

UNITED STATES AIR FORCE  
SUMMER RESEARCH PROGRAM -- 1997  
SUMMER FACULTY RESEARCH PROGRAM FINAL REPORTS

VOLUME 5B  
WRIGHT LABORATORY

RESEARCH & DEVELOPMENT LABORATORIES

5800 Uplander Way  
Culver City, CA 90230-6608

Program Director, RDL  
Gary Moore

Program Manager, AFOSR  
Major Linda Steel-Goodwin

Program Manager, RDL  
Scott Licoscas

Program Administrator, RDL  
Johnetta Thompson

Program Administrator, RDL  
Rebecca Kelly

Submitted to:

AIR FORCE OFFICE OF SCIENTIFIC RESEARCH

Bolling Air Force Base

Washington, D.C.

December 1997

20010319 054

AQM01-06-1188

# REPORT DOCUMENTATION PAGE

8

Public reporting burden for this collection of information is estimated to average 1 hour per response, including the time for reviewing the collection of information. Send comments regarding this burden estimate or any other aspect of this collection of information, Operations and Reports, 1215 Jefferson Davis Highway, Suite 1204, Arlington, VA 22202-4302, and to the Office of Management & Budget, Paperwork Project, Washington, DC 20503.

AFRL-SR-BL-TR-00-

completing and reviewing  
Directorate for Information

0958

1. AGENCY USE ONLY (Leave blank)		2. REPORT DATE December, 1997	
4. TITLE AND SUBTITLE 1997 Summer Research Program (SRP), Summer Faculty Research Program (SFRP), Final Reports, Volume 5B, Wright Laboratory			5. FUNDING NUMBERS F49620-93-C-0063
6. AUTHOR(S) Gary Moore			
7. PERFORMING ORGANIZATION NAME(S) AND ADDRESS(ES) Research & Development Laboratories (RDL) 5800 Uplander Way Culver City, CA 90230-6608			8. PERFORMING ORGANIZATION REPORT NUMBER
9. SPONSORING/MONITORING AGENCY NAME(S) AND ADDRESS(ES) Air Force Office of Scientific Research (AFOSR) 801 N. Randolph St. Arlington, VA 22203-1977			10. SPONSORING/MONITORING AGENCY REPORT NUMBER
11. SUPPLEMENTARY NOTES			
12a. DISTRIBUTION AVAILABILITY STATEMENT Approved for Public Release			12b. DISTRIBUTION CODE
13. ABSTRACT (Maximum 200 words) The United States Air Force Summer Research Program (USAF-SRP) is designed to introduce university, college, and technical institute faculty members, graduate students, and high school students to Air Force research. This is accomplished by the faculty members (Summer Faculty Research Program, (SFRP)), graduate students (Graduate Student Research Program (GSRP)), and high school students (High School Apprenticeship Program (HSAP)) being selected on a nationally advertised competitive basis during the summer intersession period to perform research at Air Force Research Laboratory (AFRL) Technical Directorates, Air Force Air Logistics Centers (ALC), and other AF Laboratories. This volume consists of a program overview, program management statistics, and the final technical reports from the SFRP participants at the Wright Laboratory.			
14. SUBJECT TERMS Air Force Research, Air Force, Engineering, Laboratories, Reports, Summer, Universities, Faculty, Graduate Student, High School Student			15. NUMBER OF PAGES
			16. PRICE CODE
17. SECURITY CLASSIFICATION OF REPORT Unclassified	18. SECURITY CLASSIFICATION OF THIS PAGE Unclassified	19. SECURITY CLASSIFICATION OF ABSTRACT Unclassified	20. LIMITATION OF ABSTRACT UL



## GENERAL INSTRUCTIONS FOR COMPLETING SF 298

The Report Documentation Page (RDP) is used in announcing and cataloging reports. It is important that this information be consistent with the rest of the report, particularly the cover and title page. Instructions for filling in each block of the form follow. It is important to *stay within the lines* to meet *optical scanning requirements*.

**Block 1. Agency Use Only** (*Leave blank*).

**Block 2. Report Date.** Full publication date including day, month, and year, if available (e.g. 1 Jan 88). Must cite at least the year.

**Block 3. Type of Report and Dates Covered.** State whether report is interim, final, etc. If applicable, enter inclusive report dates (e.g. 10 Jun 87 - 30 Jun 88).

**Block 4. Title and Subtitle.** A title is taken from the part of the report that provides the most meaningful and complete information. When a report is prepared in more than one volume, repeat the primary title, add volume number, and include subtitle for the specific volume. On classified documents enter the title classification in parentheses.

**Block 5. Funding Numbers.** To include contract and grant numbers; may include program element number(s), project number(s), task number(s), and work unit number(s). Use the following labels:

<b>C</b> - Contract	<b>PR</b> - Project
<b>G</b> - Grant	<b>TA</b> - Task
<b>PE</b> - Program Element	<b>WU</b> - Work Unit Accession No.

**Block 6. Author(s).** Name(s) of person(s) responsible for writing the report, performing the research, or credited with the content of the report. If editor or compiler, this should follow the name(s).

**Block 7. Performing Organization Name(s) and Address(es).** Self-explanatory.

**Block 8. Performing Organization Report Number.** Enter the unique alphanumeric report number(s) assigned by the organization performing the report.

**Block 9. Sponsoring/Monitoring Agency Name(s) and Address(es).** Self-explanatory.

**Block 10. Sponsoring/Monitoring Agency Report Number.** (*If known*)

**Block 11. Supplementary Notes.** Enter information not included elsewhere such as: Prepared in cooperation with....; Trans. of....; To be published in.... When a report is revised, include a statement whether the new report supersedes or supplements the older report.

**Block 12a. Distribution/Availability Statement.** Denotes public availability or limitations. Cite any availability to the public. Enter additional limitations or special markings in all capitals (e.g. NOFORN, REL, ITAR).

<b>DOD</b>	- See DoDD 5230.24, "Distribution Statements on Technical Documents."
<b>DOE</b>	- See authorities.
<b>NASA</b>	- See Handbook NHB 2200.2.
<b>NTIS</b>	- Leave blank.

**Block 12b. Distribution Code.**

<b>DOD</b>	- Leave blank.
<b>DOE</b>	- Enter DOE distribution categories from the Standard Distribution for Unclassified Scientific and Technical Reports. Leave blank.
<b>NASA</b>	- Leave blank.
<b>NTIS</b>	-

**Block 13. Abstract.** Include a brief (*Maximum 200 words*) factual summary of the most significant information contained in the report.

**Block 14. Subject Terms.** Keywords or phrases identifying major subjects in the report.

**Block 15. Number of Pages.** Enter the total number of pages.

**Block 16. Price Code.** Enter appropriate price code (*NTIS only*).

**Blocks 17. - 19. Security Classifications.** Self-explanatory. Enter U.S. Security Classification in accordance with U.S. Security Regulations (i.e., UNCLASSIFIED). If form contains classified information, stamp classification on the top and bottom of the page.

**Block 20. Limitation of Abstract.** This block must be completed to assign a limitation to the abstract. Enter either UL (unlimited) or SAR (same as report). An entry in this block is necessary if the abstract is to be limited. If blank, the abstract is assumed to be unlimited.

## **SFRP FINAL REPORT TABLE OF CONTENTS**

**i-xviii**

<b>1. INTRODUCTION</b>	<b>1</b>
<b>2. PARTICIPATION IN THE SUMMER RESEARCH PROGRAM</b>	<b>2</b>
<b>3. RECRUITING AND SELECTION</b>	<b>3</b>
<b>4. SITE VISITS</b>	<b>4</b>
<b>5. HBCU/MI PARTICIPATION</b>	<b>4</b>
<b>6. SRP FUNDING SOURCES</b>	<b>5</b>
<b>7. COMPENSATION FOR PARTICIPATIONS</b>	<b>5</b>
<b>8. CONTENTS OF THE 1996 REPORT</b>	<b>6</b>

### **APPENDICIES:**

<b>A. PROGRAM STATISTICAL SUMMARY</b>	<b>A-1</b>
<b>B. SRP EVALUATION RESPONSES</b>	<b>B-1</b>

### **SFRP FINAL REPORTS**

## PREFACE

Reports in this volume are numbered consecutively beginning with number 1. Each report is paginated with the report number followed by consecutive page numbers, e.g., 1-1, 1-2, 1-3; 2-1, 2-2, 2-3.

Due to its length, Volume 5 is bound in three parts, 5A, 5B and 5C. Volume 5A contains #1-24. Volume 5B contains reports #25-48 and 5C contains #49-70. The Table of Contents for Volume 5 is included in all parts.

This document is one of a set of 16 volumes describing the 1997 AFOSR Summer Research Program. The following volumes comprise the set:

<u>VOLUME</u>	<u>TITLE</u>
1	Program Management Report
	<i>Summer Faculty Research Program (SFRP) Reports</i>
2A & 2B	Armstrong Laboratory
3A & 3B	Phillips Laboratory
4A & 4B	Rome Laboratory
5A , 5B & 5C	Wright Laboratory
6	Arnold Engineering Development Center, United States Air Force Academy and Air Logistics Centers
	<i>Graduate Student Research Program (GSRP) Reports</i>
7A & 7B	Armstrong Laboratory
8	Phillips Laboratory
9	Rome Laboratory
10A & 10B	Wright Laboratory
11	Arnold Engineering Development Center, Wilford Hall Medical Center and Air Logistics Centers
	<i>High School Apprenticeship Program (HSAP) Reports</i>
12A & 12B	Armstrong Laboratory
13	Phillips Laboratory
14	Rome Laboratory
15B&15B	Wright Laboratory
16	Arnold Engineering Development Center

# SRP Final Report Table of Contents

Author	University/Institution Report Title	Armstrong Laboratory Directorate	Vol-Page
DR Jean M Andino	University of Florida , Gainesville , FL Atmospheric Reactions of Volatile Paint Components a Modeling Approach	AL/EQL	2- 1
DR Anthony R Andrews	Ohio University , Athens , OH Novel Electrochemiluminescence Reactions and Instrumentation	AL/EQL	2- 2
DR Stephan B Bach	Univ of Texas at San Antonio , San Antonio , TX Investigation of Sampling Interfaces for Portable Mass Spectrometry and a survey of field Portable	AL/OEA	2- 3
DR Marilyn Barger	Florida A&M-FSU College of Engineering , Tallahassee , FL Analysis for The Anaerobic Metabolites of Toulene at Fire Training Area 23 Tyndall AFB, Florida	AL/EQL	2- 4
DR Dulal K Bhaumik	University of South Alabama . Mobile , AL The Net Effect of a Covariate in Analysis of Covariance	AL/AOEP	2- 5
DR Marc L Carter, PhD, PA	Hofstra University ; Hempstead , NY Assessment of the Reliability of Ground Based Observeres for the Detecton of Aircraft	AL/OEO	2- 6
DR Huseyin M Cekirge	Florida State University , Tallahassee , FL Developing a Relational Database for Natural Attenuation Field Data	AL/EQL	2- 7
DR Cheng Cheng	Johns Hopkins University , Baltimore , MD Investigation of Two Statistical Issues in Building a Classification System	AL/HRM	2- 8
DR Gerald P Chubb	Ohio State University , Columbus , OH Use of Air Synthetic Forces For GCI Training Exercises	AL/HR1	2- 9
DR Sneed B Collard, Jr.	University of West Florida , Pensacola , FL Suitability of Ascidians as Trace Metal Biosenosrs-Biomonitors In Marine Environments An Assessment	AL/EQL	2- 10
DR Catherine A Cornwell	Syracuse University , Syracuse , NY Rat Ultrasound Vocalization Development and Neurochemistry in Stress-Sensitive Brain Regions	AL/OER	2- 11

# SRP Final Report Table of Contents

Author	University/Institution Report Title	Armstrong Laboratory Directorate	Vol-Pag
DR Baolin Deng	New Mexico Tech , Socorro , NM Effect of Iron Corrosion Inhibitors on Reductive Degradation of Chlorinated Solvents	AL/EQL	2- 11
DR Micheal P Dooley	Iowa State University , Ames , IA Copulatory Response Fertilizing Potential and Sex Ratio of Offsprings Sired by male rats Ecposed in	AL/OER	2- 13
DR Itiel E Dror	Miami University , Oxford , OH The Effect of Visual Similarity and Reference Frame Alignment on the Recognition of Military Aircraft	AL/HRT	2- 14
DR Brent D Foy	Wright State University , Dayton , OH Advances in Biologivcally-Based Kinetic Modeling for Toxicological Applications	AFRL/HES	2- 15
DR Irwin S Goldberg	St. Mary's Univ , San Antonio , TX Mixing and Streaming of a Fluid Near the Entrance of a Tube During Oscillatory Flow	AL/OES	2- 16
DR Ramesh C Gupta	University of Maine at Orono , Orono , ME A Dynamical system approach in Biomedical Research	ALOES	2- 17
DR John R Herbold	Univ of Texas at San Antonio , San Antonio , TX A Protocol for Development of Amplicons for a Rapid and Efficient Methoiid of Genotyping Hepatitis C	AL/AOEL	2- 18
DR Andrew E Jackson	Arizona State University , Mesa , AZ Development fo a Conceptual Design for an Information Systems Infrastructure To Support the Squadron	AL/HRA	2- 19
DR Charles E Lance	Univ of Georgia Res Foundation , Athens , GA Replication and Extension of the Schmidt, Hunter, and Outerbridge (1986) Model of Job Performance R	AL/HRT	2- 20
DR David A Ludwig	Univ of N.C. at Greensboro , Greensboro , NC Mediating effect of onset rate on the relationship between+ Gz and LBNP Tolerance	AL/AOCY	2- 21
DR Robert P Mahan	University of Georgia , Athens , GA The Effects of Task Structure on Cognitive Organizing Principles Implaicatins for Complex Display	AL/CFTO	2- 22

Author	University/Institution Report Title	Armstrong Laboratory Directorate	Vol-Page
DR Phillip H Marshall	Texas Tech University , Lubbock , TX Preliminary report on the effects of varieties of feedback training on single target time-to-contac	AL/HRM	2- 23
DR Bruce V Mutter	Bluefield State College , Bluefield , WV	AL/EQP	2- 24
DR Allen L Nagy	Wright State University , Dayton , OH The Detection of Color Breakup In Field Sequential Color Displays	AL/CFHV	2- 25
DR Brent L Nielsen	Auburn University , Auburn , AL Rapid PCR Detection of Vancomycin Resistance of Enteroccus Species in infected Urine and Blood	AL/AOEL	2- 26
DR Thomas E Nygren	Ohio State University , Columbus , OH Group Differences in perceived importance of swat workload dimensions: Effects on judgment and perf	AL/CFHP	2- 27
DR Edward H Piepmeier	Oregon State University , Corvallis , OR	AL/AOHR	2- 28
DR Judy L Ratliff	Murray State Univ , Murray , KY Accumulation of Storntium and Calcium by Didemnum Conchyliatum	AL/EQL	2- 29
DR Joan R Rentsch	Wright State University , Dayton , OH the Effects of Individual Differences and Team Processed on Team Member Schema Similarity and task P	AL/CFHI	2- 30
DR Paul D Retzlaff	Univ of Northern Colorado , Greeley , CO The Armstrong Laboratory Aviation Personality Survey (ALAPS) Norming and Cross - Validation	AL/AOCN	2- 31
DR David B Reynolds	Wright State University , Dayton , OH Modeling Heat Flux Through Fabrics Exposed to a Radiant Source and Analysis of Hot Air Burns	AL/CFBE	2- 32
DR Barth F Smets	University of Connecticut , Storrs , CT Desorption and Biodegradation of Dinitrotoluenes in aged soils	AL/EQL	2- 33

# SRP Final Report Table of Contents

Author	University/Institution Report Title	Phillips Laboratory Directorate	Vol-Pag
DR Graham R Allan	National Avenue , Las Vegas , NM Temporal and Spatial Characterisation of a Synchronously-Pumped Periodically-Poled Lithium Niobate O	PL/LIDD _____	3-
DR Mark J Balas	Univ of Colorado at Boulder , Boulder , CO Nonlinear Tracking Control for a Precision Deployable Structure Using a Partitioned Filter Approach	PL/SX _____	3-
DR Mikhail S Belen'kii	Georgia Inst of Technology , Atlanta , GA Multiple Aperture Averaging Technique for Measurement Full Aperture Tilt with a Laser Guide Star and	PL/LIG _____	3-
DR Gajanan S Bhat	Univ of Tennessee , Knoxville , TN Spinning Hollow Fibers From High Performance Polymers	PL/RK _____	3-
DR David B Choate	Transylvania Univ , Lexington , KY Blackhole Analysis	PL/VTMR _____	3-
DR Neb Duric	University of New Mexico , Albuquerque , NM Image Recovery Using Phase Diversity	AFRL/DEB _____	3-
DR Arthur B Edwards	9201 University City Blvd. , Charlotte , NC Theory of Protons in Buried Oxides	PL/VTMR _____	3-
DR Gary M Erickson	Boston University , Boston , MA Modeling The Magnetospheric Magnetic Field	PL/GPSG _____	3-
DR Hany A Ghoneim	Rochester Inst of Technol , Rochester , NY Focal Point Accuracy Assessment of an Off-Axis Solar Concentrator	PL/RKES _____	3-
DR Subir Ghosh	Univ of Calif, Riverside , Riverside , CA Designing Propulsion Reliability of Space Launch Vehicles	PL/RKBA _____	3- 10
DR George W Hanson	Univ of Wisconsin - Milwaukee , Milwaukee , WI Asymptotic analysis of the Natural system modes of coupled bodies in the large separation, Low-Frequency	AFRL/DEH _____	3- 11

# SRP Final Report Table of Contents

Author	University/Institution Report Title	Phillips Laboratory Directorate	Vol-Page
DR Brian D Jeffs	Brigham Young University , Provo , UT Blind Bayesian Restoration of Adaptive Optics Images Using Generalized Gaussian Markov Random Field	AFRL/DES _____	3- 12
DR Christopher H Jenkins	S Dakota School of Mines/Tech , Rapid City , SD Mechnics of Surface Precosion for Membrane Reflectors	PL/VTVS _____	3- 13
DR Dikshitulu K Kalluri	University of Lowell , Lowell , MA Mode Conversion in a Time-Varying Magnetoplasma Medium	PL/GPID _____	3- 14
DR Aravinda Kar	University of Central Florida , Orlando , FL Measurement of the Cutting Performance of a High Beam Quality Chemical Oxygen-Iodine Laser on Aerosp	AFRL/DEO _____	3- 15
DR Bernard Kirtman	Univ of Calif, Santa Barbara , Santa Barbara , CA Quantum Chemical Characterization of the elctronic Structure and Reactions of Silicon Dangling Bon	PL/VTMR _____	3- 16
DR Spencer P Kuo	Polytechnic University , Farmingdale , NY Excitation of Oscillating Two Stream Instability by Upper Hybrid Pump Waves in Ionospheric Heating	PL.GPI _____	3- 17
DR Henry A Kurtz	Memphis State University , Memphis , TN H2 Reactions at Dangling Bonds in SIO2	PL/VTMR _____	3- 18
DR Min-Chang Lee	Massachusetts Inst of Technology , Cambridge , MA Laboratory Studies of Ionospheric Plasma Effects Produced by Lightning-induced Whistler Waves	PL/GPSG _____	3- 19
DR Donald J Leo	University of Toledo , Toledo , OH Microcontroller-Based Implementation of Adaptive Structural Control	AFRL/VSD _____	3- 20
DR Hua Li	University of New Mexico , Albuquerque , NM	PL/LIDD _____	3- 21
DR Hanli Liu	Univ of Texas at Arlington , Arlington , TX Experimental Validation of Three-Dimensional Reconstruction of Inhomogenety Images in Turbid Media	AFRL/DEB _____	3- 22



# SRP Final Report Table of Contents

Author	University/Institution Report Title	Phillips Laboratory Directorate	Vol-Pag
DR M. Arfin K Lodhi	Texas Tech University , Lubbock , TX Thermoelectric Energy Conversion with solid Electrolytes	PL/VTRP	3- 23
DR Tim C Newell	University of New Mexico , Albuquerque , NM Study of Nonlinear Dynamics in a Diode Pumped Nd:YAG laser	PL/LIGR	3- 24
DR Michael J Pangia	Georgia College & State University , Milledgeville , GA Preparatory Work Towards a Computer Simulation of Electron beam Operations on TSS 1	PL/GPSG	3- 25
DR Vladimir O Papitashvili	Univ of Michigan , Ann Arbor , MI Modeling of Ionospheric Convection from the IMF and Solar Wind Data	PL/GPSG	3- 26
DR Jaime Ramirez-Angulo	New Mexico State University , Las Cruces , NM	PL/VTMR	3- 27
DR Louis F Rossi	University of Lowell , Lowell , MA Analysis of Turbulent Mixing in the Stratosphere & Troposphere	PL/GPOL	3- 28
DR David P Stapleton	University of Central Oklahoma , Edmond , OK Atmospheric Effects Upon Sub-Orbital Boost glide Spaceplane Trajectories	PL/RKBA	3- 29
DR Jenn-Ming Yang	Univ of Calif, Los Angeles , Los Angeles , CA Thermodynamic Stability and Oxidation Behavior of Refractory (Hf, Ta, Zr) Carbide/boride Composites	PL/RKS	3- 30

# SRP Final Report Table of Contents

Author	University/Institution Report Title	Rome Laboratory Directorate	Vol-Page
DR A. F Anwar	University of Connecticut , Storrs , CT Properties of Quantum Wells Formed In AlGaIn/GaN Heterostructures	RL/ERAC	4- 1
DR Milica Barjaktarovic	Wilkes University , Wilkes Barre , PA Assured Software Design: Privacy Enhanced Mail (PEM) and X.509 Certificate Specification	AFRL/IFG	4- 2
DR Stella N Batalama	SUNY Buffalo , Buffalo , NY Adaptive Robust Spread-Spectrum Receivers	AFRL/IFG	4- 3
DR Adam W Bojanczyk	Cornell Univesity , Ithaca , NY Lowering the Computational Complexity of Stap Radar Systems	RL/OCSS	4- 4
DR Nazeih M Botros	So. Illinois Univ-Carbondale , Carbondale , IL A PC-Based Speech Synthesizing Using Sinusoidal Transform Coding (STC)	RL/ERC-1	4- 5
DR Nikolaos G Bourbakis	SUNY Binghamton , Binghamton , NY Eikones-An Object-Oriented Language Forimage Analysis & Process	AFRL/IF	4- 6
DR Peter P Chen	Louisiana State University , Baton Rouge , LA Reconstructing the information Warfare Attack Scenario Guessing what Actually Had Happened Based on	RL/CA-II	4- 7
DR Everett E Crisman	Brown University , Providence , RI A Three-Dimensional, Dielectric Antenna Array Re-Configurable By Optical Wavelength Multiplexing	RL/ERAC	4- 8
DR Digendra K Das	SUNYIT , Utica , NY A Study of the Emerging Dianostic Techniques in Avionics	RL/ERSR	4- 9
DR Venugopala R Dasigi	Southern Polytechnic State Univ , Marietta , GA Information Fusion for text Classification-an Expjerimental Comparison	AFRL/IFT	4- 10
DR Richard R Eckert	SUNY Binghamton , Binghamton , NY Enhancing the rome Lab ADII virtual environment system	AFRL/IFSA	4- 11

# SRP Final Report Table of Contents

Author	University/Institution Report Title	Rome Laboratory Directorate	Vol-Page
DR Micheal A Fiddy	University of Lowell , Lowell , MA Target Identification from Limited Backscattered Field Data	RL/ERCS	4- 12
DR Lili He	Nothern Illinois University , Dekalb , IL the Study of Caaractreistics of CdS Passivation on InP	RL/EROCC	4- 13
DR Edem Ibragimov	Michigan Tech University , Houghton , MI Effects of Surface Scattering in 3-D Optical Mass Storage	RL/TRAP	4- 14
DR Phillip G Kornreich	Syracuse University , Syracuse , NY Analysis of Optically Active Material Layer Fibers	RL/OCPA	4- 15
DR Kuo-Chi Lin	University of Central Florida , Orlando , FL A Study on The Crowded Airspace Self Organized Criticality	AFRL/IFSB	4- 16
Dr. Beth L Losiewicz	Colorado College , Colorado Spring , CO The Miami Corpus Latin American Dialect Database continued Research and Documentation	RL/IRAA	4- 17
DR John D Norgard	Univ of Colorado at Colorado Springs , Colorado Spring , CO Microwave Holography using Infrared Thermograms of Electromagnetic Fields	RL/ERST	4- 18
DR Jeffrey B Norman	Vassar College , Poughkeepsie , NY Gain Spectra of Beam-Coupling In Photorefractive Semiconductors	RL/OCPA	4- 19
DR Dimitrios N Pados	State Univ. of New York Buffalo , Buffalo , NY Joint Domain Space-Time Adaptive Processing w/Small Training Data Sets	AFRL/SNR	4- 21
DR Brajendra N Panda	University of North Dakota , Grand Forks , ND A Model to Attain Data Integrity After System Invasion	AFRL/IFG	4- 22
DR Michael A Pittarelli	SUNY OF Tech Utica , Utica , NY Phase Transitions in probability Estimation and Constraint Satisfaction Problems	AFRL/IFT	4- 23

# SRP Final Report Table of Contents

Author	University/Institution Report Title	Rome Laboratory Directorate	Vol-Page
DR Salahuddin Qazi	SUNY OF Tech Utica , Utica , NY Low Data rate Multimedia Communication Using Wireless Links	RL/IWT	4- 24
DR Arindam Saha	Mississippi State University , Mississippi State , MS An Implementationa of the message passing Interface on Rtems	RL/OCSS	4- 25
DR Ravi Sankar	University of South Florida , Tampa , FL A Study ofIntegrated and Intelligent Network Management	RL/C3BC	4- 26
DR Mark S Schmalz	University of Florida , Gainesville , FL Errors inherent in Reconstruction of Targets From multi-Look Imagery	AFRL/IF	4- 27
DR John L Stensby	Univ of Alabama at Huntsville , Huntsville , AL Simple Real-time Tracking Indicator for a Freqruncy Feedback Demodulator	RL/IRAP	4- 28
DR Micheal C Stinson	Central Michigan University , Mt. Pleasant , MI Destructive Objects	RL/CAH	4- 29
DR Donald R Ucci	Illinois Inst of Technology , Chicago , IL Simulation of a Robust Locally Optimum Receiver in correlated Noise Using Autoregressive Modeling	RL/C3BB	4- 30
DR Nong Ye	Arizona State University , Tempe , AZ A Process Engineering Approach to Continuous Command and Control on Security-Aware Computer Networks	AFRL/IFSA	4- 31

# SRP Final Report Table of Contents

Author	University/Institution Report Title	Wright Laboratory Directorate	Vol-Page
DR William A Baeslack	Ohio State University , Columbus , OH	WL/MLLM	5- 1
DR Bhavik R Bakshi	Ohio State University , Columbus , OH Modeling of Materials Manufacturing Processes by NonlinearContimuum Regression	WL/MLIM	5- 2
DR Brian P Beecken	Bethel College , St. Paul , MN Contribution of a Scene Projector's Non-Uniformity to a Test Article's Output Image Non-Uniformity	AFRL/MN	5- 3
DR John H Beggs	Mississippi State University , Mississippi State , MS The Finite Element Method in Electromagnetics For Multidisciplinary Design	AFRL/VA	5- 4
DR Kevin D Belfield	University of Detroit Mercy , Detroit , MI Synthesis of Novel Organic Compounds and Polymers for two Photon Asorption, NLO, and Photorefractive	WL/MLBP	5- 5
DR Raj K Bhatnagar	University of Cincinnati , Cincinnati , OH A Study of Intra-Class Variability in ATR Systems	AFRL/SN	5- 6
DR Victor M Birman	Univ of Missouri - St. Louis , St Louis , MO Theoretical Foundations for Detection of Post-Processing Cracks in Ceramic Matrix Composites Based o	WL/FIBT	5- 7
DR Gregory A Blaisdell	Purdue University , West Lafayette , IN A Review of Benchmark Flows for Large EddySimulation	AFRL/VA	5- 8
DR Octavia I Camps	Pennsylvania State University , University Park , PA MDL Texture Segmentation Compressed Images	WL/MNGA	5- 9
DR Yiding Cao	Florida International Univ , Miami , FL A Feasibility Study of Turbine Disk Cooling by Employing Radially Rotating Heat Pipes	WL/POTT	5- 10
DR Reaz A Chaudhuri	University of Utah , Salt Lake City , UT A Novel Compatibility/Equilibrium Based Iterative Post-Processing Approach For Axisymmetric brittle	WL/MLBM	5- 11

# SRP Final Report Table of Contents

Author	University/Institution Report Title	Wright Laboratory Directorate	Vol-Page
DR Mohamed F Chouikha	Howard University , Washington , DC Detection Techniques Use in Forward-Looking Radar Signal Procesing a Literature Review	WL/AAMR _____	5- 12
DR Milton L Cone	Embry-Riddle Aeronautical University , Prescott , AZ Scheduling in the Dynamic System Simulation Testbed	WL/AACF _____	5- 13
DR Robert C Creese	West Virginia University , Morgantown , WV Feature Based Cost Modeling	WL/MTI _____	5- 14
DR William Crossley	Purdue University , West Lafayette , IN Objects and Methods for Aircraft Conceptual Design and Optimization in a Knowledge-Based Environment	WL/FIBD _____	5- 15
DR Gene A Crowder	Tulane University , New Orleans , LA Vibrational Analysis of some High-Energy Compounds	WL/MNM _____	5- 16
DR Richard W Darling	University of South Florida , Tampa , FL Geometrically Invariant NonLinear recursive Filters, with Applicaation to Target Tracking	WL/MNAG _____	5- 17
DR Robert J DeAngelis	Univ of Nebraska - Lincoln , Lincoln , NE Quantitative Description of Wire Tecxtures In Cubic Metals	WL/MNM _____	5- 18
DR Bill M Diong	Pan American University , Edinburg , TX Analysis and Control Design for a Novel Resonant DC-DC Converter	WL/POOC _____	5- 19
DR John K Douglass	University of Arizona , Tucson , AZ Guiding Missiles "On The Fly:" Applications of Neurobiologica Princioles to Machine Vision For Arma	AFRL/MN _____	5- 20
DR Mark E Eberhart	Colorado School of Mines , Golden , CO Modeling The Charge Redistribution Associated with Deformation and Fracture	WL/MLLM _____	5- 21
DR Gregory S Elliott	Rutgers:State Univ of New Jersey , Piscataway , NJ On the Development of Planar Doppler Velocimetry	WL/POPT _____	5- 22

# SRP Final Report Table of Contents

Author	University/Institution Report Title	Wright Laboratory Directorate	Vol-Page
DR Elizabeth A Ervin	University of Dayton , Dayton , OH Eval of the Pointwise K-2 Turbulence Model to Predict Transition & Separation in a Low Pressure	WL/POTT	5- 23
DR Altan M Ferendeci	University of Cincinnati , Cincinnati , OH Vertically Interconnected 3D MMICs with Active Interlayer Elements	WL/AADI	5- 24
DR Dennis R Flentge	Cedarville College , Cedarville , OH Kinetic Study of the Thermal Decomposition of t-Butylphenyl Phosphate Using the System for Thermal D	WL/POSL	5- 25
DR George N Frantziskonis	University of Arizona , Tucson , AZ Multiscale Material Characterization and Applications	WL/MLLP	5- 26
DR Zewdu Gebeyehu	Tuskegee University , Tuskegee , AL Synthesis and Characterization of Metal-Xanthic Acid and -Amino Acid Complexes Useful Ad Nonlinear	WL/MLPO	5- 27
DR Richard D Gould	North Carolina State U-Raleigh , Raleigh , NC Reduction and Analysis of LDV and Analog Raw Data	WL/POPT	5- 28
DR Michael S Grace	University of Virginia , Charlottesville , VA Structure and Function of an Extremely Sensitive Biological Infrared Detector	WL/MLPJ	5- 29
DR Gary M Graham	Ohio University , Athens , OH Indicial Response Model for Roll Rate Effects on A 65-Degree Delta wing	WL/FIGC	5- 30
DR Allen G Greenwood	Mississippi State University , Mississippi Sta , MS An Object-Based approach for Integrating Cost Assessment into Product/Process Design	WL/MTI	5- 31
DR Rita A Gregory	Georgia Inst of Technology , Atlanta , GA Range Estimating for Research and Development Alternatives	WL/FIVC	5- 32
DR Mark T Hanson	University of Kentucky , Lexington , KY Anisotropy in Epic 96&97: Implementation and Effects	WL/MNM	5- 33

# SRP Final Report Table of Contents

Author	University/Institution Report Title	Wright Laboratory Directorate	Vol-Page
DR Majeed M Hayat	University of Dayton , Dayton , OH A Model for Turbulence and Photodetection Noise in Imaging	WL/AAJT	5- 34
DR Larry S Helmick	Cedarville College , Cedarville , OH NMA Study of the Decomposition Reaction Path of Demnum fluid under Tribological Conditions	WL/MLBT	5- 35
DR William F Hosford	Univ of Michigan , Ann Arbor , MI INTENSITY OF [111]AND [100] TEXTURAL COMPONENTS IN COMPRESSION-FORGED TANTALUM	AFRL/MN	5- 36
DR David E Hudak	Ohio Northern University , Ada , OH A Study fo a Data-Parallel Imlementation of An Implicit Solution fo the 3D Navier-Stokes Equations	WL/FIMC	5- 37
DR David P Johnson	Mississippi State University , Mississippi , MS An Innovative Segmented Tugsten Penetrating Munition	WL/MNAZ	5- 38
DR Ismail I Jouny	Lafayette College , Easton , PA	WL/AACT	5- 39
DR Edward T Knobbe	Oklahoma State University , Stillwater , OK Organically Modified silicate Films as Corrosion Resistant Treatments for 2024-T3 Alumium Alloy	WL/MLBT	5- 40
DR Seungug Koh	University of Dayton , Dayton , OH Numerically Efficinet Direct Ray Tracing Algorithms for Automatic Target Recognition using FPGAs	WL/AAST	5- 41
DR Ravi Kothari	University of Cincinnati , Cincinnati , OH A Function Approximation Approach for Region of Interest Selection in synthetic Aperture Radar Image	WL/AACA	5- 42
DR Douglas A Lawrence	Ohio University , Athens , OH On the Analysis and Design of Gain scheduled missile Autopilots	WL/MNAG	5- 43
DR Robert Lee	Ohio State University , Columbus , OH Boundary Conditions applied to the Finite Vlume Time Domain Method for the Solution of Maxwell's Equ	WL/FIM	5- 44



# SRP Final Report Table of Contents

Author	University/Institution Report Title	Wright Laboratory Directorate	Vol - Page
DR Junghsen Lieh	Wright State University , Dayton , OH Develop an Explosive Simulated Testing Apparatus for Impact Physics Research at Wright Laboratory	WL/FIV _____	5- 43
DR James S Marsh	University of West Florida , Pensacola , FL Distortion Compensation and Elimination in Holographic Reocnstruction	WL/MNSI _____	5- 44
DR Mark D McClain	Cedarville College , Cedarville , OH A Molecular Orbital Theory Analysis of Oligomers of 2,2'-Bithiazole and Partially Reduced 3,3'-Dimet	WL/MLBP _____	5- 47
DR William S McCormick	Wright State University , Dayton , OH Some Observations of Target Recognition Using High Range Resolution Radar	WL/AACR _____	5- 48
DR Richard O Mines	University of South Florida , Tampa , FL Testing Protocol for the Demilitarization System at the Eglin AFB Herd Facility	WLMN/M _____	5- 49
DR Dakshina V Murty	University of Portland , Portland , OR A Useful Benchmarking Method in Computational Mechanics, CFD, adn Heat Tansfer	WL/FIBT _____	5- 50
DR Krishna Naishadham	Wright State University , Dayton , OH	WL/MLPO _____	5- 51
DR Serguei Ostapenko	University of South Florida , Tampa , FL	WL/MLPO _____	5- 52
DR Yi Pan	University of Dayton , Dayton , OH Improvement of Cache Utilization and Parallel Efficiency of a Time-Dependnet Maxwell Equation Solver	AFRL/VA _____	5- 53
DR Rolfe G Petschek	Case Western Reserve Univ , Cleveland , OH AB INITIO AUANTUM CHEMICAL STUDIES OF NICKEL DITHIOLENE COMPLEX	WL/MLPJ _____	5- 54
DR Kishore V Pochiraju	Stevens Inst of Technology , Hoboken , NJ Refined Reissner's Variational Solution in the Vicinity of Stress Singularities	AFRL/ML _____	5- 55

# SRP Final Report Table of Contents

Author	University/Institution Report Title	Wright Laboratory Directorate	Vol-Page
DR Muhammad M Rahman	University of South Florida , Tampa , FL Computation of Free Surface Flows with Applications in Capillary Pumped Loops, Heat Pipes, and Jet I	WL/POOB	5- 56
DR Mateen M Rizki	Wright State University , Dayton , OH Classification of High Range Resolution Radar Signatures Using Evolutionary Computation	WL/AACA	5- 57
DR Shankar M Sastry	Washington University , St Louis , MO	WL/MLLM	5- 58
DR Martin Schwartz	University of North Texas , Denton , TX Computational Studies of Hydrogen Abstraction From Haloalkanes by the Hydroxyl Radical	WL/MLBT	5- 59
DR Rathinam P Selvam	Univ of Arkansas , Fayetteville , AR Computation of Nonlneear Viscous Panel Flutter Using a Full-Implicit Aeroelastic Solver	WL/FIMC	5- 60
DR Yuri B Shtessel	Univ of Alabama at Huntsville , Huntsville , AL Smoothed Sliding Mode control Approach For Addressing Actuator Deflection and Deflection Rate Saturat	AFRL/VA	5- 61
DR Mario Sznaier	Pennsylvania State University , University Park , PA Suboptimal Control of Nonlneear Systems via Receding Horizon State Dependent Riccati Equations	WL/MNAG	5- 62
DR Barney E Taylor	Miami Univ. - Hamilton , Hamilton , OH Photoconductivity Studies of the Polymer 6FPBO	WLMLBP	5- 63
DR Joseph W Tedesco	Auburn University , Auburn , AL high Velocity Penetration of Layered Concrete Targets with Small Scale Ogive-nose Steel projectiles	WL/MNSA	5- 64
DR Krishnaprasad Thirunarayan	Wright State University , Dayton , OH A VHDL MODEL SYNTHESIS APPLET IN TCL/TK	WL/AAST	5- 65

# SRP Final Report Table of Contents

Author	University/Institution Report Title	Wright Laboratory Directorate	Vol-Pag
DR Karen A Tomko	Wright State University , Dayton , OH Grid Level Parallelization of an Implicit Solution of the 3D Navier-Stokes Equations	WL/FIMC	5- 60
DR Max B Trueblood	University of Missouri-Rolla , Rolla , MO A Study of the Particulate Emissions of a Well-Stirred Reactor	WL/POSC	5- 67
DR Chi-Tay Tsai	Florida Atlantic University , Boca Raton , FL Dislocation Dynamics in Heterojunction Bipolar Transistor Under Current Induced Thermal St	WL/AA	5- 68
DR John L Valasek	Texas A&M University , College Station , TX Two Axis Pneumatic Vortex Control at High Speed and Low Angle-of-Attack	WL/FIMT	5- 69
DR Mitch J Wolff	Wright State University , Dayton , OH An Experimental and Computational Analysis of the Unsteady Blade Row Potential Interaction in a Tr	WL/POTF	5- 70
DR Rama K Yedavalli	Ohio State University , Columbus , OH Improved Aircraft Roll Maneuver Performance Using Smart Deformable Wings	WL/FIBD	5- 71

# SRP Final Report Table of Contents

author	University/Institution Report Title	Arnold Engineering Development Center Directorate	Vol-Page
DR Csaba A Biegl	Vanderbilt University , Nashville , TN Parallel processing for Turbine Engine Modeling and Test Data validation	AEDC/SVT	6- 1
DR Frank G Collins	Tennessee Univ Space Institute , Tullahoma , TN Design of a Mass Spectrometer Sampling Probe for The AEDC Impulse Facility	AEDC	6- 2
DR Kenneth M Jones	N Carolina A&T State Univ , Greensboro , NC	AEDC/SVT	6- 3
DR Kevin M Lyons	North Carolina State U-Raleigh , Raleigh , NC Velocity Field Measurements Using Filtered-Rayleigh Scattering	AEDC/SVT	6- 4
DR Gerald J Micklow	Univ of Alabama at Tuscaloosa , Tuscaloosa , AL	AEDC/SVT	6- 5
DR Michael S Moore	Vanderbilt University , Nashville , TN Extension and Installation of the Model-Integrated Real-Time Imaging System (Mirtis)	AEDC/SVT	6- 6
DR Robert L Roach	Tennessee Univ Space Institute , Tullahoma , TN Investigation of Fluid Mechanical Phenomena Relating to Air Injection Between the Segments of an Arc	AEDC	6- 7
DR Nicholas S Winowich	University of Tennessee , Knoxville , TN	AEDC	6- 8
DR Daniel M Knauss	Colorado School of Mines , Golden , CO Synthesis of salts With Delocalized Anions For Use as Third Order Nonlinear Optical Materials	USAFA/DF	6- 9
DR Jeffrey M Bigelow	Oklahoma Christian Univ of Science & Art , Oklahoma City , OK Raster-To-Vector Conversion of Circuit Diagrams: Software Requirements	OCALC/TI	6- 10

# SRP Final Report Table of Contents

Author	University/Institution Report Title	Arnold Engineering Development Center Directorate	Vol-Page
DR Paul W Whaley	Oklahoma Christian Univ of Science & Art , Oklahoma City , OK A Probabilistic framework for the Analysis of corrosion Damage in Aging Aircraft	OCALC/L _____	6- 11
DR Bjong W Yeigh	Oklahoma State University , Stillwater , OK Logistics Asset Management : Models and Simulations	OCALC/TI _____	6- 12
DR Michael J McFarland	Utah State University , Logan , UT Delisting of Hill Air Force Base's Industrial Wastewater Treatment Plant Sludge	OC-ALC/E _____	6- 13
DR William E Sanford	Colorado State University , Fort Collins , CO Numerical Modeling of Physical Constraints on in-Situ Cosolvent Flushing as a Groundwater Remedial Op	OO-ALC/E _____	6- 14
DR Sophia Hassiotis	University of South Florida , Tampa , FL Fracture Analysis of the F-5, 15%-Spar Bolt	SAALC/TI _____	6- 15
DR Devendra Kumar	CUNY-City College , New York , NY A Simple, Multiversion Concurrency Control Protocol For Internet Databases	SAALC/LD _____	6- 16
DR Ernest L McDuffie	Florida State University , Tallahassee , FL A Proposed Expert System for ATS Capability Analysis	SAALC/TI _____	6- 17
DR Prabhaker Mateti	Wright State University , Dayton , OH How to Provide and Evaluate Computer Network Security	SMALC/TI _____	6- 18
DR Mansur Rastani	N Carolina A&T State Univ , Greensboro , NC Optimal Structural Design of Modular Composite bare base Shelters	SMALC/L _____	6- 19
DR Joe G Chow	Florida International Univ , Miami , FL Re-engineer and Re-Manufacture Aircraft Sstructural Components Using Laser Scanning	WRALC/TI _____	6- 20

## 1. INTRODUCTION

The Summer Research Program (SRP), sponsored by the Air Force Office of Scientific Research (AFOSR), offers paid opportunities for university faculty, graduate students, and high school students to conduct research in U.S. Air Force research laboratories nationwide during the summer.

Introduced by AFOSR in 1978, this innovative program is based on the concept of teaming academic researchers with Air Force scientists in the same disciplines using laboratory facilities and equipment not often available at associates' institutions.

The Summer Faculty Research Program (SFRP) is open annually to approximately 150 faculty members with at least two years of teaching and/or research experience in accredited U.S. colleges, universities, or technical institutions. SFRP associates must be either U.S. citizens or permanent residents.

The Graduate Student Research Program (GSRP) is open annually to approximately 100 graduate students holding a bachelor's or a master's degree; GSRP associates must be U.S. citizens enrolled full time at an accredited institution.

The High School Apprentice Program (HSAP) annually selects about 125 high school students located within a twenty mile commuting distance of participating Air Force laboratories.

AFOSR also offers its research associates an opportunity, under the Summer Research Extension Program (SREP), to continue their AFOSR-sponsored research at their home institutions through the award of research grants. In 1994 the maximum amount of each grant was increased from \$20,000 to \$25,000, and the number of AFOSR-sponsored grants decreased from 75 to 60. A separate annual report is compiled on the SREP.

The numbers of projected summer research participants in each of the three categories and SREP "grants" are usually increased through direct sponsorship by participating laboratories.

AFOSR's SRP has well served its objectives of building critical links between Air Force research laboratories and the academic community, opening avenues of communications and forging new research relationships between Air Force and academic technical experts in areas of national interest, and strengthening the nation's efforts to sustain careers in science and engineering. The success of the SRP can be gauged from its growth from inception (see Table 1) and from the favorable responses the 1997 participants expressed in end-of-tour SRP evaluations (Appendix B).

AFOSR contracts for administration of the SRP by civilian contractors. The contract was first awarded to Research & Development Laboratories (RDL) in September 1990. After completion of the

1990 contract, RDL (in 1993) won the recompetition for the basic year and four 1-year options.

## 2. PARTICIPATION IN THE SUMMER RESEARCH PROGRAM

The SRP began with faculty associates in 1979; graduate students were added in 1982 and high school students in 1986. The following table shows the number of associates in the program each year.

YEAR	SRP Participation, by Year			TOTAL
	SFRP	GSRP	HSAP	
1979	70			70
1980	87			87
1981	87			87
1982	91	17		108
1983	101	53		154
1984	152	84		236
1985	154	92		246
1986	158	100	42	300
1987	159	101	73	333
1988	153	107	101	361
1989	168	102	103	373
1990	165	121	132	418
1991	170	142	132	444
1992	185	121	159	464
1993	187	117	136	440
1994	192	117	133	442
1995	190	115	137	442
1996	188	109	138	435
1997	148	98	140	427

Beginning in 1993, due to budget cuts, some of the laboratories weren't able to afford to fund as many associates as in previous years. Since then, the number of funded positions has remained fairly constant at a slightly lower level.

### 3. RECRUITING AND SELECTION

The SRP is conducted on a nationally advertised and competitive-selection basis. The advertising for faculty and graduate students consisted primarily of the mailing of 8,000 52-page SRP brochures to chairpersons of departments relevant to AFOSR research and to administrators of grants in accredited universities, colleges, and technical institutions. Historically Black Colleges and Universities (HBCUs) and Minority Institutions (MIs) were included. Brochures also went to all participating USAF laboratories, the previous year's participants, and numerous individual requesters (over 1000 annually).

RDL placed advertisements in the following publications: *Black Issues in Higher Education*, *Winds of Change*, and *IEEE Spectrum*. Because no participants list either *Physics Today* or *Chemical & Engineering News* as being their source of learning about the program for the past several years, advertisements in these magazines were dropped, and the funds were used to cover increases in brochure printing costs.

High school applicants can participate only in laboratories located no more than 20 miles from their residence. Tailored brochures on the HSAP were sent to the head counselors of 180 high schools in the vicinity of participating laboratories, with instructions for publicizing the program in their schools. High school students selected to serve at Wright Laboratory's Armament Directorate (Eglin Air Force Base, Florida) serve eleven weeks as opposed to the eight weeks normally worked by high school students at all other participating laboratories.

Each SFRP or GSRP applicant is given a first, second, and third choice of laboratory. High school students who have more than one laboratory or directorate near their homes are also given first, second, and third choices.

Laboratories make their selections and prioritize their nominees. AFOSR then determines the number to be funded at each laboratory and approves laboratories' selections.

Subsequently, laboratories use their own funds to sponsor additional candidates. Some selectees do not accept the appointment, so alternate candidates are chosen. This multi-step selection procedure results in some candidates being notified of their acceptance after scheduled deadlines. The total applicants and participants for 1997 are shown in this table.



1997 Applicants and Participants			
PARTICIPANT CATEGORY	TOTAL APPLICANTS	SELECTEES	DECLINING SELECTEES
SFRP	490	188	32
(HBCU/MI)	( 0 )	( 0 )	( 0 )
GSRP	202	98	9
(HBCU/MI)	( 0 )	( 0 )	( 0 )
HSAP	433	140	14
TOTAL	1125	426	55

#### 4. SITE VISITS

During June and July of 1997, representatives of both AFOSR/NI and RDL visited each participating laboratory to provide briefings, answer questions, and resolve problems for both laboratory personnel and participants. The objective was to ensure that the SRP would be as constructive as possible for all participants. Both SRP participants and RDL representatives found these visits beneficial. At many of the laboratories, this was the only opportunity for all participants to meet at one time to share their experiences and exchange ideas.

#### 5. HISTORICALLY BLACK COLLEGES AND UNIVERSITIES AND MINORITY INSTITUTIONS (HBCU/MIs)

Before 1993, an RDL program representative visited from seven to ten different HBCU/MIs annually to promote interest in the SRP among the faculty and graduate students. These efforts were marginally effective, yielding a doubling of HBCU/MI applicants. In an effort to achieve AFOSR's goal of 10% of all applicants and selectees being HBCU/MI qualified, the RDL team decided to try other avenues of approach to increase the number of qualified applicants. Through the combined efforts of the AFOSR Program Office at Bolling AFB and RDL, two very active minority groups were found, HACU (Hispanic American Colleges and Universities) and AISES (American Indian Science and Engineering Society). RDL is in communication with representatives of each of these organizations on a monthly basis to keep up with their activities and special events. Both organizations have widely-distributed magazines/quarterlies in which RDL placed ads.

Since 1994 the number of both SFRP and GSRP HBCU/MI applicants and participants has increased ten-fold, from about two dozen SFRP applicants and a half dozen selectees to over 100 applicants and two dozen selectees, and a half-dozen GSRP applicants and two or three selectees to 18 applicants and 7 or 8 selectees. Since 1993, the SFRP had a two-fold applicant increase and a two-fold selectee increase. Since 1993, the GSRP had a three-fold applicant increase and a three to four-fold increase in selectees.

In addition to RDL's special recruiting efforts, AFOSR attempts each year to obtain additional funding or use leftover funding from cancellations the past year to fund HBCU/MI associates. This year, 5 HBCU/MI SFRPs declined after they were selected (and there was no one qualified to replace them with). The following table records HBCU/MI participation in this program.

SRP HBCU/MI Participation, By Year				
YEAR	SFRP		GSRP	
	Applicants	Participants	Applicants	Participants
1985	76	23	15	11
1986	70	18	20	10
1987	82	32	32	10
1988	53	17	23	14
1989	39	15	13	4
1990	43	14	17	3
1991	42	13	8	5
1992	70	13	9	5
1993	60	13	6	2
1994	90	16	11	6
1995	90	21	20	8
1996	119	27	18	7

## 6. SRP FUNDING SOURCES

Funding sources for the 1997 SRP were the AFOSR-provided slots for the basic contract and laboratory funds. Funding sources by category for the 1997 SRP selected participants are shown here.

1997 SRP FUNDING CATEGORY	SFRP	GSRP	HSAP
AFOSR Basic Allocation Funds	141	89	123
USAF Laboratory Funds	48	9	17
HBCU/MI By AFOSR (Using Procured Addn'l Funds)	0	0	N/A
<b>TOTAL</b>	<b>9</b>	<b>98</b>	<b>140</b>

SFRP - 188 were selected, but thirty two canceled too late to be replaced.

GSRP - 98 were selected, but nine canceled too late to be replaced.

HSAP - 140 were selected, but fourteen canceled too late to be replaced.

## 7. COMPENSATION FOR PARTICIPANTS

Compensation for SRP participants, per five-day work week, is shown in this table.

1997 SRP Associate Compensation

PARTICIPANT CATEGORY	1991	1992	1993	1994	1995	1996	1997
Faculty Members	\$690	\$718	\$740	\$740	\$740	\$770	\$770
Graduate Student (Master's Degree)	\$425	\$442	\$455	\$455	\$455	\$470	\$470
Graduate Student (Bachelor's Degree)	\$365	\$380	\$391	\$391	\$391	\$400	\$400
High School Student (First Year)	\$200	\$200	\$200	\$200	\$200	\$200	\$200
High School Student (Subsequent Years)	\$240	\$240	\$240	\$240	\$240	\$240	\$240

The program also offered associates whose homes were more than 50 miles from the laboratory an expense allowance (seven days per week) of \$50/day for faculty and \$40/day for graduate students. Transportation to the laboratory at the beginning of their tour and back to their home destinations at the end was also reimbursed for these participants. Of the combined SFRP and GSRP associates, 65 % (194 out of 286) claimed travel reimbursements at an average round-trip cost of \$776.

Faculty members were encouraged to visit their laboratories before their summer tour began. All costs of these orientation visits were reimbursed. Forty-three percent (85 out of 188) of faculty associates took orientation trips at an average cost of \$388. By contrast, in 1993, 58 % of SFRP associates took

orientation visits at an average cost of \$685; that was the highest percentage of associates opting to take an orientation trip since RDL has administered the SRP, and the highest average cost of an orientation trip. These 1993 numbers are included to show the fluctuation which can occur in these numbers for planning purposes.

Program participants submitted biweekly vouchers countersigned by their laboratory research focal point, and RDL issued paychecks so as to arrive in associates' hands two weeks later.

This is the second year of using direct deposit for the SFRP and GSRP associates. The process went much more smoothly with respect to obtaining required information from the associates, only 7% of the associates' information needed clarification in order for direct deposit to properly function as opposed to 10% from last year. The remaining associates received their stipend and expense payments via checks sent in the US mail.

HSAP program participants were considered actual RDL employees, and their respective state and federal income tax and Social Security were withheld from their paychecks. By the nature of their independent research, SFRP and GSRP program participants were considered to be consultants or independent contractors. As such, SFRP and GSRP associates were responsible for their own income taxes, Social Security, and insurance.

## **8. CONTENTS OF THE 1997 REPORT**

The complete set of reports for the 1997 SRP includes this program management report (Volume 1) augmented by fifteen volumes of final research reports by the 1997 associates, as indicated below:

**1997 SRP Final Report Volume Assignments**

<b>LABORATORY</b>	<b>SFRP</b>	<b>GSRP</b>	<b>HSAP</b>
<b>Armstrong</b>	2	7	12
<b>Phillips</b>	3	8	13
<b>Rome</b>	4	9	14
<b>Wright</b>	5A, 5B	10	15
<b>AEDC, ALCs, WHMC</b>	6	11	16

## APPENDIX A -- PROGRAM STATISTICAL SUMMARY

### A. Colleges/Universities Represented

Selected SFRP associates represented 169 different colleges, universities, and institutions, GSRP associates represented 95 different colleges, universities, and institutions.

### B. States Represented

SFRP - Applicants came from 47 states plus Washington D.C. Selectees represent 44 states.

GSRP - Applicants came from 44 states. Selectees represent 32 states.

HSAP - Applicants came from thirteen states. Selectees represent nine states.

Total Number of Participants	
SFRP	189
GSRP	97
HSAP	140
TOTAL	426

Degrees Represented			
	SFRP	GSRP	TOTAL
Doctoral	184	0	184
Master's	2	41	43
Bachelor's	0	56	56
TOTAL	186	97	298

SFRP Academic Titles	
Assistant Professor	64
Associate Professor	70
Professor	40
Instructor	0
Chairman	1
Visiting Professor	1
Visiting Assoc. Prof.	1
Research Associate	9
TOTAL	186

Source of Learning About the SRP		
Category	Applicants	Selectees
Applied/participated in prior years	28 %	34 %
Colleague familiar with SRP	19 %	16 %
Brochure mailed to institution	23 %	17 %
Contact with Air Force laboratory	17 %	23 %
<i>IEEE Spectrum</i>	2 %	1 %
<i>BIIHE</i>	1 %	1 %
Other source	10 %	8 %
TOTAL	100 %	100 %

## APPENDIX B -- SRP EVALUATION RESPONSES

### 1. OVERVIEW

Evaluations were completed and returned to RDL by four groups at the completion of the SRP. The number of respondents in each group is shown below.

Table B-1. Total SRP Evaluations Received

Evaluation Group	Responses
SFRP & GSRPs	275
HSAPs	113
USAF Laboratory Focal Points	84
USAF Laboratory HSAP Mentors	6

All groups indicate unanimous enthusiasm for the SRP experience.

The summarized recommendations for program improvement from both associates and laboratory personnel are listed below:

- A. Better preparation on the labs' part prior to associates' arrival (i.e., office space, computer assets, clearly defined scope of work).
- B. Faculty Associates suggest higher stipends for SFRP associates.
- C. Both HSAP Air Force laboratory mentors and associates would like the summer tour extended from the current 8 weeks to either 10 or 11 weeks; the groups state it takes 4-6 weeks just to get high school students up-to-speed on what's going on at laboratory. (Note: this same argument was used to raise the faculty and graduate student participation time a few years ago.)

## 2. 1997 USAF LABORATORY FOCAL POINT (LFP) EVALUATION RESPONSES

The summarized results listed below are from the 84 LFP evaluations received.

### 1. LFP evaluations received and associate preferences:

Table B-2. Air Force LFP Evaluation Responses (By Type)

Lab	Evals Recv'd	How Many Associates Would You Prefer To Get ?								(% Response)			
		SFRP				GSRP (w/Univ Professor)				GSRP (w/o Univ Professor)			
		0	1	2	3+	0	1	2	3+	0	1	2	3+
AEDC	0	-	-	-	-	-	-	-	-	-	-	-	-
WHMC	0	-	-	-	-	-	-	-	-	-	-	-	-
AL	7	28	28	28	14	54	14	28	0	86	0	14	0
USAF A	1	0	100	0	0	100	0	0	0	0	100	0	0
PL	25	40	40	16	4	88	12	0	0	84	12	4	0
RL	5	60	40	0	0	80	10	0	0	100	0	0	0
WL	46	30	43	20	6	78	17	4	0	93	4	2	0
Total	84	32%	50%	13%	5%	80%	11%	6%	0%	73%	23%	4%	0%

**LFP Evaluation Summary.** The summarized responses, by laboratory, are listed on the following page. LFPs were asked to rate the following questions on a scale from 1 (below average) to 5 (above average).

2. LFPs involved in SRP associate application evaluation process:
  - a. Time available for evaluation of applications:
  - b. Adequacy of applications for selection process:
3. Value of orientation trips:
4. Length of research tour:
5.
  - a. Benefits of associate's work to laboratory:
  - b. Benefits of associate's work to Air Force:
6.
  - a. Enhancement of research qualifications for LFP and staff:
  - b. Enhancement of research qualifications for SFRP associate:
  - c. Enhancement of research qualifications for GSRP associate:
7.
  - a. Enhancement of knowledge for LFP and staff:
  - b. Enhancement of knowledge for SFRP associate:
  - c. Enhancement of knowledge for GSRP associate:
8. Value of Air Force and university links:
9. Potential for future collaboration:
10.
  - a. Your working relationship with SFRP:
  - b. Your working relationship with GSRP:
11. Expenditure of your time worthwhile:

(Continued on next page)



12. Quality of program literature for associate:
13.   a. Quality of RDL's communications with you:  
      b. Quality of RDL's communications with associates:
14. Overall assessment of SRP:

Table B-3. Laboratory Focal Point Responses to above questions

	<i>AEDC</i>	<i>AL</i>	<i>USAFA</i>	<i>PL</i>	<i>RL</i>	<i>WHMC</i>	<i>WL</i>
<i># Evals Recv'd</i>	0	7	1	14	5	0	46
<i>Question #</i>							
2	-	86 %	0 %	88 %	80 %	-	85 %
2a	-	4.3	n/a	3.8	4.0	-	3.6
2b	-	4.0	n/a	3.9	4.5	-	4.1
3	-	4.5	n/a	4.3	4.3	-	3.7
4	-	4.1	4.0	4.1	4.2	-	3.9
5a	-	4.3	5.0	4.3	4.6	-	4.4
5b	-	4.5	n/a	4.2	4.6	-	4.3
6a	-	4.5	5.0	4.0	4.4	-	4.3
6b	-	4.3	n/a	4.1	5.0	-	4.4
6c	-	3.7	5.0	3.5	5.0	-	4.3
7a	-	4.7	5.0	4.0	4.4	-	4.3
7b	-	4.3	n/a	4.2	5.0	-	4.4
7c	-	4.0	5.0	3.9	5.0	-	4.3
8	-	4.6	4.0	4.5	4.6	-	4.3
9	-	4.9	5.0	4.4	4.8	-	4.2
10a	-	5.0	n/a	4.6	4.6	-	4.6
10b	-	4.7	5.0	3.9	5.0	-	4.4
11	-	4.6	5.0	4.4	4.8	-	4.4
12	-	4.0	4.0	4.0	4.2	-	3.8
13a	-	3.2	4.0	3.5	3.8	-	3.4
13b	-	3.4	4.0	3.6	4.5	-	3.6
14	-	4.4	5.0	4.4	4.8	-	4.4

### 3. 1997 SFRP & GSRP EVALUATION RESPONSES

The summarized results listed below are from the 257 SFRP/GSRP evaluations received.

Associates were asked to rate the following questions on a scale from 1 (below average) to 5 (above average) - by Air Force base results and over-all results of the 1997 evaluations are listed after the questions.

1. The match between the laboratories research and your field:
2. Your working relationship with your LFP:
3. Enhancement of your academic qualifications:
4. Enhancement of your research qualifications:
5. Lab readiness for you: LFP, task, plan:
6. Lab readiness for you: equipment, supplies, facilities:
7. Lab resources:
8. Lab research and administrative support:
9. Adequacy of brochure and associate handbook:
10. RDL communications with you:
11. Overall payment procedures:
12. Overall assessment of the SRP:
13.
  - a. Would you apply again?
  - b. Will you continue this or related research?
14. Was length of your tour satisfactory?
15. Percentage of associates who experienced difficulties in finding housing:
16. Where did you stay during your SRP tour?
  - a. At Home:
  - b. With Friend:
  - c. On Local Economy:
  - d. Base Quarters:
17. Value of orientation visit:
  - a. Essential:
  - b. Convenient:
  - c. Not Worth Cost:
  - d. Not Used:

SFRP and GSRP associate's responses are listed in tabular format on the following page.

Table B-4. 1997 SFRP &amp; GSRP Associate Responses to SRP Evaluation

	Arnold	Brooks	Edwards	Eglin	Griffis	Hanson	Kelly	Kirtland	Lackland	Robins	Tyndall	WPAFB	average
# res	6	48	6	14	31	19	3	32	1	2	10	85	257
1	4.8	4.4	4.6	4.7	4.4	4.9	4.6	4.6	5.0	5.0	4.0	4.7	4.6
2	5.0	4.6	4.1	4.9	4.7	4.7	5.0	4.7	5.0	5.0	4.6	4.8	4.7
3	4.5	4.4	4.0	4.6	4.3	4.2	4.3	4.4	5.0	5.0	4.5	4.3	4.4
4	4.3	4.5	3.8	4.6	4.4	4.4	4.3	4.6	5.0	4.0	4.4	4.5	4.5
5	4.5	4.3	3.3	4.8	4.4	4.5	4.3	4.2	5.0	5.0	3.9	4.4	4.4
6	4.3	4.3	3.7	4.7	4.4	4.5	4.0	3.8	5.0	5.0	3.8	4.2	4.2
7	4.5	4.4	4.2	4.8	4.5	4.3	4.3	4.1	5.0	5.0	4.3	4.3	4.4
8	4.5	4.6	3.0	4.9	4.4	4.3	4.3	4.5	5.0	5.0	4.7	4.5	4.5
9	4.7	4.5	4.7	4.5	4.3	4.5	4.7	4.3	5.0	5.0	4.1	4.5	4.5
10	4.2	4.4	4.7	4.4	4.1	4.1	4.0	4.2	5.0	4.5	3.6	4.4	4.3
11	3.8	4.1	4.5	4.0	3.9	4.1	4.0	4.0	3.0	4.0	3.7	4.0	4.0
12	5.7	4.7	4.3	4.9	4.5	4.9	4.7	4.6	5.0	4.5	4.6	4.5	4.6
Numbers below are percentages													
13a	83	90	83	93	87	75	100	81	100	100	100	86	87
13b	100	89	83	100	94	98	100	94	100	100	100	94	93
14	83	96	100	90	87	80	100	92	100	100	70	84	88
15	17	6	0	33	20	76	33	25	0	100	20	8	39
16a	-	26	17	9	38	23	33	4	-	-	-	30	
16b	100	33	-	40	-	8	-	-	-	-	36	2	
16c	-	41	83	40	62	69	67	96	100	100	64	68	
16d	-	-	-	-	-	-	-	-	-	-	-	0	
17a	-	33	100	17	50	14	67	39	-	50	40	31	35
17b	-	21	-	17	10	14	-	24	-	50	20	16	16
17c	-	-	-	-	10	7	-	-	-	-	-	2	3
17d	100	46	-	66	30	69	33	37	100	-	40	51	46

#### **4. 1997 USAF LABORATORY HSAP MENTOR EVALUATION RESPONSES**

Not enough evaluations received (5 total) from Mentors to do useful summary.

## 5. 1997 HSAP EVALUATION RESPONSES

The summarized results listed below are from the 113 HSAP evaluations received.

HSAP apprentices were asked to rate the following questions on a scale from  
1 (below average) to 5 (above average)

1. Your influence on selection of topic/type of work.
2. Working relationship with mentor, other lab scientists.
3. Enhancement of your academic qualifications.
4. Technically challenging work.
5. Lab readiness for you: mentor, task, work plan, equipment.
6. Influence on your career.
7. Increased interest in math/science.
8. Lab research & administrative support.
9. Adequacy of RDL's Apprentice Handbook and administrative materials.
10. Responsiveness of RDL communications.
11. Overall payment procedures.
12. Overall assessment of SRP value to you.
13. Would you apply again next year? Yes (92 %)
14. Will you pursue future studies related to this research? Yes (68 %)
15. Was Tour length satisfactory? Yes (82 %)

	Arnold	Brooks	Edwards	Eglin	Griffiss	Hanscom	Kirtland	Tyndall	WPAFB	Totals
# resp	5	19	7	15	13	2	7	5	40	113
1	2.8	3.3	3.4	3.5	3.4	4.0	3.2	3.6	3.6	3.4
2	4.4	4.6	4.5	4.8	4.6	4.0	4.4	4.0	4.6	4.6
3	4.0	4.2	4.1	4.3	4.5	5.0	4.3	4.6	4.4	4.4
4	3.6	3.9	4.0	4.5	4.2	5.0	4.6	3.8	4.3	4.2
5	4.4	4.1	3.7	4.5	4.1	3.0	3.9	3.6	3.9	4.0
6	3.2	3.6	3.6	4.1	3.8	5.0	3.3	3.8	3.6	3.7
7	2.8	4.1	4.0	3.9	3.9	5.0	3.6	4.0	4.0	3.9
8	3.8	4.1	4.0	4.3	4.0	4.0	4.3	3.8	4.3	4.2
9	4.4	3.6	4.1	4.1	3.5	4.0	3.9	4.0	3.7	3.8
10	4.0	3.8	4.1	3.7	4.1	4.0	3.9	2.4	3.8	3.8
11	4.2	4.2	3.7	3.9	3.8	3.0	3.7	2.6	3.7	3.8
12	4.0	4.5	4.9	4.6	4.6	5.0	4.6	4.2	4.3	4.5
Numbers below are percentages										
13	60%	95%	100%	100%	85%	100%	100%	100%	90%	92%
14	20%	80%	71%	80%	54%	100%	71%	80%	65%	68%
15	100%	70%	71%	100%	100%	50%	86%	60%	80%	82%

KINETIC STUDY OF THE THERMAL DECOMPOSITION  
OF *t*-BUTYLPHENYL PHOSPHATE USING THE  
SYSTEM FOR THERMAL DIAGNOSTIC STUDIES (STDS)

Dennis R. Flentge  
Professor  
Department of Science & Mathematics

Cedarville College  
P. O. Box 601  
Cedarville, OH 45314-0601

Final Report for:  
Summer Faculty Research Program  
Aero Propulsion and Power Directorate  
Wright Laboratory

Sponsored by:  
Air Force Office of Scientific Research  
Bolling Air Force Base, DC

and

Aero Propulsion and Power Directorate  
Wright Laboratory

September 1997

KINETIC STUDY OF THE THERMAL DECOMPOSITION  
OF *t*-BUTYLPHENYL PHOSPHATE USING THE  
SYSTEM FOR THERMAL DIAGNOSTIC STUDIES (STDS)

Dennis R. Flentge  
Professor  
Department of Science and Mathematics  
Cedarville College

**Abstract**

The System for Thermal Diagnostic Studies (STDS), which links a thermal reactor cell directly to a gas chromatograph/mass spectrometer (GC/MS), allows one to examine the gas phase decomposition of materials as a function of temperature, time, and atmosphere. Tertiary-butylphenyl phosphate (*t*-BPP) shows some potential for use in lubricants which must function at high temperatures. The decomposition of *t*-BPP was studied at temperatures between 300°C and 700°C, rate constants were measured, and an activation energy for the decomposition was calculated.

# KINETIC STUDY OF THE THERMAL DECOMPOSITION OF *t*-BUTYLPHENYL PHOSPHATE USING THE SYSTEM FOR THERMAL DIAGNOSTIC STUDIES (STDS)

Dennis R. Flentge

## **Introduction**

As the demands for increased efficiency and greater power are made on turbine engines, the need for lubricants that function well at higher temperatures has grown. Lubricant performance can be enhanced by using additives which reduce wear or by improving the lubricant base stock. Tricresyl phosphate (TCP) has been used widely to enhance the anti-wear characteristics of synthetic lubricants but toxilological concerns about its use exist. A related triaryl phosphate, *t*-butylphenyl phosphate (*t*-BPP), appears to be less toxic and could be a good substitute for TCP(1). A knowledge of the decomposition, reaction rate constants, and activation energies of *t*-BPP should contribute to the understanding of the processes occurring at elevated temperatures.

## **Methodology**

The System for Thermal Diagnostic Studies (STDS) was designed by Rubey of the University of Dayton Research Institute to study incineration of hazardous wastes (2, 3). Since the STDS provides control of temperature, reactive atmosphere, residence time of the reactant in the reaction vessel, pressure, and degree of mixing, it is also an excellent tool for kinetic studies of vapor phase lubricant samples(1).

The STDS contains four integrated components. First, a control console regulates the temperature of the reactor cell and the flow of the reactor gas through it.



Second, a Hewlett-Packard model 5890A gas chromatograph has been modified so that it can house the quartz reactor cell and the high temperature furnace. An unmodified model 5890A gas chromatograph is the third component. Thermal reaction products and unreacted parent material are swept into this chamber and are deposited near the beginning of the chromatographic column. Finally, a Hewlett-Packard model 5970B mass spectrometer analyzes materials separated by the gas chromatograph.

Temperature and residence time of the parent material in the reactor were components of interest in this study. The injector leading to the reactor cell was kept at 225°C and the oven surrounding the reactor cell and furnace was at 300°C. The temperature of the reactor cell, controlled by the furnace, was set at values ranging from 300°C to 700°C. Air was the reactor gas for all of the experimental trials. Residence time was established by the flow rate of the reactor gas.

A 0.2 microliter sample of the neat liquid was injected into the reaction compartment and the reactor gas carried the vaporized sample into the reactor cell. The flow was maintained for ten (10) minutes to insure that the entire sample had been carried through the reactor and that all of the products and unreacted parent material had been transported to the beginning of the gas chromatographic column. Then the reactor gas flow was reduced and the helium flow through the chromatographic column was increased. After the column was flushed two minutes to carry all of the air through the gas chromatograph and past the detectors of the mass spectrometer, the program controlling the temperature increase of the gas chromatograph and the detection of

particles in the mass spectrometer was started. The temperature was raised from 50°C to 300°C at a rate of 5°/minute and was held at 300°C for 10 minutes.

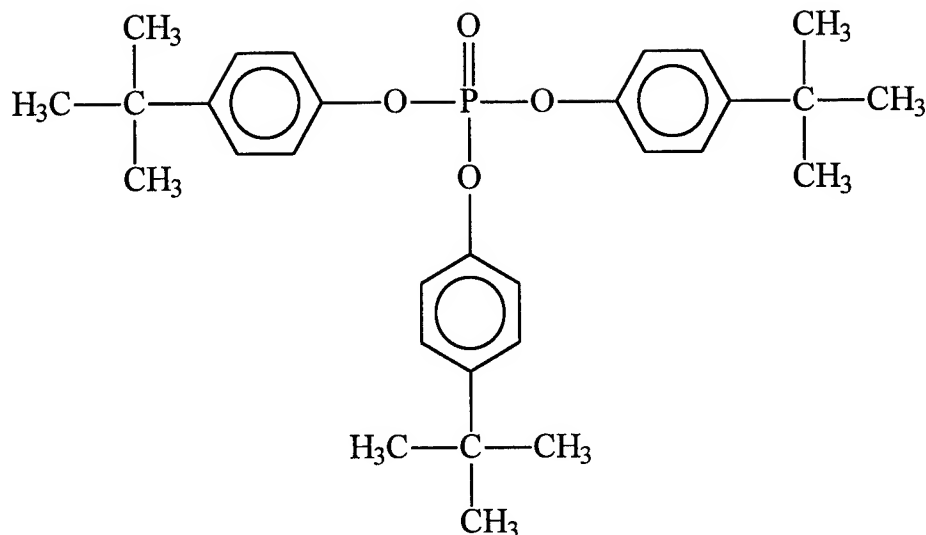
Reaction rates were followed by measuring the areas of peaks associated with fragments of *t*-BPP. The mass spectrometer looked for fragments with atomic masses ranging from 50 to 800 daltons. Computer software extracted the peak areas for samples with atomic masses of 495, 479, 423, 382, and 367 daltons. These masses represent *t*-BPP and fragments formed by the loss of methyl and *t*-butyl groups from the benzene rings. The total area of peaks from these fragments was used to measure reaction rate.

The mass spectrometer's sensitivity varied from day to day. A sample of *t*-BPP injected into the reactor set at 300°C served as the standard for each day's data. All data collected on that day were adjusted using the ratio of the total peak area of the daily standard to the average peak area of the daily standards.

The chromatographic column, which is connected directly to the mass spectrometer, draws gas into itself at a rate that is independent of the flow rate of the reactor gas. Samples of 1% dodecane dissolved in hexane were injected at several different reactor gas flow rates. A plot of the log of the peak area versus flow rate gave a relationship used to correct the data for the effect of flow rate.

Tertiarybutylphenyl phosphate is a blend of isomers with the *t*-butyl groups attached at the *meta*- and *para*- positions of the benzene ring. The groups are sterically hindered from being in the *ortho*- position. Methyl groups in the *ortho*- position seem to be an important factor in the toxicity of TCP. The structural formula for *t*-BPP is shown

below.



## **Results**

Figure 1 shows a representative gas chromatogram of *t*-BPP at 300°C. The peak areas of the 300°C chromatograms are used as the daily standard and are assumed to be the concentration at zero time for the kinetic data. The average residence time for the 300°C samples is  $2.46 \pm 0.02$  seconds.

Figure 2 shows the chromatogram for a sample at 620°C and residence time of 4.18 seconds. In addition to the peaks from *t*-BPP there are several peaks containing decomposition products of *t*-BPP. At a retention time near twelve minutes *t*-butyl phenol is found. The peak spread over the first four minutes of the chromatogram is from phenol. At shorter retention time the phenol peak is smaller and the *t*-butyl phenol peak is larger.

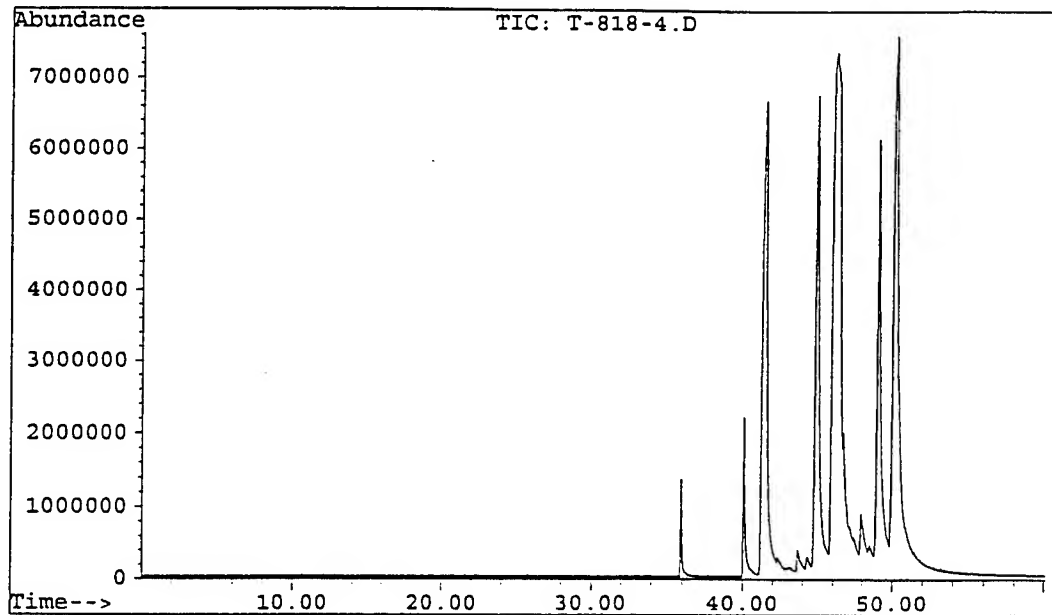


Figure 1

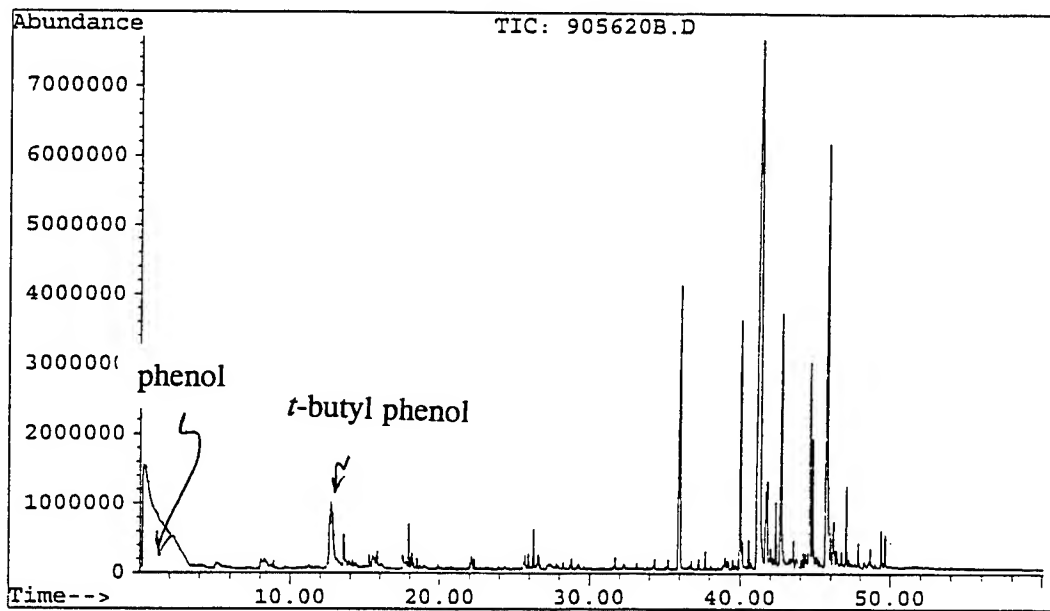


Figure 2

Wright indicated that at 650°C a change in the activation energy for the decomposition occurred and suggested that a change in the decomposition mechanism caused this(1). Our study looked at reaction rates at temperatures between 580°C and 680°C so that we could verify the activation energy change. Figure 3 shows the results for data collected at 660°C.

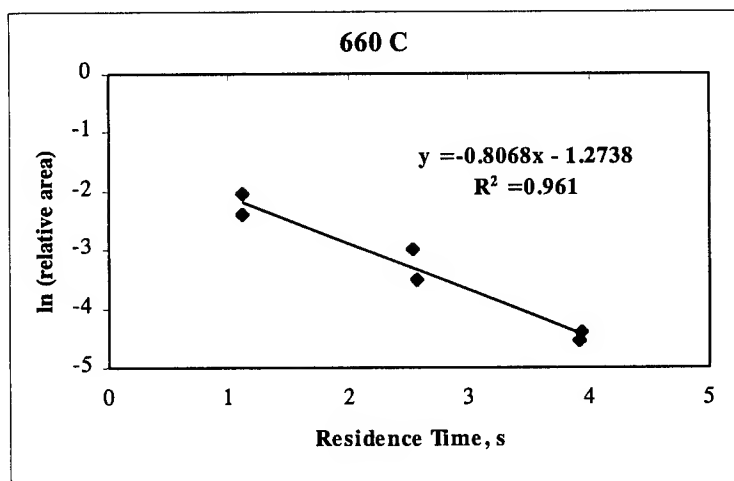
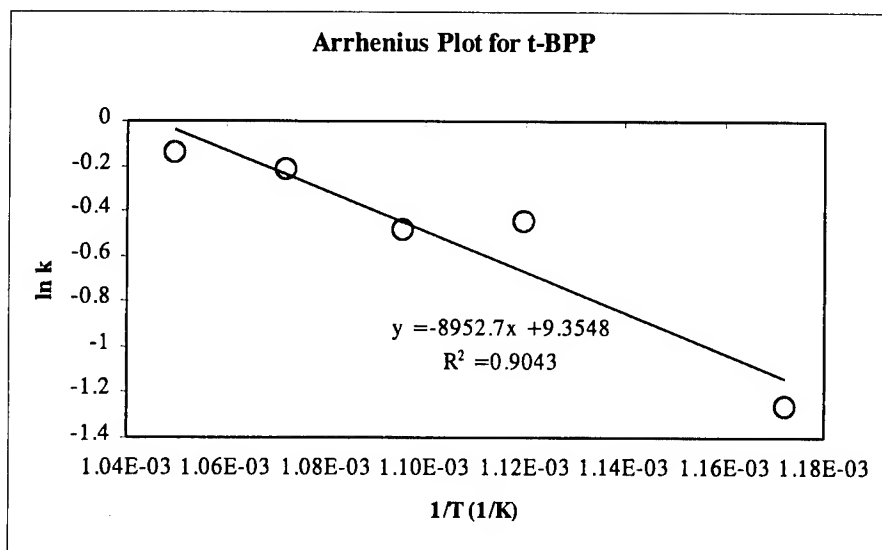


Figure 3

Table 1 contains a summary of the rate constants found from our data.

Temperature, °C	Rate Constant, k (s <sup>-1</sup> )
580	0.2830
620	0.6401
640	0.6172
660	0.8068
680	0.8722

Figure 4 shows the Arrhenius plot of the temperature and rate constant data.



The slope of the line gives an activation energy of 74.4 kJ/mol for the reaction. Wright found a value of 33 kJ/mol at temperatures below 650°C and 205 kJ/mol above 650°C(1). Wright calculated the rate constants using the two-point method. Figure 5 contains Wright's rate constants, rate constants calculated from the data in this study but using the two-point method, and rate constants calculated from linear regression analysis of the data from this study. Although there is agreement between the linear regression analysis and the two-point analysis at the lower temperatures, as the temperature approaches 700°C the results from the two methods diverge rapidly. The apparent change in activation energy at 650°C seen by Wright appears to be a consequence of his analysis of the data and not as a result of a change in reaction mechanism.

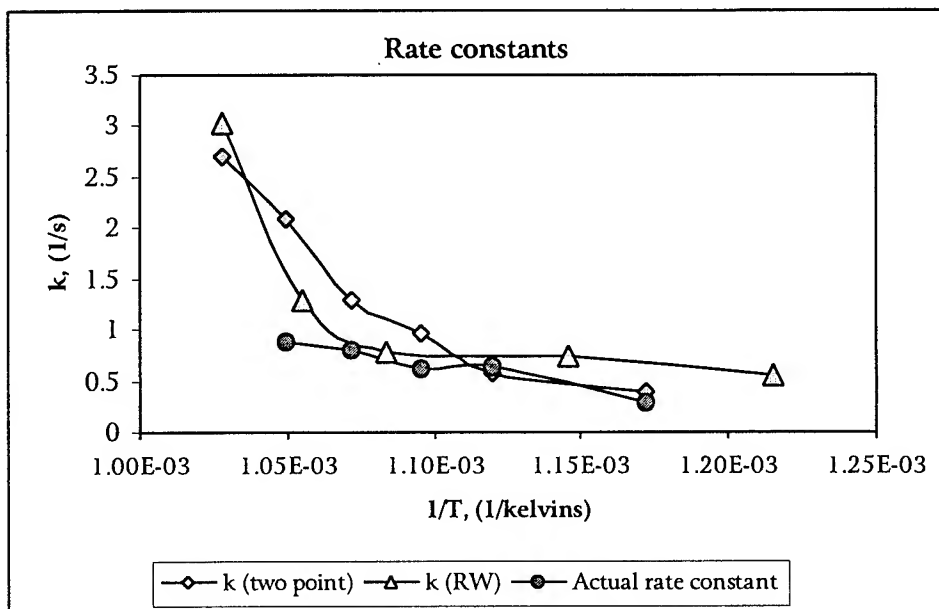


Figure 5

### Conclusions and Recommendations

The STDS shows excellent potential as an instrument to study the vapor phase decomposition of lubricants and lubricant additives. Results from the study of *t*-BPP show that high quality kinetic data can be obtained from the system. In addition to its ability to separate and analyze products that can be trapped on a column at 50°C, it can also retain molecules of lower molar mass using a cryostatic trap(2). This allows one to examine the entire range of reaction products from the thermal decomposition of the lubricants.

Additional study of the kinetics of decomposition of *t*-BPP at 300°C, 400°C, and 500°C could establish if there is a change of activation energy at any point of the decomposition process. Kinetic studies using helium as the reactor gas could also be

informative.

Other potential candidates for high temperature lubrication can also be studied using this instrument.

### **References**

- (1) Wright, Robert L., "The Gas Phase Decomposition and Trimethylolpropane Phosphate Neurotoxin Formation Potential of Tricresyl and *t*-Butylphenyl Phosphates," Technical Report WL-TR-96-2004, 1996.
- (2) Striebich, R. C. and Rubey, W. A., "A System for Thermal Diagnostic Studies," **American Laboratory**, January 1990.
- (3) Rubey, Wayne A. and Grant, Richard A., "Design Aspects of a Modular Instrumentation System for Thermal Diagnostic Studies," **Rev. Sci. Instrum.**, 59(2), February 1988.



# **MULTISCALE MATERIAL CHARACTERIZATION AND APPLICATIONS**

**George N. Frantziskonis  
Professor  
Department of Civil Engineering and Mechanics**

**University of Arizona  
611 Gould-Simpson Bldg.  
Tucson, AZ 85721**

**Final Report for:  
Summer Faculty Research Program  
Wright Laboratory**

**Sponsored by:  
Air Force Office of Scientific Research  
Bolling Air Force Base, Washington, DC**

**And**

**Wright Laboratory**

**August 1997**

# Multiscale Material Characterization and Applications

George N. Frantziskonis

## Abstract

Given the hierarchical structure of engineering materials, it is natural to seek multiscale characterization tool. This study explores wavelet analysis, a recently developed mathematical tool, for this purpose. In particular, the following problems are studied on an exploratory basis: (a) multiscale characterization of corrosion fields in aluminum alloys; (b) multiscale microstructure characterization of certain Titanium alloys; (c) discrimination of a fretted metal surface from an unfretted one using optical patterns from laser scattering. For the first problem, digitized microradiographs of corrosion in 0.74 mm Al samples with different projection magnifications (same optical magnification) are used. Through wavelet synthesis of the data at various scales, it is shown that it is feasible to obtain a quantitative measure of the corrosion field. Notably, wavelet analysis showed some periodic patterns in the images that were undetectable by the naked eye. The nature of these patterns is now being studied, yet, preliminary examinations show that they are the result of data processing and of the image capturing techniques used. It is imperative that such periodicity is understood and either eliminated or filtered out from the images. For the second problem, ultrasonic B-scan data are used for multiscale characterization of various Ti 6-4 microstructures. Two such microstructures are studied in detail for the purpose of quantitative characterization as well as for extraction of microstructural features from the B-scan data. For the third problem, preliminary results show that the optical scattering patterns should be obtained in a consistent manner, and possibly higher frequency laser beams should be used. Here, "consistent" concurs to using a fixed angle between the laser beam and the metal surface, and using the entire scattering pattern rather than pieces of it.

# Multiscale Material Characterization and Applications

George N. Frantziskonis

## Introduction

Wavelet analysis has been used very recently to rationalize experimental data examined at various scales of observation, in several branches of physical sciences ranging from particle physics and biology to electrical engineering and fluid mechanics. However, this powerful technique has not been applied extensively to materials related problems, even though several open problems and critical questions in this field can be greatly benefited from it. This work addresses this issue, and, in particular, three problems are considered, briefly addressed in the abstract and extensively in the following.

Interest in wavelet methods has increased tremendously in the past few years, with notable advances in applications, as described in several recently edited books on wavelets [Meyer, 1991; Ruskai et al, 1992; Meyer & Roques, 1993; Benedetto & Frazier, 1994; Chui et al, 1992-1995, Vols. 1-5]. It has been claimed that it is more often the case than the exception that different scales are needed to characterize physical properties. A paradigmatic illustration relevant to this work is material microstructure where the hierarchy of initial and induced heterogeneity prohibits its rational description independently of scale. Due to the capability of wavelet based techniques to rationalize data in both scale and space simultaneously, it is feasible to analyze the existence of structures and patterns for which other techniques are not adequate.

The analysis of phenomena at multiple scales has received an ever increasing level of attention in the past few years. While it is not possible to provide a detailed commentary on the contributions of the theory of wavelets (harmonic analysis, phase space analysis and renormalization, stochastic and self-similar processes, computer vision, speech, etc.), it is worthwhile to refer to an example from fluid mechanics in order to illustrate the context in which this project is undertaken and in which it should be viewed. In turbulence, wavelet analysis has shown how during the flow evolution, starting from an initial random distribution of vorticity, the smallest scales of the flow become more and more localized and concentrated in the centers of the so-called coherent structures [Farge, 1992, and references cited therein]. This led to conjecture that, contrary to generally accepted ideas, dissipation also acts at the center of coherent structures. Thus, wavelets are capable of capturing and analyzing the existence of fluid structures and patterns for which other techniques have proven inadequate, and the same is expected to be shown for solid microstructures, as described herein (on an exploratory basis).

## Wavelet Analysis

Let us present an illustrative example of use of the wavelet transform, for the purpose of further understanding and facilitating the subsequent description of the present work. Figure 1a shows a "snowflake," where the "map" depicts the spatial position of snow particles for a specific value of the magnification. Let us consider that this "map" is at the finest detail (largest magnification) possible; thus, either due to physical/experimental limitations, or due to lack of interest, information at higher scales is not available. Figures 1b,c,d show the wavelet transforms of the snowflake at three different scales (only three scales are shown for simplicity). Figure 2 shows, again, the wavelet transform of the snowflake using 32 shades from white to black. Clearly, the wavelet representation provides spectacular evidence of its capability to describe spatial "patterns" at different scales realized as magnifications. In other words, each map (Fig. 2, Fig. 1b,c,d) illustrates the spatial pattern of the snowflake for a given value of the magnification. Note that the figures show the wavelet transform rather than the wavelet representation at different scales, an issue that will be discussed in subsequent sections. In the present work, instead of a snowflake, different physical quantities are analyzed. For example, corrosion fields

detected and captured in digital form by microfocus x-ray techniques, ultrasonic B-scan data, laser scattering data from a surface. Images can, in general, be obtained at different magnifications (either originally or by processing the data at the highest magnification available) and images such as those of Fig. 2 are expected. Thus, experimentally, the wavelet transform of data is available at a range of scales. This then provides *complete* information on the spatial quantities in an image at several desired scales. In passing, here we note a relevant work [Williams & Amaratunga, 1993] about detecting certain information present at certain scales. Thus wavelets can also be used for distinguishing and/or detecting certain microstructural features.

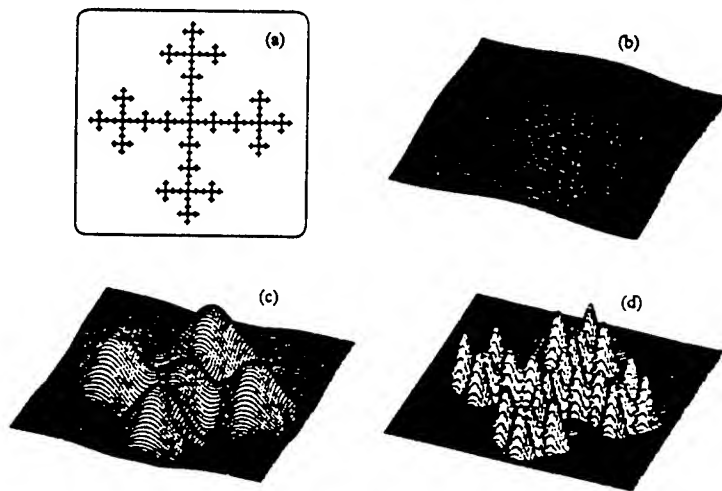


**Figure 1.** Wavelet transforms of the one-scale (fixed magnification) snowflake shown in (a). The analyzing wavelet is the second Gaussian derivative (Mexican hat, discussed in the text). The scale in (b) is three times larger than the scale in (c), and the scale in (c) is three times larger than that in (d). Figures adopted from Arneodo et al. (1992).

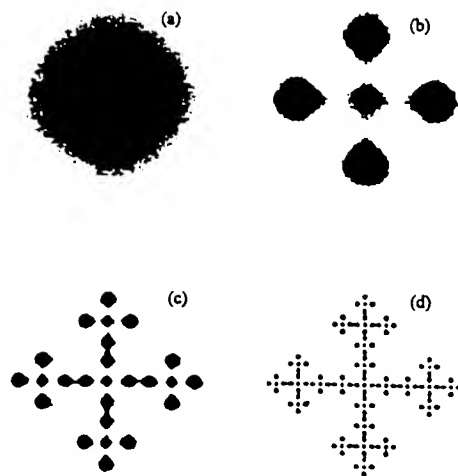


**Figure 2.** Wavelet transforms of the snowflake shown in Fig. 1. It is coded using 32 shades from white to black. Each scale is three times smaller than the previous one, i.e. the scale at (d) is three times smaller than the scale at (c). Figure adopted from Arneodo et al. (1992).

A more general goal of wavelet analysis is to provide representations of graphs (signals) as superposition of elementary functions. The corresponding representation is then used for different purposes, i.e. data compression, feature extraction, pattern recognition, etc. There are several publications on this rather new subject and applications can be found in a wide variety of scientific/engineering. Wavelet transforms provide both scale and location information about a given function. A wavelet  $\psi(x)$  (with real values in our case) transforms a function  $f(x)$  according to

$$W_f(a,b) = \int_{-\infty}^{\infty} f(x) \psi_{ab}(x) dx \quad (1)$$

The two-parameter family of functions,  $\psi_{ab}(x) = (1/\sqrt{a})\psi(\frac{x-b}{a})$  is obtained from a single one,  $\psi$ , called the mother wavelet, through dilatations by the factor  $a^{-1}$  and translations by the factor  $b$ . The factor  $1/\sqrt{a}$  is included for normalization purposes and, with it, all the wavelets have the same energy. The scale parameter  $a$  can take any value on the positive real axis. The scalars defined in (1) measure, in a certain sense, the fluctuations of  $f(x)$  around point  $b$  at the scale  $a$ .

A wavelet analysis can either be continuous or discrete. The second one, based on an orthogonal decomposition of a signal, is convenient for data in the sense that no redundant information is present and an extensive "library" of wavelets is available. In the following, we concentrate on the discrete wavelet analysis and its physical relevance to the problems addressed herein. Due to, in general, non symmetry in the discrete transform (using wavelets with full orthogonality and compact support) physical quantities may often be "misrepresented," thus for the case at hand we use symmetric bi-orthogonal wavelets.

Not every function  $\psi$  can qualify as a wavelet. In particular, its Fourier transform,

$$\bar{\psi}(k) = \int_{-\infty}^{\infty} \psi(x) e^{-2\pi i k x} dx \quad (2)$$

should ensure that the coefficient  $c_\psi$  (given below) is bounded [Chui, 1992]

$$c_\psi = \int_0^{\infty} \frac{|\bar{\psi}(k)|^2}{|k|} dk = \int_0^{\infty} \frac{|\bar{\psi}(-k)|^2}{|k|} dk < \infty \quad (3)$$

which implies, in particular, that the moment of zero-order vanish, i.e.  $\int_{-\infty}^{\infty} \psi(x) dx = 0$ . Given the wavelet coefficients  $W_f(a,b)$  associated to a function  $f$ , it is possible to reconstruct  $f$  in real space  $f = f(x)$  through the inversion formula

$$f(x) = \frac{1}{c_\psi} \int_0^{\infty} \int_{-\infty}^{\infty} W_f(a,b) \psi_{ab}(x) db \frac{da}{a^2} \quad (4)$$

The presence of the coefficient  $c_\psi$  in this inversion formula motivates the boundedness condition expressed by (3). At any given scale  $a > 0$ ,  $f$  is decomposed into the summation of a "trend" at scale  $s$  and of a "fluctuation" around this trend. The trend is the contribution from all scales  $s > a$  in (4), and the fluctuation is given by the scales  $s < a$ .

Within the context of continuous wavelet transform, wavelets commonly used are the so-called Gaussian derivatives of order  $n$ ,  $n = 1, 2, 3, \dots$ ,

$$\psi_n(x) = (-1)^n \frac{d^n}{dx^n} (e^{-x^2/2}) \quad (5)$$

For  $n = 2$  we have the so-called "Mexican hat." There are several discrete wavelet constructions present in the literature, and as mentioned above certain bi-orthogonal wavelets are advantageous for our

purpose. A good source for details on bi-orthogonal and other wavelets is the manual for the program used in this study, c.f. next section.

### *Software Used in this Study*

Data processing, wavelet analysis, and graphical presentations in this research were done with the commercially available program *Mathematica*, from Wolfram Research, Inc. A relevant package titled "Wavelet Explorer" provides information on using wavelet analysis and contains an extensive library of wavelets for discrete transforms. For wavelet analysis of two dimensional data, the product of a uniaxial wavelet in the x-direction with that in the y-direction is commonly used. Thus, a two dimensional wavelet transform includes a transform in the x-direction, one in the y-direction, and one in the x-y direction. This is illustrated schematically in Fig. 3.

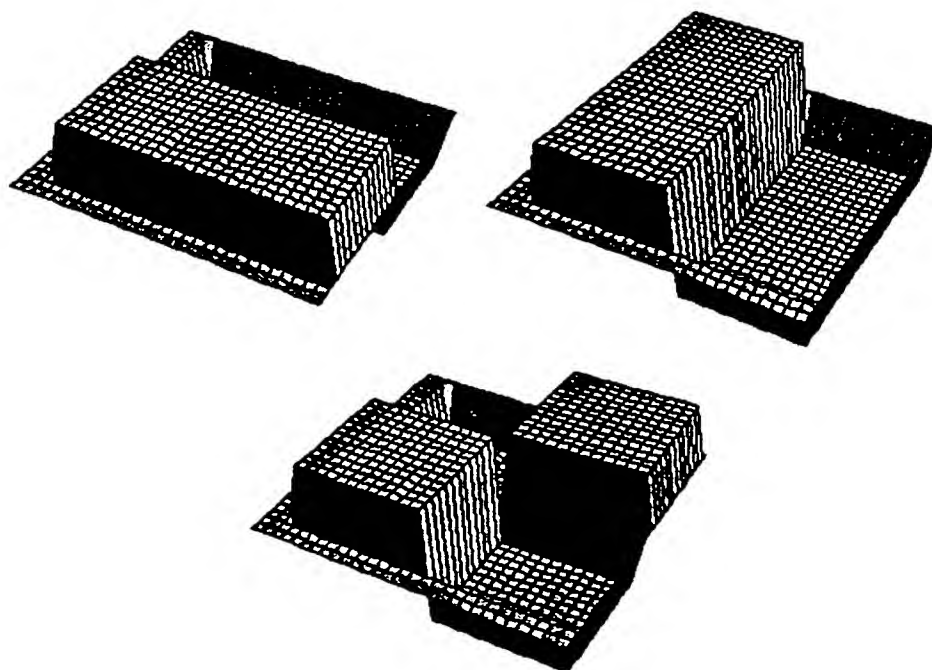


**Figure 3** Schematic of wavelets in two-dimensions, one used for the transform in the x-direction, one for the transform in the y-direction, and one for the x-y direction.

### **Towards Quantification of Corrosion Fields**

Under this project, digital microradiographs of corrosion pitting in aluminum samples were provided by Professor S. Rokhlin, Ohio State University [Rokhlin, 1997]. In particular a set of data included microradiographs with different projection magnifications (same optical magnification), Fig. 4. First, a wavelet analysis of the data was performed with each data (at different magnifications) treated as a separate image. The idea is to finally synthesize the data to a multiresolution representation. Yet, the preliminary analysis of the data revealed a periodicity in the y-direction (Figure 5) that seems

undetectable from the original images. This periodicity is rather strong to the point that it practically "dominates" the density plots of the wavelet coefficients at the first decomposition level in the y-direction. Clearly a periodicity in the y-direction is present. The problem now is to identify the origin of the periodicity, especially since it is not detectable (by the naked eye) in the original images. A straightforward way to clarify whether the periodicity is a "material property" or an "artifact" resulting from data and image processing is to capture the image from the same specimen at two different specimen orientations, one transverse to the other. This was done at 8X magnification, Fig. 6. Following the same process as before, Fig. 7 shows the density plots of the wavelet coefficients at the first level of decomposition. Clearly, the periodicity in the y-direction is practically the same for both orientations of the sample, and that indicates the periodicity has to do with the way the data are processed and with the way images are captured rather with the material. As of the time of writing this report, the problem is under investigation.

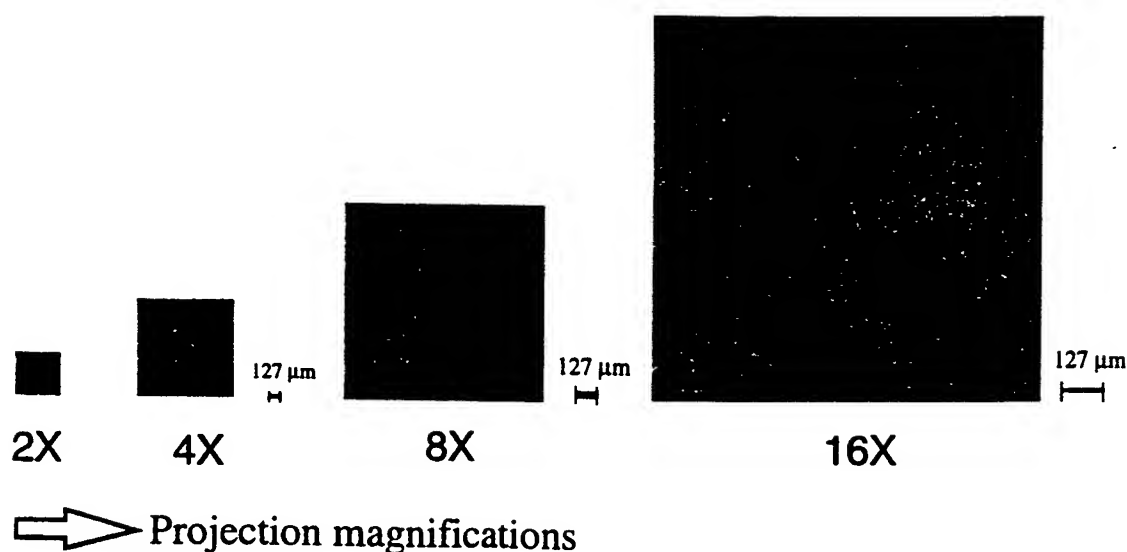


**Figure 4** Microradiographs of corrosion pitting in several projection magnifications (same optical magnification). Figure is continued on the next page.

### *Quantification of the Level of Corrosion*

An important problem is to quantify corrosion so that different levels can be distinguished and decisions can be made. Wavelets provide an efficient tool to quantify a field for the following reasons: (a) the wavelet coefficients contain important (and very compact) information about the digital image, i.e. features are represented efficiently and the local regularity of the image is easily extracted from the coefficients; (b) the coefficients contain local information, so, local irregularities, local concentrations, etc. are also easily extracted; (c) features from the image can be extracted from the wavelet coefficients, e.g. the "ridge" of the corrosion field, the distribution of "depths" (i.e. corrosion levels), location and magnitude of maximum depths, etc. In mathematical terms, the wavelet coefficients represent the local regularity of the image (usually quantified by an exponent). For example, the local maxima of the coefficients correspond to local sharp transitions, and this fact can be used for feature extraction, c.f. next section.

Since the issue of the periodicity has not been resolved adequately yet (at the writing of this report) the quantification of the corrosion fields has not been implemented yet. One way to pursue this is "similar"

to the way the wavelet coefficients have been processed for the second problem studied, presented in the following.

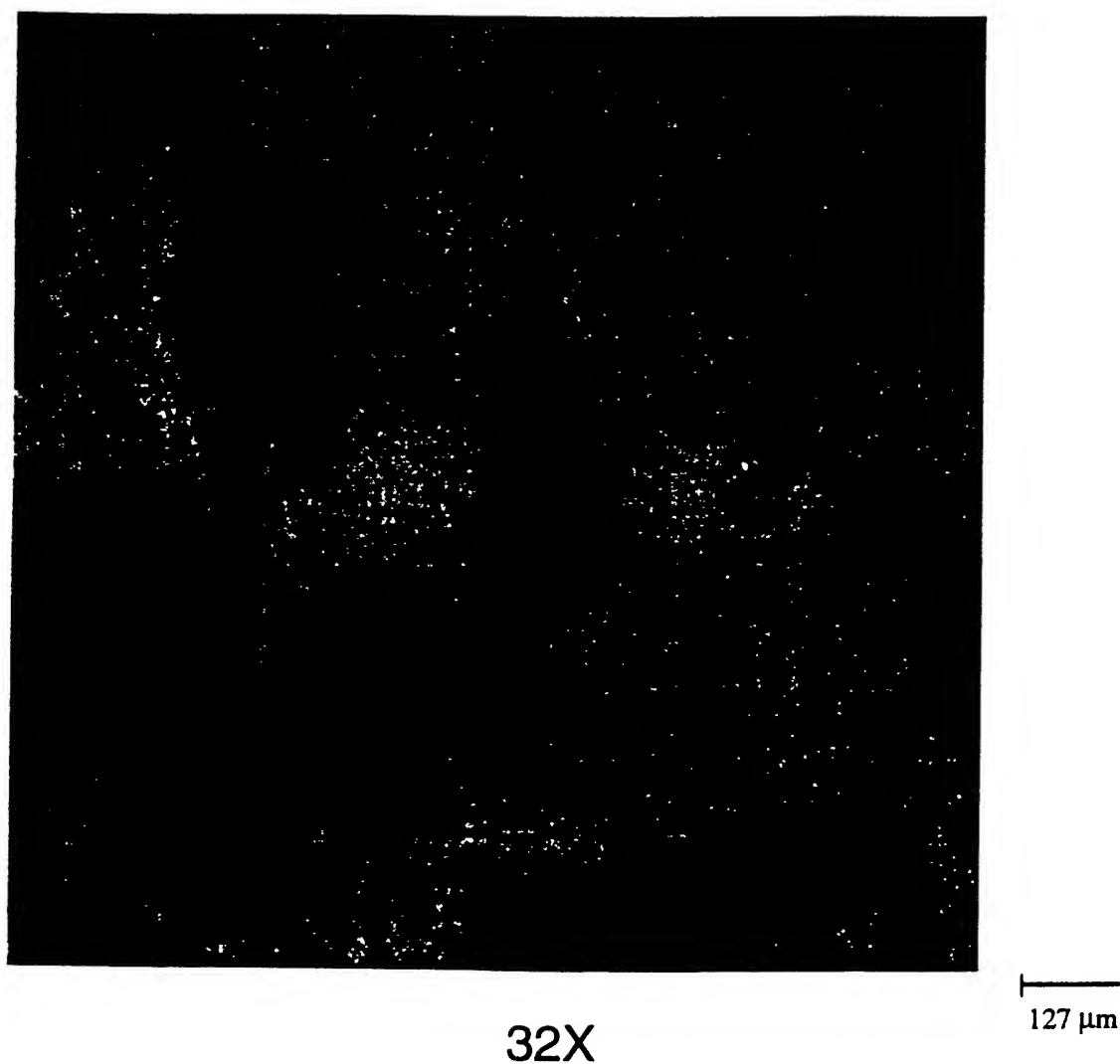


**Figure 4** Continued

One interesting point is illustrated in Fig. 8 which shows the total energy of the wavelet coefficients versus scale. It is clear that the energy of the transform increases with increasing scale. This indicates that more information (e.g. as related to the irregularity of an image) may be contained at higher magnifications (higher than 32X). It is yet to be examined (experimentally) whether "more" information is contained at higher magnifications.



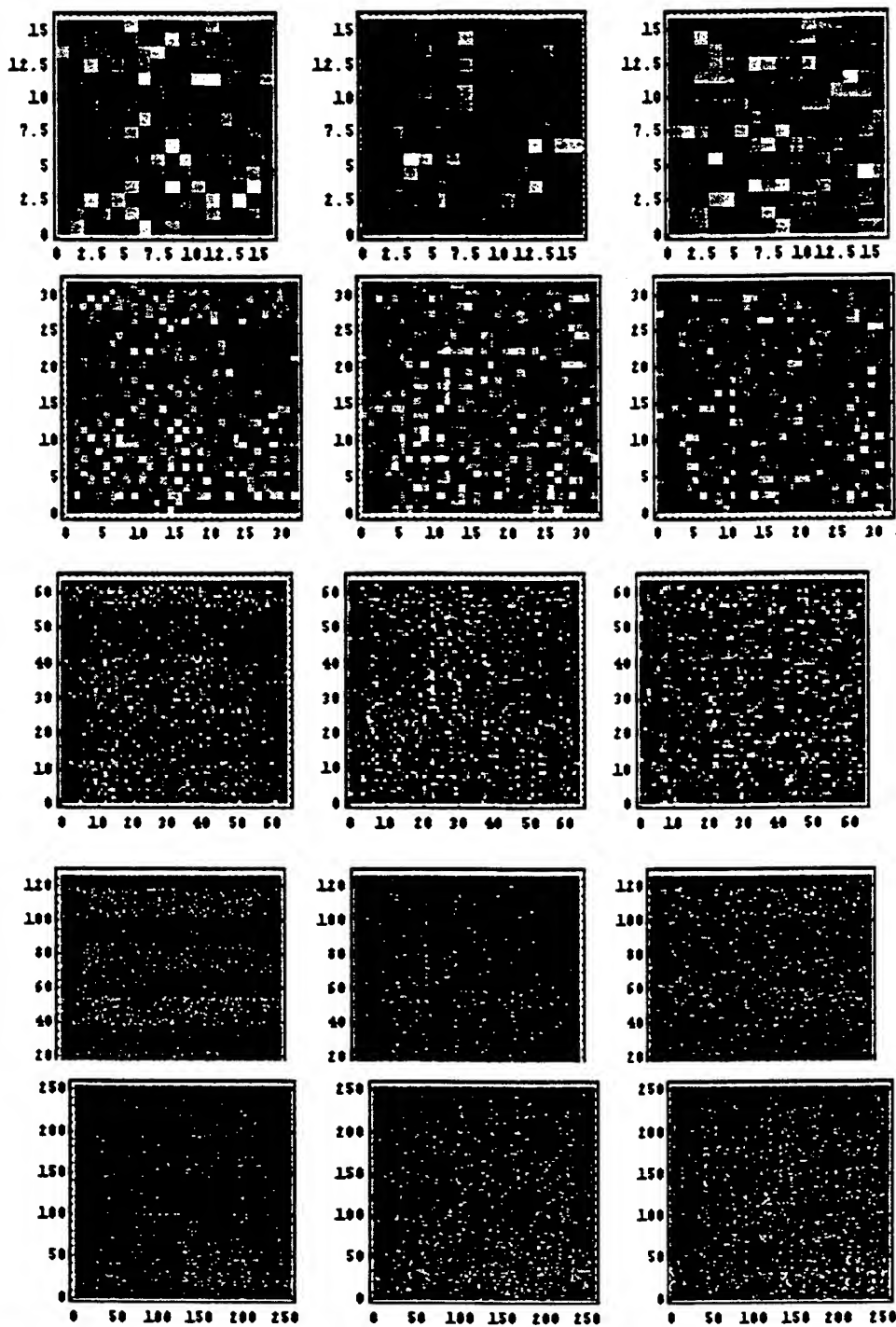


**Figure 5** Density plots of the wavelet coefficients at the first wavelet decomposition level obtained from the images shown in Fig. 4. From top to bottom the magnification increases, the first row corresponding to 2X and the last one to 32X. The first column represents wavelet coefficients from the transform in the y-direction, the second one in the x-y direction, and the third one in the x-direction.

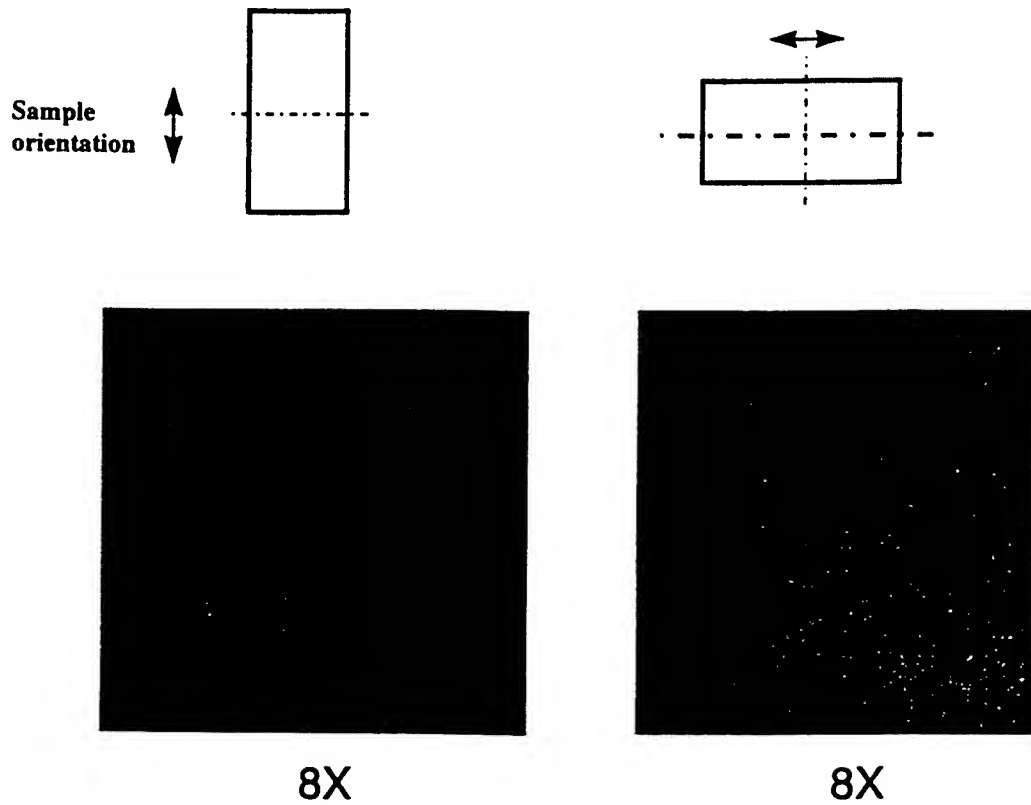


**Figure 6** Digital micrographs at constant (8X) magnifications obtained with two different sample orientations separated by 90°

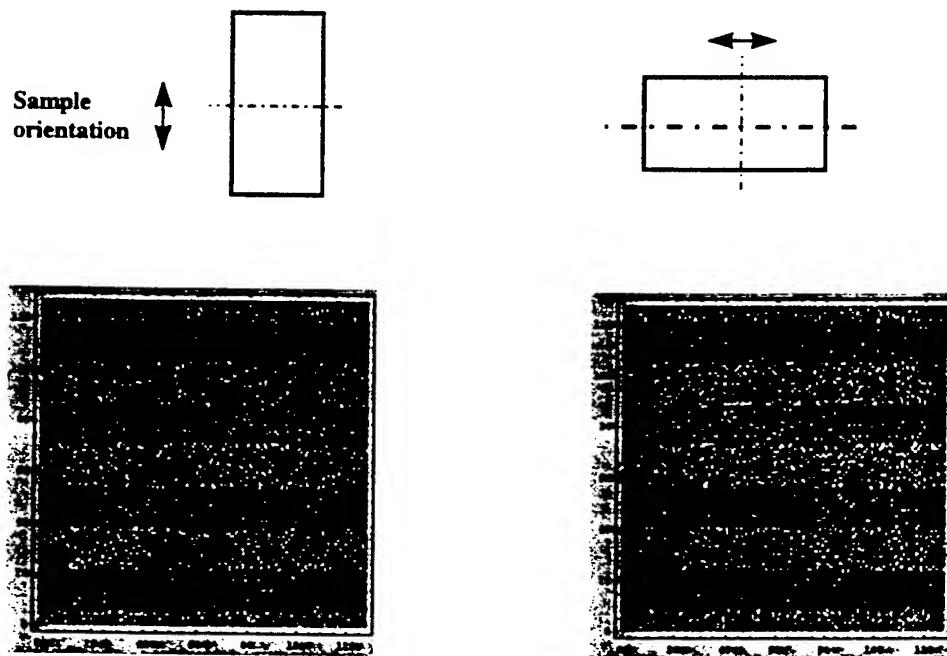


**Figure 7** Density plot of the wavelet coefficients (first level of decomposition) for the images of figure 6.

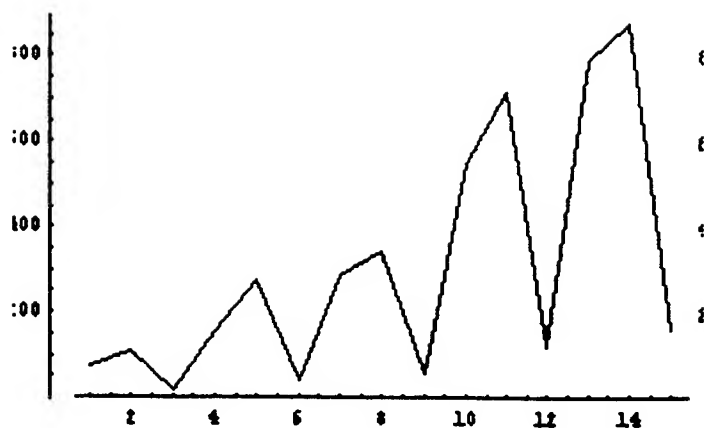


**Figure 8** Total energy of the wavelet coefficients (vertical axis) versus scale (horizontal axis). There are five scales on the horizontal axis, with points 1-3 representing the coarsest one, i.e. 2X, and 13-15 the most detailed one available, i.e. 32X. Point 1 corresponds to the wavelet transform in the y-direction, point 2 to the x-direction and point 3 to the xy-direction. Similarly points 13, 14, 15 represent the transform in the x, y, xy directions, respectively.

## Multiscale Characterization of Microstructure from Ultrasonic Tests

As is well known, the same material (e.g. Ti 6-4 which was examined in this project) can have various microstructures. The microstructure is crucial for the properties of the material and for its performance under service. Different microstructures can be produced by varying the metallurgical process., e.g. treatment temperature, cooling rate, etc. It is important to be able to characterize the microstructure, preferably in a nondestructive fashion. Furthermore it is important to be able to examine spatial uniformity, whether the intended microstructure was actually produced, and whether defects are present. Titanium 6-4 has a number of microstructures currently used for various structural purposes. Herein, we examine B-scan data from two microstructures. The first one, Fig. 9, has elongated grain "clusters" more or less parallel to one direction, and is mill annealed. For the sake of distinguishing the two microstructures examined, we term this as the "noisy" one. The second microstructure examined, herein termed as "quiet," is the so-called Widmanstaaten, Fig. 10, with relatively large grains. The term "noise" corresponds to the "ability" of the microstructure to scatter acoustic waves. In passing, it is noted that [Eylon, 1997], from the six (6) commonly used microstructures of Ti 6-4, the one shown in Fig. 9 is the second noisiest one, while the one shown in Fig. 10 is the fourth noisiest out of six.

Ultrasonic B-scan tests were performed on several specimens and various microstructures. by M.P. Blodgett, Wright-Patterson AFB [Blodgett, 1997]. Focused 10 MHz central frequency transducers were used, the focus "point" (area) being slightly below the top surface. The tests were performed on 25.4 mm thick specimens (the depth being the direction of the propagated wave). The total length of the B-scan is 32.5 mm, with 256 equally spaced points of data acquisition. Thus an image from the B-scan data can be produced where the horizontal axis is the scan direction and the vertical is along the specimen depth. The final useful image for each test consists of 256 (horizontally) by 512 (vertically) points and the total depth in the vertical direction is 19.5 mm. The distance from one B-scan to another was varied between 5mil and 50 mil. For each test a total of 10 B-scans was performed.

## *Repeatability of the Tests and Identification of Microstructure – Material Signature*

Figure 11 shows typical B-scan data for both the “noisy” and “quiet” microstructures. It is important to quantitatively assess the repeatability of the tests. Since the volume of the specimen represented in the images is large compared to the length (volume) characteristic of the microstructure, the tests should be repeatable, statistically, to say the least. In other words, all images (from the same microstructure) should have some similarity to each other, in a statistical sense. Since the volume of the specimen tested is large, a statistical description may not be necessary. This is indeed the case. As shown in the sequence, through wavelet analysis, the essential features in each image can be picked up and the repeatability of the tests can be verified. In addition, since each microstructure produces different features it is possible to assign a “material (microstructure) signature” and thus identify the microstructure from the B-scan data, without any prior knowledge.

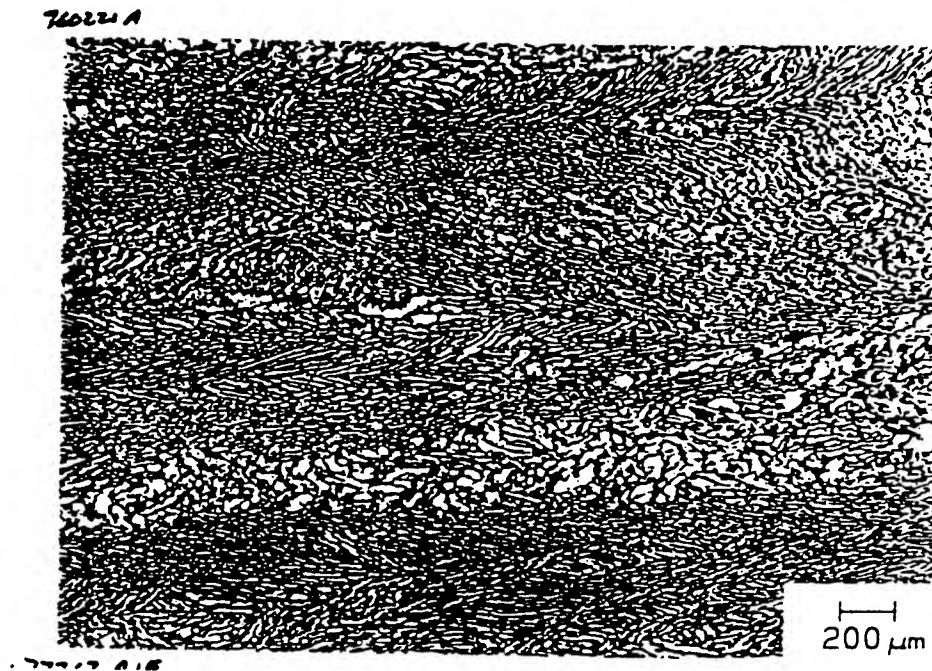


**Figure 9** Typical micrograph of the “noisy” microstructure.

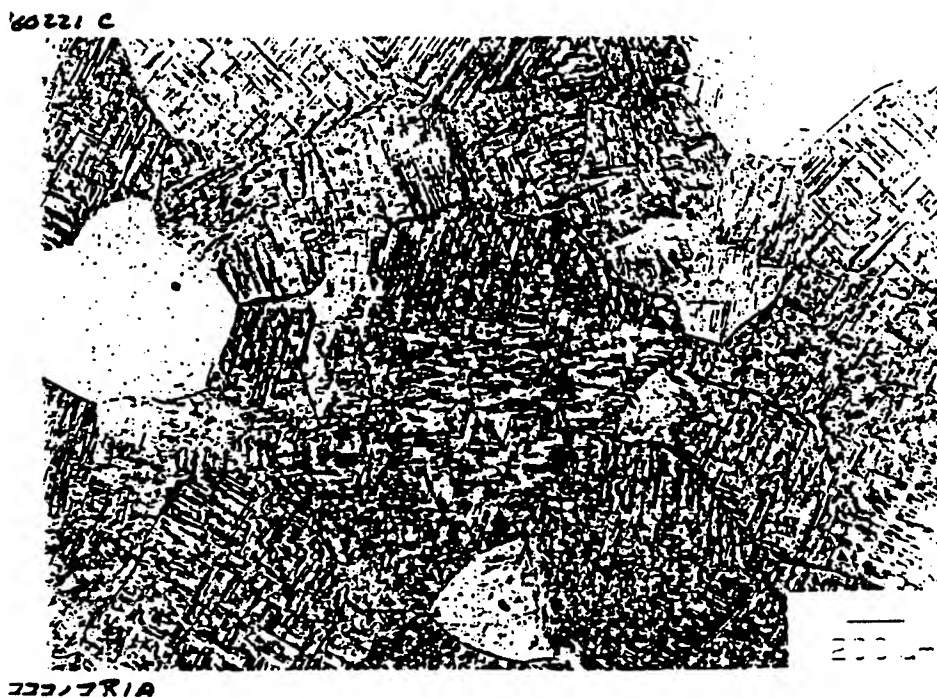


**Figure 10** Typical micrograph of the "quiet" microstructure.

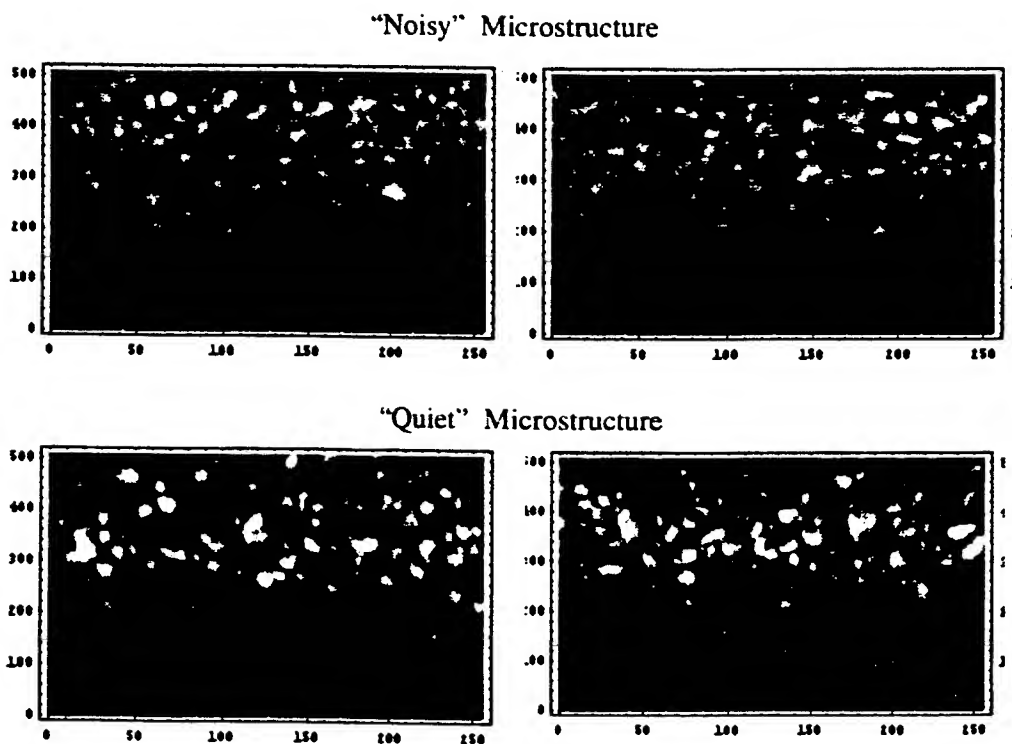


**Figure 11** Typical images from B-scan data. The horizontal axis designates the direction of the B-scan and the vertical designates sample depth. The distance between the two B-scans is 0.8 inches.

## *Physical Interpretation of the Wavelet Coefficients*

As briefly noted in the section titled "Wavelet Analysis" the wavelet coefficients represent (are related to) the local regularity of the image. In turn, this local regularity is related to the scattering of the wave and thus to the microstructure. It is feasible to track such a relation, i.e. wavelet coefficients to microstructure, analytically and/or numerically. This task (not attempted herein) would involve understanding (modeling) the scattering process through the inhomogeneous material., and will be attempted at a later stage. For the time being, it suffices to mention this relation qualitatively.

Figure 12 shows the wavelet coefficients from 4 tests (different B-scan locations) on "quiet" microstructure and 4 tests on the "noisy" one. The top four curves in each plot are from the "noisy" microstructure and the bottom ones from the "quiet" one. Clearly, the fact that each group of (four) curves are closely together indicates the repeatability of the tests. In other words the microstructure is spatially uniform in a statistical sense, and wavelets are able to capture this similarity. Of course, there should be a minimum volume below which this similarity is not repeatable for single measurements (realizations in a statistical sense).

The ability of wavelet analysis to compress an image is now well established. The same holds for the images studied herein (though, even the low valued coefficients may have information on features and feature extraction as discussed in the sequence). Figure 13 shows the compression ratio versus error for a typical image. It is seen that a compression ratio of about 60 produces an error of about 5.5%. Thus if we compress the wavelet coefficients a large number of them simply "drop out" and we are left with a signature as that of figure 14.

## *Potential Uses of the Wavelet Based Material (Microstructure) Signature*

From the metallurgical as well as the material application point of view, it is important to know whether the desired microstructure is produced consistently, whether there are regions with "undesired" microstructure, and whether there are defects. The wavelet analysis shows significant potential to address this since: (a) wavelets provide local information thus spatial irregularities are detectable; (b) the indication of repeatability of the microstructure signature provides a robust tool for discriminating one microstructure from another; (c) wavelet coefficients are sensitive enough so even small irregularities within the scanned material volume produce deviations from the signature. Importantly, these deviations have local information, e.g. they can pinpoint the region(s) where irregularities are present as well as information on the nature of the irregularities.

One important parameter is the volume of the material scanned. If this volume is small, compared to the length (volume) characteristic of the microstructure, the scan data will not be reproducible from single realizations (a large number of small sample volume data would have to be averaged. Thus it is important to identify the minimum volume of material for consistent repeatability of results.

## *Feature Extraction from the Wavelet Coefficients*

The following question is addressed in this section: is it possible to extract visual information about the microstructure, e.g. grain structure, position of grain boundaries, etc. ? As discussed before the wavelet coefficients have information on the microstructure (they represent the local regularity of the image, which is in turn related to the way the ultrasonic wave is scattered, the last being related to the microstructure). Although this relation has not been investigated yet, it may still be possible to extract relevant information from the wavelet coefficients. For example, we can use the fact that local maxima of the wavelet coefficients represent sharp transitions in the image..

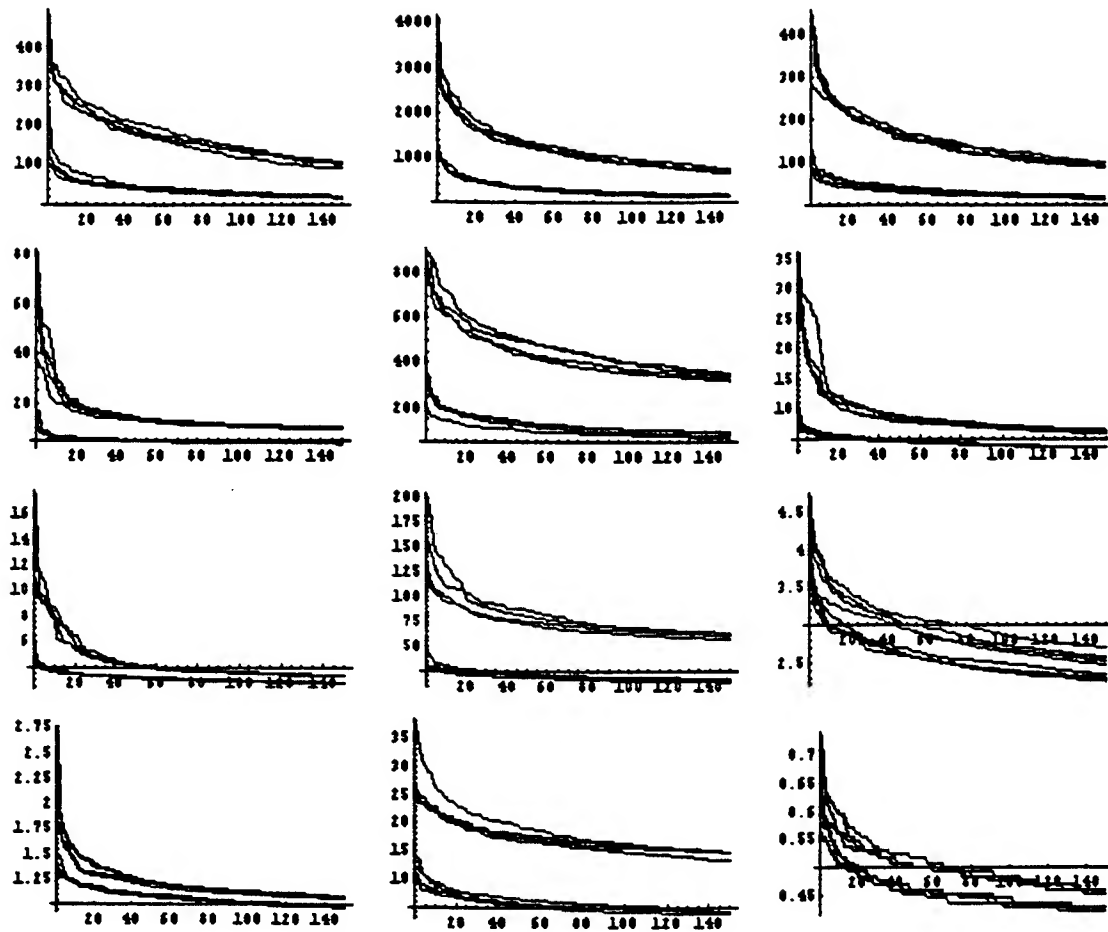


**Figure 12** Plot of wavelet coefficients (150 largest ones for each scale) obtained from four images of "noisy" microstructure (top four curves in each plot) and from four images of "quiet" microstructure (bottom four curves in each plot). The first (left) column of plots show the coefficients from the wavelet transform in the y-direction, the second one from the x, and the third one from the x-y. Scale decreases from top to bottom.

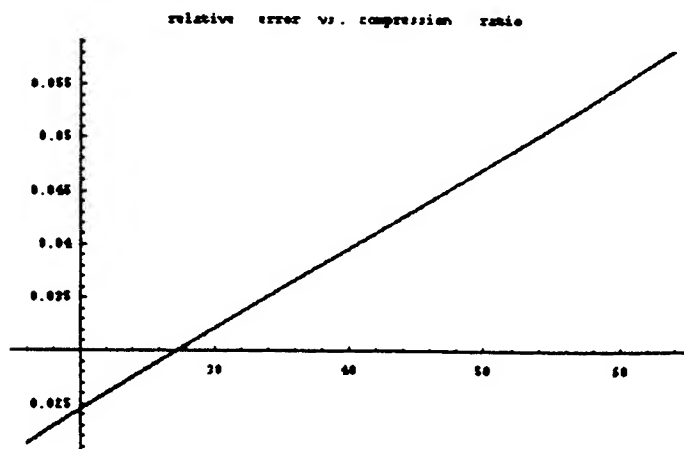


**Figure 13** Typical plot of compression ratio (horizontal axis) versus error (vertical axis) for the B-scan images.

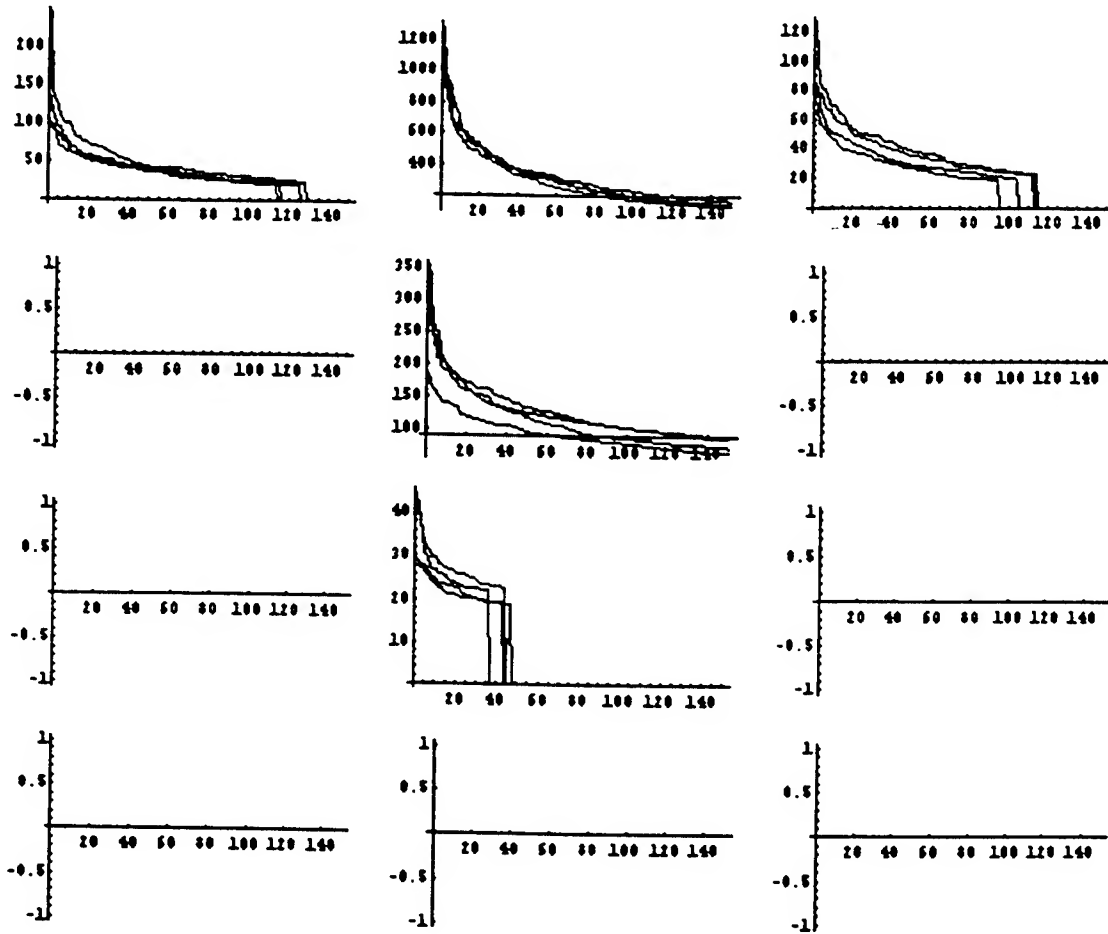
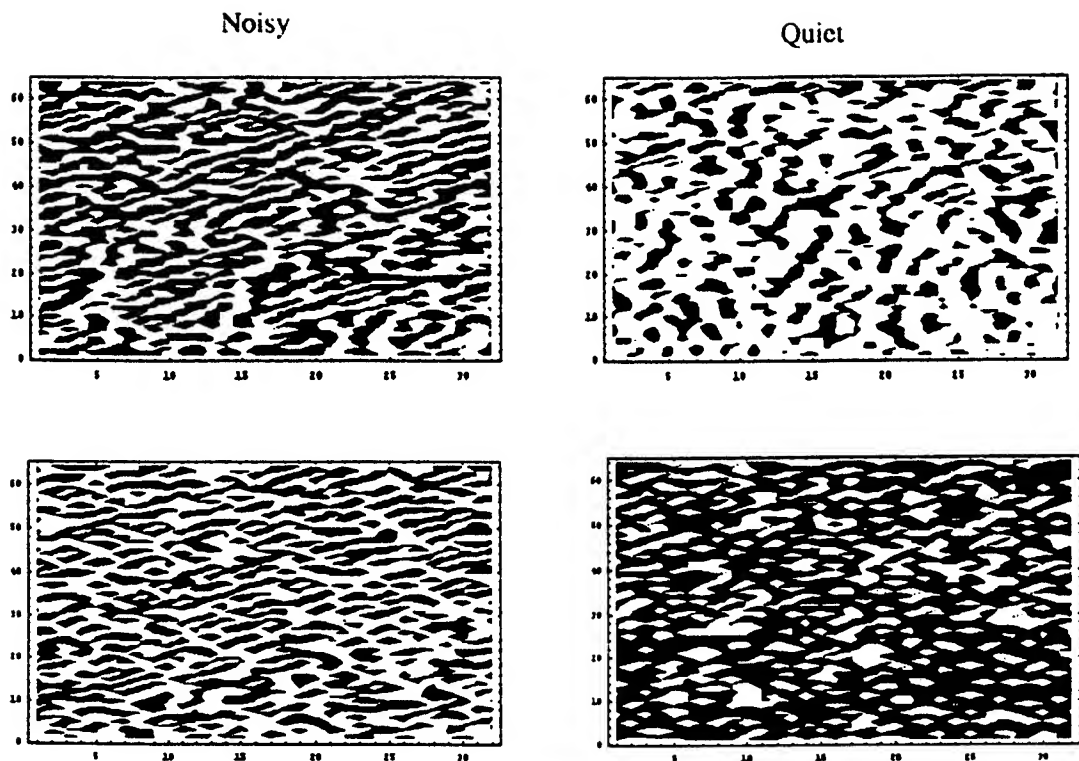


**Figure 14** Wavelet coefficients for the “quiet” microstructure that “survived” after compression with 5.5% error.

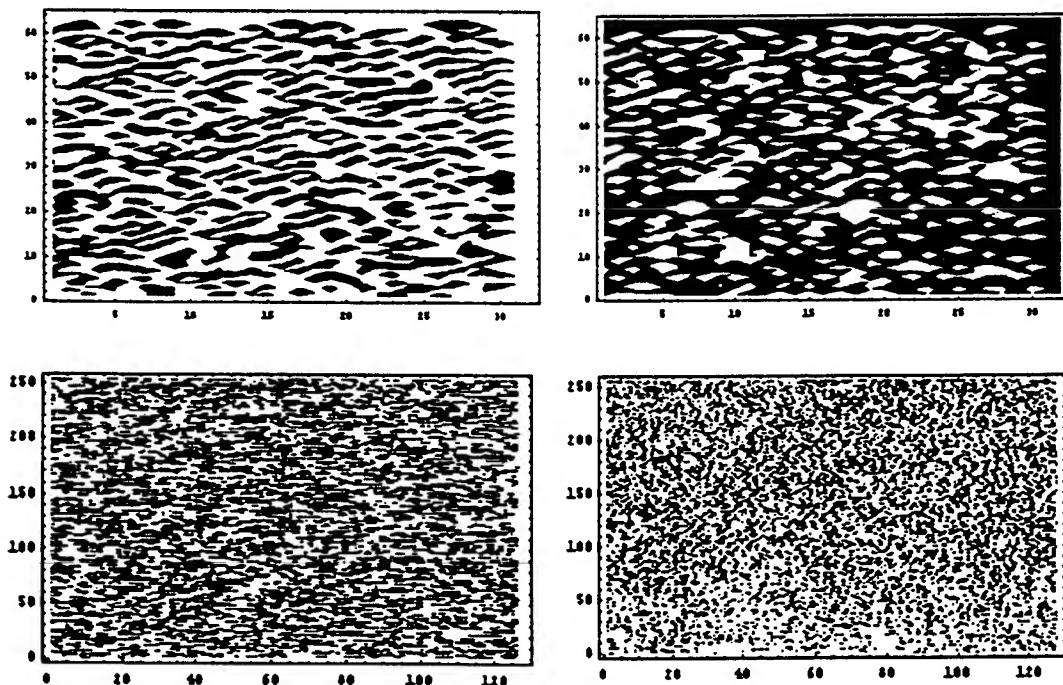
Figure 15 shows typical features extracted from the wavelet coefficient maxima. After the local maxima (and their spatial position) are evaluated, contour plots of these maxima yield the features.

Figure 16 shows the features extracted from tests different than those of Fig. 15. A clear difference in “features” can be seen (noisy vs. quiet microstructures). Furthermore the essential features of the microstructures, Fig. 9 & 10, are reproduced. Although these are only preliminary results, they illustrate the potential of the method. Several issues remain to be examined, i.e. whether the spacing used in the B-scans is adequate for detailed representation of features, whether the digitization of the signal (vertical direction) is detailed enough, etc. Furthermore, there are several ways to extract features from wavelet coefficients, and a large number of publications on the subject can be found. Here a very simple one has been explored.





**Figure 15** Features extracted from the wavelet coefficient maxima for the "noisy" (first column) and the "quiet" Note that 256 units correspond to 32.5 mm. The first row of images is the contour plot of the wavelet maxima at the corresponding scale. The second one was produced as follows: the local wavelet coefficients were averaged over a radius equal to the support of the wavelet at the corresponding scale and then the local maxima were plotted.



**Figure 16** Plots similar to those of Fig. 15, for a different B-scan test. The second row is for a different scale as can be seen from the units. Note that for such "detailed" spaces (second row) contour plotting is not as efficient in representing details.

## Discrimination of a Fretted Surface from an Unfretted one, and Quantification

Material fretting is a problem that often leads to catastrophic failures. It is important to be able to quantify the level of fretting, and one way is by studying the surface modification. Although there are issues such as subsurface plastic deformations, subsurface cracks, surface related phenomena, it is challenging to study whether there is information on fretting “encrypted” in the surface characteristics. Towards such a study, Prof. S. Gustafson, UDRI, [Gustafson, 1997] performed laser scattering experiments on fretted and unfretted surfaces. Figure 17 shows typical images obtained from the experiments.

Similarly to the images from the B-scans, the repeatability of the measurements should be examined. Figure 18 shows the wavelet coefficients from both fretted and unfretted surface. Clearly, the experiments do not repeat satisfactorily. This could be due to the way the images are captured, e.g. angle of inclination between the beam and the surface, distance of the screen from the metal (sample) surface, and/or from the fact that not the entire pattern is shown in each image. One interesting point is that the wavelet coefficients show a trend to discriminate (fretted versus unfretted) at higher scales (bottom of Fig. 18). This indicates that higher wave frequencies (e.g. blue laser) may be more efficient in studying these problems. This is, yet, to be examined.

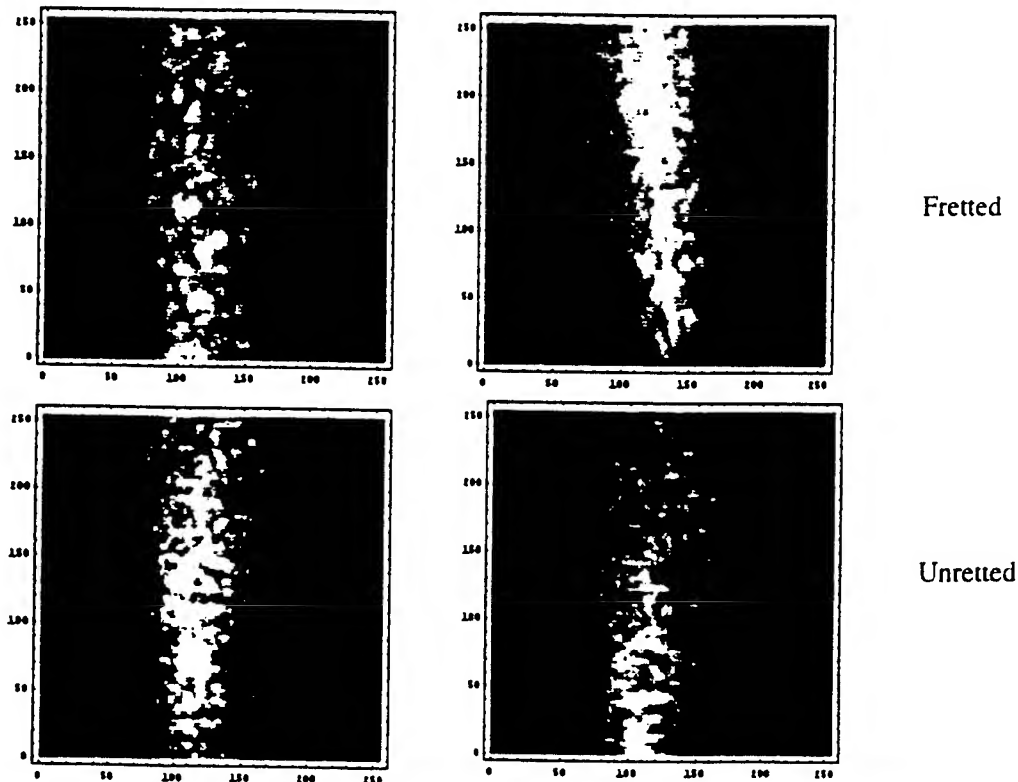


**Figure 17** Typical images obtained from laser beam scattering on fretted (top) and unfretted (bottom) surfaces. Note that some of the images do not capture the entire pattern but only part of it. The effect on this on extracting quantitative information from the images is not known at the present time.

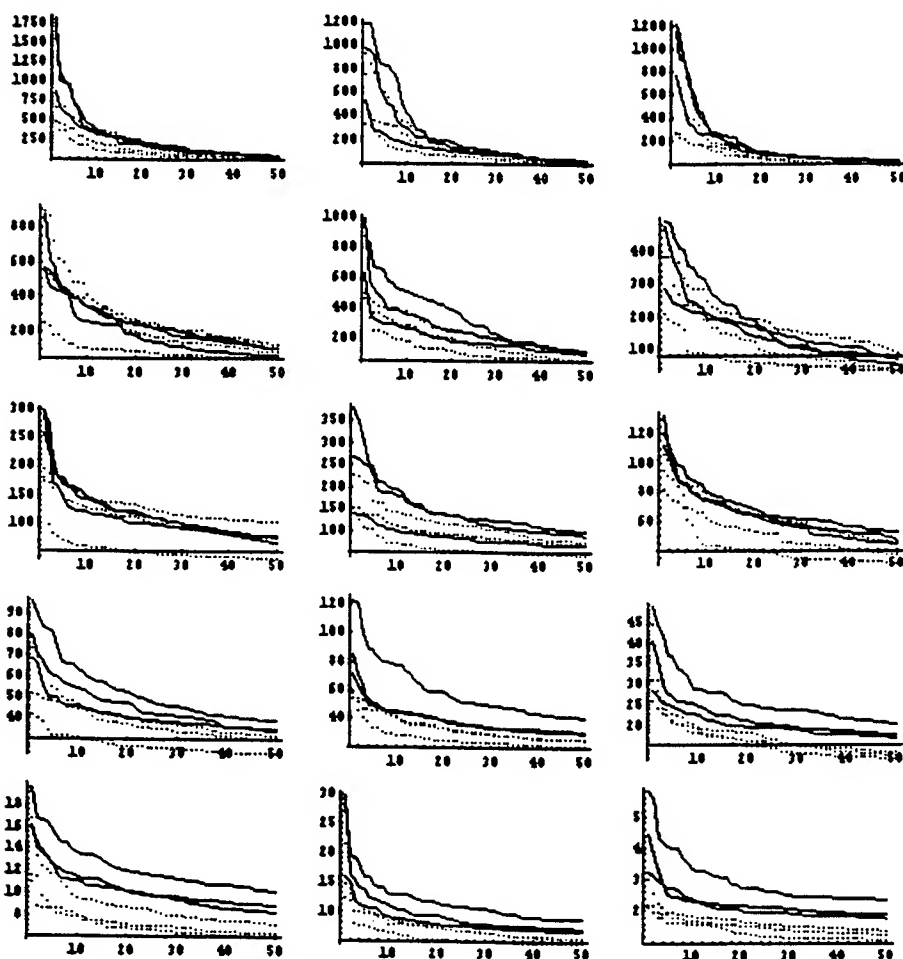


**Figure 18** Plot of wavelet coefficients (50 largest ones for each scale) obtained from images of laser scattering on unfretted surfaces (three dot lines, each corresponding to a separate unfretted surface) and from three images obtained from fretted surfaces (solid lines). The first (left) column of plots show the coefficients from the wavelet transform in the y-direction, the second one from the x, and the third one from the x-y. Scale decreases from top to bottom.

## Conclusions

A "fresh" approach to material characterization (and discrimination) with a solid mathematical background has been examined on an exploratory basis. The potential of the approach has been demonstrated through examination of (apparently) different problems. There is further work to be done until solid conclusions can be made. Yet, the proposed approach should have important consequences on material characterization and relevant properties (e.g. toughness, remaining material/structure life), nondestructive evaluation, statistically based reliability, material modeling, etc. Similarly to the success of wavelets in several fields of physical science, wavelets show to be an effective tool for investigating materials related properties at various scales.

## References

- ARNEODO A., ARGOU F., BARCY E., ELEZGARAY J., FREYSZ E., GRASSEAU G., MUZY J.F. & POULIGNY B., 1992, I. From the transition to chaos to fully developed turbulence; II. Optical wavelet transform of fractal growth phenomena. In *Wavelets and applications*, Y. Meyer (ed.), Masson, Springer-Verlag, Berlin.
- BASDEVANT C., PERRIER V., PHILIPOVITCH T. & DO KHAC M., 1993, Local spectral analysis of turbulent flows using wavelet transforms. In *Vortex flows and related numerical methods*, J.T. Beale et al. (eds.), Kluwer Academic Publishers, The Netherlands, 1-26.
- BENEDETO J.J. & FRAZIER M.W., (Eds.), 1994, *Wavelets, Mathematics and Applications*, CRC Press, Boca Raton, Florida.
- BLODGET M.P., Private communication, June-August, 1997.
- CHUI C.K., et al, 1992, *An introduction to wavelets*, Volume 1, Academic Press, San Diego, Also volumes 2,3,4 & 5, 1992-1995.
- DAUBECHIES I., 1993, Two recent results on wavelets: wavelet basis for the interval, and biorthogonal wavelets diagonalizing the derivative operator, In *Recent Advances in Wavelet Analysis*, L.L. Schumaker & G. Webb (eds.) Academic press. pp 237-257.
- EYLON D., Private communication, July-August, 1997
- FARGE M., 1992, The continuous wavelet transform of two-dimensional turbulent flows. In *Wavelets and their applications*, M. Ruskai et al. (ed.), Jones and Bartlett, Boston.
- FRANTZISKONIS G., 1995, Heterogeneity and implicated surface effects - statistical, fractal formulation and relevant analytical solution, *Acta Mechanica*, 108, 157-178.
- FRANTZISKONIS G. & LORET B., 1995, Scale dependent constitutive relations - information from wavelet analysis and application to localization problems, *A Eur. J. Mechanics A/Solids*, 14, 873-892, 1995.
- GUSTAFSON S., Private communication, July-August, 1997.
- HOUDRE H., Wavelets, probability, and statistics: some bridges, in *Wavelets*, J.J. Benedetto & M.W. Frazier Editors, CRC press, Boca Raton, 1994
- MEYER Y., ed, 1991, *Wavelets and applications*, Masson, Springer Verlag, Paris.
- MEYER Y. & ROQUES S., eds, 1993, *Wavelet analysis and applications*, Editions Frontier Press, Singapore.
- NEUHAUSER H., 1988, The dynamics of slip band formation in single crystals, *Res Mechanica*, 23, 113-135.
- ROKHLIN, S. , Private communication, July-August 1997.
- RUSKAI M.B. et al (eds.), 1992, *Wavelets and their applications*, Jones and Bartlett Publ., Boston.
- WILLIAMS J.R. & AMARATUNGA K., 1993, Hierarchical wavelet representation of geometry, *Proc. 2<sup>nd</sup> Int. Conf. on DEM*, Cambridge, MA, March 1993.
- WILLIAMS J.R. & AMARATUNGA K., 1995, A discrete wavelet transform without edge effects, IESL (MIT) technical report No. 95-02.

SYNTHESIS AND CHARACTERIZATION OF METAL-XANTHIC ACID AND -AMINO  
ACID COMPLEXES USEFUL AS NONLINEAR OPTICAL (NLO) MATERIALS

Zewdu Gebeyehu  
Assistant Professor  
Department of Chemistry

Tuskegee University  
Tuskegee, AL 36088

Final Report for:  
Summer Faculty Research Program  
Wright Laboratory

Sponsored by:  
Air Force Office of Scientific Research  
Wright-Patterson Air Force Base, Dayton, OH

and

Wright Laboratory

August 1997

# SYNTHESIS AND CHARACTERIZATION OF METAL-XANTHIC ACID AND -AMINO ACID COMPLEXES USEFUL AS NONLINEAR OPTICAL (NLO) MATERIALS

Zewdu Gebeyehu  
Assistant Professor  
Department of Chemistry  
Tuskegee University

## Abstract

Several metal complexes of xanthic acid and amino acids were synthesized by the reactions of metal chlorides or acetates with potassium salt of xanthic acid or amino acids. The isolated compounds were characterized by IR-spectroscopy and elemental analysis. The nonlinear optical properties of these complexes were also investigated using Kurtz powder test. The complexes containing the xanthate ligands, namely  $\text{Cd}(\text{S}_2\text{C-O-CHMe}_2)_2$ ,  $\text{Cd}(\text{S}_2\text{C-O-C}_2\text{H}_5)_2$  and  $\text{Pb}(\text{S}_2\text{C-O-CHMe}_2)_2$  were found to show strong second harmonic generation intensities. The other xanthate complexes,  $\text{Zn}(\text{S}_2\text{C-O-CHMe}_2)_2$  and  $\text{Sn}(\text{S}_2\text{C-O-CHMe}_2)_2$ , failed to show SHG signals. On the other hand, the amino acid complexes, Zn-L-carnosine and Cu-L-carnosine, showed no SHG, although L-carnosine is NLO active and contained a chiral center in its molecular backbone. Of all the synthesized complexes, the xanthate complexes of cadmium and lead are identified as promising candidates for frequency doubling.

# SYNTHESIS AND CHARACTERIZATION OF METAL-XANTHIC ACID AND -AMINO ACID COMPLEXES USEFUL AS NONLINEAR OPTICAL (NLO) MATERIALS

Zewdu Gebeyehu

## Introduction

Nonlinear optical materials are of tremendous importance in the fields of telecommunication industries, optical data transmission and processing and new laser technology {1}. As a result of these, the search for new materials exhibiting NLO properties is an active area of research. The synthesis of NLO materials requires a proper molecular engineering because their ease of preparation, crystal growth, damage threshold, mechanical and thermal stability ultimately determine their technological applicability.

Molecules which can crystallize in noncentrosymmetric space group, possessing highly polarizable organic group or those containing conjugated  $\pi$ -system are good candidates to be NLO materials {2-5}. Based on these criteria, we have attempted to synthesize complexes which may have the desired properties of NLO activity, by reacting transition metals or main group metals with thioacid ligands (xanthates) and amino acids. The advantage of incorporating metals to thioacid ligands or amino acids is that it results in high molecular polarization and may aid crystallization in noncentrosymmetric space group, thereby creating the necessary conditions for nonlinear optical activity. Moreover, the synthesis and crystal growth of these compounds are performed in aqueous media or using THF or methanol, which are useful solvents in growing good quality crystals with only minimum cost.

## Experimental

The preparation of all compounds were carried out in air using water as a solvent for the synthesis of metal-thioacid ligand (metal-xanthate) complexes and methanol or water for the metal-amino acid complexes. Crystals of the metal-xanthate complexes were grown from THF. All metal salts  $MX_2$  ( $M = \text{Zn, Cd, Sn, Pb}$ ;  $X = \text{Cl, CH}_3\text{COO}^-$ ) were purchased from Fluka or Aldrich. The xanthic acid potassium salts were prepared by slow addition of  $\text{CS}_2$  to a solution of KOH in the corresponding alcohol. The amino acid, L-Carnosine and L-Arginine were purchased from Aldrich and Kodak respectively. IR-spectra were recorded from 4000 - 400  $\text{cm}^{-1}$  on Perkin-Elmer FTIR spectrometer using KBr. Microanalysis was done in the analytical section of Wright Laboratory. Kurtz method was used to determine NLO activity in Wright Laboratory

using ND: YAG laser (1.06  $\mu\text{m}$ ). The powder of the materials was sieved using sieves ranging from 25 $\mu\text{m}$ -300 $\mu\text{m}$  in mesh size and packed in 1 mm thick optical cells.

### Synthesis of Metal Xanthate Complexes

#### i) Synthesis of cadmium ethyllxanthate

2.50 g (13.63 mmol) of  $\text{CdCl}_2$  was dissolved in 20 mL of water. To this solution, 4.36 g of  $\text{KS}_2\text{C-O-C}_2\text{H}_5$  in 40 mL of water was added drop by drop. A yellowish white precipitate formed immediately, which was filtered, washed three times with water and dried under vacuum. Yield = 4.75 g (98.34%). Elemental Analysis, Calculated(found)% ; C, 20.33 (19.31); H, 2.84 (2.48); S, 36.15 (30.44); Cd, 31.68 (35.60)%

#### ii) Synthesis of cadmium isopropylxanthate

5.50 g (0.03 mol) of  $\text{CdCl}_2$  was dissolved in 50 mL of distilled water. To this solution 10.46 g(0.06 mol) potassium isopropylxanthate in 70 mL of distilled water was added drop by drop while stirring the mixture. A white precipitate started forming immediately. After adding all the isopropylxanthate solution to the cadmium solution, the mixture was stirred for one more hour while heating. The white solid was filtered and washed three times with 15 mL portion of water and dried under vacuum. Yield = 11.47 g (99.98%). Elemental Analysis, Calculated(found)% ; C, 25.10 (25.22); H, 3.66 (3.70); S, 33.47 (29.79); Cd, 29.39 (29.70)%

#### iii) Synthesis of zinc isopropylxanthate

0.35 g (2.57 mmol) of  $\text{ZnCl}_2$  was dissolved in 10 mL of distilled water. 0.89 g (5.14 mmol) of potassium isopropylxanthate was also dissolved in 15 mL of water. The two solutions were mixed slowly while stirring. White precipitate formed immediately. The mixture was heated for one hour on a hot plate. The white solid was filtered and washed three times with 5 mL portion of water and dried under vacuum. Yield = 0.80 g (92.81%).

#### iv) Synthesis of lead isopropylxanthate

7.51 g (19.82 mmol) of  $\text{Pb}(\text{CH}_3\text{COO})_2 \cdot 3\text{H}_2\text{O}$  was dissolved in 75 mL of distilled water. 6.91 g (39.64 mmol) of potassium isopropylxanthate was dissolved in 100 mL water. The two solutions were mixed slowly while stirring. A white-yellowish precipitate formed immediately.



The mixture was digested by heating for one hour and filtered. The solid was washed three times with water (15 mL portion) and dried under vacuum. Yield = 9.38 g (99.26%). Elemental Analysis, Calculated(found)% ; C, 20.12 (20.17); H, 2.93 (2.86); S, 26.82 (23.76); Pb, 43.42 (44.30)%

#### v) Synthesis of tin(II) isopropylxanthate

0.213 g (0.944 mmol)  $\text{SnCl}_2 \cdot 2\text{H}_2\text{O}$  was dissolved in 20 mL of distilled water. 0.329 g (1.89 mmol) potassium isopropylxanthate was dissolved in 25 mL of distilled water. The two solutions were mixed and the mixture was stirred for one hour while heating. The formed yellowish solid was filtered and washed with water several times. Gummy substance formed which was dissolved in acetone and recrystallized as yellow powder by adding water. Yield 0.258 g (70.30%)

### Synthesis of Metal-Amino Acid Complexes

#### i) Synthesis of Zinc-L-Carnosine Complex

1.0 g (4.42 mmol) of L-Carnosine and 0.35 g (8.75 mmol) of NaOH were dissolved in 15 mL of methanol. The sodium hydroxide does not dissolve completely. To this solution, 0.97 g zinc acetate dihydrate,  $\text{Zn}(\text{CH}_3\text{COO})_2 \cdot 2\text{H}_2\text{O}$ , dissolved in 15 mL of methanol was added while stirring the mixture. A white precipitate started forming immediately. The mixture was stirred for two more hours and filtered. The white solid washed three times with 5 mL portions of methanol and dried under vacuum. Yield 1.43 g (72.59%). Elemental Analysis, Calculated(found)% ; C, 35.18 (33.95); H, 4.56 (4.58); N, 18.24(16.48); Zn, 21.17 (18.34)%

#### ii) Synthesis of Copper-L-Carnosine Complex

A solution of 0.45 g (2.0 mmol) of L-Carnosine in 10 mL distilled water was mixed with a solution of 0.034 g (2.0 mmol) of  $\text{CuCl}_2 \cdot 2\text{H}_2\text{O}$  in 5 mL of water at room temperature while stirring. The light blue color of the copper chloride changed to dark blue. The pH of the solution was raised from 4.27 to 11.0 by adding 6.0 M NaOH, and heated on a hot plate at 80°C for about two hours. Violet blue solid started to form. Reducing the volume of the solution by evaporation and cooling to room temperature gave blue powder, which was filtered, washed with acetone and dried in air. Yield 0.34 g

### iii) Reaction of Cadmium acetate with L-Carnosine

0.52 g (2.3 mmol) of L-Carnosine and 0.15 g of NaOH were dissolved in 15 mL methanol. NaOH is partially soluble. To this mixture 0.61 g (2.3 mmol) of  $\text{Cd}(\text{CH}_3\text{COO})_2 \cdot 2\text{H}_2\text{O}$  dissolved in 15 mL of methanol was added and the mixture stirred. A white precipitate formed immediately. The reaction mixture was stirred for two hours and filtered. The IR spectrum of the product showed no peaks associated to L-carnosine, confirming the formed product to be cadmium hydroxide.

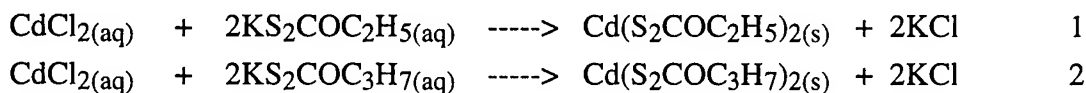
### iv) Reaction of Zinc acetate with L-Arginine

0.51 g (2.88 mmol) L-Arginine and 0.21 g of NaOH were dissolved in 20 mL of distilled water. To this, a solution of 0.63 g (2.88 mmol) zinc acetate in 15 mL of water was added and the mixture stirred for two hours. The formed white precipitate was filtered and characterized by IR-spectroscopy. No bands belonging to L-arginine were observed on the IR-spectrum.

## Results and Discussion

### i) Cadmium Xanthate

Both cadmium ethylxanthate,  $\text{Cd}(\text{S}_2\text{COC}_2\text{H}_5)_2$ , and cadmium isopropylxanthate,  $\text{Cd}(\text{S}_2\text{COC}_3\text{H}_7)_2$  were prepared by the reaction of  $\text{CdCl}_2$  and the corresponding potassium xanthate in aqueous solution in 1:2 molar ratios as shown in equations 1 and 2.



In both reactions, a yellowish-white precipitate forms mostly, although a white precipitate has been isolated for the second reaction. The yellowish color may be due to presence of small amounts of dioxanthogens, arising from oxidation of the xanthate ion during the reactions. The isolated compounds are insoluble in most organic solvents.  $\text{Cd}(\text{S}_2\text{COC}_2\text{H}_5)_2$  dissolves little in THF, from which crystal growth was possible. However,  $\text{Cd}(\text{S}_2\text{COC}_3\text{H}_7)_2$  dissolves very well in THF, and it was possible to grow x-ray quality crystals from this solution.  $\text{Cd}(\text{S}_2\text{COC}_3\text{H}_7)_2$  also dissolves in acetone in small quantity. The difference in solubility between the two cadmium xanthates is due to branching of the carbon chain in  $\text{Cd}(\text{S}_2\text{COC}_3\text{H}_7)_2$ .

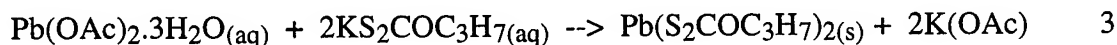
The compounds isolated were characterized by elemental analysis and IR-spectroscopy. The results of elemental analysis for both compounds show good agreement between the calculated and found value for carbon and hydrogen. However, the results obtained for sulfur and cadmium are slightly different from what was calculated. The difference may be due to mutual interference of the two elements during analysis.

The IR-spectra of both  $\text{Cd}(\text{S}_2\text{COC}_2\text{H}_5)_2$  and  $\text{Cd}(\text{S}_2\text{COC}_3\text{H}_7)_2$  are rich in bands due to various modes of vibrations of the xanthate ligands. The spectra are shown in Fig. 1 and Fig. 2. The IR-spectrum of  $\text{Cd}(\text{S}_2\text{COC}_2\text{H}_5)_2$  shows three very strong bands at 1195, 1122 and 1045  $\text{cm}^{-1}$  corresponding to chelating xanthate group. Similarly the spectrum of  $\text{Cd}(\text{S}_2\text{COC}_3\text{H}_7)_2$  shows very strong bands at 1210, 1093, and 1024  $\text{cm}^{-1}$  also due to chelating xanthate ligand. Unlike the spectrum of  $\text{Cd}(\text{S}_2\text{COC}_2\text{H}_5)_2$ , a medium band at 1144  $\text{cm}^{-1}$  is observed in the spectrum of  $\text{Cd}(\text{S}_2\text{COC}_3\text{H}_7)_2$  which may be due to increased carbon chain. Table 1 shows the vibrational frequency assignments for some of the bands observed in the IR-spectra of these two and other similar complexes.

The nonlinear optical (NLO) properties of both  $\text{Cd}(\text{S}_2\text{COC}_2\text{H}_5)_2$  and  $\text{Cd}(\text{S}_2\text{COC}_3\text{H}_7)_2$  were studied by Kurtz method. Both are found to be NLO active.

## ii) Lead isopropylxanthate

The reaction of aqueous solutions of lead acetate and potassium isopropylxanthate in 1:2 molar ratio gave yellowish-white precipitate in quantitative yield.



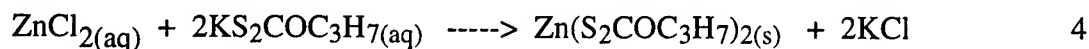
The isolated product is very well soluble in THF, benzene, and little soluble in acetone. It is insoluble in water, toluene, methylene chloride and hexane. Attempts to obtain x-ray quality crystals from the solvents in which it dissolves is not successful, despite trying different techniques of crystallization.

The compound was characterized by elemental analysis and IR-spectroscopy. The IR-spectrum shows three very strong bands between 1250 - 1000  $\text{cm}^{-1}$ , which are characteristics of chelating xanthate ligands. The IR-spectrum is shown in Fig. 3 and assignments of bands in table 1.

The NLO property of the compound was studied by Kurtz method. It showed a strong second harmonic generation (SHG) intensity.

### iii) Zinc isopropylxanthates

Aqueous solutions of the zinc chlorides and two equivalents of potassium isopropylxanthate reacted giving a white precipitate immediately.



The reaction product is insoluble in water, toluene and hexane, but soluble in  $\text{CH}_2\text{Cl}_2$  and THF. The compound was characterized by IR-spectroscopy (table 1) and tested for its NLO activity. It failed to show NLO activity.

### iv) Tin isopropylxanthate

The reaction of  $\text{SnCl}_2 \cdot 2\text{H}_2\text{O}$  with  $\text{KS}_2\text{COC}_3\text{H}_7$  in 1:2 molar ratio, gave a yellow gummy product which was insoluble in water. Dissolving the gummy substance in acetone and then adding water gave yellow-brown powder. The IR-spectrum of the powder (Fig. 4) confirms the formation of tin isopropylxanthate. The compound was tested for its NLO activity by powder test. It showed no SHG.

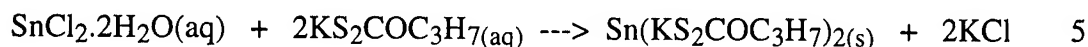


Table 1. Assignment of some absorption bands of metal xanthates ( $\text{cm}^{-1}$ ) {6}

$\text{Cd}(\text{EtXan})_2$	$\text{Cd}(\text{iPrXan})_2$	$\text{Pb}(\text{iPrXan})_2$	$\text{Sn}(\text{iPrXan})_2$	$\text{Zn}(\text{iPrXan})_2$	Assignment
2985s	2978s	2976s	2977s	2978s	$\nu(\text{CH}_3)$
1438vs	1458s	1463s	1460vs	1465vs	$\delta(\text{CH}_3)$
1391m	--	--	--	--	$\delta(\text{CH}_2)$
1365m	1372s	1370s	1371s	1371s	$\delta(\text{CH}_3)$
1195vs	1210vs	1211vs	1223vs	broad	$\nu(\text{C}_1\text{-O})$
1122vs	1092vs	1093vs	1086vs	--	$\nu(\text{C}_2\text{-O})$
1045vs	1024vs	1016vs	1027vs	--	$\nu(\text{C}=\text{S})$
860m	905s	898m	900s	900s	$\nu(\text{C}-\text{C})$
817m	821m	813m	815m	808s	$\delta(\text{CH}_3)$
659m	652s	644w	640w	650s	$\nu(\text{C}-\text{S})$
450s	468s	466s	465m	466vs	$\nu(\text{C-O-C})$

## Metal-Amino Acid Complexes

The reactions of equimolar quantities of metal salts ( $\text{MX}_2$ ,  $\text{M} = \text{Zn, Cu, Cd}$ ;  $\text{X} = \text{Cl, CH}_3\text{OO}^-$ ) in methanol or water with a mixture of L-carnosine and sodium hydroxide gave different products.  $\text{Zn}(\text{CH}_3\text{OO})_2 \cdot 2\text{H}_2\text{O}$  reacted very well with L-carnosine in the presence of NaOH giving a white crystalline product, whose IR-spectrum is rich in bands from L-carnosine. The analytical result of the compound is consistent to  $[\text{Zn}(\text{L-carnosine})](\text{OAc})_2 \cdot 2\text{H}_2\text{O}$ . Similarly the deep blue product obtained from the reaction of  $\text{CuCl}_2 \cdot 2\text{H}_2\text{O}$  and L-carnosine was characterized to be the Cu-L-carnosine complex by IR-spectrum and elemental analysis. However, the product isolated from the reaction of  $\text{Cd}(\text{OAc})_2 \cdot 2\text{H}_2\text{O}$  and L-carnosine did not give the cadmium-L-carnosine complex. This could be concluded from the IR-spectrum, which does not show the bands associated to L-carnosine. Similarly the reaction of L-arginine with the above metal salts was investigated using the same or modified procedures. Despite all attempts, it was not possible to obtain a product which could be characterized.

The isolated metal-L-carnosine complexes were investigated for their NLO properties. Both the zinc and copper complexes failed to show NLO response, although L-carnosine itself is an active NLO material.

## Conclusion

In this research, several metal-xanthate and metal-amino acid complexes were synthesized, characterized and their NLO properties investigated. Only cadmium and lead xanthate were found to demonstrate good optical frequency conversion.

## References

1. Williams, D. J. Angew. Chem. Int. Engl.. 1984, 23, 690-703.
2. Hann, R. A., Bloor, D. Eds. Organic Materials for Nonlinear Optics: Royal Society of Chemistry: London, 1989.
3. Chemla, D. S. Zyss, J. Eds. Nonlinear Optical Properties of Organic Molecules and Crystals; Academic Press: Orlando, 1987; Vols. 1 and 2.
4. Williams, D. J., Ed. Nonlinear Optical Properties of Organic and Polymeric Materials; ACS Symposium Series 233; American Chemical Society: Washington, DC, 1983.
5. Polague, T. P.; Stoner, T. C.; Dallinger, R. F.; Gilbert, T. M.; Hopkins, M. D. J. Am. Chem. Soc. 1991, 113, 703-704.
6. Rao, S. R., 'Xanthates and Related Compounds' Marcel Dekker, New York, 1971.

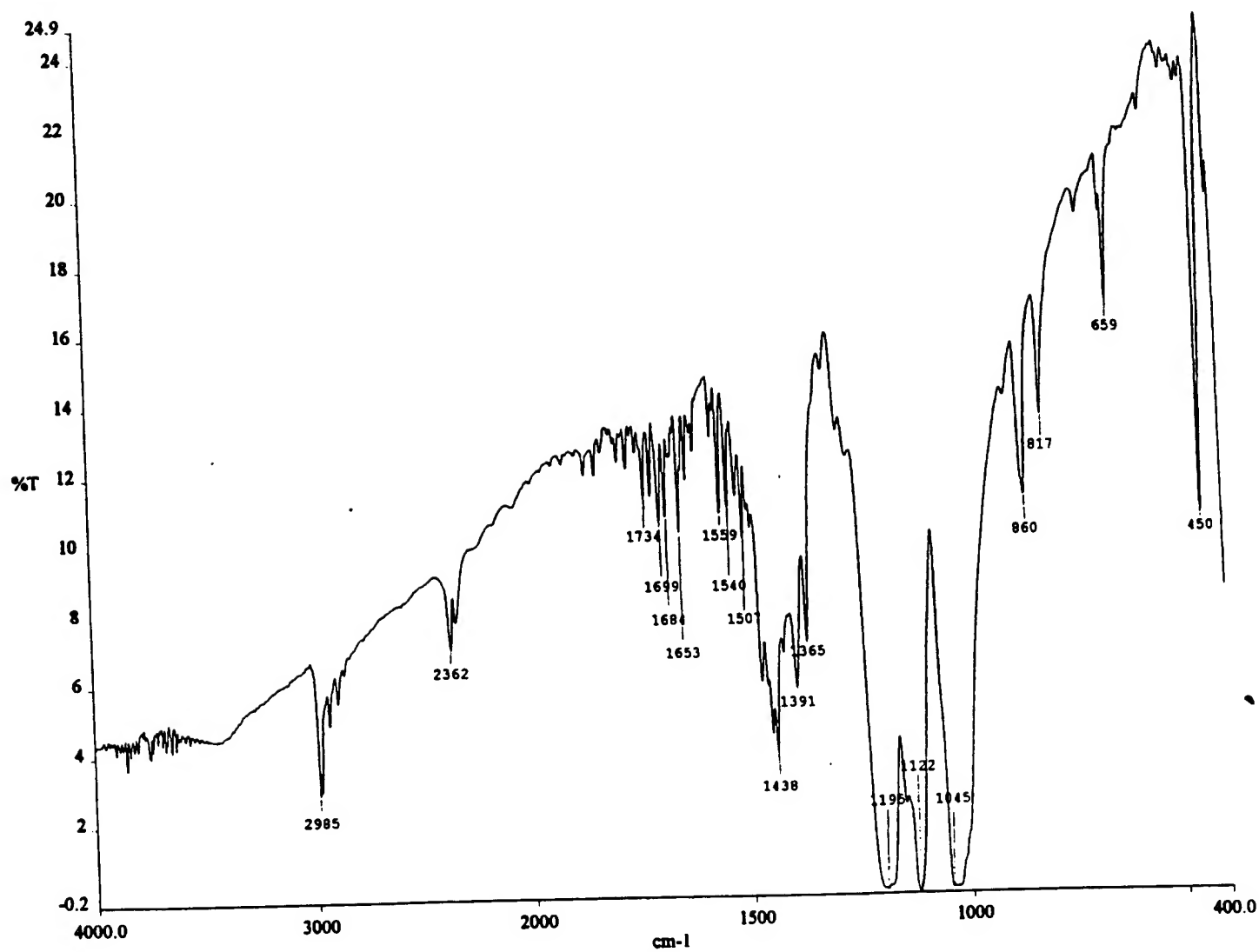


Fig. 1. IR-spectrum of  $\text{Cd}(\text{S}_2\text{COC}_2\text{H}_5)_2$

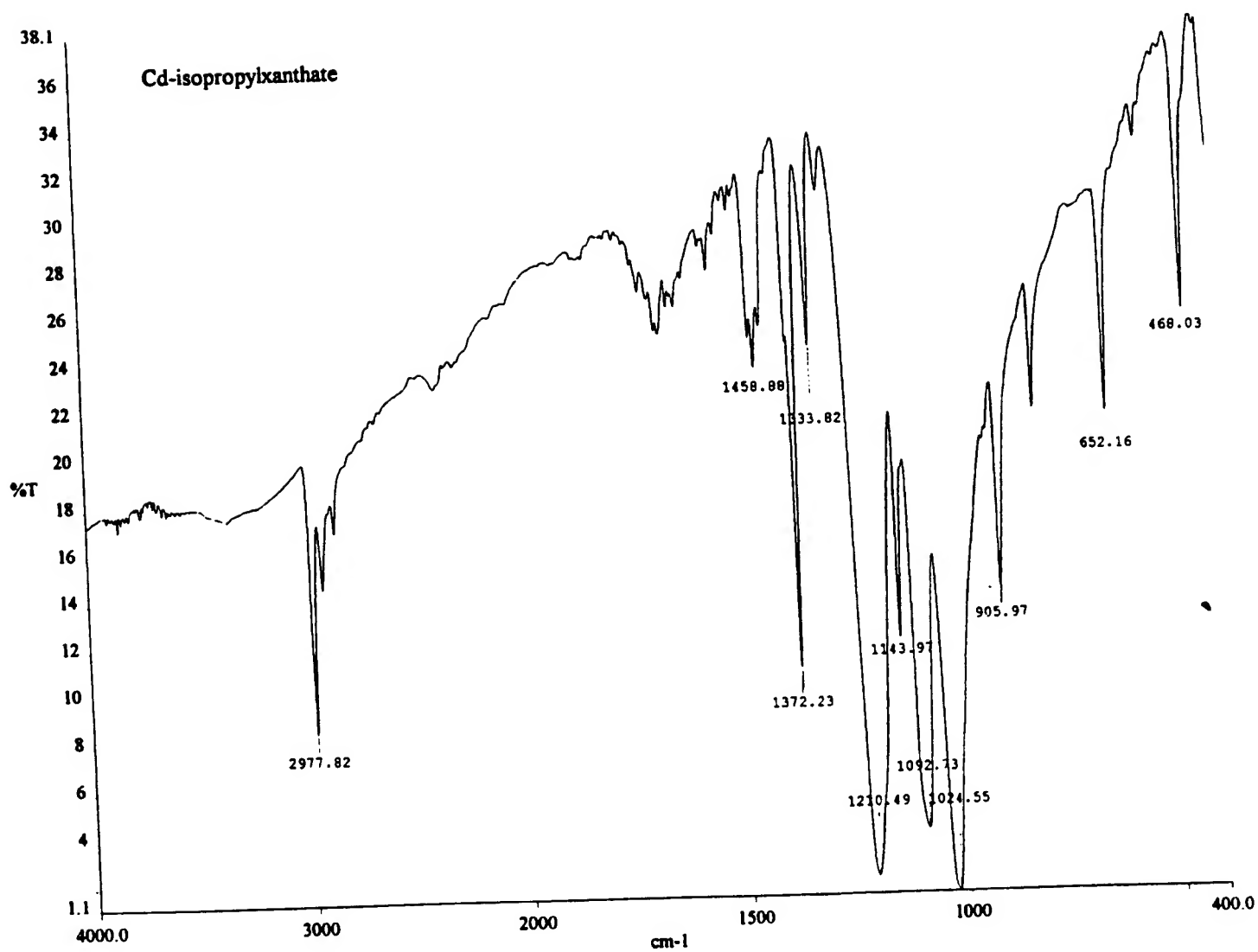


Fig. 2. IR-spectrum of  $\text{Cd}(\text{S}_2\text{COC}_3\text{H}_7)_2$

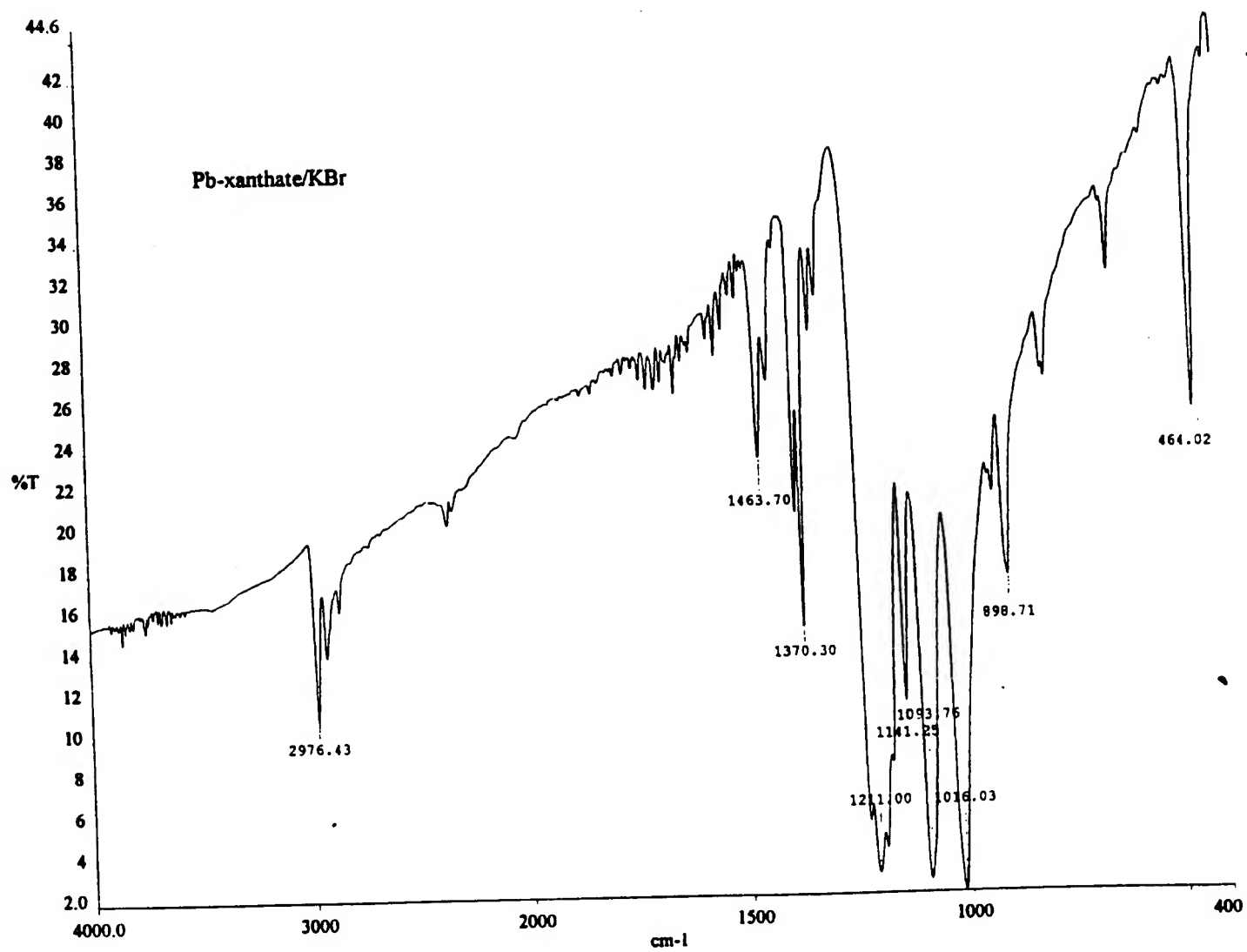


Fig.3. IR-spectrum of  $\text{Pb}(\text{S}_2\text{COC}_3\text{H}_7)_2$



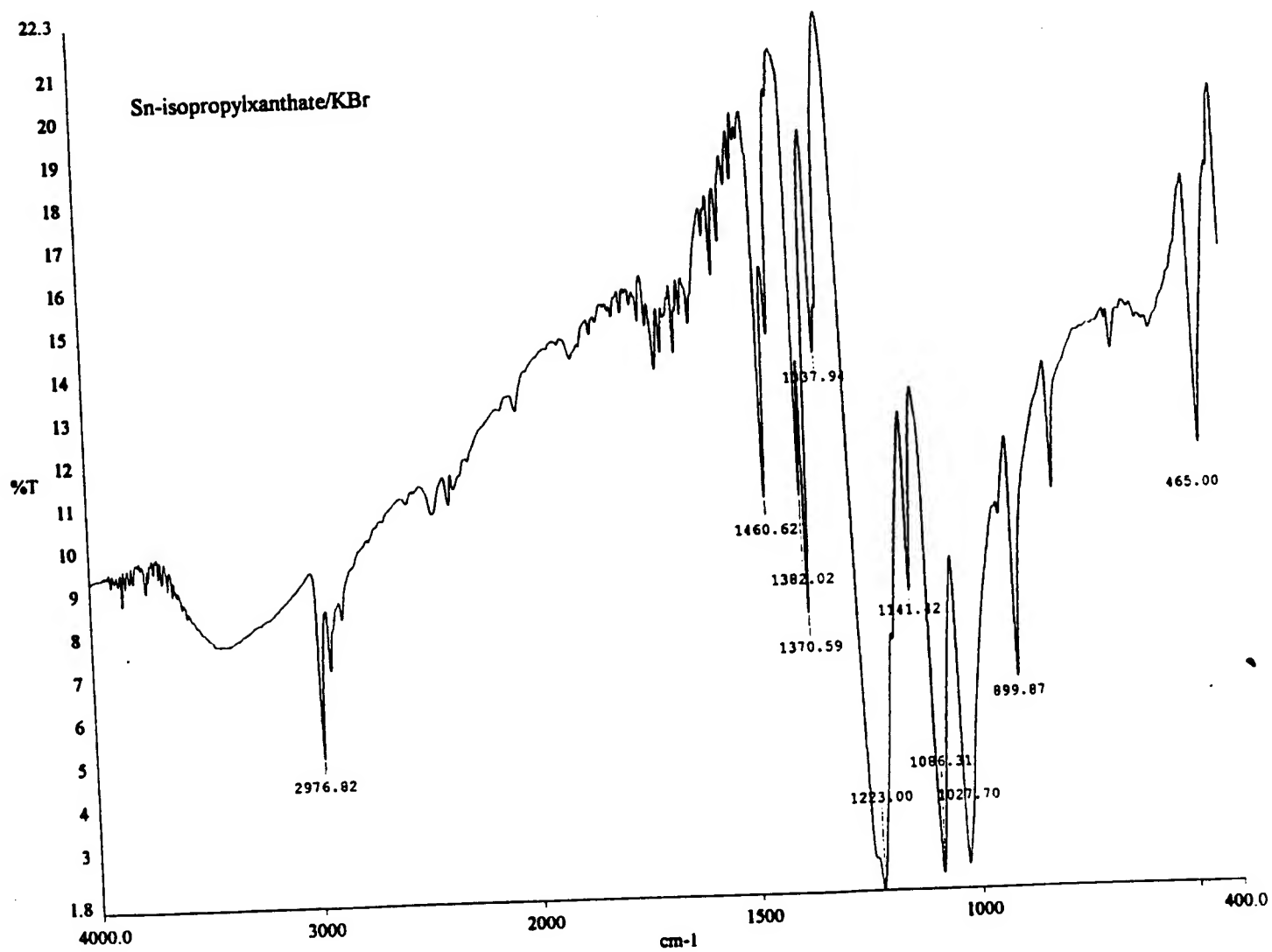


Fig. 4. IR-spectrum of  $\text{Sn}(\text{S}_2\text{COC}_3\text{H}_7)_2$

# **REDUCTION AND ANALYSIS OF LDV AND ANALOG RAW DATA**

**Dr. Richard D. Gould**  
**Professor**  
**Department of Mechanical and Aerospace Engineering**

**North Carolina State University**  
**Campus Box 7910**  
**Raleigh, NC 27695**

**Final Report for:**  
**Summer Faculty Research Program**  
**Wright Laboratory**

**Sponsored by:**  
**Air Force Office of Scientific Research**  
**Bolling Air Force Base, Washington, DC**

**And**

**Wright Laboratory**

**August 1997**

# **REDUCTION AND ANALYSIS OF LDV AND ANALOG RAW DATA**

Dr. Richard D. Gould  
Mechanical and Aerospace Engineering  
North Carolina State University  
Raleigh, NC 27695

## **ABSTRACT**

The laser Doppler Velocimeter (LDV) data analysis software used by the experimental research branch at Wright Laboratory (WL/POPT) was found to be deficient in some ways. Two new LDV data analysis software programs were developed to resolve these deficiencies. The programs named PACE2ASC and PACESTAT were written in the FORTRAN language so that they could be easily modified and recompiled at WL/POPT. Both programs read TSI PACE 1.2 acquired raw laser Doppler velocimetry files. This task first requires decoding the header information file produced by the LDV software; a task that was made extremely difficult because the header portion of the data file is of variable length. The header file length depends on the file name length, user input parameter name lengths, the number of "C" words recorded and the number of data windows selected by the RMR hardware. Once the header file is decoded the raw LDV and analog data words can be converted to velocities and signal levels. The first program, PACE2ASC, reads the TSI PACE 1.2 raw data files and writes the velocities, time between data word, RMR time word and the analog "C" words to a formatted ASCII file having the same family name as the raw data file but with the ASC extension. This program can batch process up to 10000 files at one time. The second program, PACESTAT, reads the TSI PACE 1.2 raw data files and calculates turbulence statistics up to the third moment for mixed turbulence quantities and up to the fourth moment for homogeneous turbulence quantities for up to three velocity components. A batch processing capability has been included so that up to 10000 files can be processed during each execution. A menu screen allows the user to select various run time options. In addition, it constructs and prints automatically scaled histograms of velocity PDFs with a labeled summary table of all pertinent information. These histograms and summaries can be formatted to print as an ASCII file, a postscript file or a Hewlett Packard PCL 5 file. Turbulence statistics are written to three formatted data files for later use by plotting routines or analysis programs. These statistics can be normalized with a constant reference velocity or can be normalized with different reference velocity for each data point processed during the batch job by reading a user created file which contains the reference velocities for each data point. Prior to calculating the turbulence statistics, data points lying outside of  $\pm 3$  standard deviations are discarded. This default value of 3 can be overridden by the user at run time. The program allows for three velocity bias corrections, allows for non-orthogonal laser beam angle correction, and calculates the statistical uncertainties for all quantities using the jackknife method. Lastly, the user can override the fringe spacing, frequency shift and laser wavelength in the raw data files by reading a user created file which contains the correct values for these parameters. The source code was delivered to the scientists at WL/POPT.

# **REDUCTION AND ANALYSIS OF LDV AND ANALOG RAW DATA**

Dr. Richard D. Gould

## **1. INTRODUCTION**

The purpose of this proposed research was to develop software which can be used to analyze the raw laser Doppler velocimeter (LDV) data and analog data obtained using a Thermal Systems Incorporated (TSI) IFA750 signal processor with the DL 100 DataLink Multichannel Interface and a Rotating Machinery Resolver (RMR) module. The software is necessary to provide additional important turbulence statistics and other capabilities not found in the standard TSI PACE 1.2 data acquisition and analysis software package which is shipped with the IFA 750 signal processor.

The new software, named PACESTAT, has all the capabilities of the TSI PACE 1.2 software including the ability to analyze up to three velocity components, with time between data and residence time data if these options were selected at data acquisition time, and will calculate all the standard turbulence statistics (i.e. mean velocities, standard deviation, Reynolds stresses, turbulent triple products). In addition, up to 10000 files can be analyzed at one time using the batch processing capability of this new program. A menu screen allows the user to select various run time options. Auto-scaled histograms and formatted and fully labeled summary tables are created for each data point and are formatted for one, two or three-component velocity measurements with this program. These histograms and summaries can be formatted to print as an ASCII file, a postscript file or a Hewlett Packard PCL 5 file. High and low pass data filtering based on user selected number of standard deviations is also included. The number of discarded points and revised turbulence statistics are calculated with this option. Three velocity bias correction methods, the McLaughlin-Tiederman correction, the residence time correction and the time between data correction, were included as options in this new software. Lastly, the capability to override the default fringe spacing, frequency shift and laser wavelength is also possible with this software.

This software was developed to be portable so it can be run on the UNIX based workstations and mini-computers at Wright Laboratory in the Advanced Propulsion and Power Directorate (WL/POPT) and also on Intel processor based personal computers. A modular approach was used so that subsequent modification can be accomplished easily. The fully commented FORTRAN source code consisting of one main program, 30 subroutines and 5

function programs, totaling more than 5000 lines of code, was provided to WL/POPT so that future additions and modifications can be performed. A report describing the features of this code has been given to the people at WL/POPT.

The program PACE2ASC, which contains one main program, 8 subroutines and 5 function calls totaling 1202 lines of code, will be described in more below as has the same "front end" subroutines as the PACESTAT code does, and only lacks the statistical, histogram graphics, and printing subroutines which have been described in an earlier report.

## 2. PROGRAM STRUCTURE

A modular program structure with one main calling program, named PACE2ASC, was selected for this project. The FORTRAN source code listing of the main program, showing this structure, is given in the Appendix. A flow chart of the main program is given below in Figure 1. A named common block structure was used to "pass" variables between subroutines instead of passing the variables directly between the calling program and the various subroutines using an argument. This method was selected to save memory allocation space for the "passed" variables and also allows all the subprograms which include the declared named common block access to the variables and control over their values. If variables were passed in an argument list in a subroutine call they would need to be dimensioned in both the calling program and the subroutine. This requires twice the memory space for variable storage than is required using common blocks. Ten descriptive, named common blocks were defined, instead of one large common block holding all the variables, so that only the required named common blocks for each subroutine need to be declared. It is believed that this structure makes the program more readable. A list of all the named common blocks used in PACE2ASC is given below.

```

common /ldvdat/ u(10240),v(10240),w(10240),ttu(10240),ttv(10240)
&               ,ttw(10240),c1(10240),c2(10240),curtime(10240)
&               ,c0(10240),dpoints
common /ldvset/ df1,df2,df3,fs1,fs2,fs3,wlen1,wlen2,wlen3,del,eps
&               ,scfac(5),coefk(5),coefa(5),coefb(5),coefc(5)
&               ,coefd(5),atodi(5)
common /processor/ nowpdp,tnowpdp,headbyte,c,nokdp,numctr,ctype1
&               ,ctype2,ctype3,rnr,samptim,coinwind,mode,tbd
&               ,ttime,axis,trans
common /tmatrix/ a11,a12,a13,a21,a22,a23,a31,a32,a33
common /files/ nmlen,sfname,efname,fnamein

```

## PACEASC PROGRAM FLOW CHART

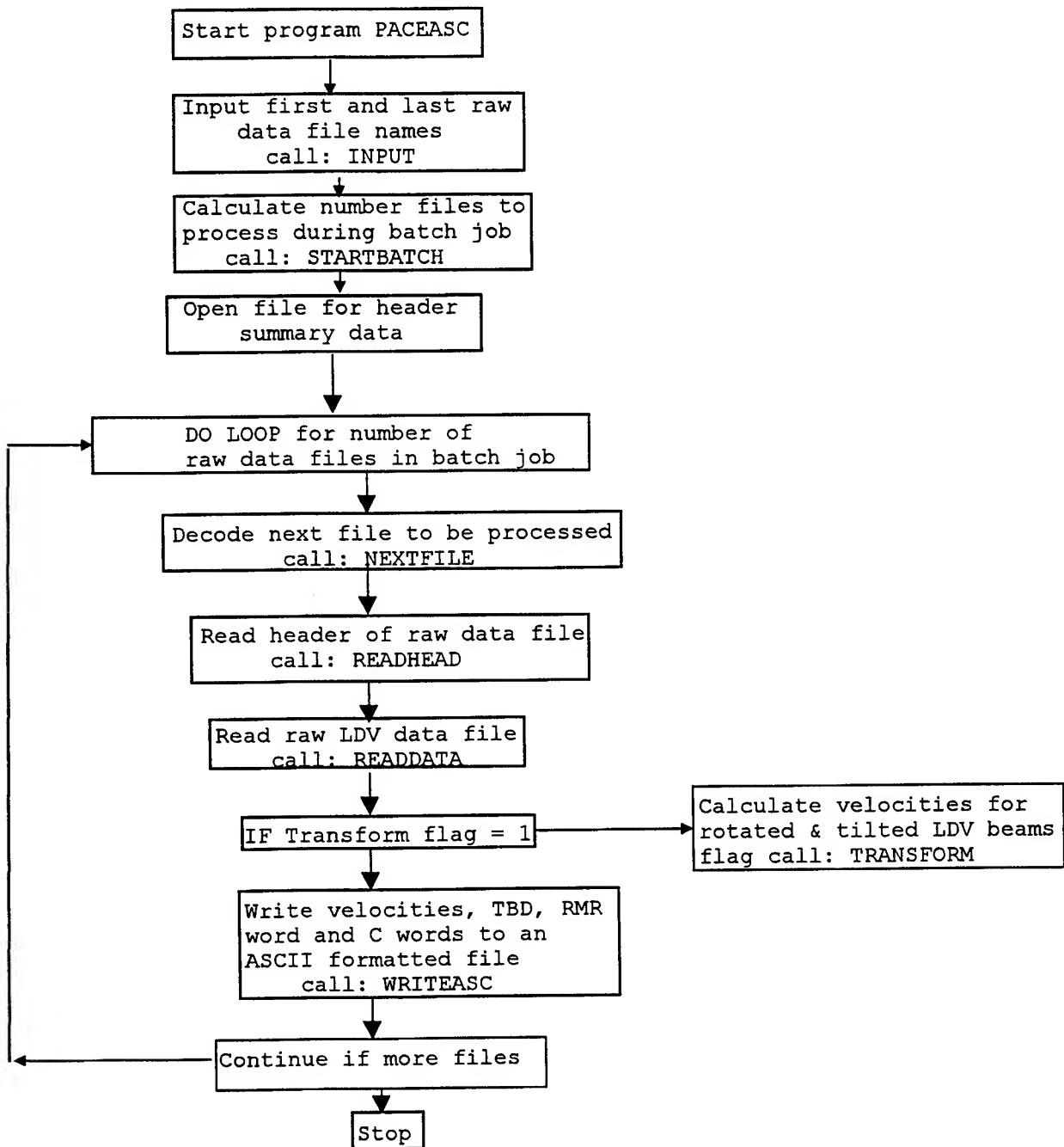


Figure 1. Flow chart of program PACEASC.

Four files are opened, assigned file names and closed during program execution. A summary table of file allocation is given below. Note that the name “family” in the file names below is replaced during program execution with the actual family name that was assigned to the raw data files being analyzed.

Table 1. File allocation.

Unit number	File name	Opening subroutine	Closing subroutine	Read or write	File type
1	Family.RAW	Readdata	Readdata	Read	direct
2	Family.ASC	Writeasc	Writeasc	Read	sequential
7	Family.SUM	Program Pace2asc	Program Pace2asc	Write	sequential
9	Family.RAW	Nextfile	Readheader	Read	sequential

### 3. SUBROUTINE DESCRIPTIONS

A brief description of all the subroutines and function programs contained in this data analysis program are given below.

#### Subroutine INPUT

Subroutine prints header to screen and queries user for the name of the starting and ending TSI PACE 1.2 generated raw data files. An example of this screen is given in Figure 2.

```

*****
*   Program reads TSI PACE acquired raw laser Doppler velocimetry   *
*   files, writes the header information of all the processed files   *
*   to a summary file and produces an ASCII file of the velocity,    *
*   time between data, and C word values (1 for each raw data file)  *
*   The ASCII data file has the same family name as the raw data     *
*   file but has an .ASC extension. Either single or batch file     *
*   processing is possible                                           *
*                                                                      *
*   Developed by: Richard D. Gould                                   *
*               Sept. 26, 1997                                       *
*               version 1.0, All rights reserved by author          *
*****

Enter first file to be processed(JUNK0000.RAW) hot0001.raw
Enter the last file to be processed(JUNK0013.RAW) hot0013.raw

```

```
13 files will be processed during batch job!
    starting with : hot0001.raw
    ending with :   hot0013.raw

A summary of the header values will be stored in file : hot0001.SUM
ASCII data files having an .ASC extension and the same family name,
one for each file, for example - hot0001.ASC will be produced

Should we continue batch job using these files?(y/[n]) y
```

Figure 2. Screen produced by subroutines INPUT AND STARTBATCH.

### **Subroutine STARTBATCH**

Subroutine decodes the starting and ending file names and determines how many files are to be processed during current execution of the program. The histograms and statistics of all the files processed during this batch job will be included in the output files. Start and end file numbers and number of files are passed back to calling program. Figure 2 shows the screen produced by this subroutine for an example where HOT0001.RAW is the first raw data file and HOT0013.RAW is the last raw data file to process during this batch job.

### **Subroutine NEXTFILE**

Subroutine encodes the integer file number in the batch process DO LOOP into the character string in the extension name of the next raw data file to be processed during batch job. Once the file name is determined it is opened as unit 9. The current file number and raw data file name in the batch job is written to screen so that the user can monitor progress.

### **Subroutine READHEADER**

Subroutine reads the header of each TSI PACE 1.2 raw data file according to the documentation given in the File Formats chapter of the TSI FIND for Windows software manual. The header contains a variable number of lines each of which can contain a variable number of characters. This made decoding the header file much more difficult than if the header was of constant length as was the case when using the older TSI FIND version 4.0 software. In any case, subroutine READHEADER was developed to handle this variable size header format and operates correctly for the 20 or so test case header files used in its development. The important variables read from the header are listed below in Table 2. The program listing for this subroutine is given in the Appendix.



Table 2. LDV and signal processor settings.

Variable name	Description
mode	1 = random, 2 = coincidence
numctr	number of signal processors
tbd	1 = on, 2 = off, 3 = even time
onaxis	Not used in PACE 1.2 software
nokdp	number of kilo data points
ttime	transit time: 1 = on, 2 = off
ctype1-3	processor type: 1=1990,2=1980,3=ifa550,4=ifa750
fd1, fd2, fd3	fringe spacing (nanometers)
fs1, fs2, fs3	frequency shift (MHz)
wlen1, wlen2, wlen3	wavelength (micrometers)
x, y, z	Position
coinwind	coincidence window(microseconds)
samptim	even time(microseconds)
c	Number of c words
rmr	1 = on, 2 = off
Numwin	Number of rmr windows
trans	1 = on, 0 off (transformation matrix flag)
del, eps	rotation about z and tilt about x angles(not used)

### **Subroutine READDATA**

Subroutine uses a calculation made in READHEADER to determines the total number of words transferred (i.e. tnowpdp) with each LDV realization based on number of signal processors, mode of operation and, whether the time between data word or transit time words are transferred, whether RMR is enabled and the number of C word analog channels that are used. Once the number of words per realization is found this subroutine reads the raw data file in this word order sequence. In order to speed the processing the raw data file is read as a single record. This requires knowledge of the total number of bytes in the raw data file which is found by knowing the header size (calculated in subroutine READHEADER) and the number of data points and the number of words with each data realization. In order to facilitate the variable length header a dynamic array was defined to hold the entire raw data file as one record. This requires using an ALLOCATE command of the Microsoft FORTRAN Powerstation compiler to dimension this array at run time instead of statically at program startup. Note that defining dynamic arrays is compiler dependent and thus the syntax may have to be changed to that of the compiler being used. The program listing for this subroutine is given in the Appendix.

## Subroutine TRANSFORM

Subroutine calculates the velocities when the beams are rotated or tilted relative to the laboratory coordinate system using the transformation coefficient matrix. These nine matrix elements are obtained from the header of the raw data file. When TRANS = 1 transformation is enabled.

### 4. SAMPLE OUTPUT

The summary of the header file, HOT0001.SUM, produced by this program looks like:

```
nokdp      mode      tbd      ttime      numctr ctype3 ctype2 ctype1
 10000      2         1         2         3         4         4         4
Coin window =      20.0 us Equal time sample interval =      1000.0 us
      fringe spc      freq shift      wavelength
channel 1      1.9020      40.0000      .5145
channel 2      -1.8054      40.0000      .4880
channel 3      4.5310      40.0000      .6328
number of c words = 2
      a/d      scale      K      A      B      C      D
cword 0      0      .0024      .0000      1.0000      .0000      .0000      .0000
cword 1      0      .0024      .0000      2.0620      .0000      .0000      .0000
cword 2      1      .0024      .0000      1.0000      .0000      .0000      .0000
RMR flag = 1      Number of RMR windows = 1
      start angle      stop angle
window 0      .0000      .1000
x =      1.000000 y =      -1.500000 z =      .000000
del =      .000000 eps =      .000000
transformation matrix enable flag (0-off, 1-on) = 1
A11 =      .707100 A12 =      .707100 A13 =      .000000
A21 =     -.707100 A22 =      .707100 A23 =      .000000
A31 =      .000000 A32 =      .000000 A33 =      1.000000
nowpdp= 7 c= 2 rmr= 1 tnowpdp=11
header bytes = 4001
```

The first 11 lines of the output ASCII file, HOT0001.ASC, looks like:

```
dpoint  channel 3  channel 2  channel 1  tbd(us)  rmr  cword 1  cword 2
 1  32.521875  -0.529364  1.114395      0    17  1.06707  9.93975
 2  18.948417  -1.130842  -2.873699     6927 1188  1.79187  9.98613
 3  30.982659  2.694894  1.420704     13870 2360 -2.70290  9.98369
 4  36.062170  -.467116  2.294192     20181 3369  .50333  9.96660
 5  24.318448  .773312  -1.991662     32749 1973 -2.27004  9.97881
 6  38.748275  .794269  -.190580     38778 2969 -1.77677  9.93731
 7  31.133275  1.080833  1.484648     99482 2605 -2.59217  9.99101
 8  33.395304  3.195963  -3.262935     99607 2625 -2.52674  9.98125
 9  33.278926  -.156375  .910760     104766 46  1.09727  9.93487
10  29.446836  .486236  .504850     146633 68  1.12244  9.89581
```

Note that these values have been validated by comparing them to the velocities, tbd, rmr and cword values produced by the TSI PACE 1.2 software. Thus all the conversion routines have

been validated. The advantage of using this code however is that you do not have to be in the PACE program to convert the files and you get a format that you can control.

## APPENDIX

```

program pace2asc
c
c*****
c    Program reads TSI PACE 1.2 acquired raw laser Doppler velocimetry
c    files and writes velocities, the time between data words, the RMR
c    word and two "C" words to a formatted ASCII file having the same
c    family name as the raw data file but with an ASC extension. Since
c    all of the data are placed in arrays with this code a user can
c    easily modify this code to whatever he/she wishes with the data.
c    A batch file processing algorithm is included.
c
c    Developed by: Richard D. Gould
c                Sept. 26, 1997
c                version 1.0, All rights reserved by author
c*****
c
c    real*4 coinwind,samptim
c    integer*4 nokdp,c,nowpdp,tnowpdp,headbyte
c    integer*2 numctr,ctype1,ctype2,ctype3,nmlen,rmr,trans
c    integer*2 nstart,nend,numfil,jfile,ifile
c    character*12 sfname,efname,fnamein
c    character*1 mode,tbd,ttime,axis
c    character*1 in
c
c    common /processor/ nowpdp,tnowpdp,headbyte,c,nokdp,numctr,ctype1
c    &                    ,ctype2,ctype3,rmr,samptim,coinwind,mode,tbd
c    &                    ,ttime,axis,trans
c    common /files/ nmlen,sfname,efname,fnamein
c
c    call input
c    call startbatch(nstart,nend,numfil,in)
c    if(in .eq. 'y') go to 1
c    if(in .eq. 'Y') go to 1
c    go to 900
1 ifile=0
  open(UNIT=7,file=sfname(1:nmlen)//'.SUM',access='sequential'
  &,status='unknown')
  do 1000 jfile=nstart,nend
    call nextfile(jfile,ifile)
    call readheader
    call readdata
    if(trans .eq. 1) call transform
    call writeasc
1000 continue
c
  close(7)
900 stop
end

```

```

subroutine readheader
c
c*****
c      Subroutine reads the header of each TSI PACE ver. 1.2 raw data file
c      according to the documentation given in the Appendix of the
c      TSI PACE/FIND software manual (Version 1.2). See PACE/FIND manual
c      for more details. TSI stands for Thermal Systems Incorporated.
c
c      Called by: Program readpace
c      Calls: function atoi20 and function atof20
c
c
c      Modified by: Richard D. Gould
c                  Sept. 26, 1997
c                  version 1.0, All rights reserved by author
c*****
c
  real*4  atof20,df1,df2,df3,fs1,fs2,fs3,wlen1,wlen2,wlen3,del,eps
&        ,x,y,z,coinwind,samptim,fs_table(17),scfac
&        ,coefk,coefa,coefb,coefc,coefd
&        ,ang1(4),ang2(4),cfs1,cfs2,cfs3,a11,a12,a13,a21,a22,a23
&        ,a31,a32,a33
  integer*4 nokdp,c,nowpdp,tnowpdp,idot,linelen,headbyte
  integer*2 atoi20,numctr,ctype1,ctype2,ctype3,i,nmlen,rmr,atodi
& ,fs1_i,fs2_i,fs3_i,numwin,cfs1u_i,cfs2u_i,cfs3u_i,trans
  character*80 string(300),temp
  character*20 cwords,nokdp_a,numctr_a,df1_a,df2_a,df3_a,fs1_a,fs2_a
1      ,fs3_a,wlen1_a,wlen2_a,wlen3_a,xpos_a,ypos_a,zpos_a
2      ,rmr_a,del_a,eps_a,c_win_a,sam_t_a,scfac_a,atod_a
3      ,coefk_a,coefa_a,coefb_a,coefc_a,coefd_a,numwin_a
4      ,ang1_a,ang2_a,cfs1_a,cfs1u_a,cfs2_a,cfs2u_a
5      ,cfs3_a,cfs3u_a,a11_a,a12_a,a13_a,a21_a,a22_a,a23_a
6      ,a31_a,a32_a,a33_a,trans_a
  character*12 sfname,efname,fnamein
  character*1 mode,tbd,ttime,ctype,axis

c
  common /ldvset/ df1,df2,df3,fs1,fs2,fs3,wlen1,wlen2,wlen3,del,eps
&        ,scfac(5),coefk(5),coefa(5),coefb(5),coefc(5)
&        ,coefd(5),atodi(5)
  common /processor/ nowpdp,tnowpdp,headbyte,c,nokdp,numctr,ctype1
&        ,ctype2,ctype3,rmr,samptim,coinwind,mode,tbd
&        ,ttime,axis,trans
  common /tmatrix/ a11,a12,a13,a21,a22,a23,a31,a32,a33
  common /files/ nmlen,sfname,efname,fnamein
  data fs_table /0.0,2.0e-3,5.0e-3,10.0e-3,20.0e-3,50.0e-3,100.0e-3
& ,200.0e-3,500.0e-3,1.0,2.0,5.0,10.0,-10.0,-20.0,40.0,-40.0/

c
  headbyte=0
  do 100 i=1,95
    read(9,10) string(i)
    temp=string(i)
    idot=80
201 continue
    if(temp(idot:idot) .eq. ' ') then
      idot=idot-1
      goto 201
    endif
    linelen=idot+1
    headbyte=headbyte+linelen
100 continue

```

```

10 format(a80)
c      ; numbers kilo data points
temp   = string(16)
nokdp_a = temp(20:27)
c      ; number of data points
nokdp   = int(atof20(nokdp_a)*1000)
c      ;processor type: 1=1990,2=1980,3=ifa550,4=ifa750
temp    = string(26)
ctype   = temp(10:12)
ctype1  = 4
ctype2  = 4
ctype3  = 4
c      ; number of signal processors
temp    = string(28)
numctr_a = temp(11:11)
numctr   = atoi20(numctr_a)
c      ; RMR enabled=1 disabled=2
temp    = string(31)
rmr_a   = temp(12:12)
rmr      = atoi20(rmr_a)
c      ; rotation about z and tilt about x angles
temp    = string(37)
del_a   = temp(10:17)
del      = atof20(del_a)
temp    = string(38)
eps_a   = temp(6:13)
eps      = atof20(eps_a)
c      ; fringe spacing (micrometers)
temp    = string(40)
df1_a   = temp(15:22)
df1      = atof20(df1_a)
temp    = string(47)
df2_a   = temp(15:22)
df2      = atof20(df2_a)
temp    = string(54)
df3_a   = temp(15:22)
df3      = atof20(df3_a)
c      ; wavelength (micrometers)
temp    = string(44)
wlen1_a = temp(12:21)
wlen1    = atof20(wlen1_a)/1000.
temp    = string(51)
wlen2_a = temp(12:21)
wlen2    = atof20(wlen2_a)/1000.
temp    = string(58)
wlen3_a = temp(12:21)
wlen3    = atof20(wlen3_a)/1000.
c      ; number of c words
temp    = string(94)
cwords  = temp(16:16)
c       = atoi20(cwords)
c
c      ; a/d conversion 0= -5 to +5 volts, 1= 0 to 10
volts
c
c      ; signal = K + A*v + B*v^2 +C*v^3 + D*v^4
c
do 101 j=1,c+1
do 102 ii=1,10
i=95+(j-1)*10+ii
read(9,10) string(i)

```

```

temp=string(i)
idot=80
202 continue
if(temp(idot:idot) .eq. ' ') then
  idot=idot-1
  goto 202
endif
linelen=idot+1
headbyte=headbyte+linelen
if(ii .eq. 4) then
  temp = string(i)
  scfac_a = temp(13:20)
  scfac(j) = atof20(scfac_a)
endif
if(ii .eq. 5) then
  temp = string(i)
  atod_a = temp(10:10)
  atodi(j) = atoi20(atod_a)
endif
if(ii .eq. 6) then
  temp = string(i)
  coefk_a = temp(3:10)
  coefk(j) = atof20(coefk_a)
endif
if(ii .eq. 7) then
  temp = string(i)
  coefa_a = temp(3:10)
  coefa(j) = atof20(coefa_a)
endif
if(ii .eq. 8) then
  temp = string(i)
  coefb_a = temp(3:10)
  coefb(j) = atof20(coefb_a)
endif
if(ii .eq. 9) then
  temp = string(i)
  coefc_a = temp(3:10)
  coefc(j) = atof20(coefc_a)
endif
if(ii .eq. 10) then
  temp = string(i)
  coefd_a = temp(3:10)
  coefd(j) = atof20(coefd_a)
endif
102 continue
101 continue
c
do 103 i=1,10
read(9,10) string(95+(c+1)*10+i)
temp=string(95+(c+1)*10+i)
idot=80
203 continue
if(temp(idot:idot) .eq. ' ') then
  idot=idot-1
  goto 203
endif
linelen=idot+1
headbyte=headbyte+linelen
if(i .eq. 7) then
  temp = string(95+(c+1)*10+i)

```

```

        numwin_a = temp(13:13)
        numwin = atoi20(numwin_a)
    endif
103 continue
c
    do 104 j=1,numwin
    do 105 ii=1,3
    i=95+(c+1)*10+11+(j-1)*3+ii
    read(9,10) string(i)
    temp=string(i)
    idot=80
204 continue
    if(temp(idot:idot) .eq. ' ') then
    idot=idot-1
    goto 204
    endif
    linelen=idot+1
    headbyte=headbyte+linelen
    if(ii .eq. 2) then
        temp = string(i)
        angl_a = temp(14:23)
        angl(j) = atof20(angl_a)
    endif
    if(ii .eq. 3) then
        temp = string(i)
        ang2_a = temp(15:24)
        ang2(j) = atof20(ang2_a)
    endif
105 continue
104 continue
c
    do 106 i=95+(c+1)*10+11+(numwin)*3,95+(c+1)*10+11+(numwin)*3+100
    read(9,10) string(i)
    temp=string(i)
    idot=80
205 continue
    if(temp(idot:idot) .eq. ' ') then
    idot=idot-1
    goto 205
    endif
    linelen=idot+1
    headbyte=headbyte+linelen
106 continue
    close(9)
c
                                ; processor mode: 1 = random, 2 = coincidence
    temp      = string(95+(c+1)*10+11+(numwin)*3+1)
    mode      = temp(6:6)
c
                                ; coincidence window(microseconds)
    temp      = string(95+(c+1)*10+11+(numwin)*3+2)
    c_win_a   = temp(11:21)
    coinwind  = atof20(c_win_a)
c
                                ; tbd: 1 = on, 2 = off, 3 = even time
    temp      = string(95+(c+1)*10+11+(numwin)*3+3)
    tbd       = temp(5:5)
c
                                ; even time(microseconds)
    temp      = string(95+(c+1)*10+11+(numwin)*3+4)
    sam_t_a   = temp(10:20)
    samptim   = atof20(sam_t_a)
c
                                ; transit time: 1 = on, 2 = off

```

```

temp      = string(95+(c+1)*10+11+(numwin)*3+6)
ttime     = temp(6:6)
c          ; frequency shift (MHz); Uses table look-up
temp      = string(95+(c+1)*10+11+(numwin)*3+36)
fsl_a     = temp(16:17)
fsl_i     = atoi20(fsl_a)
if(fsl_i .eq. 17) then
temp      = string(95+(c+1)*10+11+(numwin)*3+34)
cfs1_a    = temp(17:24)
cfs1      = atof20(cfs1_a)
temp      = string(95+(c+1)*10+11+(numwin)*3+35)
cfs1u_a   = temp(22:22)
cfs1u_i   = atoi20(cfs1u_a)
fsl       = cfs1*10**(3*(cfs1u_i-1))/10**6
else
fsl       = fs_table(fsl_i+1)
endif
temp      = string(95+(c+1)*10+11+(numwin)*3+42)
fs2_a     = temp(16:17)
fs2_i     = atoi20(fs2_a)
if(fs2_i .eq. 17) then
temp      = string(95+(c+1)*10+11+(numwin)*3+40)
cfs2_a    = temp(17:24)
cfs2      = atof20(cfs2_a)
temp      = string(95+(c+1)*10+11+(numwin)*3+41)
cfs2u_a   = temp(22:22)
cfs2u_i   = atoi20(cfs2u_a)
fs2       = cfs2*10**(3*(cfs2u_i-1))/10**6
else
fs2       = fs_table(fs2_i+1)
endif
temp      = string(95+(c+1)*10+11+(numwin)*3+48)
fs3_a     = temp(16:17)
fs3_i     = atoi20(fs3_a)
if(fs3_i .eq. 17) then
temp      = string(95+(c+1)*10+11+(numwin)*3+46)
cfs3_a    = temp(17:24)
cfs3      = atof20(cfs3_a)
temp      = string(95+(c+1)*10+11+(numwin)*3+47)
cfs3u_a   = temp(22:22)
cfs3u_i   = atoi20(cfs3u_a)
fs3       = cfs3*10**(3*(cfs3u_i-1))/10**6
else
fs3       = fs_table(fs3_i+1)
endif
c          ; transform matrix
c          ; transform enabled=1 disabled=0
temp      = string(95+(c+1)*10+11+(numwin)*3+67)
trans_a   = temp(9:9)
trans     = atoi20(trans_a)

temp      = string(95+(c+1)*10+11+(numwin)*3+71)
a11_a     = temp(5:12)
a11       = atof20(a11_a)
temp      = string(95+(c+1)*10+11+(numwin)*3+72)
a12_a     = temp(5:12)
a12       = atof20(a12_a)
temp      = string(95+(c+1)*10+11+(numwin)*3+73)
a13_a     = temp(5:12)
a13       = atof20(a13_a)

```



```

temp      = string(95+(c+1)*10+11+(numwin)*3+74)
a21_a     = temp(5:12)
a21       = atof20(a21_a)
temp      = string(95+(c+1)*10+11+(numwin)*3+75)
a22_a     = temp(5:12)
a22       = atof20(a22_a)
temp      = string(95+(c+1)*10+11+(numwin)*3+76)
a23_a     = temp(5:12)
a23       = atof20(a23_a)
temp      = string(95+(c+1)*10+11+(numwin)*3+77)
a31_a     = temp(5:12)
a31       = atof20(a31_a)
temp      = string(95+(c+1)*10+11+(numwin)*3+78)
a32_a     = temp(5:12)
a32       = atof20(a32_a)
temp      = string(95+(c+1)*10+11+(numwin)*3+79)
a33_a     = temp(5:12)
a33       = atof20(a33_a)
c
                                ; position
temp      = string(95+(c+1)*10+11+(numwin)*3+88)
xpos_a    = temp(7:14)
x         = atof20(xpos_a)
temp      = string(95+(c+1)*10+11+(numwin)*3+89)
ypos_a    = temp(7:14)
y         = atof20(ypos_a)
temp      = string(95+(c+1)*10+11+(numwin)*3+90)
zpos_a    = temp(7:14)
z         = atof20(zpos_a)
c
write(*,'(a)') ' Writing header data to summary file'
c
write(7,1002)
1002 format(4x,'nokdp',5x,'mode',7x,'tbd',5x,'ttime',
&6x,'numctr',1x,'ctype3'1x,'ctype2'1x,'ctype1')
write(7,1000) nokdp,mode,tbd,ttime,numctr,ctype3,
&ctype2,ctype1
write(7,1009) coinwind,samptim
1009 format(1x,'Coin window =',f10.1,' us',2x,
&'Equal time sample interval =',f10.1,' us')
1000 format(i8,3(9x,a1),4i8)
write(7,1003)
1003 format(15x,'fringe spc',2x,'freq shift',2x,'wavelength')
write(7,1004)df1,fs1,wlen1
1004 format(1x,'channel 1',5x,3(f10.4,2x))
write(7,1005)df2,fs2,wlen2
1005 format(1x,'channel 2',5x,3(f10.4,2x))
write(7,1006)df3,fs3,wlen3
1006 format(1x,'channel 3',5x,3(f10.4,2x))
write(7,1001) c
1001 format(1x,'number of c words =',i2)
write(7,1013)
1013 format(10x,'a/d',4x,'scale',6x,'K',9x,'A',9x,'B',9x,'C'
&,9x,'D')
write(7,1017) atodi(1),scfac(1),coefk(1),coefa(1),coefb(1)
&,coefc(1),coefd(1)
1017 format(1x,'cword 0',2x,i2,2x,6(f8.4,2x))
if(c .ge. 1) write(7,1014) atodi(2),scfac(2),coefk(2),coefa(2)
&,coefb(2),coefc(2),coefd(2)
1014 format(1x,'cword 1',2x,i2,2x,6(f8.4,2x))
if(c .ge. 2) write(7,1015) atodi(3),scfac(3),coefk(3),coefa(3)

```

```

&,coefb(3),coefc(3),coefd(3)
1015 format(1x,'cword 2',2x,i2,2x,6(f8.4,2x))
      if(c .ge. 3) write(7,1016) atodi(4),scfac(4),coefk(4),coefa(4)
&,coefb(4),coefc(4),coefd(4)
1016 format(1x,'cword 3',2x,i2,2x,6(f8.4,2x))
      write(7,1021) rmr,numwin
1021 format(1x,'RMR flag =',i2,5x,' Number of RMR windows =',i2)
      write(7,1023)
1023 format(12x,'start angle',4x,'stop angle')
      write(7,1027) angl(1),ang2(1)
1027 format(1x,'window 0',4x,2(f10.4,4x))
      if(numwin .ge. 2) write(7,1024) angl(2),ang2(2)
1024 format(1x,'window 1',4x,2(f10.4,4x))
      if(numwin .ge. 3) write(7,1025) angl(3),ang2(3)
1025 format(1x,'window 2',4x,2(f10.4,4x))
      if(numwin .ge. 4) write(7,1026) angl(4),ang2(4)
1026 format(1x,'window 3',4x,2(f10.4,4x))
      write(7,1007) x,y,z
1007 format(1x,'x = ',f12.6,2x,'y = ',f12.6,2x,'z = ',f12.6)
      write(7,1008) del,eps
1008 format(1x,'del = ',f12.6,2x,'eps = ',f12.6)
      write(7,1029) trans
1029 format(1x,'transformation matrix enable flag (0-off, 1-on) = ',i1)
      write(7,1028) a11,a12,a13,a21,a22,a23,a31,a32,a33
1028 format(1x,'A11 = ',f9.6,2x,'A12 = ',f9.6,2x,'A13 = ',f9.6,/
&1x,'A21 = ',f9.6,2x,'A22 = ',f9.6,2x,'A23 = ',f9.6,/
&1x,'A31 = ',f9.6,2x,'A32 = ',f9.6,2x,'A33 = ',f9.6)

c
c*****
c      find number of processor words per data point - nowpdp
c*****
      if ((mode .eq. '2') .and. (numctr .eq. 2)) then
        if (tbd .eq. '1') then
          nowpdp = 5
        else
          nowpdp = 4
        endif
      elseif ((mode .eq. '2') .and. (numctr .eq. 3)) then
        if (tbd .eq. '1') then
          nowpdp = 7
        else
          nowpdp = 6
        endif
      elseif (tbd .eq. '1') then
        nowpdp = 3
      else
        nowpdp = 2
      endif

c
      if(rmr .eq. 1) then
        tnowpdp=nowpdp+c+rmr
      else
        tnowpdp=nowpdp+c
      endif
      if(ttime .eq. '1') then
        tnowpdp=tnowpdp+numctr
      endif
      if(tbd .eq. '1') then
        tnowpdp=tnowpdp+1
      endif

```

```

        write(7,2001) nowpdp,c,rmr,tnowpdp
2001 format(' nowpdp= ',i2,2x,'c= ',i2,2x,'rmr= ',i2,2x,'tnowpdp=', i2)
        write(7,2002) headbyte
2002 format(' header bytes = ',i5)
c
        write(7,*)
        end
c

        subroutine readdata
c
c*****
c      Subroutine reads the binary raw data from the TSI PACE ver. 1.2
c      raw data file in the proper word order, one data point at a time,
c      according to the documentation given in the Appendix of the
c      TSI PACE/FIND software manual (Version 1.2). See PACE/FIND manual
c      for more details. TSI stands for Thermal Systems Incorporated.
c
c      Called by: Program readpace
c      Calls: function convertb, convertc, convertr
c             subroutine converta
c
c
c      Modified by: Richard D. Gould
c                  Sept. 26, 1997
c                  version 1.0, All rights reserved by author
c*****
c
        real*8 time1,time2,time3,convertb,convertc,u,v,w,ttu,ttv,ttw
        &          ,fd1,fd2,fd3,c1,c2,clraw,c2raw
        real*4 df1,df2,df3,fs1,fs2,fs3,wlen1,wlen2,wlen3,del,eps
        &          ,coinwind,samptim,scfac,coefk,coefa,coefb,coefc,coefd
        integer*4 time7500,curtime,firsttbd,dpoints,nokdp,c,nowpdp,tnowpdp
        &          ,headbyte,istart,iend,i,j,k,totbytes,error
        integer*2 time750(2),numctr,ctype1,ctype2,ctype3,nmlen,rmr,atodi
        &          ,ncycl1,ncycl2,ncycl3,addr1,addr2,addr3,word(11),c0
        &          ,trans
        character*12 sfname,efname,fnamein
        character*1 mode,tbd,ttime,axis,bytes(22)
        character*1 bytedata[ALLOCATABLE] (:)
c
        common /ldvdat/ u(10240),v(10240),w(10240),ttu(10240),ttv(10240)
        &          ,ttw(10240),c1(10240),c2(10240),curtime(10240)
        &          ,c0(10240),dpoints
        common /ldvset/ df1,df2,df3,fs1,fs2,fs3,wlen1,wlen2,wlen3,del,eps
        &          ,scfac(5),coefk(5),coefa(5),coefb(5),coefc(5)
        &          ,coefd(5),atodi(5)
        common /processor/ nowpdp,tnowpdp,headbyte,c,nokdp,numctr,ctype1
        &          ,ctype2,ctype3,rmr,samptim,coinwind,mode,tbd
        &          ,ttime,axis,trans
        common /files/ nmlen,sfname,efname,fnamein
        equivalence (time7500, time750(1))
        equivalence (word, bytes(1))
c
        if(tnowpdp .gt. 22) go to 8997
        totbytes=headbyte+nokdp*2*tnowpdp
        ALLOCATE (bytedata(totbytes), STAT = error)
        if(error .ne. 0) STOP 'Not enough storage for data; aborting ...'

```

```

c
c Note: The array bytedata( ) must be dimensioned to the exact size of the
file
c Since the header size changes based on file name lengths, variable
names
c comment string lengths, ... the only way to open the file as a
single
c direct access record (which is necessary for reasonable processing
speed
c is to dynamically allocate the array BYTEDATA. Be careful to note
that
c the syntax to allocate dynamic arrays is compiler dependent. This
c syntax is for Microsoft FORTRAN powerstation, version 1.0.
c
c open raw data file & read all bytes(including header) into 1 record
c
      open(unit=1,file=fnamein,form='binary',access='direct'
&,recl=totbytes)
      rewind(1)
      read(1, rec=1,err=8889) bytedata
      write(*,8888) totbytes
8888 format(' Done reading data file (' ,i7,' bytes)!')
      close(1)
c
      dpoints=0
      do 382 j=1,nokdp
c
c read all the words associated with each LDV data point into array
c
      k=0
      istart=headbyte+1+(j-1)*2*tnowpdp
      iend=istart+2*tnowpdp-1
      do 380, i = istart,iend
      k=k+1
      bytes(k)=bytedata(i)
380 continue
c
c decode 16 bit digital words into appropriate values
c
c Note: This sequence is for 3 LDV channels without residence time data,
c time between data words, RMR word and 2 C words.
c
      call converta(word(1),ncycl3,addr3)
      time3 = convertb(word(2),ctype1)
      call converta(word(3),ncycl2,addr2)
      time2 = convertb(word(4),ctype2)
      call converta(word(5),ncycl1,addr1)
      time1 = convertb(word(6),ctype3)
      time750(2) = word(7)
      time750(1) = word(8)
      c2raw = convertc(word(9),atodi(3),scfac(3))
      c2(j)= coefk(3)+coefa(3)*c2raw+coefb(3)*c2raw**2+coefc(3)*c2raw**3
&      +coefd(3)*c2raw**4
      clraw = convertc(word(10),atodi(2),scfac(2))
      c1(j)= coefk(2)+coefa(2)*clraw+coefb(2)*clraw**2+coefc(2)*clraw**3
&      +coefd(2)*clraw**4
      c0(j) = iand(word(11),4095)
      if(time3 .eq. 0.0 .or. time2 .eq. 0.0 .or. time3 .eq. 0.0)
&go to 381
      if(dpoints .ge. 10240) go to 8999

```

```

dpoints = dpoints + 1
fd3=(ncycl3*1000.0/time3)
fd2=(ncycl2*1000.0/time2)
fd1=(ncycl1*1000.0/time1)
w(dpoints)=(fd3-fs3)*df3
v(dpoints)=(fd2-fs2)*df2
u(dpoints)=(fd1-fs1)*df1
if (dpoints .eq. 1) firsttbd = time7500
c
if(firsttbd .gt. 0) then
c
  if(time7500 .lt. 0) then
    curtime(dpoints)=(time7500-(-2147483647))+2+(2147483647-firsttbd)
  else
    curtime(dpoints) = time7500-firsttbd
  endif
c
else
  curtime(dpoints) = time7500-firsttbd
endif
c
381 continue
382 continue
c
goto 3000
8889 write(*,*)' ERROR READING DATA FILE ',fnamein
goto 3000
8997 write(*,*)' Total number of bytes in data point > 22 array limit!'
goto 3000
8999 write(*,*)' Tried to read more than 10240 points - array limit!'
3000 continue
c
end

```

**STRUCTURE AND FUNCTION OF AN EXTREMELY SENSITIVE  
BIOLOGICAL INFRARED DETECTOR**

**Michael S. Grace Ph.D.  
Research Assistant Professor  
Department of Biology**

**University of Virginia  
Gilmer Hall  
Charlottesville, VA 22903**

**Final Report for:  
Summer Faculty Research Program  
Wright Laboratory**

**Sponsored by:  
Air Force Office of Scientific Research  
Bolling Air Force Base, Washington, DC**

**And**

**Wright Laboratory**

**August 1997**

## Structure and Function of an Extremely Sensitive Biological Infrared Detector

Michael S. Grace, Ph.D.  
Research Assistant Professor

Dept. of Biology  
University of Virginia  
Charlottesville, VA 22903-2477

### Abstract

Highly-sensitive image-forming infrared detectors are found in boid and crotalid species of snakes. These infrared-detecting systems are superior to all artificial and all known biological infrared detectors, as they combine 0.003°C thermal resolution, microscopic size, and self-repair in an uncooled system. I have performed a detailed analysis of the infrared receptor system in the boid snakes *Python molurus bivittatus* (the Burmese python), *Python regius* (the royal python), and others. Surface structural analyses of the infrared-sensitive pit by transmission electron microscopy, scanning electron microscopy, and atomic force microscopy reveal an array of plate-like structures covered by regular arrays of "micropits." These micropits were also found on the spectacle covering the eyes, but their arrangement and size there were significantly different. Infrared spectrometry of this surface material from the IR-sensitive pits showed that it was completely non-reflective of IR from 2-15µm. This material readily transmitted IR in 2 major bands, centered on 4 and 10µm. IR imaging showed that the IR-sensitive pits were non-reflective and absorptive in both the 3-5µm and 8-12µm ranges; both of these parameters were greater in the 8-12µm band. These results are particularly interesting in that these snakes normally target endothermic mammalian prey radiating maximally at 10µm. Since phosphate absorbs at 10µm, and since protein phosphorylation is an important and ubiquitous component of sensory signaling, we began biochemical analyses of tissue containing the IR-sensitive neuronal terminals. Polyacrylamide gel electrophoresis showed that the IR-sensing pits contain a variety of proteins, and that the protein pattern is distinct from that in non-pit skin, retina, and brain. Affinity chromatography successfully isolated several phosphoproteins from tissue homogenates. Immunohistochemistry on the IR-sensitive neuronal terminals showed that they are distinct from photoreceptors in the retina, in that they lack both the protein opsin and 2 calcium-binding proteins, calretinin and calbindin. However, they do contain 2 unique calcium-binding proteins, calmodulin and S-100, both of which may be involved in IR transduction, and the activities of which are regulated phosphorylation. Together, these results show that (1) IR-sensitive pits in *Python* contain an unusual surface architecture which may impart unique optical properties, (2) these pits maximally absorb in the 8-12µm range, matching the peak emission of targeted prey, and (3) IR-sensitive neuronal terminals are biochemically distinct from visible light-absorbing retinal photoreceptors, non-pit skin, and brain. Finally, these results provide a strong basis for the continued isolation and analysis of the biochemical components responsible for highly sensitive uncooled IR detection. This work may ultimately allow development of new infrared imaging technologies that take advantage of the positive features of snake infrared detectors.

## **Introduction**

Artificial infrared image-forming devices have tremendous practical applications in the military, in medicine, and in industry. While artificial infrared (IR)-sensing technology has improved dramatically in recent years, there are many reasons to seek even greater improvements in this technology. Highly sensitive image-forming IR detectors are bulky, complicated (often necessitating frequent repair or modification), and costly to maintain. In order to function with reasonable sensitivity they often must be super-cooled, adding to their bulk, cost, and potential failure. Boid and crotalid snakes, on the other hand, "see" spatial images of their thermal environments using infrared detectors that are microscopic in dimensions, self-repairing, and that function at normal ambient temperatures. Perhaps most importantly, snake infrared detectors are at least an order of magnitude more sensitive than the best artificial ones. An analysis of the extremely sensitive snake image-forming IR detector should provide insight for the development of new technologies that will result in greater sensitivity, operation at higher temperatures, and reductions in size and weight.

Snakes of the families Boidae (boas and pythons) and Crotalidae (pitvipers including the rattlesnakes) possess highly sensitive image-forming infrared sensors. In crotalids, these IR detectors are located in distinct facial invaginations or pits, one each side of the face between the nostril and eye. Most pythons and many boas also have facial pits which form an array around the rim of the mouth in or between labial scales (Fig 1). Other boid snakes are also infrared-sensitive, but simply lack the elaborate pit organ.



**Figure 1:** Head of python *Morelia spilotes* showing maxillary (upper jaw) and mandibular (lower jaw) pit organs.

Both the infrared and visual systems (along with chemical and tactile cues) are involved in prey detection by boids and pit vipers, but prey detection and localization do not require the eyes. A congenitally blind rattlesnake was shown to accurately strike prey with an efficiency and precision comparable to sighted animals of the same species (Kardong and Mackessey, 1991). When this snake's pits were covered, the snake struck prey with much less frequency and accuracy, indicating that the infrared detectors play an important role in prey detection and localization.

The boid infrared-receptive organ consists of a mass of IR-sensitive nerve terminals just under the epidermis of the skin (Fig. 2). The fibers that form these terminals originate from cells in the trigeminal ganglion (for review, see Molenaar, 1992), which in all vertebrates, subserves the senses of pressure, pain, and temperature in the face. IR information conveyed to these trigeminal neurons is sent on to the brainstem, and then to higher brain centers through multi-synaptic



connections. The projections of IR-sensitive neurons are arranged to produce a spatial representation within the brain of the snake's infrared environment. This spatial mapping is analogous to that produced by the visual projections to the brain, and in fact, these two sensory modalities merge in the optic tectum of the snake's brain. Thus, infrared-sensitive snakes "see" both visible light and infrared radiation, and these two modalities operate in precise spatial register within the brain (Hartline, Kass, and Loop 1978).

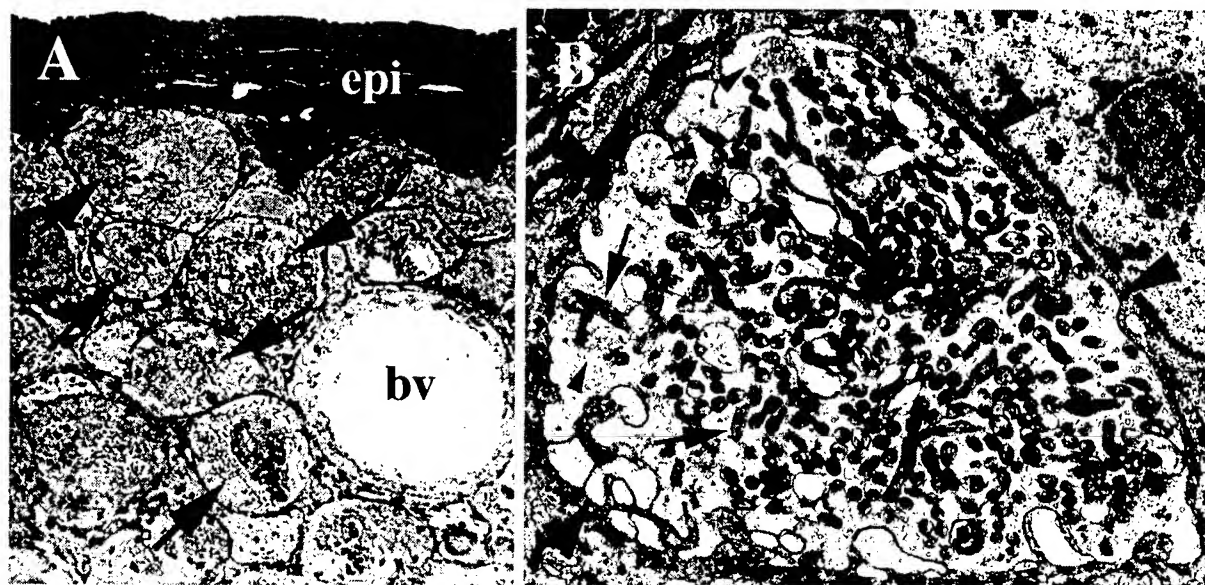


**Figure 2:** Transmission electron micrograph of a cross-section through the pit organ of the snake *Python molurus bivittatus*. **A:** low power micrograph showing many IR-sensitive neuronal terminals underlying the epidermis (epi). Note capillary (bv). **B:** A single terminal (borders indicated by large arrowheads) showing the characteristic large numbers of mitochondria (arrows) and many electron-lucent vesicles (small arrowheads) clustered near the plasma membrane.

While in the last few decades significant attention has focused upon the neuroanatomy of snake IR-sensing systems, absolutely nothing is known about the mechanisms involved in converting an IR stimulus into an electrochemical neural signal. Therefore, I have undertaken a detailed analysis of the transduction mechanism operating in the IR receptor terminal. These receptor terminals are massed within the membranes of easily recognized facial pits, and are easily removed for study. IR-sensitive neuronal terminals within the pit organ are large spherical structures, the most characteristic feature of which is the abundance of mitochondria contained within them (Fig. 2). The fact that most of the cytoplasmic space is filled with mitochondria suggests that they play a fundamental role in IR signal transduction. One report suggested that they play a primary role in signaling because they change configuration in response to infrared stimulation (Meszler, 1970). Experiments using physiologically-relevant stimuli in my laboratory, however, indicate that these earlier observations are an artifact produced by high intensity laser stimulation of the pit organ. Even so, the abundance of mitochondria indicates that they either play a primary role in signaling, or that they perform some secondary function such as providing energy for the biochemical signaling machinery. If mitochondria are a fundamental component of IR signaling, they may have unique biochemical or functional properties. Likewise, the terminal as a whole may have a biochemical makeup unique among sensory nerve endings.

The spectral sensitivity of the pit organ is also unknown. Previous experiments have employed a variety of stimulating devices including the human hand (Bullock and Diecke, 1956; Terashima and Goris, 1975), visible light sources (Terashima, Goris, and Katsuki 1968), and lasers of

various wavelengths and intensities (DeCock Buning, Terashima, and Goris, 1981a,b; Harris and Gamow, 1971; Terashima and Goris, 1977). The intensities of many of these sources were far above anything normally encountered by this sensory system. There has been no systematic effort made to determine either the spectral sensitivity of the pit organ or the spectral transmission of the tissues overlying the receptor terminals. In fact, my observations indicate that the surface of the pit organ has a structure unique to the pit. This observation suggests that the pit surface may act as a spectral filter or an anti-reflective coating.

The results reported here show that the infrared-sensitive pit organ is a highly specialized and well-organized cellular infrared detector. We found that the surface of the pit organ has a very unusual arrangement; the only other similar surface structures found were that on the spectacle covering the eye and on interscale skin (although there are significant differences between these and the pit surfaces). The highly ordered arrangement of the pit organ surface suggests that it may act as a spectral filter, functioning like a grating monochromator. Alternatively, this surface structure which overlies the receptor terminals may function as an antireflective coating. We also show that the pit organ has unusual spectral absorption/reflectance properties. Our results indicate that the pit organ may be "tuned" to a particular region of the electromagnetic spectrum, that between 8 and 12 $\mu$ m wavelength. Finally, we have begun a biochemical fractionation of the pit organ that will help elucidate the roles of several candidate biochemical components of the IR signaling cascade, and will help identify other components of the IR signal transduction system.

## **Methods**

### ***A. Animals and Tissue Preparation***

Boid snakes (family including boas and pythons) were chosen for this work because they possess one of the two most sensitive and highly organized system of image-forming biological infrared detectors known. The species used in this study were Burmese python (*Python molurus bivittatus*), ball python (*Python regius*), and others. Young (approximately 3-month old) snakes were housed individually in ventilated plastic cages containing newspaper substrate. Room temperature was maintained at 82°F, and a heat gradient was provided by directing a ceramic radiant heat source at one end of cages. Animals were fed a diet of freshly-killed laboratory mice once per week. Water was available *ad libitum*.

All snakes were anesthetized prior to removal of tissues, and no snakes used for tissue preparation were allowed to recover from anesthesia. In other cases (infrared imaging experiments), snakes were anesthetized and allowed to recover; these snakes received no painful or invasive procedures. Snakes were anesthetized with 100mg/kg ketamine HCl (subcutaneous) using an 22 gauge hypodermic needle, after having raised body temperature to approximately 30°C. Under deep anesthesia, snakes were decapitated, and tissues (IR-sensing pits, brain, trigeminal ganglia, retinae, and skin) were surgically removed. After tissue removal, animals were either be overdosed with ketamine or perfused transcardially with fixative, after which other tissues were removed for future research (beyond the scope of this report).

In addition, samples of naturally shed epidermal skin were used for surface imaging studies. These samples required no manipulation of animals. Shed skin samples were obtained from *Boa constrictor* (boa constrictor), *Epicrates cenchria* (rainbow boa), *Lampropeltis alterna* (gray-banded kingsnake), *Morelia spilotes* (carpet python), *Morelia viridis* (green tree python), and *Python regius* (ball python). Shed skins were dried flat in normal atmosphere and room temperature.

### ***B. Transmission and Scanning Electron Microscopy, and Atomic Force Microscopy***

#### **(1) Scanning electron microscopy (SEM)**

Samples of living tissues (IR-sensing pit, and dorsal skin) were fixed in a mixture of 2% paraformaldehyde and 2% glutaraldehyde in 0.1M phosphate buffer. Samples were then rinsed in 0.1M phosphate buffer, dehydrated through increasing concentrations of ethanol, and critical point dried in hexamethyldisilazine (HMDS). These samples and samples of shed skins (from IR-sensing pit, dorsal skin, and ocular spectacle) were prepared for scanning electron microscopy by mounting onto aluminum specimen holders with silver. All mounted specimens were coated with tungsten prior to SEM.

Under the conditions tested, the surface structure of shed skin samples faithfully represented the surface structure of intact isolated tissues from the species tested. Therefore, in order to reduce the number of animals killed for these experiments, many analyses were performed on shed skin samples. Freshly shed skins were immediately flattened and air dried for storage prior to preparation for SEM.

#### **(2) Atomic force microscopy (AM)**

Atomic force microscopy was used for imaging microstructure of surface structures because it allows imaging of unfixed material, and therefore eliminates the potential problem of fixation-induced artifacts including tissue shrinkage. In addition, because AFM images are computer derived from numeric data, dimensions of surface structures are readily obtainable.

Samples of shed snake skin were mounted onto metallic disks with either cyanoacrylate glue or with adhesive designed for AFM sample preparation. After initial trials, cyanoacrylate glue was the usual method, since AFM adhesive allowed significant motion in samples while collecting AFM images. Samples were imaged in tapping mode or contact mode, both of which produced detailed 3-dimensional images of surface structure. In some cases, the AFM was operated in lateral force or in phase contrast mode in attempts to determine biophysical characteristics of surface material.

As with SEM, AFM images produced from samples from shed skins faithfully represented those produced from isolated intact tissues. Therefore, in order to reduce the number of animals required, freshly shed, flattened and dried skins were used in many of the AFM analyses.

### C. Infrared Spectrometry and Imaging

#### (1) Infrared imaging

Snakes (*Python regius* and *Python molurus bivittatus*) were imaged using two infrared-sensitive cameras, one sensitive in the 3-5 $\mu$ m wavelength range and the other sensitive in the 8-12 $\mu$ m wavelength range. Data was collected at 1 frame every 0.6 sec., and was stored directly on computer. Individual frames were selected and photographed, and photographs digitized by flatbed scanner.

Large-scale images of snakes were produced by imaging with IR-transmissive lenses. Snakes were placed upon a background of half Krylon black and half aluminum foil, and a styrofoam container of liquid nitrogen used as reference. Macrovideographic images of infrared-sensitive pits were obtained by imaging with lenses removed from cameras, and snakes held in the focal plane of the collecting apparatus. In some cases, snakes were deeply anesthetized with intraperitoneal injection of 100mg ketamine HCl per mg body weight, and mounted with surgical tape onto a stereotactic positioning device which was in turn mounted in a thermal isolation chamber. This cubic chamber consisted of 5 walls lined with aluminum foil. The top (sixth wall) was a krylon black-painted pan filled with ice water to serve as a heat sink. With this apparatus, snakes were precisely positioned such that the areas of interest could be moved slowly through the focal plane of the camera's IR collector while recording.

#### (2) Infrared spectrometry

Shed snake skins from a *Boa constrictor* (boa constrictor), *Python regius* (ball python), *Morelia spilotes* (carpet python), *Epicrates cenchria* (rainbow boa), and *Lampropeltis alterna* (gray-banded kingsnake) were flattened and dried. Areas of interest were removed with scissors and placed in a homemade cardboard mount, which was then placed in a specimen holder.

The infrared spectrum of each sample was measured twenty times on a fourier-transformed infrared spectrometer (Perkin-Elmer FTIR 1725x); these measurements were then averaged to produce the final data. Infrared transmission was measured over the range of 5000 to 400 wavenumbers (2.0  $\mu$ m to 25  $\mu$ m wavelength). All measurements were performed after a 5-minute equilibration time to completely purge of the sample chamber atmosphere with dry nitrogen. An initial back ground check was run and stored in computer memory each day.

*Python regius* pits were isolated intact. Snakes were deeply anesthetized by intraperitoneal injection of 100mg ketamine HCl per kg body weight. Pit organs from the maxilla (upper jaw) were isolated under a dissecting microscope, and stored briefly in a humidified petri dish. Clusters of 5 pits were then mounted onto either aluminum foil or Krylon black-painted cardboard, covered with Glad brand plastic wrap, and subjected to direct hemispheric reflectance infrared spectrometry (DHR) over the wavelength range of 2-15 $\mu$ m.

### D. SDS-Polyacrylamide Gel Electrophoresis

Snakes were deeply anesthetized by intraperitoneal injection of 100mg ketamine HCl per kg body weight. Maxillary pit organs, retinae, brains, and skin samples were surgically isolated and homogenized in lysis buffer consisting of 2.0% Triton X-100 in a 0.1M aqueous solution of sodium phosphate. Samples were mixed with 4x sample buffer and applied to the top of a 4-10% gradient polyacrylamide gel. Gels were run at constant voltage, after which they were stained with either coomassie blue or silver.

## Results and Discussion:

### *Transmission Electron Microscopy:*

Transmission electron microscopy (TEM) performed at the University of Virginia prior to arriving at Wright Laboratories showed that the epidermis overlying infrared-sensitive nerve terminals in the *Python* pit organ contains numerous invaginations in its surface (Fig. 3).



**Figure 3:** Transmission electron micrograph of a section of epidermis (epi) overlying infrared-sensitive neuronal terminals of the pit organ (*Python molurus bivittatus*). Invaginations (arrows) were observed only in epidermis of the pit organ, and not in epidermis outside the pit organ.

These invaginations were of random widths and depths. Invaginations were observed only over the portion of the pit containing IR-sensitive terminals, and only in the outermost layer of keratinized epithelium. Outside the pit organ, the outer surface of the epidermis appeared smooth.

The appearance of surface invaginations overlying the infrared receptor terminals suggested that they may play a functional role in IR reception by the pit organ. However, given the method of tissue preparation and observation, it was unclear whether the surface invaginations were an artifact of tissue preparation, real but random in size, or real and regular in size. Therefore, scanning electron microscopy was used to image the pit organ surface in order to determine the planar spatial arrangement of the surface invaginations.

### *Scanning Electron Microscopy:*

Scanning electron microscopy (SEM) of the surfaces of isolated infrared-sensitive pit organs and pit organ-derived shed skin revealed a series of very long parallel plate-like structures with a width of 2-3 $\mu$ m (Fig. 4). These plates were joined at the long edges by interdigitating projections. The surface of each of the plates was covered by a regular array of "micropits" of less than 0.5 $\mu$ m diameter (Fig. 4). Similar observations were made using shed skins (cornified epidermis).

The spectacle overlying the eye exhibited a surface structure similar to that of the pit organ. The surface of the spectacle was composed of a parallel array of plates, each covered by micropits (Fig. 4). Here, though, the width of the plates and the diameter of the micropits are both less than those of micropits in the pit organ. In addition, micropits on the spectacle appear less regular in arrangement than those in the pit organ.

Microstructure of the pit organ and spectacle differ markedly from the microstructure of scales elsewhere on the snake's body. Python scales, for example, are covered by parallel rows of short parallel ridges (Fig. 4). Boa scales are similar, covered by very long parallel strands (see Fig. 9). Micropits were observed outside the pit and spectacle, however. Interscale skin, the epidermis occupying space between adjacent scales, was composed of large faceted "lumps" approximately 15 $\mu$ m in diameter, each of which was covered by micropits (Fig. 5).

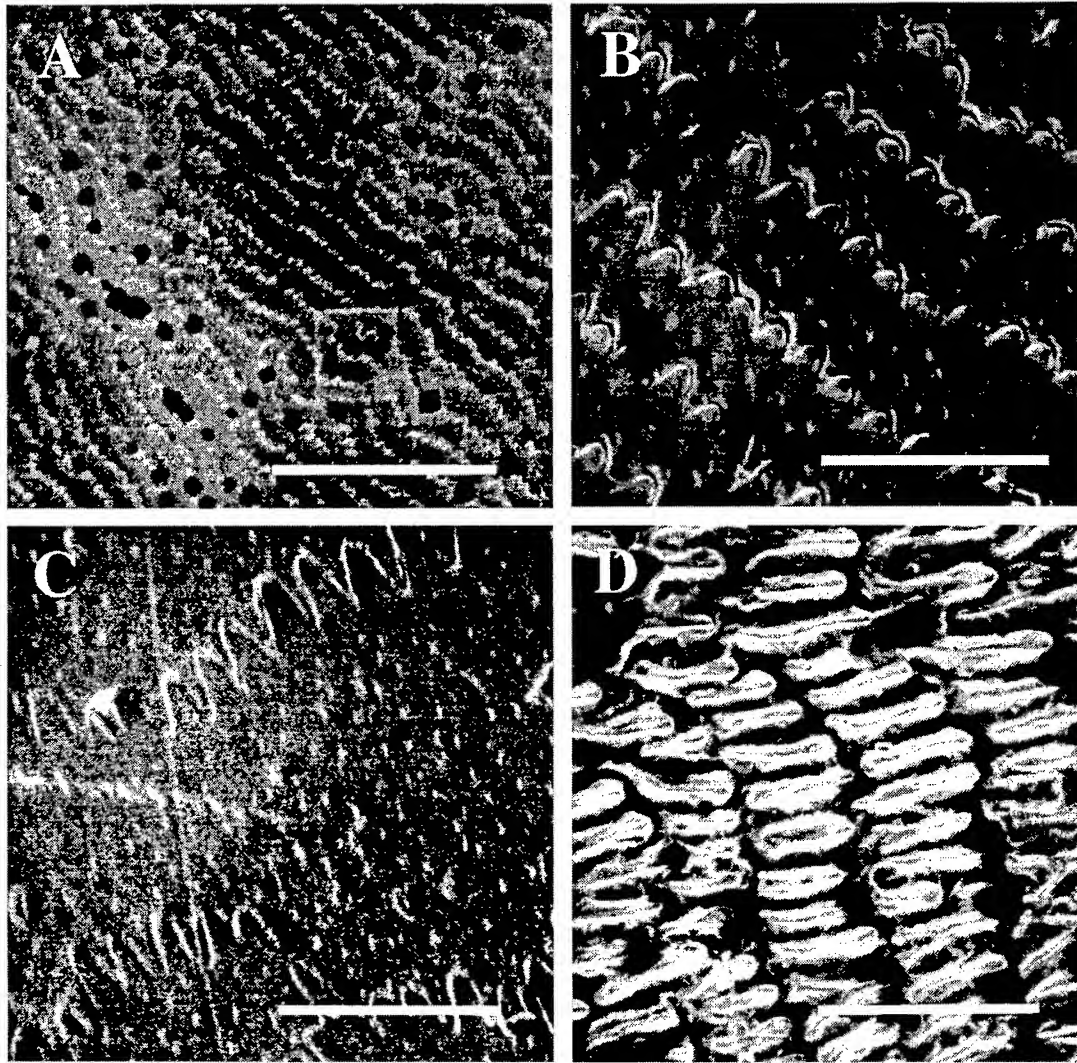


**Figure 4:** SEM of surface of python pit organ (A, B), spectacle (C), and dorsal skin (D). Note the parallel plate-like structures on pit and spectacle, and associated micropits. Dorsal skin has neither. Scale: A, 12 $\mu$ m; B,C,D 3 $\mu$ m.

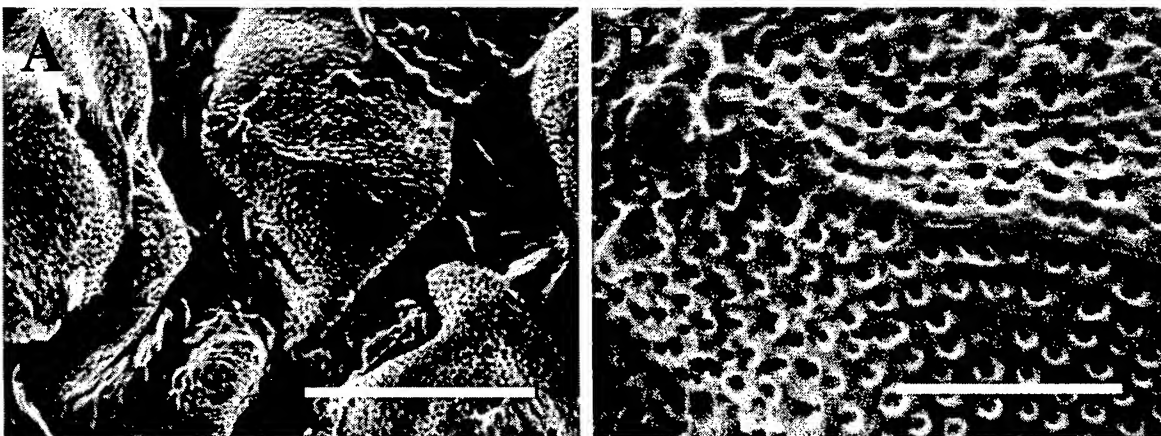


**Figure 5:** SEM of the surface of python dorsal interscale skin. A: lower magnification showing large faceted lumps; scale = 12 $\mu$ m. B: higher magnification showing micropits; scale = 3 $\mu$ m.



*Atomic Force Microscopy:*

AFM images of snake samples revealed structure essentially identical to that seen by SEM. IR-sensing pit samples exhibited an array of surface plates each covered with an array of micropits (Figs. 6-9). The spectacle was also covered by plates containing micropits, but the plates on the spectacle were longer and more narrow than those from the pit, and the micropits were smaller in both diameter and depth than those from the pit. We are investigating new approaches with AFM, including lateral force microscopy to determine frictional coefficients of sample surfaces (Fig. ). We are also using AFM to determine the distribution of hydrophilicity and/or hydrophobicity of surface structures, and are producing chemically-modified AFM probes for investigating the distribution of specific chemical residues in our samples. Finally, we are investigating the use of fluid-phase AFM in order to image single living IR-sensitive neurons in culture with the goal of detecting changes in response to IR illumination. These studies constitute part of an ongoing collaborative research effort between myself and Wright Laboratories.

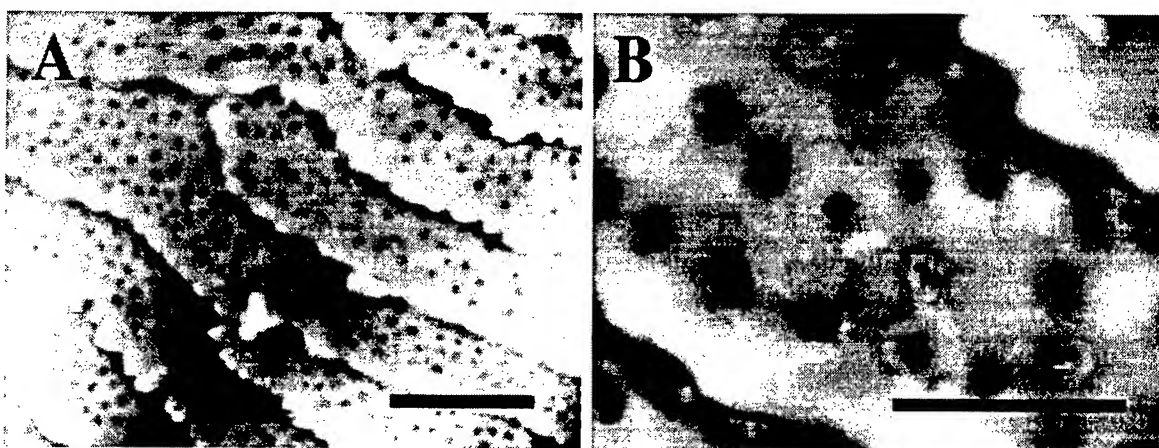


**Figure 6:** AFM images of python pit surface. note the parallel plate-like structures in A, and the numerous invaginations (“micropits”) in the surface of each plate. Scale bar = 5 $\mu$ m in A, and 2 $\mu$ m in B.

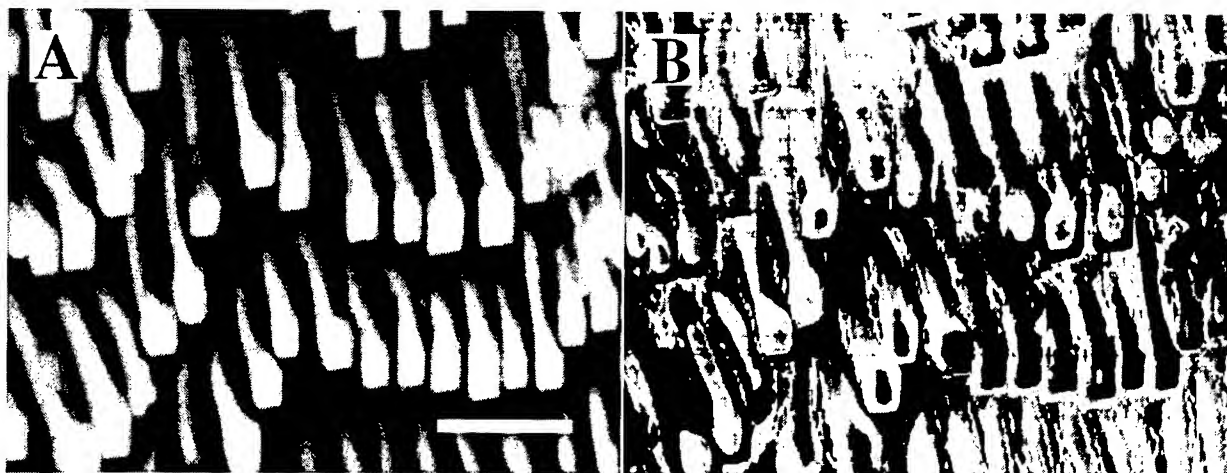


**Figure 7:** A: AFM topographic image of python (*Morelia spilotes*) non-pit skin surface. Note parallel rows of parallel ridges or cylinders and lack of plates and micropits. Scale bar = 2 $\mu$ m. B: AFM lateral force image of same sample showing frictional coefficients of surface features. Note the significant variation in frictional coefficients across individual ridges or cylinders suggesting complex chemistry or microstructure. Scale same as in A.

The presence of micropits on both the pit organ and spectacle surfaces suggests that they function in delivery of electromagnetic radiation to their respective receptors. The difference in size and spatial arrangement of the micropits and dimensions of underlying plates on the two surfaces may be related to different spectral sensitivities of the two organs. In both cases, the structure of the micropits and their plates may serve to limit spectral transmission to the receptive neurons or may act as an antireflective coating. The differences in dimensions may impose different spectral characteristics on the two tissues. The presence of the micropits on interscale skin may also function in spectral filtering or antireflectivity. In the normal relaxed resting and active positions of warm snakes, very little or no interscale skin is exposed. However, snakes are ectothermic animals, and when cold, typically bask in a coiled position, thus exposing interscale skin. Interscale skin is also exposed when snakes feed, typically on large prey items that are swallowed intact. In both cases, the animals seek to raise body temperature in order to raise metabolic rate. An antireflective or spectral filtering role of the micropits could serve to increase transmission or absorption of radiant energy in pit organ, eye, and interscale skin. The different dimensions of the microstructures of the different tissue may impart unique spectral characteristics to each tissue.

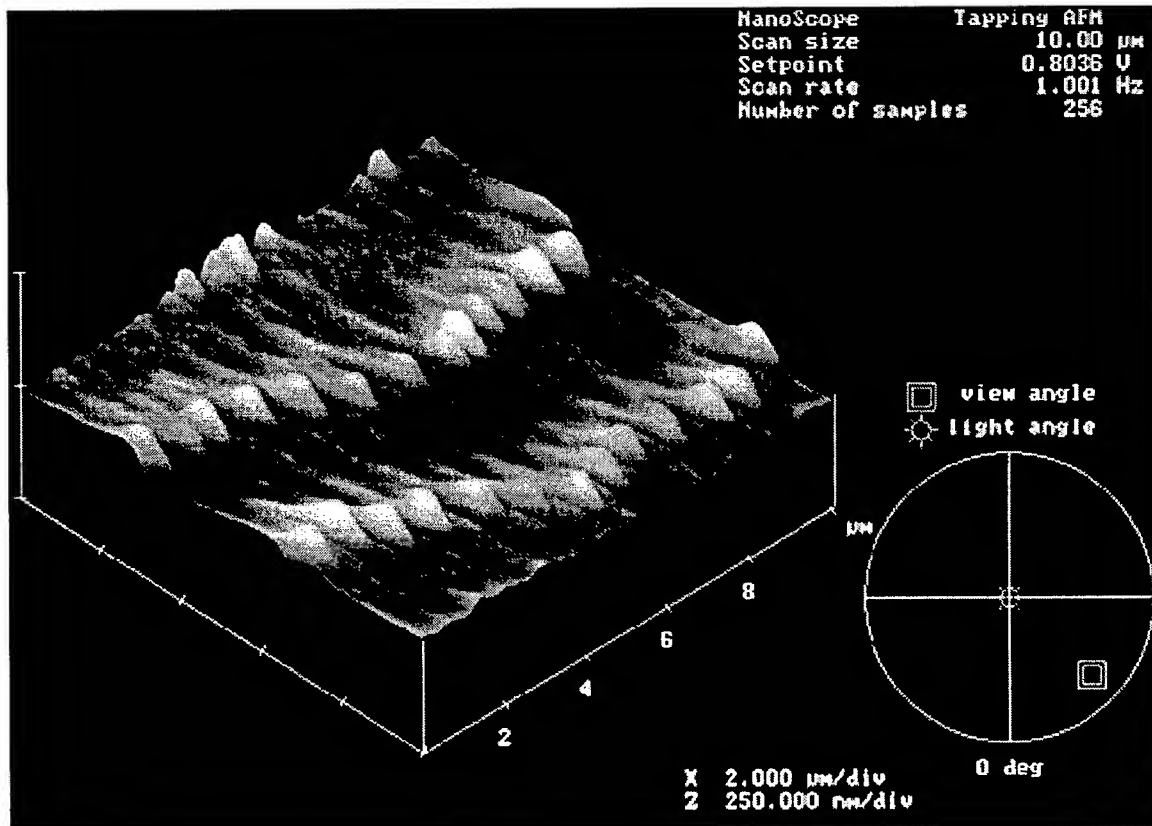


**Figure 8:** Angular view of surface of non-pit skin from the python *Morelia spilotes*. Note the parallel rows of parallel ridges or cylinders. Scale: 10 x 10μm.

In order to test whether pit organs, spectacle, and non-pit/non-spectacle epidermis exhibit different spectral properties, I investigated their spectral reflection, transmission, and absorption properties by infrared spectrometry and infrared imaging.



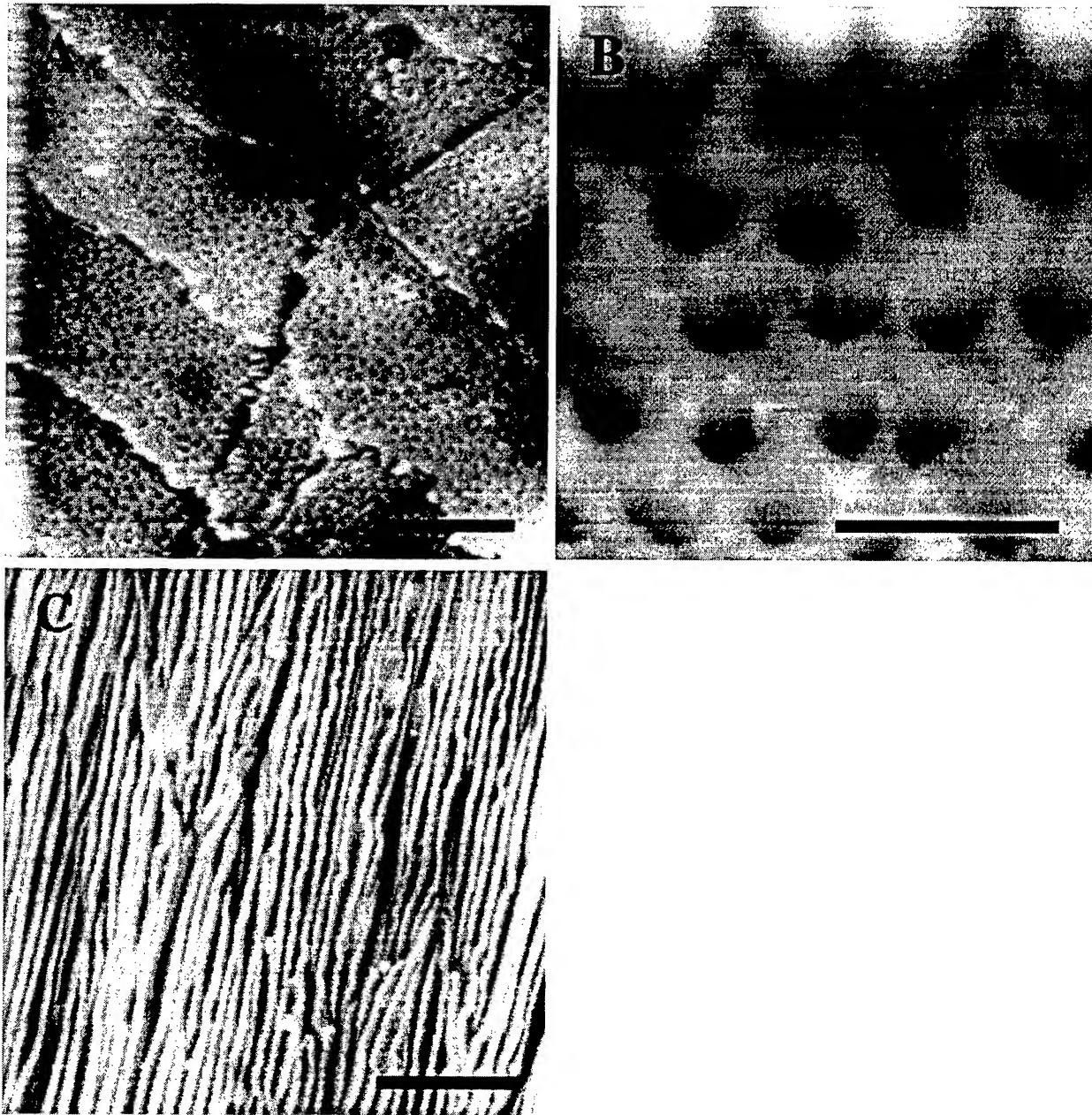


**Figure 9:** A: Low-power micrograph of the surface of a labial scale of *Boa constrictor* showing the large parallel plates covered by an array of micropits. The linear structure running from lower center to upper right is a scratch in the surface of the material. Scale bar = 5µm. B: High magnification image of labial scale of *Boa constrictor* showing regular arrangement of micropits. Scale bar = 1µm. C: Non-pit skin of *Boa constrictor*. not the parallel array of filament-like structures and lack of plates and micropits. Scale bar = 5µm.

#### *Infrared Imaging:*

Infrared video imaging was used in an initial attempt to determine the spectral reflection/absorption/transmission properties of snake tissues. Infrared imaging was performed using two IR-sensitive digital video cameras, one sensitive in the range of 3-5µm, and the other sensitive in the 8-12µm range. Images were fed directly to computer for analysis. All images collected were from live intact animals. In some cases, snakes were held with their pits at the focal plane of the cameras with lenses removed. In other cases, anesthetized snakes were mounted to a

stereotactic positioning device within an IR-shielded chamber. In both of these cases, lenses were removed in order to obtain images of IR-sensitive pit organs at high magnification. Snakes were also imaged with lenses mounted in order to determine reflectance properties over larger areas of the animal.

Imaging of pythons (in this case *Python regius*) with lenses mounted showed that the snake's rostrum, from the eyes forward to the edge of the upper jaw, exhibited much lower infrared emission and reflection than any other part of the body. While it was impossible to accurately determine the absolute temperatures of different parts of the snake's body (the emissivity was unknown), it was apparent that the rostrum was greater than 0.5°C cooler than any other part of the snake. It is also possible that the emissivity of the snake's rostrum is significantly lower than elsewhere on the body.

Imaging snakes with lenses removed from the cameras allowed magnification of the pit organs, and use of the stereotactic positioning device allowed precise control of the spatial relationship of the pit organs to the cameras' IR detectors. Viewed with either of the two cameras, the IR-sensitive pits appeared "darker" than surrounding tissue. That is, the pits themselves exhibited a greater IR absorption or lower emissivity than surrounding tissue. This effect was greater when viewed with the 8-12µm camera, indicating that the pits are IR absorptive, and that they preferentially absorb in the 8-12µm range.

In initial trials, discreet areas of the mandible and maxilla outside the pits also appeared "darker" in the IR images. However, rotating the specimen in an arc relative to the camera showed that these "dark" areas were in fact specular highlights caused by reflection of the camera's cooling system off the surface of the scale. Further tests showed that this effect could be produced by scales on any part of the snake's body. In order to determine whether the response seen within the pit was indeed greater absorption or lower emission, a warm probe (approximately 2°C above ambient temperature) was passed between the camera and the specimen. When the probe passed between the camera and scale material adjacent to the pit organ, a distinct reflection of the probe off the scale surface was observed. No such reflections were observed when the probe was passed between the pit organ and the camera, indicating that the difference in signal between pit and non-pit areas is due at least in part to greater IR absorption within the pit than by surrounding tissues.

### *Infrared Spectrometry*

Fourier-transformed infrared spectrometry was performed in order to determine the infrared transmission spectrum of intact pit samples and samples of epidermis. Spectrometry was performed over the range of 2-25µm wavelength. The outer layer of the epidermis overlies the infrared receptors, so its optical properties must influence the spectral properties of incident radiation reaching the infrared receptor nerve terminals. Since this layer of skin is periodically shed intact from the snake, and since the structure of these shed epidermal layers faithfully represents the structure in the intact living animal, we investigated the optical properties of shed skin samples. Because the structure of the outer surface of the shed skin is markedly different from that of the inner surface, we measured the infrared transmission of shed skins by placing the radiant source on the outer surface side or on the inner surface side of the skin. Results of these measurements were essentially identical with all skin samples tested. Infrared-sensitive pits in some species of snakes (*Python molurus*, for example) contain large amounts of melanin pigment granules, while those in other species (*Python regius*, for example) apparently contain no melanin. We therefore measured the infrared transmission in samples of pigmented vs. non-pigmented skin. Thus, neither pigmentation nor the direction of IR transmission altered the transmission spectral profiles.

Samples of epidermis alone exhibited 3 windows of transmission, one centered at 2-2.5µm, one at 5µm, and another at 10µm. These regions are generally within windows of atmospheric transmission, so they represent bands of IR energy that are potentially useful for IR imaging. FTIR spectrometry measurements performed on isolated intact pit organs yielded little useful information, because the intensity of the FTIR beam burned the tissue over the timecourse of the measurement.

There were significant differences in transmission spectra between epidermal samples composed of a micropit-covered surface, and those not containing micropits. Since at the time I could not get sufficient pit material for FTIR, I isolated *Boa constrictor* scale epidermal material from interscale material (interscale epidermis is covered by an array of micropits; see Fig.5), and performed FTIR on each. The results of this analysis (Fig. 10) show that micropit-covered material has a very different IR transmission profile than that of non-micropit-covered material. This result is very intriguing, and we are currently collecting epidermal samples from pit organ for more detailed analyses.

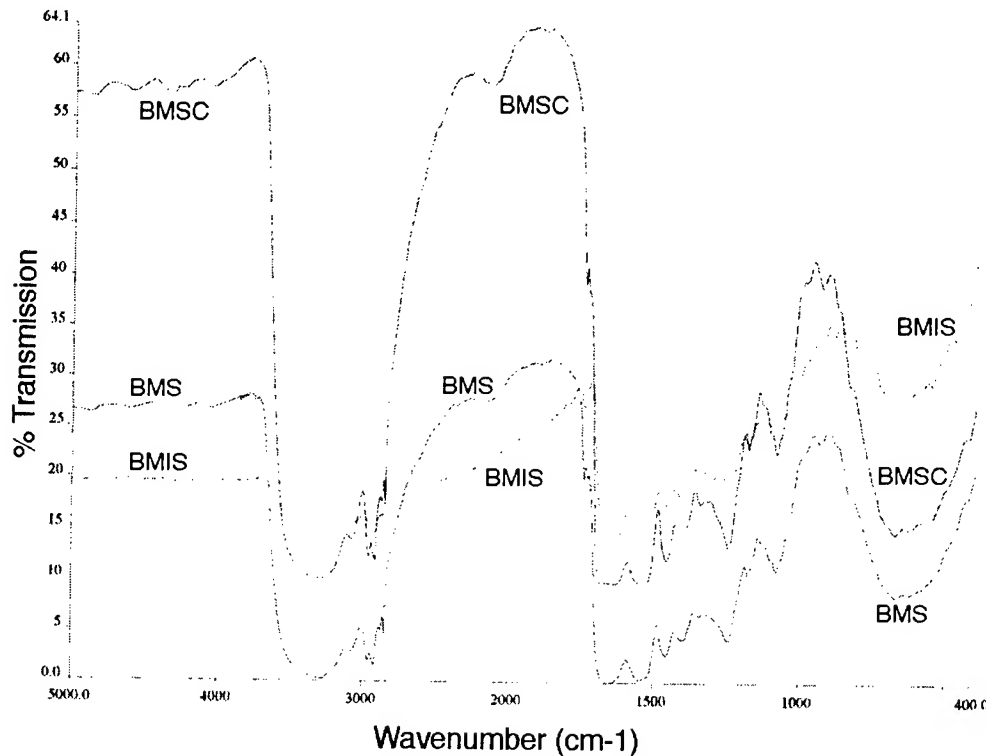


**Figure 10:** Infrared transmission spectra of *Boa constrictor* mandibular skin (intact shed epidermis, **BMS**), scale skin only (completely isolated from interscale skin, **BMSC**), and interscale skin (completely isolated from scale skin, **BMIS**).

Direct hemispheric reflectance IR spectrometry (DHR) is generally used to determine spectra of reflectance from sample surfaces. With minor modification, DHR was used here to determine both reflectance and transmission (and therefore also absorbance) properties of IR-sensitive pit material. For reflectance measurements, tissue samples were mounted on Krylon black-painted supports. These supports are completely absorbent over the range of 2-15 $\mu$ m (the spectral range used here). Thus, any radiation not reflected was absorbed by the support. For transmission measurements, samples were mounted on polished aluminum foil supports. Energy neither reflected nor absorbed by the tissue was reflected off the support to the detector. Obviously, absorption occurring under these conditions is the result of 2 passes through the sample.

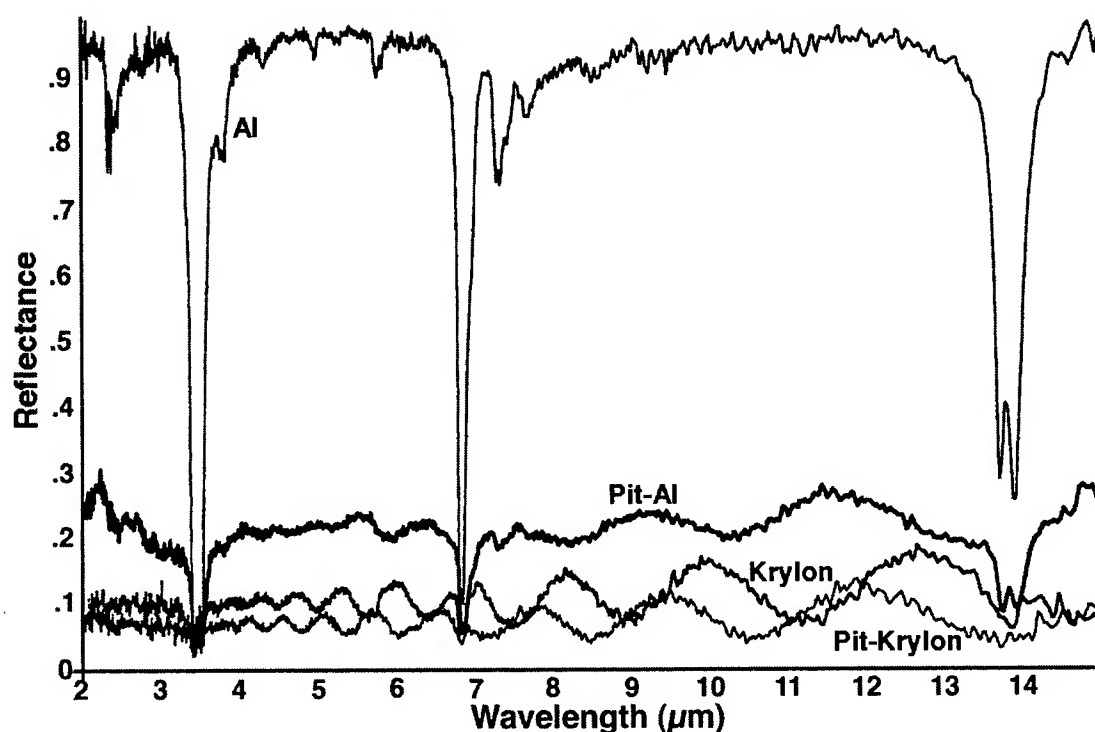


**Figure 11:** Direct hemispheric reflectance analysis of intact isolated pit organ from *Python regius*. **Krylon:** control measurement of Krylon flat black (highly absorptive). **Al:** control measurement of aluminum foil (highly reflective). **Pit-Krylon, Pit-Al:** pit organs mounted on Krylon support and aluminum foil support, respectively. All samples tested with polypropylene film overlay which produces wavy appearance of low reflectance traces.

### Biochemistry

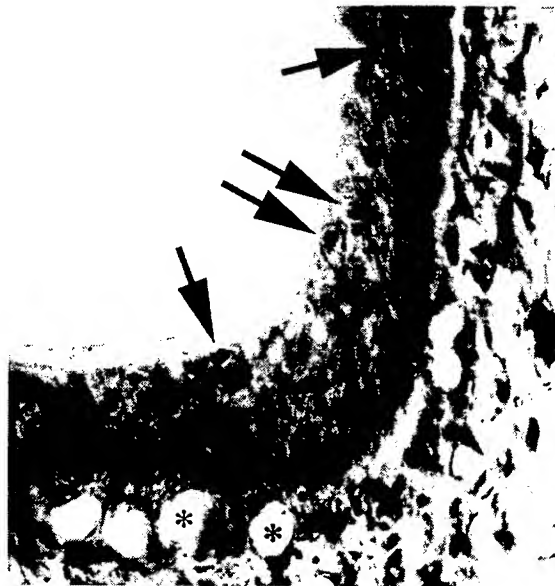
In a comparison of pit organ and retina, I localized opsins (the protein portion of the retinal photoreceptor photopigments) to photoreceptors of the retina (Table 1). I used 5 different anti-opsin antisera and found that different classes of retinal photoreceptors react with different antisera (as expected). However, none of these anti-opsin antisera labeled the IR-sensitive terminals in the pit (Table 1). This data shows that the IR receptor entity is very unlikely to be an opsin-like molecule. This answers a major question regarding the relationship between these two electromagnetic receptors, showing that they are biochemically very distinct, and that if IR sensitivity is photonic, the receptive molecule is probably unlike known retinal photopigments.

While the pit IR terminals contain no opsin, I have discovered other proteins in these terminals (Table 1). One of these, phosducin, regulates of transduction in photoreceptors, and analogous proteins have been discovered in other cells. The discovery of this regulatory protein in the IR terminals identifies another potential component of the IR transduction apparatus.

Assuming that calcium is probably involved in IR transduction at some level (it is involved in all other sensory systems), I applied a similar approach using antisera against calcium-binding proteins (Table 1, Fig. 12). I found several calcium-binding proteins in the retina (among them calretinin and calbindin), and others in IR receptors (calmodulin and S-100). Those found in photoreceptors are not found in IR receptors, and those in IR receptors do not exist in photoreceptors. This data, together with that showing the distribution of opsin immunoreactivity, shows that IR receptors are biochemically distinct from photoreceptors. From a functional point of view, the calcium-binding proteins found in IR receptors of the pit organ are calcium-regulated

**Table 1:** Immunohistochemical comparison of retinal photoreceptors and pit organ infrared-receptive neuronal terminals in *Python molurus bivittatus*.

<u>Antiserum</u>	<u>Specificity</u>	<u>Immunoreactivity</u>
<u>photoreceptor proteins</u>		
CERN-858	rod opsin	retinal photoreceptors
CERN-874	cone opsin	retinal photoreceptors
CERN-906	rod and cone opsin	some retinal photoreceptors
COS-1	cone opsin	none
OS-2	rod opsin	all retinal photoreceptors
CERN-911	phototransduction	photoreceptors, IR terminals
Phosducin	phosducin	photoreceptors, IR terminals
S-antigen	retinal s-antigen	retinal photoreceptors
<u>calcium-binding proteins</u>		
Calbindin	calbindin	inner retinal cells
Calretinin	calretinin	retinal photoreceptors
Calmodulin	calmodulin	IR terminals, inner retina
S-100	S-100	IR terminals, inner retina

**Figure 12:** Immunolocalization of calmodulin in neuronal terminals (arrows) of the infrared-sensitive pit organ of *Python molurus bivittatus*. Note that relatively few terminals are stained, suggesting functionally different classes of IR receptor cells. Asterisks: capillaries

proteins. That is, binding of calcium to these proteins causes them to change their functional activity. These proteins therefore are likely components of the IR transduction cascade. They may function by transducing the IR signal into an electrochemical signal through which neurons communicate, or they may be involved in regulating the sensitivity of the IR receptors or their recovery after stimulation. The calcium-binding proteins found in the retinal photoreceptors are not

calcium-regulated proteins, but rather calcium-sequestering proteins (that is, they actively regulate calcium concentration in the cellular cytoplasm).

There has never been any hint that, like retinal photoreceptors, there may be different functional classes of infrared receptor cells in the pit organ. My immunohistochemical results, however, argue that this may in fact be the case. While immunoreactivity for mitochondrial inner membrane proteins occurs in apparently all pit organ neuronal terminals, calcium-binding protein immunoreactivity in the pit organ occurs only in a subpopulation of neuronal terminals (Fig. 12). These results indicate that there are biochemically, and perhaps functionally, distinct classes of infrared receptor cell in the *Python* pit organ.

The discovery of these proteins in IR-sensitive nerve terminals, and the suggestion that there are biochemically-distinct classes of IR receptors are completely new findings. There has never been any hint of the biochemistry underlying infrared detection in any natural system. As such, these discoveries are some of the most important in the history of the study of this system.

The immunohistochemical studies described above were performed prior to beginning the Summer Faculty Research Program at the Wright Laboratory. In order to better define the immunohistochemically-localized components of the pit organ receptor neurons, we began immunoblotting experiments at the Wright Laboratory. These experiments involve extracting total protein from the pit organ, and separating proteins on an SDS--polyacrylamide gel. Proteins are then transferred from the gel to a nitrocellulose membrane, and this membrane is subjected to immunostaining. The visualized protein bands will show the number and molecular weights of proteins labeled by the antisera. These experiments thus far have yielded good separation of proteins, and we have developed useful staining procedures. We have not yet immunostained proteins on gels, however. These experiments comprise part of an ongoing collaborative research effort between myself and researchers at MLPJ, Wright Laboratory. We will immunostain blots using all of the antisera that have given positive results in previous experiments in which proteins were localized in tissue (see above).

Initial efforts at protein identification have focused on opsin proteins because they are the initial step in retinal phototransduction, and calcium-binding proteins because they are involved in all known sensory receptors. Another ubiquitous signaling mechanism in neurons involves protein phosphorylation/dephosphorylation. Addition or removal of phosphate groups from proteins is highly regulated in neurons, and changes in state of phosphorylation regulates phosphoprotein activity. Thus, regulation of protein phosphorylation is a likely component of IR signal transduction. In addition, the results of IR spectrophotometric analyses (see above) indicate that a potential peak of absorption by the IR receptors is centered on 10 $\mu$ m, the maximal emission of snake target prey. This is particularly interesting in that phosphate groups maximally absorb at 10 $\mu$ m. Thus, changing in protein phosphate content is not only a potential regulatory mechanism, but the phosphate groups themselves may be the absorptive entity. Therefore, we have begun isolating phosphoproteins from the pit organ. Initial attempts were made with immunoaffinity matrices. These matrices were composed of beads to which were linked antibodies directed against phosphorylated amino acids normally found in phosphoproteins (phosphoserine, -threonine, and -tyrosine). We have also used an iron affinity matrix which binds phosphoproteins. Samples applied to these matrices leave phosphoproteins bound, after which they are eluted by changing buffer chemistry. Coupling this approach with gel electrophoresis, we have isolated phosphoproteins from the pit organ. We will compare the phosphoproteins isolated from pit organ to those isolated from retina, non-pit skin, trigeminal ganglion, and brain. This approach will identify phosphoproteins unique to the pit organ, and may also identify phosphoproteins used in signal transduction in similar sensory systems. These experiments comprise part of an ongoing collaborative research effort between myself and researchers at MLPJ, Wright Laboratory.

This immunohistochemical approach, while very productive, is limited by the fact that we can only search for known components of other signaling systems. The search for phosphoproteins does not have this limitation, but is limited to proteins regulated by phosphorylation. In an effort to expand our search to any and all protein signaling components used in signal transduction by pit organ receptor neurons, we have begun generating cDNA libraries for use in a variety of experiments, most notable subtraction hybridization. We are

collecting samples of pit organ, trigeminal ganglia (location of the cell bodies sending receptor terminals to the pit organ), retina, and skin. These samples are rapidly frozen in liquid nitrogen, total RNA extracted, and poly-A RNA isolated. cDNA (copy DNA) is then produced using poly-A RNA as template. The cDNA library produced should contain coding sequences for all proteins synthesized in the tissue from which the library was made. We are in the process of collecting tissue samples for library preparation (some tissues such as trigeminal ganglia are extremely small, requiring large numbers of animals to be sacrificed over time; to maximize productivity from each animal, we are collecting tissue samples from animals used for other experiments). After cDNA libraries are prepared, we will begin the process of subtraction hybridization which will quickly and efficiently isolate cDNA fragments that are unique to the pit organ. We are comparing pit organ to non-pit skin because the IR-receptive terminals are located within the dermis of the skin. We are comparing pit organ to retina because both are image-forming radiant energy detectors. These experiments represent an ongoing collaboration between myself and researchers at MLPJ, Wright Laboratory.

### **Conclusions:**

The results described in this report are completely new findings on a novel and essentially unexplored sensory system. The infrared imaging capabilities of boid and crotalid snakes have many significant advantages over other natural IR sensors, and over current artificial infrared detection devices. The work described herein was approached from three standpoints: (1) identification of structural features of the IR sensing organ that contribute to its optical properties, (2) investigation of the IR transmission and absorption properties of the organ, and (3) biochemistry of the transduction process. The surface structure of the pit organ contributes to the transmissive, absorptive and reflective properties of the pit organ. IR spectrometric and imaging studies support this conclusion, and indicate that both atmospheric IR transmission windows (3-5 $\mu$ m and 8-12 $\mu$ m) are probably particularly important to IR sensitivity: The results of the IR spectrometric and imaging studies, together with biochemical analyses suggest that 10 $\mu$ m radiation may be particularly important. We hypothesize that protein phosphorylation may be an important component of infrared reception, and that phosphate itself, which absorbs at 10 $\mu$ m, may be the receptive entity. The results of biochemical studies have also identified several other probably proteinaceous components of the IR signal transduction cascade. The results of these investigations provide the foundation for ongoing collaborative studies between myself and researchers at Wright Laboratories.

### **Acknowledgments:**

This work described in this report was performed in collaboration with the Laser Hardened Materials and Survivability branch of the Materials Directorate, Wright Laboratories, Wright-Patterson AFB, and Systems Research Laboratories, Fairborn, Ohio. I am particularly grateful to Dr. Thomas M. Cooper, who served as Summer Faculty Research Program Point of Contact, Dr. Donald Wiff, who coordinated my visit to Wright-Patterson AFB, and Pamela Schaeffer, the MLPJ Branch Chief who provided a very productive work environment.



## References

1. Bullock, T.H. and P.J. Diecke (1956) *Properties of an infrared receptor*. Journal of Physiology, **134**:47-87.
2. DeCock Buning, T.J., S. Terashima, and R.C. Goris (1981) *Crotaline pit organs analyzed as warm receptors*. Cellular and Molecular Neurobiology, **1**:69-85.
3. DeCock Buning, T.J., S. Terashima, and R.C. Goris (1981) *Python pit organs analyzed as warm receptors*. Cellular and Molecular Neurobiology, **1**:271-278.
4. Harris, J.F. and R.I. Gamow (1971) *Snake infrared receptors: thermal or photochemical mechanism?* Science, **172**:1252-1253.
5. Hartline, P.H., L. Kass, and M.S. Loop (1978) *Merging of modalities in the optic tectum: infrared and visual integration in rattlesnakes*. Science, **199**:1225-1229.
6. Kardong, K. and G. Mackessey (1991) *The strike behavior of a congenitally blind rattlesnake*. Journal of Herpetology, **25**:208-211.
7. Meszler, R.M. (1970) *Correlation of ultrastructure and function.*, in *Biology of the Reptilia*, C. Gans and T.S. Parsons, Ed. Academic Press: London, New York. P. 305-314.
8. Molenaar, G.J. (1992) *Anatomy and physiology of infrared sensitivity of snakes*, in *Biology of the Reptilia*, C. Gans and P.S. Ulinski, Ed. University of Chicago Press: Chicago. p. 367-453.
9. Terashima, S. and R.C. Goris (1975) *Tectal organization of pit viper infrared reception*. Brain Research, **83**:490-494.
10. Terashima, S. and R.C. Goris (1977) *Infrared bulbar units in Crotaline snakes*. Proceedings of the Japanese Academy, **53**:292-296.
11. Terashima, S., R.C. Goris, and Y. Katsuki (1968) *Generator potential of Crotaline snake infrared receptor*. Journal of Neurophysiology, **31**:682-688.



**Appendix I: Presentations** by Michael S. Grace, Ph.D. during Summer Faculty Research Program at Wright-Patterson AFB:

1. Materials Lab WUD (Work Unit Directive) talk: *Mechanisms of Infrared Detection by Snakes*, 30 June, 1997
2. MLPJ (laser Hardened Materials Branch) snake group meeting talk: *Progress Report: Biomimetic Infrared Sensing Technology Initiative, WL/MLPJ, Summer 1997*, 2 July 1997
3. Wright Laboratories Education Outreach (summer high school teacher apprentice program) talk: *Snake Pit! An extremely Sensitive Natural Infrared Detector*, 16 July, 1997
4. Research Seminar (base-wide and off-base invitation): *Structure and Function of an Extremely Sensitive Image-Forming Biological Infrared Detector*, 17 July, 1997

**Appendix II: Publications** resulting from the work described in this report:

1. *Biochemistry of Snake Infrared "Vision"*, Michael S. Grace; submitted to *Nature*
2. *Retinal photoreceptors and pit organ infrared receptors in Python are biochemically distinct*. Soc. Neurosci. Abstr. 1997
3. *Characterization of snake proteins involved in infrared sensing*, Morley O. Stone\*1, Thomas M. Cooper, Drew Rolph, Don Church, and Michael Grace; abstract submitted to *Biosensors* 98
4. *Surface Structure and Optical Properties of the Infrared-Sensitive Pit Organ in Boid Snakes*, M.S. Grace, A. Campbell, T.M. Cooper, R. Crane, and D.R. Church; abstract submitted to *Biosensors* 98
5. *Biochemistry and Infrared Spectrophotometry of a Highly-Sensitive Image-Forming Infrared Detector in the Snake Python*, M.S. Grace, D.R. Church, T.M. Cooper, M. Stone, C. Kelley, and W. Lynn; abstract submitted to *Biosensors* 98
6. In preparation for peer-reviewed journals:
  - (a) *Surface structure of pit organ and non-pit organ epidermis in Biod snakes*. To be submitted to *Journal of Ultrastructural Research*.
  - (b) *Retinal photoreceptors and pit organ infrared receptors in Python are biochemically distinct*. To be submitted to the *Journal of Comparative Neurology*.
  - (c) *Infrared spectrometric analyses of Python pit organ*. To be submitted to ?.

**Appendix III: Students trained** during the course of this work:

1. Cdt. Drew Rolf, U.S.A.F. Academy cadet
2. Margaret Burns, Summer High School Student Research Prog., MLPJ, Wright-Patterson AFB

INDICIAL RESPONSE MODEL FOR ROLL ANGLE AND ROLL  
RATE EFFECTS ON A 65-DEGREE DELTA WING

Gary M. Graham  
Associate Professor  
Department of Mechanical Engineering

Ohio University  
255 Stocker  
Athens, OH 45701

Final Report for:  
Summer Faculty Research Program  
Wright Laboratories

Sponsored by:  
Air Force Office of Scientific Research  
Bolling Air Force Base, DC

and

Wright Laboratories

August 1997

**Indicial Response Model for Roll Angle and Roll Rate Effects  
on a Delta Wing during Forced Roll Oscillations**

G. M. Graham  
Ohio University  
Athens, OH 45701

**Abstract**

This paper describes an indicial response model for predicting the rolling moment on a 65° delta wing experiencing harmonic oscillations in body-axis roll at moderate to high rates. The model is formulated in the aeroballistic coordinate system and comprises two convolution integrals with one integral accounting for variations in roll angle and a second integral accounting for variations in roll rate. The model is semi-empirical in that the indicial responses are computed from experimental wind tunnel data using an optimization method. The model is extended to a nonlinear model which accounts for static nonlinearities. The nonlinear model is used to predict the moment for both harmonic rolling motions and ramp motions.

# Indicial Response Model for Roll Angle and Roll Rate Effects on a Delta Wing during Forced Roll Oscillations

G. M. Graham

## Nomenclature

- $b$  = semispan (ss) = 0.95 ft.  
 $C_{am}$  = apparent mass coefficient (ss/rad)  
 $C_l$  = rolling moment  
 $C_{l\phi}$  = roll angle "stiffness" derivative or static roll angle slope (1/rad)  
 $C_{lp}$  = roll rate "damping" derivative or static roll rate slope (ss/rad)  
 $I_{l\phi}$  = indicial response due to roll angle  
 $I_{lp}$  = indicial response due to roll rate  
 $p$  = roll rate (rad/ss)  
 $U_\infty$  = freestream velocity = 330 ft/sec  
 $\phi$  = roll angle  
 $\sigma$  = pitch angle =  $30^\circ$   
 $\tau_c$  = indicial response time constant  
 $\omega$  = oscillation frequency  
superscripts  
 $e$  = experimental parameter  
 $I$  = indicial model parameter  
 $P$  = potential flow component  
 $V$  = vortical component

## Introduction

### Background

The ability to predict the aerodynamic loading on an aircraft experiencing highly unsteady motion has been an active research topic for the past several years. Recently, Goman et al. [1] have proposed a state space model wherein the internal variable is vortex breakdown position for predicting the rolling moment on a delta wing. In the Goman model the rolling moment is computed as the solution to a first order differential equation in which the motion input (roll angle) is lagged in time in an attempt to simulate experimentally observed dynamic effects on the unsteady loading. Huang and Hanff [2] have used a delta wing surface pressure model in combination with experimentally measured vortex breakdown position to define regions on the wing surface which can be modeled using a leading edge suction analogy approach for regions in front of the breakdown position and an assumed exponential decay of pressure for regions aft of the breakdown position.

Tobak et al. [3] have developed a nonlinear indicial response model for the aerodynamic loading which can

account for both static nonlinearities as well as motion history effects on the flowfield. The indicial response is by definition the loading response to a step change in a motion parameter, such as angle of attack or roll angle, as the step height approaches zero. In addition, the NIR model has been extended to account for the possibility of critical states at which solution bifurcations may exist [4,5]. Etkin [6] has formulated the aircraft equations of motion using a linear form of the indicial method.

Recent wind tunnel data acquired at the Air Force SARL facility have provided a large amount of force and moment data on a 65° delta wing over a wide range of flight conditions [7]. This paper describes a semi-empirical indicial response model for predicting the rolling moment on a delta wing undergoing harmonic roll oscillations wherein the SARL data are used to compute the indicial responses. These indicial responses may then be integrated using a superposition integral to compute the time varying rolling moment for a specified motion.

For analyzing the SARL data of Reference [7] it is convenient to describe the wing motion in the aeroballistic coordinate system. Jenkins [8] has shown that in this coordinate system "single degree of freedom roll motions in wind tunnel experiments must be seen as the superposition of two characteristic motions." For a single degree of freedom rolling motion (when viewed in the aeroballistic coordinate system) these characteristic motions correspond to variations in roll angle,  $\phi$  (designated  $\Psi$  in References [3,8]) which are due to pure translation, and body-axis roll rate,  $p$ , corresponding to pure rotation. Therefore, any mathematical representation of the aerodynamic loading should account for both effects. The situation is analogous to the pitch-plane case in which single degree of freedom rotations produce the combined effects of plunge ( $\dot{\alpha}$ ) and pitch ( $q$ ). In the wind tunnel  $\phi$  and  $p$  are kinematically related  $p = \dot{\phi}$ . Nevertheless, when formulating the aerodynamic response in the aeroballistic coordinate system, the independence of the response to each motion parameter must be acknowledged. This is accomplished in the present model by using a separate superposition integral for the angle and rate effects.

#### Comment on the Use of Stability Derivatives

The stability derivative approach for predicting aerodynamic forces on aircraft has been in use for many years. While this method is concise and may be adequate for quasisteady motions, it may introduce significant error in highly unsteady cases. For predicting the rolling moment coefficient due to oscillations in roll angle, Fourier analysis of small-amplitude harmonic data yields an in-phase linear roll angle or "stiffness" derivative and an out-of-phase linear roll rate or "damping" derivative. Alternatively, the stiffness derivative may be computed from static data. The rolling moment is formulated as

$$C_l(t) = C_{l\phi}^e \phi(t) + C_{lp}^e p(t) \quad (1)$$

where  $C_{l\phi}^e$  and  $C_{lp}^e$  may be functions of roll angle but are generally not considered to be functions of rate or frequency. The assumption contained in Eq. (1) is that the aerodynamic response is "fast" compared to the motion rate.

The above aerodynamic derivatives have been computed from harmonic data acquired at five nondimensional frequencies ( $\omega b/U_\infty$ ) and are shown in Figures 1a and 1b (square symbols). The harmonic data were acquired at a constant pitch angle of 30°, 0° roll angle offset, and an amplitude of 2°. In relation to the stability derivative

approach, it is important to note the variation in these derivatives with frequency. An illustration of the importance of the frequency dependence may be seen in Figure 2a which shows experimental roll moment data for a nondimensional frequency of 0.04. Also shown is a prediction of the moment using Eq. (1) wherein  $C_{l\phi}^e$  has been measured from static data at  $\phi=0^\circ$  and  $C_{lp}^e$  has been computed from harmonic data at the same frequency. The agreement between the experiment and Eq. (1) is poor. Figure 2b shows a similar calculation wherein  $C_{l\phi}^e$  and  $C_{lp}^e$  have both been computed from harmonic data acquired at a reduced frequency of 0.14. The agreement is again poor. From the foregoing it can be concluded that the stability derivative approach, whether based on static or dynamic tests, does not provide the required sensitivity to rate (frequency) effects and a model which contains more of the physics of the flow, such as noninstantaneous response times, is needed. It is possible to add higher order terms to Eq. (1), however, this will introduce additional (and possibly unstable) roots into the vehicle's characteristic equation.

### Mathematical Model

#### Indicial Response Model

The superposition integral method for describing the response of linear systems has been applied in many branches of engineering. This approach is based on the superposition of indicial responses which by definition is the response of the system to a step input in a boundary condition such as angle of attack or roll angle. Of particular interest to the flight mechanist is the method of Reference [3] wherein the superposition integral is extended to accommodate the occurrence of a nonlinear indicial response (NIR) which may include static nonlinearities and motion history effects on the flowfield.

Following Reference [3], for a delta wing experiencing body-axis roll at constant total pitch angle, the full nonlinear form of the superposition integral for the rolling moment (formulated in the aeroballistic coordinate system [8]) is

$$C_l(t) = C_{l0} + \int_0^t I_{l\phi}[\phi(\xi), p(\xi); t, \tau] \frac{d\phi(\tau)}{d\tau} d\tau + \int_0^t I_{lp}[\phi(\xi), p(\xi); t, \tau] \frac{dp(\tau)}{d\tau} d\tau \quad (2)$$

where  $\phi$  is the roll angle,  $p$  is the roll rate, and it is understood that  $\phi$  and  $p$  are independent motion parameters. Variations in  $\phi$  are due to translational motion only and it is defined by:  $\tan\phi = v/w$ , where  $v$  and  $w$  are the  $y$  and  $z$  components of velocity measured in the body-fixed coordinate system. Variations in rate  $p$  are due to pure rotation about the body-fixed  $x$  axis.

In Eq. (2),  $I_{l\phi}$  is the aerodynamic roll angle NIR which is defined as the moment response to a step change in  $\phi$  by translation while  $p$  is held constant, and  $I_{lp}$  is the NIR to a step change in  $p$  while  $\phi$  is held constant (see Reference [8]). The notation of Eq. (2) is intended to indicate that both NIRs are functionals of the motion history described by  $\phi(\xi)$  and  $p(\xi)$ . For motions which are analytic the NIR can be written as a function of the motion parameters and their time derivatives ( $\phi(\tau), \dot{\phi}(\tau), \dots, p(\tau), \dot{p}(\tau), \dots$ ), and elapsed time  $(t-\tau)$  from step onset. Assuming the NIR to be dependent only on  $\phi(\tau)$ ,  $p(\tau)$ , and elapsed time, Eq. (2) simplifies to

$$C_l(t) = C_{l0} + \int_0^t I_{l\phi}(\phi(\tau), p(\tau), t-\tau) \frac{d\phi(\tau)}{d\tau} d\tau + \int_0^t I_{lp}(\phi(\tau), p(\tau), t-\tau) \frac{dp(\tau)}{d\tau} d\tau \quad (3)$$

where the indicial responses remain nonlinear since they depend on the motion; although in a simplified way. The linearized form of Eq. (2) is

$$C_l(t) = C_{l0} + \int_0^t I_{l\phi}(t-\tau) \frac{d\phi(\tau)}{d\tau} d\tau + \int_0^t I_{lp}(t-\tau) \frac{dp(\tau)}{d\tau} d\tau \quad (4)$$

where the indicial responses are functions of elapsed time only. Although linear, Eq. (4) retains the capability of predicting significant lags in the rolling moment response. This paper describes an application of Eqs. (3) and (4) wherein the wind tunnel data of Reference [7] have been used to compute the indicial responses.

As discussed below, the present approach is predicated on the existence of rolling moment data at the same mean angle and same amplitude, but at different frequencies. In this paper attention is focused on the following motion

$$\begin{aligned} \phi(t) &= \phi_0 - \Delta\phi \cos(\omega t) \\ \sigma &= 30^\circ \text{ (pitch angle)} \end{aligned} \quad (5)$$

where  $\Delta\phi = 2^\circ$  or  $4^\circ$ . The negative sign and the use of a cosine function (as opposed to sine) in the first equation is arbitrary and used only for convenience since this is the form into which a data reduction program (for smoothing) places the data. Rolling moment data were taken at five nondimensional frequencies ( $\omega b/U_\infty$ ) of 0.02, 0.04, 0.06, 0.08, and 0.14 at a Mach number of 0.3. Also considered below is the case of a "ramp" motion from  $\phi = -4^\circ$  to  $\phi = +4^\circ$ . Details of the experiments can be found in Reference [7].

#### Static Data

An important prerequisite for indicial response modeling is the existence of detailed static loading data. This is important for at least two reasons. First, the indicial response, whether linear or nonlinear, must approach the static value as time goes to infinity. Second, static data contain information on the location of critical states. Critical states are points where there is a change in flow topology which may cause the system to bifurcate to a new equilibrium solution branch[4,5]. Static data for the present delta wing are shown in Figure 3 which shows the *slope* of the rolling moment data. The slope has been computed numerically by performing a central difference on the static moment data. There is a significant asymmetry in the data. The reason for the asymmetry is not completely understood, however, it may be due to freestream asymmetry caused by a tear in one of the tunnel screens. Nevertheless, so long as the indicial response model is faithful to the static data the model should be valid. The region  $-4^\circ < \phi < 4^\circ$  is believed to be free of critical states [5].

Unfortunately, there are no experimental data for the steady state dependence on roll rate which are directly applicable to the present study. Future static data acquired on (induced) cambered wings [9,10] or on a rotary test rig may be of significant value in the advancement of the indicial response parameter identification. In the induced camber concept an uncambered wing undergoing variations in roll rate is replaced by an equivalent static wing having a camber distribution which yields the same angles of attack along the leading edge.

#### Form of the Indicial Response

For applying Eq. (3) or (4), the task at hand becomes the identification of the indicial responses  $I_{l\phi}$  and  $I_{lp}$ . Data acquired for "slow ramp" and "ramp-and-hold" motions [11] suggest the following forms may be adequate

$$\begin{aligned} I_{l\phi}(t) &= C_{l\phi} (1 - Ae^{-t/\tau_c}) \\ I_{lp}(t) &= C_{lp} (1 - Be^{-t/\tau_c}) \end{aligned} \quad (6)$$

where  $C_{l\phi}$  is the known local static moment curve slope (Figure 3), and the constants  $C_{lp}$  (steady rate slope),  $A$ ,  $B$ , and  $\tau_c$  are determined from the SARL data using an optimization method as described below.

In the present work the indicial responses are considered to be the sum of an instantaneous potential flow contribution, and superimposed thereon a transient viscous indicial response having a finite time constant. The components of the indicial response are illustrated in Figure 4 for the roll angle response ( $I_{l\phi}$ ) only, the concept being the same for the roll rate response ( $I_{lp}$ ).

The assumption of an instantaneous potential flow contribution to the indicial responses stems from two observations. The first is illustrated in Figure 5 which shows rolling moment data for ramp-up and ramp-down motions. For each curve there is an inflection point where the second derivative of the curve changes sign. For the static data this occurs at zero degrees roll angle. Flow visualization data indicate that, at the inflection points, the vortex breakdown position is approximately the same on both the right and left wings. Therefore, assuming that the strengths of the right and left vortices are approximately equal the vortical effects should cancel leaving only the potential flow contribution. Also shown on Figure 5 is the static potential flow curve obtained from the commercial code QUADPAN. The static potential flow results correlate well with the dynamic data at the inflection points. The conclusion is that there is a part of the aerodynamic response which is very fast and this corresponds closely to the value predicted by potential flow theory. One might intuitively expect the time scale of the potential flow contribution to be on the order of the convection time scale for the flow, which is known to be much smaller than observed lags due to vortex breakdown. The second justification for the assumption of a fast-acting potential flow contribution to the indicial response requires an expansion of Eq. (4) for the motion under consideration and will be discussed in detail later.

#### Linear Indicial Response Model

The linear indicial response model (Eq. (4)) has been applied to the case of  $2^\circ$  amplitude harmonic oscillations in body-axis roll about four different offset angles of  $\phi_0 = 0^\circ, 3^\circ, 6.5^\circ$ , and  $8^\circ$ . Representative results for the  $0^\circ$  and  $8^\circ$  cases are presented here. No attempt was made to account for the effects of critical state crossings which are known to exist at values of  $\phi$  near  $5^\circ$  and  $8^\circ$  [5]. In the linear model the parameters  $C_{l\phi}$ ,  $C_{lp}$ ,  $A$ ,  $B$ , and  $\tau_c$  appearing in the indicial responses of Eqs. (5) are assumed to be constants. The static slope  $C_{l\phi}$  is known from Figure 3 and is taken to be the average slope over the  $2^\circ$  range of the harmonic motion. As has been mentioned, there are no static data for the roll rate effect and, therefore, this is treated as an unknown parameter.

Substitution of Eqs. (5) and (6) into Eq. (4) yields

$$\begin{aligned} C_l(t) = & C_{l0} + C_{l\phi} \Delta\phi \omega \int_0^t (1 - Ae^{-(t-\tau)/\tau_c}) (\sin\omega\tau) d\tau + \\ & C_{lp} \Delta\phi \omega^2 \int_0^t (1 - Be^{-(t-\tau)/\tau_c}) (\cos\omega\tau) d\tau + C_{am}\dot{\phi}(t) \end{aligned} \quad (7)$$



where the last term is an instantaneous apparent mass term added to account for variations in  $\phi$  due to linear accelerations. The terminology "apparent mass" seems appropriate when considering that  $\phi$  is a function of the linear velocity in the y and z directions so that accelerations in these directions will cause  $\phi$  (and therefore  $C_l$ ) to change. Integrating Eq. (7) and separating into in-phase (i.e.  $-\cos\omega t$ , see Eq. (5)) and out-of-phase ( $\sin\omega t$ ) components yields

$$C_l(t) = C_{l0} + C_{l\phi}^I \Delta\phi \cos(\omega t) + C_{lp}^I \Delta\dot{\phi} \sin(\omega t) \quad (8)$$

where

$$C_{l\phi}^I = [C_{l\phi}(1 + \omega^2 \tau_c^2(1 - A)) + C_{lp} B \omega^2 \tau_c] / (1 + \omega^2 \tau_c^2) \quad (9)$$

$$C_{lp}^I = [-C_{l\phi} A \tau_c + C_{lp}(1 + \omega^2 \tau_c^2(1 - B))] / (1 + \omega^2 \tau_c^2) + C_{am}$$

In this form  $C_{l\phi}^I$  and  $C_{lp}^I$  represent the indicial model counterparts to the aerodynamic "stiffness" and "damping" derivatives, respectfully, and are seen to be functions of frequency. Note that in Eq. (7) *each integral contributes to both  $C_{l\phi}^I$  and  $C_{lp}^I$* . Within the context of the present model, therefore, harmonic wind tunnel data which have been reduced to in-phase and out-of-phase derivatives cannot be associated solely with angle and rate effects, respectively. The lag in both angle and rate indicial responses causes each integral to contribute both an in-phase and out-of-phase component.

If the frequency is specified, and inasmuch as  $C_{l\phi}$  is known from static tests, there are five unknowns in Eqs. (9), namely:  $C_{lp}$ , A, B,  $\tau_c$ , and  $C_{am}$ . The optimization method known as the variable metric method [12] has been used to solve for these constants. The function, F, chosen to be optimized is

$$F = \sum_{i=1}^N [(C_{l\phi}^e(\omega_i) - C_{l\phi}^I(C_{lp}, A, B, \tau_c; \omega_i))^2 + (C_{lp}^e(\omega_i) - C_{lp}^I(C_{lp}, A, B, \tau_c, C_{am}; \omega_i))^2] = 0 \quad (10)$$

where N is the number of frequencies tested (at a given offset roll angle),  $C_{l\phi}^e$  and  $C_{lp}^e$  are the experimental aerodynamic derivative such as those shown in Figures 1a and 1b for the case of zero offset, and  $C_{l\phi}^I$  and  $C_{lp}^I$  are functions of the unknown parameters indicated in parenthesis ( $\omega_i$  is of course known).

Two additional equations which force the indicial responses instantaneously to the potential flow values are also optimized with Eq. (10) given by

$$[C_{l\phi}(1 - A) - C_{l\phi}^P]^2 = 0 \quad \text{and} \quad [C_{lp}(1 - B) - C_{lp}^P]^2 = 0 \quad (11)$$

where the potential flow derivatives have been computed using the commercial code QUADPAN. Eqs. (11) are simply added into the summation of Eq. (10). Note from Eqs. (9), (10), and (11) that it is possible to differentiate the function, F, with respect to the unknown constants which is a prerequisite for implementing the variable metric method algorithm of Reference [12]. The variable metric method is a descent method which makes use of the derivatives of the optimization function with respect to the unknown parameters to locate local minima. In this method it is important to have good initial estimates for the unknown parameters because the function to be optimized may have numerous local minima. A method for determining the initial estimates in the present problem is described in Reference [13].

Eqs. (10) and (11) are solved (optimized) for  $C_{lp}$ , A, B,  $\tau_c$ , and  $C_{am}$ . Once a solution is obtained, Eqs. (11) are

removed and Eq. (10) is solved alone using the previous solution as an initial estimate. This is done to check the validity of the assumed potential flow behavior. The second solution to Eq. (10) has been found to differ by only a small amount from that with Eqs. (11) enforced. The results are shown in Figures 1a,b for the aerodynamic derivatives. In Figures 1a,b a correlation coefficient (coefficient of multiple determination) of 0.99 was computed. The individual contributions of the roll angle response and the roll rate response to each of the aerodynamic derivatives are also shown as dashed lines. Once the unknown indicial responses have been computed the rolling moment may be computed from Eq. (7) or (8).

It is important to recognize the central role which the frequency dependence of the aerodynamic derivatives plays in the present analysis and the availability of data across a range of frequencies. Strong frequency dependence indicates that significant lags in the aerodynamic response are present. It is the exploitation of the frequency dependence which permits the identification of the individual roll angle and roll rate contributions to the total response.

The second justification mentioned above for the assumption that the fast-acting component of the indicial response corresponds to a potential flow may now be discussed. For a harmonic oscillation in roll, as the frequency approaches infinity it is only the instantaneous component of the indicial response (Eqs. (6)) which survives. The vortical lag component (see Figure 4) has an initial value of zero and will contribute nothing at infinite frequency. This can be seen by taking the limit of Eq. (8) as  $\omega$  approaches infinity. Shown in Figure 1a is the value of the slope of the steady potential flow rolling moment with respect to roll angle computed at  $\phi = 0^\circ$ . It can be seen that the computed indicial model roll angle component of the stiffness derivative approaches this value as frequency increases. The conclusion is that the initial value of the roll angle indicial response (the first of Eqs.(6)) should be close to the steady potential flow value. The same observation can be made in relation to the roll rate response as seen in Figure 1b.

#### Present Model in Relation to Reference [1]

There is a relatively straight forward comparison which can be made between the present formulation and that of Goman et al.[1]. Using the concept that the rolling moment may be written as the sum of a potential flow component and a vortical component (i.e.  $C_l = C_l^P + C_l^V$ ) the vortical component of Eq. (7) can be shown to be can be shown to be a solution to

$$\tau_c \frac{dC_l^V}{dt} + C_l^V = C_{l\phi}^V \phi(t) + C_{lp}^V p(t) \quad (12)$$

Eq. (12) is in a form which may be convenient for incorporating the above model into a control system with only minor departure from conventional practice [14]. In Reference [1] the rolling moment given as the solution to

$$\tau_c \frac{dC_l^V}{dt} + C_l^V = C_{l\phi}^V (\phi(t) - \tau_3 \dot{\phi}(t)) \quad (13)$$

where the dot superscript indicates the time derivative of  $\phi$ , and  $\tau_3$  is a time constant which serves to lag the roll angle and is computed using a least squares fit to experimental data. Eq. (13) has no dependence on roll rate,  $p$ . For a single degree of freedom body-axis roll (as in the wind tunnel), the roll angle and roll rate are kinematically

related by  $p = \dot{\phi}$ , so that Eq. (12) becomes

$$\tau_c \frac{dC_l^V}{dt} + C_l^V = C_{l\phi}^V \phi(t) + C_{lp}^V \dot{\phi}(t) \quad (14)$$

A comparison of Eqs. (13) and (14) shows that the two models will be equivalent if the rate terms satisfy

$$-\tau_3 C_{l\phi}^V = C_{lp}^V \quad (15)$$

for which there would seem to be no physical basis. Furthermore, the angle and rate slope terms,  $C_{l\phi}^V$  and  $C_{lp}^V$ , are both known to be positive. Therefore, in order for Eq. (15) to be satisfied  $\tau_3$  would have to be negative which would seem to contradict the physical reasoning behind the form of Eq. (13). Attempts to apply the model of Reference [1] have yielded a negative value for  $\tau_3$ . It appears, therefore, that the form of Eq. (13) is insufficient for modeling the rate effects on the present delta wing. The authors in no way intend the above comments to be a criticism of the excellent work reported in Reference [1], but rather an attempt to explain the difficulties encountered when applying the method to the SARL data of Reference [7].

### Nonlinear Formulation of Indicial Response Model

For larger amplitude motions than those considered in the above linear model there are significant nonlinearities in the static rolling moment (see Figure 3) curve. Experimental data have been acquired for harmonic motions about a  $0^\circ$  offset with a  $4^\circ$  amplitude. To account for the nonlinearity in this region the convolution integral model is written in nonlinear form as

$$C_l(t) = C_{l0} + \int_0^t C_{l\phi}(\phi(\tau)) (1 - Ae^{-(t-\tau)/\tau_c}) \frac{d\phi(\tau)}{d\tau} d\tau + C_{lp} \int_0^t (1 - Be^{-(t-\tau)/\tau_c}) \frac{dp(\tau)}{d\tau} d\tau + C_{am} \dot{\phi}(t) \quad (16)$$

where the variation in the static slope is now accounted for in the roll angle response integral. Because there are no experimental data for the steady rate slope,  $C_{lp}$ , the linear form of the second integral is retained. The constants A and B are again computed based on the assumption that the indicial responses go instantly to the potential flow values.

A third order curve fit for the static slope  $C_{l\phi}(\tau)$  has been used and is shown in Figure 3. The agreement with the experimental data is not excellent, however, most of the features of the static data are captured; in particular the points at which the slope changes sign and the strong nonlinearity between  $-4^\circ < \phi < -2^\circ$ .

In the linear analysis the optimization method for solving for the indicial response parameters is based in fitting in and out-of-phase experimental derivatives. For the larger amplitude motions considered here, the real-time rolling moment data are used in the optimization routine. Four data sets for harmonic motions ( $\phi_0 = 0^\circ$ ,  $\Delta\phi = 4^\circ$ ) at reduced frequencies of 0.02, 0.04, 0.08, and 0.14 each having 256 data points over one cycle of motion have been optimized simultaneously. The function, F, which is optimized is given by

$$F = \sum_{j=1}^{NF} \sum_{i=1}^{ND} [C_l^e(\omega_j, t_i) - C_l(\omega_j, t_i)]^2 = 0 \quad (17)$$

where NF is the number of frequencies, ND is the number of data points in each set,  $C_1^e$  are the experimental data, and  $C_1$  are the values predicted by Eq. (16). The linear results have been used as the initial estimates for the unknown parameters. The computation time on a Silicon Graphics INDIGO workstation is near one minute.

The optimized indicial response results have been applied to two cases. The first is a harmonic oscillation about  $0^\circ$  offset with a  $4^\circ$  amplitude (from which the indicial responses were obtained). In this case the integration of Eq. (16) has been performed analytically retaining only the steady state terms. The resulting expression for  $C_1(t)$  is quite long and is omitted here. The second motion is a ramp motion at constant rate. In this case the integration has been performed numerically using a trapezoidal rule. Note that in this case all transient terms must be retained since the system may not reach steady state over the duration of the motion. The transient effects fall naturally out of the numerical integration.

## Results

### Linear and Nonlinear Results for Harmonic Motions

Harmonic motions about four offset angles of  $\phi_0 = 0^\circ, 3^\circ, 6.5^\circ$ , and  $8^\circ$  have been modeled using the linear model of Eq. (4). Only representative results for the  $0^\circ$  and  $8^\circ$  cases are presented here. In the linear case ( $2^\circ$  amplitude), the approach has been to exploit the frequency dependence of the experimental aerodynamic derivatives to compute the indicial model roll angle and roll rate effects. The indicial response results are then integrated to yield the rolling moment prediction in real time. The optimized results for an offset angle of  $0^\circ$  have been shown in Figures 1a and 1b where it is seen that each aerodynamic derivative has a contribution from both the roll angle response and the roll rate. This again illustrates the point that in-phase and out-of-phase derivatives cannot be attributed directly to angle and rate effects, respectively. The aerodynamic derivatives and optimized solutions for the  $8^\circ$  offset case are shown in Figures 6a and 6b where it can be seen that the optimized solution agrees well with the experimental values.

The rolling moment coefficient results are shown in Figures 7a-d for the  $0^\circ$  offset case at five nondimensional frequencies of 0.02, 0.04, 0.06, 0.08. These results are representative of the other offset angles considered ( $3^\circ, 6.5^\circ$ , and  $8^\circ$ ). In each figure the total rolling moment has been decomposed into the contributions of the roll angle response (first integral in Eq. (7)), the roll rate response (second integral), and the apparent mass contribution. The cross hatch on each curve indicates the simultaneous values. In each case there is relatively good agreement between the indicial response (IR) model and the experimental data. The present indicial response model results are in much better agreement than the stability derivative calculations shown in Figures 2a and 2b. It can also be seen in Figures 7a-d that the apparent mass effect is small.

In the nonlinear analysis only the data at  $0^\circ$  offset angle have been analyzed. The rolling moment results for the three nondimensional frequencies of 0.02, 0.06, and 0.14 are shown in Figures 8a-c, respectively. The agreement is relatively good at each frequency. In order to check the validity of the results, the indicial response solutions at  $4^\circ$  amplitude have been used to predict a  $2^\circ$  amplitude motion at the same offset angle with acceptable accuracy [13].

### Ramp Motion

The indicial responses computed for the nonlinear harmonic motion of the previous section have been used to compute the rolling moment for a ramp motion between  $-4^\circ < \phi < 4^\circ$ . The integration has been performed numerically so that all transients are retained. The results are shown in Figures 9a-c which are for nondimensional roll rates (based on semispan) of 0.0029, 0.011, and 0.014, respectively. Also shown are the SARL data as well as the various components of the total analytic moment. The agreement is relatively good, however, in each case, particularly at the lowest roll rate, the data exhibit some unsteady behavior which is not fully predicted by the NIR model. The reason for this is not presently well understood. Future computations may focus on performing the optimization on the ramp data alone and a comparison with the present results for harmonic motion. The range of roll angles for the harmonic and ramp data are the same, however, the roll rate is obviously completely different for both motions. There may be some nonlinearity (i.e  $p(\tau)$  dependence in Eq. (16)) associated with this fact that is not accounted for in the present formulation. The authors are not aware of any purely rate dependent experimental data which might provide some guidance in this problem.

### Conclusion

The present work provides a framework for practical application of indicial response modeling for an aircraft configuration. The formulation for the rolling moment has been performed in the aeroballistic coordinate system wherein roll angle and roll rate must be treated as independent motion parameters. Consequently two superposition integrals are required. In the linear case (small amplitude), the frequency dependence of the experimental aerodynamic stiffness and damping derivatives has been used to separate the roll angle and roll rate effects. The indicial response model has been shown to accurately predict the rolling moment for harmonic oscillations in body-axis roll. The analysis has been extended to larger amplitude motions wherein static nonlinearities in the roll angle component are significant. There remains much yet to be learned. In particular, the availability of purely roll rate dependent experimental data would be valuable information in that one of the principal unknowns ( $C_{lp}$ ) in the model would be quantified directly. These data may be acquired perhaps from induced camber models or from rotary rig tests.

The application of indicial responses computed from harmonic data to the case of a ramp motion have displayed some inaccuracies which are presently not well understood. They may be attributed to the fact that the variation in roll rate in the respective motions are completely different. Static roll rate data may also provide some information relevant to this problem.

### Acknowledgement

This author gratefully acknowledges the support of the Air Force Office of Scientific Research under the 1997 Summer Faculty Program and to Wright Laboratories.

### References

- <sup>1</sup>Goman, M. and Khrabrov, A., "State Space Representation of Aerodynamic Characteristics of an Aircraft at High Angles of Attack," *AIAA J. of Aircraft*, Vol. 31, No. 5, Sept.-Oct. 1994.
- <sup>2</sup>Huang, X. Z. and Hanff, E.S., "Prediction of Normal Force on a Delta Wing Rolling at High Incidence," *AIAA Paper 93-3686*, August 1993.

<sup>3</sup>Tobak, M. and Schiff, L.B., "Aerodynamic Mathematical Modeling-Basic Concepts," AGARD Lecture Series No.114, Paper 1, March 1981.

<sup>4</sup>Tobak, M., Chapman, G.T., "Nonlinear Problems in Flight Mechanics Involving Aerodynamic Bifurcations," AGARD CP-386, 1985, pp. 25-1 to 25-15.

<sup>5</sup>Jenkins, J.E., Myatt, J.H., and Hanff, E.S., "Body-Axis Rolling Motion Critical States of a 65-Degree Delta Wing," *AIAA J. of Aircraft*, Vol. 33, No. 2, March-April 1996.

<sup>6</sup>Etkin, B., *Dynamics of Atmospheric Flight*, Wiley and Sons, Inc., 1972, p. 165.

<sup>7</sup>Jenkins, J.E. and Hanff, E.S., "Highlights of the IAR/WL Delta Wing Program," AIAA Workshop on Delta Wings: Unsteady Aerodynamics and Modeling", August 1995.

<sup>8</sup>Jenkins, J.E. and Graham, G.M., "Aerodynamic Responses to Body-Axis Rolling Motions," *AIAA J. of Aircraft*, to be published.

<sup>9</sup>Ericsson, L.E., "Unique High-Alpha Roll Dynamics of a Sharp-Edged 65° Delta Wing," AIAA Paper 92-0276, Jan. 1992.

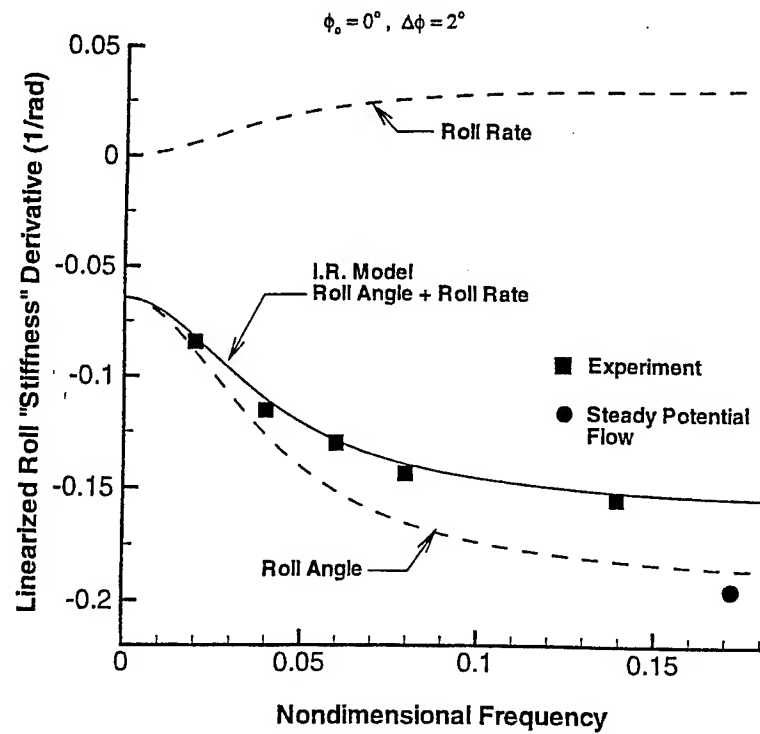
<sup>10</sup>Huang, X.Z. and Hanff, E.S., "Roll Rate Induced Camber Effect on Delta Wing Leading-Edge Vortex Breakdown," AIAA Paper 95-1793, June 1995.

<sup>11</sup>Grismer, D.S. and Jenkins, J.E., "Critical-State Transients for a Rolling 65-Delta Wing," *AIAA Journal of Aircraft*, Vol. 34, No. 3, May-June 1997.

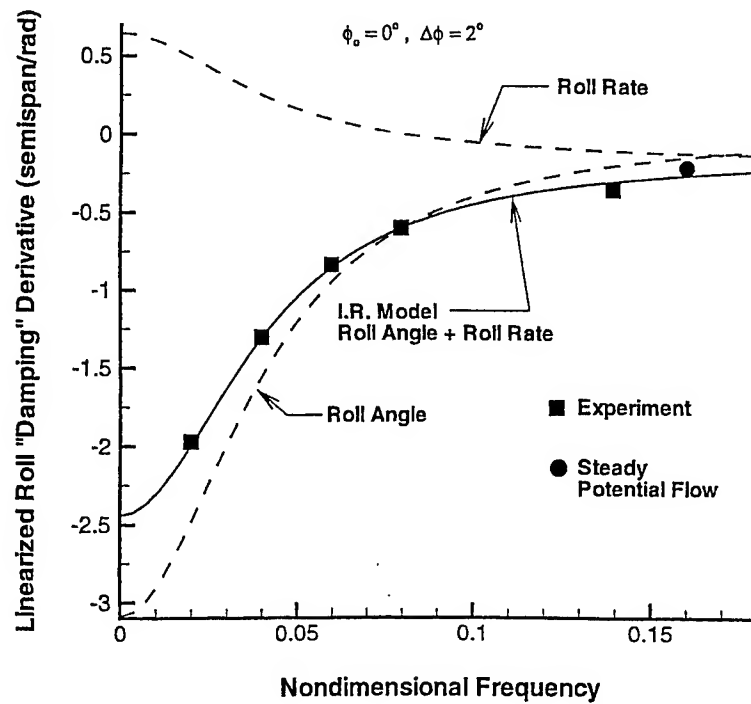
<sup>12</sup>Press, W.H., Flannery, B.P., Teukolsky, S.A., and Vetterling, W.T., *Numerical Recipes*, Cambridge University Press, 1989.

<sup>13</sup>Graham, G.M. and Jenkins, J.E., "Semi-Empirical Indicial Response Model for a 65° Delta Wing Oscillating in Roll," AIAA Paper 97-0326, Jan. 1997.

<sup>14</sup>McKeehen, P.D., Myatt, J.H., Grismer, D.S., and Buffington, J.M., "Simulation of a Tailless Aircraft Using Nonlinear Indicial Response Aerodynamic Modeling Methods," AIAA Paper No. 97-3790, Aug. 1997.

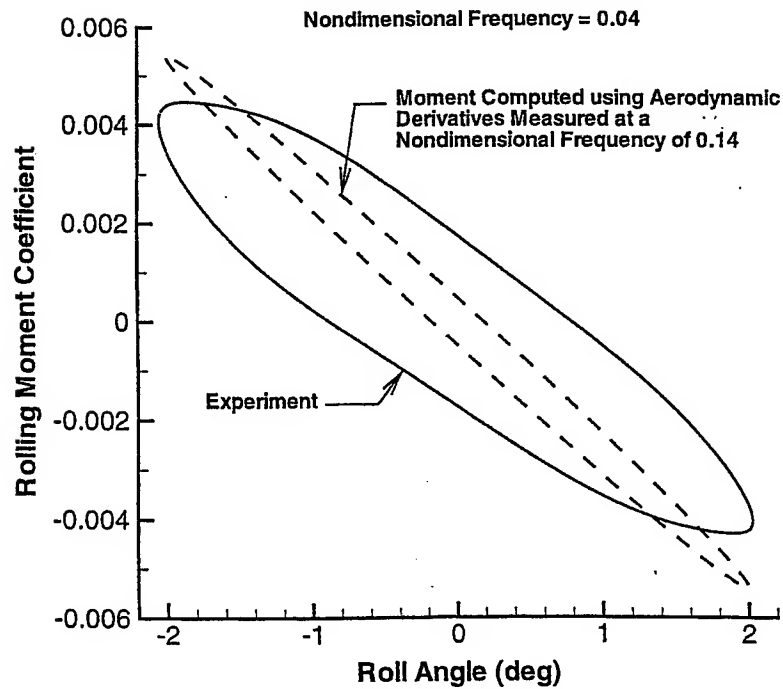
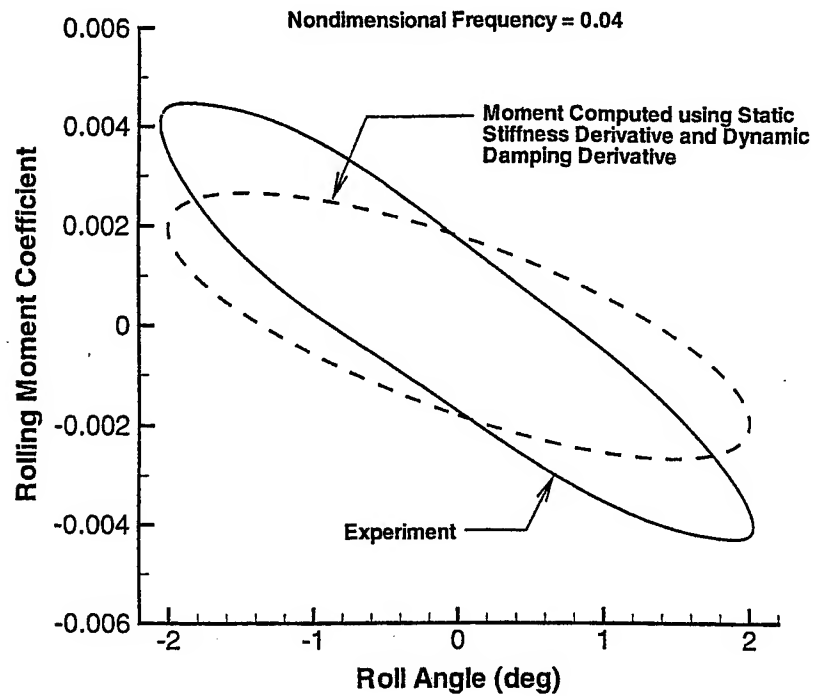


(1a)



(1b)

Figures 1a and 1b. Aerodynamic Derivatives for  $\phi_0 = 0^\circ, \Delta\phi = 2^\circ$ .



Figures 2a and 2b. Rolling Moment Computed Using Stability Derivatives.



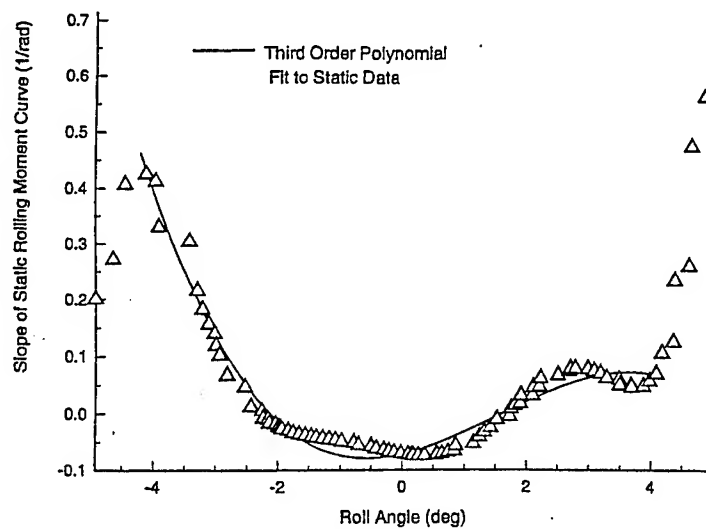


Figure 3. Slope of Static Rolling Moment.

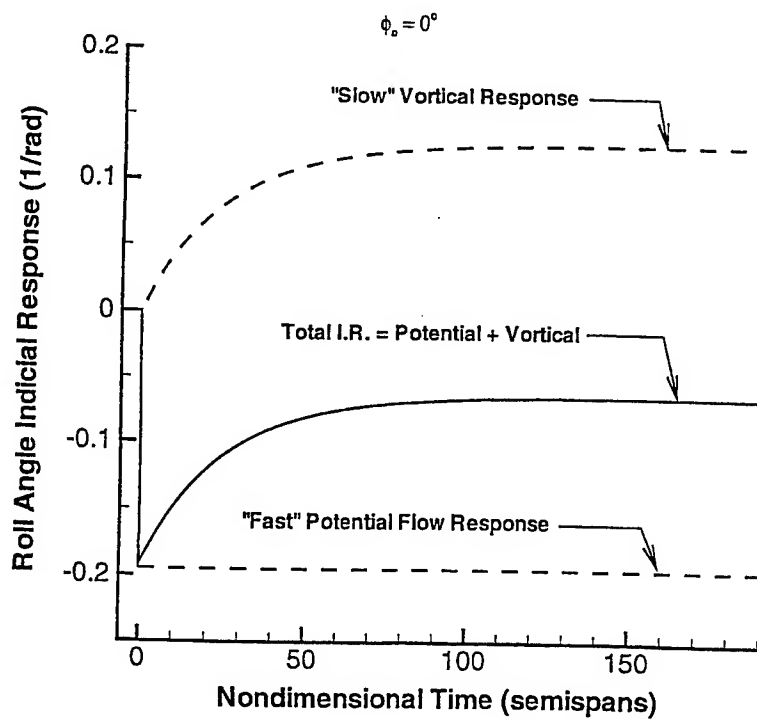
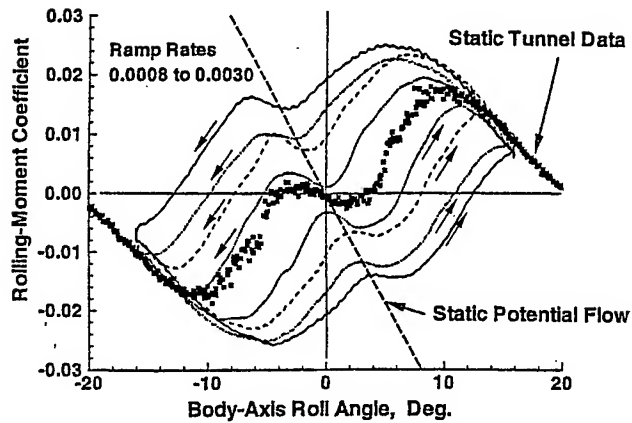


Figure 4. Computed Linear Roll Angle Indicial Response for  $\phi_0 = 0^\circ$ .

## Multiple Time Scales

$$M = 0.3, \sigma = 30^\circ$$



Large lags – Increase with rate

Inflection points - Symmetric vortex breakdown

- Aligned with potential flow contribution

Figure 5. Comparison of Ramp Data with Potential Flow Theory.

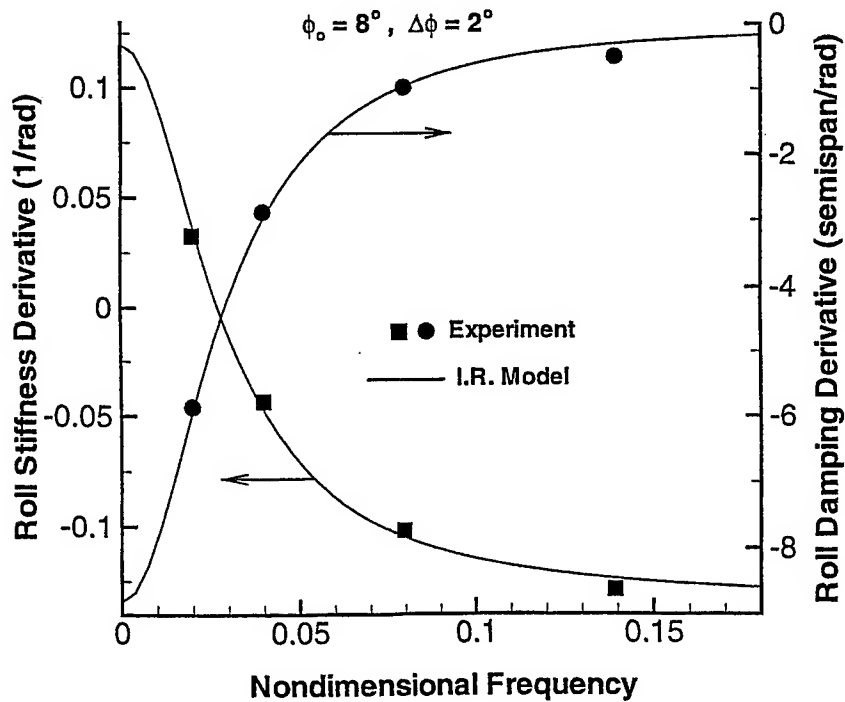


Figure 6. Aerodynamic Derivatives for  $\phi_0 = 8^\circ, \Delta\phi = 2^\circ$ .

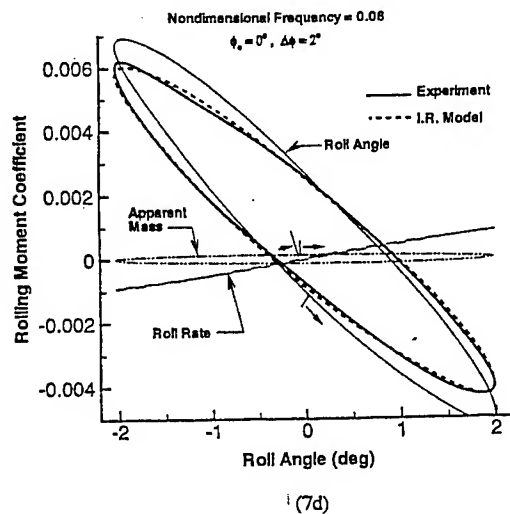
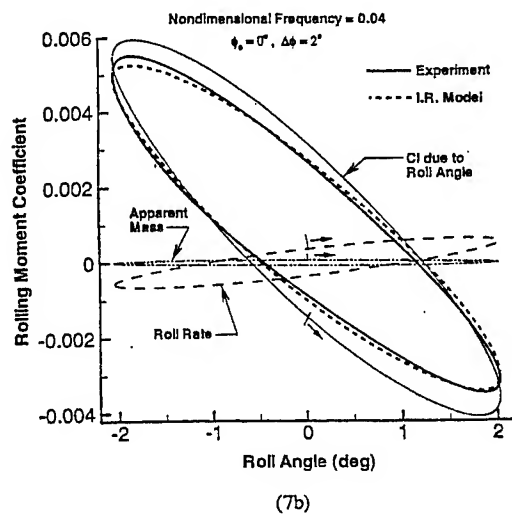
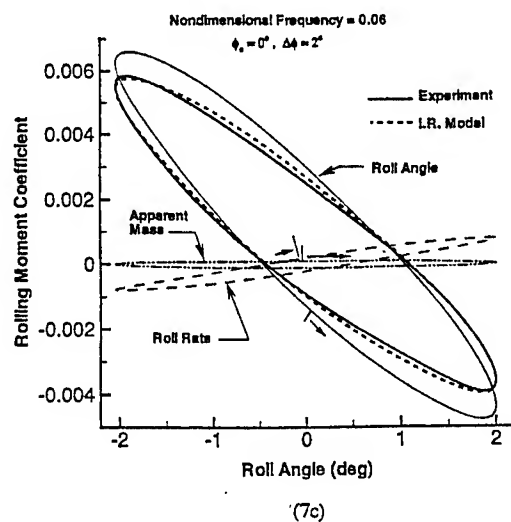
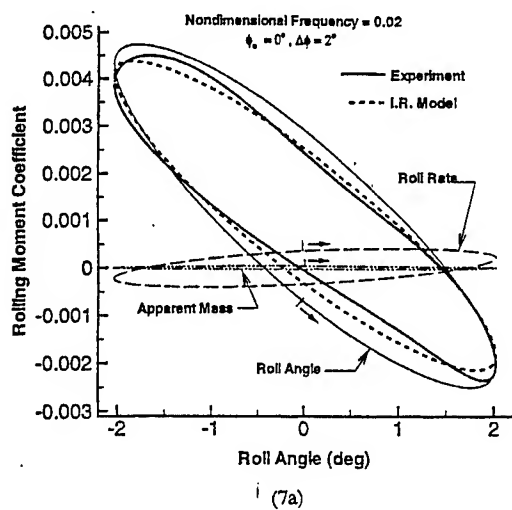
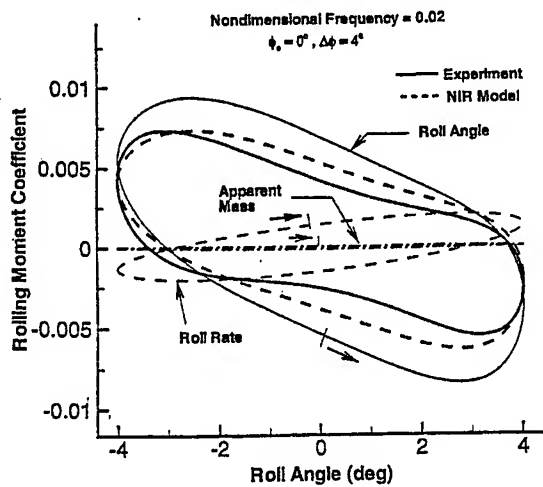
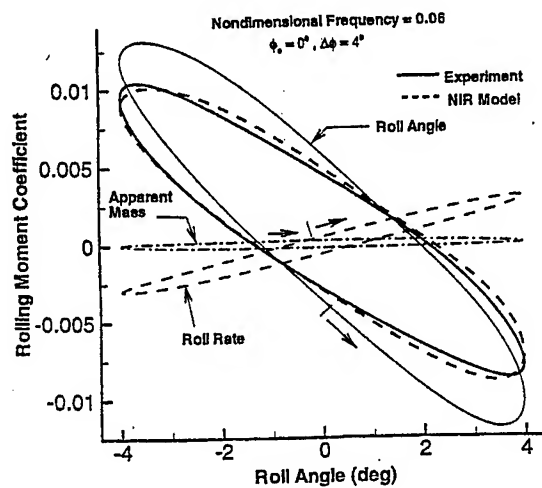


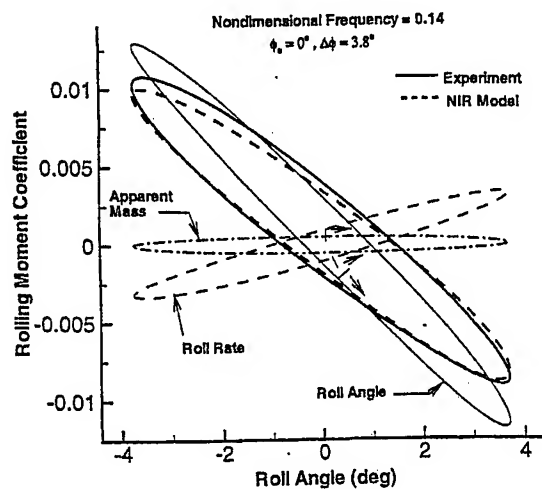
Figure 7a-d. Linear Indicial Response Model Results for Harmonic Motion.



(8a)



(8b)



(8c)

Figure 8a-c. Nonlinear Indicial Response Model Results for Harmonic Motion.

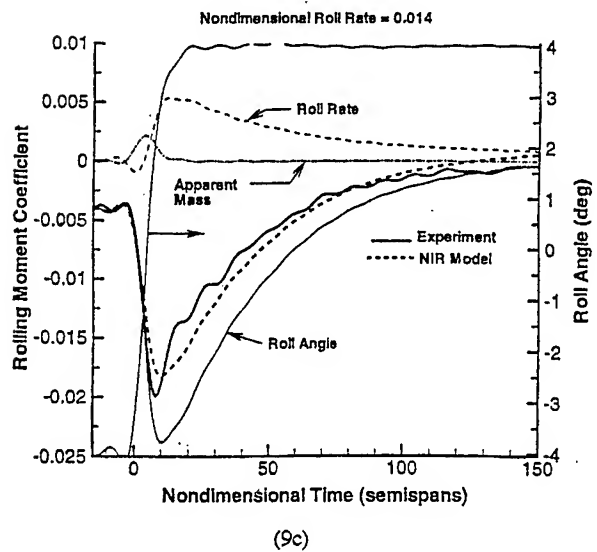
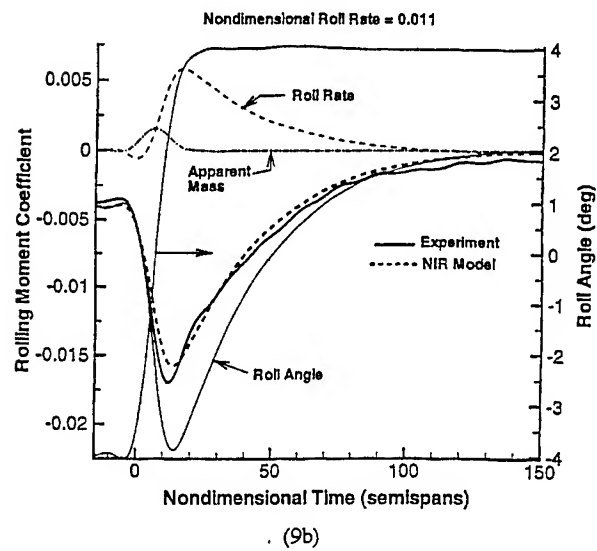
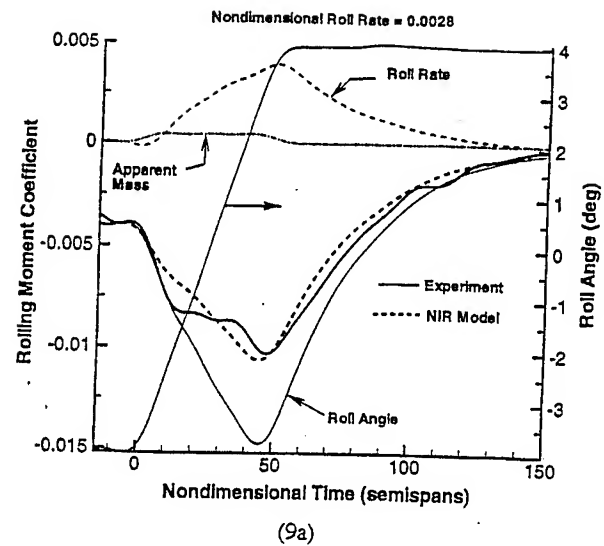


Figure 9a-c. Nonlinear Indicial Response Model Results for Ramp Motion.

**AN OBJECT-BASED APPROACH FOR INTEGRATING COST ASSESSMENT  
INTO PRODUCT/PROCESS DESIGN**

Allen G. Greenwood  
Associate Professor  
Department of Industrial Engineering

Mississippi State University  
P. O. Box 9542  
125 McCain Engineering Building  
Mississippi State, MS 39762

Final Report for:  
Summer Faculty Research Program  
Wright Laboratory / Manufacturing Technology Directorate  
Manufacturing and Engineering Systems Division

Sponsored by:  
Air Force Office of Scientific Research  
Bolling Air Force Base, DC

and

Wright Laboratory  
Wright-Patterson Air Force Base, OH

August 1997

# **AN OBJECT-BASED APPROACH FOR INTEGRATING COST ASSESSMENT INTO PRODUCT/PROCESS DESIGN**

Allen G. Greenwood  
Associate Professor  
Department of Industrial Engineering  
Mississippi State University

## **ABSTRACT**

The design, development, and manufacture of affordable products is a major concern in both military and commercial production. One critical element in designing affordable products is the concurrent consideration of product and process cost early in the design process. This research provides an approach for integrating cost assessment into the product/process design environment. The underlying concept is based upon the simultaneous consideration of the components of the product triad – form, material, and process – through the application of object-oriented technologies. This paper (1) provides a conceptual representation of an object-based, cost-assessment approach that supports the design process, (2) defines the objects, properties, hierarchies, and underlying object structure that are used in the approach, and (3) describes an initial view of the application environment and software that would be used to implement the approach as a design support system.

# AN OBJECT-BASED APPROACH FOR INTEGRATING COST ASSESSMENT INTO PRODUCT/PROCESS DESIGN

Allen G. Greenwood

## INTRODUCTION

Defense system requirements have shifted from performance at all costs, to one of ensuring superiority, yet being affordable. As a result, affordability has become the primary focus of weapon system procurement. In fact, affordability is the driving force in today's manufacturing environment, both military and commercial. Affordability is defined as the balance among requirements, costs, and budgets and considers both product performance and cost. A technology is considered affordable if it meets the customer's requirements, is within the customer's budget, and has the best value among available alternatives ([1], p. 2)

Design can be defined as the "process of producing a set of descriptions of an artifact that satisfy a set of given performance measures and constraints." ([2], p. 6). As stated above, the design of affordable products must concurrently consider and trade off elements of performance and cost. Therefore, in order to design, develop, and produce affordable products, product design and manufacturing process design, as well as "total" product/process cost, must be considered concurrently and early in the design phase. However, major barriers exist that preclude supportive cost estimating to be a key element in integrated product and process development (IPPD) and concurrent engineering. Those barriers include cost models and tools, cost data, and the costing process itself.

Cost models and tools are disjointed, often proprietary, and not well understood by most designers. Traditionally, cost model drivers are often not related to product features and design variables, nor are they related to characteristics of manufacturing processes. Most cost models also do not adequately address the relationships between direct product/process costs and indirect costs.

Cost data are also disjointed, often proprietary, and not well understood by most designers. In addition, the data needed to support the design process are typically not available because legacy data systems do not track the information to the required level of detail and legacy data are often based on processes and methods that are no longer used.

In order to develop affordable products, cost assessment must move away from the traditional sequential, "over-the-wall" approach and toward a concurrent engineering approach, as illustrated in Figure 1. The traditional approach depicted in the left panel of Figure 1, converts requirements into product mostly through manipulation of form and material with little consideration for producibility. Cost assessment is a post-design activity that may possibly feed back to design in order to spawn alternatives. As Yoshimura describes ([3], p. 163), "in usual design optimization, consideration is only



given to the improvement of the product performance ... the product manufacturing and cost factors concerning manufacturing processes are scarcely considered." On the other hand, a concurrent engineering approach, as represented in the right panel of Figure 1, transforms customer requirements into product through the consideration of process as an integral element with form and material and cost assessment is at the core of the IPPD or concurrent engineering process.

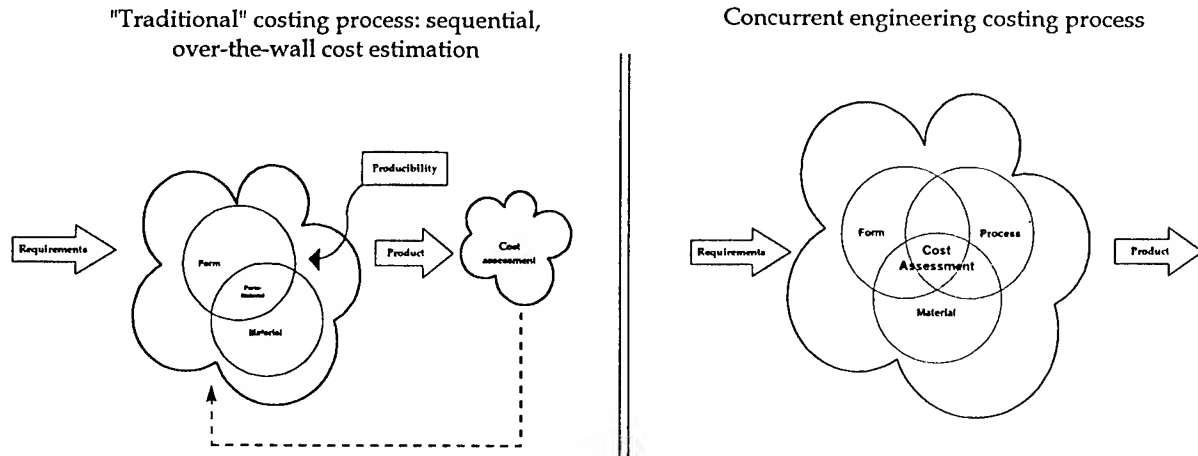


Figure 1: Comparison of traditional and concurrent costing processes.

Cost estimating methodologies are generally grouped into four categories [4]: (1) judgment – use of expert opinion of one or more qualified experts in the area to be estimated, (2) parametric -- mathematical expressions, often referred to as cost estimating relationships or CERs, that relate cost to independent cost driving variables, (3) analogy – use of actual costs from a similar existing or past programs with adjustments for complexity, technical or physical differences, to derive a new system estimate, and (4) grass roots, also referred to as “engineering build up” or “detailed estimate” are performed at the functional level of the Work Breakdown Structure. The object-based approach described in this paper supports the application of any, and all, of these methodologies as an integral part of the design process.

In order for product/process cost estimating to be an effective tool in design, the aforementioned barriers must be broken and a totally new approach to costing is required. It is time to *engineer* cost estimating and move toward a cost “science” that provides a structured, understandable, and tractable process. It is necessary to investigate how cost assessment *should* be integrated into the IPPD process and leverage information technology to build effective and supportive tools. These tools must be flexible, robust, and adaptive in order to be able to respond to rapid changes in the design environment (forms,

materials, and processes) as well as be responsive to new costing approaches (e.g. activity based costing, throughput accounting). Development of such an approach will both create a basis upon which to investigate and develop new tools and methodologies, as well as to make cost assessment an essential and integrated computer-aided engineering (CAE) methodology.

This research builds upon a framework that defines the modeling and analysis progression from product features to an enterprise view of the production of the product and provides the foundation for manufacturing-oriented, design-directed cost estimating (MODDCE). The MODDCE framework, as shown in Figure 2, is composed of five levels that progress from a hierarchical decomposition of a product's features through three intermediate steps to an enterprise-level model that links product features with manufacturing and non-manufacturing entities throughout the enterprise. The highest or enterprise level provides the most comprehensive analysis capabilities for assessing the effect of changes in product and process design on the enterprise and the resulting effect of those changes on "total" cost. The progression to each level requires the completion of an activity. For example, in order to move from the hierarchical decomposition of a product's features to the corresponding manufacturing elements that create those features, requires an activity that maps or associates features with transformation elements. Each of the activities that link the five levels is described in [5].

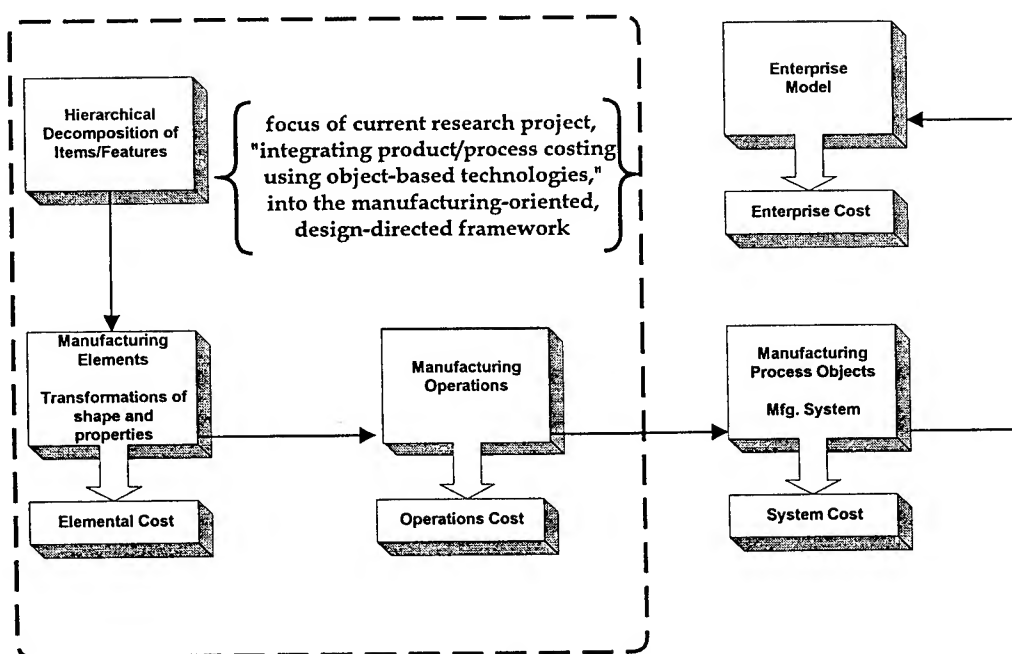


Figure 2: MODDCE framework links product features to an enterprise view of production.

As shown in Figure 2, this research focuses on the left-hand portion of the framework, where a product's design evolves, in terms of what it looks like, what it is made of, and how it will be constructed. This paper describes a general object-based approach for integrating product/process cost assessment as

early in the design phase as possible and provide a means to track changes in cost as a design evolves. It provides (1) conceptual definitions of the objects and object structure that comprise the cost-assessment approach and (2) preliminary description of the design support system that would be developed to implement and apply the approach.

## OBJECT-BASED APPROACH TO INTEGRATED PRODUCT/PROCESS COSTING

As part of this project, object-based technologies were investigated in order to assess their applicability for facilitating the development and use of an integrated costing environment that effectively supports concurrent product and process design. It was found, and as demonstrated in this paper, that an object-based approach offers a strong promise for meeting this goal and breaking down some of the barriers described earlier. There is a plethora of information available on object orientation and it is beyond the scope of this paper to provide a comprehensive review of this literature. However, a brief description of the broad area of object-based technologies and general definitions are provided below. The sources that were reviewed as part of this project include: [2], [6], [7], [8], [9], [10], [11], [12].

Object orientation provides a more natural and easier means -- as compared to more traditional systems analysis, design, programming, and database approaches -- to represent and model complex systems from individual components. In object-oriented applications, data objects that represent real-world entities are often the focus; whereas, applications that employ a conventional programming approach are often procedure focused. Therefore, from a modeling perspective, as noted by Khoshafian and Abnous [8], decomposition of a system from an object-oriented perspective is more intuitive and involves well-defined behaviors and encapsulated algorithms; in contrast, procedure-based decomposition is unnatural, in most cases.

From an object-oriented perspective, a system or process that is being modeled is represented in terms of multiple objects that are associated with or related to each other. In general, *objects* (1) contain information, often referred to as *properties*, instance variables, or attributes and (2) offer behavior to other objects by means of operations or *methods*. A set of objects with identical properties and structure is defined as a *class*. All objects are created to conform to the description of a particular class and are said to be *instances* of that class. Objects are distinguished from each other by the value of their properties; i.e. the representation of an instance is stored in its properties. *Inheritance* is an important feature of object-based systems. A class can inherit properties and behavior from another class or from multiple classes. That is, an instance of the inheriting class will obtain all of the operations and properties that are contained in both the inheriting and inherited classes. An underlying object-oriented database structure provides an effective means to integrate diverse data types and applications necessary develop complex and flexible systems.

This research uses object-based technologies to represent a design-supporting, cost-assessment process. It is based upon the premise that cost assessment must concurrently consider three primary design dimensions, or what may be referred to as the product triad – *form*, *material*, and *process*. That is, in order to adequately cost an item, one must know its form, what it is made of, and how it will be produced. The last element is the one that has received the least consideration in the past. However, in order to design and build affordable products and to make meaningful trades among alternatives, all three elements must be an integral part of the design process and “cost” is a natural metric to tie them together. While the amount and level of information available early in the design phase may be limited, manufacturing process still must be addressed and assumptions must be made as to how the product will be produced. A similar notion is put forth by Shankar and Jansson ([13], pp. 256-257) in what they refer to as coupling, “in concurrent engineering or DFM (design for manufacturability) strategy, the impact of each design decision on both functional and production requirements must be assessed. ... When this happens, the design is said to be coupled and the parameter is referred to as the coupling variable. ... Coupling as it affects manufacturability may be classified into the following categories: material-based coupling, process-based coupling, and configuration-based coupling.” The author prefers the term “form” rather than “configuration.” Form refers to the shape and structure of something; whereas, configuration is more restrictive, in that it relates more to the arrangement of parts or interrelationships of elements. In the approach described in this paper, the arrangement and interrelationships of parts is considered in the “item structure” that is defined below.

The proposed object-based, product-triad approach is represented conceptually in the left portion, panel (a), of Figure 3. The three primary design dimensions, or product triad – form, material, and process – are defined as objects and are represented as circles in the figure. Similarly, they are represented as circles in the object structure in the right-hand portion, panel (b), of Figure 3. As will be described in more detail later, each of the three primary objects are considered to be object hierarchies. Secondary objects, shown as the intersection of two primary objects in panel (a) and represented by ovals in the object structure in panel (b), are complex objects, in that they inherit properties from two primary objects. For example, the Form-Material object inherits properties from both the Form and Material hierarchies. Complex objects will be defined in more detail later in the paper. There is a second type of complex object, shown as the intersection of all three primary objects in panel (a) and the triangle in panel (b). This Form-Material-Process (F-M-P) object inherits properties from all three hierarchies. This object is especially important since it provides the basis for cost assessment; i.e. costing cannot be completed until the design has considered the item’s form, material, and manufacturing process. It should be noted that an instance of the F-M-P object may result from the combination of a secondary and primary object, e.g., the combination of the Form-Material object and a Process object.

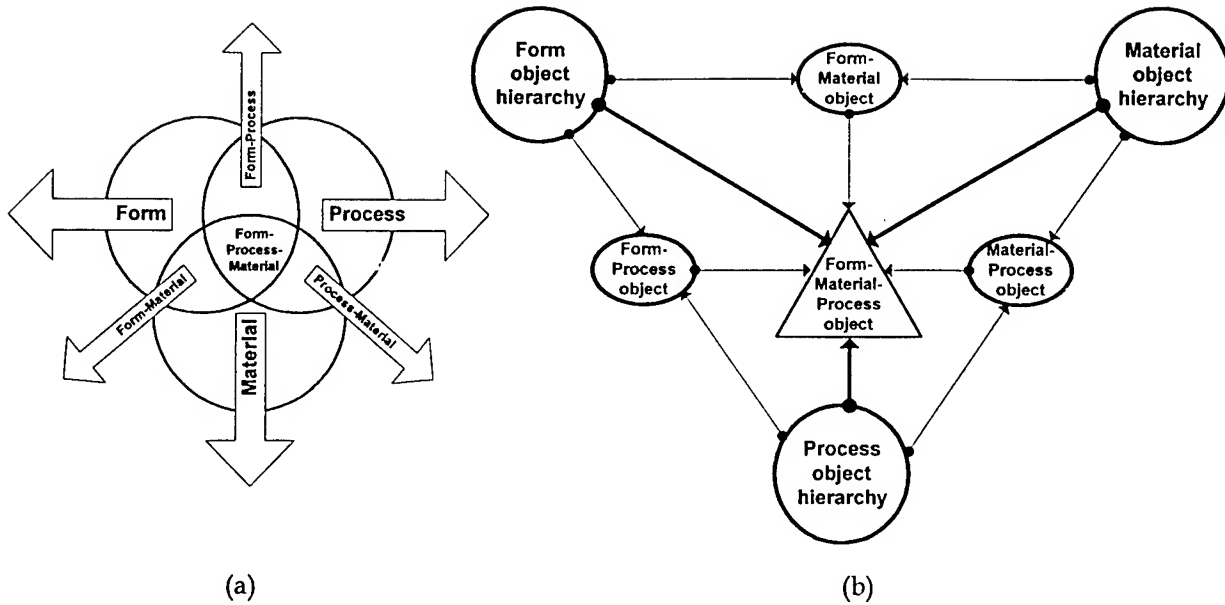


Figure 3: Conceptual representation and fundamental structure of object-based cost assessment.

#### PRELIMINARY DEFINITION OF OBJECTS AND OBJECT STRUCTURE

Examples of the three object hierarchies are provided in Figures 4, 5, and 6. These hierarchies are provided to illustrate fundamental concepts and demonstrate feasibility of the approach. As a result, they are generic and not completely defined; further research is required to refine the structure and content of the hierarchies, objects, and properties. This refinement will result from applying the object-based cost-assessment approach to specific problem domains and addressing the needs of IPTs working in those problem domains. It should be noted that in general, the hierarchies, objects, and their corresponding properties can be developed to support a “complete” design environment, including a variety of computer-aided engineering tools, methods, and resources, as well as detailed descriptions of manufacturing processes and their capabilities. However, the focus of the elements developed in this research is on cost assessment. As a result, only those properties, methods, etc. that are directly related to cost are considered.

An example Form object hierarchy is provided in Figure 4. It illustrates a variety of ways in which an item’s form may be considered. For example, it may be represented by a set of either two- or three-dimensional geometric primitives, by an indicator of complexity such as Woodward’s classification [14] of shape complexity, or by like items, such as aircraft structural components (skins, ribs, spars, etc.). The figure indicates that a cylinder is a type of three-dimensional primitive and pipes and solids are types of cylinders. The solid cylinder is shown to possess three properties – name, outside diameter, and length. It is assumed that the representation and description of an item’s form does not have to be as completely defined in order to estimate cost, at least early in the design process, as it may for other engineering

applications. That is, the form does not have to be a full specification for building or testing the item, but only provide enough definition to identify the types of manufacturing processes necessary to produce the item.

The manner in which the item's form is represented depends upon the complexity of the item being designed and the phase of design (e.g. conceptual, preliminary, detailed). It is expected that an item's form representation will evolve over time, as more design detail becomes available. An object-based system would facilitate tracking the design history of items.

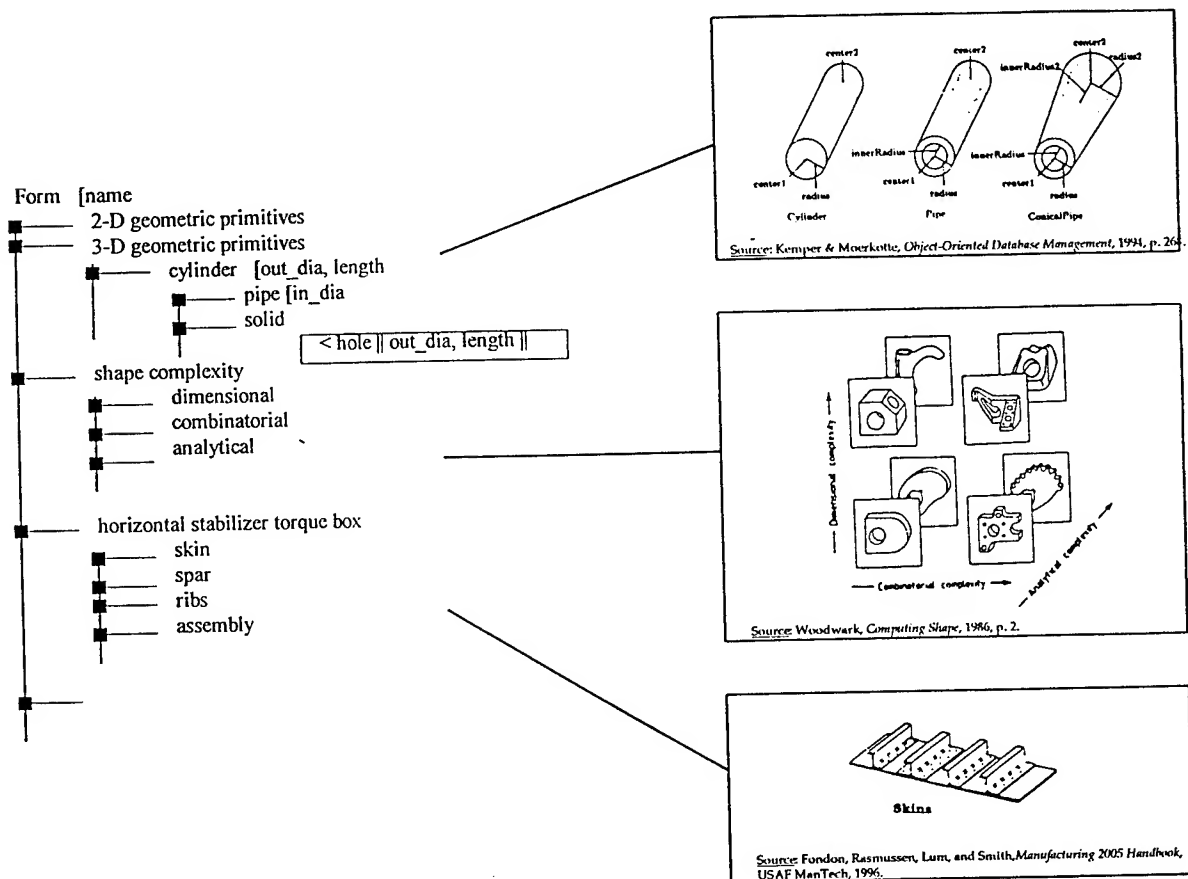


Figure 4: Form object hierarchy.

An example material hierarchy is provided in Figure 5 and is used to illustrate the concept of inheritance. As shown at the root of the hierarchy, all materials have the following properties: type, description, density, form, and cost; however, materials such as metals and composites have different properties. For example, whether a material is heat treated or not is only relevant to metals; and, properties such as matrix, fiber type, and fiber length are only relevant to composite materials. Therefore, a specific material's properties will depend upon which object it is associated with in the hierarchy.

Instances of two materials, aluminum and polymer-matrix composites, illustrate in Figure 5, the differing properties; example instance property values are provided in the boxed text.

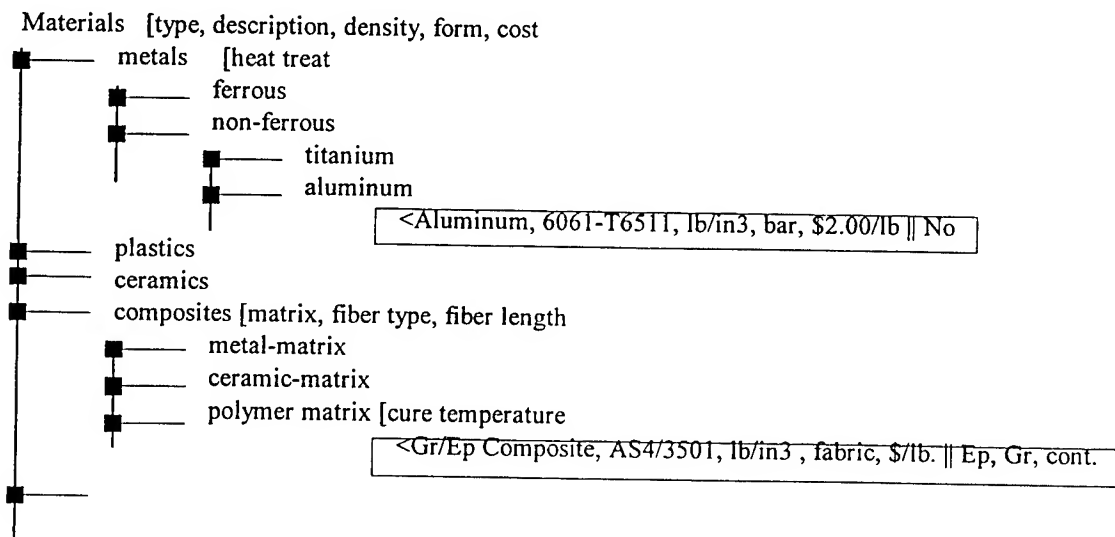


Figure 5: Material object hierarchy.

The third object hierarchy provides a taxonomy of manufacturing processes. As shown in Figure 6, these processes are grouped into machining, casting, forging, composites, assembly, etc. This taxonomy is one that would likely correspond to the structure of a company's overhead pool. As companies move more towards activity-based costing systems, the object-based structure provides the flexibility to accommodate more refined overhead assignments. An alternative structure to that in Figure 6 would be to group processes by their function. For example, Todd [15] groups manufacturing processes by mass, thermal, and chemical reduction, consolidation, deformation, thermal joining, etc.

The choice of a manufacturing process is dictated by such considerations as: ([16], p. 1232) characteristics and properties of the workpiece material, shape, size, and thickness of the part, tolerances and surface finish requirements, functional requirements for the expected service life of the item, production volume (and schedule), level of automation required to meet production volume and rate, and costs involved in individual and combined aspects of the manufacturing operation. Many of these considerations are addressed when a specific Form instance and Material instance are linked with a Process instance to create a representation of the item being designed. Numerous guidelines are available on the capabilities of various manufacturing processes for producing items from different materials, shape characteristics, tolerance and shape characteristics, etc. Some of these guidelines are beginning to be incorporated into CAD software in order to provide real-time feedback to the designer. Cost guidelines are also available, usually on a relative basis. All too often however, these guidelines represent general trends and are not related to specific processes and product features. For example, a graph in Kalpakjian

([16], p. 1237) illustrates the exponential relationship between tolerance and relative cost for an unspecified material and process (e.g. relative to a tolerance of 0.030, an item manufactured with a tolerance of 0.015 is twice as expensive to produce, a tolerance of 0.005 is five times the cost, and a tolerance of 0.001 is seventeen times the cost of the 0.030 tolerance item.) Few guidelines are available on the cost impact of production volume, rate, lead time, etc. These are factors that are becoming increasingly important to address during design when fewer new defense systems are being procured and there is a growing need to sustain systems that are no longer being procured.

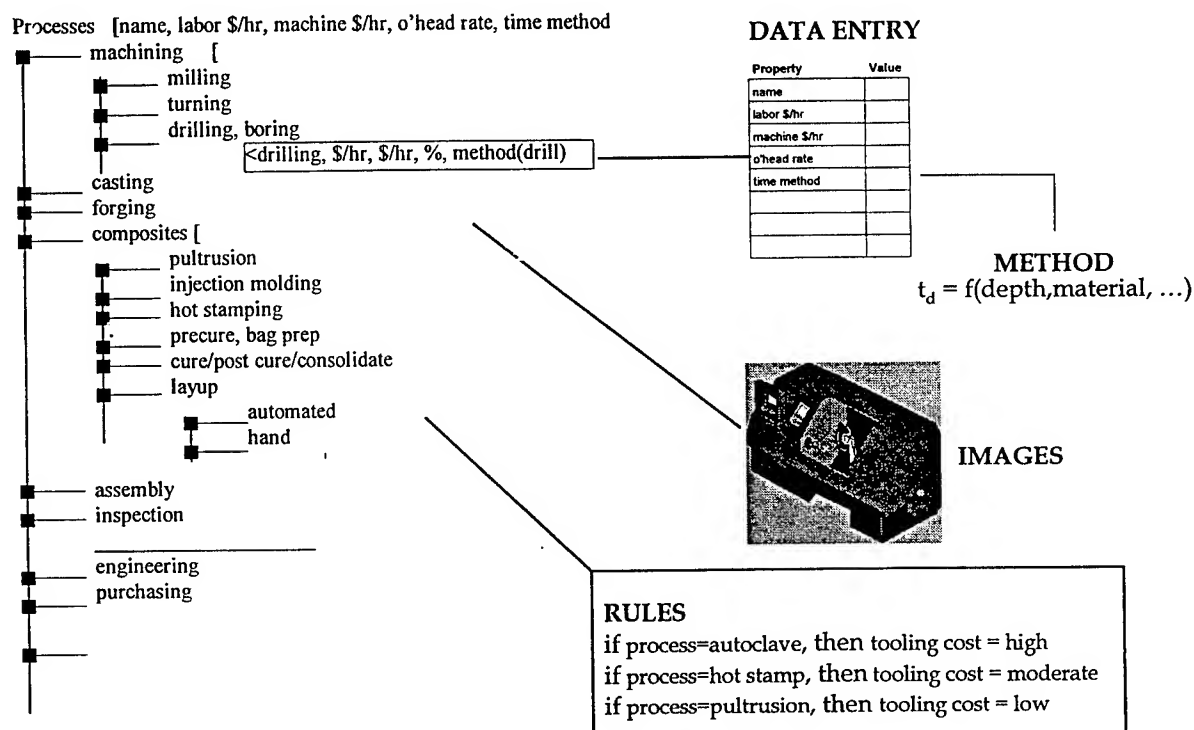


Figure 6: Process object hierarchy.

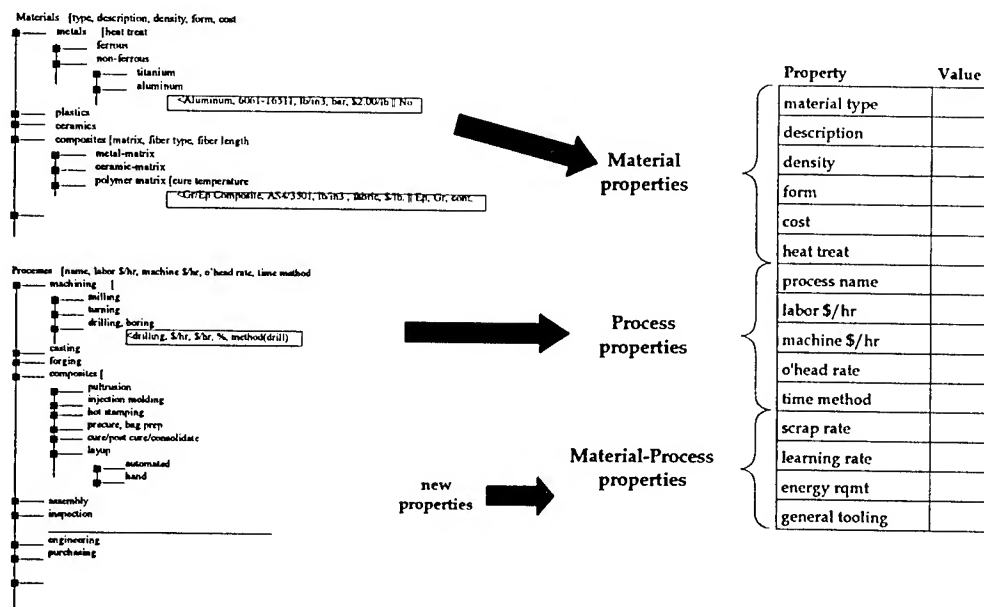
It should be noted that the Process hierarchy is not limited to manufacturing processes. It may include such non-manufacturing entities as engineering, purchasing, etc., as well as external entities, such as customers and suppliers. This provides for enterprise-level costing, as defined in the MODDCE framework [5], where the impact of changes in product/process design on indirect entities in the enterprise is assessed, and conversely, the impact on changes in indirect entities on manufacturing processes, and hence on the product, is also assessed.

Figure 6 also illustrates some of the capabilities of the objects in the hierarchy. Instances of the objects in the hierarchy provide the specific data values that describe an item and drive its cost. Property or attribute values may be specified for a particular instance through data-entry windows similar to the one shown in Figure 6. In addition to numeric and character values, methods may be specified. For



example, the production time for a process may be defined by a formula or algorithm that, in the case of drilling, depends upon the depth of the hole, material, etc. These values would be instantiated when the Process instance is "linked" with specific Form and Material instances. In addition to computational methods, objects may contain a rule base to help guide design and cost assessment. In order to help define, describe, document, and clarify objects and their properties and methods, both still and video clip images, as well as textual narration, need to be a part of the object structure.

The three object hierarchies described above are taxonomies of general information about ways to represent form, describe engineering materials, and characterize production processes. In the object-based approach developed in this paper, a particular item that is being designed is represented as a complex object or “collection” of instances from several different objects. A complex object is illustrated in Figure 7 -- it is referred to as a Material-Process object and is a combination of a Process object and a Material object. The particular Material-Process object shown in Figure 7 represents drilling aluminum; this object inherits all of the properties from the aluminum material object and all of the properties from the drilling process object. Note that had the Material-Process object been formed from a different material, e.g. a composite, it would have inherited different properties, i.e. only those relevant to composite materials. Complex objects not only inherit all of the properties from the simple objects from which they are formed, but contain additional properties that are associated with the particular complex object. For example, in the case of the Material-Process object in Figure 7, such properties as scrap rate, learning rate, etc. are added to the complex object and are not inherited from either simple object. This follows from the general notion that scrap rate is not solely attributed to material or solely attributed to process, but depends upon a specific material-process combination.



**Figure 7: Material-process object.**

As described above and illustrated in Figure 3, a cost assessment of a particular design requires specification of form, material, and process. However, as shown in Figure 8, two additional elements are required in order to complete a cost assessment. First, the item being designed must be considered in its context as a part of some larger system or product, as illustrated by the item structure in Figure 8. The item structure primarily provides programmatic information, such as quantity, schedule, etc. These properties are often important factors in design since, for example, low production rate or quantity may preclude an item from being produced by certain processes because they would result in prohibitive costs and become unaffordable. Cost structure is the second element that must be combined with the Form-Material-Process design definition. The cost structure defines the types of cost that are addressed in the analysis.

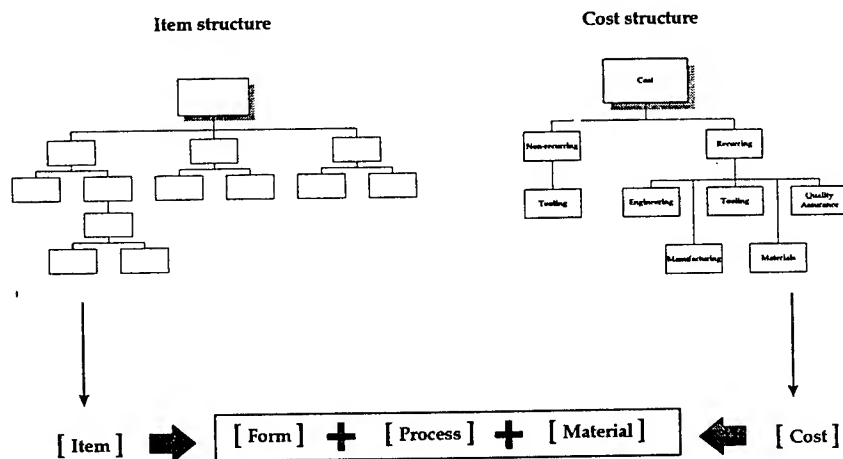


Figure 8: Cost assessment is based upon the interaction of cost structure and item structure with a Form-Material-Process instance.

## APPLICATION OF OBJECT-BASED COST ASSESSMENT

This section briefly describes how the aforementioned objects tie together and how the approach, when developed into a computer-aided engineering tool, would be used in the design process. Figure 9 illustrates the overall application of the object-based cost assessment approach to support product/process design. The process begins in the lower-left portion of the figure, where an item that is to be designed is defined in terms of form, material, and process. The large arrows emanating from the "item design" box represent the creation of an instance of an object within each of the three object hierarchies. Those three instances are "related" or "collected" into a single complex instance, as represented by three arrows that connect each hierarchy to the Form-Material-Process (F-M-P) object. The F-M-P object contains all of the information – in terms of property values, methods, rules, etc. – sufficient

to develop an estimate of the item's cost. In the example in Figure 9, the item's cost is composed of six cost elements. The costs for each item are linked to an item structure; this facilitates combining and rolling-up costs for an entire system or product.

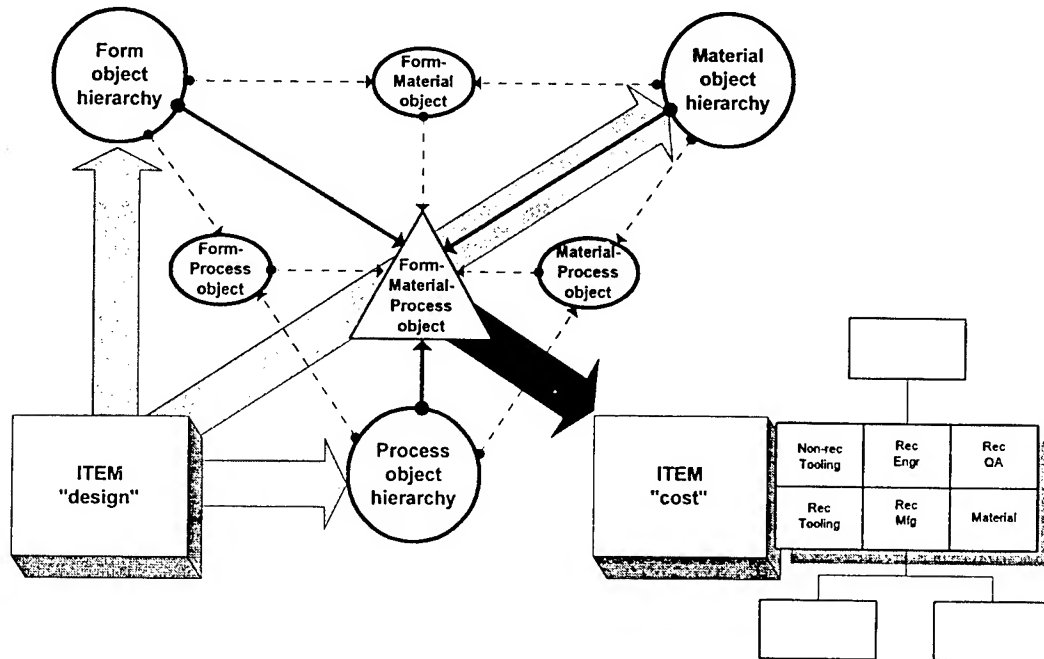


Figure 9: Linkage between item "design" and item "cost" through an object-based structure.

A software implementation of the object-based cost assessment approach described in this paper is illustrated in Figure 10. The system – referred to as OCEANS, Object-based Cost Estimation and Assessment for design Support – is shown in the context of its application environment. OCEANS, when developed and implemented as a software system, would provide cost assessments as an integral part of the design environment and would be considered a standard computer-aided engineering (CAE) tool. Such a system would provide a strong link between members of an IPT and the product/process design environment. The system would be considered an evolving application, in that its capabilities and resources would continually be updated and enhanced based on lessons learned by the IPTs and through research projects. The system would itself be a valuable research tool and would provide a powerful learning environment for academe and industry.

The primary components of the system that would implement the concepts and approach described in this paper are shown in the shaded OCEANS box. The F-M-P (Form-Material-Process) database contains instances of the object classes discussed earlier. The knowledge base contains rules, element descriptions, notes and annotations from past use, etc. that further define and support the development of relationships among the objects that are used to assess product/process cost. The system is composed of numerous methods, models, tools, etc. that define the behavior of objects and provide the

computational capability of the system. Providing effective feedback to designers and IPTs, in forms that are meaningful and useful to them, is critical to any system's success. Therefore, "interfaces" is defined as a primary element of the system. Interface includes the means for all users of the system to effectively and efficiently provide input to and receive output from OCEANS. As a result, a primary capability of OCEANS is an ability to construct "views" that represent information contained in the system to support a variety of specific needs. Another important capability of OCEANS is the generation of standard and ad hoc reports to document and support the design process.

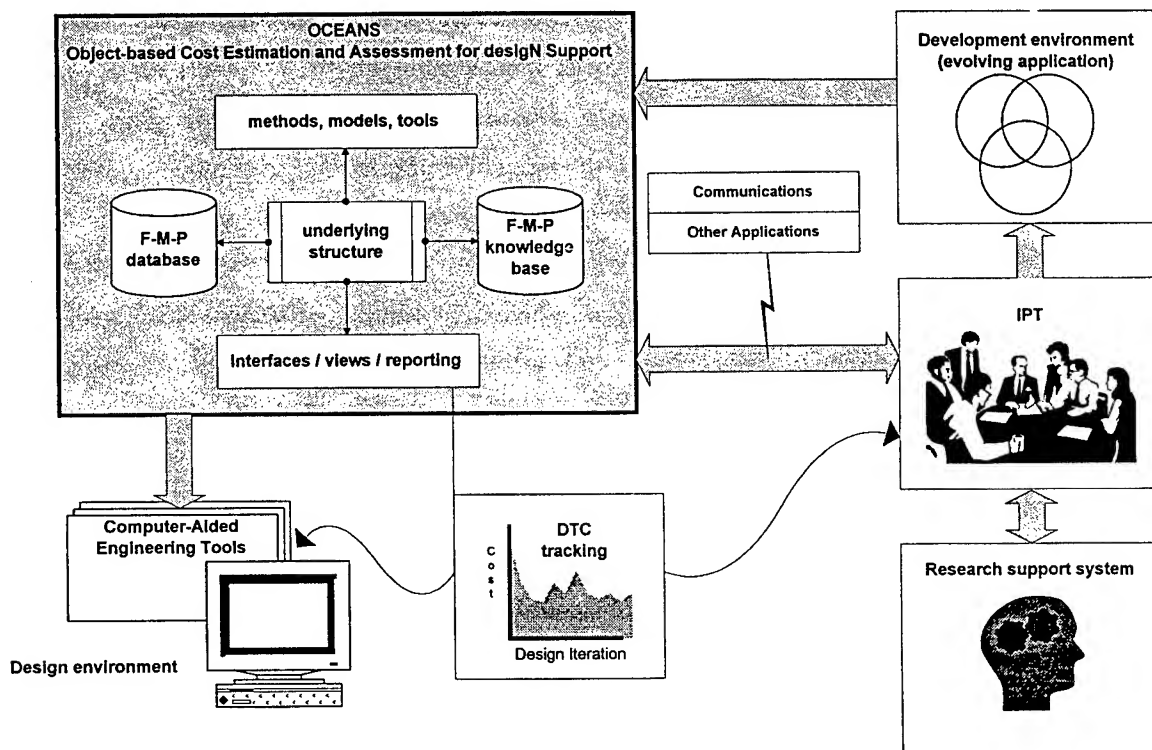


Figure 10: Application environment for an object-based cost assessment system.

The final major component of the OCEANS software system is its underlying structure. An object-based framework provides the needed flexibility that allows different users to represent, manage, and query the data, objects, methods, output, etc. to best meet their needs. That is, the system can easily be redefined or reconfigured to best represent a specific product, project or company organization, level of expertise, design requirements and considerations, etc. Similarly, the object-based structure accommodates increasing levels of detail as designs evolve.

In order to effectively support the design and IPPD processes, it is imperative that the system facilitate and encourage communication and collaboration among member of the IPT. It must also easily and seamlessly link to and integrate with methods, models, and tools from other applications. This

capability is represented in Figure 10 by the items to the right of the OCEANS box that are linked with the arrow connecting OCEANS and the IPT.

One of the strengths of the object-based approach is that as the database becomes populated with a variety of design alternatives, new design considerations will be able to draw upon and effectively use this history. As shown by the box figure below OCEANS, the object-based structure provides a means to track product costs and the reasons for changes in cost, as they evolve through the design process. For example, one possible application of OCEANS is a design-to-cost (DTC) system. Through the use of object-based technologies, such a system could easily be extended to track costs through production and operation. Reporting from this type of system would be used to refine and calibrate cost models, as well as provide feedback to the design process.

Since this paper defines a basic conceptual approach to enhance the cost assessment process during IPPD and outlines the fundamental structure for a software implementation, the next logical step is to develop a prototype of an application environment that implements OCEANS. The prototype would demonstrate and test the preliminary concepts defined in this paper, as well as the application of object-based technologies to the cost-modeling domain. At this time, the best software in which to develop and test a prototype application is Knowledge Base Engineering's *IKE (Integrated Knowledge Environment)* and *Oz (Object cZar)*. *IKE* is an integrated set of process-oriented, multimedia application development tools that manage data, objects, graphics, forms, and images. *Oz* provides capabilities to manage hierarchical object structures, create and maintain objects, object metrics, object collections, and object views.

As part of the prototyping process, it is necessary to further explore the representation of the three design dimensions and elements of the costing process as objects. The most effective way to develop a prototype system is through the use of an actual case example(s). That is, represent a specific problem domain in an object-based context. This includes interaction between the developers of OCEANS and industry-based IPTs that are designing "real" products and using "real" processes. A better understanding of the design and IPT processes will result in an application that best meets the commercial and military needs to develop more affordable products. Therefore, an important next step in the evolution of an OCEANS system is to involve an industry partner(s) that would provide the knowledge and data that are necessary to further define the approach and populate the object base. One such potential source is the Military Products using Best Commercial Practices (MP-C/MP) Program [17], [18]. This project is an Industrial Base Pilot program that is jointly funded the Air Force Wright Laboratory, Manufacturing Technology Directorate and the C-17 System Program Office (SPO). For example, a prototype of OCEANS would be developed around the design and manufacture of the C-17 horizontal stabilizer outer torque box, considering both all aluminum and mostly composite structures. A second possible partner is Small Business Innovation Research Engineering Companies (SBIRE) in Drumright, OK. SBIRE is a virtual manufacturing enterprise in Oklahoma that consists of a coalition of

small and high technology manufacturing organizations that have combined resources in order to produce small quantities of re-manufactured aircraft components for DoD. The author has been involved with both of these projects during the 1996 and 1997 AFOSR Summer Faculty Research Programs.

## CONCLUSIONS

This paper addresses a critical concern in today's commercial and military manufacturing environments - the design and manufacture of affordable products. One of the barriers to developing affordable products is the lack of supportive cost assessment tools that can be applied early in the design process, where the most cost benefit can be obtained. To effectively trade-off performance and cost, the designer and integrated product team must be able to address process design issues at the same time as they address product design issues.

A result of the research that was conducted during the 1997 Summer Faculty Research Program (SFRP) is an innovative approach that specifically addresses these issues. The approach, as described in this paper, provides the foundation for the development of a system that permits cost estimation and assessment to become a computer-aided engineering tool for assessing product/process costs early in the design process. The approach takes a concurrent engineering costing process perspective that would supplant the traditional, sequential, "over-the-wall" costing process. Object-based technologies are proposed to provide the means to directly and simultaneously link the consideration of form and material in product design with the consideration of manufacturing processes.

This research provides a conceptual representation of an object-based, cost-assessment approach that supports the design process, defines the objects, properties, hierarchies, and underlying object structure that are utilized in the approach, and describes an initial view of the application environment and software system that would be used to implement the approach. The next step for this research, in addition to further refining the objects, properties, and hierarchies, is to develop a prototype of the proposed system. This design support system, named OCEANS - Object-based Cost Estimation and Assessment for design Support, would best be developed through the use of actual case examples from industry. As a result of contacts made during the SFRP, the author is currently soliciting involvement from potential industry partners.

## ACKNOWLEDGEMENTS

The author expresses his sincere appreciation and gratitude to Mr. E. I. (Sam) Nusinow, President, Knowledge Base Engineering, Centerville, OH, Mr. John W. Fondon, Jr., Systems Engineering, Northrop-Grumman Commercial Aircraft Division, Dallas, TX, and Mr. Mike Lee, President, SBIRE, Drumright, OK for generously and graciously contributing their time, ideas, and support to this project.

## REFERENCES

- [1] Wright Laboratory Affordability Strategy Team, "Affordability in Science and Technology Development," Wright-Patterson Air Force Base, OH: Wright Laboratory, July 9, 1993.
- [2] R. D. Coyne, M. A. Rosenman, A. D. Radford, M. Balachandrian, and J. S. Gero, *Knowledge-Based Design Systems*. Reading, MA: Addison-Wesley Publishing Company, 1990.
- [3] M. Yoshimura, "Concurrent optimization of product design and manufacture," in *Concurrent Engineering: Contemporary issues and modern design tools*, H. R. Parsaei and W. G. Sullivan, Editors London: Chapman & Hall, 1993, pp. 159-183.
- [4] Modern Technology Corporation, "Integrated Weapon Systems Management (IWSM) "How to" Manual for Manufacturing Cost Assessment (MCA)," Dayton, OH: Modern Technologies Corporation (MTC), September 27, 1995.
- [5] A. G. Greenwood, "A Framework for Manufacturing-Oriented, Design-Directed Cost Estimation," Final report for Summer Faculty Research Program, Bolling Air Force Base, DC: Air Force Office of Scientific Research, September 1996.
- [6] I. Jacobson, M. Ericsson, and A. Jacobson, *The Object Advantage: Business Process Reengineering with Object Technology*. Reading, MA: Addison-Wesley Publishing Company, 1995.
- [7] A. Kemper and G. Moerkotte, *Object-Oriented Database Management: Applications in Engineering and Computer Science*, Englewood Cliffs, NJ: Prentice Hall, 1994.
- [8] S. Khoshafian and R. Abnous, *Object Orientation Concepts, Languages, Databases, User Interfaces*. New York: John Wiley & Sons, Inc., 1990.
- [9] J. Martin and J. J. Odell, *Object-Oriented Analysis and Design*. Englewood Cliffs, NJ: Prentice Hall.
- [10] S. Shlaer and S. J. Mellor, *Object-Oriented Systems Analysis: Modeling the World in Data*. Englewood Cliffs, NJ: Yourdon Press, 1988.
- [11] Pilot Software, "An Introduction to OLAP," <http://www.pilotsw.com/olap/olap.html>: Pilot Software, 1997.
- [12] B. Wu, "Object-oriented systems analysis and definition of manufacturing processes," *International Journal of Production Research*, vol. 33, pp. 955-974, 1995.
- [13] S. R. Shankar and D. G. Jansson, "A generalized methodology for evaluating manufacturability," in *Concurrent Engineering: contemporary issues and modern design tools*, H. R. Parsaei and W. G. Sullivan, Eds. London: Chapman & Hall, 1993, pp. 248-263.
- [14] J. Woodwark, *Computing Shape*. London: Butterworths, 1986.
- [15] R. H. Todd, *Manufacturing Process Reference Guide*. New York: Industrial Press Inc., 1994.
- [16] S. Kalpakjian, *Manufacturing Engineering and Technology*. Reading, MA: Addison-Wesley Publishing Company, 1992.

- [17] J. W. Fondon, Jr., D. Rasmussen, D. Lum, and S. Smith, "Large Composite Structure -- Commercial Military Integration (Military Products Using Best Commercial Practices) Phase I -- Manufacturing 2005 Business Practices, Manufacturing Infrastructure, Process Technology Development, Volume II -- Manufacturing 2005 Handbook," Wright-Patterson Air Force Base, OH: Manufacturing Technology Directorate, Wright Laboratory, Air Force Materiel Command, January 1996.
- [18] M. K. Riseley, T. Houpt, and S. Wheeler, "Large Composite Structure -- Commercial Military Integration (Military Products Using Best Commercial Practices) Phase I -- Manufacturing 2005 Business Practices, Manufacturing Infrastructure, Process Technology Development, Volume I -- Program Review," Wright-Patterson Air Force Base, OH: Manufacturing Technology Directorate, Wright Laboratory, Air Force Materiel Command, January 1996.



**RANGE ESTIMATING FOR RESEARCH AND DEVELOPMENT  
ALTERNATIVES**

**Rita A. Gregory  
Assistant Professor**

**Georgia Institute of Technology  
Atlanta, GA 30332**

**Final Report for:  
Summer Research Program  
Wright Laboratory**

**Sponsored by:  
Air Force Office of Scientific Research  
Bolling Air Force Base, Washington, DC**

**And**

**Wright Laboratory**

**August 1997**

## RANGE ESTIMATING FOR RESEARCH AND DEVELOPMENT ALTERNATIVES

Rita A. Gregory  
Assistant Professor  
School of Civil and Environmental Engineering  
Construction Engineering and Management  
Georgia Institute of Technology

### Abstract

This research was designed to assist Wright Laboratory Air Base Technology Branch in identifying limiting factors and cost drivers for emerging technologies. By identifying the limiting factors and cost drivers, technology developers can better focus their research to find alternatives to overcome limitations or to develop more “affordable” solutions in these times of decreasing budgets. As part of their Air Base facilities research, the Air Base Technology Branch has a long, successful history of developing telerobotic and autonomous construction equipment for rapid runway construction and repair and for remediating hazardous waste and unexploded ordnance. The specific request for this summer research was to develop a methodology to analyze these field data to identify limiting factors and cost drivers that in turn could be used to focus future research thrusts. These field data are results of complex, multivariate problems that include integration of telerobotic search operations; vehicle navigation; guidance and control; remote communications; global positioning links; automated damage assessment; automated target location, identification, and recognition; end effector integration; commercial off-the-shelf applications; and associated computer technologies. The methodology prototyped, after researching many alternatives, was an application of Artificial Neural Networks. This paper will discuss the alternative methodologies and the rationale for selecting Artificial Neural Networks. Complementing this paper are two graduate student papers to complete this summer research project: “Cost-Based Risk Predictions and Identification of Project Cost Drivers Using Artificial Neural Networks” (Pearce 97-0415) and “Data Simulation Supporting Range Estimating for Research and Development Alternatives” (Williams 97-0416).

## **RANGE ESTIMATING FOR RESEARCH AND DEVELOPMENT ALTERNATIVES**

**Rita A. Gregory**

### **INTRODUCTION**

This research was sponsored by the Air Force Office of Scientific Research, Bolling AFB, DC and the Air Force Wright Laboratory Air Base Technology Branch (WL/FIVC-OL Tyndall AFB, FL) as part of the Summer Faculty Research Program. This research was designed to assist Wright Laboratory Air Base Technology Branch in identifying limiting factors and cost drivers for emerging technologies. By identifying the limiting factors and cost drivers, technology developers can better focus their research to find alternatives to overcome limitations or to develop more "affordable" solutions in these times of decreasing budgets. As part of their Air Base facilities research, the Air Base Technology Branch has a long, successful history of developing telerobotic and autonomous construction equipment for rapid runway construction and repair and for remediating hazardous waste and unexploded ordnance (Nease 1994). Part of the laboratory's research includes collecting and analyzing field data on actual unexploded ordnance digs and hazardous waste clean-ups (USAF 1995a,b). The specific request for this summer research was to develop a methodology to analyze these field data to identify limiting factors and cost drivers that in turn could be used to focus future research thrusts (Nease 1997). These field data are results of complex, multivariate problems that include integration of telerobotic search operations; vehicle navigation; guidance and control; remote communications; global positioning links; automated damage assessment; automated target location, identification, and recognition; end effector integration; commercial off-the-shelf applications; and associated computer technologies. The methodology prototyped, after researching many alternatives, was an application of Artificial Neural Networks. This paper will discuss the alternative methodologies and the rationale for selecting Artificial Neural Networks. Complementing this paper are two graduate student papers to complete this summer

research project: "Cost-Based Risk Predictions and Identification of Project Cost Drivers Using Artificial Neural Networks" (Pearce 97-0415) and "Data Simulation Supporting Range Estimating for Research and Development Alternatives" (Williams 97-0416).

Review of alternative methodologies was the first step of this research. Traditional parametric estimating, most often used in the early stages of research and development programs such as the robotic research in the Wright Lab, require historical data and/or input to learning curve theory to develop cost estimating relationships. Neither is available for robotic systems in environmental operations. Nor, in the case of automated excavation equipment, is data available for credible engineering-build-up or quantity-take-off estimating (Burns 1995; Burns 1993; Gregory 1993; Gregory 1992; Thurston 1995). This paper, as part of the summer research, will discuss the alternative methods considered.

An especially difficult aspect of this summer research was to keep separate the complexities of the field data from the complexities of developing a new application of Artificial Neural Networks. The field tests (USAF 1995a,b) were designed to demonstrate engineering prototypes and the data collection was a "fallout" or extra benefit. There was no formal data collection protocol designed to collect information from which cost drivers could be deduced. Also, most of the data collected in the field tests were not collected under conditions considered "clean" where variables could be independently observed or analyzed. For example, time motion studies from which productivity advantages can be deduced were not conducted. One of the first problems of this summer research was to design a data set that was "clean" enough to prototype a methodology. To prove the methodology prototype and not get confused between complex data and complex methodology, this data set also needed to be on a subject that was simple and well understood. When designing a new approach for data analysis on a complex, multivariate problem such as the robot digging unexploded ordnance, it would be especially difficult to understand the interactions among the complex field data and complex algorithms of Artificial Neural Networks. To overcome these difficulties, this researcher directed the development of a "clean" data set by simulating multivariate data using the USAF

Parametric Automated Cost Engineering System (PACES) for vertical construction. The concept was that if we could "prove" the application of Artificial Neural Networks on a data set that was thoroughly understood (vertical construction) and "clean" (simulated), then we could have confidence in applying the technique on an unknown, multivariate, and complex data set such as the data collected in the robot field tests. Ms Laura Williams, a graduate student supporting this research, has documented this data simulation in "Data Simulation Supporting Range Estimating for Research and Development Alternatives" (Williams 97-0416). Ms Annie Pearce, another graduate student supporting this research, discusses the prototype of Artificial Neural Networks in analyzing the PACES generated data in her paper "Cost-Based Risk Predictions and Identification of Project Cost Drivers Using Artificial Neural Networks" (Pearce 97-0415). The final goal of analyzing the robot field data using Artificial Neural Networks will be a follow-on or continuation of this summer methodology prototyping.

#### **ALTERNATIVE APPROACHES**

Extensive literature exists on the general subjects of cost estimating, cost analyses, and range estimating (Gregory 1992). Several professional societies (e.g., American Association of Cost Engineers, International Society of Parametric Analysts, and Society of Cost Estimating and Analysis) set their charters around the advancement, training and regulation of cost control, cost analysis, and/or cost estimating. Almost all references begin with a classification of methods of estimating, the accuracy expected with different classifications, and the applications at differing stages of design or development. For example Hardie uses two broad titles-- approximate estimates and detailed estimates (Hardie date unknown)--while Sinclair divides the types into conceptual estimates, preliminary estimates, and final design/bid estimates (Sinclair 1988). Regardless of categorizations and projections of accuracies the techniques for this research can be generally grouped into engineering build up estimates, parametric estimates, and expert systems for estimating.

## **Engineering-Build-Up**

The traditional estimating technique of engineering-build-up, called quantity-take-off estimating in construction engineering, is the most commonly used when a system has matured enough to provide the details needed for this technique. Quantity-take-off estimating is a process of counting every component of a design to the lowest level of detail. The term literally comes from counting (measuring the quantities of) material, labor, and equipment from detail design (take-off from the drawings). A traditional engineering build-up or quantity takeoff estimate is developed at the latter stages of the design phase (or in research and development at the systems development stage) once the drawings are complete. A quantity-take-off estimate is done by developing a work breakdown structure and counting the individual components “taken off” the detailed design plans. This can be done using several approaches. One approach to consider is using an assemblies format to structure the estimate. This involves taking the facility under consideration and breaking it up into assemblies such as foundations and exterior enclosure (R.S. Means 1997). Comparatively, a component breakdown could be done where the actual components of the facility or engineering design such as a robot are counted individually and entered as line items in a spreadsheet format. Regardless of the approach, once the quantities are available, pricing must take place. Prices can be found through contacting the material suppliers or consulting subcontractor bids. The advantage of this system is that it is very accurate if it is completed successfully. “Successfully” refers to the completion of the estimate without any errors or omissions which inherently requires the completion of the design (Mosely 1997).

Engineering-build-up or quantity-take-off estimating would only be applicable to the robot program to estimate a specific design of equipment. It is not suitable for cost analysis to determine cost drivers or to develop range estimates to focus future research and development thrusts.

## **Parametric Estimating.**

Traditional parametric estimating uses comparative techniques by applying some form of regression analysis on historical data. The estimate is derived by comparing a current project to past projects--thus the term comparative. Comparative estimates include unit costs, square foot costs, and parametric estimates derived from historical cost curves. A major problem in developing comparative estimates is that there is no standard method of defining the technical or descriptive characteristics of the individual systems or collecting historical costs associated with the specific characteristics. If the original data are not collected with the system's or scenario's unique characteristics spelled out, no amount of statistical manipulation or regression analyses can account for the differences with reliability or validity. This problem of data characterization is especially difficult in hazardous waste clean up and unexploded ordnance because of the multitude of complex interrelated variables from the system complexities and the soil geophysics. Typical statistical requirements such as independence and conditionality are not suitable for variables and parameters in these scenarios.

This technique is not suitable for analyzing the robotic field data because the data was not collected with a formal protocol and the data does not flag or identify the special system design characteristics needed for range estimating or deducing cost drivers. Plus, an unsolvable problem in using comparative estimating for research and development, is that if the project is a new or one-of-a-kind system, there is no cost history or data from which a valid cost comparison can be made. There is no historical data in the robot program from which valid cost comparisons can be made.

## **Artificial Intelligent and Expert Systems**

The need for artificial intelligence and expert systems is expanding at an unprecedented rate. The information explosion and the rapid communication systems of today and tomorrow require near immediate synthesis of data and expert knowledge to solve complex technical

problems. Construction engineering is no exception to the information explosion. New materials; computerized control systems; voluminous legal, regulatory, environmental, and safety requirements; and construction technologies are just a few examples of the rapidly expanding information fields that the construction engineer must synthesize today (Gregory 1992).

Although most references graphically display artificial intelligence systems in discrete boxes, the set of tools could be more accurately described as a continuum of emerging tools with overlapping applications (Gregory 1992). Harmon and Maus describe artificial intelligence as “an academic research program” with five most active areas of commercial application: natural language, robotics, improved human interfaces, exploratory programming, and expert systems. The expert systems area, as described by Harmon and Maus, is “a program that manifests some combination of concepts, procedures, and techniques to allow people to design and develop computer systems that use knowledge and inference techniques to analyze and solve problems” (Harmon and Maus 1988).

Three key areas from artificial intelligence research that apply to this summer research are 1) new ways to represent knowledge, 2) heuristic search, and 3) the separation of knowledge from inference and control (Harmon and Maus 1988). In context of expert systems, Harmon defines knowledge as a body of information about a particular topic that is organized to be useful. Knowledge-based programs rely on rules-of-thumb or heuristics rather than algorithms and mathematical certainty; therefore, they allow the analyst to look at problems that are unorganized or have incomplete or not clean data (Gregory 1991). These techniques allow an expert to examine the contents of data without knowing how the content is derived or manipulated (Gregory 1991). A key element of knowledge engineering is that a database and a knowledge base can look similar, but the way in which the information is organized and manipulated is significantly different (Gregory 1991). A knowledge base can incorporate such heuristics as simple as a step functions or the complex ability to make on-course corrections from



real time feedback from complex, multiple sensor fusion. Artificial intelligence systems allow knowledge bases to adjust the body of procedures and selected algorithms to create and apply new algorithms. This is a breakthrough that knowledge-based expert systems provide. These processes are not and cannot be modeled with mathematical algorithms. The attribute that a knowledge system can generate the decisions to which the algorithms and the calculations are applied is the theory that makes this technique applicable for the robot data analyses.

Another breakthrough in artificial intelligence is the ability of a computer program to "learn" or "teach itself." When a new data element or algorithm is added, all existing models can access and use that new component without being completely reprogrammed. The organization of the knowledge bases and work break down structure allows multiple, almost unlimited paths through the decision steps in molding construction engineering applications (Gregory 1991).

This study concentrates on artificial intelligence tools designed to enable computers to assist experts in analyzing and solving complex problems. Artificial Neural Networks are a modeling tool based loosely on the computational paradigm of the human brain and have proven to be robust and reliable for tasks of forecasting, classification, and interpretation or processing of data (Pearce 1997). In the third phase of this summer research, Ms Pearce in her paper "Cost-Based Risk Predictions and Identification of Project Cost Drivers Using Artificial Neural Networks," examines the potential of Artificial Neural Networks as a tool to support the task identifying cost drivers in an array of complex, multivariate data. Application of this prototype to robot field data will be a follow-on research project.

## CONCLUSIONS

The ability to analyze data from robot field tests is complicated by the integrated, complex, multivariate aspects of the robot functions. These field data are results of complex, multivariate problems that include integration of telerobotic search operations; vehicle navigation; guidance and control; remote communications; global positioning links; automated damage assessment; automated target location, identification, and recognition; end effector

integration; commercial off-the-shelf applications; and associated computer technologies.

Traditional cost analysis techniques are not suitable for identifying limiting factors or deducing cost drivers from which research and development programs can focus future thrusts. Artificial intelligent systems are being developed that can simulate the thinking process and heuristics common in human decision making and thinking. An application of Artificial Neural Networks, using clean, simulated data was prototyped and proved the concept of using artificial intelligent systems for analyzing complex, multivariate data. The prototype application developed in this summer research is reported in three complementary papers: this one plus “Cost-Based Risk Predictions and Identification of Project Cost Drivers Using Artificial Neural Networks” (Pearce 97-0415) and “Data Simulation Supporting Range Estimating for Research and Development Alternatives” (Williams 97-0416). Future research can be a follow-on application of this prototype system.

## BIBLIOGRAPHY

- Burns, T., Thurston, M., and Edgar, M. H. (1995). "Case study: using a parametric model for environmental remediation cost estimating." Federal Facilities Environmental Journal, Summer, John Wiley and Sons, Inc.
- Burns, T., and Gregory, R. A., et al. (1993). "Totally integrated construction cost estimating, analysis, and reporting system." U.S. Patent and Trademark Office, U.S. Patent 5,189,606 Washington DC.
- Gregory, R. A., and Rast, R., et al. (1993). "Remedial action cost engineering and requirements environmental estimating (RACER/ENVEST), analysis, and reporting system." U.S. Patent Application S/N 08/051,551. AF Inv, 20918, Air Force Legal Services Agency, Wright-Patterson AFB, OH 45433-7109.
- Gregory, R. A. (1992). "Development of a knowledge-based system approach for decision making in construction projects," Dissertation, University of Florida, Gainesville, FL.
- Gregory, R. A. (1991). Letter to AF/JACPD "Response to your 26 Feb 91 letter, subj: S/N 07/400,764-Thomas J. Burns et al.-Totally Integrated Construction Cost Estimating, Analysis, and Reporting System," Tyndall AFB, FL.
- Hardie, G.M. (date unknown). Construction Estimating Techniques, British Columbia Institute of Technology, Prentice-Hall, Inc. Englewood Cliffs, NJ.
- Harmon, P. and Maus, R. (1988). Expert Systems: Tools and Applications, Wiley and Sons, Inc., New York, NY.
- Mosley, M. (1997). "Quantity Takeoff Estimating vs. Parametric Estimating," CE 4900 Individual Study, Georgia Institute of technology, School of Civil and Environmental Engineering, Atlanta, GA.

- Nease, A. D. and Grosskopf, K. (1997). Unstructured Interview, Tyndall AFB, FL, June 1997.
- Nease, A. D., and Alexander, E. F. (1994). "Air Force construction automation/robotics." *Automation in Construction*, Elsevier Science Publishers B.V., Air Force Materiel Command, Wright Laboratories, Air Base Operability and Repair Section, Tyndall AFB, FL 32403.
- Pearce, A. 1997. "Cost-Based Risk Predictions and Identification of Project Cost Drivers Using Artificial Neural Networks," AF/OSR Summer Research Program (97-0415).
- R.S. Means Company. (1997). *Assemblies Cost Data*, 22nd Annual Ed., R.S. Means Company, Kingston, MA.
- Sinclair, N.D. (1988). Estimating for Abnormal Conditions, Industrial Press, Inc., New York.
- Thurston, M., Reid, M., and Ove, T. (1995). "Automated cost estimating for ordnance and explosive waste remediation." Delta Research Corporation, Niceville, FL 32578.
- USAF WL/FIVCO (USAF). (1995a). "Live site advanced technology demonstration standard validation data sheet, U.S. Army Jefferson proving ground, IN." Air Force Materiel Command, Wright Laboratories, Air Base Operability and Repair Section, Tyndall AFB, FL 32403, June-July.
- USAF WL/FIVCO (USAF). (1995b). "Area clearance program." Air Force Materiel Command, Wright Laboratories, Air Base Operability and Repair Section, Tyndall AFB, FL.
- Williams, L. 1997. "Data Simulation Supporting Range Estimating for Research and Development Alternatives," AF/OSR Summer Research Program (97-0416).

# **ANISOTROPY IN EPIC 96&97:IMPLEMENTATION AND EFFECTS**

**Mark T. Hanson  
Assistant Professor  
Department of Mechanical Engineering**

**University of Kentucky  
Lexington, KY 40506**

**Final Report for:  
Summer Research Program  
Wright Laboratory**

**Sponsored by:  
Air Force Office of Scientific Research  
Bolling Air Force Base, Washington, DC**

**And**

**Wright Laboratory**

**September 1997**

## ANISOTROPY IN EPIC 96&97: IMPLEMENTATION AND EFFECTS

Mark T. Hanson  
Associate Professor  
Department of Mechanical Engineering  
University of Kentucky

### Abstract

Computer simulations of high velocity impact events provide efficient and effective means for analyzing weapons and armor systems. Today this is true more than ever before with the continuing trend towards faster computers at lower cost. Hence computer codes which perform these simulations have become an indispensable tool to the present day weapons designer. The availability of higher powered computers has allowed these computer codes to be modified and expanded to model currently used materials in a more realistic way. Furthermore this has also provided the weapons designer with a chance to consider new and potentially more effective materials which respond to loading in a more complicated manner.

The computer code of interest here, termed EPIC (Elastic Plastic Impact Code), is a finite element based continuum hydrocode. Previous versions of EPIC have only included the capability to analyze isotropic materials. This isotropic constitutive model has worked well to study the behavior of currently used materials such as copper which exhibits minimal direction dependence in its properties. However materials of increasing interest to the Air Force in its weapons development program do not generally follow this isotropic behavior. One such material of particular interest to the Air Force is tantalum. The heavy compression that occurs during processing of this body centered cubic metal results in a preferred orientation of the grains referred to as texture. The presence of texture gives a directional dependence to the material properties which leads it to obey an anisotropic constitutive law.

Recent versions of EPIC (1996&97) have included the ability to analyze anisotropic materials, particularly in the post yield realm of material behavior. Hence it was the main focus of the present work to investigate the implementation of anisotropy in this hydrocode and to conduct an initial numerical investigation as to how significant are the effects of anisotropy. For the numerical analysis, simulations of the Taylor impact test were used. It is shown that anisotropy in the plastic deformation properties can have significant effects on high velocity impact. In particular quantities such as wave front position, effective stress and equivalent plastic strain, and strain rate can be substantially different as compared to isotropic materials.

## ANISOTROPY IN EPIC 96&97: IMPLEMENTATION AND EFFECTS

Mark T. Hanson

### Introduction

Pure metals like many other substances are generally referred to as polycrystalline materials. This means they are composed of large numbers of very small crystals or grains. Each individual grain is comprised of atoms arranged in specific periodically located positions termed a lattice structure. It is well known that an individual grain of a certain metal may have different material properties in different directions (Here material properties refers to Young's modulus, Poisson's ratio and other artifacts of mechanical testing techniques). Since the individual grains are small (in the 100 micron range), a sample of a material may contain an extremely large number of grains which are most often randomly oriented. The random nature to the distribution of grains dictates that the polycrystalline material will essentially have the same material properties in all directions. If the material properties of a sample are directionally independent the material is said to be *isotropic*.

Deformation of a polycrystal occurs by the sliding of planes of atoms over one another. These slip planes have a specific orientation within an individual grain. Under large deformation this slip within a grain can cause a rotation of the lattice structure itself, thus altering its orientation within the polycrystalline material. If the polycrystal loses its random grain orientation as a result of this deformation, crystallographic texture is said to have developed. The existence of preferred orientations of the grains in a polycrystal allows the directional dependence of the individual grain's material properties to be transferred to the polycrystal as a whole. Thus the existence of crystallographic texture may strongly affect the properties of the overall material. If the material properties of a sample are directionally dependent the material is said to be *anisotropic*.

Some materials are anisotropic by their very nature. Examples include wood, fiber reinforced composite laminates, and single crystals of metals as noted above. Of particular interest to the Air Force is polycrystalline materials with texture, namely tantalum. After heavy compression of a cylinder of tantalum into a flat sheet, the grains of this bcc (body centered cubic) metal become preferentially oriented such that their  $\langle 111 \rangle$  or  $\langle 100 \rangle$  directions are aligned with the sheet normal. The anisotropy induced by this large deformation will effect the performance of this material in potential weapons applications. The present study seeks to investigate some of the consequences of this anisotropic behavior.

Present purposes will be fulfilled by a numerical investigation of the Taylor impact test. This test is a useful tool in evaluating material behavior for potential weapons applications. Here the explicit dynamic finite element code EPIC (Elastic Plastic Impact Code) will be used in the analysis.

Recent versions of EPIC (1996 & 1997) have incorporated an anisotropic material capability. The details of the implementation for anisotropic behavior in a finite element code such as EPIC can be found in Maudlin and Schiferl (1996). Here the effects of anisotropy on high rate impact loadings are of interest. The Taylor impact test is reviewed next and then the EPIC code is briefly discussed. Some aspects to the anisotropic analysis will be presented and finally some numerical results for Taylor impact of an anisotropic cylinder are obtained.

### **Taylor Impact Test**

Taylor (1948) along with co-workers (Whiffin 1948, Carrington and Gayler, 1948) is credited for first introducing a dynamic impact test in an effort to deduce the yield stress of materials subjected to high strain rates. In this experiment a right circular cylinder composed of the material to be investigated is impacted against a flat rigid target, as shown in Figure 1 (House, 1989; Rule, 1995). A smooth-bored gun is used with the aid of gun powder to project the cylinder at its desired velocity. The gun barrel is approximately 25 in. long and calibers (cylinder diameters) from 0.17 in. to 0.50 in. can be used. The velocity can be adjusted (by the amount of powder used) to approximately achieve the desired high strain rate which can be up to  $10^5/s$ . The target is heavy, weighing approximately 80 lb., and it is made from a hardened and polished steel. This produces an extremely hard and smooth surface that minimizes frictional effects and thus simulates a rigid smooth object.

As noted above, the specimens are launched through the use of a specific amount of commercial grade gun powder which is placed in a primed shell casing. The casing is then loaded in the gun behind the cylindrical specimen. A remotely operated solenoid is used to activate the firing pin that strikes the primer which in turn detonates the powder. The powder burns at an extremely fast rate creating a very high pressure in the barrel which forces the specimen down the barrel towards the target. The pressure can be measured with pressure transducers along the barrel which allows the specimen velocity to be calculated (House, 1989). Alternatively a laser system can be used to accurately determine the projectile velocity at a location closer to the target face as depicted in Figure 1. Powder curves (specimen velocity versus mass of powder) have been developed which allow easy calculation of the amount of powder required to achieve a desired velocity.

As the cylinder strikes the target face, a dynamic stress field is created in the specimen. This initiates at the target-specimen interface and propagates along the cylindrical specimen. The impact velocity used is sufficient to generate stresses above the yield strength of the material and thus cause plastic flow of the specimen. A typical experimental result for a copper specimen is shown in Figure 2 from House (1998) where the impact velocity was 189 m/s. The left image shows an undeformed specimen and the right image displays its geometry after a typical impact event which lasts on the average of a few hundred micro-seconds. The plastic deformation is largest at the end which strikes



the target causing the diameter to become enlarged. The other end of the specimen retains its original shape. The geometrical change in the specimen is captured during this short time period by the use of an extremely high speed Cordin camera (House, 1989). Film images during the impact duration allow the position of the wave front (characterized by a specific level of strain in the specimen) to be followed in time.

### **EPIC Finite Element Code**

It is evident from the above discussion that the Taylor impact test produces a visual picture record of the changing specimen geometry during dynamic loading. Elements of this final geometry were the basis of the simple yet insightful analytical model developed by Taylor (1948) to extract quantitative and hence useful results. Recent work, such as by Jones et al. (1985, 1987, 1991, 1996), has been directed at developing a more in-depth understanding of the wave propagation phenomenon that occurs during impact in the Taylor test. Although this new analysis of high rate impact loading has provided a considerable improvement in the basic understanding of the fundamental mechanics occurring, it has been limited by the desire to stay within an engineering analysis where closed form analytical expressions are obtainable for developing their models.

A contrasting approach to analyzing more general problems of this nature has relied on the rapidly expanding numerical analysis capabilities that faster computers have provided. Computer codes mainly based on finite element analysis have been continually developed, improved and expanded towards more accurately modeling high rate loading phenomenon. The code of interest here termed EPIC was initially put forth more than two decades ago (Johnson, 1977) and since that time has undergone continual development. EPIC is a general purpose explicit dynamic finite element code useful in analyzing a multitude of dynamic high rate problems. As with any finite element code of this nature, the basic governing differential equations are satisfied on an element by element basis and the numerical solution for the physical quantities of interest are found compatible with a specified set of initial and boundary conditions.

The problems for which EPIC is designed to analyze are extremely complex and a complete discussion is far beyond the present scope. Pertinent to the Taylor test it is noted that problems of this nature may involve shock loading resulting in extremely high pressure during the transient stage of impact with subsequent quasi-steady wave propagation followed by specimen deceleration during the terminal transient period. In EPIC the stress state is decomposed into a hydrostatic pressure and a deviatoric component. The deformation occurring during loading is related to these two stress components through constitutive laws which reflect the material behavior.

The high hydrostatic pressures are related to volume changes through what is termed an equation of state (EOS). As an example a commonly used EOS incorporated into EPIC termed the Mie-Gruneisen EOS is given as

$$P = (K_1\mu + K_2\mu^2 + K_3\mu^3)(1 - \Gamma\frac{\mu}{2}) + \Gamma E_s(1 + \mu) \quad , \quad \mu = \frac{\rho}{\rho_0} - 1$$

Here  $\rho_0$  and  $\rho$  are the initial and subsequent densities respectively, and thus  $\mu$  represents the degree to which the material is being compressed. Also  $E_s$  is the internal energy and  $K_1$ ,  $K_2$ ,  $K_3$  and  $\Gamma$  are coefficients that are material dependent. Other EOS models are also included but not discussed presently.

Of more relevance to present considerations is the deviatoric component of the stress which is related to plastic flow. The essence of the plastic flow analysis rests on two features. First a yield function is required that dictates when the three-dimensional stress state has reached a point at which yielding of the material occurs and plastic flow commences. Previous versions of EPIC considered isotropic materials for which the traditional yield function  $f(\sigma_{ij})$  has the Von Mises form

$$f(\sigma_{ij}) = (\sigma_{xx} - \sigma_{yy})^2 + (\sigma_{yy} - \sigma_{zz})^2 + (\sigma_{zz} - \sigma_{xx})^2 + 6(\sigma_{xy}^2 + \sigma_{xz}^2 + \sigma_{yz}^2) - 2\sigma_e^2 = 0$$

where  $\sigma_{ij}$  is the Cartesian stress tensor and  $\sigma_e$  is the effective stress (uniaxial yield stress). In terms of principle stresses  $\sigma_1$ ,  $\sigma_2$ ,  $\sigma_3$  the above expression becomes

$$f = (\sigma_1 - \sigma_2)^2 + (\sigma_2 - \sigma_3)^2 + (\sigma_3 - \sigma_1)^2 - 2\sigma_e^2 = 0$$

One may think of the above equation as defining the effective stress under multi-axial loading and when the effective stress reaches the yield stress, plastic flow will occur.

The yield stress (or material strength) depends on several factors. These include past load history, strain rate and temperature. Thus the yield stress evolves as the material deforms. This strength function is generally based on uniaxial stress strain measurements and incorporates factors such as strain hardening, temperature and strain rate dependence. A commonly used strength function available in EPIC was put forth by Johnson and Cook (1983) and has the form

$$\sigma_e = (C_1 + C_2\epsilon^N)(1 + C_3\ln\dot{\epsilon}^*) (1 - T^{*M})$$

where  $\sigma_e$  is the stress level at which plastic flow initiates,  $C_1, C_2, C_3, N$  and  $M$  are material dependent constants and  $\epsilon, \dot{\epsilon}^*$  and  $T^*$  are the effective plastic strain, effective plastic strain rate and the homologous temperature, respectively. A more modern strength function incorporated into EPIC is the Mechanical Threshold Stress (MTS) model and is more fundamentally based on material behavior. It is constructed from a postulate that structure of the material is the important state variable and the current structure is dependent on the deformation history. Although it is more fundamentally based, it is also considerably more complicated to discuss than present space limitations allow. The interested reader can find the important details in Follansbee and Kocks (1988) and its implementation in EPIC by Maudlin, Davidson and Henninger (1990). The incorporation of these strength functions into the anisotropic capability in EPIC will now be discussed.

### Anisotropic Plasticity Modifications

The yield function presented above applies to isotropic materials. If one considers principal stress space ( $\sigma_1, \sigma_2, \sigma_3$  are the axes) the yield function appears as an infinite circular cylinder centered along the line  $\sigma_1 = \sigma_2 = \sigma_3$  as shown in Figure 3. Yielding occurs as the stress state reaches the cylindrical surface from within. A stress state outside the cylinder can never be attained. The yield function does not depend upon the value of the hydrostatic pressure which is represented by the axis of the cylinder. Also shown in Figure 3 is a view looking down the cylinder axis which is referred to as the  $\pi$  plane ( $\sigma_1 + \sigma_2 + \sigma_3 = 0$ ). In the  $\pi$  plane view, the polygon inscribed within the circle represents the Tresca (maximum shear stress) yield criterion.

For anisotropy, the directional dependence of the material properties requires a different yield function. A quadratic yield function for anisotropic materials (with stress denoted by  $s$  and coordinate directions by 1, 2 and 3) was given by Hill (1948) as

$$f(s_{ij}) = \frac{1}{2} [H(s_{11} - s_{22})^2 + F(s_{22} - s_{33})^2 + G(s_{33} - s_{11})^2 + 2Ns_{12}^2 + 2Ms_{13}^2 + 2Ls_{23}^2] - s_e^2 = 0$$

where  $H, F, G, N, M$ , and  $L$  are constants. These can be evaluated from the different yield stresses in the different directions. Note that this function still gives an infinite cylinder independent of the hydrostatic pressure however it now has an elliptical cross-section in the  $\pi$  plane. Details of the implementation of this Hill - 48 yield criterion in EPIC 96&97 are now discussed.

The focus will now be on the Taylor test and a schematic is shown in Figure 5. A cylindrical coordinate system is used where the axis of the cylinder is taken as the 2 direction, 1 is radial and 3 is measured circumferentially in the hoop direction. For the special case of cylinder

impact the 1 - 3 planes perpendicular to the cylinder axis will be taken as planes of material isotropy. In this case  $F = H$ ,  $L = N$  and  $F + 2G - M = 0$ . Axial symmetry requires that  $s_{13} = s_{23} = 0$  as well as  $s_{33} = -(s_{11} + s_{22})$ . With these results the yield function becomes

$$f(s_{ij}) = \frac{1}{2} [2(2G+F)s_{11}^2 + (5F+G)Ms_{22}^2 + 2(2G+F)s_{11}s_{22} + 2Ns_{12}^2] - s_e^2 = 0$$

A  $\pi$  plane transformation as  $s_{12} = -s_z/\sqrt{3}$ ,  $s_{11} = 2s_y/3$  and  $s_{22} = -s_y/3 - s_x/\sqrt{3}$  leads to the form

$$f = As_x^2 + Bs_y^2 + Cs_z^2 + Ds_xs_y - s_e^2 = 0$$

with A, B, C and D being combinations of the previous constants. For isotropy  $A = B = C = 1$ ,  $D = 0$ . (In EPIC,  $D = 0$  always).

If the uniaxial yield stresses are introduced as X in the radial (1) direction, Y in the axial (2) direction and Z as the shear yield in the (1 - 2) plane the result is

$$\frac{1}{3} [1 + \frac{2Y^2}{X^2}] s_x^2 + s_y^2 + \frac{X^2}{3Z^2} s_x^2 + \frac{2}{\sqrt{3}} [\frac{Y^2}{X^2} - 1] s_x^2 - X^2 = 0$$

where implemented in EPIC with  $D = 0$  the slightly different form is obtained

$$\frac{1}{3} [\frac{4X^2}{Y^2} - 1] s_x^2 + s_y^2 + \frac{X^2}{3Z^2} s_x^2 - X^2 = 0$$

Numerical results below from EPIC 96&97 are a thus based on this last equation.

As a final comment it is important to note that isotropic plasticity numerical analysis is based on the radial return algorithm which returns the stress point to the yield surface in a radial direction. For anisotropic plasticity, the yield surface is not circular and radial return is no longer valid. An appropriate normal return algorithm is incorporated into EPIC to account for this. The details are omitted due to space limitations.

## Numerical Results

Three cases of Taylor impact are now considered as shown in Figure 5. The material considered is OFE copper (half hard) and the Mechanical Threshold Stress constitutive model is used to evaluate the yield stress in the radial direction X. Planes perpendicular to the cylinder axis are taken as isotropic and hence  $Z = X/\sqrt{3}$ . In the first case the cylinder is isotropic and therefore  $Y = X$ .

Note that for an isotropic material the coefficients of each term in the above equation are one. In the second case the cylinder has been axially softened compared to the radial direction such that  $Y = 0.7559X$ . In the third case the axial direction has been hardened with  $Y = 1.25X$ . These numbers were chosen to give a coefficient of approximately 2.0 or 0.5 for the first term in the above equation. Figure 4 shows the yield surface in the  $\pi$  plane for the three cases considered. The axially hardened case noticeably expands the surface while the softened case gives a significant contraction.

The effect of the material anisotropy is revealed in the following figures. Figure 6 displays the final cylinder shape after impact. Clearly the axially hardened case exhibited the least radial plastic flow and retained the longest final length while the axially softened cylinder showed the largest radial deformation and the greatest reduction in length. The equivalent plastic strain versus time for the three cases is shown in Figure 7. The results are plotted at three locations; near the cylinder axis, at the outer boundary and half way in-between. At the outer boundary the equivalent plastic strain was the largest for the axially softened material and smallest for the axially hardened case. The steady state difference between these extremes is almost a factor of two. Towards the cylinder interior the deviation caused by the anisotropy decreased but was still noticeable.

An interesting result is shown in Figure 8 which reveals the Von Mises stress versus time during the impact event. It is clear that the axially hardened case produced the largest values during the duration of impact while the axially softened case was the lowest. In this regard it is important to note that although the EPIC code produced the Mises stress, it is truly only meaningful for an isotropic material. Since the Mises stress is based on the Von Mises isotropic yield criterion, the formula for effective stress in the anisotropic case would be more appropriate. This observation is also true for the equivalent plastic strain from Figure 7 above. An examination of the EPIC subroutine seemed to reveal that the isotropic equivalent plastic strain measure was being calculated. It is known that the correct form to the equivalent plastic strain is one which is the work conjugate to the effective stress (Hill, 1950). Although these quantities may not be the correct ones to consider, they do at least provide some mechanism for a comparison of results.

## Conclusions

It is well known that the processing of metals can have a significant impact on the crystallographic texture and the resulting plastic deformation properties of the workpiece. If considerable texture is present, an anisotropic plasticity analysis may be appropriate for high rate impact loading studies. The present numerical investigation of the Taylor impact test confirms this since substantial differences were found to exist in final geometry and measures of effective stress and strain during the impact event when anisotropic material properties were considered. It was also found that EPIC, although incorporating an appropriate anisotropic yield function, produced results

for effective stress and equivalent plastic strain that are appropriate only for an isotropic analysis. This suggests an area for possible future work which would be of great benefit. Furthermore the incorporation of a higher order yield criteria (with an exponent of 6 or 8) which better fits crystallographic texture calculations would also be of high value. Also the expansion to a three-dimensional anisotropic plasticity calculation capability would facilitate the prediction of the elliptical impact face which sometimes occurs from the Taylor impact test.

### Acknowledgments

The author is grateful for support provided by the AFOSR summer Faculty Research Program which made this learning experience possible. The author is also deeply indebted to Dr. Joel House, Wright Lab., Eglin AFB for suggesting this topic, contributing with many fruitful discussions and assisting in the numerical computations. Also thanks to the other staff at Eglin I had the pleasure of interacting with and who also made this such a pleasurable experience.

### References

- Barrett, C. S., 1950, *Structure of Metals*, J. Wiley.
- Carrington, W. E. and Gayler, M. L. V., 1948, "The Use of Flat-Ended Projectiles for Determining Dynamic Yield Stress: Part III. Changes in Microstructure caused by deformation under impact at high-striking velocities", *Proc. Roy. Soc. London, Series A*, Vol. 194, pp. 323-331.
- Follansbee, P. S. and Kocks, U. F., 1988, "A Constitutive Description of the Deformation of Copper Based on the Use of Mechanical Threshold Stress as an Internal State Variable", *Acta Metall.*, Vol. 36, pp. 81-93.
- Hill, R., 1950, *The Mathematical Theory of Plasticity*, Oxford University Press, Oxford.
- House, J. W., 1989, "Taylor Impact Testing", Report No. AFATL-TR-89-41, Air Force Armament Laboratory, Eglin AFB, FL, September 1989.
- House, J. W., 1998, *Wave Propagation in the Taylor Impact Experiment*, Ph.D. Dissertation, University of Kentucky.
- Johnson, G. R., 1977, "EPIC-3, A Computer Program for Elastic-Plastic Impact Calculations in 3 Dimensions", Final Report, Honeywell Inc., Defense Systems Division, May 1977.
- Johnson, G. R. and Cook, W. H., 1983, "A Constitutive Model and Data for Metals Subjected to Large Strains, High Strain Rates, and High Temperatures.", 7th International Symposium on Ballistics, The Hague, The Netherlands, April, 1983.
- Jones, S. E. and Gillis, P. P., 1985, "An Elementary Scaling Law for Rod Impact Specimens," *International Journal of Impact Engineering*, Vol. 4, pp. 195.
- Jones, S. E., Gillis, P. P. and Foster, J. C., 1987, "On the Equation of Motion of the Undeformed Section of a Taylor Specimen" *J. Appl. Phys.*, Vol. 61, pp. 15.

Jones, S. E., Gillis, P. P., Foster, J. C. and Wilson, L. L., 1991, "A One-Dimensional Two-Phase Flow Model for Taylor Impact Specimens" *ASME Journal of Engineering Materials and Technology*, Vol. 113, pp. 228.

Jones, S. E., Maudlin, P. J. and Foster, J. C., 1996, "An Engineering Analysis of Plastic Wave Propagation in the Taylor Test" *International Journal of Impact Engineering*.

Maudlin, P. J., Davidson, R. F. and Henninger, R. J., 1990, "Implementation and Assessment of the Mechanical Threshold Stress Model Using the EPIC2 and PINON Computer Codes, Los Alamos National Laboratory, Report No. LA-11895-MS.

Maudlin, P. J. and Schiferl, S. K., 1996, "Computational Anisotropic Plasticity for High Rate Forming Operations", *Comput. Methods Appl. Mech. Engrg.*, Vol. 131, pp. 1-30.

Rule, W. K., 1995, "Taylor - A Preprocessor, Postprocessor, and Optimizer for Numerically Modeling Taylor Impact Specimens with EPIC", Final Report, AFOSR Summer Faculty Fellowship, December 1995.

Taylor, G. I., "The Use of Flat-Ended Projectiles for Determining Dynamic Yield Stress: I. Theoretical Considerations", *Proc. Roy. Soc. London, Series A*, Vol. 194, pp. 289-299.

Whiffin, A. C., 1948, "The Use of Flat-Ended Projectiles for Determining Dynamic Yield Stress: Part II. Tests on Various Metallic Materials", *Proc. Roy. Soc. London, Series A*, Vol. 194, pp. 300-322.

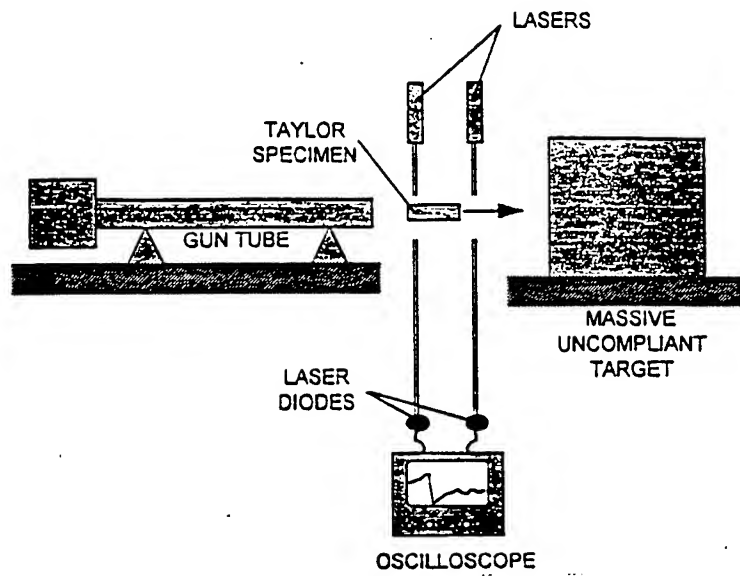


Figure 1. Schematic of Taylor impact test (from Rule, 1995)



Figure 2. Copper Taylor impact specimen geometry (from House, 1998)



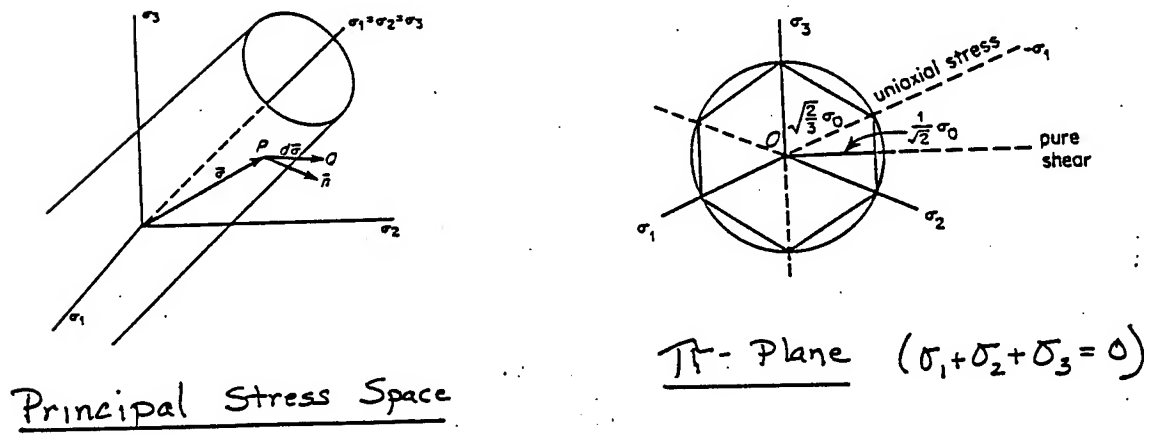


Figure 3. Isotropic yield surface and  $\pi$  plane.

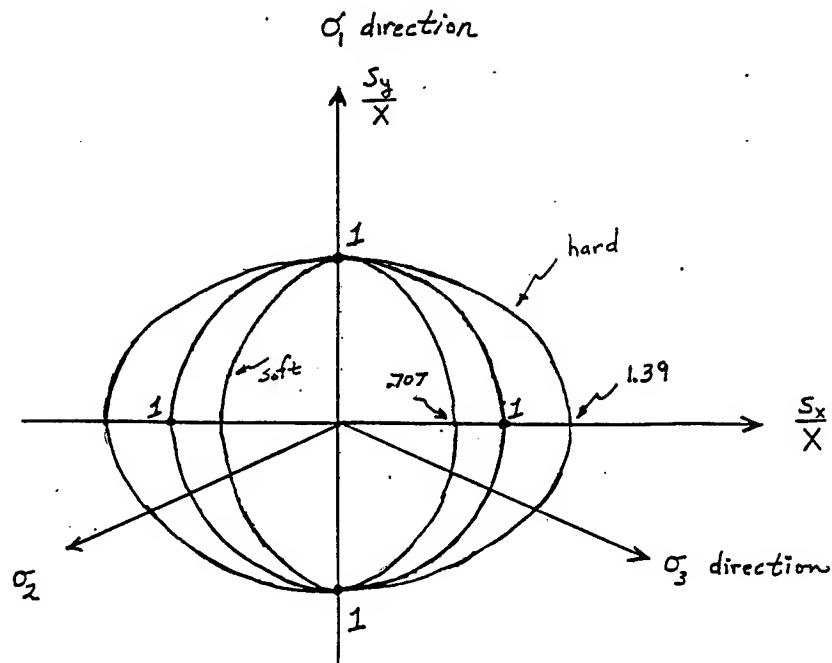
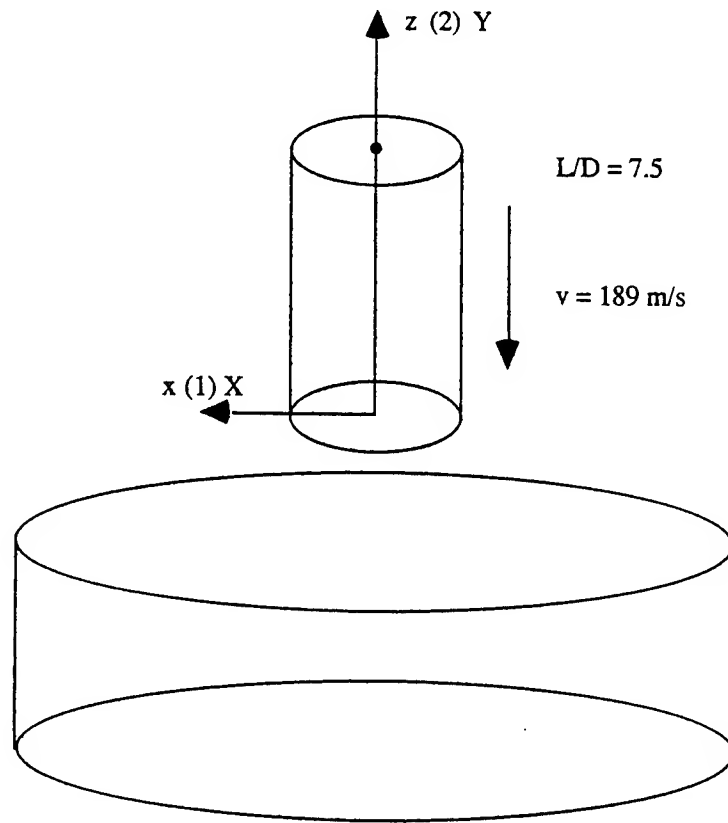


Figure 4. Yield loci in the  $\pi$  plane for an isotropic, axially hardened and axially softened cylinder.



Three Test Cases:

Isotropy	$Y = X$	$Z = X/\sqrt{3}$
Axial Softened	$Y = .7559X$	$Z = X/\sqrt{3}$
Axial Hardened	$Y = 1.25X$	$Z = X/\sqrt{3}$

$X$  from MTS (Mechanical Threshold Stress) Material Model for OFE Copper (Half Hard)

Figure.. 5. Taylor impact schematic.

Taylor Impact Test  
Mechanical Threshold Stress Material Model  
OFE Copper (Half Hard)

Isotropic Versus Anisotropic Response

06/02/96

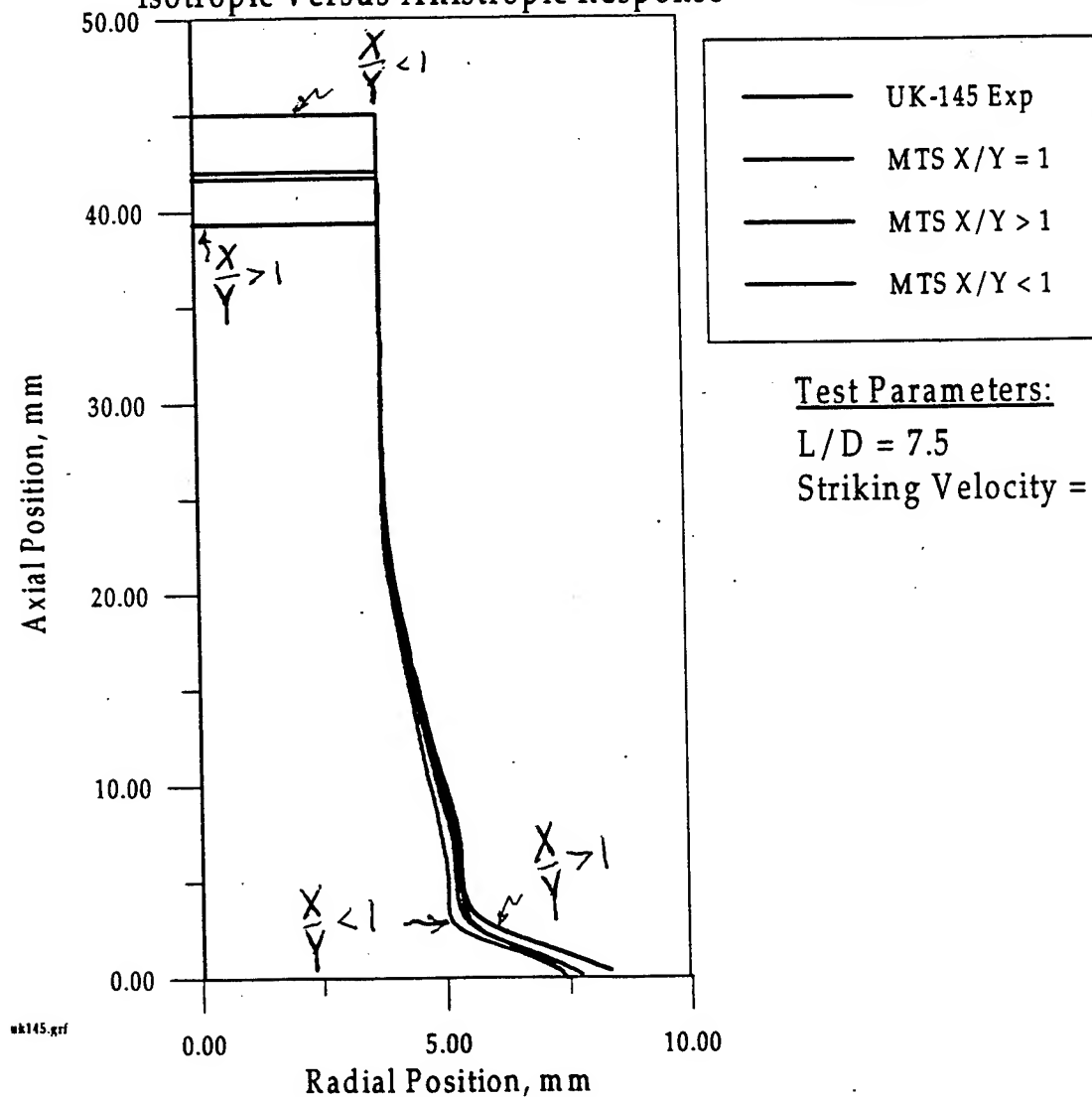


Figure 6. Final specimen shape.

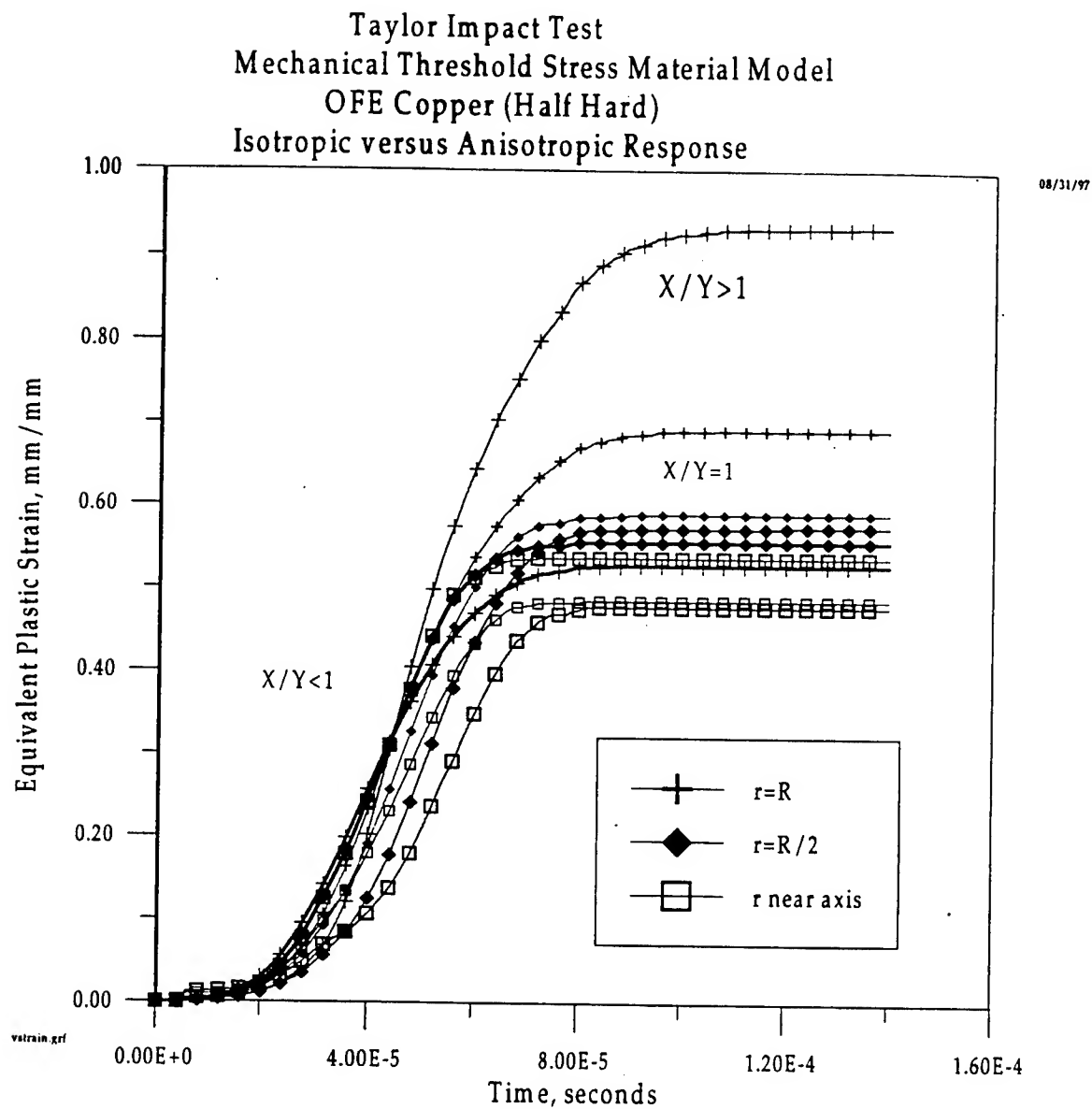


Figure 7. Equivalent plastic strain for Taylor impact test.

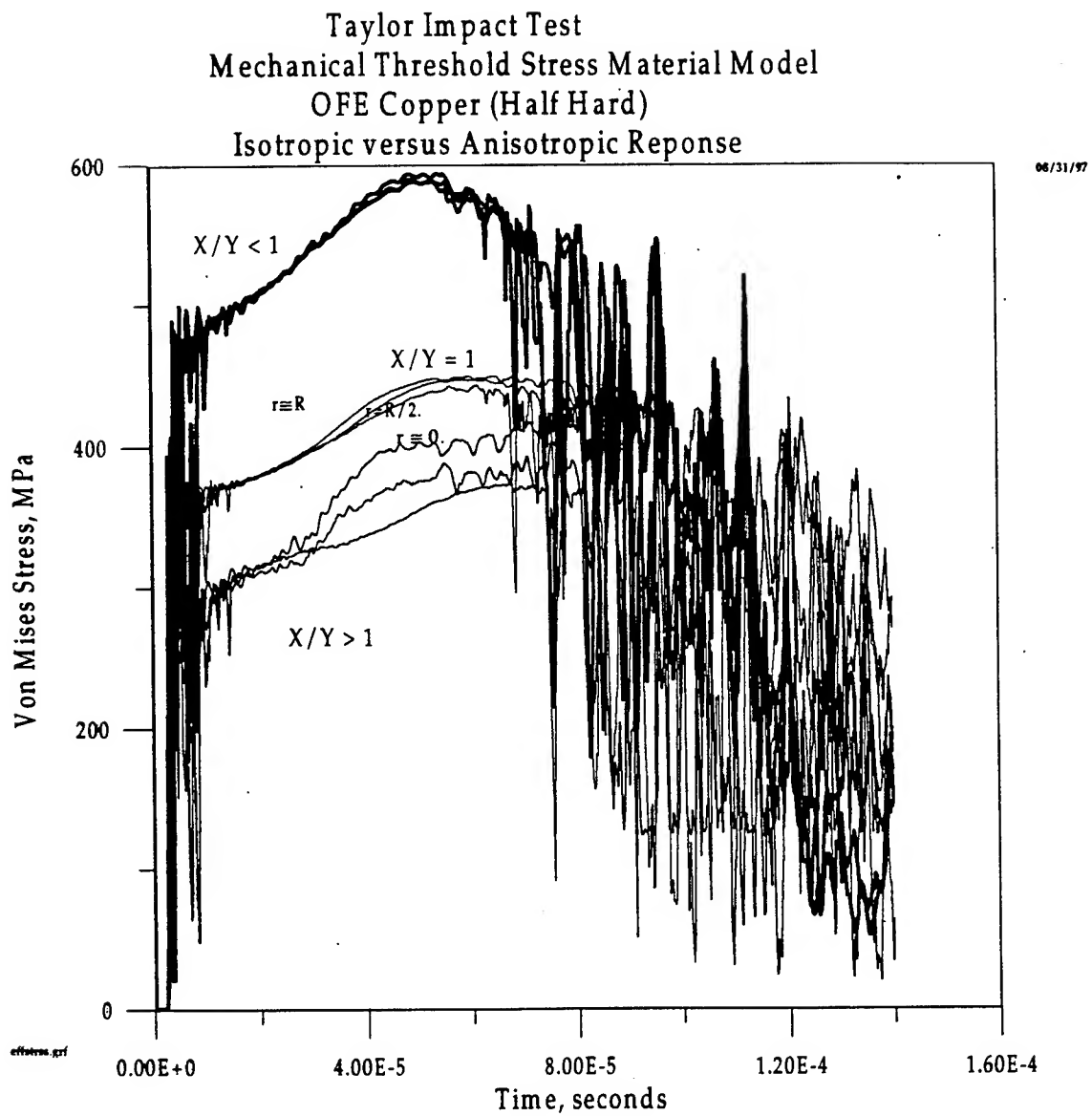


Figure 8. Von Mises stress for Taylor impact test.

**A MODEL FOR TURBULENCE AND PHOTODETECTION NOISE IN  
IMAGING SYSTEMS**

**Majeed M. Hayat  
Assistant Professor  
Department of Electro-Optics**

**University of Dayton  
300 College Park  
Dayton, OH 45469**

**Final Report for:  
Summer Research Program  
Wright Laboratory**

**Sponsored by:  
Air Force Office of Scientific Research  
Bolling Air Force Base, Washington, DC**

**And**

**Wright Laboratory**

**September 1997**

# A MODEL FOR TURBULENCE AND PHOTODETECTION NOISE IN IMAGING SYSTEMS

Majeed M. Hayat  
Assistant Professor  
Electro-Optics Graduate Program  
University of Dayton

## Abstract

A stochastic model is developed to describe image degradation due to turbulence and uncertainty in photodetection and intensification in gated imaging systems. The results of simulation indicate that real-time integration imaging results in a superior performance than frame-by-frame averaging if the time between frames is relatively large. The effect of turbulence is modeled by assuming a slowly time varying random thin screen in the aperture plane which introduces a time-varying random tilt. The variation in the tilt, due to the change in the thin screen from frame to frame, can become large for sufficiently large times between frames. When images are averaged, simulations suggest that there is a tradeoff between the number of successive frames used and atmospheric blur. This tradeoff requires further research to optimize the exposure time for minimizing the mean square error. Reduction in the resolution and contrast due to the uncertainty in the response of TE photocathode detectors and MCP image intensifiers is also considered. A model has been developed that captures the degrading effect of dark current. Simulations show that when the MCP is operated in the saturation mode, dark current significantly reduces contrast. The model also captures the spread introduced by the MCP, electron focusing error, and the random multiplication gain associated with the MCP stages. Analytical expressions are derived for the mean and the variance of the point spread function of the intensifier. The model for the detection/intensification is combined with the model for turbulence to give a complete stochastic model for the imaging system.

## I. Introduction

The goal of this study is to provide a model for coherent and incoherent imaging systems using gated cameras under turbulent atmospheric conditions. The degrading effects of atmospheric turbulence and photodetection noise associated with the gated cameras are examined. Consider the block diagram representation of Fig. 1. The object  $O(x)$  is thought



Figure 1. Block diagram of the imaging system

of as the intensity in incoherent imaging and as the complex amplitude of a plane wave in coherent imaging. The atmosphere affects the object  $O$  through its variable refractive index. At each instant, a realization of the refractive index profile (in planes parallel to the aperture along the ray paths) introduces phase and amplitude changes in the plane waves at the aperture of the optical components prior to photodetection. It is customary to represent this block by a random screen at the aperture plane [24]. The cumulative effect of the variation in the index of refraction can be lumped in a single screen. The distorted wave is then focused onto a detector (or array of detectors) where each incident photon is converted to a free electron with a certain probability determined by the quantum efficiency of the detector. The detectors of interest are transferred-electron (TE) photocathodes [5] for which quantum efficiencies as high as 20% have been demonstrated in the 0.95 – 1.7 micron range. These tubes suffer, however, from a high level of dark noise. Dark noise can degrade the collected image by reducing the contrast. Furthermore, when saturation-mode image intensification follows the photodetection, the effect of dark noise becomes more prominent since it is likely that each dark electron may saturate the intensifier. This effect may result in specks in the collected image. Intensification can be accomplished by means of microchannel plates (MCP's). MCP's can operate in two modes of gain. At low gains the device operates in an unsaturated mode for which the statistics of the gain (the distribution of the charge pulse height) is negative exponential [25]. In this mode the uncertainty in the gain increases with the gain. However, if the gain is increased beyond a certain limit, a space



charge effect occurs resulting in a reduction in the uncertainty of the gain. In the saturation mode, the gain statistics is almost Gaussian with a variance which is less than that obtained in the unsaturated mode [25]. Usually, two slightly angled stages of MCP's are cascaded in order to reduce positive ion feedback. The benefit of this technique is accompanied by the possibility of electron spread. In particular, an electron transferring from a channel in the first stage to the second may enter a neighboring channel [25, 21]. The above effects degrade the performance of the imaging system. The development of a mathematical model for the imaging system incorporating the above degrading effects can provide a platform for developing statistical image recovery algorithms. Such a task requires the knowledge of the model parameters. These parameters must be obtained using manufacturer's data and further measurements. We plan to address these issues in a subsequent study.

In Section II a stochastic model is developed for the random screen representing turbulence. This model allows a slow random variation in the phase screen in time. This effect is important since it is the accumulated effect of change in the phase screen that results in image blur in the image when multiple frames of the same image are averaged. Also, this effect causes blur in application when the gating time is comparable to the variation time in the phase screen. In Section III a stochastic model for the response of the image intensifier is developed. This model captures the effects of electron focusing error, the spread of electrons from one channel to neighboring channels, and the random gain of the microchannel tubes. In Section IV we use the models introduced in Sections II and III to determine the performance of the imaging system. The effect of the key factors representing the temporal variation in the phase screen, spread of the point spread function of the image intensifiers, background photon noise, and shot noise are investigated using computer simulation. Section VII includes summary and conclusions.

## II. A stochastic model for turbulence in gated imaging

Consider a general coherent imaging system consisting of an object, a collection of optical components, and an image. Let  $u_i(\mathbf{x})$  and  $u_o(\mathbf{x})$  denote the complex amplitudes of the image and object fields, respectively. If we denote the imaging system impulse response by  $h_o$ , then

the image field can be expressed as (under Fresnel paraxial conditions):

$$u_i(\mathbf{x}) = u_o(\mathbf{x}) * h_o. \quad (1)$$

The term  $h_o$  accounts for aberrations due to finite aperture and nonideal optical components. In the case of aperture-limited imaging,  $h_o$  is given by the Fourier transform of the pupil function  $W$ . Now suppose that the fields are disturbed as a result of propagation through a medium with a nonuniform (and random) refractive index such as the atmosphere. Following [24], the pupil function can be generalized to additionally account for atmospheric turbulence. As the field propagates thorough the random medium it experiences a randomly varying distribution of the index of refraction. Aberrations due to this effect can be modeled by placing a fictitious thin screen at the aperture plane. More precisely, we replace the pupil function  $W$  by  $Wt_s(\mathbf{x})$ , where  $t_s(\mathbf{x})$  is a random screen which is expressed in terms of the log-amplitude perturbation  $\chi(\mathbf{x})$  and the phase perturbation  $\psi(\mathbf{x})$  as follows:

$$t_s(\mathbf{x}) = e^{\chi(\mathbf{x}) + j\psi(\mathbf{x})}. \quad (2)$$

In short exposure imaging, the atmosphere is assumed to be "frozen" for the duration of the frame. The imaging system does, however, experience aberrations due to the perturbed distribution of the refractive index. This perturbation is the result of a single realization of the atmospheric induced perturbation. It is well known [24, 10] that the dominant degrading effect in short-exposure imaging is the random tilt. Tilt can be mathematically attributed to the linear term in the Taylor series expansion of the phase function  $\psi(\mathbf{x})$ . Tilt results in a shift in the location of the image in the image plane. In short exposure imaging, most of the degradation is attributed to tilt [24]. In fact, it has been shown that tilt constitutes a factor of 0.9 of the total power of the phase perturbations [10]. In long exposure imaging, the accumulated effect of individual tilts (as the tilt varies from one instant to the other) accounts for most of the degradation. Another application for which the accumulated effect of tilt can be noticed is when multiple short-exposure frames are obtained and then averaged. In this scenario, each frame will be subject to a independent tilt. When averaging is performed the multiple shifts result in a blur. Long-time exposure or multiple short-exposure frames are unavoidable in weak-light (small photon count per pixel) applications where the effect

of quantum noise is a limiting factor in the performance. Thus, on one hand, we need more photons, i.e., long exposure time or multiple frames, and on the other hand, degradation due to the turbulent medium (manifested in time varying shift) is more severe if the exposure time is long.

In this study, we will consider the effect of tilt on resolution and contrast in multiple frame short-exposure imaging. We assume hereafter that  $\psi(\mathbf{x}) = \mathbf{k} \cdot \mathbf{x}$ , where the vector  $\mathbf{k}$  represents the magnitude and direction of the tilt for each realization of the turbulence. The thin screen is therefore given by

$$t_s(\mathbf{x}) = e^{j\mathbf{k} \cdot \mathbf{x}}. \quad (3)$$

We now consider the random temporal variation of the tilt parameter  $\mathbf{k}$  when the time between successive frames is sufficiently small so that the change in the amount of the shift is small.

#### A. A random walk model for the random thin screen

Let  $\mathbf{k}_n$ ,  $n = 1, 2, \dots$ , denote the shift associated with the  $n$ th realization of turbulence. Assuming that the real time between consecutive realizations is sufficiently small, the random process  $\mathbf{k}_n$  can be modeled by a 2-dimensional random walk [16]. Let us quantize the possible values of  $\mathbf{k}$  by requiring it to take values in a discrete set (in an increasing order)  $E_B \triangleq \{\beta_1, \dots, \beta_q\}$ . In order to express the “term” slow in a probabilistic sense, we will assume that if  $\mathbf{k}_n = \beta_k$  then the conditional probability (or transition function) of  $\mathbf{k}_{n+1}$  depends only on  $\beta_k$ . Furthermore, the likelihood that  $\mathbf{k}_{n+1}$  takes a value which is near  $\beta_k$  is high. Mathematically, this conditional probability is given by the random-walk transition function

$$P\{\mathbf{k}_{m+1} = \beta_l | \mathbf{k}_m = \beta_k\} = \begin{cases} 1 - p, & l = k, \\ p/2, & l = k \pm 1, \end{cases} \quad (4)$$

where  $p$  is a model parameter to be estimated *a priori* using real data. Special care must be taken in handling cases when  $k = 1, 2, q - 1$ , and  $q$  corresponding to cases when the value of  $\mathbf{k}$  is near the boundary of the set of possibilities  $E_B$ . What this stochastic model basically implies is that once a shifted point is at a specific location, it can either stay at its location at

the next time frame, or it can go to a nearby location with certain probabilities. By limiting the number of neighboring states, the "slow" variation in the tilt can be modeled. Similar types of random walk have been extensively used in many areas of science and engineering to model random phenomena that vary slowly in time. The most famous example is the well-known Brownian motion which is indeed a limiting case of a simple random walk [2]. The random walk is a special case of Markov chains.

## B. Diffraction and turbulence limited imaging

### 1. Coherent imaging

In this section, we characterize the impulse response  $h_{OT}$  of the imaging system considering the effects of the finite aperture and turbulence. This impulse can then be substituted in (1) to yield the field at the image plane. In order to include the effect of turbulence, we replace the pupil function  $W(\mathbf{x})$  by the turbulence-modified pupil function  $W_t(\mathbf{x}) = W(\mathbf{x})t_s(\mathbf{x})$ , where  $t_s(\mathbf{x})$  is given in (3). Using  $W_t$  as the new pupil function, standard Fourier optics [12] yields

$$h_{OT} = \mathcal{F}\{W_t(\mathbf{f}\lambda d_i)\}, \quad (5)$$

where  $\lambda$  is the optical wavelength and  $d_i$  is the distance between the exiting pupil and the image plane. The intensity  $i(\mathbf{x})$  at the image plane can then be calculated using the relation

$$i(\mathbf{x}) = |u_i(\mathbf{x})|^2 = |u_o(\mathbf{x}) * h_{OT}|^2. \quad (6)$$

### 2. Incoherent imaging

In some cases, the speckle effect due to interference of coherent light can be filtered out (e.g., by using a suitable low-pass filter) without significantly affecting the resolution of the image. In these cases, it is computationally advantageous to assume that the illumination is incoherent since the effect of interference is ignored. The image intensity then takes the simplified form [12]

$$i(\mathbf{x}) = o(\mathbf{x}) * |h_{OT}(\mathbf{x})|^2. \quad (7)$$

The quantity  $h_{OT}(\mathbf{x})$  is the diffraction and turbulence limited point spread function (PSF). It is customary in Fourier incoherent imaging to use a normalized version of  $o(\mathbf{x}) = |h_{OT}(\mathbf{x})|^2 / \int |h_{OT}(\mathbf{x})|^2 d\mathbf{x}$

What is new in (7) is that the PSF  $|h_{OT}(\mathbf{x})|^2$  is random and its temporal variation obeys the random walk random mechanism described in II-A.

### III. A stochastic model for noise an image intensifier

The resolving power of micro-channel plate image intensifiers is governed by geometrical and operational considerations. The absolute highest resolution of an image obtained from a MCP tube is governed by the diameter of each tube. This limit is not achieved in physical devices due to other factors such as electron lens focusing error and spread of electrons from one channel to adjacent channels as they are transferred from the first plate to the second plate. Factors limiting the contrast include scintillation noise resulting from positive ions striking the channel surface generating secondary electrons, random gain of the intensifier, and dark current generated at the photodetection stage. We will now develop a stochastic model that captures the above effects.

Each incident photon is transformed into a free electron in space (by means of a TE photocathode tube) with probability  $\eta$  representing the quantum efficiency of the photodetector. Each liberated electron is focused (by electrostatic or electromagnetic means [7]) onto a desired location on the microchannel plate tube surface. The actual location of the electron is within a random error  $\epsilon$  of the desired location. It is typical to assume that  $\epsilon$  is normally distributed with zero mean and variance  $\sigma_\epsilon^2$ . Each electron initiates a series of secondary electron emissions in the microchannel. The statistics of the number of secondary electrons  $G$  depends on the mode of operation. If the MCP is operated in a saturation mode with ion feedback suppression (e.g., the Chevron configuration [6]), then experiments [14] showed that  $G$  is Gaussian. On the other hand, if the device is operating in the unsaturated mode, then  $G$  obeys a negative exponential distribution resulting in high fluctuations. As each secondary electron enters the second stage of the MCP, it is transferred to the desired channel of second plate with a certain probability, and it is transferred to neighboring channels with certain probabilities. Similarly to the first stage of the MCP, each secondary electron initiates a random number  $A$  of secondary electrons in the second stage. Thus, the operation of the detector and image intensifier results in fluctuations in the gain as well as random spread.

An important factor affecting the performance of the camera is dark current associated with the TE tube and the scintillation noise associated with the MCP. Dark current noise is due to the spontaneous generation of electron in TE tubes [4]. These dark electrons are then amplified in the PCM. Scintillation noise results from the generation of secondary electrons in the PCM due to the collision of positive ions the MCP walls [25]. We now proceed to give a mathematical model for the foregoing factors.

### A. Point spread function of the MCP

Let  $h_d(\mathbf{x})$  denote the point spread function of the MCP, i.e., the response of the camera when a single photon at location  $(0, 0)$  is incident on it. (The spatial variable  $\mathbf{x}$  can now be thought of as the discrete index of a pixel define by the area of each microchannel.) The quantity  $h_d$  accounts for the random MCP gain and spread. More precisely,

$$h_d(m, n) = \sum_{k=1}^G g_k(m, n),$$

where  $G$  is the random gain of the first MCP stage. The probability distribution of  $G$  can be modeled by a Gaussian or a negative exponential law depending on the mode of operation of the MCP. The term  $g_k(m, n)$  represents the gain and spread at the output of the second MCP stage associated with the  $k$ th electron from the first stage:

$$g_k(m, n) = A_k \sum_i \sum_j \Xi_{ij}^k \delta(m - i, n - j), \quad (8)$$

where  $A_k$  is the random gain of the second MCP stage associated with the  $k$ th electron from the first stage, and for each  $k$ ,  $\Xi_{ij}^k$  is a binary random variable which is one only if the  $k$ th electron from the first MCP stage had migrated to the  $(i, j)$ th secondary channel. The probability distribution of  $\Xi_{ij}^k$  is assumed to be known by performing estimates from measurer data. For example, one may make the physical assumption that  $\Xi_{ij}^k$  can assume a value 1 only if the point  $(i, j)$  is within a certain range of  $(0, 0)$ . We will also make the assumption that events associated with different electron are independent, and that events associated with different MCP stages are also independent. The effect of scintillation noise can be included in the random gain  $G$ .

## 1. Modeling dark noise

Electrons generated spontaneously in the TE tube can be modeled as a totally randomly distributed electrons whose mean total number can be determined from the experimental results [5, 4]. Due to the random nature of the dark electron generation, the actual total random number of electrons can be assumed to be a Poisson random variable. The dark current noise can therefore be modeled as a random image (superimposed with the actual image) for which each pixel may contain a random number of electrons with a Poissonian distribution. This random image is represented by:

$$\mathfrak{S} = \sum_{ij} N_{ij} \delta(m - i, n - j), \quad (9)$$

where  $N_{ij}$  is the random number of dark electrons in the  $(i, j)$ th pixel.

## IV. The overall imaging model

We now combine the effects of atmospheric turbulence and the degrading effects associated with the camera to present a model for the imaging system of Fig. I. Let  $o(m, n)$  and  $I(m, n)$  denote the object and its image, respectively. An upper case is used for the image to emphasize that it is random. In light of the models of the preceding sections, the object and the image are related by:

$$I(m, n) = \sum_{ij} (N_{ij} + N^{object}_{ij}) h_d(i - m, j - n), \quad (10)$$

where  $N_{ij}$  is the number of dark-noise electrons at the MCP's  $(i, j)$ th input pixel, and  $N^{object}_{ij}$  is the number of object photoelectrons at the  $(i, j)$ th pixel of the MCP generated by the TE photocathode. The random quantity  $N^{object}$  is assumed to be Poissonian with a mean value that is proportional to the atmospherically blurred image intensity  $i$ . Note that  $i$  is obtained using (6) or (7).

## V. Statistical analysis

In this section, we provide expressions for the mean and the variance of the of the some random quantities introduced in earlier sections.

## A. Statistics of the PSF of the MCP

By taking an ensemble average (denoted by the symbol  $E$ ) of the expression given by (III-A) we obtain

$$E[h_d(m, n)] = \mu_G \mu_A h_o(m, n),$$

where  $\mu_G = E[G]$  and  $\mu_A = E[A_k]$  are the means of the gain associated with the first and second stages of the MCP, respectively. The function  $h_o(m, n)$  is defined as

$$h_o(m, n) = \sum_i \sum_j p_{ij} \delta(m - i, n - j),$$

where  $p_{ij}$  is the probability that an electron at location  $(0, 0)$  in the first stage is transferred to location  $(i, j)$  in the second stage. A more detailed analysis yields an expression for the variance  $\sigma_{h_d}^2$  of (III-A):

$$\sigma_{h_d}^2 = \left\{ \mu_G (\sigma_A^2 + \mu_A^2) + (\sigma_G^2 - \mu_G) \mu_A^2 h_o(m, n) \right\} h_o(m, n),$$

where  $\sigma_G^2$  and  $\sigma_A^2$  are the variances of  $G$  and  $A_k$ , respectively.

The autocorrelation function of  $h_d$  is necessary in determining the variance of the detected image. The expression for the autocorrelation function is lengthy and it is not included in this report. However, its effect on the variance of the output image will be given. In particular, if we assume that an object  $i(m, n)$  is applied as the input to a system represented by a random PSF  $h_d$ , then it is straight forward to show that the mean of the output  $E[y(m, n)]$  is given by the convolution  $i(m, n) * E[h_d]$ , and the variance  $\sigma_y^2$  is given by

$$\begin{aligned} \sigma_y^2 &= (\sigma_G^2 + \mu_G^2 - \mu_G) (h_o(m, n)^2 * i(m, n)) \\ &+ (\mu_G^2 - \mu_G) (h_o(m, n) * i(m, n))^2 \\ &+ \mu_G (\sigma_A^2 - \mu_A) (h_o(m, n) * i^2(m, n)). \end{aligned}$$

The above expression shows that the NMP spread is determined by the width of the function  $h_o(m, n)$ .



## VI. Simulation results

The combined model given in (10) was simulated using a test image shown in Fig. 2 which consists of a 64 by 64 binary image. The simulations are performed using MATLAB (version 5.0) on a Pentium PC and SPARC-20 SUN Workstation. The author will provide

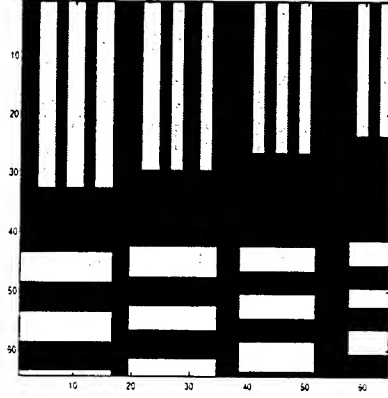


Figure 2. Test image used in all simulations

the reader with a copy of the MATLAB programs upon request. All the simulations make the following assumptions: The gains of each MCP is 100, and their variances is 10. The available number of photons per pixel is 50. The detector quantum efficiency is unity, and the tilt is at most a single pixel per consecutive frames.

### A. Single frame results

Figure 3 shows the image obtained when four consecutive frames are observed for various values of background noise. The signal-to-noise parameter is defined as the ratio of the image photons to the noise photons. The MCP maximal spread is assumed to be 2. Figures 3 (a)-(c) assumes the operation in an unsaturated mode while (d) assumes a saturation mode.

The degrading effect of background noise on contrast is noticeable in general but becomes much more severe when the MCP is operated in the saturation mode. This result is expected since any pixel containing as low as a single dark electron will result in a bright (saturated) pixel).

The key issue here is that the tilt can change by at most one pixel from frame to frame. However, this tilt can build up to generate a blur if the frames are averaged. The results of this subsection correspond to the case when the time between frames is short enough that the change in the refractive index of the atmosphere is small. This small change in the refractive index may result in a maximum change of one pixel in the tilt. As discussed in Section II, the location of the shift obeys a random walk process in two dimensions. A MCP spread of 2 and 3 are assumed in generating Figs. 4 and 5, respectively. The increase in blur is evident from these figures as the MCP spread increases.

### **B. Independent multiple frames**

When frames are separated by a relatively long periods of time, the individual shifts can be assumed to be statistically independent. The change in the tilt can therefore be more than one pixel per frame. A limit on the maximum change in tilt should be imposed based to physical assumptions about the physics of turbulence. Figures 6 and 7 show an average over four independent frames. It is seen that the performance is inferior to that of consecutive frames.

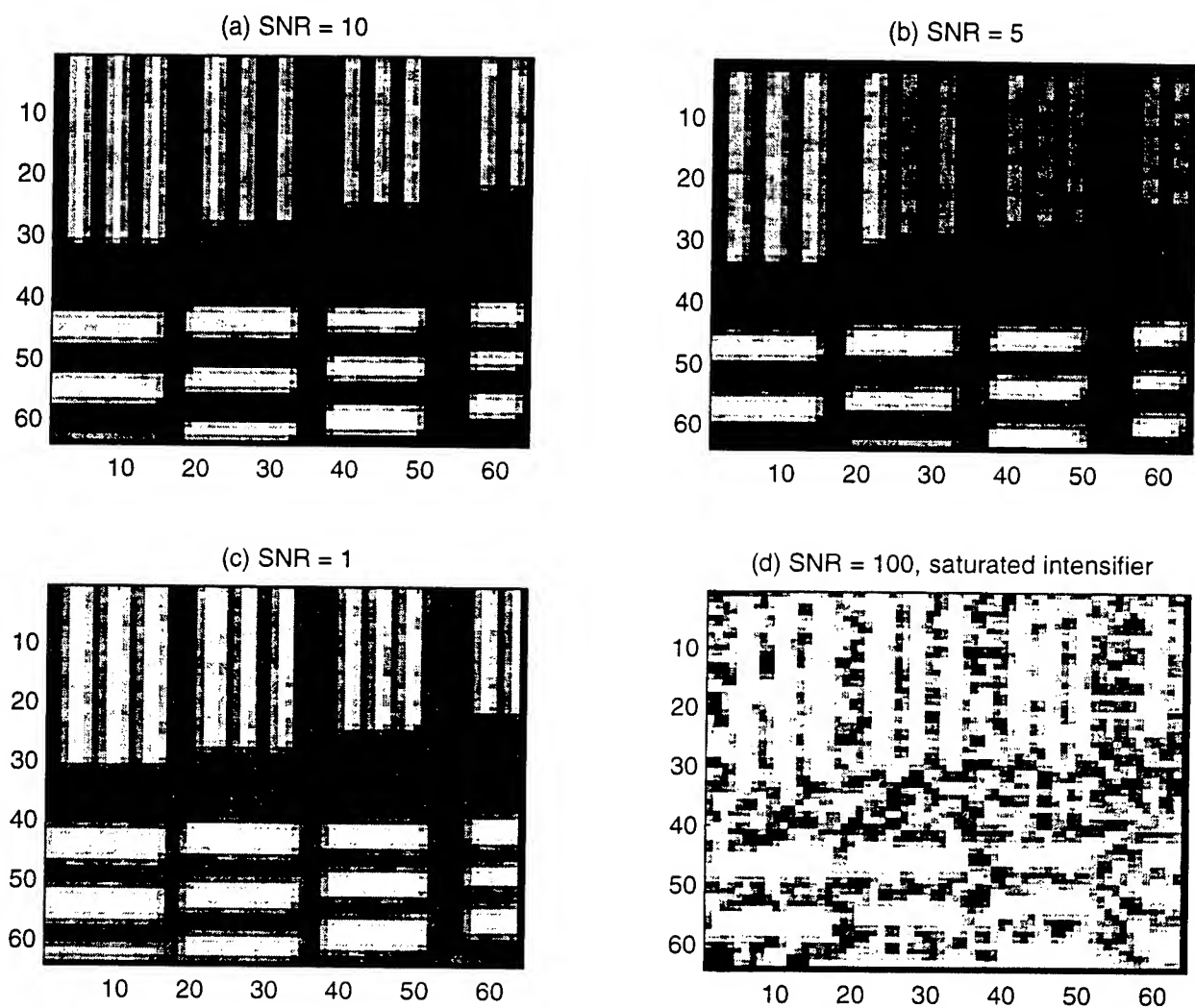


Figure 3. Simulation of the imaging system using four frames for different values of SNR. The image in (d) is obtained when the MCP is in a saturation mode.

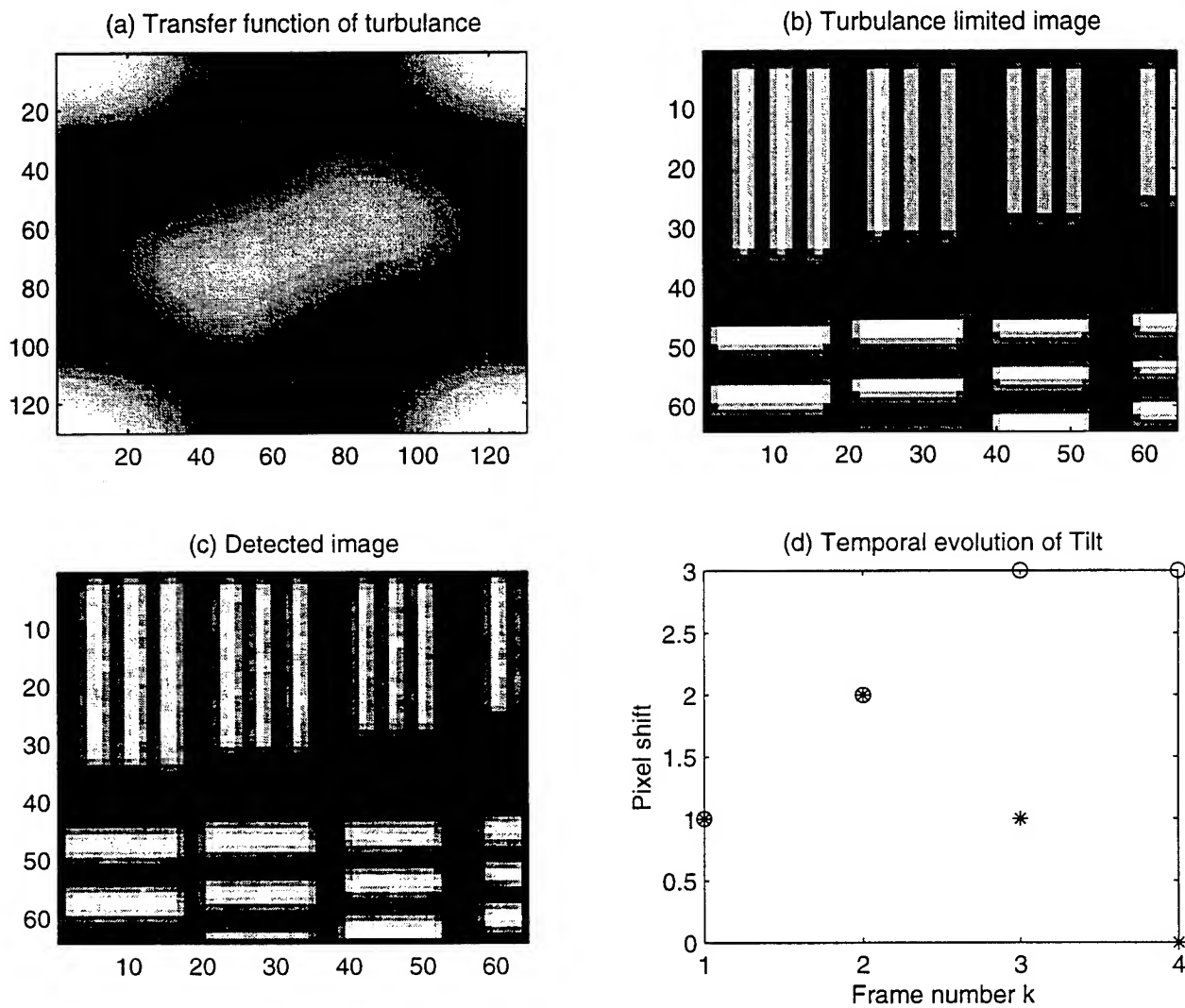


Figure 4. Simulation of the imaging system using four consecutive frames for  $\text{SNR} = 2$  and MCP spread of 2 pixels. (a) DFT of the turbulence-limited point spread function; (b) turbulence limited image, and; (c) detected image, and; (d) horizontal (\*) and vertical (o) tilt as a function of frame number  $k$ . The MCP is assumed to be in an unsaturated mode.

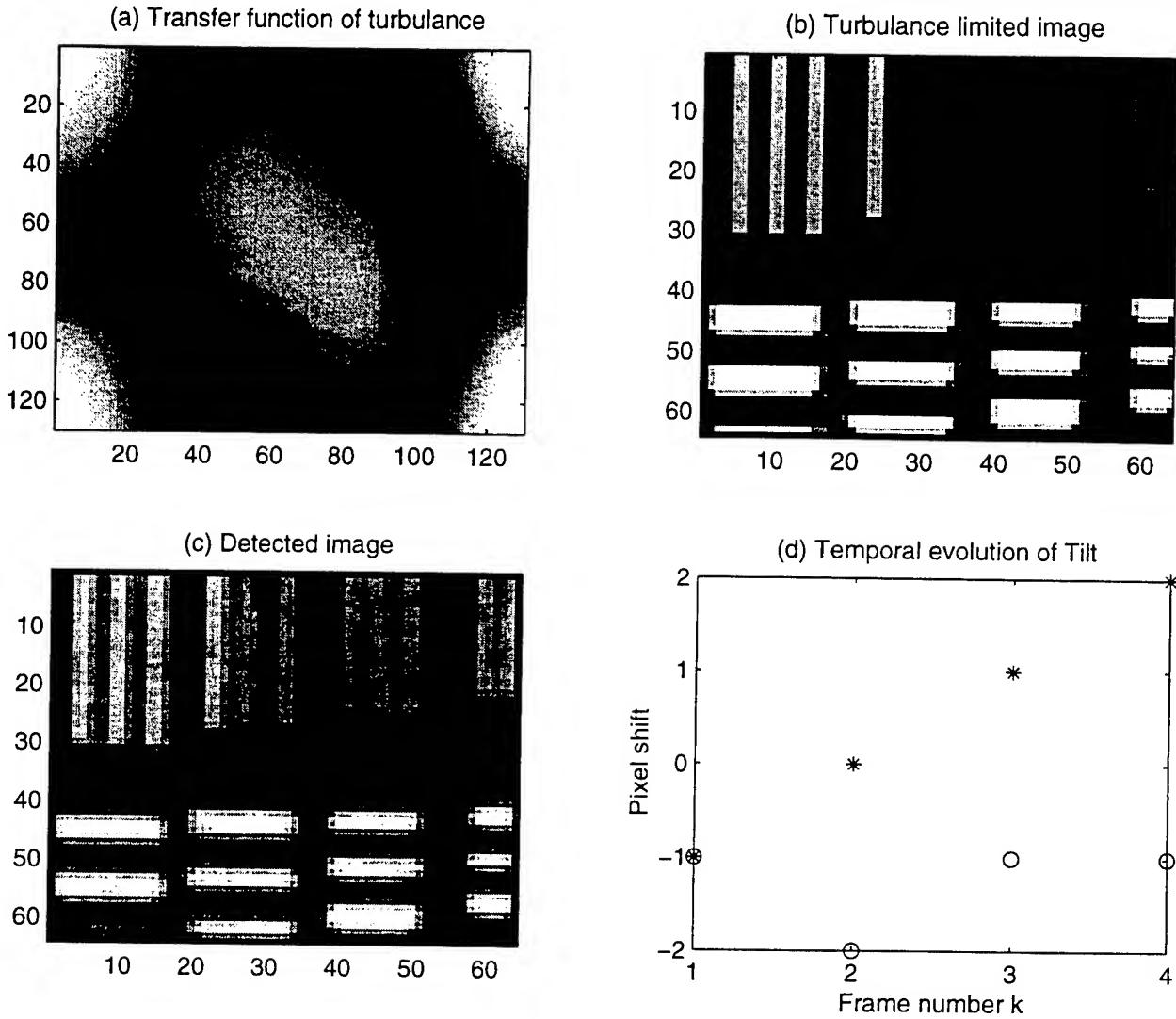


Figure 5. Simulation of the imaging system using four consecutive frames for  $\text{SNR} = 3$  and MCP spread of 2 pixels. (a) DFT of the turbulence-limited point spread function; (b) turbulence limited image, and; (c) detected image, and; (d) horizontal (\*) and vertical (o) tilt as a function of frame number  $k$ . The MCP is assumed to be in an unsaturated mode.

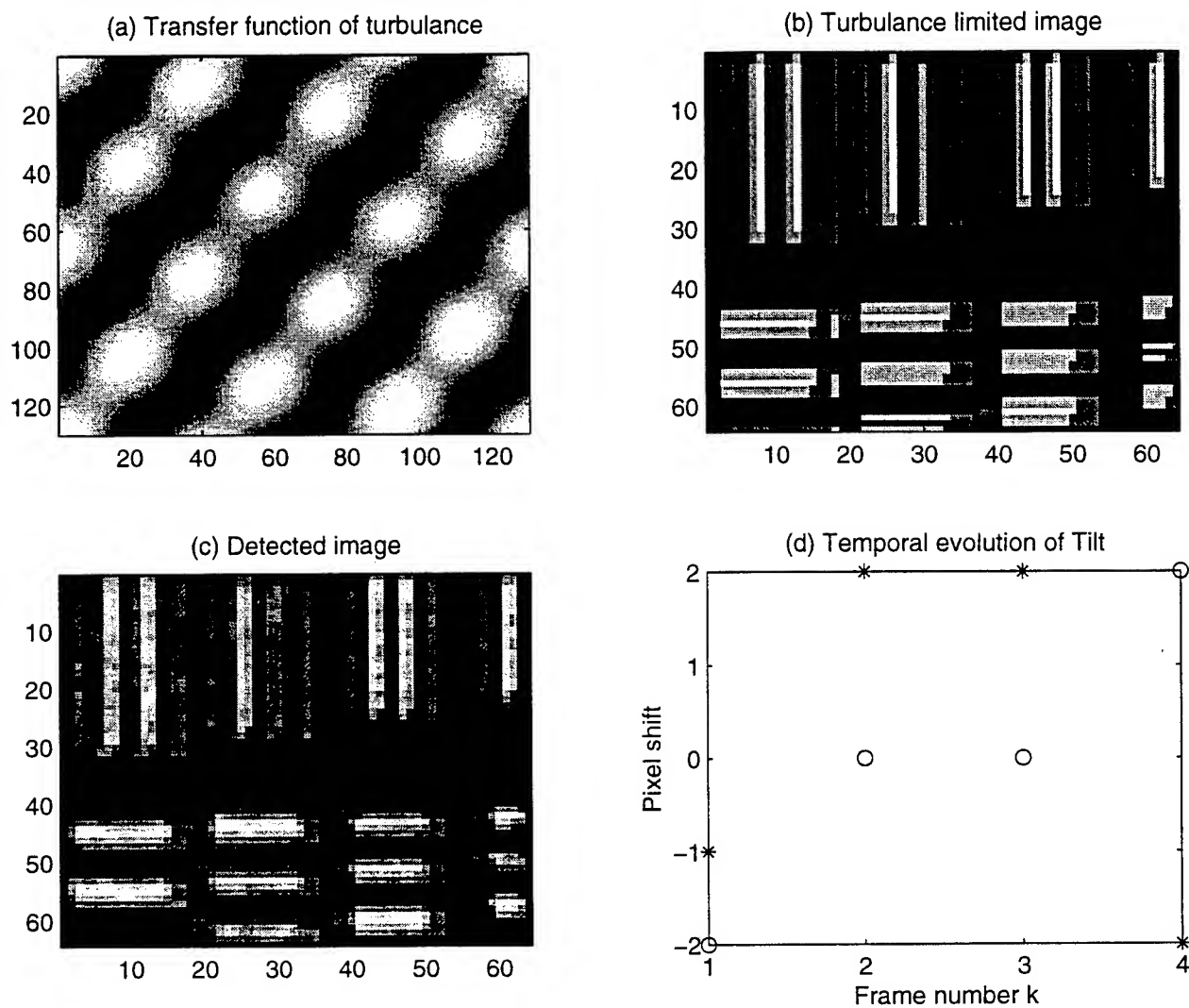


Figure 6. Simulation of the imaging system using four consecutive frames for  $\text{SNR} = 2$  and MCP spread of 2 pixels. (a) DFT of the turbulence-limited point spread function; (b) turbulence limited image; (c) detected image, and; (d) horizontal (\*) and vertical (o) tilt as a function of frame number  $k$ . The MCP is assumed to be in an unsaturated mode.

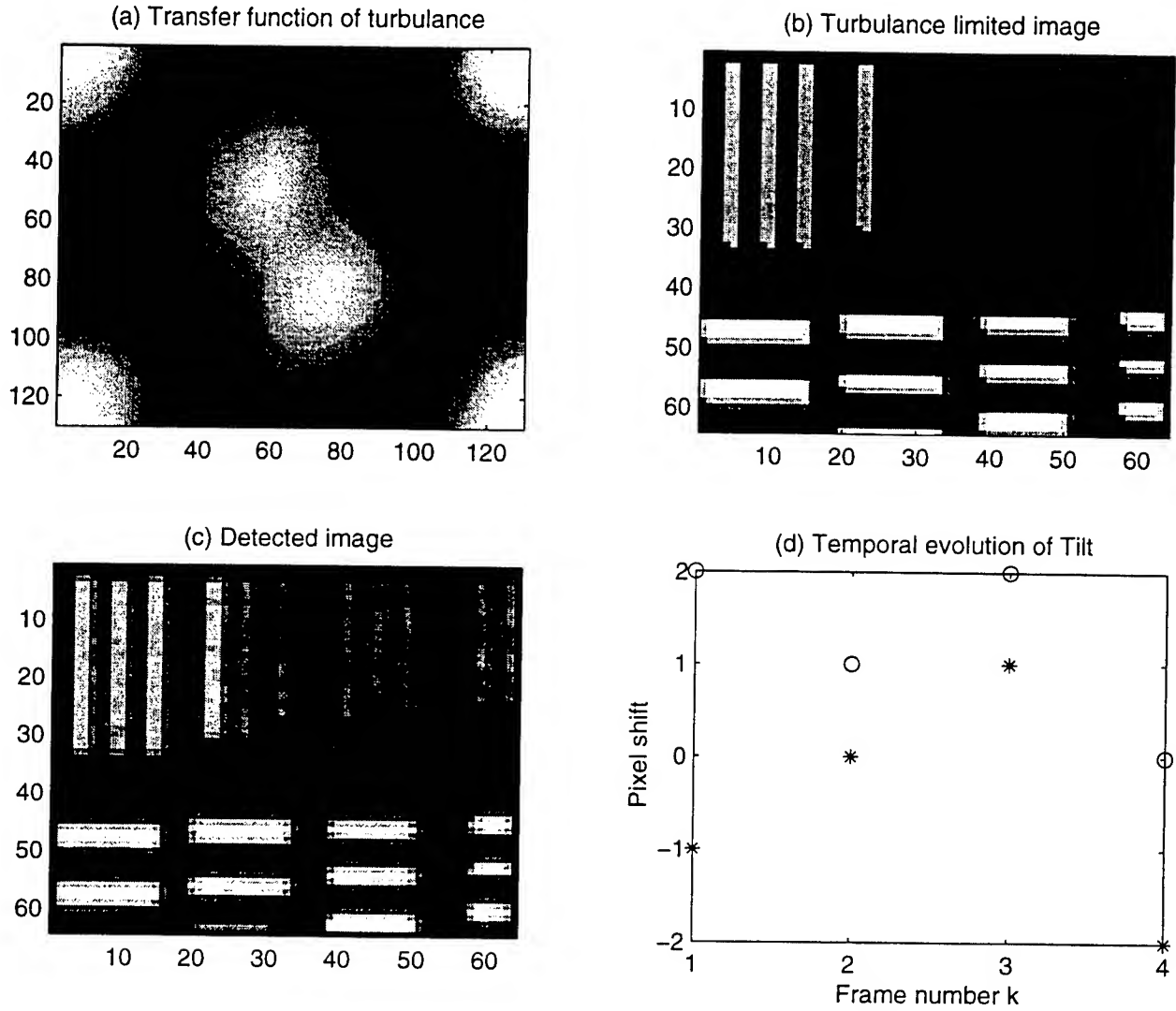


Figure 7. Simulation of the imaging system using four consecutive frames for  $\text{SNR} = 3$  and MCP spread of 3 pixels. (a) DFT of the turbulence-limited point spread function; (b) turbulence limited image; (c) detected image, and; (d) horizontal (\*) and vertical (o) tilt as a function of frame number  $k$ . The MCP is assumed to be in an unsaturated mode.

## VII. Conclusions

We have developed a stochastic model that captures aspects of degradation due to turbulence and uncertainty in photodetection and intensification in gated imaging systems. Experimental results in the literature have shown that real-time integration imaging results in a superior performance than frame-by-frame averaging. This study models turbulence by a slowly time varying random thin screen in the aperture plane. We consider only the tilt effect the thin screen since tilt represents the major source of degradation. By developing a stochastic model with slow time variation for the thin screen, we have been able to simulate the main features of the the experimental results. The slow variation in the thin screen is modeled by a a two-dimensional random walk. When captured images are separated by large time intervals, realizations of the thin screen are practically independent. The tilt from frame to frame can therefore be much larger than the case when frames are collected within a short time (as is the case in real-time integration). This model thus asserts that the tilt can vary within a certain small range from frame to frame if the time between frames is small. On the other hand, if the time between frames is large, there will be a random buildup of tilt variation in the time between frames resulting in large overall change on tilt. Our simulations suggest that there is a tradeoff between the number of successive frames used and atmospheric blur if images are averaged. This raises a fundamental question in statistical image recovery: What is the optimal exposure time in the sense of minimizing the mean square error? In principle, this questions can be addressed in the context of statistical signal processing now that a statistical model for the temporal variation in the image is formulated. The author plans to pursue this question in future studies.

This study also addresses the reduction in the resolution and contrast due to uncertainty in the response of TE photocathode detectors and MCP image intensifiers. A model has been developed that captures the degrading effect of dark noise. Simulations show that when the MCP is operated in the saturation mode, dark current significantly reduces contrast. The model also captures the spread introduced by the MCP as a result of electron spreading to neighboring channels as they are transferred from one stage of the MCP to the other. In addition, the random multiplication gain associated with the MCP stages are also captured in the model. We have derived analytical expressions for the mean and the variance of the



point spread function of the intensifier. Different MCP spread parameters were considered in the simulations to illustrate the blur associated with the MCP intensifiers. The parameters of the model can be estimated from measured test data a-priori. The model for the detection/intensification is then combined with the model for turbulence to give a complete stochastic model for the imaging system.

## References

- [1] V. Aebi, K. Costello, G. Davis, and R. Weiss, and V. Aebi, "Photocathode development for a 1300-nm streak tube," *Proc. SPIE*, vol. 2022, pp. 34-44, 1993.
- [2] P. Billingsley, *Probability and Measure*, 2nd ed. New York: Wiley 1986.
- [3] M. B. Corbett and B. N. Laprade, "Performance of long-life curved channel microchannel plates," *Proc. SPIE*, vol. 1072, pp. 130-137, 1989.
- [4] K. Costello, V. Aebi, G. Davis, R. La Rue, and R. Weiss, "Transferred electron photocathode with greater than 20% quantum efficiency beyond 1 micron," *Proc. SPIE*, vol. 2550, pp. 177-188, 1995.
- [5] K. Costello, G. Davis, R. Weiss, and V. Aebi, "Transferred electron photocathode with greater than 5% quantum efficiency beyond 1 micron," *Proc. SPIE*, vol. 1449, pp. 40-50, 1991.
- [6] W. B. Colson, J. McPherson, and F. T. King, *Rev. Sci. Inst.*, vol. 44, p. 1694, 1973.
- [7] I. P. Csorba, *Image Tubes*. Sams, 1985.
- [8] J. Dupuy, "The "super second generation" image intensifiers," *Proc. SPIE*, vol. 1072, pp. 13-18, 1989.
- [9] W. B. Feller, L. M. Cook, G. W. Fraser, J. F. Pearson, S. S. Murray, and M. R. Garcia, "Low noise microchannel plates," *Proc. SPIE*, vol. 1072, pp. 138-148, 1989.
- [10] D. L. Fried, "Optical resolution through a randomly inhomogeneous medium for very long and very short exposures," *J. Opt. Soc. Am.*, vol. 56, pp. 1372-1379, 1966.
- [11] L. K. van Geest and L. A. Bosch, "Gated image intensifiers and applications," *Proc. SPIE*, vol. 1072, pp. 19-29, 1989.
- [12] J. W. Goodman, *Introduction to Fourier Optics*. New York: McGraw-Hill, 1968.
- [13] J. W. Hardy, "Adaptive optics," in *Proc. SPIE on Active and Adaptive Optical Components*, vol. 1542, pp. 2-17, 1991.
- [14] P. Henkle, R. Roy, and J. L. Wiza, *IEEE Trans. Nucl. Sci.*, vol. NS-25, p. 548, 1978.
- [15] G. C. Holst, *CCD Arrays, Cameras, and Displays*. SPIE Optical Engineering Press, Bellingham, Washington, 1996.
- [16] S. Karlin and H. M. Taylor, *A First Course in Stochastic Processes*. Academic Press: New York, 1975.
- [17] M. Lampton, "The microchannel image intensifier," *Scientific American*, vol. 245, no. 5, 1981.
- [18] R. A. La Rue, J. P. Edgecumbe, G. A. Davis, S. Gospe, and V. Aebi, "High quantum efficiency photomultiplier with fast time response," *Proc. SPIE*, vol. 2022, pp. 64-73, 1993.
- [19] A. G. Milnes and D. L. Feucht, "Heterojunction photocathode concepts," *Applied Physics Letters*, vol. 19, no. 10, pp. 383-385, 1971.
- [20] A. Papoulis, *Probability, Random Variables, and Stochastic Processes*, New York: McGraw Hill, third ed., 1991.
- [21] W. Parkes, K. D. Evans, and E. Matheison, *Nucl. Instr. and Meth.*, no. 121, p. 151, 1974.
- [22] F. Roddier, "The effects of atmospheric turbulence in optical astronomy," in *Progress in Optics*, E. Wolf, ed., vol. XIX, New York: North-Holland, 1981.
- [23] M. C. Roggemann, E. L. Caudill, D. W. Tyler, M. J. Fox, M. A. Von Bokern, and C. L. Matson, "Compensated speckle imaging: theory and experimental results," *Appl. Opt.*, vol. 33, pp. 3099-3110, 1994.
- [24] M. C. Roggemann and B. Welsh, *Imaging Through Turbulence*. CRC Press: New York, 1996.
- [25] J. L. Wiza "Microchannel plate detectors," in *Nuclear Instruments and Methods*, vol. 162, pp. 587-601, 1979.

**NMR STUDY OF THE DECOMPOSITION REACTION PATH OF DEMNUM  
FLUID UNDER TRIBOLOGICAL CONDITIONS**

**Larry S. Helmick  
Professor  
Department of Science of Mathematics**

**Cedarville College  
Box 601  
Cedarville, OH 45314**

**Final Report for:  
Summer Research Program  
Wright Laboratory**

**Sponsored by:  
Air Force Office of Scientific Research  
Bolling Air Force Base, Washington, DC**

**And**

**Wright Laboratory**

**August 1997**

NMR STUDY OF THE DECOMPOSITION REACTION PATH OF  
DEMNUM FLUID UNDER TRIBOLOGICAL CONDITIONS

Larry S. Helmick  
Professor of Chemistry  
Department of Science and Mathematics  
Cedarville College

Abstract

It has previously been shown using  $^{19}\text{F}$  nuclear magnetic resonance (NMR) spectroscopy that Demnum fluid undergoes decomposition by a disproportionation reaction mechanism to form acid fluorides when heated in the presence of aluminum chloride. It is shown in this study that Demnum fluid decomposes at 345C in the presence of dry air and bearing steels to form the same acid fluorides. Consequently, the same disproportionation reaction mechanism must be involved under these conditions as well. Then it is shown that these acid fluorides readily undergo hydrolysis to carboxylic acids when they are exposed to atmospheric moisture. Finally, carboxylic acids, not acid fluorides, were detected in highly stressed Demnum fluids exposed to the atmosphere after recovery from fatigue testing experiments. Therefore, it is concluded that under tribological conditions, Demnum fluid initially decomposes in the presence of bearing steels by a disproportionation reaction mechanism to form acid fluorides which subsequently react with atmospheric moisture to form carboxylic acids.

# NMR STUDY OF THE DECOMPOSITION REACTION PATH OF DEMNUM FLUID UNDER TRIBOLOGICAL CONDITIONS

Larry S. Helmick

## Introduction

Perfluoropolyalkyl ethers (PFPAE) are presently being investigated as liquid lubricants for aerospace applications because of their broad liquid temperature range, favorable temperature/viscosity characteristics, and low chemical reactivity (1-3). However, it is now known that PFPAE fluids are susceptible to decomposition under tribological conditions (4,5), or when simply heated in the presence of metallic structural and bearing materials (6,7). Decomposition appears to occur because the surfaces of these materials can easily be converted to metal fluorides which catalyze decomposition of the fluid (6,8).

The reaction mechanism for decomposition of Demnum fluid to acid fluorides in the presence of the Lewis acid catalyst aluminum chloride has been reported (9,10). However, at elevated temperatures in a Cameron-Plint tribometer where the fluid is exposed to metal surfaces as well as the atmosphere, carboxylic acids, not acid fluorides, have been detected by Fourier transform infrared (FTIR) spectroscopy (11-13). A possible decomposition reaction path (Figure 1) involving initial formation of acid fluorides followed by hydrolysis of the acid fluorides to carboxylic acids by moisture in the atmosphere was suggested to account for these results. However, no specific experimental data was presented to support this potential reaction path.

It is important to know this reaction path in order to devise potential ways to prevent it from occurring and thus improve the chemical and thermal stability of the fluid under high temperature tribological conditions. Therefore, it was the purpose of this study to demonstrate that Demnum fluid does indeed initially decompose in the presence of bearing steels to produce acid fluorides, and that the acid fluorides can readily be hydrolyzed by moisture in the air to form carboxylic acids. Thus, detection of carboxylic acids, not acid fluorides, following tribological experiments involving bearing steels in the presence of ambient air would be expected.

#### Experimental Procedures

**Materials:** Demnum S-65, a commercially available linear PFPPE fluid produced by Daikin Industries, was used in this study. It has a C/O ratio of 3/1 and a kinematic viscosity of 12 cst at 100C. The five bearing steels used in the thermal tests were 4140, 52100, 410, M50, and 440C.

**Thermal Tests:** Twenty mL of Demnum was heated at 345C for 48 hours in a standard micro oxidation-corrosion apparatus (14) containing the five bearing metals with 1 L/Hr flow of dry air. Low boiling decomposition products which distilled out were collected with a 10C condenser protected from atmospheric moisture with a calcium sulfate drying tube. Both the residual Demnum remaining in the reaction tube as well as the distillate were transferred to NMR tubes in a dry bag to protect from atmospheric moisture any acid fluorides which may have been formed. The NMR tubes were capped and immediately analyzed to determine the structure of the decomposition products. The caps were then removed to expose the solutions to the atmosphere at room

temperature to determine if the reaction products could readily be hydrolyzed by atmospheric moisture to carboxylic acids.

NMR: A Varian VXR-300 300MHz NMR was used to obtain the proton as well as the  $^{19}\text{F}$  spectra of the fluids. Samples were dissolved in fluorotrichloromethane (approximately 50% concentration). Chemical shifts are slightly concentration dependent. For proton spectra, 512 scans were obtained at 299.9 MHz over a range of 16 ppm. Chemical shifts of the proton spectra are reported relative to chloroform at 7.24 ppm. For  $^{19}\text{F}$  spectra, 1000 scans were collected at 282.2 MHz over a range of 210 ppm. Chemical shifts of  $^{19}\text{F}$  are reported relative to fluorotrichloromethane at 0 ppm.

Tribometer: Fluids were stressed until failure (27-35 hours) on a modified Ball-on-Rod Rolling Contact Fatigue Tester (15) using M50 steel balls at 316C, 3600 rpm, and 4.8 GPa load. The fluid was dripped unto the bearing and was stressed in the hot contact zone, which was not open to the atmosphere, for several seconds before draining into a collection reservoir exposed to the atmosphere. NMR spectra were run on the recovered fluid after exposure to the atmosphere.

### Results

Figure 1 shows the reaction path previously proposed for decomposition of Demnum fluids under tribological conditions (12). It also shows the NMR chemical shifts for the various types of fluorine found in Demnum, the acid fluoride, and the final carboxylic acid products. These chemical shift

assignments for Demnum and the acid fluoride are in agreement with those previously reported by Kasai and Wheeler (10).

Figure 2 is the  $^{19}\text{F}$  NMR spectrum of unstressed Demnum with the chemical shift assignments for fluorines 1-8 shown. The signal at 0 ppm is the fluorotrichloromethane reference.

Figure 3 shows the  $^{19}\text{F}$  NMR spectrum of the distillate obtained from the oxidation-corrosion apparatus by heating Demnum in the presence of bearing metals and dry air. The decrease in intensity of peaks 4-6 relative to peaks 1-3 is due to the decrease in molecular weight of the material as the polymer is cleaved. That this material consists primarily of acid fluorides is easily determined from the presence of a carbonyl stretch absorption band at  $1883\text{ cm}^{-1}$  in the FTIR spectrum, the characteristic acyl fluorine (11) at +23.3 ppm, and the two distinctive  $\text{CF}_2$  groups (9 and 10) next to the carbonyl group (-85.5 and -121.4 ppm) in the NMR spectrum. Integration shows  $y$  to have an average value of 2, but that there must be a small amount of additional material present which contains  $\text{C}_3\text{F}_7$  on both ends of the molecule.

Gas chromatography/chemical ionization mass spectrometry (GC/CIMS) shows that there may actually be as many as eight different compounds present in this material. All three of the acid fluorides with  $y=1-3$  are definitely present. Then there are probably two more acid fluorides present with  $y=2$  or 3 which have  $\text{C}_2\text{F}_5$  rather than  $\text{C}_3\text{F}_7$  end groups. In addition, there are probably two compounds with  $\text{C}_3\text{F}_7$  groups on both ends of the molecule as expected from the NMR spectrum,  $\text{C}_3\text{F}_7(\text{OC}_3\text{F}_6)_y\text{OC}_3\text{F}_7$  where  $y=2$  or 3. And finally, there is

probably one corresponding compound with one  $C_2F_5$  end group,  $C_2F_5(OC_3F_6)_3OC_3F_7$ . All of these compounds would be expected to be formed if Demnum decomposes by a disproportionation reaction mechanism under these conditions.

This NMR spectrum and the one for the residue (not shown) are essentially identical to those obtained by Kasai and Wheeler (10) for the distillate and residue resulting from heating Demnum in the presence of aluminum chloride. Consequently, the same reaction mechanism must be occurring under both sets of conditions. This is reasonable to expect since the surfaces of bearing steels are well known to be readily converted to metal fluorides by the initial decomposition products of PFPAE fluids. The metal fluorides then act as catalysts for further decomposition by the same disproportionation reaction mechanism observed for aluminum chloride (11).

Figure 4 shows the  $^{19}F$  spectrum after the acid fluoride has been exposed to the atmosphere for several hours. That this must be the spectrum of a carboxylic acid is easily determined from the absence of the acyl fluorine absorption band at +23 ppm as well as the subtle change in chemical shift for the two  $CF_2$  groups (12 and 13) next to the carbonyl group (-85.3 and -122.2 ppm). Furthermore, the proton NMR spectrum (not shown) displays a characteristic carboxyl proton peak at +9.9 ppm. Both the O-H stretch and the C=O stretch are observed in the FTIR spectrum (3556 and  $1775\text{ cm}^{-1}$ ) as well.

Finally, Figure 5 shows the  $^{19}F$  spectrum of fluid recovered from a typical fatigue test after exposure to the atmosphere. The vertical scale is expanded



to show the weak peaks. (Very weak positive and negative peaks from -10 to -120 ppm are due to noise which is visible because of the expanded scale.) The absence of acid fluorides is apparent from the lack of absorption at +23 ppm. The weak bands at -85.2 and -122.1 ppm correspond to those of the two CF<sub>2</sub> groups (12 and 13) next to the carbonyl group of a carboxylic acid, not an acid fluoride. In addition, the carboxyl proton (14) is seen at +9.3 ppm in the proton NMR spectrum, and the O-H and C=O stretches appear at 3556 and 1775 cm<sup>-1</sup> in the FTIR spectrum. Consequently, it is clear that the same carboxylic acids produced in oxidation-corrosion tests are also produced in tribology experiments involving bearing steels if the fluid is exposed to atmospheric moisture.

### Conclusion

The NMR data support the previously suggested decomposition reaction path. Under tribological conditions, Demnum fluids decompose initially to acid fluorides by a disproportionation reaction mechanism. These compounds then undergo hydrolysis to form carboxylic acids by reacting with moisture in the atmosphere. Consequently, detection of carboxylic acids, not acid fluorides, following tribological experiments involving bearing steels in the presence of ambient air is to be expected.

### Acknowledgments

Fluids from fatigue tests were kindly supplied by Hitesh K. Trivedi, UES, Inc. FTIR spectra were obtained by Jim Liang, University of Dayton Research Institute.

### Disclaimer

The U. S. Air Force does not endorse or criticize the materials used in this study.

### References

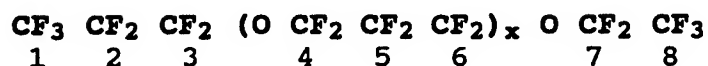
1. Fusaro, R.L., "Tribology Needs for Future Space and Aeronautical Systems," NASA TM-104525, 1991.
2. Jones, W.R., Jr., "The Properties of Perfluoropolyethers Used for Space Applications," NASA TM-106275, 1993.
3. Masuko, M., Jones, W.R., Jr., and Helmick, L.S., "Tribological Characteristics of Perfluoropolyether Liquid Lubricants Under Sliding Conditions in High Vacuum," NASA TM-106257, 1993.
4. Karis, T.E., Novotny, V.J., and Johnson, R.D., "Mechanical Scission of Perfluoropolyethers," J. Appl. Polym. Sci., **50**, 1357-1368 (1993).
5. Vurens, G., Zehringer, R., and Saperstein, D., "The Decomposition Mechanism of Perfluoropolyether Lubricants during Wear," Chapter 10 in Surface Science Investigations in Tribology, Chung, Y.W., Homola, A.M., Sheet, G.B., eds., ACS Symposium Series, American Chemical Society, 1992.
6. Zehe, M.J., and Fout, O.D., "Acidic attack of Perfluorinated Alkyl Ether Lubricant Molecules by Metal Oxide Surfaces," Trib. Trans., **33**, 634-640 (1990).
7. Deimers, J.R., Gschwender, L.J., and Snyder, C.E., "A New Technique for the Investigation of Liquid Lubricant Degradation: The Oxidation Corrosion Conductivity Test," Lubr. Eng., **51**, 321-327 (1995).
8. Kasai, P.H., Tang, W.T., and Wheeler, P., "Degradation of Perfluoropolyethers Catalyzed by Aluminum Oxide," Appl. Surf. Sci., **51**, 201-211 (1991).
9. Kasai, P.H. "Perfluoropolyethers: Intramolecular Disproportionation," Macromolecules, **25**, 6791-6799 (1992).
10. Kasai, P.H., and Wheeler, P., "Degradation of Perfluoropolyethers Catalyzed by Aluminum Chloride," Appl. Surf. Sci., **52**, 91-106 (1991).
11. Helmick, L.S., and Sharma, S.K., "Effect of Humidity on Friction and Wear for a Linear Perfluoropolyalkyl Ether Fluid Under Boundary Lubrication Conditions," Lubr. Eng., **52**, 6, 437-442 (1996).
12. Liang, J., and Helmick, L.S., "Tribochemistry of a PFPPE Fluid on M-50 Surfaces by FTIR Spectroscopy," STLE Preprint No. 95-TC-5A-2, (1995).

13. Liang, J., Tung, Y.S., Henderson, D.O., and Helmick, L.S., "A Study of Boundary Lubricating Thin Films Produced from a Perfluoropolyalkylether Fluid on M-50 Surfaces Part 2: Humidity Effect and Topography Studies," Submitted for Publication (1996).

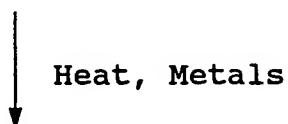
14. Harsacky, F.J., and Dolle, R.E., "A Chronological History of the Development of High Temperature Oxidation-Corrosion Evaluation Methods Including an Improved Micro Oxidation-Corrosion Procedure for the Investigation of Advanced Gas Turbine Engine Lubricants," Technical Report No. AFML-TDR-64-291, (1965).

15. Trivedi, H.K., Gerardi, D.T., Forster, N.H., Rosado, L. and Givan, G.D., "A Modified Ball-on-Rod Type Rolling Contact Fatigue (RCF) Tester for Accelerated Testing of Candidate Lubricants and Bearing Materials," SAE Technical Paper Series 951041 (1995).

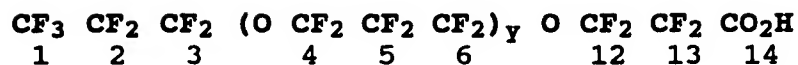
**Figure 1: DECOMPOSITION REACTION PATH OF DEMNUM  
UNDER TRIBOLOGICAL CONDITIONS**



**Demnum**



**Acid Fluorides**



**Carboxylic Acids**

<u>GROUP</u>	<u>CHEMICAL SHIFT (PPM)</u>
1	-81.8
2	-130.1
3	-84.2
4	-83.2
5	-129.1
6	-83.2
7	-88.5
8	-87.4
9	-85.5
10	-121.4
11	+23.3
12	-85.3
13	-122.2
14	+9.9 (IN PROTON SPECTRUM)

Figure 2:  $^{19}\text{F}$  NMR SPECTRUM OF UNSTRESSED DEMNUM

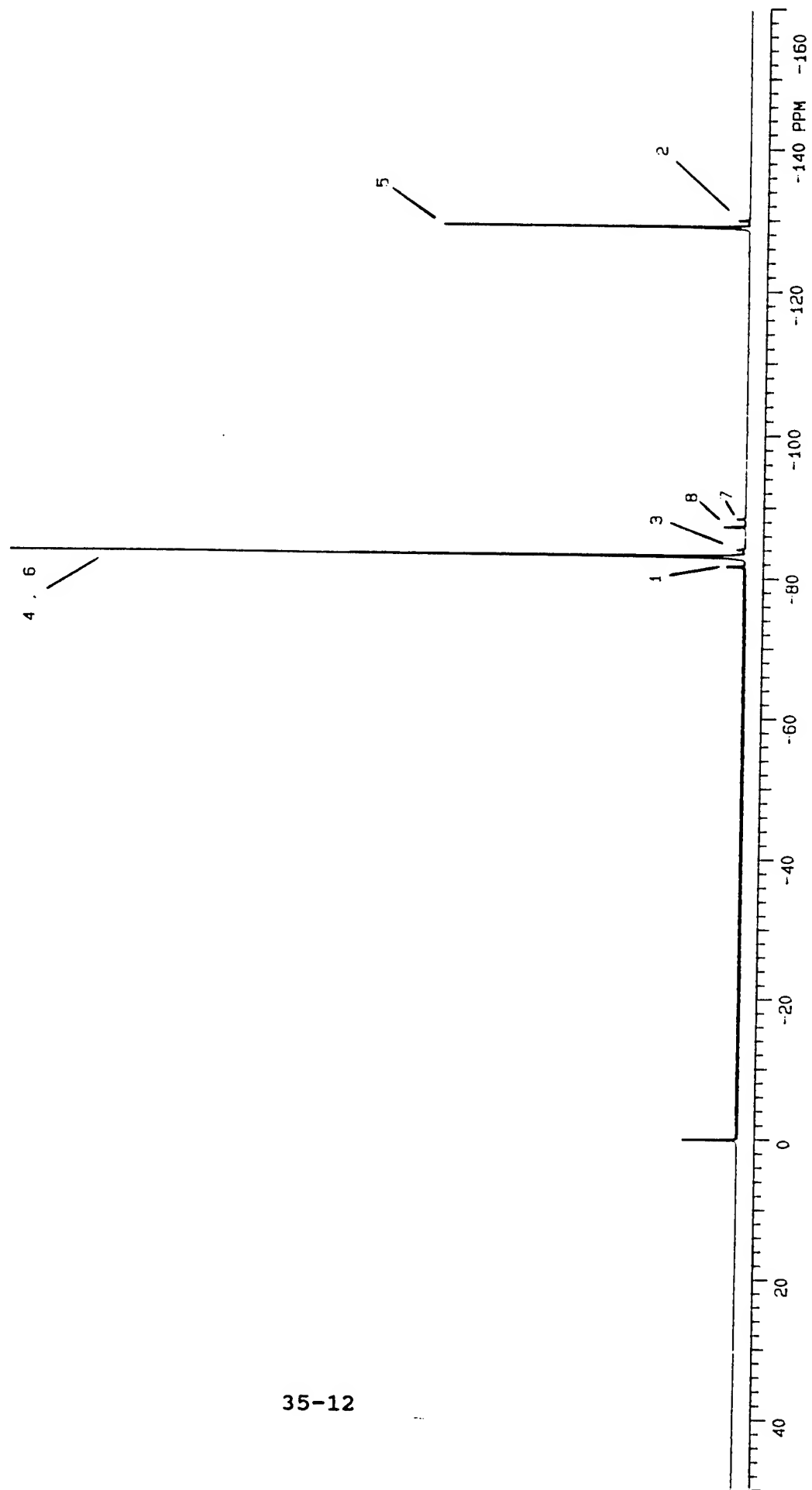


Figure 3:  $^{19}\text{F}$  NMR SPECTRUM OF THE ACID FLUORIDE

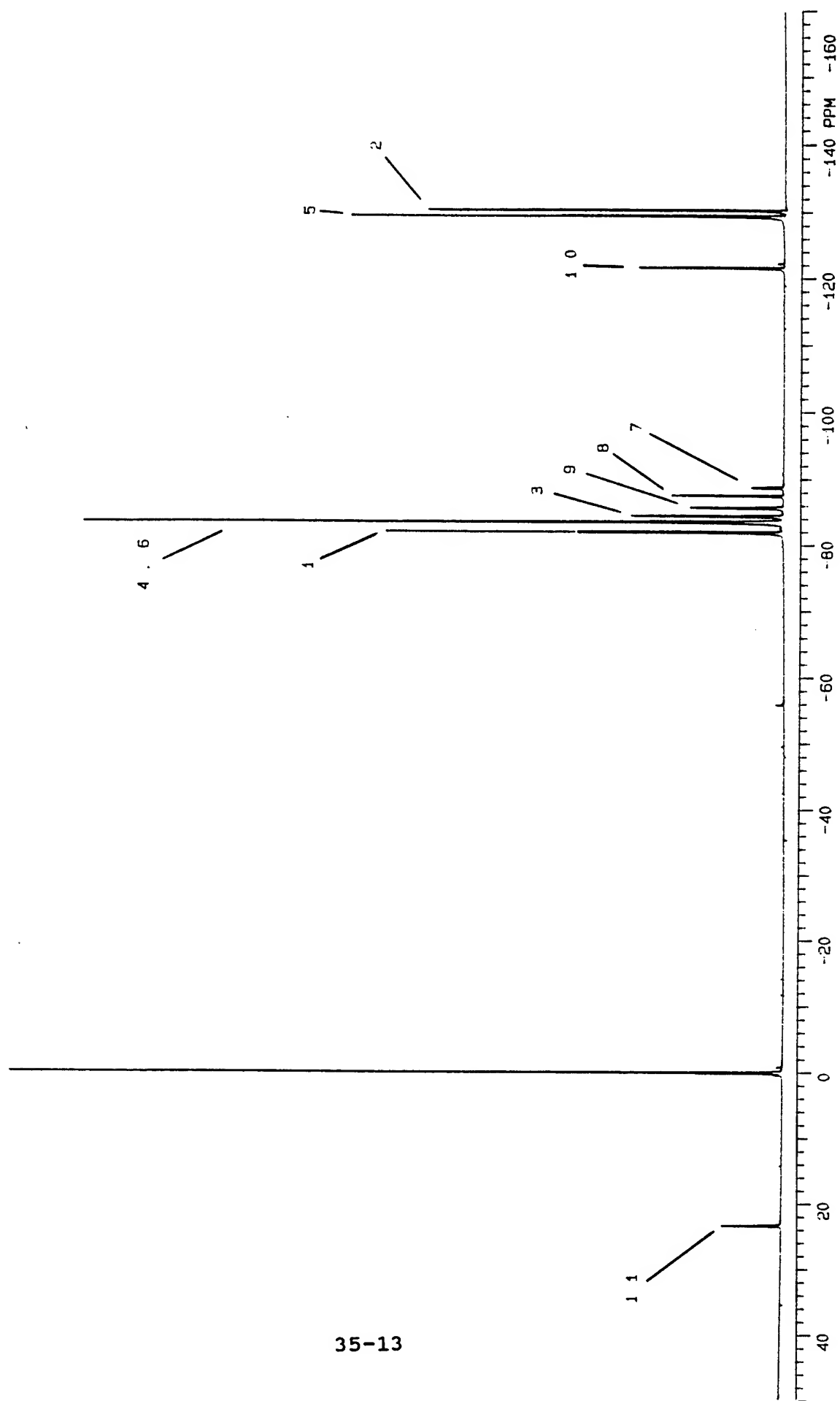


Figure 4:  $^{19}\text{F}$  NMR SPECTRUM OF THE CARBOXYLIC ACID

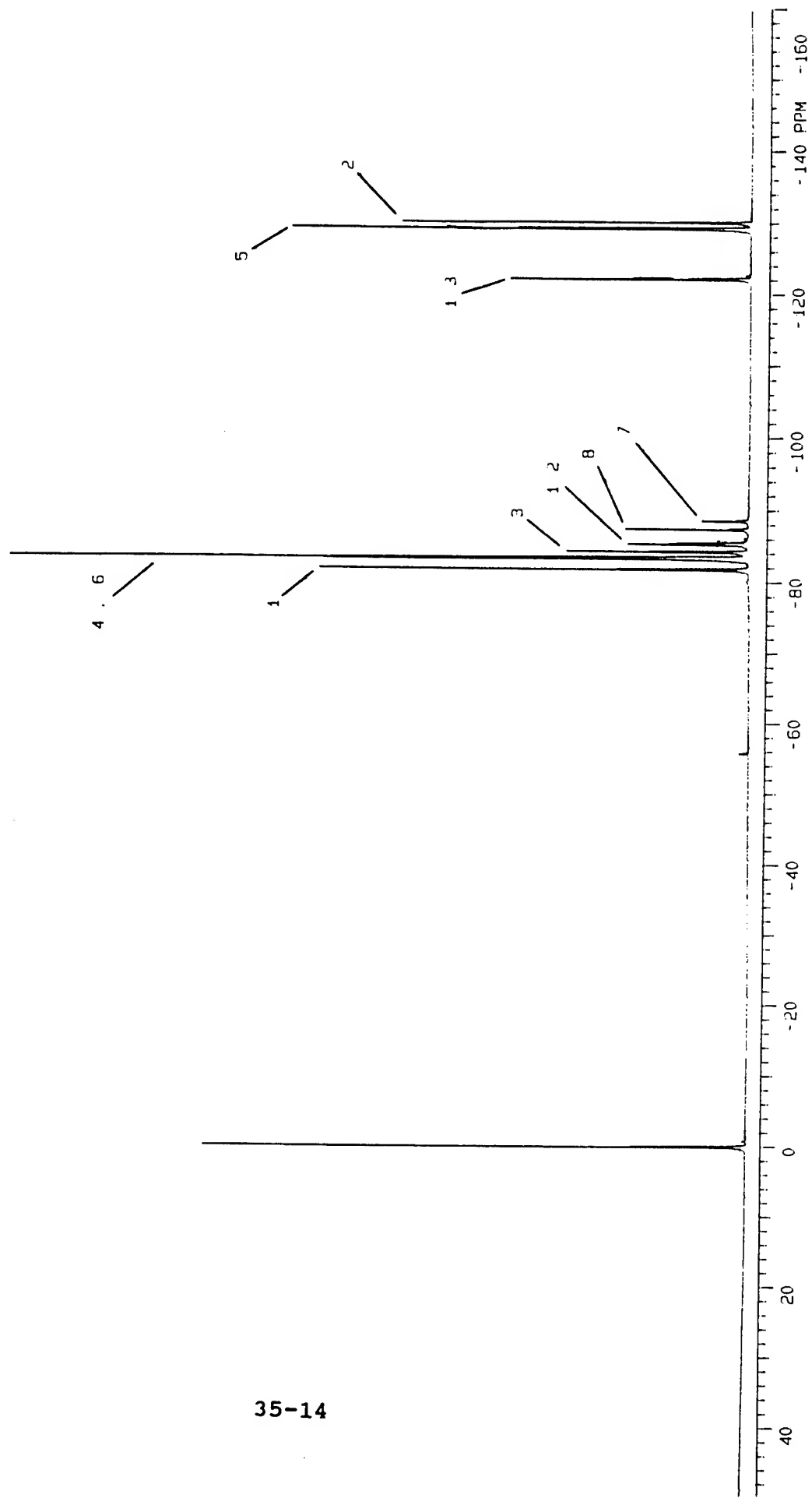
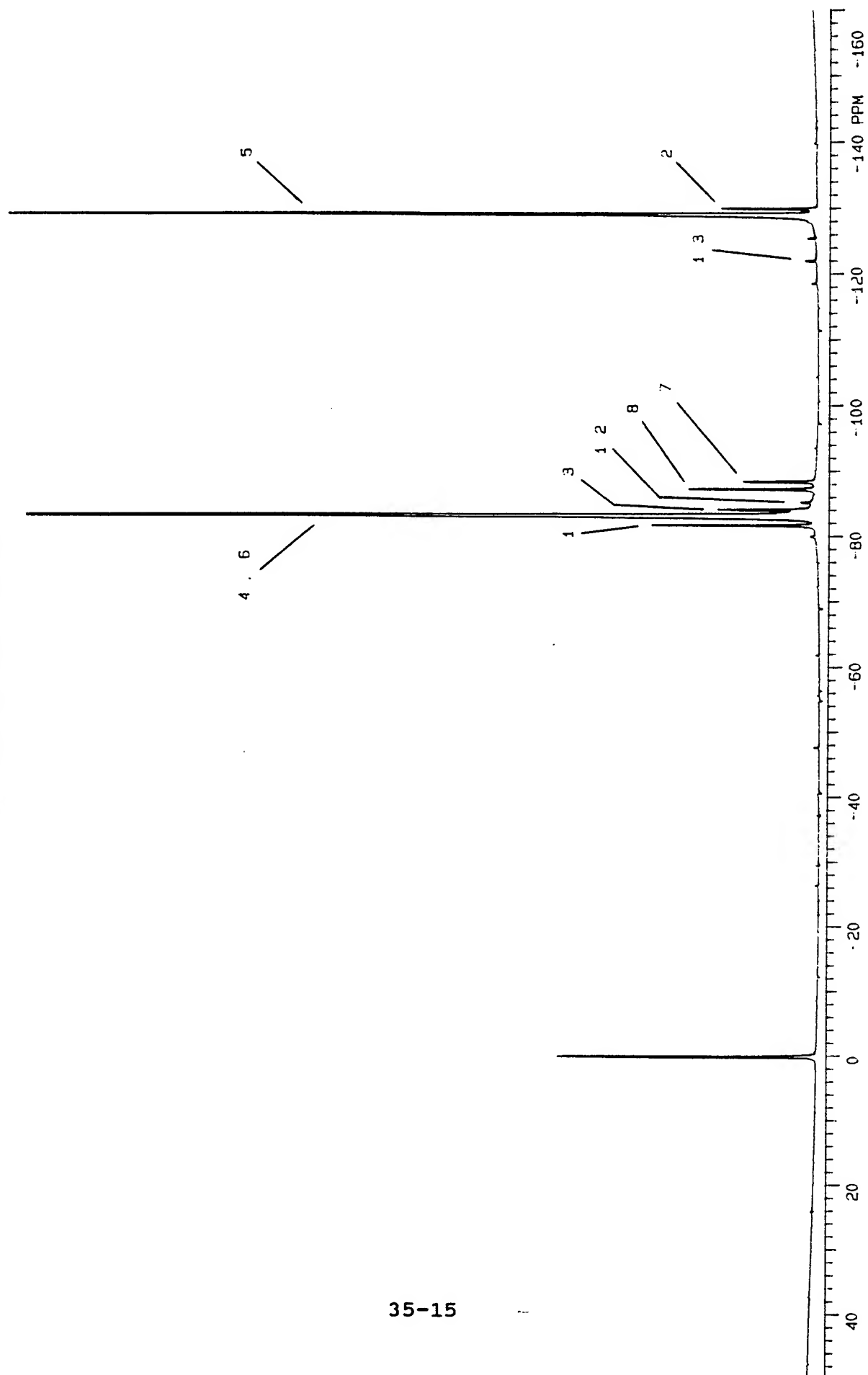


Figure 5:  $^{19}\text{F}$  NMR SPECTRUM OF DEMNUM STRESSED  
IN THE FATIGUE TESTER





# **INTENSITY OF [100] TEXTURAL COMPONENTS INCOMPRESSION-FORGED TANTALUM**

William F. Hosford  
Professor  
Department of Materials Science and Engineering

University of Michigan  
Ann Arbor, Michigan, 48109-4788

Final Report for:  
Summer Faculty Research Program  
Wright Laboratory  
Eglin Air Force Base, FL. 32542

Sponsored by:  
Air Force Office of Scientific Research  
Bolling Air Force Base, DC

And

Wright Laboratory

July, 1997

# INTENSITY OF [111] AND [100] TEXTURAL COMPONENTS IN COMPRESSION-FORGED TANTALUM

W. F. Hosford

Professor

Department of Materials Science and Engineering

University of Michigan

## Abstract

Crystallographic textures in compressed tantalum were studied. A method has been devised to analyze the strength of the individual textural components in materials with fiber textures. Analyses of three batches of tantalum indicate that the final texture after forging is composed of [111] and [100] components. The relative strength of the two components depends on the texture before compression. Since the final mechanical properties depend strongly on texture, control of properties requires control of texture, including the starting texture. It is suggested that a program to predict quantitatively the end texture from the starting texture would allow tighter control of the starting material.

# INTENSITY OF [111] AND [100] TEXTURAL COMPONENTS IN COMPRESSION-FORGED TANTALUM

W. F. Hosford

## Introduction

Deformation of polycrystalline materials occurs by slip within the grains on specific planes and in specific directions. Such slip in a grain causes a rotation of the lattice changing its orientation. The result is a statistical orientation of the grains, or crystallographic texture. The existence of these textures strongly affects the properties of the material.

Of particular interest to the Air Force are the textures developed in tantalum. After heavy compression of bcc metals many grains become oriented so that either their  $\langle 111 \rangle$  directions or  $\langle 100 \rangle$  directions are aligned with the sheet normal [1]. Experiments [2] and theoretical work [3] have shown that the relative number with each orientation depends on the texture before the compression and that the degree of the alignment increases with the compressive strain. Since the properties depend on the texture, to obtain reproducible properties it is necessary to control the texture. Of particular interest here is the relative number of grains oriented near [111] and near [100]. A very strong [111] component together with a weak [100] component would be desirable.

Textures are measured by x-ray diffraction techniques. Today, the usual way of reporting the results of these measurements is in the form, of an inverse pole figure. These are plots of the frequency of a characteristic specimen direction (e.g. the fiber axis for a rod) relative to the cubic axes of the crystals. Figure 1 is an example of an inverse pole figure. It represents the orientation of the compression axis of a tantalum powder sample after radial compression to a strain of 0.83. It is clear that there are concentrations of orientations near [111] and near [100]. However it is not possible from this representation to determine the fractions of grains near these poles. One of the objectives of this work was to develop a method to quantitatively describe the textures. This was done by calculating from the numerical ODF output, the percent of the grains within a fixed angle of the two poles. Details of the calculation method are given in Appendix I.

### Samples from Compressed Powder

The first data set is from a disk made by isostatic compression of tantalum powder. One group of samples were then compressed various amounts in the through-thickness and another was compressed in the radial direction. Figures 2-4 are plots showing the percentage of material within  $2.5^\circ$ ,  $7.5^\circ$  and  $12.5^\circ$  of  $\langle 111 \rangle$  and  $\langle 100 \rangle$  poles. These figures indicate that the texture is fairly well developed by the time the true compressive strain equals 0.30 and fully developed at a true compressive strain of 0.60 (height reduction of 49%). The reason for the drop in the intensities for the radial specimens above a strain of 0.6 is not known, In principle the two sets of curve should coincide because the starting material was randomly oriented and there is no intrinsic difference between the two directions.

### Rolled Plate

The second set of data is from specimens cut from a rolled plate. Half of the specimens were then compressed parallel to rolling direction and half in the transverse direction. Figures 5-8 show the development of their texture in these samples as a function of the amount of compression. Because the starting material was not isotropic, the curves for the rolling and transverse direction differ.

### Rod Material

A third set of data is from earlier work by O'Brien *et al* [2] conducted under an Air Force SBIR contract. The starting material was a round bar with a very strong  $[110]$  texture. Figure 9 shows that 80% of the material is initially oriented within  $12.5^\circ$  of a  $\langle 110 \rangle$  pole. Figures 10 and 11 show that with this starting texture, compression produces a very strong  $[111]$  texture with few grains being oriented near  $[100]$ .

### Conclusions

This work shows that the relative amounts of  $[111]$  and  $[100]$  components developed by compression depend on the texture before compression. Some orientations rotate toward  $[111]$  and some toward  $[100]$ . The resulting properties depend on the strengths of these two components. A  $[111]$  texture has the highest possible strength and the highest possible R-value while a  $[100]$  texture has the lowest possible strength and the lowest possible R-value.

### Needed Work

A computer model is needed to track the rotations of individual starting orientations. While there has been some computer modeling of texture development in bcc metals, it is not possible from the published results to determine the rotation of individual grains, nor how the relative intensities of the two components depend on the starting texture. [3]. Furthermore the model used was not a pure pencil-glide model.

The basic orientation triangle can be divided into the regions representing orientations that will eventually rotate to [111] or [100] under continued compression. Figure 12 shows this schematically. Work to establish the boundary between the two regions should be done. The results would allow prediction of end textures from starting rod textures. It could even be the basis for specification of material to be forged, since it would allow early rejection of material that would not meet the necessary property requirements after forging.

### Summary

A method has been devised to analyze the texture strength in tantalum.

Analyses of three batches of tantalum indicate that the final texture after forging is composed of [111] and [100] components. The relative strength of the two components depends on the texture before compression.

Since the final properties depend strongly on texture, control of properties requires control of texture, including the starting texture. A program to predict quantitatively the end texture from the starting texture would allow tighter control of the starting material.

### References:

1. C. S. Barrett, *Structure of Metals*, 2nd. ed., 1950, J. Wiley
2. J. M. O'Brien, W. F. Hosford, and R. L. Landrum, "Mechanical and Physical Properties of Cold Forged Tantalum," WL-TR-7075, SBIR final report, 1996.
3. B-J. Lee, K. S. Vecchio, S. Azhi and S. Schoenfeld, "Modeling the Mechanical Behavior of Tantalum," *Met. and Mat., Trans. A*, **28A** (1997) pp. 113-122.

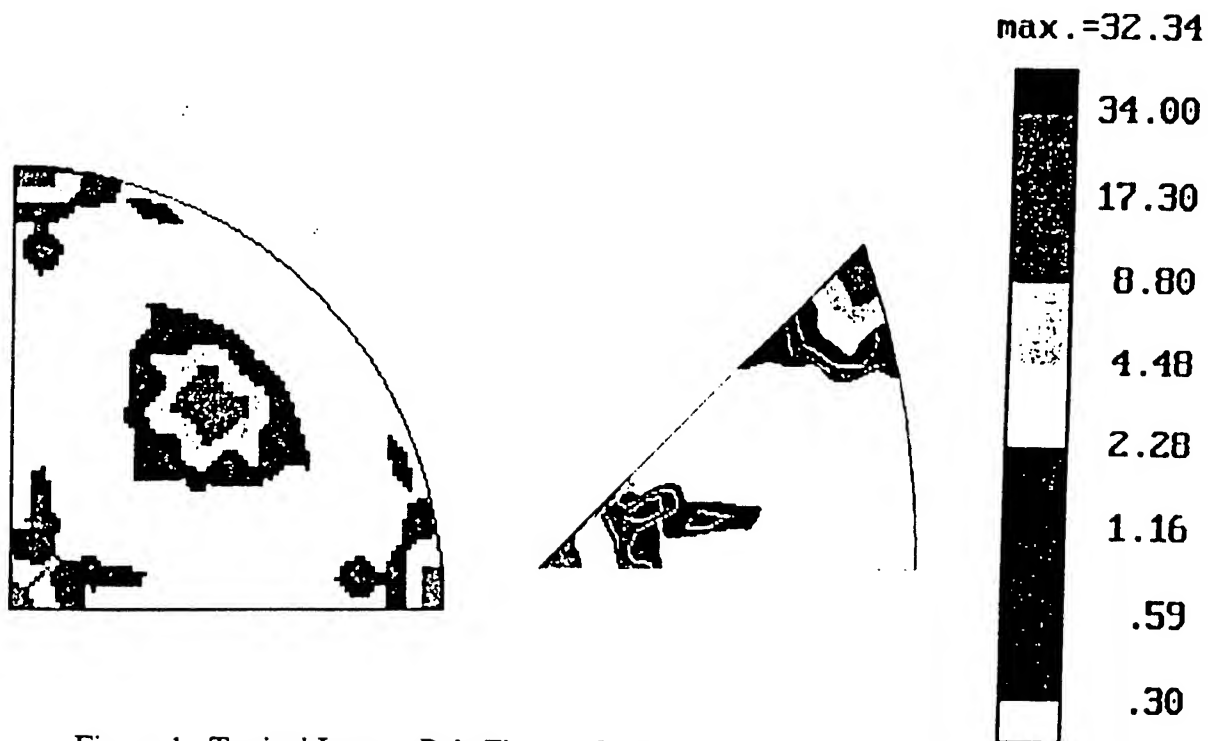


Figure 1. Typical Inverse Pole Figure of a Quadrant of a Tantalum after Compression (left). The peaks at the north pole and at 0 and 90° on the equator indicate strong [100] component. The center peak indicated a strong [111] texture component. The same texture data is plotted at right in the basic orientation triangle with corners at [100], [010] and [111]. Note that, although the strong [100] and [010] components are obvious, the relative numbers of grains with near-[100] and near-[111] orientations are not apparent from this inverse pole figure.

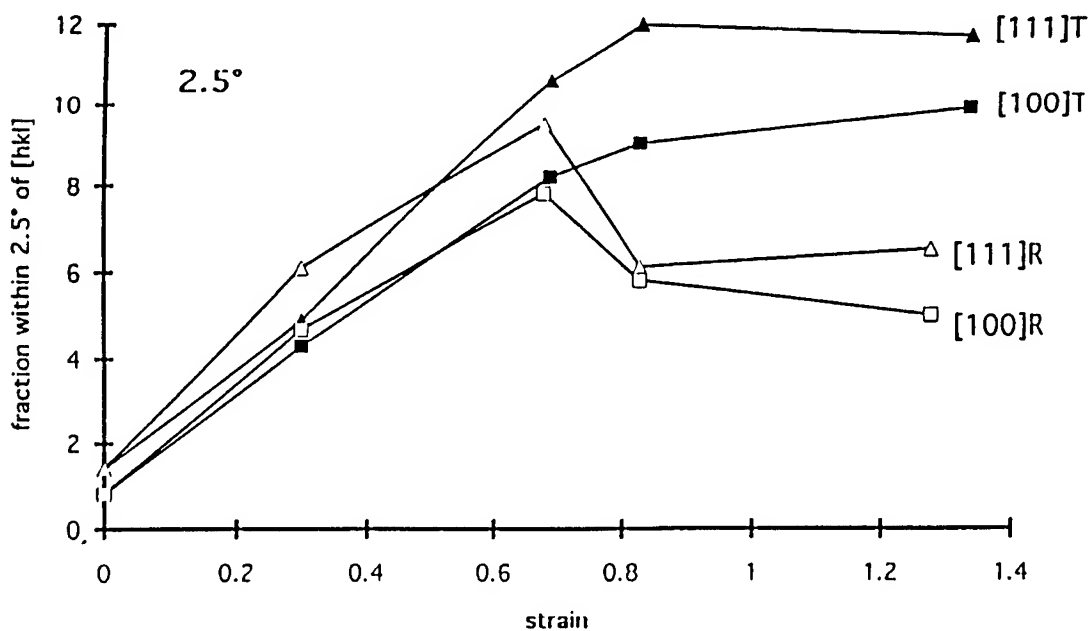


Figure 2 The percent of the grains oriented within 2.5° of [111] and of [100] in the powder metallurgy tantalum after compression in two directions. T indicates through-thickness compression and R indicates radial direction compression.

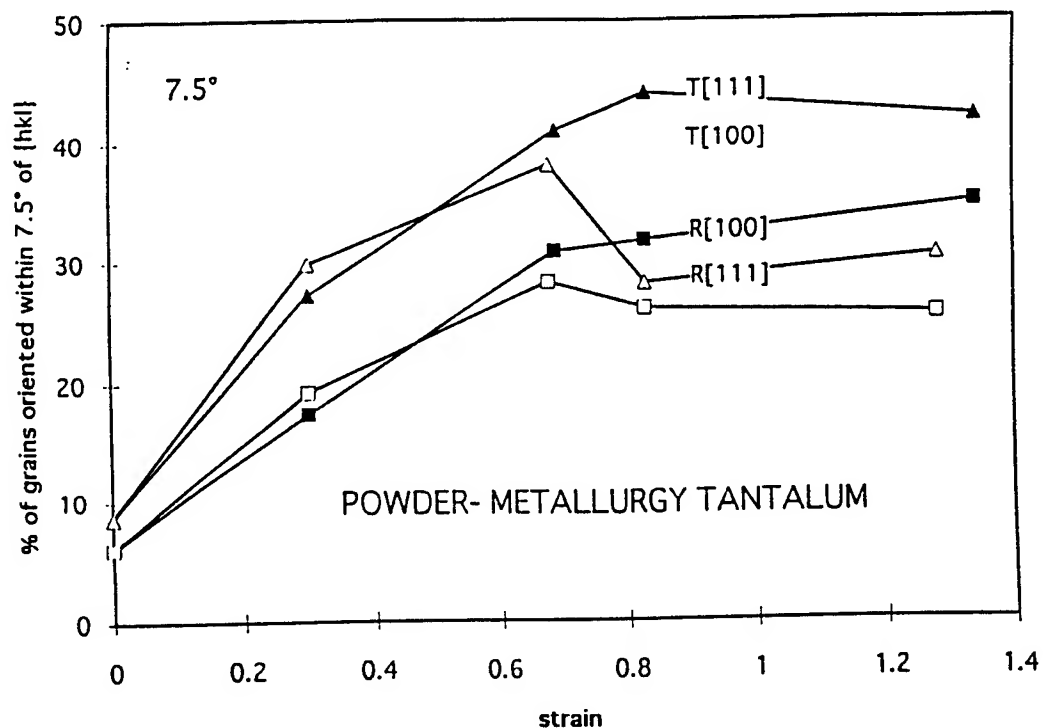


Figure 3 The percent of the grains oriented within  $7.5^\circ$  of [111] and of [100] in the powder metallurgy tantalum after compression in two directions. T indicates through-thickness compression and R indicates radial direction compression.

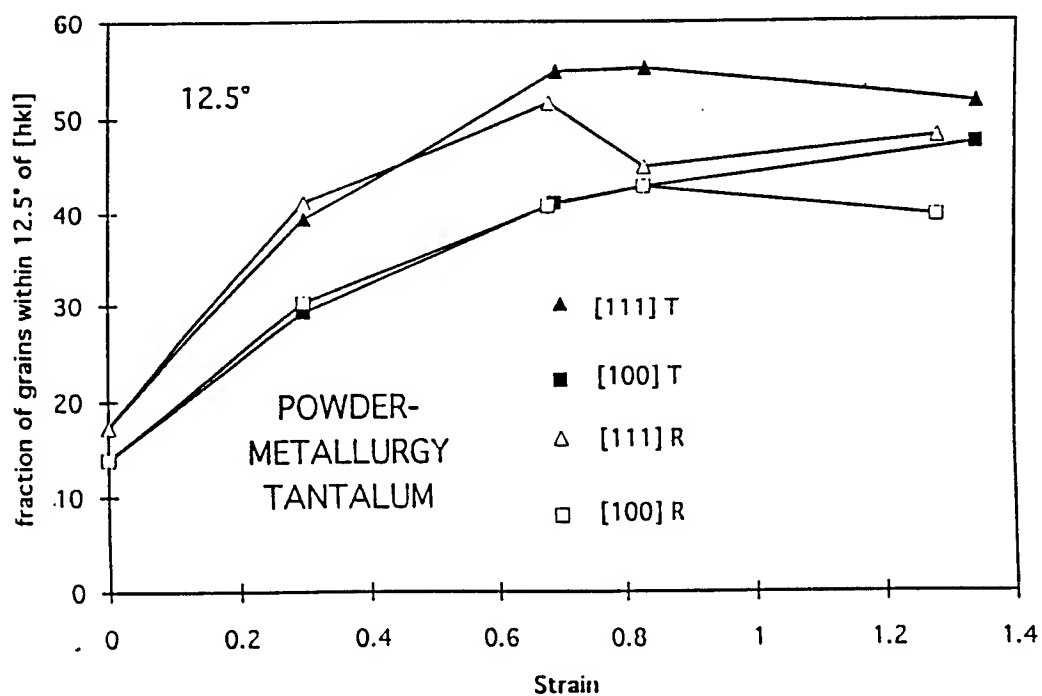


Figure 4 The percent of the grains oriented within  $12.5^\circ$  of [111] and of [100] in the powder metallurgy tantalum after compression in two directions. T indicates through-thickness compression and R indicates radial direction compression.

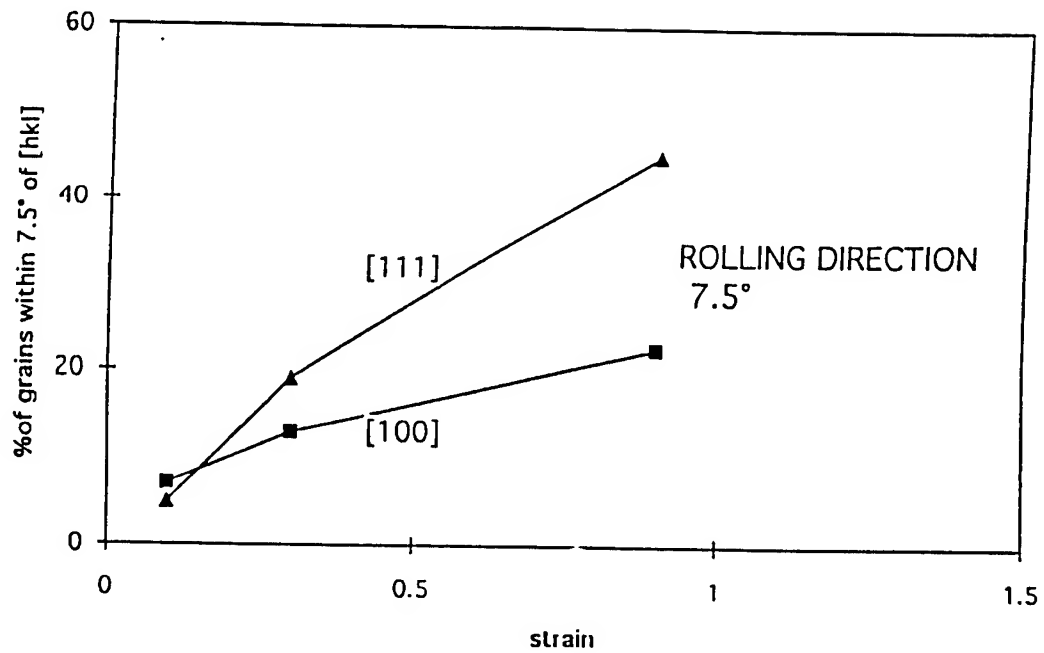


Figure 5 The percent of the grains oriented within 7.5° of [111] and of [100] in the tantalum plate after compression in the rolling direction.

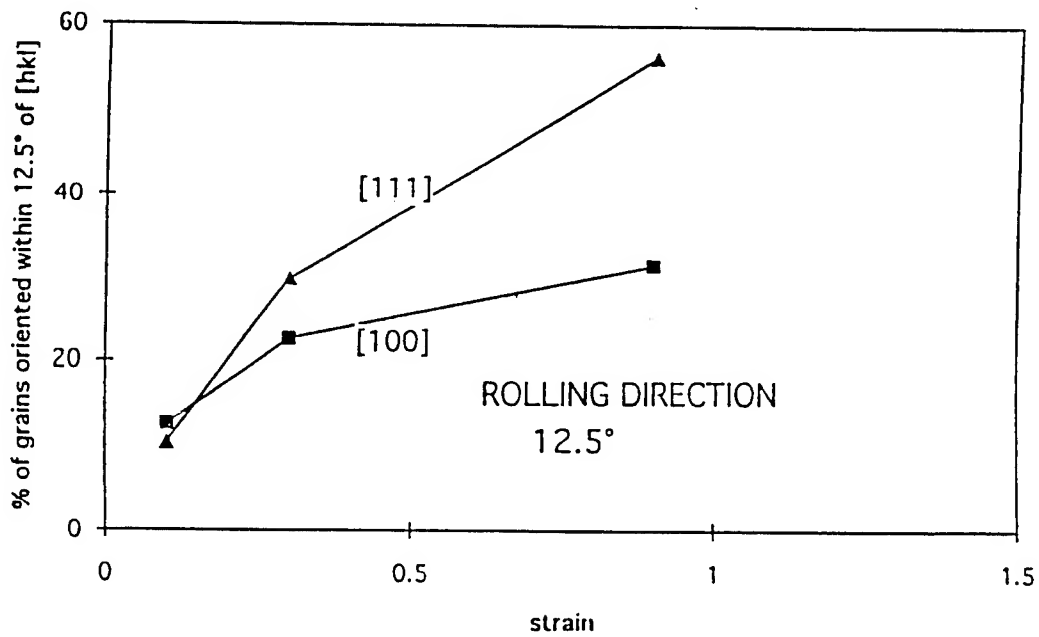


Figure 6 The percent of the grains oriented within 12.5° of [111] and of [100] in the tantalum plate after compression in the rolling direction.



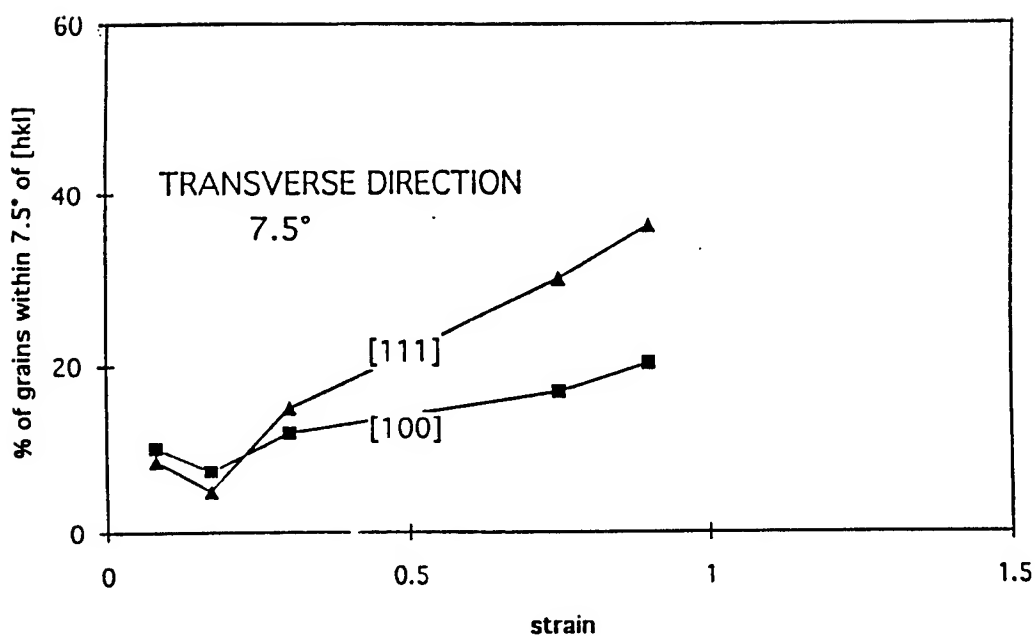


Figure 7. The percent of the grains oriented within  $7.5^\circ$  of  $[111]$  and of  $[100]$  in the tantalum plate after compression in the transverse direction.

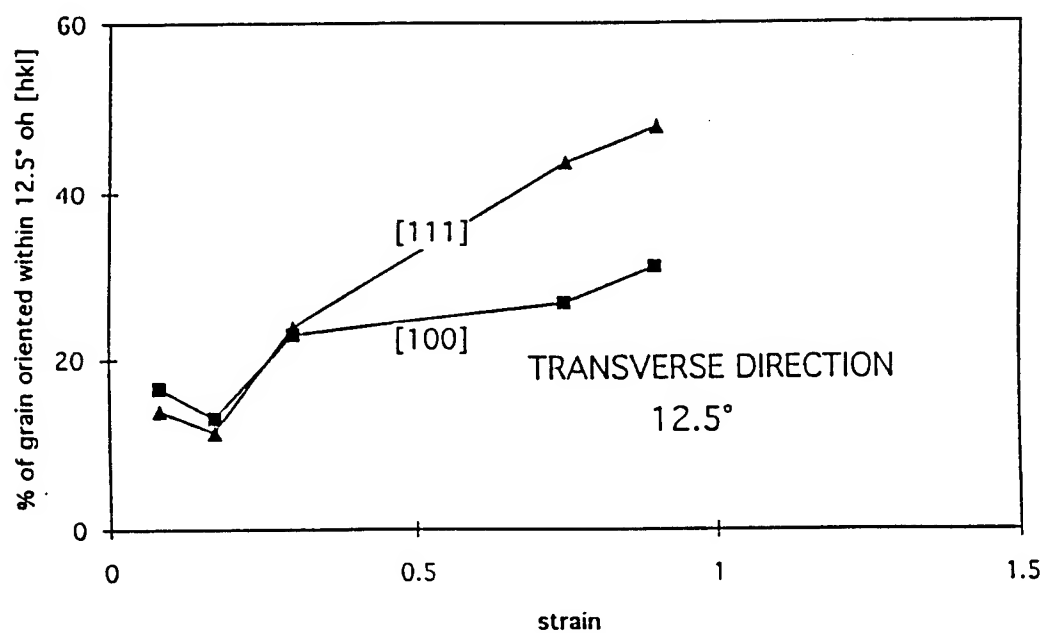


Figure 8. The percent of the grains oriented within  $12.5^\circ$  of  $[111]$  and of  $[100]$  in the tantalum plate after compression in the transverse direction.

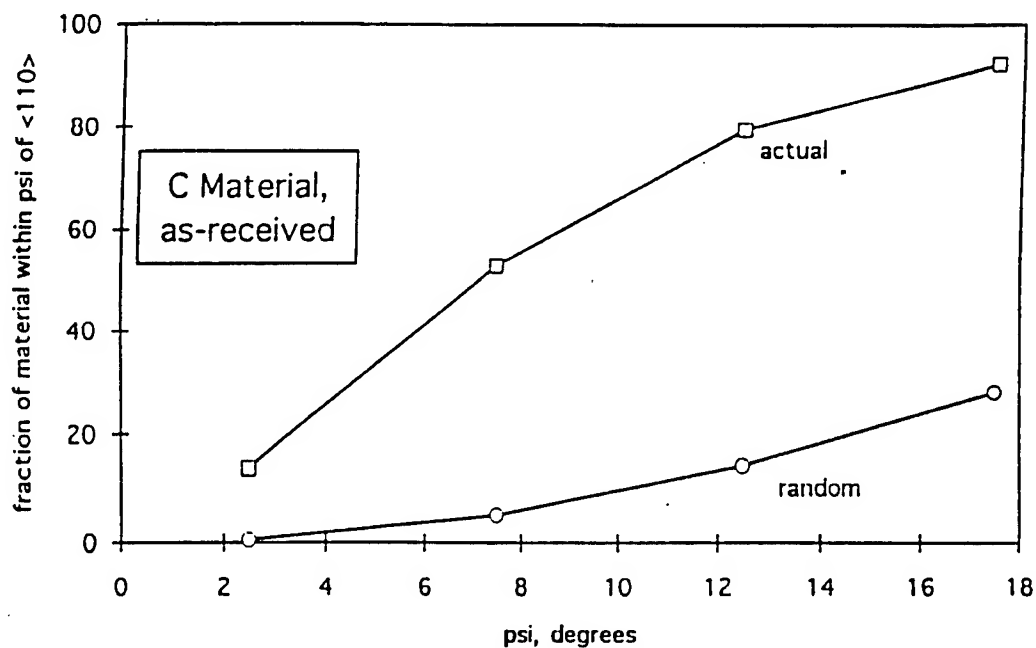


Figure 9. The intensity of the [110] rod texture in the C-material in the as-received condition. Note that about 80% of the material is oriented within 12.5° of [110], whereas if the texture were random only 14% would be. The data is from

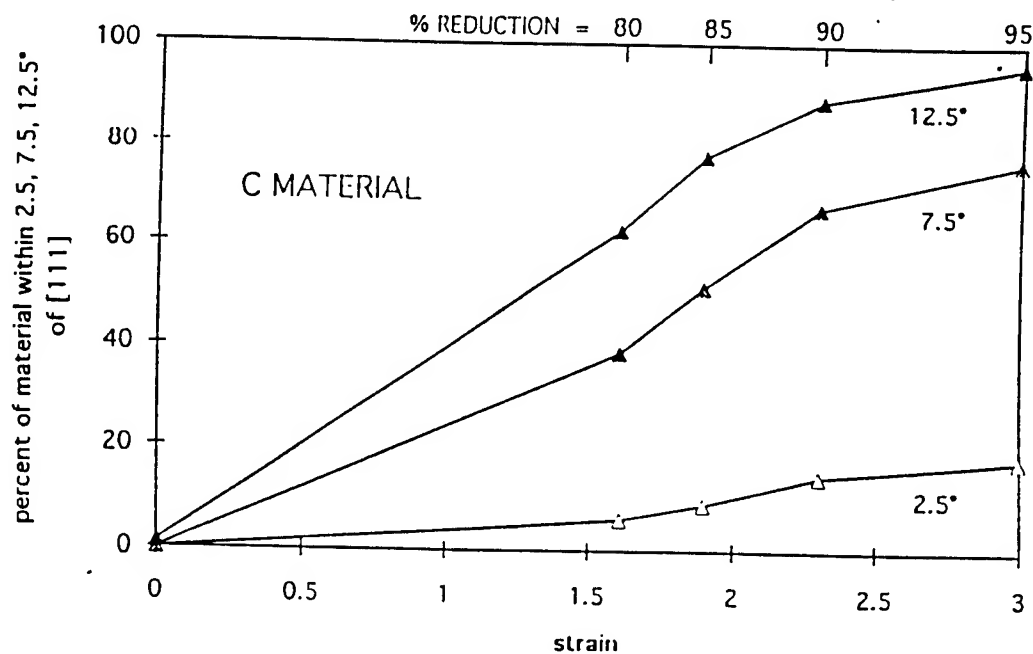


Figure 10. Intensity of the [111] texture in the C material after compression forging. Note that after a 95% reduction over 95% of the grains are oriented within 12.5° of [111]. Processing of material C was reported in ref. 2.

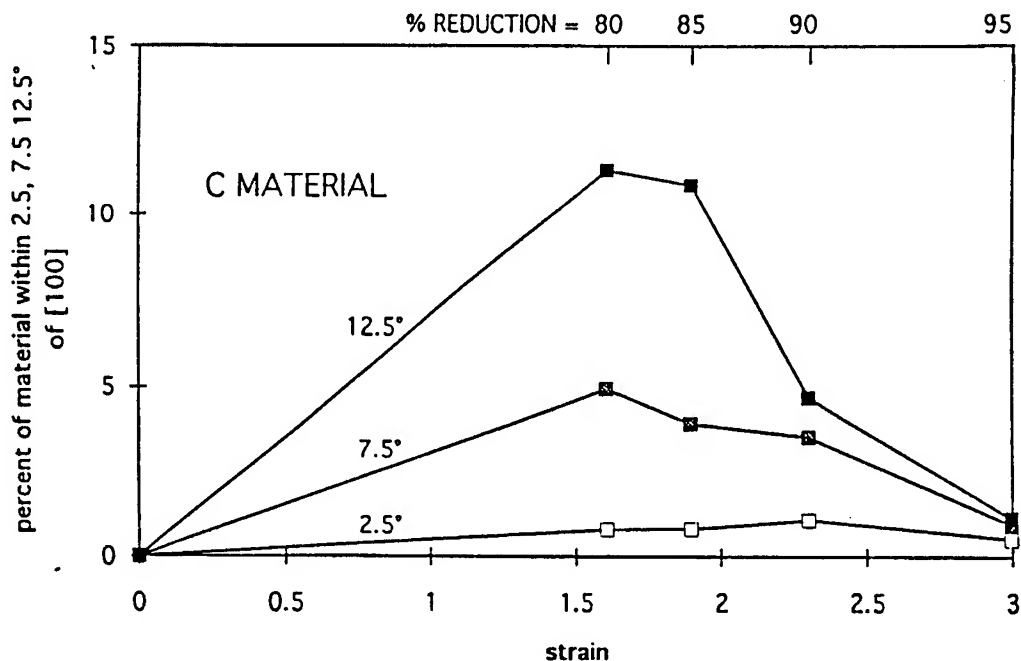


Figure 11. Intensity of the [100] texture in the C material after compression forging. Note that after a 95% reduction less than 2% of the grains are oriented within 12.5° of [100]. Data from ref. 2.

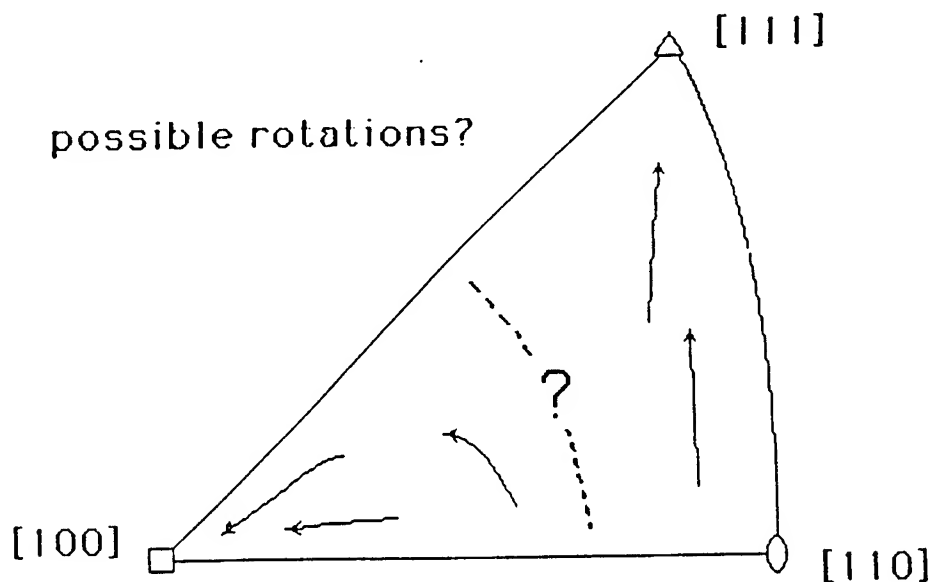


Figure 12. Schematic drawing of the basic stereographic orientation triangle, showing possible rotations of grains toward [111] or [100]. Establishment of the boundary separating these two rotations would permit prediction of the relative intensity of [111] and [100] components after compression forging. Data from reference 2.

## APPENDIX: Method of Analysis.

A typical set of data for a fiber textured material orientation quadrant is shown in Table 1. The data are arranged in the rows that can be thought of as latitude,  $\phi$ , and columns that are analogous to longitude,  $\theta$ , (figure A-1). These are intensities of the fiber axis plotted relative to the cubic crystal axes with [001] at the north pole (top row), [100] at the lower left hand corner, and [010] at the lower right hand corner. The [111] pole is located at a latitude  $\phi = 35.26^\circ$  and a longitude,  $\theta = 45^\circ$ . The matrix is symmetric about  $\theta = 45^\circ$ .

For bcc metals compression tends to form a crystallographic texture with two major components with  $\langle 111 \rangle$  and  $\langle 100 \rangle$  aligned with the fiber axis in an inverse pole figure (Figure 1 of the text). Although these two components are apparent, a quantitative figure for the relative strengths is not apparent.

One simple way of quantifying the texture is determine the fraction of the grains oriented within a fixed angle,  $\psi^*$ , of these two ideal orientations. For this report,  $\psi^* = 2.5^\circ, 7.5^\circ$  and  $12.5^\circ$  were taken as the fixed angle. To accomplish this, the following method of analysis was adopted. Each datum in the data set represents the intensity over a region of  $\Delta\theta = 5^\circ$  by  $\Delta\phi = 5^\circ$ , except at the north pole and at the equator where the  $\Delta\phi$  represented is  $2.5^\circ$ . The relative number of poles within  $\psi^*$  of hkl,  $N(\theta, \phi, \psi^*)$ , was calculated as

$$N(\theta, \phi, \psi^*) = \sum_{\theta} \sum_{\phi} [I(\theta, \phi) \cdot A(\theta, \phi) \cdot F(\theta, \phi, \psi^*)] \quad 1$$

where  $I(\theta, \phi)$  is the intensity datum at  $(\theta, \phi)$  (e.g. Table I),  $A(\theta, \phi)$  is the relative spherical area represented by the datum at  $\theta, \phi$ , and  $F(\theta, \phi, \psi^*)$  is the fraction of the spherical area within  $\psi^*$  of hkl.

The term,  $A(\theta, \phi)$ , is the spherical area represented by the datum. The area of a spherical zone bounded by the latitude  $\phi_1$  and  $\phi_2$  is, zone area =  $2\pi(\cos\phi_1 - \cos\phi_2)$ , where  $\phi_1$  and  $\phi_2$  are the bounding values of the spherical zone represented by the data at  $\phi$ . For all of the points between  $5^\circ \leq \phi \leq 85^\circ$ ,  $\phi_1 = \phi - 2.5^\circ$  and  $\phi_2 = \phi + 2.5^\circ$ . For the data at  $\phi = 0^\circ$ ,  $\phi_1 = 0^\circ$  and  $\phi_2 = 2.5^\circ$ . For  $\phi = 90^\circ$ ,  $\phi_1 = 87.5^\circ$  and  $\phi_2 = 90^\circ$ .

The area  $A(\theta, \phi)$  represented by a datum at  $\phi, \theta$  is

$$A(\theta, \phi) = (\sin\phi_1 - \sin\phi_2)\Delta\theta \quad 2$$

where  $\Delta\theta$  is  $5^\circ$  for  $5^\circ \leq \theta \leq 85^\circ$  and  $2.5^\circ$  for  $\theta = 0^\circ$  and  $90^\circ$ .

The term  $F(\theta, \phi, \psi^*)$  is the fraction of the spherical area represented by the data point that lies within an angle,  $\psi^*$ , of hkl. First the angles,  $\psi$ , between the orientations,  $(\theta, \phi)$  and the hkl pole were calculated using the relations for a spherical triangle as below:

For the [111],

$$\cos\psi = \sqrt{(1/3)}\sin\phi + \sqrt{(2/3)}\cos\phi\cos(45-\theta), \quad 3$$

for [001],

$$\cos\psi = 90-\phi, \quad 4$$

and for [100] and [010],

$$\cos\psi = \cos\phi\cos\theta \quad \text{and} \quad \cos\psi = \cos\phi\sin\theta. \quad 5$$

For [101],

$$\cos\psi = [(1/\sqrt{2})\sin\phi + (1/\sqrt{2})\cos\phi\cos\theta], \quad 6..$$

for [011]

$$\cos\psi = [(1/\sqrt{2})\sin\phi + (1/\sqrt{2})\cos\phi\sin\theta] \quad 7.$$

and for [001]

$$\cos\psi = [\cos\phi\cos(\theta-45)] \quad 8.$$

The calculated values  $\psi$  are listed in Table II. These were used to calculate the values of  $F(\theta, \phi, \psi^*)$  as

$$F(\theta, \phi, \psi^*) = 1 \text{ for } \psi \leq (\psi^* - 2.5^\circ) \quad 9.$$

(i.e. when the sector represented by  $(\theta, \phi)$  lies entirely within  $\psi^*$ ) or as

$$F(\theta, \phi, \psi^*) = 0 \text{ for } \psi \geq (\psi^* + 2.5^\circ) \quad 10.$$

(i.e. when the sector represented by  $(\theta, \phi)$  lies entirely outside of  $\psi^*$ ) or as

$$F(\theta, \phi, \psi^*) = (\psi^* + 2.5^\circ - \psi)/5^\circ \text{ for } (\psi^* - 2.5^\circ) \leq \psi \leq (\psi^* + 2.5^\circ) \quad 11.$$

(i.e. if the sector represented by  $(\theta, \phi)$  lies partially within  $\psi^*$ ).

The values of  $F(\theta, \phi, \psi^*)$  are given in Table III for  $\psi^* = 2.5^\circ, 7.5^\circ$  and  $12.5^\circ$ .

To normalize  $N(\theta, \phi, \psi_0)$  so that it represents the fraction of the grains within  $\psi^*$  of hkl, it is divided by the total number of grains in the hemisphere:

$$N_{\text{total}} = \sum_{\theta} \sum_{\phi} [I(\theta, \phi) \cdot A(\theta, \phi)], \quad 12.$$

which is equivalent to equation 1 with  $F(\theta, \phi, \psi^*) = 1$  for all elements.

Therefore the fraction of the grains oriented within  $\psi^*$  of hkl,  $f(\psi^*, \text{hkl})$ , is

$$\begin{aligned} f(\psi^*, \text{hkl}) &= N(\theta, \phi, \psi^*)/N_{\text{total}} \\ &= \sum_{\theta} \sum_{\phi} [I(\theta, \phi) \cdot A(\theta, \phi) \cdot F(\theta, \phi, \psi^*)] / \sum_{\theta} \sum_{\phi} [I(\theta, \phi) \cdot A(\theta, \phi)], \end{aligned} \quad 13.$$

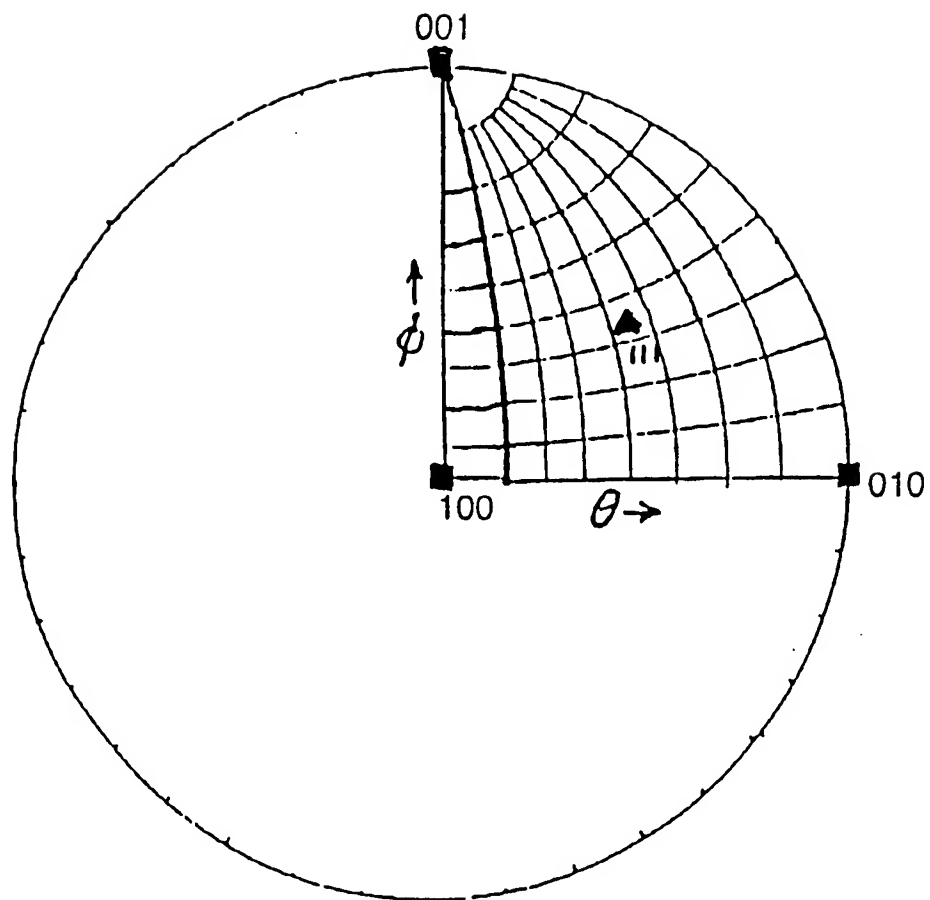


Figure A-1 Standard Cubic Projection, with [001] at the North Pole and [100] at the Center. Showing the Angles  $\theta$  and  $\phi$ . The [111] pole is located at  $\theta = 45^\circ$  and  $\phi = 35.26^\circ$

Table I A Typical Set of Data from the ODF Output.

$\phi$	0	5	10	15	20	25	30	35	40	45	50	55	60	65	70	75	80	85	90
90	763	762	762	762	762	762	762	762	762	763	762	762	762	762	762	762	762	762	763
85	617	618	618	615	612	609	561	636	633	630	633	636	561	609	612	615	618	618	617
80	290	96	92	97	113	119	128	135	118	720	118	135	128	119	113	97	92	96	290
75	48	47	47	89	98	135	132	17	33	33	33	17	132	135	98	89	47	47	48
70	29	29	40	54	56	31	15	18	34	33	34	18	15	31	56	54	40	29	29
65	24	23	33	41	19	12	14	48	24	12	24	48	14	12	19	41	33	23	24
60	8	21	22	13	8	19	26	32	58	26	58	32	26	19	8	13	22	21	8
55	17	7	3	6	3	28	16	60	70	116	70	60	16	28	3	6	8	7	17
50	9	10	16	2	20	21	26	82	113	102	113	82	26	21	20	2	16	10	9
45	15	10	10	1	7	17	55	291	372	192	372	291	55	17	7	1	10	10	15
40	9	10	2	2	8	36	69	90	882	731	882	90	69	36	8	2	2	10	9
35	17	5	6	6	18	49	294	267	894	875	894	267	294	49	18	6	6	5	17
30	8	22	3	16	15	84	118	192	911	726	911	192	118	84	15	16	3	22	8
25	24	31	14	15	64	104	100	117	306	93	306	117	100	104	64	15	14	31	24
20	29	57	35	47	39	37	60	27	51	26	51	27	60	37	39	47	35	57	29
15	48	96	26	33	23	35	16	18	8	13	8	18	16	35	23	33	26	96	48
10	290	119	33	30	20	14	12	3	2	2	2	3	12	14	20	30	33	119	290
5	617	629	119	96	54	31	21	9	10	10	10	9	21	31	54	96	119	629	617
0	763	617	290	48	29	24	8	17	9	15	9	17	8	24	29	48	290	617	763

Table II Angles,  $\psi$ , between Various Orientations and [hkl]

<u>Angles, <math>\psi</math>, from [111]</u>		$\psi = \cos^{-1}[(1/\sqrt{3})\sin\phi + \sqrt{(2/3)}\cos\phi\cos(\theta - 45)]$				
phi	theta/	45°	40°/50°	35°/55°	30°/60	25°/65°
20		15.264	15.887	17.624	20.186	23.300
25		10.264	11.133	13.405	16.508	20.054
30		5.264	6.739	9.923	13.666	17.61
35		0.264	4.097	8.179	12.259	16.33
40		4.736	6.171	9.219	12.768	16.49
45		9.736	10.454	12.359	15.000	18.051
50		14.736	15.179	16.436	18.336	20.698
55		19.736	20.036	20.909	22.286	24.074

<u>Angles, <math>\psi</math>, from [100] and [010]</u>		$\psi = \cos^{-1}[\cos\phi\cos\theta]$ or $= \cos^{-1}[\cos\phi\sin\theta]$				
phi	theta /	0°/90°	5°/85°	10°/80°	15°/75°	20°/70°
0		0	5.000	10.000	15.000	20.000
5		5	7.0666	11.169	15.793	20.591
10		10	11.169	14.106	17.964	22.269
15		15	15.793	17.964	21.091	24.814
20		20	20.591	22.269	24.814	27.991

<u>Angles, <math>\psi</math>, from [001],</u>		$\psi = \phi$
phi	all theta values	
0	0.000	
5	5.000	
10	10.000	
15	15.000	
20	20.000	

<u>Angles, <math>\psi</math>, from [101] and [011]</u>		$\psi = \cos^{-1}[(1/\sqrt{2})\sin\phi + (1/\sqrt{2})\cos\phi\cos\theta]$ or $= \cos^{-1}[(1/\sqrt{2})\sin\phi + (1/\sqrt{2})\cos\phi\sin\theta]$					
phi\theta	0,90	5,85	10,80	15,75	20,70	25,65	30,60
25	20	20.400	21.572	23.385			
30	15	15.507	16.937	19.081	21.720		
35	10	10.703	12.576	15.188	18.218	21.480	
40	5	6.209	8.898	12.112	15.522	19.031	
45	0	3.535	7.067	10.591	14.106	17.606	21.07
50	5	6.031	8.393	11.862	14.354	17.520	20.72
55	10	10.497	11.862	13.835	16.189	18.722	
60	15	15.295	16.146	17.469	19.160	21.124	
65	20	20.190	20.747	21.641			

<u>from [110]</u>		$\psi = \cos^{-1}[\cos\phi\cos(\theta-45)]$			
phi\theta	45	40,50	35,55	30,60	25,65
0	0	5	10	15	20
5	5	7.061	11.117	15.793	20.591
10	10	11.117	14.106	17.963	22.269
15	15	15.793	17.963	21.091	
20	20	20.591	22.269		



Table III Fraction of Data,  $F(\theta, \phi, \psi^*)$ , within  $\psi^* = 2.5^\circ, 7.5^\circ$  and  $12.5^\circ$  of  $[hkl]$

<u>[111], <math>\psi^* = 2.5^\circ</math></u>			
phi	theta/	45°	40°/50°
30		0.0	0.0
35		0.9472	0.1806
40		0.05288	0.0
45		0.0	0.0

<u>[100] and [010], <math>\psi^* = 2.5^\circ</math></u>			
phi	theta/	0/90°	5/85°
0		1.0	0
5		0.0	0.0

<u>[001], <math>\psi^* = 2.5^\circ</math></u>		
phi	all theta values	
0	1.0	
5	0.0	

<u>[111] <math>\psi^* = 7.5^\circ</math></u>					
phi	theta/	45°	40/50°	35/55°	
25		0.0	0.0	0.0	0.0
30		0.9472	0.6522	0.0154	0.0
35		1.0	1.0	0.3642	0.0
40		1.0	0.7658	0.1562	0.0
45		0.053	0.0	0.0	0.0

<u>[100] and [010], <math>\psi^* = 7.5^\circ</math></u>				
phi	theta/	0/90°	5/85°	80/10°
0		1.0	1.0	0.0
5		1.0	0.867	0.0
10		0.0	0.0	0.0

<u>[001], <math>\psi^* = 7.5^\circ</math></u>		
phi	all theta values	
0	1.0	
5	1.0	
10	0.0	

Table III (continued)

[111],  $\psi^* = 12.5^\circ$

phi	theta/	45°	40/50°	35/55°	30/60
20	0.0	0.0	0.0	0.0	0.0
25	0.9472	0.7734	0.319	0.0	0.0
30	1.0	1.0	1.0	0.2668	0.0
35	1.0	1.0	1.0	0.5482	0.0
40	1.0	1.0	1.0	0.4460	0.0
45	1.0	0.9092	0.5282	0.0	0.0
50	0.0528	0.0	0.0	0.0	0.0
55	0.0	0.0	0.0	0.0	0.0

[100] and [010]  $\psi^* = 12.5^\circ$

phi	theta/	0/90°	5/85°	10/80°	15/75°
0	1.0	1.0	1.0	0.0	0.0
10	1.0	1.0	0.7662	0.0	0.0
15	1.0	0.7662	0.1788	0.0	0.0
20	0.0	0.0	0.0	0.0	0.0

[001],  $\psi^* = 12.5^\circ$

phi	all theta values
0	1.0
5	1.0
10	1.0
15	0.0

[101] & [011]  $\psi^* = 2.5^\circ$

phi\theta	0,90°	5,85°	10,80°
40	0	0	0
45	1.0	0.293	5
50	0	0	0

[110]  $\psi^* = 2.5^\circ$

phi\theta	45°	40,50°
0	1	0
0	0	

[101] & [011]  $\psi^* = 7.5^\circ$

phi\theta	0,90°	5,85°	10,80°	15,75°
35	0	0	0	0
40	1	0.7582	0.2204	0
45	1	1	0.5866	0
50	1	0.7398	0.3214	0

[110]  $\psi^* = 7.5^\circ$

phi\theta	45°	40,50°	35,55°
0	1	1	0
5	1	0.5878	0
10	1	0	0
15	0	0	0

Table III (continued)

<u>[101] &amp; [011]</u>		$\psi^* = 12.5^\circ$				
phi\theta		0,90°	5,85°	10,80°	15,75°	20,80      25,85
30	0	0	0	0	0	
35	1	0.8594	0.4854	0	0	
40	1	1	1	0.5776	0	
45	1	1	1	0.8818	0.1788	0
50	1	1	1	0.6276	0.1292	0
55	1	0.9006	0.6276	0.2330	0	
60	0	0	0	0		

<u>[110]</u>		$\psi^* = 12.5^\circ$			
phi\theta		45°	40,50°	35,55°	30,60°
0	1	1	1	0	
5	1	1	0.7766	0	
10	1	0.7766	0.1788	0	
15	0	0	0	0	

<u>[101] &amp; [011]</u>		$\psi^* = 17.5^\circ$					
phi\theta		0,90°	5,85°	10,80°	15,75°	20,80	25,85
25	0	0	0	0			
30	1	0.8986	0.6126	0.18387	0		
35	1	1	1	0.9624	0.3464	0	
40	1	1	1	1	0.8956	0.1938	0
45	1	1	1	1	1	0.4788	0
50	1	1	1	1	1	0.4960	0
55	1	1	1	1	0.7622	0.2556	0
60	1	0.9410	0.7708	0.5062	0.1680	0	
65 0	0	0	0	0	0		

<u>[110]</u>		$\psi^* = 17.5^\circ$				
phi\theta		45°	40,50°	35,55°	30,60°	25,65
0	1	1	1	1	0	
5	1	1	1	0.8414	0	
10	1	1	1	0.4074	0	
15	1	0.8414	0.4074	0		
20	0	0	0			

# A STUDY OF A DATA-PARALLEL IMPLEMENTATION OF AN IMPLICIT SOLUTION OF THE 3D NAVIER-STOKES EQUATIONS

David E. Hudak  
Associate Professor  
Department of Mathematics and Computer Science

Ohio Northern University  
Ada,, OH 45810

Final Report for:  
Summer Faculty Research Program  
Wright Laboratory  
Aeromechanics Division

Sponsored by:  
Air Force Office of Scientific Research  
Bolling Air Force Base, DC

And

Wright Laboratory

August, 1997

# A STUDY OF A DATA-PARALLEL IMPLEMENTATION OF AN IMPLICIT SOLUTION OF THE 3D NAVIER-STOKES EQUATIONS

David E. Hudak  
Associate Professor  
Department of Mathematics and Computer Science

Ohio Northern University

A preliminary parallel version of the FDL3DI application from Wright Laboratory was developed using MPI on an IBM SP2. This report describes the overall design of the parallel code and estimates the performance of the code. For this data-parallel implementation, a single grid is broken into subgrids and each subgrid is assigned to a separate processor. The boundary points are exchanged between processors as necessary. Parallel I/O features were written which produce identical results for sequential and parallel restart files, allowing restart files to be moved between sequential and parallel platforms.

This approach required extensive modifications to the source but allows for high levels of parallelism. Experimental runs show that the solution for a grid of size  $140 \times 140 \times 140$  exhibits a speedup of 2.9 on four processors. These preliminary results demonstrate that parallel systems can provide significant performance improvements for this application.

# A STUDY OF A DATA-PARALLEL IMPLEMENTATION OF AN IMPLICIT SOLUTION OF THE 3D NAVIER-STOKES EQUATIONS

David E. Hudak

## 1 Introduction

The potential of massively parallel computer systems (MPPs) for the solution of large computational aeroscience problems has yet to be realized. In order for an application to attain high performance on a parallel computer it is essential that the problem is decomposed into subproblems such that the work is shared among the processors. This decomposition of a single problem into subproblems exploits *data parallelism*, and is achieved by splitting the global data set among the processors in such a way that the work load is distributed equitably, communication cost is kept as small as possible and the numerical accuracy of the problem is not compromised. However, the goals of balancing the work load, minimizing communication and maintaining accuracy within an application are often at odds, complicating the task.

In this project, I performed performance analysis and implemented I/O functionality for a data-parallel version of the FDL3DI application currently under development at the the Aeromechanics Division of Wright Laboratory. FDL3DI solves the three-dimensional Navier-Stokes equations using the approximate-factorization algorithm of Beam and Warming in conjunction with a Newton subiteration procedure to enhance the accuracy for rapid fluid motion. The parallel version of the code was written using the MPI message-passing library on an IBM SP2. The sample problem was a model of uniform flow over a flat plate.

This report is organized as follows. The sequential version of the FDL3DI application is examined and performance improvements are suggested in Section 2. The implementation of the data-parallel solution is discussed in Section 3. Experimental runs on the IBM SP2 are described in Section 4.

## 2 Performance Estimate of Sequential Code

### 2.1 Profiling

In order to make recommendations on the improvement of sequential performance, statistics on the relative performance of subroutines were generated for the code. In order to understand the organization of the code, the FORGE Explorer [1] application was used to analyze the code. Explorer reported the call tree for the entire application. This information is included in Appendix A.

Two basic methods of profiling were used. First, PC-sampling was used on the CRAY C90 and the Silicon Graphics workstations. Varying grid sizes and numbers of time steps were used to assess the impact of workload variation on the relative performance of sections of the code. The code was found to maintain relative performance independent of the size of the grid or number of time steps. Table 1

Machine	Routine	Hit Count
CRAY	RHSXZ	11%
CRAY	SQRT	9.5%
CRAY	VCROX	6.3%
CRAY	VCROSY	5.9%
CRAY	VCROZ	5.8%
SGI	VCROX	13.7%
SGI	RHSXZ	10.7%
SGI	SQRT	8.3%
SGI	VCROSY	6.6%
SGI	VCROZ	6.5%

Table 1: Performance Results from PC-Sampling Profiles.

Routine	Number of Calls
SQRT	5867355
RHSXZ	195
VCROZ	195
VCROSY	195
SPENTA	1170
TXIRHS	195
VCROX	195

Table 2: Performance Results from Basic-Block Count Profile on the SGI.

summarizes important routines.

Second, in order to more accurately determine the behavior of the routines in the code, pixie was used to obtain a basic-block count profile of the code on the Silicon Graphics machines. The grid size for this experiment was  $41 \times 41 \times 41$ , so there were 39 interior points along each dimension. This information is summarized in Table 2.

## 2.2 Analysis

Due to the large impact of sqrt time on overall performance, the calls to sqrt were examined. At several locations in the code, a call to sqrt was found to be redundant since the value computed,  $(1./\text{sqrt}(2.))$ , is a constant. I replaced the call to sqrt with the value of the constant and again used basic-block counting to obtain the results in Table 3.

Using this data, it is possible to model the number of calls made to sqrt. Let  $N$  be the number of interior grid points along one dimension (for the  $41 \times 41 \times 41$  grid,  $N = 39$ ). The total number of calls made to sqrt per time step is  $19N^3 + 30N^2 + 20N$ . Clearly the 19 occurrences of sqrt which are called cubic-ally on  $N$  are the dominant factors.

The space requirements for the application were generated by examining the data storage in COMMON blocks. The storage can be approximated by  $33N^3 + 6N^2 + 5N + 100$ . Again, the 33 cubic terms

Routine	Number of Calls
SQRT	5866575
RHSXZ	195
VCROSZ	195
VCROSY	195
SPENTA	1170
TXIIRHS	195
VCROSX	195

Table 3: Basic-Block Count Profile on the SGI without some sqrt calls.

dominate.

## 2.3 Algorithmic Restructuring

Restructuring of computations is possible to reduce the total number of calls to the sqrt function.

1. **Computation involving GAM, P, and RHO.** Computations involving Gamma, P, and RHO occur in TMSTEP, SPECTX, SPECTY, SPECTZ, SDIAGX, SDIAGY and SDIAGZ. These computations can be consolidated. The number of calls to sqrt would be reduced from  $6N^3$  to  $N^3$ , a savings of  $5N^3$ . The total number of calls to sqrt would be reduced by 25%, for an estimated savings of 2.5% of the total execution time. The overhead involves increasing storage by  $N^3$ . This would require an approximate 3% increase in overall storage. This restructuring will produce the greatest reduction in calls to sqrt. If the coding is feasible, I would recommend it.
2. **Computation involving XMU.** Computations involving XMU occur in SWEEPJ1, SWEEPI, SWEEPK and SWEEPJ2. These can be consolidated by expanding XMU to a three-dimensional array. The number of calls to sqrt will be diminished from  $4N^3$  to  $N^3$ , a savings of  $3N^3$ . The total number of calls to sqrt would be reduced by 15%, for an estimated savings of 1.5% of the total execution time. The overhead involves increasing storage for XMU from  $N^2$  to  $N^3$ . This would require an approximate 3% increase in overall storage. Again, if the coding is feasible, I would recommend it.
3. **Removal of constant calculation.** Computations of  $(1./\text{sqrt}(2.))$  occur in routines NIHRs, PIRHS, TXIIRHS and TZETRHS. Removal of these calculations will only save  $4N$  calls to sqrt per time step. However, there is no significant storage overhead involved in this optimization. I recommend its inclusion.
4. **Other possibility.** Optimizations similar to the ones described above may be possible on the ETAX/ETAY computations in NIHRs and PIHRs.

If all optimizations mentioned above were incorporated, the number of calls to sqrt would decrease by 40% overall and the execution time could be expected to drop by 4%. The additional storage requirements



would increase overall storage by 6%. Since storage will be adequate on the SP2 to accommodate these restructurings, I urge their consideration.

### 3 Parallelization Strategy

Parallelization of an application for a message-passing system such as the IBM SP-2 involves two decisions. First, a partition must be defined which allocates portions of the global data sets to the local memories of individual processors. Second, a format for messages must be established to ensure that processors are sending information according to the correct protocol, i.e., the right data to the right processor.

#### 3.1 Partitioning Strategy

Valid partitions are required to satisfy the following conditions similar to [7] [6].

1. Tessellation. The partition must tile the data set so that each point in the iteration space is assigned to exactly one processor.
2. Identical by translation. Each partition should be the image of any other one by a translation, except for parts located near boundaries of the iteration space. This property ensures reasonable load balancing and efficient code generation.
3. Straight Line Perimeters. In order to ensure tiling and simplify code generation, the perimeter of each part is composed of planes.
4. Symmetry. This requirement is satisfied by most shapes that tessellate and are simple to code.

The partitioning strategy chosen for this application was an extension of the multipartitioning strategy devised by Smith et. al. [9] and examined by Jun [8]. Assume that a  $N \times N \times N$  is being partitioned for  $P$  processors. In this case, the algorithm creates  $P^2$  different partitions, each of size

$$\left\lceil \frac{P}{N} \right\rceil \times \left\lceil \frac{P}{N} \right\rceil \times N \quad (1)$$

as illustrated for  $P = 4$  in Fig. 1. Each of the major three-dimensional arrays, X, Y, Z, U, V, W, P, RHO and EDDY, are partitioned in this manner.

The major computation in this problem centers around dimensional sweeps. For example, a sweep along the I dimension would compute  $U(1,1,1)$ ,  $U(2,1,1)$ ,  $U(3,1,1)$ , etc. This partition allows for all processors to simultaneously work during the sweeps along the J and K dimensions. The sweep along the I dimension remains sequentialized for this implementation of the code.

In order to automate the process of assigning data parts to processors, the parts are numbered in a two-dimensional fashion as demonstrated by the  $NB$  and  $JB$  labels in Fig. 1. A part at location  $NB = x$  and  $JB = y$  for  $P$  processors is assigned to processor  $pid$ , where

$$pid = \text{mod}(x + y, P) \quad (2)$$

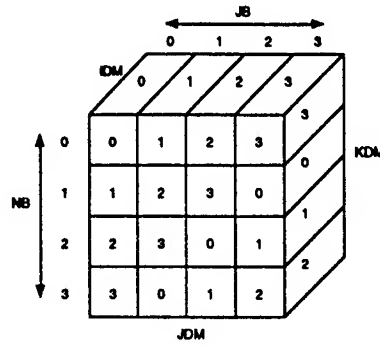


Figure 1: 2D Multipartitioning Strategy

Border	Expression for $NB$	Expression for $JB$
Top ( $K = 1$ )	0	$pid$
Bottom ( $K = KDM$ )	$NB$	$mod(pid + 1, P)$
Left ( $J = 1$ )	$pid$	0
Right ( $J = JDM$ )	$mod(pid - 1, P)$	$JB$

Table 4: Expressions for calculating border parts.

In addition, the global boundaries can be computed from the processor identifier,  $pid$ , as described in Table 4. These boundary expressions were used in the periodic boundary conditions of the flat-plate problem.

### 3.2 Interprocessor Communication

Interprocessor communication occurs during the sweeps along the parallelized dimensions. In order to compute the correct answer, each processor must know whom it is sending data to, what data to send and how it should be packed into messages. Let us consider each question individually.

In the partition illustrated by Fig. 1, sweeps along either parallelized dimension result in cyclical communication patterns. For example, in a sweep along the K-dimension, processor 0 always sends to processor 1, processor 1 always sends to processor 2, and so on as illustrated in Fig. 2. Note that for dimensional sweeps in the opposite direction (e.g., sweeping "down" along the K dimension and then sweeping "up") the communication pattern is reversed.

The amount of data transmitted between processors may be different for the dimensional sweep along the K dimension as along the J dimension. In each case, the data transmitted (the border of the part) takes the shape of a two-dimensional plane. For communication along the K dimension, this plane has size  $\lceil \frac{JDM}{P} \rceil \times IDM$  and has size  $\lceil \frac{KDM}{P} \rceil \times IDM$  for sweeps along the J dimension. These borders must be transmitted for each of the nine three-dimensional arrays.

The current implementation of the code uses the MPI library for message passing [5]. In this implementation, one MPI message consists of a vector from each array involved in the computation. This means that the average message size is  $9 \times IDM$  and approximately  $\lceil \frac{N}{P} \rceil$  messages are sent for a general

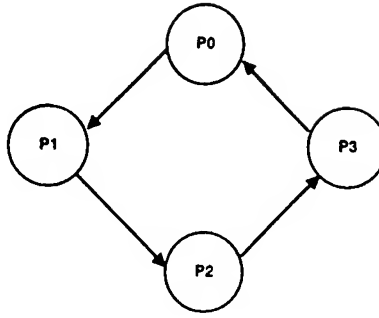


Figure 2: Communication Patterns for Parallel Sweeps

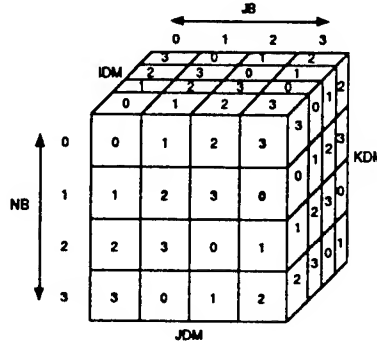


Figure 3: 3D Multipartitioning Strategy

$N \times N \times N$  array in order to communicate across one border.

It may be more efficient to use MPI datatypes for communication. For example, the periodic boundary conditions in the flat-plate problem were coded using an MPI datatype for a two-dimensional border. Using this border, I was able to send 9 messages of size  $\lceil \frac{N}{P} \rceil \times IDM$  as opposed to the strategy discussed in the preceding paragraph. This method greatly reduces the number of message sent and will reduce message start-up overhead.

### 3.3 Parallel I/O and Postprocessing

I/O capabilities were built into this version of the code. Each processor currently reads in the entire restart file and updates its portion of the global data set. When computation is finished, each processor writes its own portion of the global data set into an output file. These data sets are then reassembled using a postprocessor into a single output file. This parallel I/O and postprocessor produce identical results for sequential and parallel restart files, allowing restart files to be moved between sequential and parallel platforms.

### 3.4 Potential 3D Partitions

Although not implemented, it is possible to extend the partitioning strategy to three dimensions. The partition is illustrated in Fig. 3. This would allow for more computation to be parallelized and hence

Processors	$N = 41$	$N = 61$	$N = 81$	$N = 100$	$N = 140$
1	4.5	17.7	45.4	92.4	261
2	2.3	9.0	18.8	37.6	120
3	2.2	8.1	18.1	35.6	100
4	3.2	8.6	18.8	34.2	90

Table 5: Timing in Seconds per Timestep of Flat Plate Problem

should generate higher levels of parallel efficiency. However, this benefit must be weighed against the amount of communication and the programming difficulty.

When evaluating computation and communication requirements of such partitions, it is useful to compare the volume of the partitions (which is proportional to the amount of computational load) and the surface area of the partitions (which is proportional to the amount of interprocessor communication) [4]. For the two-dimensional partitioning in Fig. 1 involving an  $N \times N \times N$  array split among  $P$  processors, the volume per part is  $\frac{N}{P} \times \frac{N}{P} \times N$  and the total volume for all  $P$  parts per processor is  $\frac{N^3}{P}$ . The surface area for an interior part is  $4 \times \frac{N}{P} \times N$  and, at  $P$  parts per processor has a total of  $4N^2$ . For the three-dimensional partitioning in Fig. 3, the volume per part is  $\frac{N}{P} \times \frac{N}{P} \times \frac{N}{P}$  and the total volume for all  $P^2$  parts per processor is again  $\frac{N^3}{P}$ . The surface area for an interior part is  $6 \times \frac{N}{P} \times \frac{N}{P}$  and, at  $P^2$  parts per processor has a total of  $6N^2$ .

From the above analysis, it is clear that the three-dimensional partitioning will generate considerably more communication (50% more). In addition, given that the experimental results in Section 4 demonstrate that a fairly large part size is required to generate good parallel efficiency, I recommend staying with the current partitioning strategy.

## 4 Performance Analysis of Parallel Code

A problem was generated simulating uniform flow over a flat plate. This problem was run in parallel on an IBM SP2 [3] [10] [2]. The execution time is given in Table 5. Speedup, defined as the ratio of sequential execution time to parallel execution time for an identical problem, is listed in Table 6. Parallel efficiency, defined as the speedup divided by the number of processors, is given in Table 7. Note that both speedup and parallel efficiency improve as the problem size increases. This indicates that this code will scale well to larger test cases and greater numbers of processors, provided that the size of each part remains large.

## 5 Conclusion and Future Work

In this report I have demonstrated that FDL3DI can be parallelized using a data-parallel decomposition across processors. There are a collection of items which must be investigated to allow for maximum performance. These remain important areas for future work. First, algorithmic restructuring which reduces redundant computations as described in Section 2.3 should be examined. In addition, it may be

Processors	$N = 41$	$N = 61$	$N = 81$	$N = 100$	$N = 140$
1	1.00	1.00	1.00	1.00	1.00
2	1.95	1.96	2.41	2.46	2.18
3	2.05	2.19	2.51	2.60	2.61
4	1.40	2.06	2.41	2.70	2.90

Table 6: Parallel Speedup of Flat Plate Problem

Processors	$N = 41$	$N = 61$	$N = 81$	$N = 100$	$N = 140$
1	100%	100%	100%	100%	100%
2	97.5%	98.0%	120%	123%	109%
3	68.3%	73.0%	83.6%	86.7%	87.0%
4	35.0%	51.5%	60.3%	67.5%	72.5%

Table 7: Parallel Efficiency of Flat Plate Problem

possible to gain additional performance in the sqrt sections of the code by using optimized sqrt functions. The IBM SP2 has two different sqrt libraries: the IEEE Math Library (libm.a) and the System V Math Library (libmsaa.a).

The parallel efficiency of the code can be improved in multiple ways. First, the data alignment of the code can be improved. Current data alignment is consecutive by partition number. Alignment along the I dimension will improve performance. Second, the inclusion of MPI data types as described in Section 3.2 will improve parallel efficiency as well. Finally, if additional parallelism is required, three-dimensional partitioning could be used.

## 6 Acknowledgements

Thanks to Miguel Visbal and Joseph Shang for giving me the opportunity to work with the FIMC research group. Thanks to Drs. Sadayappan, Visbal, Tomko and Pan for their insight and advice. Thanks also to my student, Mark Fitzpatrick, for providing initial prototypes of the preprocessor and postprocessor. Additional computer resources were provided by the Ohio Supercomputer Center, Columbus OH.

# A FDL3DI Source Code Charts

Call Subchain... {	Node	Status
1:	NSCODE	
2:	INITIA	
3:	INITIA/DO 1 L	
4:	INITIA/DO 1 K	
5:	INITIA/DO 1 J	
6:	INITIA/DO 1 I	
7:	INITIA/DO 2 K	
8:	INITIA/DO 2 J	
9:	INITIA/DO 2 I	
10:	INITIA/DO 21 J	
11:	INITIA/DO 21 I	
12:	INITIA/DO 3 M	
13:	INITIA/DO 3 L	
14:	INITIA/DO 3 I	
15:	METRIC1	
16:	METRIC1/DO 1 K	
17:	METRIC1/DO 1 J	
18:	METRIC1/DO 1 I	
19:	METRIC1/DO 2 II	
20:	METRIC1/DO 21 K	
21:	METRIC1/DO 21 J	
22:	METRIC1/DO 3 II	
23:	METRIC1/DO 31 K	
24:	METRIC1/DO 31 I	
25:	METRIC1/DO 4 II	
26:	METRIC1/DO 41 J	
27:	METRIC1/DO 41 I	
28:	TNSTEP	
29:	TNSTEP/DO 1 K	
30:	TNSTEP/DO 1 J	
31:	TNSTEP/DO 1 I	
32:	TNSTEP/DO 2 K	
33:	TNSTEP/DO 2 J	
34:	TNSTEP/DO 21 I	
35:	TNSTEP/DO 22 I	
36:	TNSTEP/DO 3 K	
37:	TNSTEP/DO 3 J	
38:	TNSTEP/DO 31 I	
39:	TNSTEP/DO 32 I	
40:	TNSTEP	<See 28>
41:	UPDTQO	
42:	UPDTQO/DO 1 K	
43:	UPDTQO/DO 1 J	
44:	UPDTQO/DO 1 I	
45:	TNSTEP	<See 28>
46:	SWEEPJ1	
47:	SWEEPJ1/DO 1 JF	
48:	CXNU	
49:	CXNU/DO 1 II	
50:	CXNU/DO 11 I	
51:	RHSXZ	
52:	RHSXZ/DO 1 L	
53:	RHSXZ/DO 1 K	
54:	RHSXZ/DO 1 I	
55:	RHSXZ/DO 11 K	
56:	RHSXZ/DO 11 I	
57:	RHSXZ/DO 2 K	
58:	RHSXZ/DO 2 I	
59:	RHSXZ/DO 21 L	
60:	RHSXZ/DO 21 K	
61:	RHSXZ/DO 21 I	
62:	RHSXZ/DO 27 K	
63:	RHSXZ/DO 27 I	
64:	RHSXZ/DO 28 K	
65:	RHSXZ/DO 28 I	
66:	RHSXZ/DO 29 L	
67:	RHSXZ/DO 29 K	
68:	RHSXZ/DO 29 I	
69:	RHSXZ/DO 31 K	
70:	RHSXZ/DO 31 I	
71:	RHSXZ/DO 32 K	
72:	RHSXZ/DO 32 I	
73:	RHSXZ/DO 33 L	
74:	RHSXZ/DO 33 K	
75:	RHSXZ/DO 33 I	
76:	VCROSY	
77:	VCROSY/DO 1 K	
78:	VCROSY/DO 1 I	
79:	VCROSY/DO 2 K	
80:	VCROSY/DO 21 I	
81:	VCROSY/DO 3 L	
82:	VCROSY/DO 31 K	
83:	VCROSY/DO 31 I	
84:	VCROSY/DO 4 L	
85:	VCROSY/DO 4 K	
86:	VCROSY/DO 4 I	
87:	CONVRT	
88:	CONVRT/DO 1 II	
89:	CONVRT/DO 11 I	
90:	DAMPZ	
91:	DAMPZ/DO 5 K	
92:	DAMPZ/DO 5 I	
93:	DAMPZ/DO 1 L	
94:	DAMPZ/DO 2 K	
95:	DAMPZ/DO 2 I	
96:	DAMPZ/DO 3 I	
97:	DAMPZ/DO 4 I	
98:	SDAMPZ	
99:	SPECZ	
100:	SPECZ/DO 1 K	
101:	SPECZ/DO 1 I	
102:	SPECZ/DO 2 K	
103:	SPECZ/DO 2 I	
104:	SDAMPZ/DO 1 I	
105:	SDAMPZ/DO 11 K	
106:	SDAMPZ/DO 12 K	
107:	SDAMPZ/DO 2 I	
108:	SDAMPZ/DO 4 I	
109:	SDAMPZ/DO 4 K	
110:	SDAMPZ/DO 5 I	
111:	SDAMPZ/DO 6 I	
112:	SDAMPZ/DO 6 K	
113:	SDAMPZ/DO 7 I	
114:	SDAMPZ/DO 8 I	
115:	SDAMPZ/DO 9 K	
116:	SDAMPZ/DO 10 K	
117:	RHSSUB	
118:	RHSSUB/DO 1 K	
119:	RHSSUB/DO 1 I	
120:	RHSSUB/DO 2 L	

Call Graph of FDL3DI generated from FORGExplorer

```

121: | | | | RHSSUB/DO 2 K
122: | | | | RHSSUB/DO 2 I
123: | SWEEPI
124: | | SWEEPI/DO 1 IF
125: | | | CXNU1
126: | | | | CXNU1/DO 1 K
127: | | | | CXNU1/DO 1 J
128: | | | VCROSI
129: | | | | VCROSI/DO 1 K
130: | | | | VCROSI/DO 1 J
131: | | | | VCROSI/DO 2 K
132: | | | | VCROSI/DO 21 J
133: | | | | VCROSI/DO 3 L
134: | | | | VCROSI/DO 31 K
135: | | | | VCROSI/DO 31 J
136: | | | | VCROSI/DO 4 L
137: | | | | VCROSI/DO 4 K
138: | | | | VCROSI/DO 4 J
139: | SWEEPK
140: | | SWEEPK/DO 1 KF
141: | | | CXNU
142: | | | RHSY
143: | | | | RHSY/DO 9 J
144: | | | | RHSY/DO 9 I
145: | | | | RHSY/DO 1 J
146: | | | | RHSY/DO 1 I
147: | | | | RHSY/DO 2 L
148: | | | | RHSY/DO 2 J
149: | | | | RHSY/DO 2 I
150: | | | | RHSY/DO 21 J
151: | | | | RHSY/DO 21 I
152: | | | | RHSY/DO 22 J
153: | | | | RHSY/DO 22 I
154: | | | | RHSY/DO 23 L
155: | | | | RHSY/DO 23 J
156: | | | | RHSY/DO 23 I
157: | | | VCROSZ
158: | | | | VCROSZ/DO 1 J
159: | | | | VCROSZ/DO 1 I
160: | | | | VCROSZ/DO 2 J
161: | | | | VCROSZ/DO 21 I
162: | | | | VCROSZ/DO 3 L
163: | | | | VCROSZ/DO 31 J
164: | | | | VCROSZ/DO 31 I
165: | | | | VCROSZ/DO 4 L
166: | | | | VCROSZ/DO 4 J
167: | | | | VCROSZ/DO 4 I
168: | | | COEVRT
169: | | | DAMPX
170: | | | | DAMPX/DO 5 J
171: | | | | DAMPX/DO 5 I
172: | | | | DAMPX/DO 1 L
173: | | | | DAMPX/DO 2 J
174: | | | | DAMPX/DO 2 I
175: | | | | DAMPX/DO 3 J
176: | | | | DAMPX/DO 4 J
177: | | | DAMPY
178: | | | | DAMPY/DO 5 J
179: | | | | DAMPY/DO 5 I
180: | | | | DAMPY/DO 1 L

```

<See 48>

<See 87>

```

181: | | | | DAMPY/DO 2 J
182: | | | | DAMPY/DO 2 I
183: | | | | DAMPY/DO 3 I
184: | | | | DAMPY/DO 4 I
185: | | | SDAMPX
186: | | | | SPECX
187: | | | | SPECX/DO 1 J
188: | | | | SPECX/DO 1 I
189: | | | | SPECX/DO 2 J
190: | | | | SPECX/DO 2 I
191: | | | | SDAMPX/DO 1 J
192: | | | | SDAMPX/DO 11 I
193: | | | | SDAMPX/DO 12 I
194: | | | | SDAMPX/DO 2 J
195: | | | | SDAMPX/DO 4 J
196: | | | | SDAMPX/DO 4 I
197: | | | | SDAMPX/DO 6 J
198: | | | | SDAMPX/DO 6 J
199: | | | | SDAMPX/DO 6 I
200: | | | | SDAMPX/DO 7 J
201: | | | | SDAMPX/DO 8 J
202: | | | | SDAMPX/DO 9 I
203: | | | | SDAMPX/DO 10 I
204: | | | SDAMPY
205: | | | | SPECY
206: | | | | SPECY/DO 1 J
207: | | | | SPECY/DO 1 I
208: | | | | SPECY/DO 2 J
209: | | | | SPECY/DO 2 I
210: | | | | SDAMPY/DO 1 I
211: | | | | SDAMPY/DO 11 J
212: | | | | SDAMPY/DO 12 J
213: | | | | SDAMPY/DO 2 I
214: | | | | SDAMPY/DO 4 I
215: | | | | SDAMPY/DO 4 J
216: | | | | SDAMPY/DO 5 I
217: | | | | SDAMPY/DO 6 I
218: | | | | SDAMPY/DO 6 J
219: | | | | SDAMPY/DO 7 I
220: | | | | SDAMPY/DO 8 I
221: | | | | SDAMPY/DO 9 J
222: | | | | SDAMPY/DO 10 J
223: | | | SWEEPK/DO 11 J
224: | | | SWEEPK/DO 11 I
225: | | | BTRID
226: | | | | BTRID/DO 1 I
227: | | | | FILLNX
228: | | | | CHATA
229: | | | | CHATA/DO 1 J
230: | | | | CHATA/DO 2 J
231: | | | | CHATA
232: | | | | CHATA
233: | | | | FILLNX/DO 1 M
234: | | | | FILLNX/DO 1 L
235: | | | | FILLNX/DO 1 J
236: | | | | CHATA
237: | | | | FILLNX/DO 2 M
238: | | | | FILLNX/DO 2 L
239: | | | | FILLNX/DO 2 J
240: | | | | CHATV1

```

<See 228>

<See 228>

<See 228>

Call Graph of FDL3DI generated from FORGEExplorer

```

241: | | | | | CHATV1/DO 1 J
242: | | | | | CHATV1/DO 2 J
243: | | | | | CHATV1 <See 240>
244: | | | | | CHATV1 <See 240>
245: | | | | | FILLMX/DO 3 M
246: | | | | | FILLMX/DO 3 L
247: | | | | | FILLMX/DO 3 J
248: | | | | | CHATV1 <See 240>
249: | | | | | FILLMX/DO 4 J
250: | | | | | FILLMX/DO 5 M
251: | | | | | FILLMX/DO 51 L
252: | | | | | FILLMX/DO 51 J
253: | | | | | FILLMX/DO 52 J
254: | | | | | FILLNY
255: | | | | | CHATB
256: | | | | | CHATB/DO 1 I
257: | | | | | CHATB/DO 2 I
258: | | | | | CHATB <See 255>
259: | | | | | CHATB <See 255>
260: | | | | | FILLNY/DO 1 M
261: | | | | | FILLNY/DO 1 L
262: | | | | | FILLNY/DO 1 I
263: | | | | | CHATB <See 255>
264: | | | | | FILLNY/DO 2 M
265: | | | | | FILLNY/DO 2 L
266: | | | | | FILLNY/DO 2 I
267: | | | | | CHATV2
268: | | | | | CHATV2/DO 1 I
269: | | | | | CHATV2/DO 2 I
270: | | | | | CHATV2 <See 267>
271: | | | | | CHATV2 <See 267>
272: | | | | | FILLNY/DO 3 M
273: | | | | | FILLNY/DO 3 L
274: | | | | | FILLNY/DO 3 I
275: | | | | | CHATV2 <See 267>
276: | | | | | FILLNY/DO 4 I
277: | | | | | FILLNY/DO 5 M
278: | | | | | FILLNY/DO 51 L
279: | | | | | FILLNY/DO 51 I
280: | | | | | FILLNY/DO 52 I
281: | | | | | FILLNZ
282: | | | | | CHATC
283: | | | | | CHATC/DO 1 I
284: | | | | | CHATC/DO 2 I
285: | | | | | CHATC <See 282>
286: | | | | | CHATC <See 282>
287: | | | | | FILLNZ/DO 1 M
288: | | | | | FILLNZ/DO 1 L
289: | | | | | FILLNZ/DO 1 I
290: | | | | | CHATC <See 282>
291: | | | | | FILLNZ/DO 2 M
292: | | | | | FILLNZ/DO 2 L
293: | | | | | FILLNZ/DO 2 I
294: | | | | | CHATV3
295: | | | | | CHATV3/DO 1 I
296: | | | | | CHATV3/DO 2 I
297: | | | | | CHATV3 <See 294>
298: | | | | | CHATV3 <See 294>
299: | | | | | FILLNZ/DO 3 M
300: | | | | | FILLNZ/DO 3 L

```

```

301: | | | | | FILLNZ/DO 3 I
302: | | | | | CHATV3 <See 294>
303: | | | | | FILLNZ/DO 4 I
304: | | | | | FILLNZ/DO 5 M
305: | | | | | FILLNZ/DO 51 L
306: | | | | | FILLNZ/DO 51 I
307: | | | | | FILLNZ/DO 52 I
308: | | | | | BTRID/DO 2 L
309: | | | | | BTRID/DO 2 J
310: | | | | | BTRID/DO 3 J
311: | | | | | BTRID/DO 33 J
312: | | | | | BTRID/DO 4 M
313: | | | | | BTRID/DO 4 J
314: | | | | | BTRID/DO 6 II
315: | | | | | BTRID/DO 7 L
316: | | | | | BTRID/DO 7 J
317: | | | | | SWEEPK/DO 12 L
318: | | | | | SWEEPK/DO 12 J
319: | | | | | SWEEPK/DO 12 I
320: | | | | | SWEEPK/DO 13 L
321: | | | | | SWEEPK/DO 13 J
322: | | | | | SWEEPK/DO 13 I
323: | | | | | BTRID <See 225>
324: | | | | | SWEEPK/DO 14 J
325: | | | | | SWEEPK/DO 14 I
326: | | | | | TXIIRMS
327: | | | | | TXIIRMS/DO 1 J
328: | | | | | TXIIRMS/DO 1 I
329: | | | | | SDIAGX
330: | | | | | SDIAGX/DO 21 J
331: | | | | | SDIAGX/DO 21 I
332: | | | | | SDIAGX/DO 22 J
333: | | | | | SDIAGX/DO 22 I
334: | | | | | SDIAGX/DO 1 J
335: | | | | | SDIAGX/DO 2 I
336: | | | | | SDIAGX/DO 3 I
337: | | | | | SDIAGX/DO 4 J
338: | | | | | SDIAGX/DO 5 J
339: | | | | | SPENTA3
340: | | | | | SPENTA3/DO 1 J
341: | | | | | SPENTA3/DO 2 I
342: | | | | | SPENTA3/DO 2 J
343: | | | | | SPENTA3/DO 3 J
344: | | | | | SPENTA3/DO 4 J
345: | | | | | SPENTA3/DO 5 II
346: | | | | | SPENTA3/DO 6 J
347: | | | | | SDIAGX/DO 6 J
348: | | | | | SDIAGX/DO 7 I
349: | | | | | SDIAGX/DO 8 I
350: | | | | | SDIAGX/DO 61 J
351: | | | | | SPENTA
352: | | | | | SPENTA/DO 1 J
353: | | | | | SPENTA/DO 2 I
354: | | | | | SPENTA/DO 2 J
355: | | | | | SPENTA/DO 3 J
356: | | | | | SPENTA/DO 4 J
357: | | | | | SPENTA/DO 5 II
358: | | | | | SPENTA/DO 6 J
359: | | | | | SDIAGX/DO 9 J
360: | | | | | SDIAGX/DO 9 I

```

Call Graph of FDL3DI generated from FORGEExplorer



361:         SDIAGI/DO 62 J		
362:         SPENTA	<See 351>	
363:         SWEEPK/DO 15 J		
364:         SWEEPK/DO 15 I		
365:         WIRHS		
366:         WIRHS/DO 1 J		
367:         WIRHS/DO 1 I		
368:         SDIAGY		
369:         SDIAGY/DO 21 J		
370:         SDIAGY/DO 21 I		
371:         SDIAGY/DO 22 J		
372:         SDIAGY/DO 22 I		
373:         SDIAGY/DO 1 I		
374:         SDIAGY/DO 2 J		
375:         SDIAGY/DO 3 J		
376:         SDIAGY/DO 4 I		
377:         SDIAGY/DO 5 I		
378:         SPENTA3	<See 339>	
379:         SDIAGY/DO 7 J		
380:         SDIAGY/DO 7 I		
381:         SDIAGY/DO 8 J		
382:         SDIAGY/DO 8 I		
383:         SDIAGY/DO 61 I		
384:         SPENTA	<See 351>	
385:         SDIAGY/DO 9 J		
386:         SDIAGY/DO 9 I		
387:         SDIAGY/DO 62 I		
388:         SPENTA	<See 351>	
389:         SWEEPK/DO 16 J		
390:         SWEEPK/DO 16 I		
391:         SWEEPJ2		
392:         SWEEPJ2/DO 1 JF		
393:         CXNU	<See 48>	
394:         SDAMPZ1		
395:         SPECZ	<See 99>	
396:         SDAMPZ1/DO 1 I		
397:         SDAMPZ1/DO 11 K		
398:         SDAMPZ1/DO 12 K		
399:         SDAMPZ1/DO 2 I		
400:         SWEEPJ2/DO 11 K		
401:         SWEEPJ2/DO 11 I		
402:         BTRID	<See 225>	
403:         PIRHS		
404:         PIRHS/DO 1 K		
405:         PIRHS/DO 1 I		
406:         SDIAGZ		
407:         SDIAGZ/DO 21 K		
408:         SDIAGZ/DO 21 I		
409:         SDIAGZ/DO 22 K		
410:         SDIAGZ/DO 22 I		
411:         SDIAGZ/DO 1 I		
412:         SDIAGZ/DO 2 K		
413:         SDIAGZ/DO 3 K		
414:         SDIAGZ/DO 4 I		
415:         SDIAGZ/DO 5 I		
416:         SPENTA3	<See 339>	
417:         SDIAGZ/DO 7 K		
418:         SDIAGZ/DO 7 I		
419:         SDIAGZ/DO 8 K		

420:         SDIAGZ/DO 8 I		
421:         SDIAGZ/DO 61 I		
422:         SPENTA	<See 351>	
423:         SDIAGZ/DO 9 K		
424:         SDIAGZ/DO 9 I		
425:         SDIAGZ/DO 62 I		
426:         SPENTA	<See 351>	
427:         TZETRHS		
428:         TZETRHS/DO 1 K		
429:         TZETRHS/DO 1 I		
430:         SWEEPJ2/DO 12 K		
431:         SWEEPJ2/DO 12 I		
432:         SWEEPJ2/DO 13 K		
433:         SWEEPJ2/DO 13 I		
434:         CRESID		
435:         CRESID/DO 1 K		
436:         CRESID/DO 1 J		
437:         CRESID/DO 1 I		
438:         BNDRYC		
439:         BNDRYC/DO 4 K		
440:         BNDRYC/DO 4 I		
441:         BNDRYC/DO 5 LL		
442:         BNDRYC/DO 6 K		
443:         BNDRYC/DO 6 I		
444:         BNDRYC/DO 7 K		
445:         BNDRYC/DO 8 I		
446:         BNDRYC/DO 9 K		
447:         BNDRYC/DO 9 J		
448:         BNDRYC/DO 3 J		
449:         BNDRYC/DO 3 I		
450:         CRESID	<See 434>	
451:         LIFT		
452:         CXNU	<See 48>	
453:         LIFT/DO 1 I		
454:         LIFT/DO 4 I		
455:         SECOND	Unknown	
456:         SECOND	Unknown	

Call Graph of FDL3DI generated from FORGEExplorer

## References

- [1] Applied Parallel Research, Sacramento, CA 95825. *ForgeX Version 2.1 User's Guide*, October 1995.
- [2] Eric L. Boyd, Gheith A. Abandah, Hsien-Hsin Lee, and Edward S. Davidson. Modeling computation and communication performance of parallel scientific applications: A case study of the IBM SP2. Technical Report CSE-TR-236-95, University of Michigan, Department of Electrical Engineering and Computer Science, May 1995.
- [3] T. Agerwala et al. SP2 system architecture. *IBM Systems Journal*, 34(2):152-184, 1995.
- [4] G. Fox, M. Johnson, G. Lyzenga, S. Otto, J. Salmon, and D. Walker. *Solving Problems on Concurrent Computers*, volume I. Prentice-Hall, Englewood Cliffs, NJ, 1988.
- [5] W. Gropp, E. Lusk, and A. Skjellum. *Using MPI: Portable Parallel Programming with the Message-Passing Interface*. MIT Press, Boston, MA, 1994.
- [6] David E. Hudak and Santosh G. Abraham. *Compiling Parallel Loops for High Performance Computers: Partitioning, Data Assignment, and Remapping*. Kluwer Academic Publishers, 1993.
- [7] F. Irigoien and R. Triolet. Supernode partitioning. In *Proceedings of the 15th Annual ACM SIGACT-SIGPLAN Symposium on Principles of Programming Languages*, pages 319-329, 1988.
- [8] Yong-Du Jun. *Parallel Implementation of Factored Alternating Direction Implicit Method for Strongly Coupled Navier-Stokes and K-E Equations*. PhD thesis, University of Cincinnati, Cincinnati, OH, 1996.
- [9] Merritt H. Smith, Rob F. Van der Wijngaart, and Maurice Yarrow. Improved multi-partition method for line-based iteration schemes. In *Computational Aerosciences Workshop, NASA Ames Research Center*, March 1995.
- [10] M. Snir, P. Hochschild, D. D. Frye, and K. J. Gildea. The communication software and parallel environment of the IBM SP2. *IBM Systems Journal*, 34(2):185-204, 1995.

# **AN INNOVATIVE SEGMENTED TUNGSTEN PENETRATING MUNITION**

**David P. Johnson  
Assistant Professor  
Department of Aerospace Engineering**

**Mississippi State University  
M. S. 9549  
Mississippi State, MS 39762**

**Final Report for:  
Summer Research Program  
Wright Laboratory**

**Sponsored by:  
Air Force Office of Scientific Research  
Bolling Air Force Base, Washington, DC**

**And**

**Wright Laboratory**

**August 1997**

# **An Innovative Segmented Tungsten Penetrating Munition**

David P. Johnson  
Assistant Professor  
Dept. Aerospace Engineering  
Mississippi State University

## **ABSTRACT**

One of the factors that governs the penetration depth of a penetrating munition is the ratio of the penetrator's weight to its cross-sectional area ( $W/A$ ). Dense metal ballast significantly increases  $W/A$ , but yields some structural challenges. Tungsten, in particular, while being very dense, typically has low ductility and toughness in bulk form, and is difficult to fabricate and machine. The purpose of this work was to investigate the feasibility of developing a segmented dense metal ballasted penetrating munition. Allowing the use of segments greatly facilitates the manufacturing of the tungsten portion of the munition.

The use of a segmented ballast requires a strong, tough member to maintain structural integrity during impact. In this work, steel was considered for this purpose. Two configurations were considered: a steel rod, with tungsten rings placed around it, and a steel shell, with tungsten disks placed inside it. Both linear and non-linear structural and material response were considered, using analytical techniques. A 3-D finite element analysis was also initiated, but has not yet reached completion as of the submission of this report.

The analytical work suggests that a segmented tungsten penetrator is indeed feasible, and should be pursued. Using a non-linear structural and material response analysis, coupled with an empirical external loads model from a computer code called AMPLL, by William K. Rule, it was demonstrated that a representative segmented tungsten ballasted penetrator could withstand impact angles of up to about  $20^\circ$  off vertical ( $\beta = 70^\circ$ ), and angles of attack ( $\alpha$ ) of up to about  $1^\circ$ .

It was found that the shell configuration was more robust than the steel rod configuration. The members of the structure can be sized (with satisfactorily small amounts of steel in the cross-section) such that no permanent shape change occurs during impact. This means that not only will the structure survive impact, but that adverse thermodynamic effects will be minimized.

# An Innovative Segmented Tungsten Penetrating Munition

David P. Johnson

## INTRODUCTION

The purpose of this work was to investigate the feasibility of developing a segmented dense metal ballasted penetrating munition. The motivation behind a ballasted penetrator is to increase the penetration depth into a given target material. Penetration depth is typically modeled using experimentally validated empirical expressions of the following form [1]:

$$D = C_1 S N \left( \frac{W}{A} \right)^{C_2} f_1(V, W) \quad 1$$

Here,  $C_1$  and  $C_2$  are empirical constants,  $S$  is the penetrability of the target,  $N$  is a nose performance coefficient,  $W$  is the weight of the penetrator,  $A$  is the cross-sectional area of the penetrator, and  $f_1(V, W)$  is a function of the velocity  $V$ , and of  $W$ , that depends on the target type. It is the potential benefit of increasing  $W/A$  that leads to the desire to investigate dense metal ballasted penetrators.

Because of obstacles to the use of depleted uranium for such an effort, a certain amount of work has been done to determine if tungsten could be used as a ballasting material. However, the fabrication of tungsten in bulk quantities under current technology yields a material that is relatively weak and brittle. In addition, large billets of tungsten are difficult to make, and to handle.

One possible solution to this dilemma is to make the tungsten ballast in segments of smaller size, and to

connect them with a strong, tough tensile member designed to withstand the bending loads that a penetrator would experience upon impact. Although the concept may be generalized for other cases where a segmented penetrator may be desirable, the work herein will reference specifically the use of a steel tensile member used to apply compressive stresses to a segmented tungsten ballasted penetrator.

Part of the scope of this research was to investigate how to arrange the steel tensile member and the tungsten such that the penetrating performance is maximized. Culp [2] performed an initial study of this problem. In his study, Culp investigated a specific configuration for the tungsten/steel penetrator structure, as illustrated in Figure 1. The configuration chosen was a series of stepped tungsten segments compressed by a steel rod or bolt running through the center of the structure. The steps in the tungsten were designed to take shear loads in the tungsten. The Culp study did not include a dynamic finite element analysis, and did not provide an in-depth treatment of the mechanics of the penetrator structure under load. The tungsten segments had to be configured so that a penetrator analysis software application called AMPLL (Analytical Model of Penetration with Lateral Loads), done by Rule [3], could be used to approximate the maximum stresses in the steel and the tungsten of a limited number of cases. Various sizes of bolt, and values of preload (torque on the bolt) were used with different impact conditions to see which con-

figurations would survive a given impact, and which would fail. Based upon his work, Culp found that a segmented penetrator should be feasible and that further work should be done. Unfortunately, the version of AMPLL that Culp had access to contained a bug [4], and stress levels were substantially under predicted .

The current work was an extension and amplification of the Culp study. As part of this work, a dynamic 3-D finite element study was initiated. However, as of the completion date of this report, the final 3-D finite element results were not available, although initial work seemed encouraging.

## CONFIGURATION ISSUES

Three configuration issues were addressed before the analytical work commenced. The first issue was how to configure the tungsten segments themselves. Culp recommended a stepped, rather than a flat segment configuration. Second, there is the issue of the configuration of the tensile member. While Culp proposed a central steel rod as the tensile member, it was felt that a steel shell configuration should also be investigated. The analytical work described later addressed both of these issues. Finally, the main objective of the analytical work was to size the structural elements such that the munition could survive a set of desired impact conditions while maximizing the effective sectional density ( $W/A$ ).

### Disk Configuration

The Culp study [2] included stepped tungsten disks. These steps were intended to take shear loads when the structure was subjected to lateral loads upon impact. However, some issues of concern arise with such a configuration. The main issue is that the corrected version

of AMPLL indicates that the compressive loading that the tungsten would be required to take is considerably higher than what Culp was considering. This necessitates that more of the surfaces between segments be in contact in order to distribute the compressive stresses, and avoid yield in the tungsten. Only a portion of the cross-sectional area was specified in the Culp report as bearing surfaces. There is also the added cost of machining the steps, and the possibility that the relatively brittle tungsten may be susceptible to stress concentrations induced by the corners. To address these issues, the shear stresses in the steel portion of the structure were investigated in order to determine if flat (unstepped) mating surfaces could be used instead. In order to do so, a worst case scenario was adopted. Namely, the segments were assumed to be short, and the mating surfaces were assumed to be frictionless so that the tungsten did not share in supporting shear stresses, which were taken instead entirely by the steel. In reality, the tungsten may share some of the shear loading with the steel.

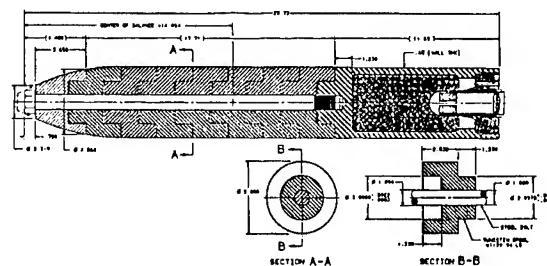


Figure 1. Segmented penetrator proposed by Culp [2].

### Tensile Member Configuration

The Culp study [2] investigated essentially a steel bolt as the tensile member. This bolt ran through holes in the centers of the tungsten disks (Figure 1). The current work employed analytical techniques to compare stresses in a steel rod tensile member, such as that pro-

posed by Culp, and an external steel shell tensile member (Figure 2). The goal was to discover which of the two configurations is more structurally efficient, and thus which would require less steel in the cross section. Less steel leads to a higher effective density, and maximizes the penetrating efficiency of the munition.

### Sizing of Structural Elements

Sizing and tradeoff studies were carried out using both linear and non-linear mechanics of materials techniques. This required a priori knowledge of the internal axial force, shear force, and bending moment as functions of time throughout the impact, and position along the structure. External loads were approximated by the projectile penetration code AMPLL (Analytical Model of Penetration with Lateral Loads) by Rule [3], and modifications to the existing code were introduced in order to calculate and output the internal load information. The modifications to the existing code used the external loads calculated by AMPLL, and performed a rigid body dynamics analysis of the penetrator structure to arrive at the internal axial force, shear force, and bending moment. These internal reactions were calculated at various time steps throughout the impact event, over the length of the structure, so that it could be determined where the maximum stresses would occur. This removed the typical assumption that maximum stresses occur at the centroid.

As a simulated impact event proceeded, the internal reaction data generated by the modified version of AMPLL were output to text files. The normal and shear stresses on a surface perpendicular to the penetrator axis could then be calculated analytically, with the goal of investigating failure of the structure. The structure's members

could then be sized appropriately such that it would survive a desired set of impact conditions.

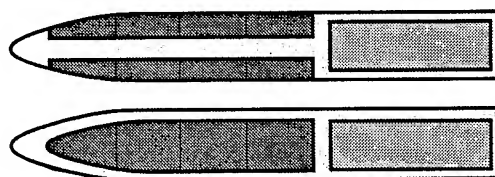


Figure 2. Steel rod and shell configurations of a segmented penetrator.

### ANALYTICAL PROCEDURE

The AMPLL code obtained from Rule [3] could not be used directly to predict the structural response of the penetrator configurations under consideration. The simple beam-type finite elements used in the code were not capable of handling a non-homogeneous, and prestressed structure. Hence, in order to predict the structural response, an analytical stress-based approach was adopted. Both linear and non-linear stress studies were carried out in order to investigate the feasibility of the segmented penetrator concept. However, in order to find the stresses in the structure, it was first necessary to know the internal force and moment reactions in the structure as functions of time and position along the penetrator. This was accomplished using AMPLL as a loads model, and then using the tools of rigid body structural dynamics to find the internal reactions. Once these internal reactions were calculated, the stresses could be determined using either linear or non-linear mechanics of materials developments. Stresses for both the steel rod, and steel shell configurations shown in Figure 2 were developed.

In addition, the issue of thermal strain was addressed. Since the coefficient of thermal expansion of the tungsten is only about half that of steel, the preload in the steel tends to change as the structure is exposed to

changing temperature. The main issue would be whether the performance of the structure would be changed given the fact that the weapon would likely be exposed to a cold thermal soak as the aircraft used as the delivery platform flew at altitude to the target.

### Dynamics Model

The penetrator was modeled as a slender rod under the action of external distributed axial ( $T$ ) and lateral ( $W$ ) forces. The mass moment of inertia for this structure about its centroid was calculated by AMPLL. The equations of motion for the centroid of the body are:

$$\begin{aligned} \int_0^{\ell} T(x) dx &= m \bar{a}_x \\ \int_0^{\ell} W(x) dx &= m \bar{a}_y \\ \int_0^{\ell} W(x) x dx &= \bar{I}_m \alpha + m \bar{a}_x \bar{x} \end{aligned} \quad 2$$

where  $\bar{m}$  is the mass of the penetrator,  $\bar{I}_m$  is the mass moment of inertia,  $\bar{a}_x$  and  $\bar{a}_y$  and  $\alpha$  are the centroidal accelerations, and  $\bar{x}$  is the distance from the nose of the penetrator to its centroid. Given  $W$  and  $T$  from AMPLL, the centroidal accelerations could be found.

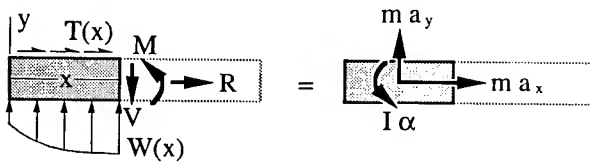


Figure 3. Free body and acceleration diagrams of a portion of the penetrator.

Next, the internal forces and moments in the structure could be found. To do this, it is useful to consider the free body and acceleration diagrams of a section of the body, of arbitrary length  $x$  (Figure 3). The primed quantities refer to the portion shown, not the entire penetrator.

The accelerations  $a'_x$  and  $a'_y$  of the centroid of this portion of the body are expressed as:

$$\begin{aligned} a'_x &= \bar{a}_x \\ a'_y &= \bar{a}_y - \alpha (\bar{x} - \bar{x}') \end{aligned} \quad 3$$

where  $\bar{x}'$  is the distance from the nose of the penetrator to the centroid of the above portion. It is assumed that the angular speed  $\omega$  of the body is small enough not to affect the axial acceleration  $a'_x$ . The equations of motion of this portion of the body can be written as:

$$\begin{aligned} \int_0^x T(\zeta) d\zeta + R &= m' a'_x \\ \int_0^x W(\zeta) d\zeta - V &= m' a'_y \\ \int_0^x W(\zeta) d\zeta - Vx + M &= \bar{I}'_m \alpha + m' a'_y \bar{x}' \end{aligned} \quad 4$$

These equations can be solved for the axial force  $R$ , shear force  $V$ , and bending moment  $M$  as functions of position  $x$  in the body, given the distributed axial  $T$  and lateral  $W$  forces.

The usual conventions that  $R$  is positive when tensile, and  $M$  is positive when causing compressive stresses above the  $z$ -axis, were used. During an impact event,  $R$  will usually be compressive (negative) throughout the body.

### Linear Normal Stress

For the linear stress analysis, it was assumed that no gaps between tungsten segments formed (i.e. stresses remained compressive in the tungsten), and that plastic yielding of the steel and tungsten did not occur.

The penetrator was modeled using mechanics of materials techniques. A tensile preload was required in the steel to keep the stresses in the tungsten compressive



during impact. This preload was found by considering the structure to be a composite, residual stressed structure under combined axial force, shear force and bending moment. The effective bending stiffness  $\overline{EI}$  of a composite body is as follows:

$$\overline{EI} = E_{st} I_{st} + E_{tu} I_{tu} \quad 5$$

where  $E_{st}$ ,  $I_{st}$ ,  $E_{tu}$ , and  $I_{tu}$  are Young's modulus and the second moment of area about the centroid for steel and tungsten, respectively. It was assumed that no separation between disks occurred (i.e. the normal stress in tungsten remained compressive throughout the cross-section), so the cross-section remained circular, and the centroid was in the center.

For the composite rod and ring structure being considered (Figure 4), the normal stress in the steel or tungsten, on a plane perpendicular to the axis of the structure can be found in terms of the internal bending moment, and the internal axial force, as follows:

$$\sigma = \frac{F}{A} - \frac{MEy}{EI} \quad 6$$

where  $F$  is the internal axial force,  $A$  is the cross-sectional area of the steel or tungsten,  $M$  is the internal bending moment,  $E$  is the stiffness of the steel or tungsten, and  $y$  is the position above the  $z$ -axis. Positive axial force is tensile, and positive bending moment contributes to compressive stresses when  $y$  is positive.

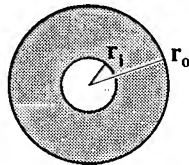


Figure 4. Cross section of rod and ring structure.

The axial force  $F$  is composed of two parts, namely any preload  $P$  plus any internal axial force  $R$  due to the impact loads. Furthermore, the preload in the steel will be tensile, while the preload in the tungsten will be compressive.

$$\begin{aligned} F_{st} &= P + R_{st} \\ F_{tu} &= -P + R_{tu} \end{aligned} \quad 7$$

The steel will take some ( $R_{st}$ ) of the axial load  $R$  due to impact, and the tungsten will take the remainder ( $R_{tu}$ ). In order to find how much goes in each, it must be noted first that the sum of the forces in the steel and the tungsten must be equal to the axial impact force  $R$ , and second that the normal strain due to  $R_{st}$  and  $R_{tu}$  will be equal.

$$\begin{aligned} R_{st} + R_{tu} &= R \\ \epsilon_{st} = \frac{R_{st}}{A_{st} E_{st}} &= \frac{R_{tu}}{A_{tu} E_{tu}} = \epsilon_{tu} \end{aligned} \quad 8$$

Substituting in expressions for the area of the steel and the tungsten for each configuration being considered, these two equations may be solved simultaneously to find  $R_{st}$  and  $R_{tu}$  for the steel rod and steel shell configurations:

$$\begin{aligned} R_{st} &= \frac{R f A_{st}}{f A_{st} + k (1 - f A_{st})} \\ R_{tu} &= \frac{R (1 - f A_{st})}{f A_{st} + k (1 - f A_{st})} \end{aligned} \quad 9$$

where  $f A_{st}$  is the ratio of the area of steel in the cross section to the total area of the cross section (the fractional area of steel in the cross section), and  $k$  is the ratio of the stiffness of tungsten to the stiffness of steel.

Referring to Equations 6 and 7, the value of the preload required to keep gaps from forming between adjacent

tungsten segments still needs to be found. With some manipulation it can be shown that the stress in the tungsten for each configuration can be expressed as:

$$\begin{aligned}\sigma_{tu}^r &= \frac{-P}{\pi r_o^2 (1 - fA_{st})} + \frac{k (R - 4 M y)}{\pi r_o^2 (fA_{st} + (1 - fA_{st}))} \\ \sigma_{tu}^s &= \frac{-P}{\pi r_o^2 fA_{st}} + \frac{k (R - 4 M y)}{\pi r_o^2 (fA_{st} + (1 - fA_{st}))}\end{aligned}\quad 10$$

where the superscripts  $r$  and  $s$  denote steel rod, and steel shell configurations, respectively, and  $r_o$  is the outside radius of the structure (see Figure 4). The preload  $P$  can then be found with the condition that the normal stress in the tungsten must be zero at maximum. Substituting  $\sigma_{tu} = 0$ , and the appropriate value for  $y$  into Equations 10, and solving for  $P$  yields:

$$\begin{aligned}P^r &= k (1 - fA_{st}) \left\{ \frac{R}{fA_{st} + k (1 - fA_{st})} + \frac{4 |M|}{r_o [fA_{st}^2 + k (1 - fA_{st}^2)]} \right\} \\ P^s &= k (1 - fA_{st}) \left\{ \frac{R}{(1 - fA_{st}) + k fA_{st}} + \frac{4 |M| \sqrt{1 - fA_{st}}}{r_o [fA_{st} (2 - fA_{st}) + k (1 - fA_{st}^2)]} \right\}\end{aligned}\quad 11$$

Here,  $|M|$  (absolute value of  $M$ ) is used to remove the ambiguity that arises by constraining  $\sigma_{tu}$  at  $y = -r_2$  to be zero, given that  $M$  may in reality be negative. The moment may indeed switch from positive to negative during impact, in what is commonly called tail slap. Equations 11, 9 and 7 can be substituted back into Equation 6, and the stresses in the tungsten and steel for each configuration can be found, given the bending moment and axial load at a cross-section. For the steel rod configuration, the stresses are:

$$\begin{aligned}\sigma_{st}^r &= \frac{[k - fA_{st}^2 (k - 1)] r_o^2 R + 4 [(1 - fA_{st}) k r_o - fA_{st} y] |M|}{fA_{st} [k - fA_{st}^2 (k - 1)] \pi r_o^4} \\ \sigma_{tu}^r &= \frac{-4 k (r_o + y) |M|}{[k - fA_{st}^2 (k - 1)] \pi r_o^4}\end{aligned}\quad 12$$

For the steel shell configuration, the stresses are:

$$\begin{aligned}\sigma_{st}^s &= \frac{[k - fA_{st} (k - 1) (2 - fA_{st})] r_o^2 R + 4 [(1 - fA_{st})^{3/2} k r_o - fA_{st} y] |M|}{fA_{st} [k - fA_{st} (k - 1) (2 - fA_{st})] \pi r_o^4} \\ \sigma_{tu}^s &= \frac{-4 k (\sqrt{1 - fA_{st}} r_o + y) |M|}{[k - fA_{st} (k - 1) (2 - fA_{st})] \pi r_o^4}\end{aligned}\quad 13$$

Thus, for a given penetrator and area fraction of steel ( $fA_{st}$ ), the stresses in the tungsten and steel can be found for a known set of loads ( $R$  and  $M$ ). The maximum tensile stress in the steel may be found by substituting  $r_i$  or  $r_o$  into  $y$  for the steel rod and steel shell configurations, respectively. The maximum compressive load in the tungsten may be found by substituting  $-r_o$  or  $-r_i$  into  $y$  for the steel rod and steel shell configurations, respectively (see Figure 4). Recall that stresses in the tungsten have been constrained to be compressive throughout the cross-section. In order to maximize the cross-sectional density, we want to minimize the amount of steel in the cross-section ( $fA_{st}$ ) subject to the constraint that the stresses in each material remain below their respective yield stresses.

## Linear Shear Stress

Normal stress constitutes only part of the picture. Failure of ductile materials like steel is typically modeled using the Maximum Distortion Energy, or von Mises failure criterion [5]. For a state of plane stress, this failure theory can be reduced to the following:

$$\sigma_{vM} = \sqrt{\sigma_x^2 + 3 \tau_{xy}^2}\quad 14$$

Hence, it is necessary to find the shear stress in the steel. To do this, one must make an assumption about whether the tungsten will share in taking shear loads. If not (i.e. if there is no friction between tungsten segments), then all shear force must be taken by the steel. If the tungsten does participate in sharing the shear force, a scheme similar to Equations 8 must be devel-

oped, stating that the shear force is to be divided among the steel and tungsten, and that the average shear strains in the steel and tungsten are equal. However, the worst case is represented when the steel must take all shear load. The shear stress in the steel can then be written as:

$$\tau = \frac{VQ}{It} \quad 15$$

where  $I$  is the moment of inertia of the steel portion of the cross-section about the center of the cross-section;  $Q = A_o \bar{y}$ ; and  $A_o$ ,  $\bar{y}$ , and  $t$  for the maximum shear stress in both configurations are defined in Figure 5.

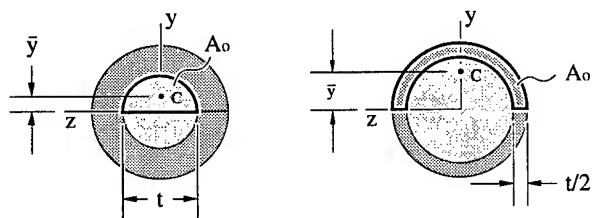


Figure 5. Definitions of geometric quantities for the steel rod and shell configurations.

Then the maximum shear stress can be expressed as:

$$\tau_{max}^r = \frac{4V}{3\pi r_o^2 f A_{st}} \quad 16$$

$$\tau_{max}^s = \frac{4V(1 - f A_{st}^{3/2})}{3\pi r_o^2 (1 - f A_{st}^2)(1 - \sqrt{f A_{st}})}$$

### Non-linear Normal Stress

The non-linear stress development relaxes two constraints imposed by the linear stress model; namely, inelastic material behavior is allowed, and gaps are allowed to form between adjacent tungsten disks. The strain in the steel and tungsten are functions of two factors. One is the preload, and the other is the bending occurring in the structure. The strains in the two materials can be expressed as:

$$\epsilon_{st} = \frac{P}{\pi r_o^2 f A_{st} E_{st}} + \frac{(y + y^*)}{\rho} \quad 17$$

$$\epsilon_{tu} = \frac{-P}{\pi r_o^2 (1 - f A_{st}) E_{tu}} + \frac{(y + y^*)}{\rho}$$

where  $P$  is the preload applied to the structure, as in the linear case,  $\rho$  is the radius of curvature to which the structure is bent,  $y$  is the position in the cross-section (with  $y = 0$  being at the center of the circular cross-section), and  $y^*$  is an unknown distance that must be solved for.

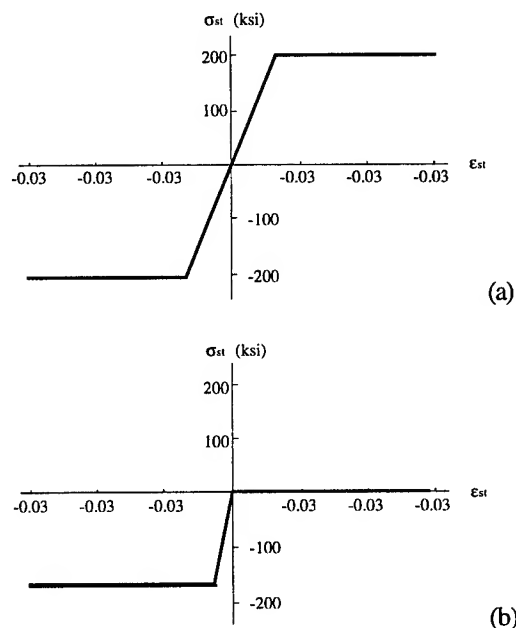


Figure 6. Material behavior of steel (a) and tungsten (b). Then, for a given preload  $P$ , and radius of curvature  $\rho$ , the normal strain at a given position in the cross-section can be used to find the normal stress at that location by using the non-linear stress/strain response of the material (Figure 6). Notice that the tungsten cannot exhibit tensile stresses, as segments are allowed to separate.

Again, the normal stress at any location in the cross-section can be found for given values of  $P$  and  $\rho$ , except

that  $y^*$  is still unknown. The value of  $y^*$  is found by requiring that the integral of the normal stress over the cross-section be made equal to the internal axial force  $R$ .

$$\int_A \sigma dA = R \quad 18$$

Recall that the value of  $R$  is calculated by AMPLL for a given impact event. In fact, because of the way AMPLL calculates the external loads [3],  $R$  is independent of the impact velocity, and the angles of attack and impact. The only things significantly affecting  $R$  are the cross-sectional area and the weight of the penetrator, the penetrability of the target, and the nose shape. Hence, for a given penetrator and target,  $R$  is virtually constant for any impact conditions.

Numerical integration techniques can be used to converge on a solution for  $y^*$  using Equation 18. After this is accomplished, the moment required to bend the penetrator into the specified radius of curvature  $\rho$  is found by integrating the moment of the normal stress, thus:

$$M = \int_A \sigma y dA \quad 19$$

Picking successively larger values of curvature ( $1/\rho$ ), one can construct a plot of the bending moment versus curvature for the structure. The moment tends to level off at some maximum value at larger values of curvature, allowing for a convenient means of defining when the penetrator "breaks."

### Temperature Analysis

The equations governing the structure's behavior under thermal excursions are very similar to those determining how much of the axial impact load was shared by each

material. In order to write the governing equations, it is necessary to note two things. First, any change in the load in the tensile member must be accompanied by an equal and opposite change in the load in the tungsten. Second, the strains (thermal and mechanical) in the two members must be equal, as before. These two observations lead to the following:

$$\begin{aligned} \Delta P_{st} &= -\Delta P_{tu} \\ \epsilon_{st} &= \frac{\Delta P_{st}}{A_{st} E_{st}} + \alpha_{st} \Delta T = \frac{\Delta P_{tu}}{A_{tu} E_{tu}} + \alpha_{tu} \Delta T = \epsilon_{st} \end{aligned} \quad 20$$

where  $\alpha$  is the coefficient of thermal expansion. The areas of the steel and tungsten can be expressed in terms of  $fA_{st}$ , and the above equations can be solved for  $\Delta P_{st}$ :

$$\Delta P_{st} = \frac{(\alpha_{tu} - \alpha_{st}) \Delta T k \pi r_t^2 f A_{st} (1 - f A_{st})}{f A_{st} + k (1 - f A_{st})} \quad 21$$

### MODIFICATIONS TO AMPLL

At this point, given the internal axial load  $R$ , shear force  $V$ , and bending moment  $M$ , it is now possible, at an arbitrary location along the length of the penetrator, to monitor the normal stresses and strains in the steel and tungsten during both linear and non-linear response, as well as the maximum shear stress in the steel during linear response. The question then arises: at what location along the length of the penetrator do the maximum stresses occur? Typically, it is assumed that the stresses will be highest at the centroid of the body. However, since the stresses can be found explicitly as functions of the axial and lateral forces on the penetrator, it is possible to find where the stresses are highest without assuming anything a priori. The only requirement is a knowledge of what these forces are as functions of position and time throughout an impact event. This infor-

mation can be supplied by making modifications to the software package AMPLL, as discussed earlier.

Among other things, AMPLL was designed to find stresses in penetrators during impact. However, the analysis employed by AMPLL cannot accommodate composite, preloaded structures such as the one under discussion. Therefore, it was necessary to modify AMPLL so that its output could be used in the analysis developed above.

AMPLL discretizes the penetrator into a given number of elements (connected at nodepoints) along its length as part of its analysis of stresses, using a 1-D beam-type finite element analysis. As part of this analysis, the axial and lateral forces at each nodepoint are calculated. However, there was no option to output these forces to a text file for use in finding stresses in the current work. Therefore, an additional subroutine was created, and several of the existing subroutines were modified.

The additional subroutine takes the nodal axial and lateral forces and employs the structural dynamics analysis discussed above to find the internal axial force, shear force, and bending moment at each nodepoint in the structure for all time steps throughout the impact. In order to do this, the dynamics analysis was discretized, by replacing integral relationships involving distributed loads with summations involving nodal forces. The subroutine simply creates three ASCII text files, one for each of the three internal reactions ( $R$ ,  $V$ , and  $M$ ), and writes each nodal value for every  $n^{\text{th}}$  time step, where  $n$  can be changed from within the code. This yields a record of all nodal reactions throughout a given impact.

## RESULTS AND DISCUSSION

Using the output from the new subroutine in the modified version of AMPLL, and the expressions developed above, the tools are now available for the analysis of the penetrator under consideration. Both linear and non-linear stress cases are discussed.

### Linear Analysis

This part of the analysis was a direct follow-on to Culp's work [2], making the assumption that neither yield, nor separation between tungsten segments should not be allowed. It was assumed that once structural or material non-linearities occurred, structural failure would soon follow.

After the expressions were developed for the analysis of this structure, it was necessary to develop some criterion for defining failure. Expressions for both normal stress and shear stress, on a surface perpendicular to the axis of the structure, have been developed. Critical locations in the cross-section at which stresses were monitored were points  $A$  and  $B$  in the steel, and point  $C$  in the tungsten, as defined by Figure 7.

For a bending moment parallel to the  $z$ -axis, and a shear force parallel to the  $y$ -axis, points  $A$  and  $B$  represent the locations of maximum normal stress and maximum shear stress, respectively, in the steel. And point  $C$  represents the location of maximum compressive normal stress in the tungsten. In the steel, the von Mises stress (Equation 14) at  $B$  must be compared to the normal stress at  $A$  (the first of Equations 12 and 13), for a given cross-section.

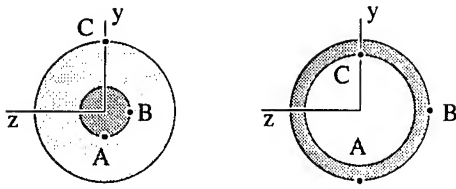


Figure 7. Various locations in rod and shell configurations.

As it turns out, the shear stresses are relatively small where the bending stresses are high, because of the relationship between the shear force and the bending moment. Because  $V = dM/dx$ , the shear force is near or equal to zero where the bending moment is maximum. And where the shear forces are large, the bending moment is significantly smaller. Therefore, it was found that the normal stresses would govern failure of the structure.

Hence, Figures 8 and 9 show plots of maximum normal stress vs.  $fA_{st}$  in both the steel and tungsten, for both the rod and shell configurations. Equations 12 and 13, along with the data from the modified version of AMPLL were used for the calculation of the stresses. The penetrator was a 6 in. diameter, 36 in. long tungsten/steel penetrator impacting a 3 ft thickness of reinforced concrete at 1300 ft/s,  $85^\circ$  angle of impact ( $\beta$ ),  $0^\circ$  angle of attack ( $\alpha$ ) (see Figure 10). Note that for the same maximum stress, the rod configuration requires less steel in the cross-section than the shell configuration, and will therefore lead to a slightly more dense penetrator.

If the yield stress of the steel is taken as 200 ksi, and that of the tungsten as 175 ksi, the smallest possible  $fA_{st}$  of about 0.3 leads to imminent yield in both the steel and the tungsten. This indicates that  $\alpha = 0^\circ$ ,  $\beta =$

$85^\circ$  is as severe an impact as can be survived under the assumptions of the linear analysis.

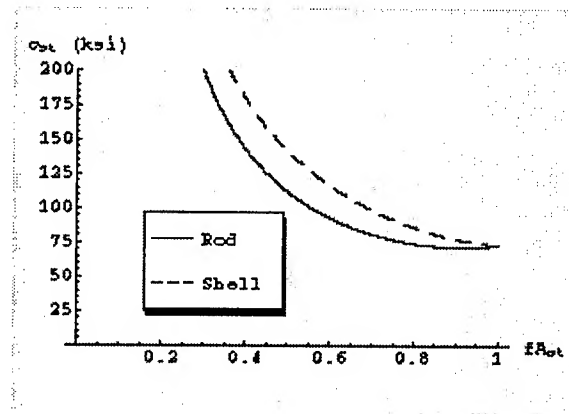


Figure 8. Maximum normal stress in steel vs.  $fA_{st}$ .

One serious drawback to this arrangement is that the preload required by Equations 11 is nearly 90% of the yield stress of the steel. Introduction of this preload to the structure during fabrication may not be feasible.

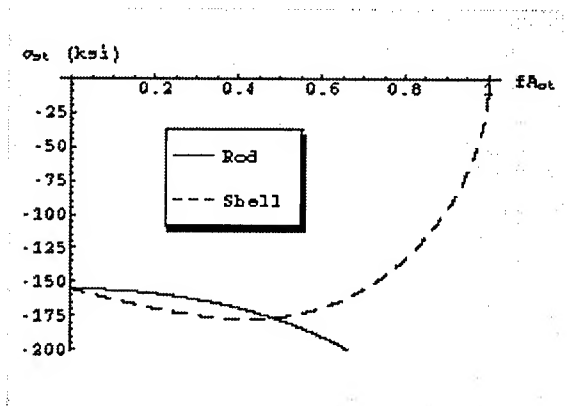


Figure 9. Maximum compressive stress in tungsten vs.  $fA_{st}$ .

Selecting the minimum allowable values for  $fA_{st}$  (Figure 8) of approximately 0.3 and 0.36 for the rod and shell configurations, respectively, Figure 11 shows the normal stresses on a line that lies along the y-axis (Figure 7) and runs from the top to the bottom of the cross-section. Note that in each of the configurations,

the maximum stress in the steel is 200 ksi (the yield strength of the steel), and the stress in the tungsten varies from zero (as constrained in the analysis) to near its yield strength of 175 ksi.

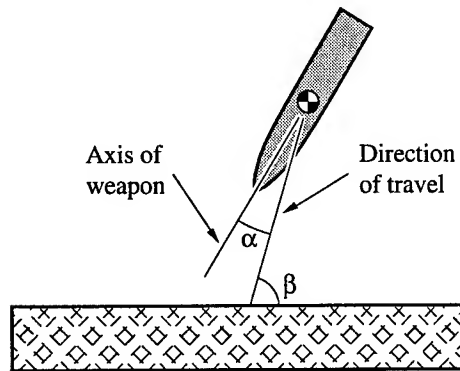


Figure 10. Definitions of  $\alpha$  and  $\beta$ .

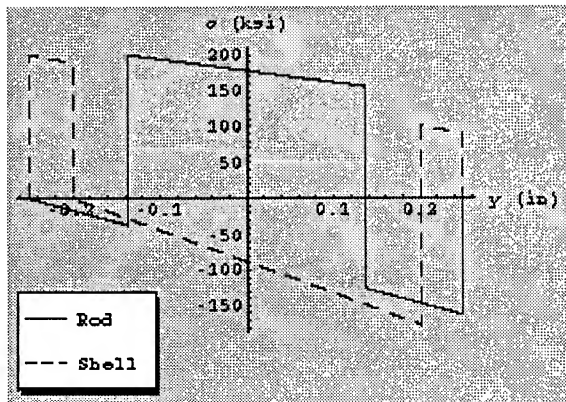


Figure 11. Normal stress throughout cross-section for the rod and shell configurations.

Figure 12 shows schematics of the relative sizes of the members for both the rod and shell configurations corresponding to their minimum allowable fractional areas of steel ( $fA_{st}$ ) of about 0.3 and 0.36, respectively (see Figure 8). In this figure, the steel is represented as darker gray. The effective density of the cross-section may be found using a rule of mixtures calculation, and the densities of tungsten and steel, as follows:

$$\rho_{eff} = \rho_{st} fA_{st} + \rho_{tu} (1 - fA_{st})$$

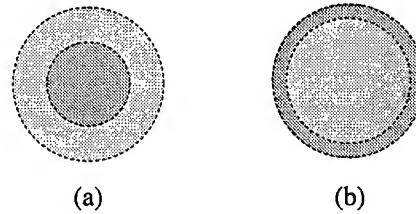


Figure 12. Schematics showing the relative scale of the tungsten and steel members for the rod with  $fA_{st}=0.3$  (a), and the shell with  $fA_{st}=0.35$  (b).

It is clear that when no yielding or segment separation occurs in the structure, the steel rod configuration leads to a somewhat lower  $fA_{st}$ , and hence a more dense cross-section than the steel shell configuration does. This is because the tungsten is stiffer than the steel, and its location at greater distances from the centroid makes the structure more efficient in bending. However, it is not clear that the steel rod would be a better configuration if the loads were such that some material and structural non-linearities were allowed to occur. Motivation for allowing non-linear structural response to occur lies in the possibility of allowing higher off-vertical angles of impact, or in reducing the amount of steel required in the cross-section.

### Non-linear Analysis

Assuming that plastic deformation can occur in the constituent materials, and that separation may occur between adjacent tungsten segments, the question then arises: how will one know if the structure really does "break"? What will be the new failure criterion? Obviously, it is undesirable for too much curvature to be present in the structure, otherwise adverse dynamic effects (steering) may be present after target penetration. Also, if the impact angles  $\alpha$  and  $\beta$  (Figure 10) are too severe, the structure will simply collapse.

In order to investigate the response of the structure to bending moment, it is necessary to refer to Equations 17. Recall that in order to go through the non-linear analysis, one has to first assume values for the preload  $P$ , fractional area of steel  $fA_{st}$ , and radius of curvature  $\rho$ . Once these are specified, Equations 18 and 19 are used to find the moment  $M$  required to produce a curvature of  $1/\rho$ . One can then step through various values of curvature, and produce a moment vs. curvature plot. Figure 13 shows this plot for a steel rod configuration structure with a given  $P$ , and  $fA_{st}$ .

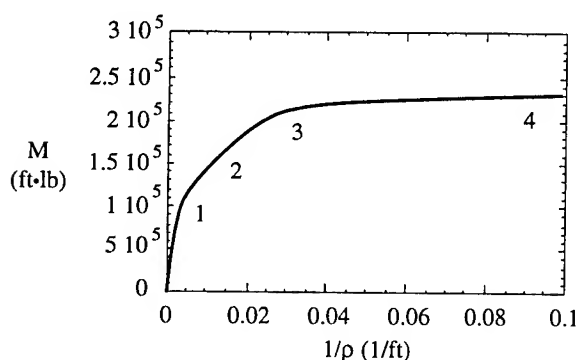


Figure 13. Plot of moment ( $M$ ) vs. curvature ( $1/\rho$ ).

Note that there exists a critical moment ( $M_{cr}$ ) above which, the curvature becomes very large. We can take this critical moment as our failure criterion. If the maximum  $M$  calculated by AMPLL for a given impact lies above  $M_{cr}$ , the structure collapses. If not, then the structure survives.

Recall the plot given in Figure 11. This is a plot of stress across the cross-section following the  $y$ -axis. Figure 14 shows plots of the same thing for various values of curvature along the moment vs. curvature plot (rod configuration only). The four plots in Figure 14 roughly correspond to the four numbered locations on this curve in Figure 13.

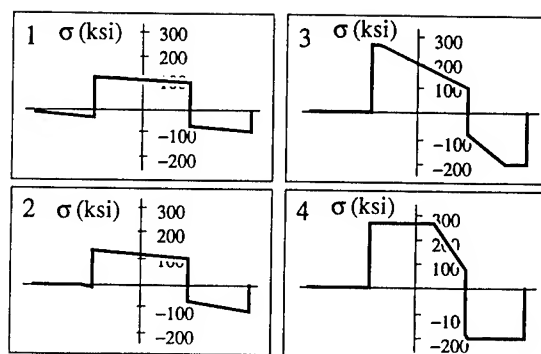


Figure 14. Normal stress along  $y$ -axis (Figure 7) at various values of curvature.

Up to point 1 in Figure 13, no yielding or separation between segments has occurred. This corresponds to the linear analysis performed previously. After this point, adjacent segments of tungsten actually separate, and a "crack" is formed between them. In other words, the stress cannot go tensile, so it simply goes to zero. This is shown in plot 2 in Figure 14. As the curvature continues to increase, the separated region continues to grow. At point 3 in Figure 13, the rod and the tungsten begin to yield (plot 3 in Figure 14). Beyond point 3, it continues to develop into a fully yielded cross-section (point 4).

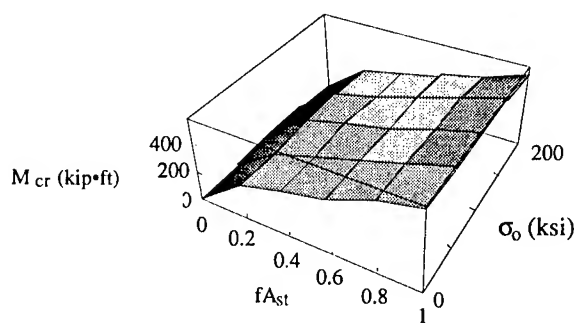


Figure 15. Critical moment vs. fractional area of steel and stress in the steel due to the preload.

Another matter that must be considered is how the critical bending moment  $M_{cr}$  varies as a function of the preload  $P$ . Recall that for Figures 13 and 14,  $fA_{st}$  and  $P$



were arbitrarily assigned. Figure 15 shows the value of  $M_{cr}$  as functions of  $fA_{st}$  and  $\sigma_p = P/A_{st}$  (the stress in the steel due to the preload).

Of course, as expected,  $M_{cr}$  is quite a strong function of  $fA_{st}$ , with the maximum value corresponding to an all steel cross-section ( $fA_{st}=1$ ).

But, as it turns out,  $M_{cr}$  is almost entirely independent of the preload.  $M_{cr}$  is virtually constant over the entire range of preloads from zero to yield in the steel. This is because in order to get to  $M_{cr}$  in the  $M$  vs.  $1/\rho$  curve, we had to yield almost all of the cross-section. Different preloads will change the shape of the  $M$  vs.  $1/\rho$  curve, but will not change its ultimate value,  $M_{cr}$ . This means that any value of  $P$  can be chosen, and the concern with the linear analysis of being able to introduce high values of preload into the structure is eliminated.

Finally, Figure 16 shows several moment vs. curvature plots; three plots for each configuration (rod and shell), each at different values of  $fA_{st}$ . For the sake of comparison, the most severe impact that could be survived under the linear stress analysis corresponded to a maximum bending moment (from AMPLL) of about  $1.8 \times 10^5$  ft•lb, and it took a fractional area of steel of 0.3 to do it. Compared to Figure 16, bending moments of greater magnitude are survivable, with fractional areas of steel significantly below 0.3.

Whereas the rod configuration seemed slightly better than the shell configuration under the linear analysis, it is quite clear that the shell configuration is actually a much more robust configuration. This makes sense when one considers Figure 17 in conjunction with Equation 19. As the structure is bent, and segments be-

gin to separate, the shell configuration has more stressed material further away from the center of the cross-section. Hence, Equation 19 will yield a higher moment for a given radius of curvature.

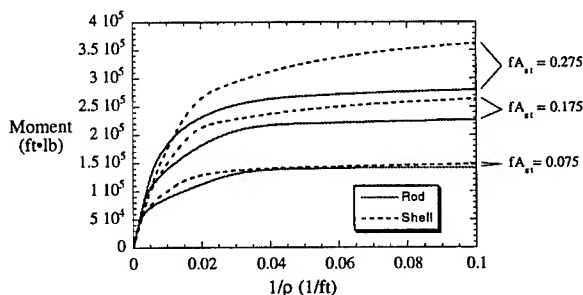


Figure 16. Moment vs. curvature for various values of  $fA_{st}$ , for both the rod and shell configurations.

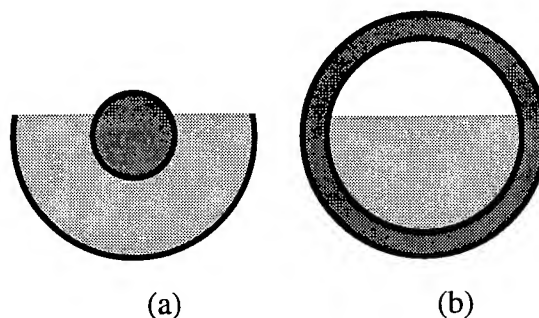


Figure 17. Schematic of cross-sections of the rod (a) and shell (b) configurations showing development of gaps between tungsten (lighter grey) segments.

The question that then arises is how severe an impact is it desired to survive. With the non-linear analysis developed herein, the envelope of impact conditions has been broadened considerably over that of the linear stress analysis. For instance, a 6 in. diameter, 36 in. long shell configuration tungsten/steel penetrator impacting a 3 ft thickness of reinforced concrete at 1300 ft/s,  $70^\circ$  angle of impact ( $\beta$ ),  $1^\circ$  angle of attack ( $\alpha$ ) (see Figure 10) could survive an impact with quite acceptable values of  $fA_{st}$  (around 0.25). More severe impacts could be survived with greater area fractions of steel in the cross-

section. It would be a matter of further study to find the optimal configuration of a final penetrator.

Figure 18 shows a schematic of a possible revision of Culp's [2] proposed penetrator. The segments could be placed inside the steel shell, and a threaded plug could then be inserted, as shown. Since the non-linear analysis showed that it is not critical, it would not be necessary to introduce large levels of preload into the structure.

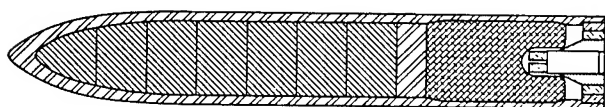


Figure 18. Schematic of proposed configuration of segmented penetrator.

Lastly, recall from Figures 13 and 14 that most of the performance in the moment vs. curvature curve is in the elastic region. Plastic yielding in the constituent materials doesn't happen until point 3 in Figure 13. Hence, if the moment due to impact loading remains below this point 3 in Figure 13, there will be no permanent bending of the structure. This would minimize adverse terradynamic effects that permanent bending would create.

### Temperature Effects

From Equation 21, the change in preload of the tensile member due to temperature changes can be found. With a thermal soak at a temperature change of 30°C (55°F), there is only about a 2.5% change in the preload. This is an amount that is quite acceptable.

### CONCLUSIONS AND FUTURE WORK

Although the 3-D finite element work was not finished by the completion date of the project, the work is ongoing

and will be completed. However, the analytical work suggests that a segmented tungsten penetrator is indeed feasible, and should be pursued. Using a non-linear structural and material response analysis, coupled with the modified version of AMPLL developed in this work, it has been demonstrated that a segmented tungsten ballasted penetrator, of the configuration shown in Figure 18, could withstand impact angles of up to about 20° off vertical ( $\beta = 70^\circ$ ), and angles of attack ( $\alpha$ ) of up to about 1° (see Figure 10).

It was found that the shell configuration was more robust than the steel rod configuration. See Figure 2. The members of the structure can be sized (with satisfactory area fractions of steel in the cross-section) such that no permanent shape change occurs upon bending during impact. This means that not only will the structure survive impact, but that adverse terradynamic effects will be minimized.

It turns out, from the non-linear analysis, that a large preload in the steel tensile member is not necessary. This avoids a problem that was anticipated concerning how the preload would be introduced into the structure. It also alleviates any concerns about changing loads due to temperature effects.

The next logical step after the current research would be to fabricate and test a scaled prototype of the segmented penetrator design. For the sake of cost minimization, the first prototype could be made entirely of steel. This would eliminate the cost of fabricating tungsten segments. If this design performs well, a tungsten segmented penetrator could then be built. The analytical tools developed in the current work would aid in the analysis of any experimental work done.

## REFERENCES

- 1 Young, C.W., "Depth Prediction for Earth-Penetrating Projectiles," J. of the Soil Mechanics and Foundations Division, ASCE, 95(SM3), 803-817, 1969.
- 2 Culp, M., "Tungsten Disk Penetrator Design Study-December 1996," Full Spectrum Technologies, Inc., 503 Golf View Dr. Suite 200, San Jose, CA 95127.
- 3 Rule, W.K., "Development of the Analytical Model of Penetration with Lateral Loading (AMPLL) Program," Final Report for the Department of the Air Force, Wright Laboratory, Eglin Air Force Base, FL, Purchase Order F08630-94-M-0009, September 1994.
- 4 Rule, W.K., Private Communication, 8 July 1997.
- 5 Craig, R.C., Mechanics of Materials, John Wiley & Sons, Inc., New York.

**Associate did not participate in the program.**

ORGANICALLY MODIFIED SILICATE FILMS AS CORROSION RESISTANT  
TREATMENTS FOR 2024-T3 ALUMINUM ALLOY

Edward T. Knobbe  
Assoc. Professor of Chemistry and  
Director of the Environmental Institute

Oklahoma State University  
201 CITD  
Stillwater, OK 74078

Final Report for:  
Summer Faculty Research Program  
Wright Patterson Air Force Base

Sponsored by:  
Air Force Office of Scientific Research  
Bolling Air Force Base, DC  
and  
Wright Patterson Air Force Base

September 1997

# ORGANICALLY MODIFIED SILICATE FILMS AS CORROSION RESISTANT TREATMENTS FOR 2024-T3 ALUMINUM ALLOY

Robert L. Parkhill<sup>1</sup> and Edward T. Knobbe<sup>1,2</sup>

<sup>1</sup>Thin Film Materials Processing Group

Department of Chemistry and

<sup>2</sup>the Environmental Institute

Oklahoma State University

## Abstract

Organically modified silicates (ormosils) sol-gel films coated on aluminum alloy 2024-T3 coupons were investigated for the purpose of developing an environmentally-compliant replacement for chromate-based surface treatments. The effect of surfactants, hybrid organic content, and alkoxide size effects on resultant films were evaluated for corrosion protection in comparison to Alodine-1200 type surface treatments. Results indicate that pinhole surface defects were present in most films; these limit the ultimate performance of sol-gel treatments. Even with pinhole defects, however, 4 orders of magnitude improvement in corrosion protection was demonstrated for sol-gel treated coupons with respect to Alodine 1200 surface treatments. Selected single-layer sol-gel compositions were found to rival the performance of the chromate-laden paint system (e.g., Alodine/primer/topcoat) currently used by the Air Force.

# ORGANICALLY MODIFIED SILICATE FILMS AS CORROSION RESISTANT TREATMENTS FOR 2024-T3 ALUMINUM ALLOY

Robert L. Parkhill and Edward T. Knobbe

## **I. Introduction**

Recently, the Air Force has identified corrosion of aluminum-skinned aircraft and the development of improved environmentally-compliant surface treatments of aluminum alloys to be high priority topics. Changing federal regulations dictate the use of fundamentally new coating systems which are capable of meeting more strict environmental standards [1]. Coating processes which rely on the use of chromate-based passivating agents, such as strontium chromate (e.g., Alodine 1200-type treatments) will no longer be approved for use. The issue becomes more problematic as the service lifetimes of aging weapons systems such as the C/KC-135 are now projected to be 80 years and longer. Replacement coating systems must be capable of satisfying the substantial need for dramatically extended lifetimes, must be compatible with present and future environmental requirements, and must be easily integrated into the current primer/topcoat paint systems.

Recent research has been directed toward the development of a new coating process based on the sol-gel process. Preliminary investigations indicate that the one of the most promising approaches involve a sol-gel coating system doped with corrosion-inhibiting additives [2-5]. The studies described herein suggest that selected sol-gel compositions may provide a fundamentally new protective barrier capable of meeting both environmental and corrosion-protection performance goals.

## **II. Approach**

Over the past two summers, researchers from Oklahoma State University (Parkhill and Knobbe) have investigated the use of organically modified silicate (ormosil) films as potential replacement treatments for the passivation of aluminum alloys (AAs). Ormosils

provide a route to the preparation of hybrid organic-inorganic materials composed of intimately mixed network polymer systems. Sol-gel films prepared using ormosil precursors are of particular interest, because they blend the mechanical and chemical characteristics from both network types. The ceramic hybrid component may be optimized to provide improved film adhesion to AA substrates and impart greater hardness, while the organic hybrid network component contributes to increased film density, flexibility, and functional compatibility with organic polymer paint systems. Hybrid films may be tailored to have exceptional durability and adhesion, while still providing a dense, flexible barrier to permeation of water and corrosion initiators such as  $\text{Cl}^-_{(\text{aq})}$ .

Last year's studies showed that alcohol based sol gel films possessed superior corrosion protection compared to standard chromate treatments such as Alodine 1200 [6]. Ormosil coatings were found to exhibit substantial improvement, by up to six orders of magnitude, in corrosion resistance with respect to chromate-based conversion coatings. Thus, sol-gel films demonstrated much promise for the development of environmentally-compliant replacements to chromated surface treatments.

In addition to chromate elimination, viable replacement systems must have low or zero component volatile organic compounds (VOCs). Thus, it is desirable to investigate entirely or largely water-based processes. This aspect introduces several new problems for sol gel materials and processes, including high solution surface tension (and resultant poor surface wetting), precursor solubility, and sol stability. Very few published studies have successfully employed water based sol gel solutions for coating systems. However, research results described herein provide a basis for developing dramatically improved, water-based sol gel coatings capable of meeting the future need for low VOC formulations.



### III. Background

In general terms, the sol-gel method consists of hydrolysis and condensation reactions in which alkoxy-silanes react with water to form a polymeric network of nanoporous material. The sol-gel process is extensively described in the work by Brinker and Scherer [7]. Organically-modified silicate hybrid materials consist of a comparable reaction sequence with the addition of organic functionality which can be blended into the hybrid system to tailor material properties for the desired functionality. In such systems the influences of organic groups and cross-linking agents, water content, and alkoxide precursors have been shown to have profound effects on the chemical reaction kinetics and upon the resultant hybrid.

#### *III.a Water Based Systems*

Under conditions of excess water (i.e., more than that needed for complete alkoxide hydrolysis), the hydrolysis and condensation reaction rates are significantly altered. Aelien *et al.* found the acid-catalyzed hydrolysis of TEOS to be first order with respect to  $H_2O$  concentrations [7,8]. Increased water concentrations result in more rapid and complete hydrolysis of alkoxide species. Since water is a by-product of the condensation step, elevated water levels slow condensation and polymerization. Increased water content tends to stabilize the sol phase, resulting in the development of more branched colloidal structures. Sols composed of highly branched particles tend to yield films having increased porosity and lower film density. Conversely, more linear particles tend to yield denser, harder films. Thus, it is clear that the water/alkoxide ratio can substantially influence reaction kinetics in a way which impacts film porosity and hardness characteristics.

In addition to perturbing reaction kinetics, water content also effects solution viscosity and surface tension. Unlike typical sol-gel derived solution's used for thin film coatings, which generally rely on the use of organic co-solvents, water-based systems tend to have substantially greater surface tensions and viscosities. Methanol, for example, has a surface tension (23 dynes/cm<sup>2</sup>) which is only one third that of water (72 dynes/cm<sup>2</sup>) [9].

Solutions having large surface tensions can result in poor substrate surface wetting characteristics; they also tend toward slow evaporation rates of volatile compounds subsequent to film formation. It is known that sol viscosity increases as a function of particle growth and reduced alcohol content. Ultimately, water content substantially impacts film thicknesses and sol stability. In order to develop an understanding of chemical effect (i.e., precursor alkoxide group, water content, hydrolysis rate, surface tension, viscosity, dilution, *etc.*) on film morphology, an integrated series of studies on related parameters was performed. One of the goals of the summer project was to improve film quality and corrosion protection characteristics through the development of dense films having improved surface wetting characteristics compared with films prepared during the '96 summer program.

### *III.b. Surfactants*

Surfactant use in coating systems has been shown to be one of the primary mechanisms for improving film quality. Research by Murakata, T. *et. al* has shown that various salt additives and ionic surfactants can profoundly alter the surface area and pore diameters of silica samples [10]. Other studies have utilized surfactants to aid in surface wetting of high energy surfaces [11,12]. Currently, many industrial sources offer surfactants which can be tailored to a particular system for reducing surface tensions and improving wetting. By introducing various surfactants, the morphology of film coatings can be optimized for improved corrosion protection.

In this study, a dual surfactant system was investigated to improve wetting behavior on clean AA surfaces. Surfactants were chosen on the basis of reducing surface tension in aqueous solution. Vender-supplied literature indicates surface tension reduction in aqueous media may be decreased from 72 dynes/cm<sup>2</sup> to 22 dynes/cm<sup>2</sup> through the use of selected surfactants. Surface tension effects on wetting, overall film quality, and corrosion

protection have been investigated, and the impact of surfactant use on corrosion protection has been quantified

### *III.c. Precursor Use*

Alkoxide precursors can largely effect hydrolysis and condensation reaction kinetics through steric bulk and electron donating (or withdrawing) characteristics. Short chain alkoxides react much faster than large chain alkoxides due to a lower degree of steric hindrance and less stability due to electron donation characteristic [7]. Precursor sols incorporating small alkoxide side groups, such as tetramethoxy silane (TMOS), hydrolyze more readily than those incorporating larger alkoxide side groups (i.e., tetraethoxy silanes, (TEOS), tetrapropoxy silane, (TPOS), *etc.*), resulting in a more chemically reactive solution. Thus, precursor alkoxide side chains can be utilized to control reaction kinetics and/or the stability of a sol system. Ormosils prepared using TMOS, TEOS, and organically modified silicate precursors were coated onto AA substrates. The impact of alkoxy side group size on film morphology and corrosion protection have been assessed.

The presence of organic functional side chains in a hybrid silica system can effect film wetting and surface compositions. Research has shown that organic content can change the chemical nature of colloidal surfaces in sol-gel systems [12-15]. In the case of low organic content in the sol-gel derived network polymer, the organic functional groups have been shown to be more or less evenly dispersed throughout the ormosil composition. With elevated organic concentration, however, the functionalities have been found to segregate, yielding organic-rich regions which are preferentially positioned at surface sites. Thus, film characteristics can be dramatically altered by varying the relative amount of polymer components. Elevated organic content tends to produce surfaces with a hydrophobic surface character.

## **4. Experimental Methods**

### **4.1. Materials and Reagents**

Substrates consisted of aluminum 2024-T3 coupons which were polished with 300 and 600 grit silicon carbide sand paper followed by cleaning in an ultrasonic bath using isopropanol and hexane solvents. Alkoxide reagents (i.e., TEOS, TMOS, and ormosil) reagents were used as received from Aldrich. Surfactants were incorporated by direct dissolution into the aqueous sol phase. Spectroscopic grade isopropanol and hexane were used as received from Aldrich. Nitric acid was used to catalyze the hydrolysis reaction.

### **4.2. Sol-gel Preparations**

Preparation of the ormosil solutions was performed as follows: 25.0 ml of TEOS was placed in a beaker with 18.7 ml of acidified water. The resultant two-phase solution was vigorously stirred to induce mixing and initiate hydrolysis. The bi-phasic solution became a clear single phase sol approximately 2 hours after initial mixing. Once the solution cleared, organically modified precursors were added and thoroughly mixed. One hour later, additional water and surfactants additives were added in a drop-wise manner until the desired concentrations were obtained. The final solution was stirred continuously in a closed container held at room temperature until its use in dip-coating. Immediately prior to coating, the sol was transferred to a teflon cells into which the AA substrate were dipped.

### **4.3. Coating and Curing Methods**

Aluminum 2024-T3 substrates were dipped into precursor sols using a Chematic Technology Inc. model 201 dip-coater. The sol gel coatings were applied using a single dip step. 30 ml of sol were transferred to the teflon dipping cell. Dip-coating was done using a dwell time of 10 seconds in the coating sol. The withdrawal speed was 10 cm/s into RT air. After dipping, samples were cured using selected time/temperature conditions.

Curing temperatures included room temperature, 60°C, 100°C, and 150°C. Cure times at these temperatures ranged from 1 to 24 hours. After heat treatment, samples were removed from the ovens and allowed to cool to room temperature before characterization and analysis.

#### 4.4. Characterization

Film morphologies were characterized using an OPTIPHOT-POL Nikon polarizing microscope equipped with a 5.0X microscope objectives. Film thickness was determined using a Sloan Dektak IIA profilometer.

The corrosion potentials were determined from potentiodynamic polarization curves using a Gamry potentiostat. Sweep potentials were varied from -1.0V to 0.2V vs. SCE after coated samples were immersed in a 3% NaCl solution. Specimens were maintained in the 3% NaCl for 1 hour prior to potentiodynamic polarization measurement, except in cases where the effects of longer term immersion are noted. Data were analyzed using CMS100 software.

### 5. Results and Discussion

Film performance and morphology were characterized as functions of surfactant addition, organic content, and chemical nature of alkoxide precursors used. Compositional parameters were varied in order to develop optimal corrosion protection. Film protection characteristics were determined in relation to one of three protection standard specimens: untreated 2024-T3 aluminum alloy, Alodine 1200 treated 2024-T3, or a "standard" complete paint system (i.e., Alodine surface treatment/chromated primer/topcoat) applied to a 2024-T3 coupon. Preliminary assessments of protection afforded by sol-gel surface treatments were made on the basis of film morphology, thickness, and screening potentiodynamic polarization measurements.

### 5.1. Corrosion Protection as a Function of Surfactants Addition.

Table I represents profilometer measurements from 2 sets of ormosil coatings. Films were prepared using water/alkoxide molar ratios concentrations as indicated in Table I. In each specimen set, film thicknesses were found to increase as water ratios were reduced. Surfactant addition caused film thickness to increase for a given water/alkoxide ratio.

Table I. Thickness Variation in Ormosil Coatings due to Surfactant Addition.

<u>Sample</u>	<u>Water:Alkoxide Ratio</u>	<u>Surfactant</u>	<u>Thickness</u>
1	2:1	no	1.8 $\mu\text{m}$
2	2:1	yes	2.2 $\mu\text{m}$
3	4:1	no	0.8 $\mu\text{m}$
4	4:1	yes	1.5 $\mu\text{m}$

Thickness reduction due to increased water content is expected as a result of simple dilution effects. However, surfactant-induced film thickness increases are not so easily explained. Surfactant addition caused the sol to become observably more viscous. The mechanism which leads to such a substantial viscosity increase is not well understood or documented in the literature. Upon dipping into the more viscous, surfactant-containing sol, the deposited layer entrained substantially more liquid. Gelatin of this thick viscous layer resulted in a substantially thicker coating as indicated in Table I..

Figure 1 shows optical micrographs of samples 1 and 2. At 50X, micrographic images revealed the significance of surfactant addition. Sample 1 (containing no surfactant) had a large areal pinhole number (# pinholes/area). Pinhole sizes generally ranged from 10 to 80  $\mu\text{m}$ . Sample 2, which contained surfactant additives, was found to have two types of pinholes. Small pinholes were estimated to have diameters of less than 10  $\mu\text{m}$ , with an

areal number of 45 holes/mm<sup>2</sup>. Larger pinholes were randomly positioned with estimated diameters between 20 and 50  $\mu\text{m}$  and an areal number of 3 pinholes/mm<sup>2</sup>.

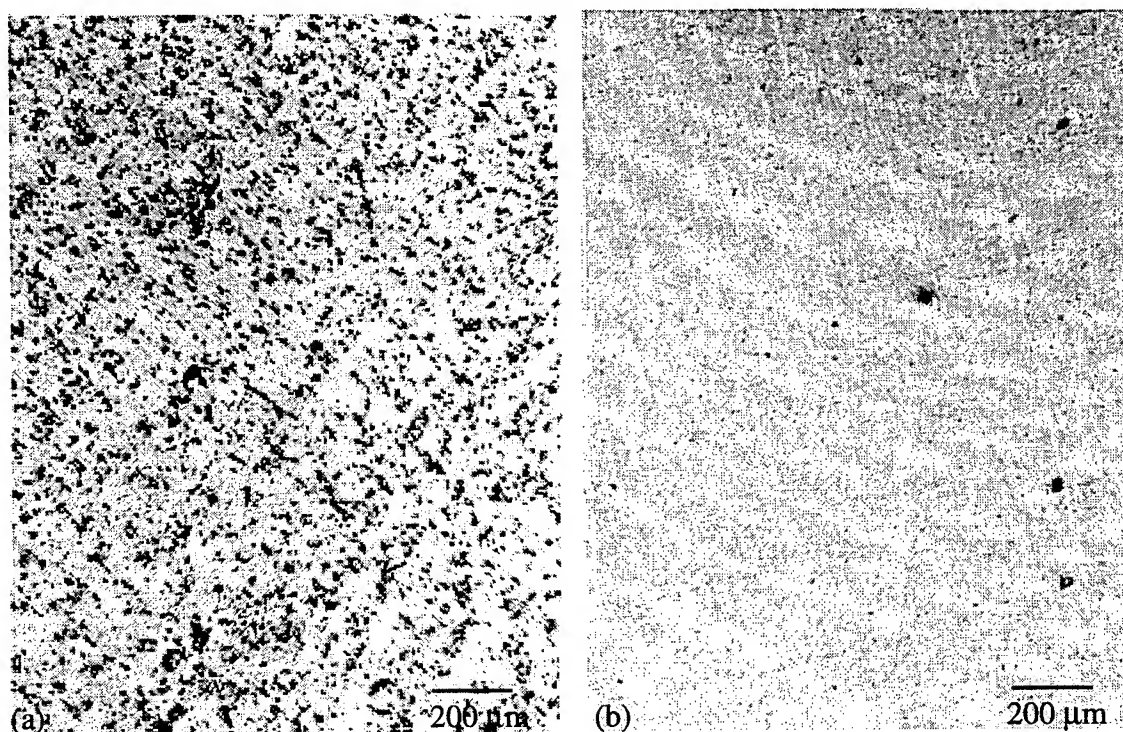


*Figure 1* : Aluminum 2024-T3 substrates coated with an ormosil coating with a water : alkoxide ratio of 4:1: (a) No surfactant sample 1 (b) Surfactant sample 2.

The development of extensive pinholes in the ormosil films is postulated to occur as a result of the high surface tension found in water-based sols. As water evaporates during film formation, large capillary forces cause the free energy of the solid-liquid interface to increase. In order to compensate, the remaining sol can minimize the interfacial energy by decreasing the liquid-solid interface. As water continues to evaporate, the sol begins to bead on the AA surface, leaving voids at the interface (Figure 2a). With surfactant addition, the surface tension of the sol was estimated to be reduced by as much as two thirds. Reduced surface tension lowers the capillary forces, which permits the sol to spread more uniformly across the substrate (Figure 2b). It is clear from examination of Figures 1(a) and

(b) that pinhole formation was significantly reduced through the use of appropriate surfactant additives.

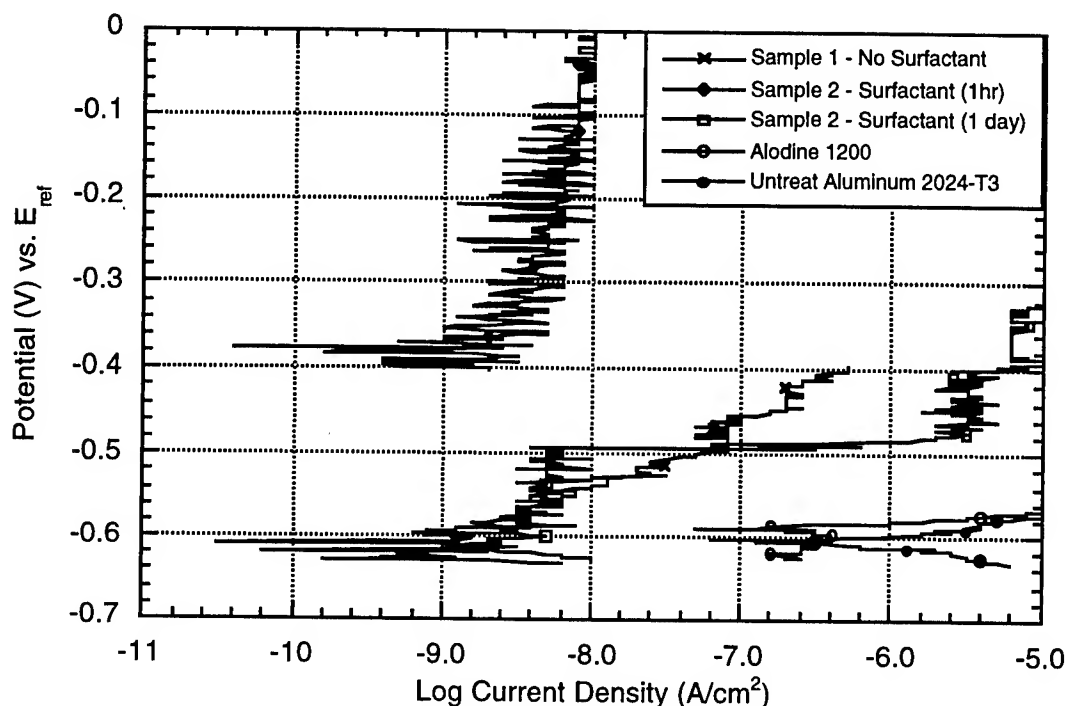


*Figure 2:* Anodic behaviors for a non surfactant ormosil film, ormosil film with surfactant, Alodine 1200-treated, and untreated aluminum 2024-T3 coupons.

Electrochemical evaluation of Samples 1 and 2 demonstrated the excellent corrosion resistance imparted by the surfactant system. Figure 2 represents an anodic electrochemical polarization spectroscopy measurements used to assess ormosil corrosion protection (with and without surfactant addition) compared to Alodine 1200-treated and untreated aluminum 2024-T3 substrates. Untreated 2024-T3 coupons had a corrosion potential ( $E_{oc}$ ) of -610mV and did not exhibit a passive region before pitting. Alodine 1200 had an  $E_{oc}$  of -580mV and showed a small (0.04V) passive zone prior to pitting. Sample 1 (no surfactant) had an ( $E_{oc}$ ) of -610mV with little observable pre-pitting passivation. Sample 2 (surfactants added) had an  $E_{oc}$  of -380mV and showed a passive zone of 0.4V without measurable



pitting after a 1 hour soak in 3% NaCl solution. After 24 hours of immersion, Sample 2 showed a  $E_{oc}$  of -620mV and a small passive zone of 0.13V before the onset of pitting. Comparison of the passivation current densities indicate that surfactant-enhanced ormosil coatings have a 4 order of magnitude improvement in field-induced corrosion rate when compared to the Alodine 1200 surface treatment.

These results clearly indicate that surfactant addition provides dramatically-improved corrosion protection. The evidence is consistent with the dominant corrosion failure mechanism proposed for in the ormosil films; i.e., pinhole defects. The rapid failure of sample 1 indicates incomplete barrier protection, consistent with the large areal pinhole number found for such specimens. However, the comparatively small current density at elevated potentials implies that the corrosion rates for such specimen is slow. It is postulated that the gradual increase in current density as a function of applied field (above the corrosion potential) was due to pinhole enlargement from dissolution of aluminum at local defect sites. The pitting observed in sample 2 was attributed to catastrophic film failure (i.e. localized coating delamination and/or cracking). As water permeates through film defects, interfacial stresses develop leading to film failure. The rapid increase in current density suggests the onset of pitting, resulting from an instantaneous change in the exposed AA surface. Post electrochemical test examination of the films revealed significant cracking near and around pinholes, which is consistent with the proposed failure mechanism. Thus, the overall improvement in corrosion protection associated with surfactant addition is presumed to be a direct result of significant reduction in areal defect number.

## 5.2. Organic Composition:

Table II represents profilometer measurements from 3 sets of ormosil coatings as a function of organic component. Film compositions are presented as water:alkoxide molar ratios. In each set, film thickness was shown to decrease with elevated water content. The

thickness differences found to exist between 20 and 33 percent organic composition gels were not significant (within experimental measurement error).

Table II Thickness results of ormosil films with variable dilutions and organic content

<u>Sample</u>	<u>Water:Alkoxide Ratio</u>	<u>Organics</u>	<u>Thickness</u>
O1	2:1	20%	1.7 $\mu\text{m}$
O2	2:1	33%	1.5 $\mu\text{m}$
O3	4:1	20%	0.9 $\mu\text{m}$
O4	4:1	33%	1.0 $\mu\text{m}$
O5	6:1	20%	0.7 $\mu\text{m}$
O6	6:1	33%	0.8 $\mu\text{m}$

Variations in organic content (i.e., 20% vs. 33%) resulted in minimal observable surface morphology variation. Figure 4 represents two ormosil films typical of the 20% and 33% organic components (specimen O3 and O4). Ormosils with 33% organics were found to have two types of pinholes. Small pinholes were estimated to have diameters of less than 10  $\mu\text{m}$  with an areal number of 45 holes/ $\text{mm}^2$ . Larger pinholes were randomly positioned with diameters of 20 to 50  $\mu\text{m}$  and areal number of 3 holes/ $\text{mm}^2$ . Ormosils containing 20% organics were shown to have similar pinhole types, with areal pinhole numbers of 25 holes/ $\text{mm}^2$  and 2 holes/ $\text{mm}^2$  for small and large pinholes, respectively.

These results suggest that ormosil films containing 20% organic components have moderately improved wetting characteristics. The lower areal pinhole number indicates that reduced surface tensions may have occurred as a result of lowered organic content (increased surface tensions are associated with poorer sol wetting behavior).

The electrochemical evaluation for the organic component (20% and 33%) ormosil films and a complete paint system on aluminum 2024-T3 substrates are presented in Figure 5. The 33% organic ormosil had an  $E_{oc}$  of -630mV a passive zone of nearly 0.14V after 1

day of immersion in 3% NaCl solution. The 20% organic film showed an  $E_{oc}$  of -460mV and a passive zone of 0.45V after 1 day of exposure to 3% NaCl solution (no pitting).

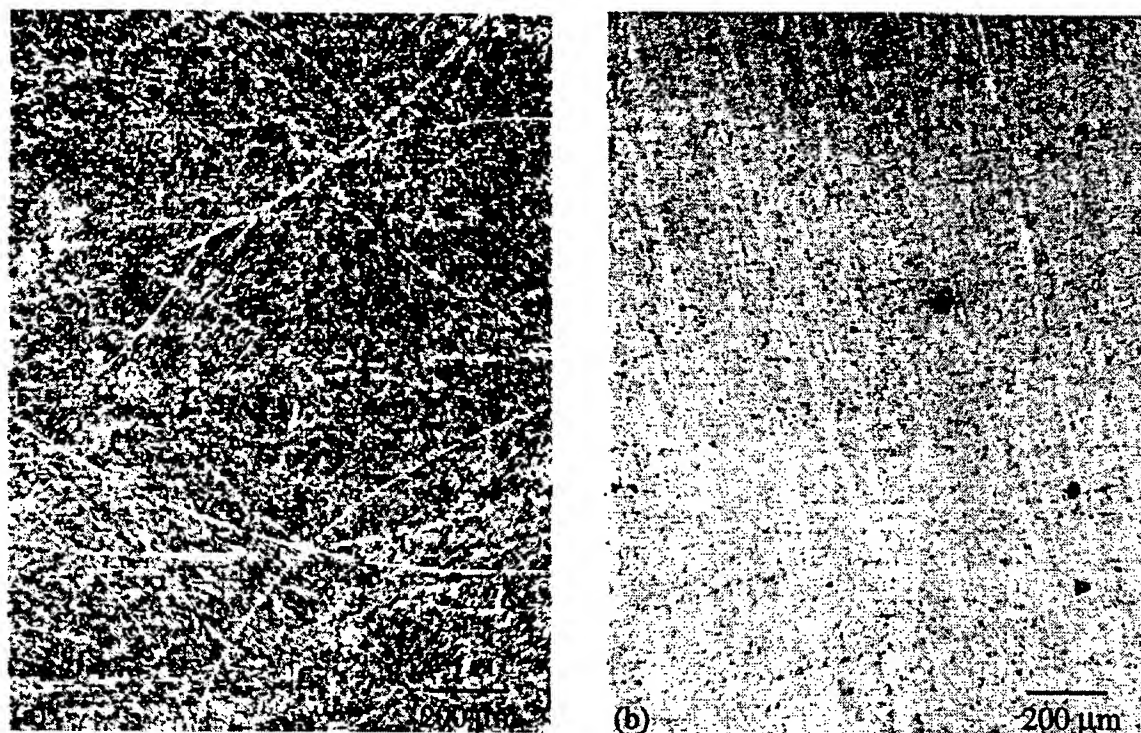


*Figure 4:* Aluminum 2024-T3 substrates coated with ormosil films containing different concentrations of organic material (a) 20% (b) 33 %.

The film eventually failed after 3 days of immersion in the salt water solution; at that time these films exhibited an  $E_{oc}$  of -620mV and a reduced passive zone (0.08V). These films are shown in Figure 3 compared to the performance of a complete paint system (CPS; i.e., Alodine surface treatment/chromated epoxy primer/polyurethane topcoat). The CPS exhibited an  $E_{oc}$  value of -300mV after 3 days immersion in 3% NaCl solution, with a passive zone of 0.3V. Direct comparison of the anodic polarization behavior of these specimens clearly shows that the single layer, chromate-free 20% organic ormosil coating offers a level of corrosion protection which is very similar to that afforded by a chromate-laden CPS.

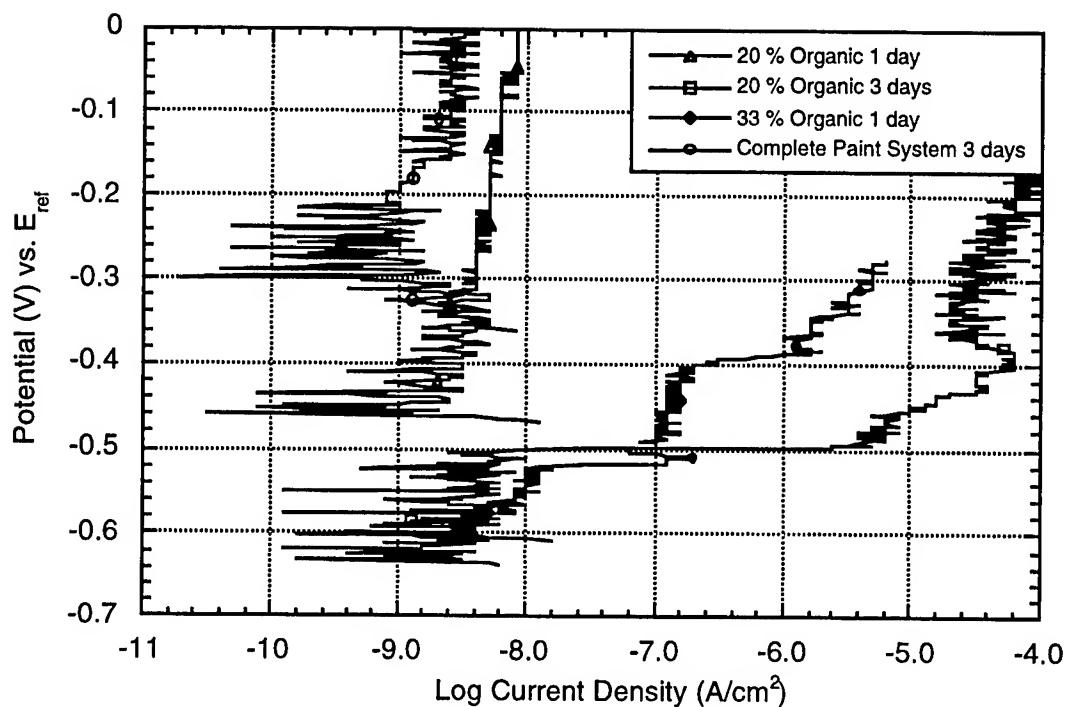


*Figure 5:* Polarization behaviors for 20% organic ormosil, 33 % organic ormosil, and complete paint system coated on aluminum 2024-T3 coupons.

The electrochemical evaluation showed greatly improved corrosion resistance for the 20% organic ormosil film compared to the 33% organic film. In both systems, the pitting initiation appear to be caused by localized film fracture induced at defect sites by internal stresses. Thus, the extended protection provided by the lower organic content ormosil can be attributed to both a reduction in pinhole density and lower water/ $\text{Cl}^-_{(\text{aq})}$  permeability through such films.

### 5.3 Silica Precursor:

Table III represents profilometer measurements from 3 sets of ormosil coatings with different silicon alkoxide precursors. The films are presented as water:alkoxide molar

ratios. In each set, film thickness was shown to decrease as water ratios increased. The thickness differences between alkoxide precursors was negligible.

Table III

<u>Sample</u>	<u>Water:Alkoxide Ratio</u>	<u>Precursor</u>	<u>Thickness</u>
M1	4:1	TMOS	1.4 $\mu\text{m}$
E1	4:1	TEOS	1.7 $\mu\text{m}$
M2	6:1	TMOS	0.8 $\mu\text{m}$
E2	6:1	TEOS	0.9 $\mu\text{m}$
M3	8:1	TMOS	0.5 $\mu\text{m}$
E3	8:1	TEOS	0.7 $\mu\text{m}$
M4	10:1	TMOS	0.3 $\mu\text{m}$
E4	10:1	TEOS	0.4 $\mu\text{m}$

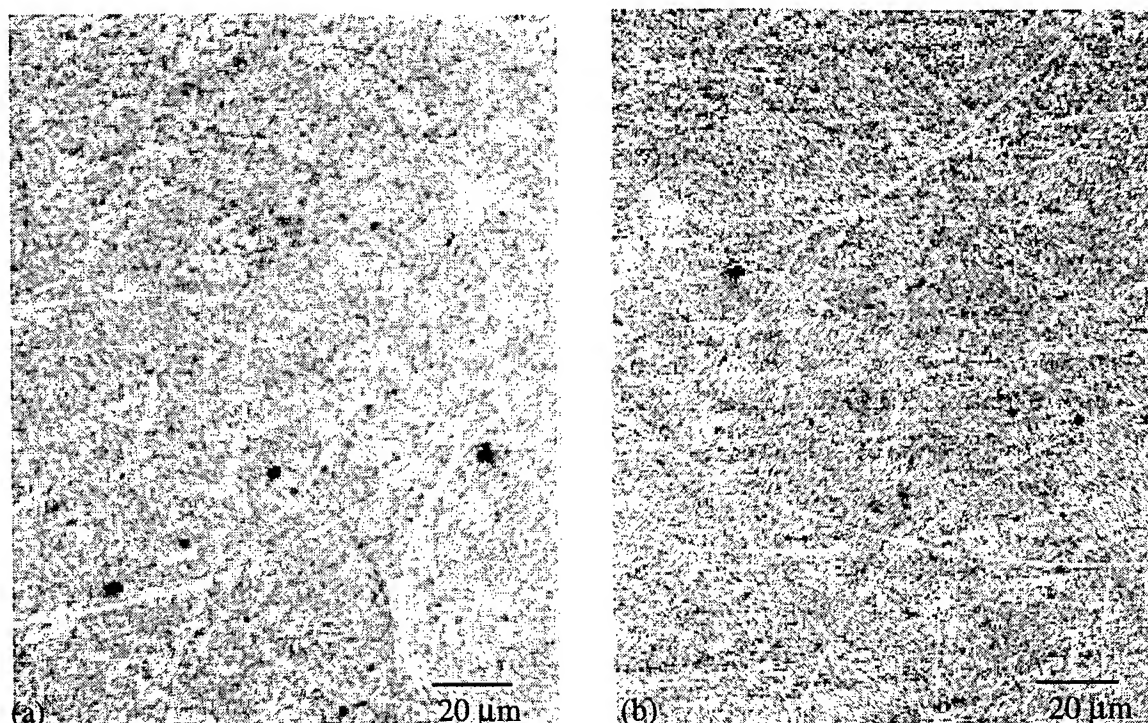


Figure 6. Optical micrographs of two ormosil films with different silica alkoxide precursors. (a) TMOS (b) TEOS

The small variation in film thickness can be attributed to the nature of the alcoholic by-products of the hydrolysis reaction for TMOS (methanol-generating alkoxide) precursor

versus the TEOS (ethanol-generating alkoxide) precursor. The two system are primarily composed of water, but alcohol by-products can influence the viscosity of the sol.

The use of different alkoxide precursors showed only small variation in surface morphology. Figure 6 represents optical micrographs of two typical ormosil films derived from TMOS and TEOS alkoxide precursors. The TMOS ormosil film was found to have two types of pinholes. Small pinholes were estimated to have diameters of less than 10  $\mu\text{m}$  and an areal pinhole number of 35 holes/ $\text{mm}^2$ . Larger pinholes were randomly scattered with diameters between 50 and 100  $\mu\text{m}$  and an areal pinhole number of 4 holes/ $\text{mm}^2$ . The TEOS ormosil film was shown to have similar population densities, but pore diameters of less than 10  $\mu\text{m}$  for small pinholes and between 20 and 50  $\mu\text{m}$  for large pinholes.

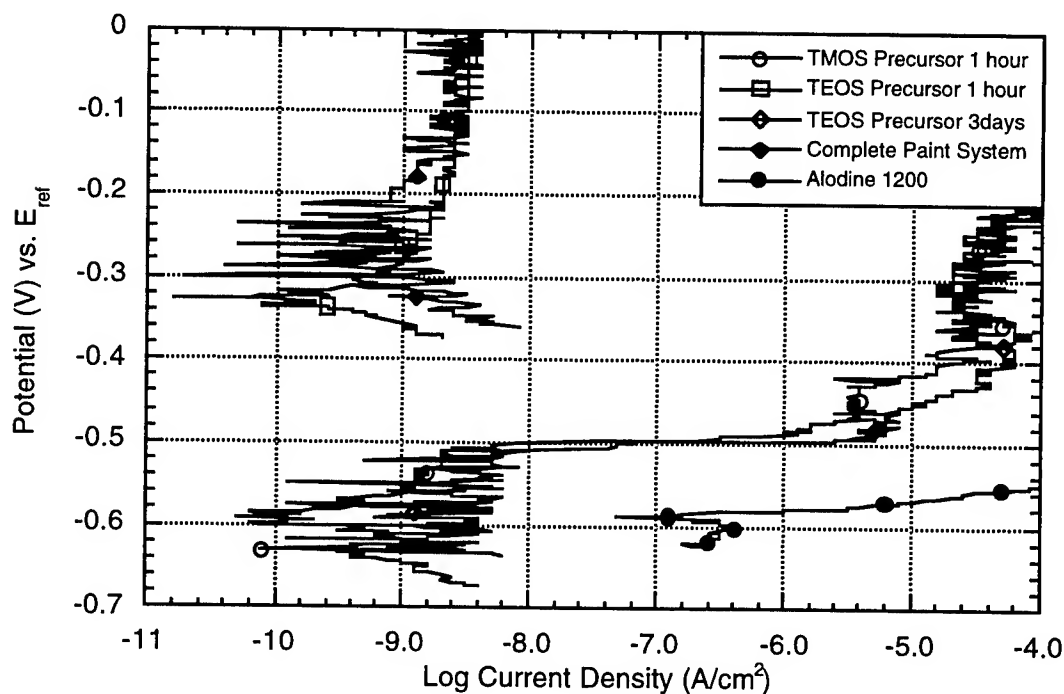


Figure 7. Anodic polarization behavior of silica precursors, Alodine 1200, and a complete paint system .

Figure 7 represents electrochemical analysis for a TEOS ormosil film, TMOS ormosil film, Alodine 1200, and complete paint system on aluminum 2024-T3 substrates. The TMOS ormosil film had an  $E_{oc}$  of -630mV and a passive zone of 0.13 after 1 hour of immersion in 3% NaCl solution. The TEOS ormosil film had an  $E_{oc}$  of -330mV and a passive zone of 0.35V after 1 hour of immersion in 3% NaCl solution. The film failed only after 3 days of continuous immersion in salt water and showed an  $E_{oc}$  of -590mV and a passive zone of 0.09V. The complete paint system showed an  $E_{oc}$  of -300mV and a passive zone of 0.3V after 3 day of immersion in 3% NaCl solution.

TEOS derived films were shown to provide superior corrosion protection compared to TMOS derived films. In both cases, the mechanism of failure is postulated to be film cracking. The comparatively early failure of TMOS-derived ormosils suggests that such films are (a) more porous and/or (b) more highly strained. The TMOS-derived sol is believed to have resulted in the development of more branched particulate structures during the colloidal particle growth phase due to the more reactive nature of the methoxy precursor. A higher degree of branching could lead to more porous film structures with a subsequent lowering of film integrity. Thus, less reactive silicon alkoxide precursors appear to yield films having improved corrosion protection due to the denser gel network which results.

## 6. Summary and Conclusion

The corrosion resistance of aluminum alloy 2024-T3 substrates coated with water based ormosil film preparations were investigated. Corrosion performance and surface morphology were assessed as a function of surfactant addition, organic content, and silicon alkoxide precursors. Films were characterized by profilometry, optical spectroscopy, and electrochemical impedance spectroscopy analysis.

Results of the summer term project showed that water based sol-gel coatings provided corrosion protection values which were several orders of magnitude better than

the current Alodine 1200 treatments on aluminum 2024-T3 coupons, and equivalent to the alcohol based sol-gel systems previously investigated. Optimization of surfactant addition, organic content, and silicon alkoxide group selection results in substantial reduction in the pinhole defect areal number. Chromate-free ormosil films provide corrosion protection of up to ten thousand times that of conventional chromate-based surface treatments. Selected single-layer compositions yielded corrosion protection values which equaled or exceeded that afforded by chromate-laden complete paint systems. Thus, water-based sol-gel coatings were found to exhibit great potential for the replacement of chromate based conversion coatings presently used in the passivation of aircraft aluminum alloys.

## 7. References

1. Private Communication, Dr. Michael Donley, Coating Research Program POC, Wright Laboratory, Wright Patterson Air Force Base, Dayton OH.
2. K. Kato, *J. Mater. Sci.*, **28**(1993) p4033.
3. F.M. Seon, *J. Less-Comm. Metals*, **148**(1989) p73.
4. S. Roure, F. Czerwinski, and A. Petric, *Oxid. Met.*, **42**(1994) p75.
5. V.A.C. Haanappel, T. Franssen, B. Geerdink, and P.J. Gellings, *Oxid. Met.*, **30**(1988) p201.
6. R. Parkhill and E.T. Knobbe, AFOSR 1996 summer report.
7. C.J Brinker and G.W. Scherer, *Sol-gel Science*, Academic Press, San Deigo, (1990)
8. R. Aelion, A. Loebel, and F. Eirich, *J.Am.Chem.Soc.*, **72**(1950) p5705.
9. D. R. Lide, *CRC Handbook of Chemistry and Physics*, CRC Press, Boston, (1991).
10. T. Murakata, S. Sato, T. Ohgawara, T. Watanabe, and T. Suzuki, *J.Mater.Sci.*, **27**(1992) p1567.
11. D. Quere, A. de Ryck, and O. Ou Ramidane, *Europhysics Lett.*, **37**(1997) p305.
12. D.R. Karsa, *Additives for Water-Based Coatings*, Royal Society of Chemistry, Great Brittan, (1990)
13. J. Mackenquie, Q. Huang, T. Iwamotot, *J.Sol.Sci.&Tech.*, **7** (1996) p151.
14. B.M. De Witte, D. Commers, and J.B. Uytterhoeven, *J. Non-Cryst. Solids*, **202**(1996) p35.
15. C. Della Volpe, S. Dire, and E. Pagani, *J.Non-Cryst. Solids*, **209**(1997) p51.



# Numerically Efficient Direct Ray Tracing Algorithms for Automatic Target Recognition using FPGAs

Seungug Koh  
Assistant Professor  
Department of Electrical and Computer Engineering

University of Dayton  
300 College Park  
Dayton, OH 45469-0226

Final Report for:  
Summer Faculty Research Program  
Wright Laboratory

Sponsored by:  
Air Force Office of Scientific Research  
Bolling Airforce Base, DC

and

Wright Laboratory

August 1997

# Numerically Efficient Direct Ray Tracing Algorithms for Automatic Target Recognition using FPGAs

Seungug Koh  
Assistant Professor  
Department of Electrical and Computer Engineering  
University of Dayton

## Abstract

Numerically efficient direct ray tracing algorithms are developed in closed form to automatically recognize targets in hard real-time situations. The developed algorithms have been implemented in high level language C/C++ employing both fixed-point-only or floating-point-only operations. The new algorithms' accuracy and execution time speedup have been validated against various benchmarks utilizing both fixed-point and floating-point operation based C/C++ programs. Xilinx XC4000 FPGA based software-to-hardware mapping using VHDL has also been studied to rapidly and optimally implement the developed algorithms into hardware platform. The developed ray tracing algorithms are accurate, Numerically efficient, thereby, ideal for hard real-time automatic target recognition applications in the avionics environment.

# 1 Introduction

Shooting & Bouncing Ray (SBR) techniques used for XPATCH can effectively predict target radar signatures, thereby, automatically recognizing targets by correlating the target radar signatures with the detected radar signals. SBR techniques are based on numerical ray tracing algorithms coupled with algebraic surface interpolation algorithms applicable to objects of arbitrary shape. However it is known to be very difficult to deploy the SBR techniques for automatic target recognition in real-time due to the long computation time.

It has been proposed to embed the ray tracing algorithms into the dedicated Xilinx Field Programmable Gate Array (FPGA) boards so that execution time of the ray tracing can be significantly improved. The Xilinx XC4000 family has been selected as a target architecture for its known benefits of reconfiguration, high-capacity, high-speed operations. VHDL-based top-down design methodology has also been adopted to allow the streamlined the design processes by rapidly prototyping FPGA hardware configurations through automatic synthesis processes.

This report summarizes 1) numerically direct ray tracing algorithms suitable for the real-time automatic target recognition applications and 2) architectural study of embedding direct ray tracing algorithms into Xilinx XC4000 family-based hardware to be suitable to real-time automatic target recognition applications. Chapter 2 discusses the underlining problems with the existing XPATCH ray tracing computations. Chapter 3 outlines various approaches employed to resolve the problems discussed in Chapter 2. These approaches include innovative computationally efficient direct ray tracing al-

gorithms and their implementation in C/C++. Chapter 4 summarizes the simulation results for several benchmark cases. Finally Chapter 5 concludes with accomplishments and suggested future activities.

## 2 Discussion of Problems

Automatic target recognition in real-time requires that detected radar signals have to be correlated with the pre-calculated target radar signatures within a specified time. SBR techniques used in XPATCH can accurately predict the target radar signatures from arbitrary surfaces [1]. SBR techniques of XPATCH rely on the third-order interpolation polynomials by using cubic splines [6] [7]. SBR guarantees that the interpolated surfaces are smooth to the second-order derivatives and it can calculate reasonably accurate hit points and bouncing angles [4] [5]. But SBR consumes a tremendous amount time for computation to obtain the target radar signatures. Furthermore the computation time for SBR algorithm is unpredictable due to the iterative processes employed in the XPATCH's ray tracing algorithms. So it inhibits the practical implementation of XPATCH for automatic target recognition in hard real-time environment.

It has been proposed to embed the ray tracing algorithms into the dedicated Xilinx Field Programmable Gate Array (FPGA) boards so that execution time of the ray tracing can be significantly improved. The Xilinx XC4000 family has been selected as a target architecture for its known benefits of reconfiguration, high-capacity, high-speed operations [2]. Since the Xilinx FPGAs have limited number of Configurable Logic Blocks (CLBs), Input/Output Blocks (IOBs), and routing channels, it becomes

necessary to consider an alternative ray tracing algorithm suitable for software-to-hardware mapping. It is also desirable to develop a direct algorithm as opposed to a iterative algorithm, if hard real time automatic target recognition is required [3]. The iterative ray tracing algorithm of cubic spline interpolation is very difficult to be embedded in a hardware platform. From these observations, computationally efficient direct ray tracing algorithms have been studied and developed.

### 3 Methodology

This chapter summarizes the direct ray tracing algorithms suitable for Xilinx XC4000 family based hardware implementation. Geometrical ray tracing algorithms has been well studied by the optics community to design and implement various optical lenses, like telescopic and microscope objective lenses. Due to the unavailable numerical calculation devices, like the modern digital calculators and computers, the geometrical optical system designers of the past relied on efficient and closed-form mathematical equations for their design. These traditional ray tracing methods are direct and computationally efficient to be useful for XPATCH as an alternative ray tracing algorithm [3].

By adopting the optical lens design methodology, geometrical surfaces can modeled in second-order surface equations. These second-order surface equations include circular, elliptical, parabolic and hyperbolic equations and arbitrary geometrical surfaces can be modeled using these equations. Once source/target coordinates, target surface equations and incoming radar ray vectors are specified, the direct ray tracing (DRT)

algorithm can calculate the target hit points, bouncing ray angle and return points at the radar receivers. Furthermore DRT determines whether the incoming radar rays hit the target at the early stage of computation. And it also can automatically select the front surface of hit points if there exists both front and rear surface hit points.

The following equations are used to calculate hit points and bouncing ray angles of circular objects. The distance between radar source and target is arbitrary. The incoming radar ray vectors and positions of target and radar source are also arbitrary vectors.

$$X1 = X - d + D\alpha \quad (1)$$

$$Y1 = Y + D\beta \quad (2)$$

$$Z1 = Z + D\gamma \quad (3)$$

The definitions for the symbols of the above equations are described in Figure 1. A point  $(X1, Y1, Z1)$  is a hit point on a sphere and a vector  $(\alpha, \beta, \gamma)$  represents the normalized incoming ray. A point  $(X, Y, Z)$  is a coordinate of radar source. The distance  $D$  between radar source and hit point can be calculated using the following equations.

$$D = l + t \quad (4)$$

with

$$l = \alpha(d - X) - \beta Y - \gamma Z \quad (5)$$

$$t = \alpha r - \sqrt{(\alpha r)^2 - M^2 + 2rM_x} \quad (6)$$

Note that vector  $M$  can be calculated using the following equations and  $M_x$  is a x component of vector  $M$ . Further information related to the direct ray tracing can be found in reference [3].

$$M = (X - d + \alpha l)\hat{i} + (Y + \beta l)\hat{j} + (Z + \gamma l)\hat{k} \quad (7)$$

$$M_x = X - d + \alpha l \quad (8)$$

In Chapter 4 the simulation results of DRT algorithms are reported using three different benchmarks; paraxial, off-axial and fixed/floating point ray tracings.

## 4 Results

C/C++ programs for DRT algorithms have been implemented and various benchmarking has also been performed using these programs. The DRT algorithms are implemented using both fixed-point-only and floating-point-only operations to determine the necessary hardware components and to select suitable target FPGA architectures. The following C code execution results show the validity of the proposed approach.

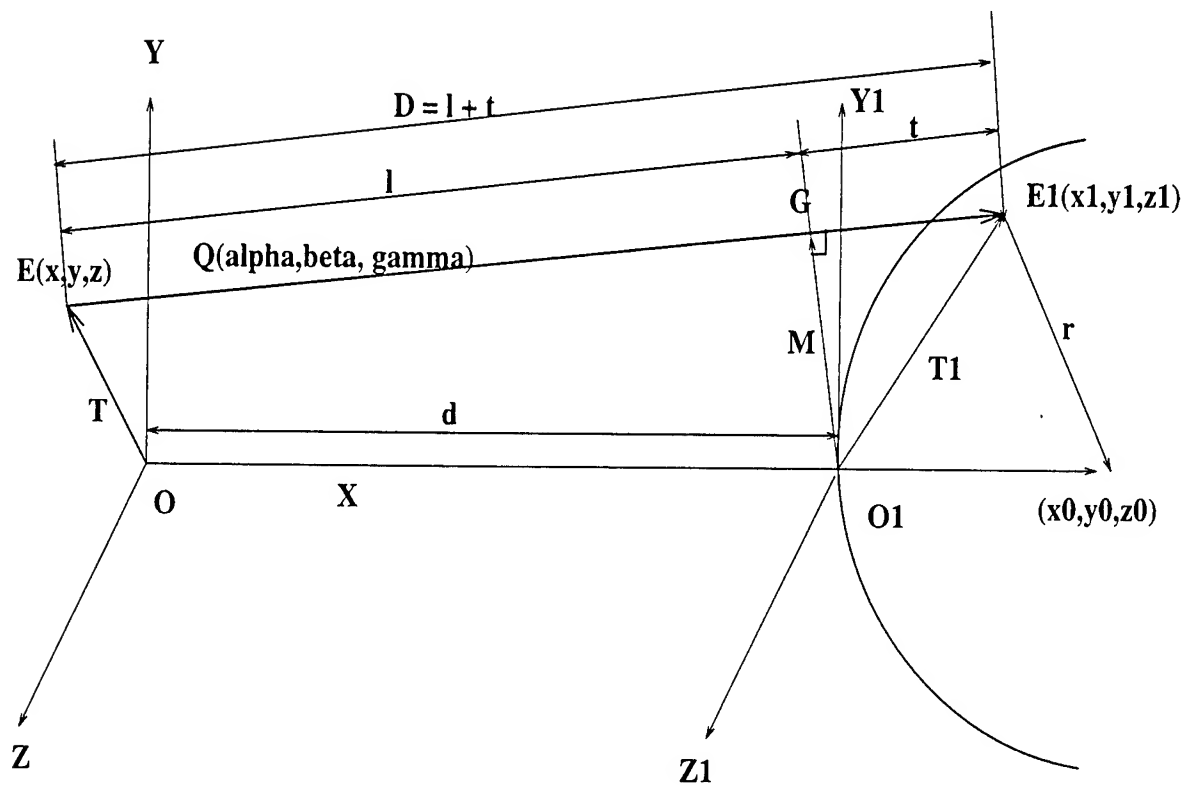


Figure 1: Direct Ray Tracing for Second-Order Surfaces



a) testbench 1: paraxial ray tracing using floating-point-only operations

The paraxial rays to the circular surface will be bounced back to the source because the bouncing ray vector is identical to the incoming ray vector except for the reversed propagation direction. The benchmark result indicate that the bouncing ray vector actually return back to the radar source.

```
*****
Ray Tracing Method: with input ray and known sphere.
Assumption: X-coordinate of ray overlapped with x_coord of the sphere
*****
Describe the input ray position by: x_i + y_j + z_k
input : x  y  z
0 0 0
==> accepted values are: x=0.000000, y=0.000000, z=0.000000
and input ray direction by vector: alpha_i + beta_j + gamma_k
input: alpha  beta  gamma
1 0 0
==> accepted values are: alpha=1.000000, beta=0.000000, gamma=0.000000
*****
==> normalized values are: alpha=1.000000, beta=0.000000, gamma=0.000000
Describe the sphere by: pow(x1-r) + pow(y1) +pow(z1) = pow(r)
input: r
100
==> accepted value: r=100.000000
*****
Given the distance between ray and sphere origins (along x_coord)
input: d
1000
==> accepted value: d=1000.000000
*****
Given the distance between receiving plane and sphere origins (along x_coord)
input: dprime ( using positive value)
1000
==> accepted value: d'=1000.000000
*****
==> Hit point on the sphere: x1=0.000000, y1=0.000000, z1=0.000000
*****
The reflected-ray intersects with the receiving plane :
x = 0, y = 0.000000, z = 0.000000
```

b) testbench 2: off-axis ray tracing using floating-point-only operations

When the incoming ray is not paraxial, the bouncing angle will not return to the radar source. The hit points and bouncing angle depend on the incoming ray vector, radar source coordinates, target coordinates and surface geometry of the target. The DRT program automatically determines the front hit points of the target and produce the bouncing ray vector.

```
*****
Ray Tracing Method: with input ray and known sphere.
Assumption: X-coordinate of ray overlapped with x_coord of the sphere
*****
Describe the input ray position by: x_i + y_j + z_k
input : x  y  z
0 1 1
==> accepted values are: x=0.000000, y=1.000000, z=1.000000
and input ray direction by vector: alpha_i + beta_j + gamma_k
input: alpha  beta  gamma
100 1 1
==> accepted values are: alpha=100.000000, beta=1.000000, gamma=1.000000
*****
==> normalized values are: alpha=0.999900, beta=0.009999, gamma=0.009999
Describe the sphere by: pow(x1-r) + pow(y1) + pow(z1) = pow(r)
input: r
100
==> accepted value: r=100.000000
*****
Given the distance between ray and sphere origins (along x_coord)
input: d
1000
==> accepted value: d=1000.000000
*****
Given the distance between receiving plane and sphere origins (along x_coord)
input: dprime ( using positive value)
1000
==> accepted value: d'=1000.000000
*****
==> Hit point on the sphere: x1=1.220129, y1=11.012201, z1=11.012201
*****
```

The reflected-ray intersects with the receiving plane :  
x = 0, y = 251.048946, z = 251.048946

c) benchmark 3: fixed-point-only vs floating-point-only operations

The DRT algorithms are implemented using 32-bit fixed-point-only operations and 64-bit floating-point-only operations. Fixed point operations are ideal for hardware implementations but it showed relatively large values of error propagation. For example the off-axis ray tracing of testbench 2 is treated like a paraxial ray tracing in the case of the fixed-point-only DRT program. Since the Z component of the incoming ray vector is much larger than X and Y components, fixed-point-only DRT program is treating the incoming ray vector as a paraxial ray. The hit points at the radar receive becomes (0,1,1) as compared to the previous testbench value of (0, 251.048946, 251.048946).

```
*****
Ray Tracing Method: with input ray and known sphere.
Assumption: X-coordinate of ray overlapped with x_coord of the sphere
*****
Describe the input ray position by: x_i + y_j + z_k
input : x  y  z
0 1 1
==> accepted values are: x=0, y=1, z=1
and input ray direction by vector: alpha_i + beta_j + gamma_k
input: alpha  beta  gamma
100 1 1
==> accepted values are: alpha=100, beta=1, gamma=1
*****
==> normalized values are: alpha=1, beta=0, gamma=0
Describe the sphere by: pow(x1-r) + pow(y1) + pow(z1) = pow(r)
input: r
100
==> accepted value: r=100
*****
Given the distance between ray and sphere origins (along x_coord)
input: d
1000
```

```

==> accepted value: d=1000
*****
Given the distance between receiving plane and sphere origins (along x_coord)
input: dprime ( using positive value)
1000
==> accepted value: d'=1000
*****
==> Hit point on the sphere: x1=0, y1=1, z1=1
*****
The reflected-ray intersects with the receiving plane :
x = 0, y = 1, z = 1

```

The simulation benchmark suggests the following findings.

- The DRT algorithm provides fast, accurate results as long as the target can be modeled as second-order surface equations.
- The DRT benchmarks indicate that fixed-point-only operations are relatively inaccurate. The fixed-point hardware implementation has to consider the scaling factors and round off errors when the digital designers select a particular hardware platform.
- The DRT programs have a very predictable software response time and is very ideal for the hard real-time applications.
- The estimated number of Configurable Logic Blocks (CLBs) for DRT algorithms is about 20,000 to 40,000 depending on the datapath/controller implementations. It is estimated to require a minimum two to four XC4028EX Xilinx devices for DRT algorithms and FPGA implementation is planned as a next level of research.

## 5 Conclusion

Numerically efficient DRT algorithms are developed in closed forms to automatically recognize targets for real-time applications. The DRT algorithms have been implemented in C/C++ using both fixed-point and floating-point operations. The accuracy and computation speedup factor of DRT algorithms have been validated against various benchmarks using both fixed-point and floating-point operations. The Xilinx XC4000 FPGA-based software-to-hardware mapping using VHDL has also been studied to rapidly embed the developed algorithms into hardware. Automatic target recognition in hard real-time application can be performed by the accurate and numerically efficient ray tracing algorithms being developed.

The current DRT algorithms can be further refined by incorporating multiple bouncing problems, multilayer surface geometry of coated targets and phase shift evaluations. Once the above improvements are implemented, DRT algorithms could provide extremely fast but still very accurate target signature calculation capabilities to the modern avionics systems.

## References

- [1] User's Manual for XPATCH, DEMACO, Inc., June 1, 1995
- [2] The Programmable Logic Data Book, Xilinx, 9/96
- [3] Seungug Koh, "Forward Light Scattering from Optical Fibers", MS Thesis, Rose-Hulman Institute of Technology, Terre Haute, IN, 1990
- [4] Daniel L. Toth, "On Ray Tracing Parametric Surfaces", ACM SIGGRAPH '85, Vol 19, No 3, 1985
- [5] Tomojuki Nishita, Thomas W. Sederberg and Masanori Kakimoto, "Ray Tracing Trimmed Rational Surface Patches", ACM Computer Graphics, Vol 24, No 4, August 1990
- [6] H. Ling, R.C. Chou, and S.W. Lee, "Shooting and Bouncing Rays: Calculating the RCS of an Arbitrarily shaped cavity," IEEE Trans. Antennas & Propagations, Vol. 37, pp. 194-205, 1989
- [7] D.J. Andersh, M. Haxlett, S.W. Lee, D.D. Reeves, D.P. Sullivan, and Y. Chu, "Xpatch: A high frequency electromagnetic-scattering prediction code and environment for complex three-dimensional objects," IEEE Trans. Antennas & Propagations, Vol 36, pp. 65-69, Feb. 1994

# A Function Approximation Approach for Region of Interest Selection in Synthetic Aperture Radar Images

Ravi Kothari  
Assistant Professor  
Department of Electrical & Computer Engineering & Computer Science

University of Cincinnati  
P. O. Box 210030  
Cincinnati, OH 45221-0030

Final Report for:  
Summer Faculty Research Program  
Wright Laboratory

Sponsored by:  
Air Force Office of Scientific Research  
Bolling Air Force Base, DC

and

Wright Laboratories (WL/AACA)

September 1997

# A Function Approximation Approach for Region of Interest Selection in Synthetic Aperture Radar Images

Ravi Kothari

Assistant Professor

Department of Electrical & Computer Engineering & Computer Science  
University of Cincinnati

## Abstract:

One of the first steps in Automatic Target Recognition (ATR) is the grading of an image to identify, for further analysis, candidate regions which may have potential targets. To be most effective, this initial detection (or focus of attention) stage needs to reject clutter (noise or countermeasures which provide target like characteristics), while ensuring regions with true targets are not missed.

This report outlines the procedure and some results obtained towards using the model order of an artificial neural network to characterize disjoint block in Synthetic Aperture Radar (SAR) images. The approach is based on the premise that regions with targets would require a model with more free parameters (higher model order) to approximate the distribution of the return. Consequently, we use recently developed neural network algorithms [17]-[20] *which can self-regulate their model order*, to approximate disjoint squares of the image. Squares of the image which require a larger model order (more free parameters) are then labeled as candidate regions likely to have potential targets.

Simulations from several target and clutter images from the MSTAR PUBLIC CD-ROMS were used to evaluate the efficacy of the proposed approach.



# A Function Approximation Approach for Region of Interest Selection in Synthetic Aperture Radar Images

Ravi Kothari

## 1 Introduction

Automatic Target Recognition (ATR) in its simple form consists of the three steps shown below:

1. Region of interest selection (often also called pre-processing or segmentation).
2. Extraction of features from the regions identified in Step 1 above.
3. Classification of the object (if any) in the regions of interest based on the features extracted in Step 2 above.

The set of outcomes for the last of these steps includes *targets* (e.g. T72), *unknown target*, as well as *clutter*. The distinction between *unknown target* and *clutter* is subtle, but nonetheless one that is important. The categorization as *clutter* implies the lack of a target, while the categorization as an *unknown target* implies that it is not possible to assign an exact class label, though the region seems to have characteristics that are more 'target-like'.

When information from multiple sensors is available, one can form a single data stream on which the above three steps can be applied. This could be termed as data level fusion. Alternatively, each of the three steps may be independently applied to data from each sensor followed by a categorization which is negotiated between the categorization obtained from each data stream (decision level fusion). Time varying information (motion provides a clue as to the functionality of the observed) can also provide discriminatory features.

Whatever be the configuration of sensors used, Step 1 (region of interest selection) is an important step in an ATR system. When a large number of regions (larger than actual) are labeled as containing potential targets, a significant amount of time is wasted in Steps 2 and 3 above. When a small (smaller than actual) number of regions are labeled as containing potential targets, true targets may be missed. The goal of this first step is to remove clutter (noise or countermeasures which provide target like characteristic), or conversely to mark non-clutter areas as regions of interest.

This report focuses on region of interest selection in Synthetic Aperture Radar (SAR) images though I believe that the concept may also be applicable to data available from other sensors (e.g. Ultra-High Resolution Radar, Forward Looking Infrared, or Hyperspectral data).

The rest of this report is organized as follows. In Section 2, a short summary of related work is presented. In Section 3, the concept of the *model order* is introduced and it is shown that the model order (or the number of free parameters) is a valuable cue in characterizing the underlying surface producing a certain return. In Section 4, a neural network is presented as a mechanism for estimating the model order. Simulation results are presented in Section 5 and conclusions in Section 6.

## 2 Previous Work In Regions of Interest Selection

Histograms of SAR images, because of the low contrast that is typical of SAR images, typically tend to be uni-modal making it difficult to obtain a threshold for the purposes of region of interest selection. When the clutter characteristics are stationary and Gaussian, the so called Constant False Alarm Rate (CFAR) filter, which uses the pixel intensity relative to the local mean can be used (see [1] for modifications in the non-Gaussian case). Various filters (such as the whitening filter in [2], or the

BCS/FCS as in [3]) can be used to enhance the contrast prior to CFAR application. Multi-parameter CFAR may also be used as in [4]. A macro Gabor filter composed of a set of real Gabor functions has also been proposed [5].

The region of interest selection can itself utilize Steps 2 and 3 that I have outlined in the previous section. Thus features may be extracted (say from disjoint squares) and a classifier constructed to label a square as 'interesting' or otherwise. For example, in [6] a feed-forward neural network trained using back-propagation [7] is used to obtain regions of interest. Inputs to this network are derived from Gabor filters. A similar approach reported in [8] uses Radial Basis Function neural networks operating on the wavelet decomposition of an image to obtain regions of interest.

A disadvantage of any supervised region of interest detection scheme is that its performance is directly influenced by the amount and quality of data that was used in training it. Due to the large variability of clutter characteristics it may be very difficult to arrive at a training data set which captures this variability. Consequently, adaptive clutter characterization have also been proposed. These approaches assume that there will always be a large amount of clutter available in a SAR image and hence adaptive characterization is possible. For example, in [9], a Gibbs distribution model is constructed towards approximating the joint pdf of pixels. Such a pdf can for example be used in Bayesian inference to ascertain if an image region is consistent with the pdf or deviates from it. In [10], clutter is characterized based on statistical pattern recognition techniques.

In [8], unsupervised methods based on vector quantization (with the number of clusters decided *a priori*) is used to obtain regions of interest. Due to the difficulty in *a priori* deciding the number of clusters, the authors also report results using a topology representing network proposed by [11]. This idea is similar to my previous usage of Self-Organizing Feature Maps [12] towards obtain a reduced number of colors to represent an image.

This short review of previous work is no way exhaustive, neither has an attempt been made to make it so. Specifically, only those works are discussed which lets the reader put into perspective the general classes of techniques that have been used as pertaining to the SAR images considered here (to be described later) were discussed. Specifically, methods which utilize motion or those which can locate embedded targets or those not pertaining to SAR images have been omitted.

### 3 The Model Order and Region of Interest

To begin the discussion, it is worthwhile to envision a SAR image as a function  $f(x, y)$ . The value of the function at a point  $(x, y)$  is  $f(x, y)$  — the intensity of the return at a point<sup>1</sup>. An alternative view of the SAR image is then a function in two dimensions. The left and right panels of Figure 1 shows 8x8 squares of a SAR image extracted from regions containing clutter and target respectively. Note that due to the large variability of clutter, Figure 1 should not be considered a typical situation — it is one illustration.

Given the scenario as described above, a valid question to ask is: *What is the lowest order of an approximator that will minimize  $\|f(x, y) - \hat{f}(x, y)\|$ , where  $\hat{f}(x, y)$  is the approximation produced by a given approximator (e.g. polynomial, splines, neural networks).* The lowest order of the approximator that can produce  $\|f(x, y) - \hat{f}(x, y)\| < \epsilon$  is the model order. The model order then refers to the number of independent parameters (e.g. number of polynomial coefficients) that may produce such a return. A polynomial with order 1 can only produce planes (flat returns). A second order polynomial can only produce quadratic surfaces. Quite clearly, higher order approximators can produce more complex returns. In other words, the complexity of the approximator characterizes the complexity of the return.

In its above form, there are two issues that deserve further clarification.

---

<sup>1</sup>For most of this report only the magnitude portion of the SAR return is considered.

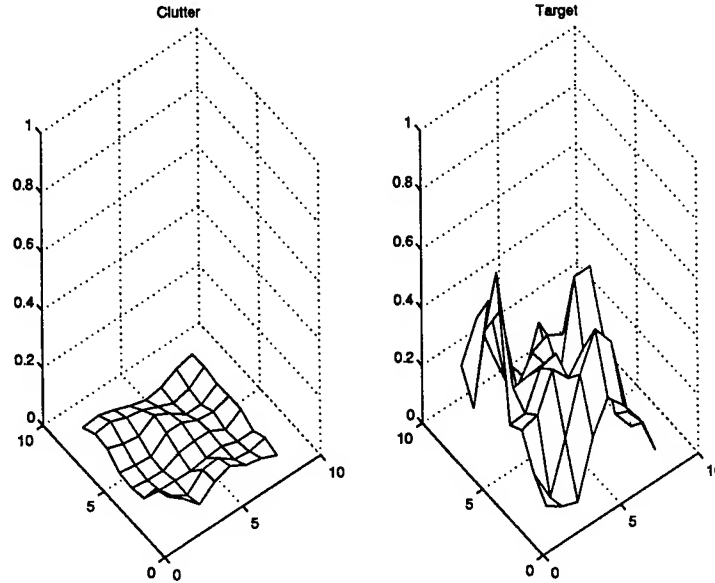


Figure 1: 8x8 squares extracted from a SAR image. Data for the left panel was obtained from a region of the image containing clutter while data for the right panel was obtained from a region known to contain a target

- The first is the issue of *generalization* i.e. we would like to produce a smooth approximation of the function. In the polynomial case, if the order of the polynomial approaches the number of points defining the function (64 in this case), we can reproduce the function exactly. Any noise in  $f(x, y)$  would thus also be "learnt" by the approximator. The point of the approximation is to learn the underlying function which generated the data (return), and not any noise that is present in the return. Consequently, we require the lowest order approximation.
- The second issue has to do with the approximator that is used. In this work, a feed-forward neural network is used due to several attractive properties that such networks have. These include:
  1. Multi-layered feed-forward neural networks are model free estimators i.e. they adapt based on examples and do not require *a priori* characterization of the variables.
  2. A feed-forward network with a single hidden layer consisting of an *arbitrary* number of sigmoidal hidden neurons can approximate continuous functions defined on the compact set  $\mathcal{R}^n$  [14] (see also [15] for some results relating to the nature of non-linearities used in the hidden layer neurons).
  3. A feed-forward network with a single hidden layer of  $m$  sigmoidal neurons achieves an integrated squared error of  $O(1/m)$ . In contrast, a linear combination of a set of  $m$  fixed basis functions achieves an integrated squared error of  $O(1/m^{2/d})$ , where  $d$  is the dimension of the input [16]. Thus with increasing dimensionality of the input space, the rate of parameter growth is much smaller in a neural network than say in polynomial or spline approximators.

Points 1, and 3 above facilitate favorable consideration of feed-forward neural networks as computational models. Point 2 above is an *existence* theorem that establishes the capabilities of a feed-forward neural network but does not allow for procedural determination of the number of

hidden neurons to use in a given situation. The number of hidden layer neurons sharply influence the performance of a network — too few neurons and the model will approximate poorly; too many neurons and the network will overfit the training data.

In the next section we briefly review some fundamental results that allow a feed-forward neural network to self-regulate its order [17]-[20]. Note that determining the number *effective* or *free* parameters is much more complicated in the case of non-linear approximators such as feed-forward neural networks.

## 4 Self-Regulation of Model Order Using Lateral Connections in a Feed-Forward Neural Network

The proposed architecture consists of a feed-forward network with lateral connection from neuron  $(j - 1)$  in the hidden layer to neuron  $j$  in the hidden layer, as illustrated in Figure 2. The network has  $n$  inputs,  $m$  neurons in the hidden layer, and  $o$  neurons in the output layer. We denote the weight from hidden neuron  $j$  to input  $k$  as  $w_{jk}$ ; weights from hidden neuron  $j$  to output neuron  $i$  are denoted by  $W_{ij}$ ; and the lateral weight from hidden neuron  $(j - 1)$  to hidden neuron  $j$  are denoted by  $q_{j,j-1}$ . The  $p$  input-output training pairs are denoted by  $\{(\xi^\mu, \zeta^\mu) : \mu = 1, 2, \dots, p\}$ . The net input,  $h_j^\mu$ , received by a hidden layer neuron, when pattern  $\mu$  is presented is:

$$h_j^\mu = \begin{cases} \sum_{k=1}^n w_{jk} \xi_k^\mu & j = 1 \\ \sum_{k=1}^n w_{jk} \xi_k^\mu + q_{j,j-1} h_{j-1}^\mu & 1 < j \leq m \end{cases} \quad (1)$$

The output of a hidden layer neuron,  $z_j^\mu$ , is a (non-linear) function of its net input:

$$z_j^\mu = f(h_j^\mu) \quad (2)$$

An output layer neuron produces as output,  $y_i^\mu$ , defined as:

$$y_i^\mu = f(s_i^\mu) = f\left(\sum_{j=1}^m W_{ij} z_j^\mu\right) \quad (3)$$

The adjustment of the weights are done to minimize the sum of squared error between the output  $y_i^\mu$  and the desired output  $\zeta_i^\mu$ , i.e.  $J = \sum_{\mu=1}^p J^\mu$ , where:

$$J^\mu = \frac{1}{2} \sum_{i=1}^o (\zeta_i^\mu - y_i^\mu)^2 \quad (4)$$

To obtain the learning algorithm, we use gradient descent to minimize  $J^\mu$ . For the hidden to the output layer weights, we obtain:

$$\Delta W_{ij}^\mu = -\eta \frac{\partial J^\mu}{\partial W_{ij}} = (\zeta_i^\mu - y_i^\mu) f'(s_i^\mu) z_j^\mu = \eta \delta_i^\mu z_j^\mu \quad (5)$$

where,  $\delta_i^\mu = (\zeta_i^\mu - y_i^\mu) f'(s_i^\mu)$ , and  $\eta$  is a constant (forward learning rate).

The weight update equations for the lateral weights are:

$$\Delta q_{j,j-1}^\mu = -\eta_q \frac{\partial J^\mu}{\partial q_{j,j-1}} = \eta_q \left[ \frac{\delta_j^\mu}{\delta_{j-1}^\mu} + \left( \sum_{\beta=j+1}^m \frac{\delta_\beta^\mu}{\delta_{\beta-1}^\mu} \prod_{\alpha=j+1}^{\beta} q_{\alpha,\alpha-1} \right) \right] h_{j-1}^\mu \quad (6)$$

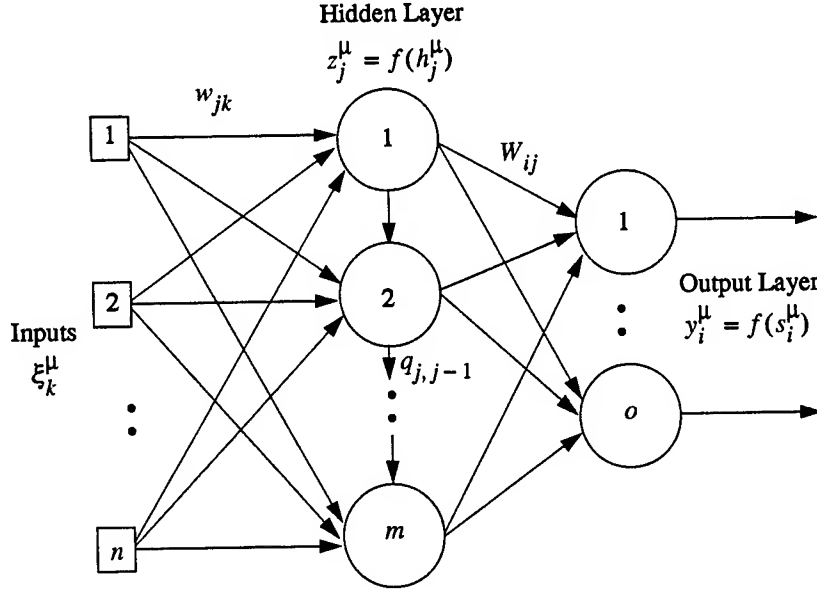


Figure 2: Lateral connections in a feed-forward architecture. Inputs, and hidden layer neurons are fully connected as are hidden layer and output layer neurons. Neuron  $j$  in the hidden layer also receives the net input of neuron  $(j - 1)$  in the hidden layer through a lateral connection

where,  $\underline{\delta}_j^\mu = \left( \sum_{i=1}^o \delta_i^\mu W_{ij} f'(h_j^\mu) \right)$ , and  $\eta_q$  is a constant (lateral learning rate). The update equations for the input to the hidden layer weights are similar to the above:

$$\Delta w_{jk}^\mu = -\eta \frac{\partial J^\mu}{\partial w_{jk}} = \eta \left[ \underline{\delta}_j^\mu + \left( \sum_{\beta=j+1}^m \underline{\delta}_\beta^\mu \prod_{\alpha=j+1}^{\beta} q_{\alpha,\alpha-1} \right) \right] \xi_k^\mu \quad (7)$$

These weight update equations, details of which are available in [17], indicate that the error at a hidden layer neuron is dependent on the error at other hidden layer neurons. Equations (5)–(7) are identical to what one might obtain using back-propagation for the proposed architecture. For ease of reference however, we term back-propagation for a feed-forward network with lateral connections as lateral back-propagation.

Now if all the lateral weights are initialized to be equal i.e.,  $q_{j,j-1} = q^*$ , all the input to hidden weights are initialized to be equal i.e.  $w_{jk} = w^*$ , and all the hidden to output weights are initialized to be equal i.e.  $W_{ij} = \tilde{W}^*$ , we obtain:

$$h_j^\mu = \sum_{k=1}^n w^* \xi_k^\mu (1 + q^* + q^{*2} + \dots + q^{*(j-1)}) = \left( \frac{1 - q^{*j}}{1 - q^*} \right) \sum_{k=1}^n w^* \xi_k^\mu \quad (8)$$

From equation (8), one may observe that beyond some value  $t$  corresponding to a neuron position in the hidden layer, the net input to the hidden neurons will be the same for  $j > t$ , where  $1 \leq t \leq m$ , when  $q^* < 1$ . In other words,  $h_j^\mu = \tilde{h}$ ; for  $t < j \leq m$ . Similarly by expanding equations (5)–(7) one obtains three regions in the hidden layer neurons: neurons 1 through  $t$  differentiate, neurons  $t$  through  $T$  behave identically, and neurons  $T$  through  $m$  differentiate. A detailed proof of this is available in [17]. Under equal weight initialization one always obtains the three regions, with the unspecialized neurons in the center of the hidden layer behaving similarly to reduce the *effective* order of the network.

## 4.1 New Enhancements

When one looks at equation (1), it is immediately clear that the decision boundaries implemented by each hidden layer neuron is still a hyperplane. The signal arriving through the lateral connection from neuron  $(j-1)$  can be absorbed in the weighted sum of neuron  $j$ . Towards making this into a more powerful paradigm and to allow localization, a modified architecture was developed. In this architecture, the lateral connections carry the weighted sum of neuron  $(j-1)$  passed through a Gaussian activation function. Specifically,

$$h_j^\mu = \begin{cases} \sum_{k=1}^n w_{jk} \xi_k^\mu & j = 1 \\ \sum_{k=1}^n w_{jk} \xi_k^\mu + q_{j,j-1} e^{-\frac{(h_{j-1}^\mu - C_j)^2}{\sigma^2}} & 1 < j \leq m \end{cases} \quad (9)$$

where,  $C_j$  is the center of the Gaussian, and  $\sigma^2$  its variance. Note that when the first term of the above equation dominates one gets a linear (or almost linear) decision boundary (open half space). When the second term dominates, one gets a closed decision boundary, as in a Radial Basis Function network. The advantages of both forms (localization with closed decision boundary and slow rate of parameter growth with linear decision boundaries) can thus be realized. The update equation for the most part remain the same with the exception of  $\frac{\partial h_{j+1}^\mu}{\partial h_j^\mu}$  that appears in the derivation. The update equations then are:

$$\begin{aligned} \Delta q_{j,j-1}^\mu &= -\eta_q \frac{\partial J^\mu}{\partial q_{j,j-1}} \\ &= \eta_q \left[ \underline{\delta}_j^\mu h_{j-1}^\mu + \left( \sum_{\beta=j+1}^m \underline{\delta}_\beta^\mu \prod_{\alpha=j+1}^{\beta} q_{\alpha,\alpha-1} e^{-\frac{(h_{\alpha-1}^\mu - C_\alpha)^2}{\sigma^2}} \left( -2 \frac{(h_{\alpha-1}^\mu - C_\alpha)}{\sigma^2} \right) \right) e^{-\frac{(h_{j-1}^\mu - C_j)^2}{\sigma^2}} \right] \end{aligned} \quad (10)$$

and,

$$\Delta w_{jk}^\mu = -\eta \frac{\partial J^\mu}{\partial w_{jk}} = \eta \left[ \underline{\delta}_j^\mu + \left( \sum_{\beta=j+1}^m \underline{\delta}_\beta^\mu \prod_{\alpha=j+1}^{\beta} q_{\alpha,\alpha-1} e^{-\frac{(h_{\alpha-1}^\mu - C_\alpha)^2}{\sigma^2}} \left( -2 \frac{(h_{\alpha-1}^\mu - C_\alpha)}{\sigma^2} \right) \right) \right] \xi_k^\mu \quad (11)$$

If required similar update equations can be updated for  $C_j$  and  $\sigma^2$ . In preliminary simulations though adjustment of  $C_j$  was done and  $\sigma^2$  was held constant. The exact value of  $\sigma$  should be set based on the smallest target (small bump) that needs to be approximated. Further results will be reported separately in upcoming papers [21],[22]. Nonetheless, the effects of the inclusion can be seen from Figure 3 below. Note that the decision boundaries formed from the new architecture can take on more complex shapes.

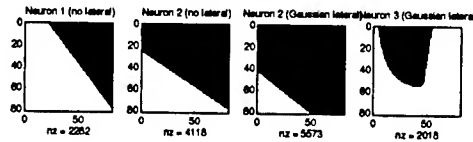


Figure 3: Gaussian Lateral connections in a feed-forward architecture and its effect. Neuron 1 in the hidden layer feeds to neuron 2 in the hidden layer, and neuron 2 feeds to neuron 3 and so on

## 5 Simulation Results with SAR Data

Extensive programs in C and Matlab were written to obtain *preliminary* results regarding the efficacy of the proposed methodology.

### 5.1 Simulation Set 1

The first result illustrated relates to the approximation of the clutter and target patches shown in Figure 1. Figure 4 shows the approximation obtained with a network of 2 inputs ( $x$  and  $y$  coordinates), 15 sigmoidal hidden neurons (and hence 14 lateral weights), and 1 sigmoidal output. The forward weights were initialized to 0.1, and the lateral weights were initialized to 0.01. The forward learning rate ( $\eta$ ) was 0.3, and the lateral learning rate ( $\eta_q$ ) was 0.1. The left column of the figure shows the approximation obtained for the clutter data, and the values of the lateral weights at the end of the training. The right panel shows the corresponding plots for the target data. In both cases all parameters and the number of training epochs were equal. Note that while 2 lateral weights was used for the clutter data, 9 lateral weights were used for the target data. The rest of the lateral weights behave similarly in each case and hence do not contribute to the number of *free* or *independent* parameters of this approximator. Clearly, from the number of hidden neurons (the same behavior is observed from a plot of the forward weights), one can conclude that a smaller model order was required for approximating clutter. The number of the lateral weights behaving differently (same as the number of hidden neurons behaving differently) thus *allows for identification of the region of interest*.

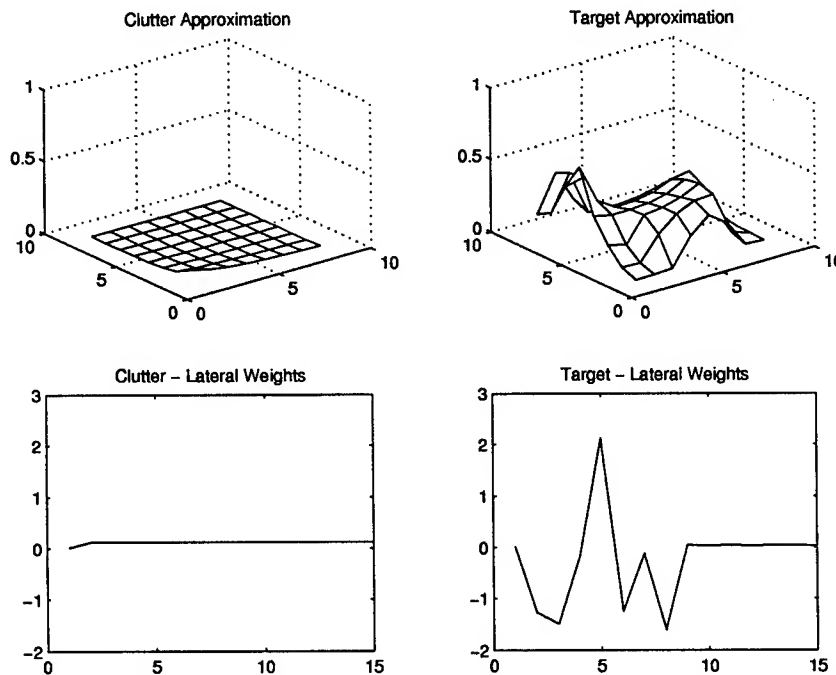


Figure 4: Approximation and status of the lateral weights at the end of the training for the clutter data of Figure 1 (left column) and the target data of Figure 1 (right column)

## 5.2 Simulation Set 2

This above simulation may tempt one to consider that since the signal intensity is greatly different in each case, perhaps a simple threshold would have sufficed. As mentioned earlier, SAR images tend to be uni-modal and make it difficult for a global threshold to be identified. Furthermore, consider Figure 5 which shows in the left panel (top row), raw clutter data and in the right column (top row) clutter data has been artificially shifted (by 0.8) with induced random noise ( $\pm 0.2$ ). The simulation was created to show that the model order is unaffected by the addition of noise or shifting. Note however, that multiplication affects the variance of the function, and hence affects the model order. The bottom row of Figure 5 shows the lateral weights obtained in each of the two cases. Note the model order is the same in each case.

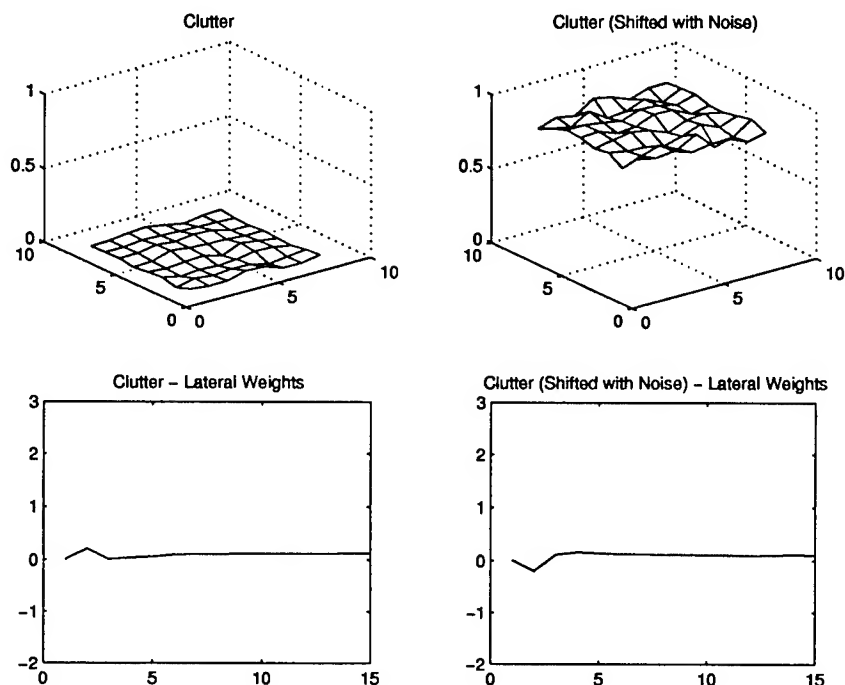


Figure 5: Clutter (left top) and clutter shifted and noise added (right top). The bottom row shows the corresponding lateral weights obtained from a network with identical parameters as those with which Figure 4 was obtained



### 5.3 Simulation Set 3

The above proposed methodology was applied to four different target chip images (which contain the target and the clutter) as found on the MSTAR PUBLIC TARGET CD-ROM. Disjoint squares of 8x8 were considered and the above algorithm was applied to each resulting square. All training parameters were held as discussed above. Figure 6 shows the raw image (T72/HB03838.015) and Figure 7 shows the number of hidden neurons<sup>2</sup>. In Figure 7, each grid rectangle reflects a block of the image, and the height of the peak indicates the model order required to produce the gray level surface of that block. Note that the actual target has been well isolated. These results can obviously be made better since the block may partially fall onto the target. Perhaps once the block has been noted to contain a target, a larger block can be grown around the detected block. Nonetheless over several simulations, the target was always detected despite such effects. Figures 8 through 13 repeat these simulations for different image files containing different targets.

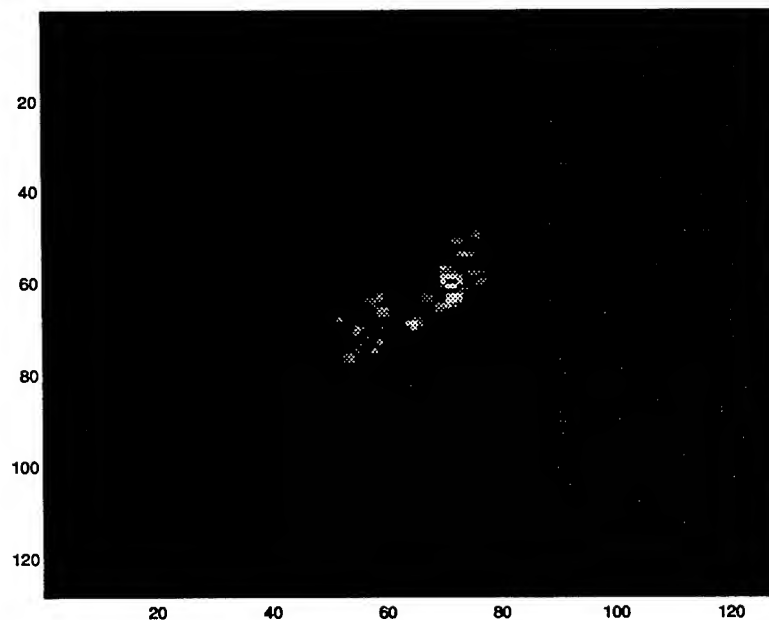


Figure 6: Sample SAR image containing a target (T72/HB03838.015)

---

<sup>2</sup>The model order is solely a function of the number of hidden neurons used, the number of inputs and the number of outputs. Since the number of inputs and outputs are fixed, the model order is indicated by the number of hidden neurons that are used.

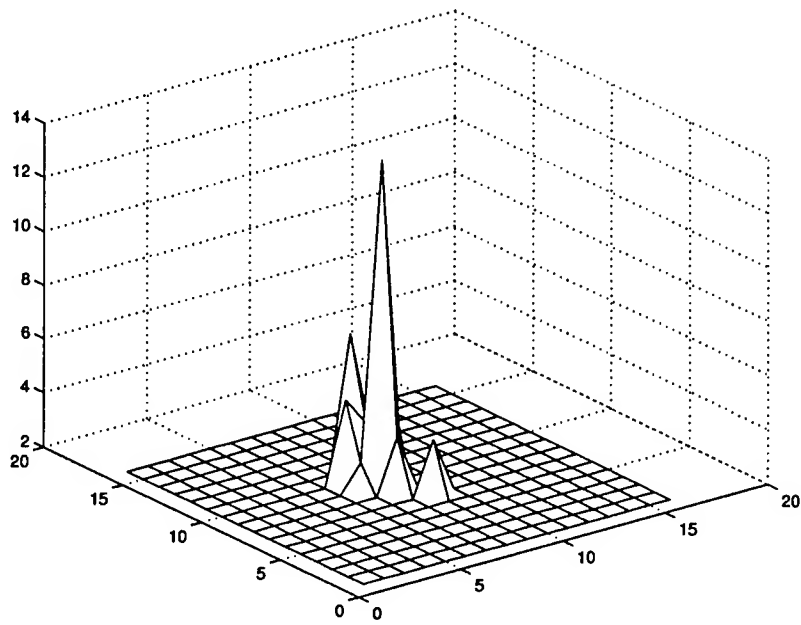


Figure 7: Model Order for 8x8 blocks as determined (T72/HB03838.015)

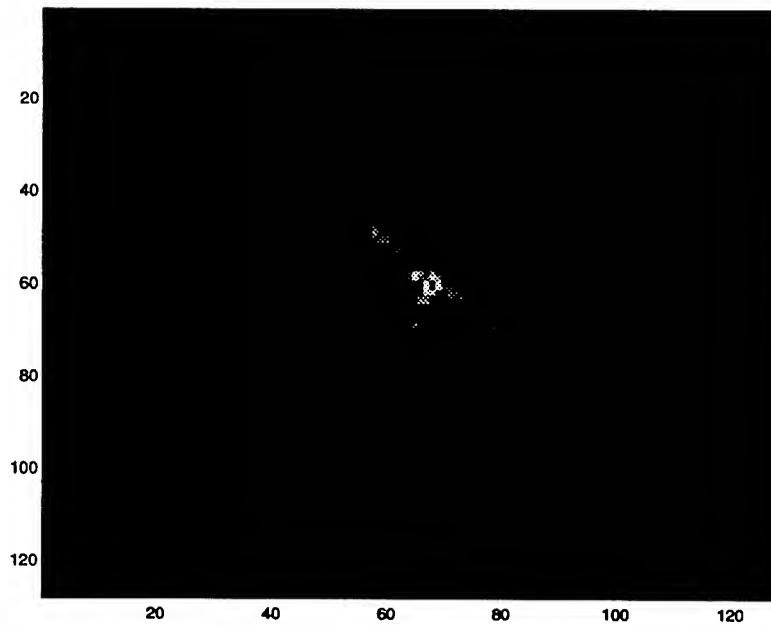


Figure 8: Sample SAR image containing a target (Bmp2/HB03834.000)

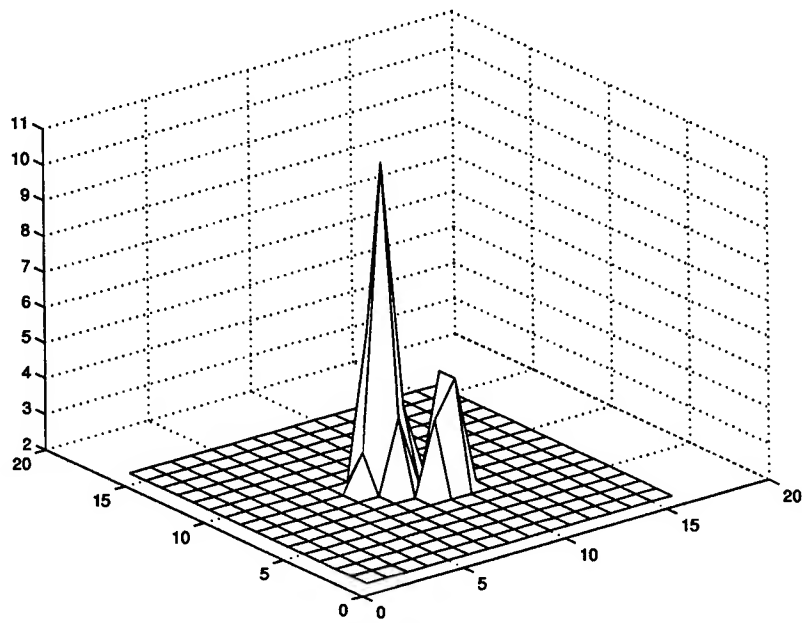


Figure 9: Model Order for 8x8 blocks as determined (Bmp2/HB03834.000)



Figure 10: Sample SAR image containing a target (Btr70/HB03797.004)

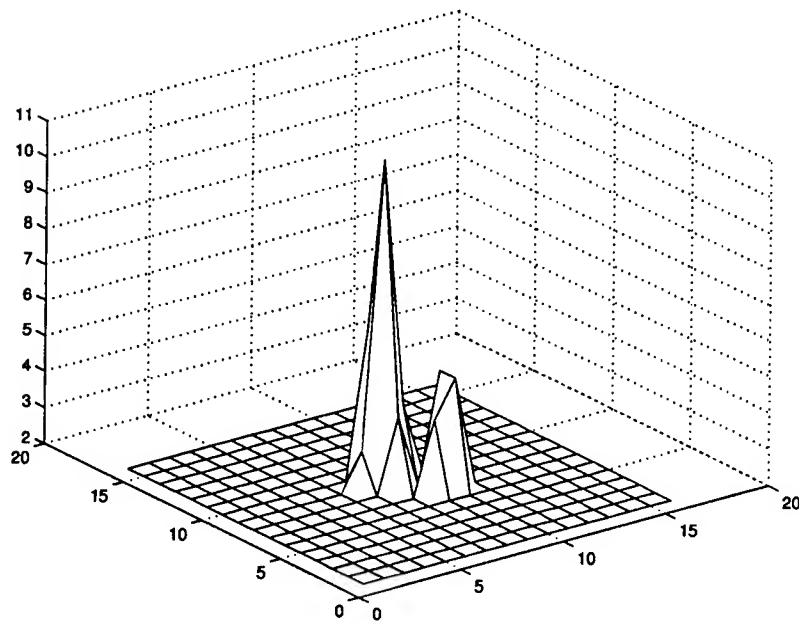


Figure 11: Model Order for 8x8 blocks as determined (Btr70/HB03797.004)

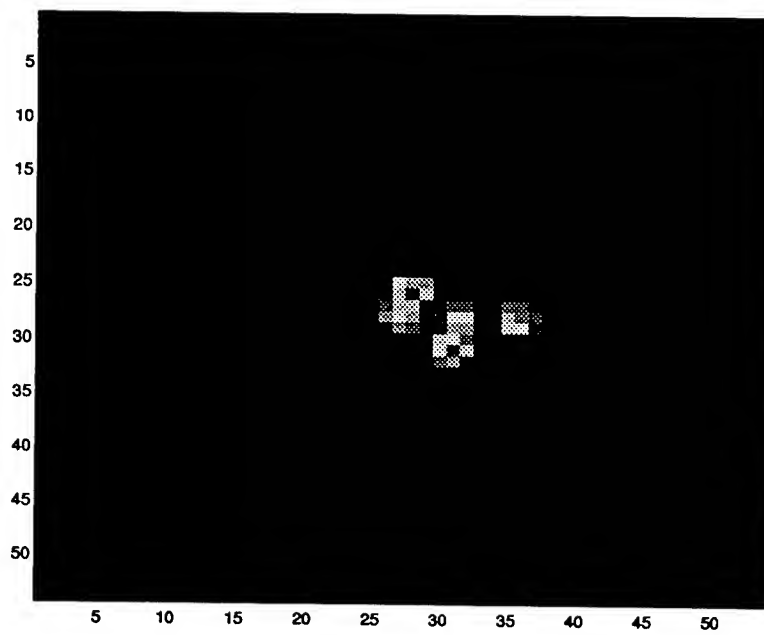


Figure 12: Sample SAR image containing a target (Slicy/HB14977.015)

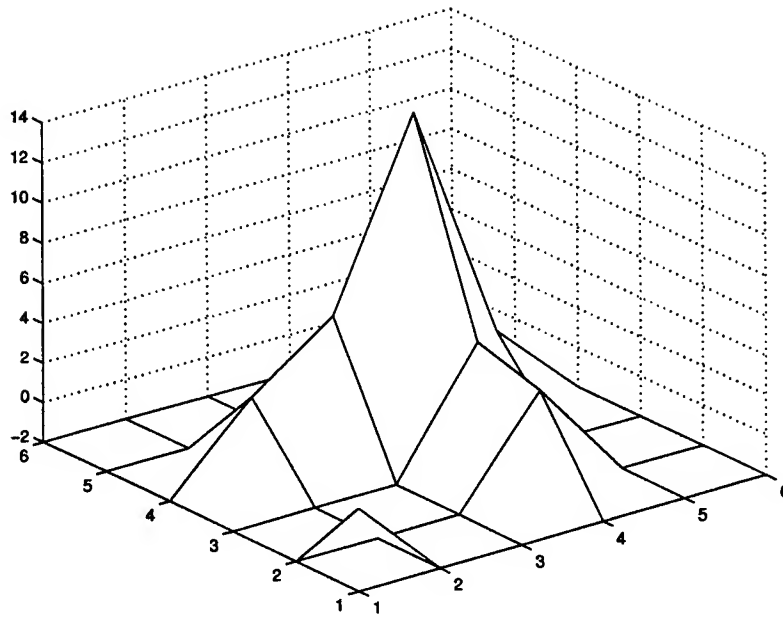


Figure 13: Model Order for 8x8 blocks as determined (Slicy/HB14977.015)

#### 5.4 Simulation Set 4

The above proposed methodology was applied to images found on the MSTAR PUBLIC CLUTTER CD-ROM. Figure 14 shows a clutter image, and the corresponding model order is shown in Figure 15. Due to the large sizes of these images, and the limited computational resources that were available, mean for disjoint 32x32 blocks in the image were computed. Typically, those blocks that fall below a threshold are assigned the same model order as the first block (2 in the previous simulations). Other statistics could also be considered. In particular, skewness seems like a good measure due to some indications that clutter is negatively skewed. To show the locations where the computation of model order was actually done in this simulation, the blocks for which the mean was lower than the threshold are shown with 0 model order. Those blocks with non-zero model order were actually computed. One may observe that the few locations where the model order was computed, the model order came out to be 2. These clutter images typically result in a number of false alarms though no published results were available on the typical number of false alarms that contemporary algorithms produce. Nonetheless, this representative simulation clearly shows that the model order is much less than what typical targets give rise to (compare the peaks to those in the earlier Figures).

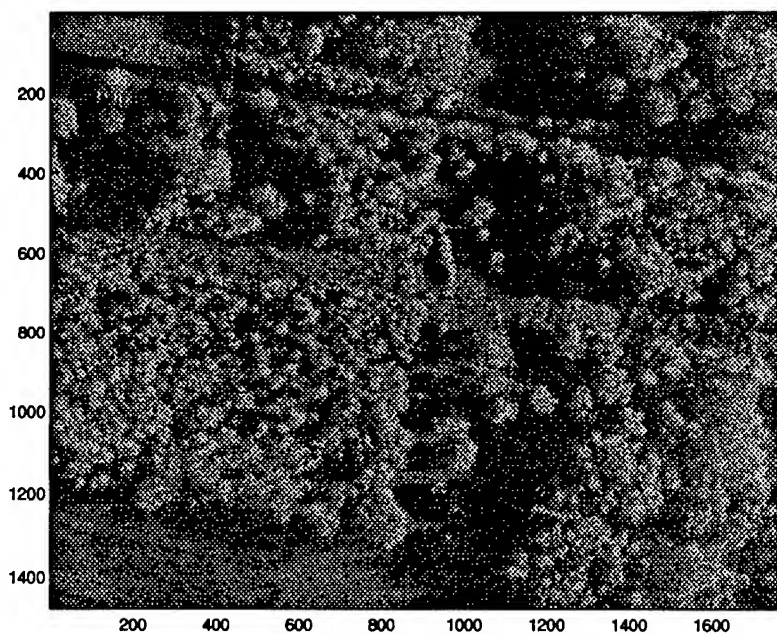


Figure 14: Sample clutter image (HB06197)

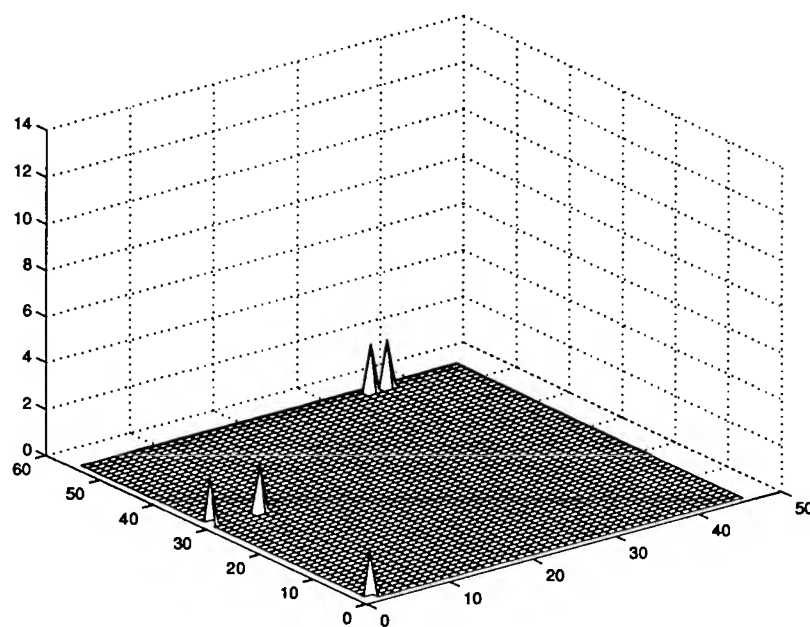


Figure 15: Model Order for 32x32 blocks as determined (HB06197)

## 6 Conclusions

The minimization of false alarm is necessary to minimize the bottleneck that is likely at the recognition stage of an ATR system. Towards that end, this research used an innovative idea to allow for identification of region of interest with minimal amount of false alarm. In the simulations that were run, model order provided discriminatory information regarding the location of potential targets. Clearly, model order deserves further attention as a tool for false alarm reduction in SAR images. Additional related topics for further investigation include:

- The overall speed of the proposed model order based technique is much slower than that of other implementations (e.g. CFAR). Since the proposed networks always start from the same initial weights for each block and same training parameters, the trajectory of error decrease can be correlated to the model order without going through the entire training. Thus, a sophisticated table lookup can be used to reduce the processing time.
- The advanced algorithm (with Gaussian Lateral Connections) was developed concurrently with the ROI determination. The advanced algorithm allows more sophisticated approximation of less strong returns. A more extensive testing of this algorithm is necessary (some of it will be reported in [21]).
- Other forms of lateral connectivity in the network need to be investigated.
- Other model selection criterion such as unbiased estimate of variance, final prediction error, Bayesian information criterion, and generalized cross validation can also be used in a framework to calculate the model order. This aspect was initiated in the Summer research but was only fleetingly evaluated.
- Only the magnitude aspect of the return was used in the above simulations. The phase of the return also contains significant information and is anticipated to aid the determination of ROI's.

## References

- [1] G. B. Goldstein, "False Alarm Regulation in Log Normal and Weibull Clutter," *IEEE Transactions on Aerospace and Electronic Systems*, Vol. 9, pp. 84-92, 1973.
- [2] L. M. Novak, and M. C. Burl, "Optimal Speckle Reduction in Polarimetric Sar Imagery," *IEEE Transactions on Aerospace and Electronic Systems*, Vol. 26, pp. 293-305, 1990.
- [3] S. Grossberg, and E. Mingolla, "Neural Dynamics of Surface Perception: Boundary Webs, Illuminants, and Shape from Shading," *Computer Vision, Graphics, and Image Processing*, Vol. 37, pp. 116-165, 1987.
- [4] A. M. Waxman et al., "Neural Processing of SAR Imagery for Enhanced Target Detection," *Proc. SPIE on Algorithms for Synthetic Aperture Radar Imagery II*, Vol. 2487, pp. 201-210, 1995.
- [5] D. Casasent, and J. S. Smokelin, "Real, Imaginary, and Clutter Gabor Filter Fusion for Detection with Reduced False Alarms," *Optical Engineering*, Vol. 33, pp. 2255-2263, 1994.
- [6] G. Tarr, "Multi-Layered Feedforward Neural Networks for Image Segmentation," *Ph.D. Dissertation, Air Force Institute of Technology*, OH, 1991.

- [7] D. E. Rumelhart, and J. L. McClelland, *Parallel Distributed Processing: Explorations in the Microstructure of Cognition*, vol. 1, Cambridge, MA:MIT Press, 1986.
- [8] S. Rogers et al., "Neural Networks for Automatic Target Recognition," *Neural Networks*, Vol. 8, pp. 1153-1184, 1995.
- [9] S. P. Luttrell, "A Hierarchical Network for Clutter and Texture Modelling," *Proc. SPIE on Adaptive Signal Processing*, pp. 518-528, 1991.
- [10] J. Chernick et al., "Background Characterization Techniques for Target Detection Using Scene Metrics and Pattern Recognition," *Optical Engineering*, Vol. 30, pp. 254-258, 1991.
- [11] T. Martinez, and K. Schulten, "Topology Representing Networks," *Neural Networks*, Vol. 7, pp. 507-522, 1994.
- [12] T. Kohonen, *Self Organizing Maps*, Berlin: Springer Verlag, 1995.
- [13] X. Chen, R. Kothari, and P. Klinkhachorn, "Reduced Color Image Based on Adaptive Color Selection Using Neural Networks," *Proc. World Congress on Neural Networks*, Vol. I, pp. 555-558, 1993.
- [14] G. Cybenko, "Approximation by Superpositions of a Sigmoidal Function," *Math. Contr. Signals, Syst.*, vol. 2, pp. 303-314, 1989.
- [15] T. Chen, H. Chen, R. Lin, "Approximation Capability in  $C(\mathcal{R})$ " by Multilayer Feedforward Networks and Related Problems," *IEEE Trans. Neural Networks*, vol. 6, pp. 25-30, 1995.
- [16] A. R. Barron, "Universal Approximation Bounds for Superposition of a Sigmoidal Function," *IEEE Trans. Information Theory*, vol. 39, pp. 930-945, 1993.
- [17] R. Kothari, and K. Agyepong, "On Lateral Connections in Feed-Forward Neural Networks," *Proc. IEEE International Conference on Neural Networks*, pp. 13-18, 1996.
- [18] R. Kothari, and K. Agyepong, "Self-Regulation of Model Order in Feed-Forward Neural Networks," *Proc. IEEE International Conference on Neural Networks*, pp. 1966-1971, 1997.
- [19] K. Agyepong, and R. Kothari, "Controlling Hidden Layer Capacity through Lateral Connections," *Neural Computation*, Vol. 9, No. 6, pp. 1381-1402, 1997.
- [20] R. Kothari, and K. Agyepong, "Induced Specialization of Context Units for Temporal Pattern Recognition and Reproduction," In *IEEE Neural Networks for Signal Processing VII*, 1997, To Appear.
- [21] R. Kothari, and D. Ensley, "Decision Boundaries and Generalization Performance of Feed-Forward Networks With Local Lateral Connections," *Proc. SPIE Application and Science of Computational Intelligence*, 1998 (Submitted).
- [22] R. Kothari, and D. Ensley, "On the Use of Model Order for Detecting Potential Target Locations in SAR Images," *Proc. SPIE Algorithms for Synthetic Aperture Radar Imagery V*, 1998 (Submitted).



**ON THE ANALYSIS AND DESIGN  
OF GAIN SCHEDULED MISSILE AUTOPILOTS**

**Douglas A. Lawrence  
Associate Professor  
School of Electrical Engineering  
and Computer Science**

**Ohio University  
Athens, Ohio 45701**

**Final Report for:**

**Summer Faculty Research Program  
Wright Laboratory  
Armament Directorate  
Eglin Air Force Base**

**Sponsored by:**

**Air Force Office of Scientific Research  
Bolling Air Force Base, DC**

**and**

**Wright Laboratory  
Armament Directorate  
Eglin Air Force Base**

**August 1997**

ON THE ANALYSIS AND DESIGN  
OF GAIN SCHEDULED MISSILE AUTOPILOTS

Douglas A. Lawrence  
Associate Professor  
School of Electrical Engineering  
and Computer Science  
Ohio University

**Abstract**

The application of a recently developed methodology for gain scheduled control system synthesis to the design of a pitch channel missile autopilot is described. Conditions are given under which a nonlinear gain scheduled autopilot exists that linearizes to a prescribed family of linear autopilots designed over specified operating envelope. A combination of techniques are employed to satisfy these conditions. Nonlinear simulation results indicate satisfactory performance over the flight envelope.

# ON THE ANALYSIS AND DESIGN OF GAIN SCHEDULED MISSILE AUTOPILOTS

Douglas A. Lawrence

## 1. Introduction

Controlling the behavior of a missile or aircraft over a wide operating envelope is a challenging problem in large part due to the presence of significant nonlinear effects. Existing flight control systems typically employ some form of gain scheduling to compensate for these nonlinearities and yet preserve a linear controller architecture. Documented studies of gain scheduling methods applied to flight control problems have appeared in the literature. [1], [4], [8] - [15]

A methodology proposed in [7] that focuses on nonlinear systems aspects of gain scheduling can be described in broad terms by the following steps:

- Determine a nonlinear plant's family of constant operating points, parameterized by a designated set of scheduling variables.
- For the corresponding family of linearized plants, design a family of linear controllers to meet prescribed design goals at each constant operating point.
- Construct a gain scheduled controller that linearizes to the appropriate linear controller at each constant operating point.
- Check nonlocal performance of the resulting nonlinear control system.

In this methodology, the emphasis is on the linearization requirement of the third step. Specifically, technical conditions are derived for the existence of a nonlinear controller with this property. Further, it is shown that failure to satisfy these conditions will introduce so-called *hidden coupling terms* in any attempt to schedule the family of linear controllers constructed in the second step. These hidden coupling terms can potentially degrade system performance.

This report describes the application of the above gain scheduling methodology to the design of a pitch channel autopilot for a hypothetical tail-controlled missile. The primary objective of this effort is to investigate the impact of a recently described interpolation strategy for linear point designs on the nonlinear controller implementation. In addition to advantages pointed out in [5], this technique allows one of the technical existence conditions to be met without imposing any constraints on the linear point designs. Moreover, this approach leads to a gain scheduled autopilot that has an appealing structure. The remainder of this report is organized as follows. The nonlinear missile model is presented in the next section. The gain scheduled autopilot design is described in Section 3. Simulation results are discussed in Section 4. Finally, concluding remarks are given in Section 5.

## 2. Missile Description

A missile's longitudinal behavior is characterized by the following variables:

$V_m$	missile speed in <i>feet/sec</i>
$\alpha$	angle-of-attack in <i>radians</i>
$Q$	pitch rate in <i>radians/sec</i>
$\delta$	tail fin deflection in <i>radians</i>
$\theta$	pitch attitude angle in <i>radians</i>
$\eta_z$	normal acceleration in <i>gees</i>
$h$	altitude in <i>feet</i>
$M$	mach number.

The short-period longitudinal aerodynamics are described by

$$\begin{aligned}\dot{\alpha} &= \frac{1}{V_m} \left[ \frac{\bar{q}S}{m} [C_N \cos(\alpha) - C_A \sin(\alpha)] + g \cos(\theta - \alpha) \right] + Q \\ \dot{Q} &= \frac{\bar{q}Sd}{I_y} C_M\end{aligned}\quad (1)$$

and the remaining longitudinal aerodynamics are described by

$$\begin{aligned}\dot{V}_m &= \frac{\bar{q}S}{m} [C_A \cos(\alpha) + C_N \sin(\alpha)] - g \sin(\theta - \alpha) \\ \dot{\theta} &= Q \\ \dot{h} &= V_m \sin(\theta - \alpha)\end{aligned}\quad (2)$$

Normal acceleration is given by

$$\eta_z = \frac{\bar{q}S}{mg} C_N + \cos(\theta). \quad (3)$$

The aerodynamic coefficients  $C_A$ ,  $C_N$ , and  $C_M$  characterize the aerodynamic axial force, normal force, and pitching moment, respectively, of the missile. For the particular missile model used in this study, these aerodynamic coefficients are given by ([8])

$$\begin{aligned}C_A &= a_a \\ C_N &= a_n \alpha^3 + b_n |\alpha| \alpha + c_n (2 - M/3) \alpha + d_n \delta \\ C_M &= a_m \alpha^3 + b_m |\alpha| \alpha + c_m (-7 + 8M/3) \alpha + d_m \delta + e_m Q\end{aligned}$$

with polynomial coefficient values listed Table 1. Finally, dynamic pressure,  $\bar{q}$ , is determined from

$$\bar{q} = \frac{1}{2} \rho V_m^2 \quad (4)$$

where  $\rho$  is the altitude-dependent air density. The tail fin actuator is modeled by

$$\frac{d}{dt} \begin{bmatrix} \delta \\ \dot{\delta} \end{bmatrix} = \begin{bmatrix} 0 & 1 \\ -\omega_a^2 & -2\zeta_a \omega_a \end{bmatrix} \begin{bmatrix} \delta \\ \dot{\delta} \end{bmatrix} + \begin{bmatrix} 0 \\ \omega_a^2 \end{bmatrix} \delta_c \quad (5)$$

where  $\delta_c$  is the commanded tail fin deflection in *radians*. Additional missile and actuator parameters are listed in Table 2.

### 3. Gain Scheduled Autopilot Design

The first step in the design process involves calculating the missile's family of constant operating points or equilibria. This poses an immediate difficulty in that true equilibria cannot exist for a ballistic missile since the condition  $\dot{V}_m = 0$  cannot be achieved without thrust. As an alternative, we consider only short-period equilibria. Specifically, we are interested in constant solutions to the algebraic equations resulting from the constraints  $\dot{\alpha} = \dot{Q} = 0$ :

$$\begin{aligned} 0 &= \frac{1}{V_m^\circ} \left[ \frac{\bar{q}^\circ S}{m} [C_N^\circ \cos(\alpha^\circ) - C_A^\circ \sin(\alpha^\circ)] + g \cos(\theta^\circ - \alpha^\circ) \right] + Q^\circ \\ 0 &= \frac{\bar{q}^\circ S d}{I_y} C_M^\circ. \end{aligned} \quad (6)$$

For any such solution, the corresponding normal acceleration value is

$$\eta_z^\circ = \frac{\bar{q}^\circ S}{mg} C_N^\circ + \cos(\theta^\circ). \quad (7)$$

We note that solutions to (6) will not yield zero derivatives in (2).

Acknowledging the potential hazards of our approach, we continue with the design and recognize that, since (6) constitutes two equations in six unknowns, there is a continuous family of solutions which can be parameterized in several ways. Here we parameterize by angle-of-attack, mach number, altitude, and pitch attitude angle and determine pitch rate, tail fin deflection, and normal acceleration as functions of these variables to obtain the relationships

$$\begin{aligned} Q^\circ &= Q^\circ[\alpha^\circ, M^\circ, h^\circ, \theta^\circ] \\ \delta^\circ &= \delta^\circ[\alpha^\circ, M^\circ, h^\circ, \theta^\circ] \\ \eta_z^\circ &= \eta_z^\circ[\alpha^\circ, M^\circ, h^\circ, \theta^\circ]. \end{aligned} \quad (12)$$

In addition, the actuator dynamics yield

$$\delta_c^\circ = \delta^\circ[\alpha^\circ, M^\circ, h^\circ, \theta^\circ]. \quad (13)$$

For the remainder of this report, we ignore the dependence of this constant operating point family on pitch attitude and define  $\Theta = [\alpha \ M \ h]$  which will allow us to compactly write  $Q^\circ(\Theta)$ , and so on. Also,  $\Theta$  will play the role of the scheduling variable in the remainder of the design process.

For the second step in the design process, we focus on the short period aerodynamics (1), the actuator dynamics (5), and normal acceleration (3) for which (12) and (13) characterize a parameterized family of constant operating points. For the associated parameterized family of linearizations, we consider a parameterized family of linear autopilots of the form

$$\begin{aligned}
\dot{x}_I &= \eta_c - \eta_z \\
\dot{x}_C &= A(\Theta)x_C + B(\Theta)[x_I \quad \eta_z \quad Q]^T \\
\delta_c &= C(\Theta)x_C + D(\Theta)[x_I \quad \eta_z \quad Q]^T
\end{aligned} \tag{14}$$

where  $\eta_c$  is a commanded normal acceleration. The linear autopilot family was constructed as follows.

For the cell in the scheduling variable set defined by

$$\{\Theta \in R^3 \mid 0 \leq \alpha \leq 10^\circ, 3.0 \leq M \leq 3.5, 20k \leq h \leq 30k \text{ ft.}\}$$

linear  $H_2$  point designs were constructed at the eight vertices. On the interior of the cell, the control signals generated by each of the autopilots were linearly interpolated. This leads to a parameterized family of autopilots (14) with

$$\begin{aligned}
A(\Theta) &= A = \begin{bmatrix} A_1 & \cdots & 0 \\ \vdots & \ddots & \vdots \\ 0 & \cdots & A_8 \end{bmatrix} \\
B(\Theta) &= B = \begin{bmatrix} B_1 \\ \vdots \\ B_8 \end{bmatrix} \\
C(\Theta) &= [\rho_1(\Theta)C_1 \quad \cdots \quad \rho_8(\Theta)C_8] \\
D(\Theta) &= [\rho_1(\Theta)D_1 \quad \cdots \quad \rho_8(\Theta)D_8]
\end{aligned}$$

where  $(A_i, B_i, C_i, D_i), i=1, \dots, 8$  are state space realizations of the eight point designs and linear interpolation of the individual control signals is achieved by the  $\rho_i(\Theta)$ 's. An important feature of this interpolation scheme as it relates to the construction of a nonlinear gain scheduled autopilot in the next step of the design procedure is that the  $A$  and  $B$  matrices above are independent of  $\Theta$ .

As an indication of the performance and stability robustness achieved by the family of linear autopilots over the cell under consideration we consider the operating point corresponding to the center of the cell: 5 degrees angle-of-attack, mach 3.25, and 25k ft altitude. For the associated linearized short-period aerodynamics, actuator dynamics, and linear autopilot a closed-loop unit step response is given in Fig. 1 and a bode plot of the open-loop return difference is given in Fig 2. This situation essentially represent worst case linear performance achieved over the cell and yet these plots indicate acceptable transient response behavior and stability margin.

It is important to note that in order to implement this interpolation strategy over an entire flight envelope, the corresponding scheduling variable set must be divided into an appropriate number of cells, with the above construction repeated on each cell. Further, a procedure to switch between parallel banks of linear autopilots as scheduling variable trajectories cross cell boundaries is required. These important issues are not pursued in this study.

The next step in the design process is to construct a nonlinear autopilot of the form

$$\begin{aligned}
\dot{x}_I &= \eta_c - \eta_z \\
\dot{x}_C &= a(x_C, x_I, \eta_z, Q, \Theta) \\
\delta_c &= c(x_C, x_I, \eta_z, Q, \Theta)
\end{aligned} \tag{15}$$

that schedules the family of linear autopilots in the sense that the following two requirements are met.

**Requirement 1.** At each constant operating point, the nonlinear autopilot generates the correct constant control value. Specifically, there must exist functions  $x_I^\circ(\Theta), x_C^\circ(\Theta)$  that satisfy (suppressing arguments)

$$\begin{aligned}
a(x_C^\circ, x_I^\circ, \eta_z^\circ, Q^\circ, \Theta) &= 0 \\
c(x_C^\circ, x_I^\circ, \eta_z^\circ, Q^\circ, \Theta) &= \delta^\circ
\end{aligned} \tag{16}$$

**Requirement 2.** At each constant operating point, the nonlinear autopilot linearizes to the appropriate linear autopilot. Specifically, the following partial derivative identities must hold.

$$\begin{aligned}
\frac{\partial a}{\partial x_C}(x_C^\circ, x_I^\circ, \eta_z^\circ, Q^\circ, \Theta) &= A \\
\frac{\partial a}{\partial(x_I, \eta_z, Q)}(x_C^\circ, x_I^\circ, \eta_z^\circ, Q^\circ, \Theta) &= B \\
\frac{\partial c}{\partial x_C}(x_C^\circ, x_I^\circ, \eta_z^\circ, Q^\circ, \Theta) &= C(\Theta) \\
\frac{\partial c}{\partial(x_I, \eta_z, Q)}(x_C^\circ, x_I^\circ, \eta_z^\circ, Q^\circ, \Theta) &= D(\Theta)
\end{aligned} \tag{17}$$

and

$$\begin{aligned}
\frac{\partial a}{\partial \Theta}(x_C^\circ, x_I^\circ, \eta_z^\circ, Q^\circ, \Theta) &= 0 \\
\frac{\partial c}{\partial \Theta}(x_C^\circ, x_I^\circ, \eta_z^\circ, Q^\circ, \Theta) &= 0.
\end{aligned} \tag{18}$$

The identities in (18) reflect the fact that the family of linear autopilots does not exhibit linear terms in the scheduling variables. The following theorem establishes necessary and sufficient conditions for the existence of a nonlinear autopilot that meets these two requirements.

**Theorem.** There exists a nonlinear autopilot (15) that meets Requirements 1 and 2 if and only if there exist functions  $x_I^\circ(\Theta), x_C^\circ(\Theta)$  that satisfy

$$\begin{aligned}
A \frac{\partial x_C^\circ}{\partial \Theta} + B \begin{bmatrix} \partial x_I^\circ / \partial \Theta \\ \partial \eta_z^\circ / \partial \Theta \\ \partial Q^\circ / \partial \Theta \end{bmatrix} &= 0 \\
C(\Theta) \frac{\partial x_C^\circ}{\partial \Theta} + D(\Theta) \begin{bmatrix} \partial x_I^\circ / \partial \Theta \\ \partial \eta_z^\circ / \partial \Theta \\ \partial Q^\circ / \partial \Theta \end{bmatrix} &= \frac{\partial \delta^\circ}{\partial \Theta}
\end{aligned} \tag{19}$$

**Proof.** For necessity, suppose there is a nonlinear autopilot that satisfies Requirements 1 and 2. Then differentiating (16) with respect to  $\Theta$  and substituting the identities in (17) and (18) yields (19). For sufficiency, suppose there are functions  $x_I^\circ(\Theta), x_C^\circ(\Theta)$  that satisfy (19) and consider

$$\begin{aligned}
a(x_C, x_I, \eta_z, Q, \Theta) &= A x_C + B \begin{bmatrix} x_I \\ \eta_z \\ Q \end{bmatrix} \\
c(x_C, x_I, \eta_z, Q, \Theta) &= \delta^\circ(\Theta) + C(\Theta) [x_C - x_C^\circ(\Theta)] + D(\Theta) \begin{bmatrix} x_I - x_I^\circ(\Theta) \\ \eta_z - \eta_z^\circ(\Theta) \\ Q - Q^\circ(\Theta) \end{bmatrix}
\end{aligned} \tag{20}$$

Since  $A$  and  $B$  are independent of  $\Theta$ , the first identity in (19) gives

$$A x_C^\circ(\Theta) + B \begin{bmatrix} x_I^\circ(\Theta) \\ \eta_z^\circ(\Theta) \\ Q^\circ(\Theta) \end{bmatrix} = 0 \tag{21}$$

which gives the first identity in (16). It is also clear that the first two identities in (17) and the first identity in (18) are satisfied. Next, it is easy to see that the second identity in (16) and the last two identities in (17) hold for any choice of functions  $x_I^\circ(\Theta)$ ,  $x_C^\circ(\Theta)$  and it remains to check that the second identity in (18) is satisfied. Differentiating (20) with respect to  $\Theta$  and evaluating at any constant operating point yields

$$\frac{\partial c}{\partial \Theta}(x_C^\circ, x_I^\circ, \eta_z^\circ, Q^\circ, \Theta) = \frac{\partial \delta^\circ}{\partial \Theta} - C(\Theta) \frac{\partial x_C^\circ}{\partial \Theta} - D(\Theta) \begin{bmatrix} \partial x_I^\circ / \partial \Theta \\ \partial \eta_z^\circ / \partial \Theta \\ \partial Q^\circ / \partial \Theta \end{bmatrix} \tag{22}$$

which is zero due to the second identity in (19).

□□□

It is worth emphasizing that since this particular interpolation scheme leads constant  $A$  and  $B$  matrices, the first identity in (19) is equivalent to (21). Consequently, for any choice of  $x_I^\circ(\Theta)$ , we can satisfy the first identity in (19) by taking

$$x_C^\circ(\Theta) = -A^{-1}B \begin{bmatrix} x_I^\circ(\Theta) \\ \eta_z^\circ(\Theta) \\ Q^\circ(\Theta) \end{bmatrix} \tag{23}$$

since the linear point designs will have each  $A_i$  invertible. Also, the second identity in (19) can be rewritten as

$$K_{DC}(\Theta) \begin{bmatrix} \partial x_I^\circ / \partial \Theta \\ \partial \eta_z^\circ / \partial \Theta \\ \partial Q^\circ / \partial \Theta \end{bmatrix} = \frac{\partial \delta^\circ}{\partial \Theta} \tag{24}$$

where

$$K_{DC}(\Theta) = -C(\Theta)A^{-1}B + D(\Theta)$$

is the DC gain of the interpolated linear autopilot. Hence, the existence conditions reduce to a single equation (24) which can be solved for  $\partial x_I^\circ / \partial \Theta$  to yield a partial differential equation of the form



$$\frac{\partial x_I^\circ}{\partial \Theta} = G(\Theta) = [G_1(\Theta) \ G_2(\Theta) \ G_3(\Theta)] \quad (25)$$

This equation has a solution  $x_I^\circ(\Theta)$  if and only if the following mixed-partial derivative conditions are satisfied

$$\frac{\partial G_i}{\partial \Theta_j} = \frac{\partial G_j}{\partial \Theta_i}, \quad 1 \leq i < j \leq 3 \quad (26)$$

When these conditions are satisfied, a solution to (24) can be expressed by a line integral of the form

$$x_I^\circ(\Theta) = C_0 + \int_{\gamma} G(\bar{x}) \cdot d\bar{x}$$

where  $\gamma$  is a suitably smooth but otherwise arbitrary path from a fixed point  $\Theta_0$  to  $\Theta$  and  $C_0 = x_I^\circ(\Theta_0)$ . Unfortunately, these conditions are restrictive and typically will not be satisfied. It is always possible, however, to construct a function for which any one of the three scalar identities in (25) is satisfied. This is done by choosing the path of integration along the coordinate axes in a specified order. For example, to achieve equality for the first scalar identity in (25), take

$$x_I^\circ(\Theta) = \int_{\alpha_0}^{\alpha} G_1(x, M, h) dx + \int_{M_0}^M G_2(\alpha_0, y, h) dy + \int_{h_0}^h G_2(\alpha_0, M_0, z) dz \quad (27)$$

where we have taken  $C_0 = 0$  and have used the notation  $\Theta = [\alpha \ M \ h]$  and  $\Theta_0 = [\alpha_0 \ M_0 \ h_0]$ . Taking the terms on the right hand side in reverse order, the third term corresponds to integrating along the  $\Theta_3 = h$  axis from  $(\alpha_0, M_0, h_0)$  to  $(\alpha_0, M_0, h)$ . The second term corresponds to integrating along the  $\Theta_2 = M$  axis from  $(\alpha_0, M_0, h)$  to  $(\alpha_0, M, h)$ . Finally, the first term corresponds to integrating along the  $\Theta_1 = \alpha$  axis from  $(\alpha_0, M, h)$  to  $(\alpha, M, h)$ . Direct calculations then give

$$\begin{aligned} \frac{\partial x_I^\circ}{\partial \alpha}(\Theta) &= G_1(\Theta) \\ \frac{\partial x_I^\circ}{\partial M}(\Theta) &= G_2(\Theta) + \int_{\alpha_0}^{\alpha} \left[ \frac{\partial G_1}{\partial \Theta_2}(x, M, h) - \frac{\partial G_2}{\partial \Theta_1}(x, M, h) \right] dx \\ \frac{\partial x_I^\circ}{\partial h}(\Theta) &= G_3(\Theta) + \int_{\alpha_0}^{\alpha} \left[ \frac{\partial G_1}{\partial \Theta_3}(x, M, h) - \frac{\partial G_3}{\partial \Theta_1}(x, M, h) \right] dx \\ &\quad + \int_{M_0}^M \left[ \frac{\partial G_2}{\partial \Theta_3}(\alpha_0, y, h) - \frac{\partial G_3}{\partial \Theta_2}(\alpha_0, y, h) \right] dy \end{aligned}$$

It can be seen that the first identity in (25) indeed holds. Also, the mismatch in the last two identities depends on the difference of the mixed partial derivatives.

In summary, the gain scheduled autopilot takes the final form

$$\begin{aligned}
\dot{x}_I &= \eta_c - \eta_z \\
\dot{x}_C &= A x_C + B \begin{bmatrix} x_I \\ \eta_z \\ Q \end{bmatrix} \\
\delta_c &= \delta^\circ(\Theta) + C(\Theta) [x_C - x_C^\circ(\Theta)] + D(\Theta) \begin{bmatrix} x_I - x_I^\circ(\Theta) \\ \eta_z - \eta_z^\circ(\Theta) \\ Q - Q^\circ(\Theta) \end{bmatrix} \\
&= C(\Theta) x_C + D(\Theta) \begin{bmatrix} x_I \\ \eta_z \\ Q \end{bmatrix} + \lambda(\Theta)
\end{aligned} \tag{28}$$

where

$$\begin{aligned}
\lambda(\Theta) &= \delta^\circ(\Theta) - C(\Theta) x_C^\circ(\Theta) - D(\Theta) \begin{bmatrix} x_I^\circ(\Theta) \\ \eta_z^\circ(\Theta) \\ Q^\circ(\Theta) \end{bmatrix} \\
&= \delta^\circ(\Theta) - K_{DC}(\Theta) \begin{bmatrix} x_I^\circ(\Theta) \\ \eta_z^\circ(\Theta) \\ Q^\circ(\Theta) \end{bmatrix}
\end{aligned} \tag{29}$$

with  $x_I^\circ(\Theta)$  given by (27). This gain scheduled autopilot generates a control signal that is composed of two distinct pieces. The first component corresponds to the linear interpolation of the control signals generated by the eight linear autopilots operating in parallel. The second component can be thought of as a correction term that addresses the previously described requirements imposed on the autopilot. Even though this correction term only removes the hidden coupling term corresponding to angle-of-attack, its impact on system performance is significant.

In the fourth step of this gain scheduling methodology, nonlocal performance over the entire operating point envelope is normally analyzed under the assumption that all exogenous signals acting on the system are sufficiently slowly-varying. [3] [6] Here there is some concern over the fact that linear designs were performed about operating points that are not equilibria for the overall longitudinal aerodynamics. On the other hand, gain scheduled pitch channel autopilots are traditionally designed using a short-period approximation in a manner similar to that described here and work well in practice. This outcome can be explained as follows. The overall closed-loop system can be decomposed into two subsystems in a feedback configuration. The first subsystem consists of the short-period aerodynamics (1), the actuator (5), and the autopilot (28) with appropriately defined inputs and outputs. The second subsystem consists of the remaining longitudinal aerodynamics (2) whose inputs are the outputs of the first subsystem and vice-versa. It can be shown using the analysis of [6], that the first subsystem is locally finite-gain input-output stable. [2] It also can be shown using energy considerations that the output of the second subsystem is uniformly bounded. It can then be shown using the small gain theorem that the overall system possesses a stability property consistent with behavior exhibited in simulation studies.

#### 4. Simulation Results

A *Simulink*<sup>TM</sup> simulation was constructed for the closed-loop system consisting of the aerodynamics (1) and (2), the actuator dynamics (5), and the gain scheduled autopilot (28). Simulation results are presented here for an initial condition corresponding to the constant operating point parameterized by:

angle-of-attack	0 degrees
mach number	3.5
altitude	25,000 feet
pitch attitude	0 degrees

and a -40 g normal acceleration step command at  $t = 0$ . This scenario was selected to generate a scheduling variable profile that spans much of previously specified cell in order to test the validity of the point design interpolation scheme. Various responses are shown in Figs. 3 through 9. Fig. 3 shows the normal acceleration response when the correction term (29) is included (solid curve) and when it is omitted (dashed curve). With the correction term in place, the response is in good agreement with linearized responses throughout the operating envelope. With the correction term removed, the destabilizing effects of a hidden coupling term due to angle-of-attack that is necessarily present are apparent. The remaining figures depict responses with the correction term in place.

#### 5. Concluding Remarks

In this report, the application of a recently developed methodology for gain scheduling to a missile autopilot design problem has been described. A key feature of the design is the incorporation of a control signal interpolation strategy which allows one of the technical existence conditions to be satisfied without imposing any constraints on the linear point designs. Moreover, this approach leads to a nonlinear gain scheduled autopilot that has the structure of a linear parameter-varying autopilot plus a correction term.

The gain scheduling methodology employed in this work presumes that linear controller designs are computed based on plant linearizations about constant operating points or equilibria. In the autopilot design studied here, this was not possible and the alternative was to use short-period equilibria assuming all other variables are constant. This appears to be common practice and results in autopilots that perform well. A mathematical justification of this phenomenon can be derived using standard stability results.

## 6. References

- [1] R.A. Hyde and K. Glover, "The Application of Scheduled H-Infinity Controllers to a VSTOL Aircraft," *IEEE Transactions on Automatic Control*, Vol. AC-38, No. 7, pp. 1021-1039, 1993.
- [2] H. K. Khalil, *Nonlinear Control Systems*, Second Edition, Prentice-Hall, 1996
- [3] M. Kelemen, "A Stability Property," *IEEE Transactions on Automatic Control*, Vol. AC-31, No. 8, pp. 766-768, 1986.
- [4] M.G. Kellett, "Continuous Scheduling of H-Infinity Controllers for a MS760 Paris Aircraft," In *Robust Control System Design Using H-Infinity and Related Methods*, P.H. Hammond (Ed.), pp. 197-223, Institute of Measurement and Control, London, 1991.
- [5] J. H. Kelly and J. H. Evers, "An Interpolation Strategy for Scheduling Dynamic Compensators," *Proceedings of the 1997 AIAA Guidance, Navigation and Control Conference*, New Orleans, Louisiana, 1997.
- [6] D.A. Lawrence and W.J. Rugh, "On a Stability Theorem for Nonlinear Systems with Slowly Varying Inputs," *IEEE Transactions on Automatic Control*, Vol. AC-35, No. 7, pp. 860-864, 1990.
- [7] D.A. Lawrence and W.J. Rugh, "Gain Scheduling Dynamic Linear Controllers for a Nonlinear Plant," *Automatica*, Vol. 31, No. 5, pp. 381-390, 1995.
- [8] C. P. Mracek and J. R. Cloutier, "Full Envelope Missile Longitudinal Autopilot Design Using the State-Dependent Riccati Equation Method," *Proceedings of the 1997 AIAA Guidance, Navigation and Control Conference*, New Orleans, Louisiana, 1997.
- [9] R. Nichols, R. Reichert, W.J. Rugh, "Gain Scheduling for H-Infinity Controllers: A Flight Control Example," *IEEE Transactions on Control Systems Technology*, Vol. 1, No. 2, pp. 69-79, 1993.
- [10] A. Ostroff, "High-Alpha Application of Variable-Gain Output Feedback Control," *AIAA Journal of Guidance, Control, and Dynamics*, Vol. 15, pp. 491-497, 1992.
- [11] R.T. Reichert, "Dynamic Scheduling of Modern-Robust-Control Autopilot Designs for Missiles," *IEEE Control Systems Magazine*, Vol. 12, No. 5, pp. 35-42, 1992.
- [12] J.S. Shamma and J.R. Cloutier, "Gain-Scheduled Missile Autopilot Design Using Linear Parameter Varying Transformations," *AIAA Journal of Guidance, Control, and Dynamics*, Vol. 16, No. 2, pp. 256-263, 1993.
- [13] White, J. Wozniak, D. Lawrence, "Missile Autopilot Design Using a Gain Scheduling Technique," *Proceedings of the 26th Southeastern Symposium on System Theory*, pp. 606-610, Athens, Ohio, 1994.

Axial Force Coefficient	Normal Force Coefficient	Pitch Moment Coefficient
$a_a = -0.300$	$a_n = 19.373$	$a_m = 40.440$
	$b_n = -31.023$	$b_m = -64.015$
	$c_n = -9.717$	$c_m = 2.922$
	$d_n = -1.948$	$d_m = -11.803$
		$e_m = -1.719$

Table 1. Aerodynamic Coefficient Parameters

Symbol	Description	Value
S	surface area	0.44 feet <sup>2</sup>
m	mass	13.98 slug
g	acceleration due to gravity	32.2 feet/sec <sup>2</sup>
d	reference length	0.75 feet
I <sub>y</sub>	pitch moment of inertia	182.5 slug-feet <sup>2</sup>
$\zeta_a$	actuator damping ratio	0.7
$\omega_a$	actuator natural frequency	150 radians/sec

Table 2. Missile and Actuator Parameters

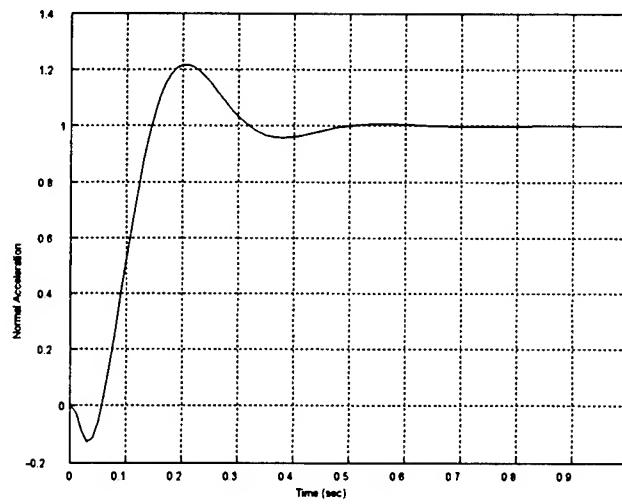


Fig 1. Linearized Normal Acceleration Step Response.

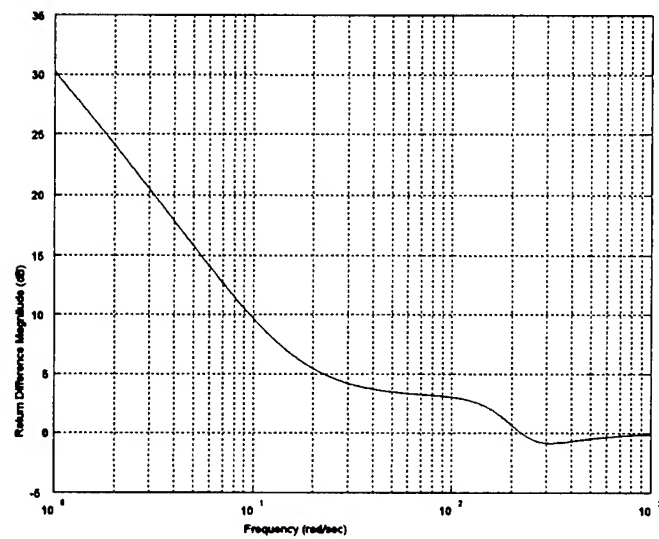


Fig. 2. Linearized Return Difference Frequency Response.

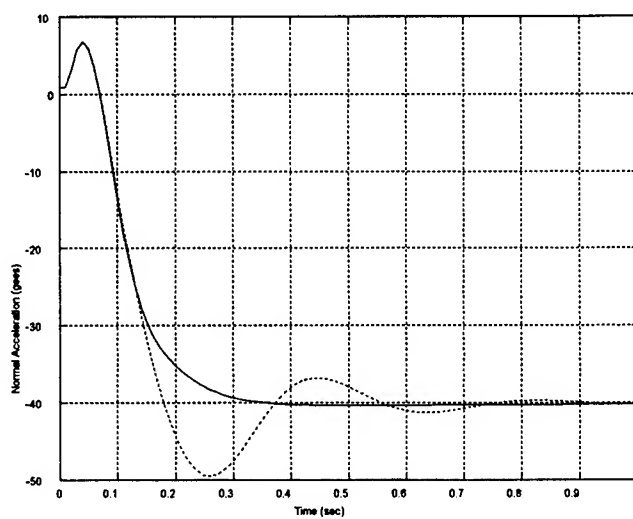


Fig. 3 Nonlinear Normal Acceleration Responses.

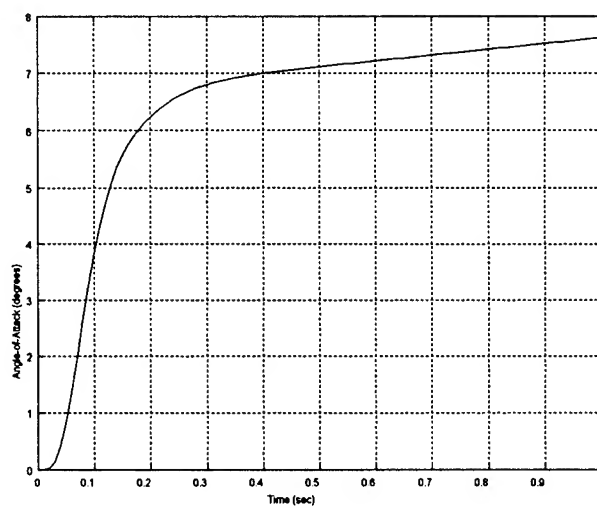


Fig. 4 Nonlinear Angle-of-Attack Response.

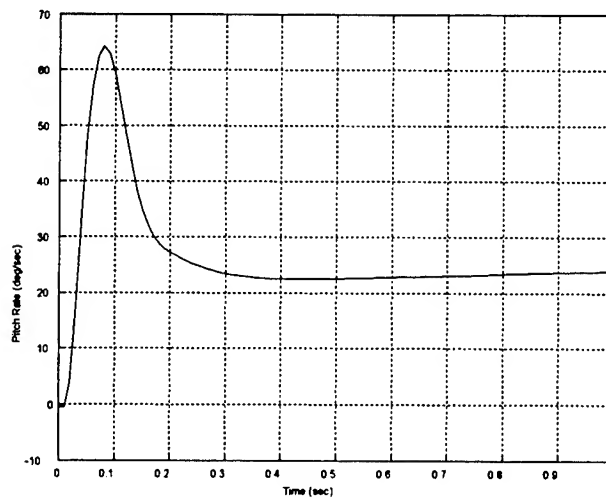


Fig. 5 Nonlinear Pitch Rate Response.

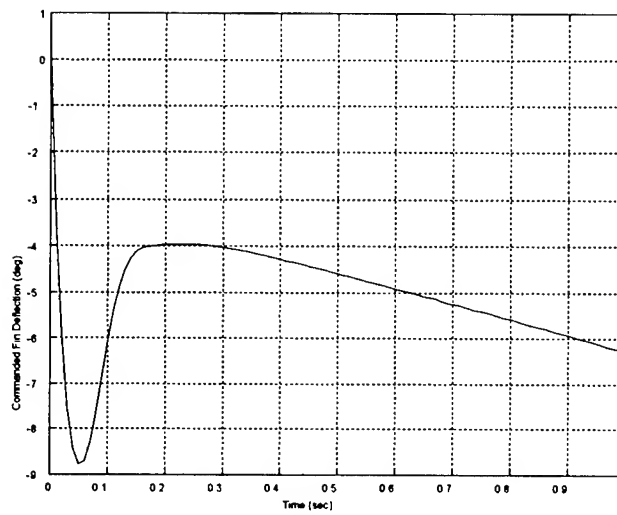


Fig. 6 Nonlinear Commanded Tail Fin Deflection Response.



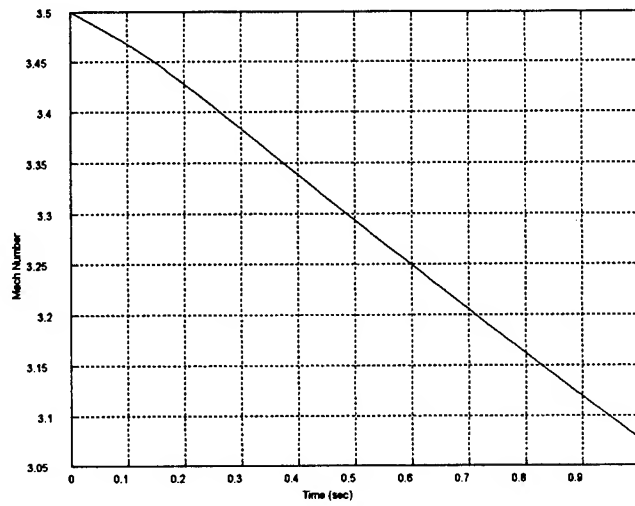


Fig. 7 Nonlinear Mach Response.

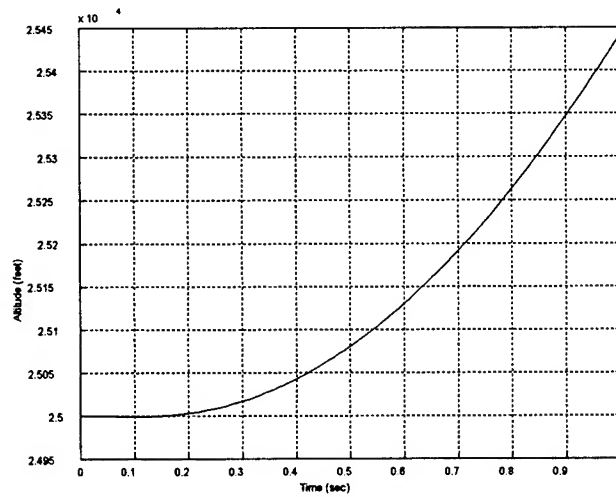


Fig. 8 Nonlinear Altitude Response.

BOUNDARY CONDITIONS APPLIED TO THE  
FINITE VOLUME TIME DOMAIN METHOD  
FOR THE SOLUTION OF MAXWELL'S EQUATIONS

Robert Lee  
Associate Professor  
Department of Electrical Engineering

The Ohio State University  
2015 Neil Avenue  
Columbus, OH 43210

Final Report for:  
Summer Faculty Research Program  
Wright Laboratory

Sponsored by:  
Air Force Office of Scientific Research  
and  
Wright Laboratory

August 1997

**BOUNDARY CONDITIONS APPLIED TO THE  
FINITE VOLUME TIME DOMAIN METHOD  
FOR THE SOLUTION OF MAXWELL'S EQUATIONS**

Robert Lee

Associate Professor

Department of Electrical Engineering

The Ohio State University

**Abstract**

In this report, we consider the application of the anisotropic perfectly matched layer (PML) absorbing boundary condition to the finite volume time domain (FVTD) method. At this point, the anisotropic PML has been applied to both the finite difference time domain method and the finite element method in the frequency domain; however, no work has been done for extending this method to FVTD. This report contains a review of FVTD applied to electromagnetics. It is followed by a review of the general theory of the anisotropic PML. Finally we formulate the PML for the FVTD method.

# BOUNDARY CONDITIONS APPLIED TO THE FINITE VOLUME TIME DOMAIN METHOD FOR THE SOLUTION OF MAXWELL'S EQUATIONS

Robert Lee

## I.. Introduction

The concept of using a lossy material to absorb an outgoing wave in order to simulate an infinite region of free space for finite methods is not a new one [1]. However, this method of truncation has not gained widespread use because of the reflections which occur at the free space/material interface. One idea to minimize the reflections at this interface is to choose a low loss for the material. Unfortunately, the lossy region must be sufficiently large to attenuate the wave, which can significantly reduce the computational efficiency.

Berenger [2] has introduced a modification to Maxwell's equations in order to allow for the specification of material properties which result in a reflectionless lossy material. The material is reflectionless in the sense that a plane wave propagating through an infinite free space/lossy material interface has no reflection for any angles of incidence. Berenger refers to this material as a perfectly matched layer or PML. Although Berenger demonstrates the validity of his approach with numerical experiments, the physical meaning of his modifications to Maxwell's equations is not very clear. Chew and Weedon [3] provide a systematic analysis of the PML in terms of the concept of "coordinate stretching". They demonstrate that Berenger's modifications to Maxwell's equations can be derived from a more generalized form of Maxwell's equations. There has also been additional work done on the PML, including that of Mittra and Pikel [4] and Rappaport [5].

Recently, it has also been discovered by Sacks et al. [6] that the reflectionless properties of a material can be achieved if the material is assumed to be anisotropic. Unlike Berenger's approach, this one does not require a modification of Maxwell's equations, making it easier to analyze in the general framework of electromagnetics. One of the important issues to resolve is the differences between the PML proposed by Berenger and the anisotropic PML proposed by Sacks et al. In this paper, we review the derivation of the two PML methods in order to demonstrate that they produce different field results even though the associated differential equation and tangential field boundary conditions are the same. In this report, we present the theory of the anisotropic PML and its application to FVTD. In this report, we consider the electromagnetic boundary

## II.. Finite Volume Time Domain Method

The general time domain form of Maxwell's equations in the absence of sources for materials which are linear, isotropic, and lossless can be written as

$$\nabla \cdot \vec{D} = 0 \quad (1)$$

$$\nabla \cdot \vec{B} = 0 \quad (2)$$

$$\nabla \times \vec{E} = -\frac{\partial \vec{B}}{\partial t} \quad (3)$$

$$\nabla \times \vec{H} = \frac{\partial \vec{D}}{\partial t} \quad (4)$$

where  $\vec{B} = \mu \vec{H}$  and  $\vec{D} = \epsilon \vec{E}$ . The variables  $\mu$  and  $\epsilon$  are the permeability and permittivity, respectively, of the material. Note that equations (1) and (2) can be derived from equations (3) and (4) through the application of the divergence operator and a stipulation on the initial conditions (zero fields for  $t < 0$ ). Thus, the two

curl equations ((3) and (4)) can be used to fully determine the electromagnetic field solution.

The two curl equations can be represented in the cartesian coordinate system as

$$\frac{\partial \vec{U}}{\partial t} + \frac{\partial \vec{F}_x}{\partial x} + \frac{\partial \vec{F}_y}{\partial y} + \frac{\partial \vec{F}_z}{\partial z} = 0 \quad (5)$$

where

$$\vec{U} = [E_x, E_y, E_z, H_x, H_y, H_z]^T \quad (6)$$

$$\vec{F}_x = [0, -H_z/\epsilon, H_x/\epsilon, 0, E_z/\mu, -E_y/\mu]^T \quad (7)$$

$$\vec{F}_y = [H_z/\epsilon, 0, -H_x/\epsilon, -E_z/\mu, 0, E_x/\mu]^T \quad (8)$$

$$\vec{F}_z = [-H_y/\epsilon, H_x/\epsilon, 0, E_y/\mu, -E_x/\mu, 0]^T \quad (9)$$

The terms  $\vec{F}_i$ ,  $i = x, y, z$  are commonly referred to as flux vectors. Although the above equations are for the Cartesian coordinate system, we can obtain similar forms for other coordinate systems. In fact, the extension to a general curvilinear coordinate system can be found in [1].

Let us rewrite equation (5) in a more compact form:

$$\frac{\partial \vec{U}}{\partial t} + \nabla \cdot \vec{\bar{F}} = 0 \quad (10)$$

where

$$\vec{\bar{F}} = \hat{x}\vec{F}_x + \hat{y}\vec{F}_y + \hat{z}\vec{F}_z \quad (11)$$

The form of (10) is useful for FVTD. To demonstrate this, let us apply FVTD to a sample cell shown in Figure 1. The cell is a hexahedral with volume  $V$  and surface  $S$ . The typical edge length of the cell is  $h$ . The unit vector  $\hat{n}$  is pointed in the outward normal direction to the surface  $S$ . In the FVTD formulation, we use the

approximation that (10) is satisfied in the weak sense within  $V$ , i.e.,

$$\iiint_V \left[ \frac{\partial \vec{U}}{\partial t} + \nabla \cdot \vec{F} \right] dv = 0 \quad (12)$$

An application of the divergence theorem to the second term in (12) leads to

$$\frac{\partial(V\tilde{U})}{\partial t} + \iint_S \hat{n} \cdot \vec{F} ds = 0 \quad (13)$$

where  $\tilde{U}$  is the average value of  $\vec{U}$  within the cell and is given by

$$\tilde{U} = \frac{1}{V} \iiint_V \vec{U} dv \quad (14)$$

We choose the unknown field quantities in  $\vec{U}$  to be located at the centroid of the cell. Let us call this value  $\hat{\vec{U}}$ . It can be shown [8] that for smooth solutions,  $\hat{\vec{U}} = \tilde{U} + O(h^n)$  when the approximation for the flux at the cell surfaces is accurate to within  $O(h^n)$ . There are a variety of different interpolation schemes to determine the flux at the cell surfaces in terms of  $\vec{U}$ . A common choice is the MUSCL scheme [9].

The time stepping algorithm is important for determining both the accuracy and stability of the FVTD method. The two-stage, second-order-accurate Runge Kutta scheme has been applied successfully to FVTD [10]. More recently, the multi-stage fourth-order-accurate Runge-Kutta scheme has been implemented [8]. This scheme requires twice the number of arithmetic operations as the two-stage algorithm; however, it produces more accurate results, and its superior stability properties allow one to choose a larger time step.

### III.. Outer Boundary Condition: The Perfectly Matched Layer

(a) *Anisotropic PML Theory*

The derivation here is based on [6], but there are some slight changes in notation to help in the comparison with Berenger's PML. The time-harmonic form of Maxwell's equations can be written as

$$\begin{aligned}
 \vec{\nabla} \cdot [\bar{\epsilon}] \vec{E} &= 0 \\
 \vec{\nabla} \cdot [\bar{\mu}] \vec{H} &= 0 \\
 \vec{\nabla} \times \vec{E} &= -j\omega[\bar{\mu}] \vec{H} \\
 \vec{\nabla} \times \vec{H} &= j\omega[\bar{\epsilon}] \vec{E}
 \end{aligned} \tag{15}$$

where  $[\bar{\mu}]$  and  $[\bar{\epsilon}]$  are the effective permeability and permittivity of Region 2, respectively. In this paper, we concentrate on materials with  $[\bar{\mu}]$  and  $[\bar{\epsilon}]$  diagonal in the same coordinate system.

$$\begin{aligned}
 [\bar{\mu}] &= \begin{pmatrix} \mu_x + \frac{\sigma_M^x}{j\omega} & 0 & 0 \\ 0 & \mu_y + \frac{\sigma_M^y}{j\omega} & 0 \\ 0 & 0 & \mu_z + \frac{\sigma_M^z}{j\omega} \end{pmatrix} \\
 [\bar{\epsilon}] &= \begin{pmatrix} \epsilon_x + \frac{\sigma_E^x}{j\omega} & 0 & 0 \\ 0 & \epsilon_y + \frac{\sigma_E^y}{j\omega} & 0 \\ 0 & 0 & \epsilon_z + \frac{\sigma_E^z}{j\omega} \end{pmatrix}
 \end{aligned} \tag{16}$$

Furthermore, we select  $[\bar{\epsilon}]$  and  $[\bar{\mu}]$  such that

$$\frac{[\bar{\epsilon}]}{\epsilon} = \frac{[\bar{\mu}]}{\mu}$$

to match Region 2 to Region 1. Thus, we can write,

$$[\bar{\mu}] = \mu[\Lambda] = \mu \begin{pmatrix} a & 0 & 0 \\ 0 & b & 0 \\ 0 & 0 & c \end{pmatrix}$$



$$[\vec{\epsilon}] = \epsilon[\Lambda] = \epsilon \begin{pmatrix} a & 0 & 0 \\ 0 & b & 0 \\ 0 & 0 & c \end{pmatrix} \quad (17)$$

where  $a, b, c$  are in general complex. Consequently, Eq. (15) reduces to

$$\begin{aligned} \vec{\nabla} \cdot \epsilon[\Lambda] \vec{E} &= 0 \\ \vec{\nabla} \cdot \mu[\Lambda] \vec{H} &= 0 \\ \vec{\nabla} \times \vec{E} &= -j\omega\mu[\Lambda] \vec{H} \\ \vec{\nabla} \times \vec{H} &= j\omega\epsilon[\Lambda] \vec{E} \end{aligned} \quad (18)$$

As in Berenger's PML, we must specify a further condition to the PML material to make it reflectionless to a plane wave. For a wave propagating in the  $z$  direction, we must specify  $a = b = 1/c$ . For a propagating wave to decay exponentially, we must specify that the  $\text{Im}(a) < 0$ . Also, the  $\text{Re}(a)$  can be specified for the desired absorption of evanescent waves.

#### (a.1) Use of anisotropic PML for FVTD

The above formulation for the anisotropic PML is for the frequency domain. In order to find the time domain equations for the PML, we must modify the PML equations. We derive the equations for the case where the absorption is along the  $z$  direction. The matrix term  $[\Lambda]$  is written as

$$[\Lambda] = \begin{pmatrix} a & 0 & 0 \\ 0 & a & 0 \\ 0 & 0 & 1/a \end{pmatrix} \quad (19)$$

where we specify  $a = \alpha + \sigma/j\omega = (\sigma + j\omega\alpha)/j\omega$  with  $\alpha$  and  $\sigma$  being values which we choose. The constitutive relations for  $\vec{B}$  and  $\vec{E}$  leads to

$$\begin{aligned}
 j\omega B_x &= \mu_0(\sigma + j\omega\alpha)H_x \\
 j\omega B_y &= \mu_0(\sigma + j\omega\alpha)H_y \\
 (\sigma + j\omega\alpha)B_z &= j\omega\mu_0H_z \\
 j\omega D_x &= \epsilon_0(\sigma + j\omega\alpha)E_x \\
 j\omega D_y &= \epsilon_0(\sigma + j\omega\alpha)E_y \\
 (\sigma + j\omega\alpha)D_z &= j\omega\epsilon_0E_z
 \end{aligned} \tag{20}$$

$$\begin{aligned}
 j\omega D_x &= \epsilon_0(\sigma + j\omega\alpha)E_x \\
 j\omega D_y &= \epsilon_0(\sigma + j\omega\alpha)E_y \\
 (\sigma + j\omega\alpha)D_z &= j\omega\epsilon_0E_z
 \end{aligned} \tag{21}$$

Substituting (20) and (21) into the frequency domain form of Maxwell's equations and then transforming to the time domain produces the following eight scalar equations:

$$\frac{\partial H_x}{\partial t} + \frac{\sigma}{\alpha}H_x = \frac{1}{\alpha\mu_0} \left( \frac{\partial E_y}{\partial z} - \frac{\partial E_z}{\partial y} \right) \tag{22}$$

$$\frac{\partial H_y}{\partial t} + \frac{\sigma}{\alpha}H_y = \frac{1}{\alpha\mu_0} \left( \frac{\partial E_z}{\partial x} - \frac{\partial E_x}{\partial z} \right) \tag{23}$$

$$\frac{\partial B_z}{\partial t} = \frac{\partial E_x}{\partial z} - \frac{\partial E_z}{\partial y} \tag{24}$$

$$\frac{\partial B_z}{\partial t} + \frac{\sigma}{\alpha}B_z = \frac{\mu_0}{\alpha} \frac{\partial H_z}{\partial t} \tag{25}$$

$$\frac{\partial E_x}{\partial t} + \frac{\sigma}{\alpha}E_x = \frac{1}{\alpha\epsilon_0} \left( \frac{\partial H_z}{\partial y} - \frac{\partial H_y}{\partial z} \right) \tag{26}$$

$$\frac{\partial E_y}{\partial t} + \frac{\sigma}{\alpha}E_y = \frac{1}{\alpha\epsilon_0} \left( \frac{\partial H_x}{\partial z} - \frac{\partial H_z}{\partial x} \right) \tag{27}$$

$$\frac{\partial D_z}{\partial t} + D_z = \frac{\partial H_y}{\partial x} - \frac{\partial H_x}{\partial y} \tag{28}$$

$$\frac{\partial D_z}{\partial t} + \frac{\sigma}{\alpha}D_z = \frac{\epsilon_0}{\alpha} \frac{\partial E_z}{\partial t} \tag{29}$$

The application of the PML to FVTD requires some modification of the original FVTD equations. Equation (5) is only for lossless media. Also, the variables are not

well-suited for the PML region. A more suitable set of FVTD equations are

$$\frac{\partial \vec{U}}{\partial t} + [A]\vec{U} + \frac{\partial \vec{F}_x}{\partial x} + \frac{\partial \vec{F}_y}{\partial y} + \frac{\partial \vec{F}_z}{\partial z} = 0 \quad (30)$$

where

$$\vec{U} = [E_x, E_y, D_z, H_x, H_y, B_z]^T \quad (31)$$

$$\vec{F}_x = [0, -H_z/(\epsilon_0\alpha), H_x/, 0, E_z/(\mu_0\alpha), -E_y]^T \quad (32)$$

$$\vec{F}_y = [H_z/(\epsilon_0\alpha), 0, -H_x, -E_z/(\mu_0\alpha), 0, E_x]^T \quad (33)$$

$$\vec{F}_z = [-H_y/(\epsilon_0\alpha), H_x/(\epsilon_0\alpha), 0, E_y/(\mu_0\alpha), -E_x/(\mu_0\alpha), 0]^T \quad (34)$$

and the matrix  $[A]$  is given by

$$\begin{pmatrix} \sigma/\alpha & 0 & 0 & 0 & 0 & 0 \\ 0 & \sigma/\alpha & 0 & 0 & 0 & 0 \\ 0 & 0 & 0 & 0 & 0 & 0 \\ 0 & 0 & 0 & \sigma/\alpha & 0 & 0 \\ 0 & 0 & 0 & 0 & \sigma/\alpha & 0 \\ 0 & 0 & 0 & 0 & 0 & 0 \end{pmatrix} \quad (35)$$

The above equation (30) in conjunction with (25) and (29) forms the basic FVTD equations for the PML region with the wave being absorbed in the z direction. Similar equations can be derived to absorb the wave in the x and y directions.

#### IV.. References

- [1] R. Holland and J. W. Williams, "Total-field versus scattered field finite-difference codes: A comparative assessment," *IEEE Trans. Nucl. Sci.*, Vol. NS-30, pp. 4583-4588, 1983.
- [2] J. P. Berenger, "A perfectly matched layer for the absorption of electromagnetic waves," *J. Comp. Physics*, Vol. 114, pp. 185-200, October, 1994.

- [3] W. C. Chew and W. H. Weedon, "A 3D perfectly matched medium from modified Maxwell's equations with stretched coordinates," *Microwave and Optical Technology Letters*, pp. 599-604, September, 1994.
- [4] R. Mittra and U. Pekel, "A new look at the perfectly matched layer (PML) concept for the reflectionless absorption of electromagnetic waves," *Microwave and Guided Wave Letters*, Vol. 5, pp. 84-86, March, 1995.
- [5] C. M. Rappaport, "Perfectly matched absorbing boundary conditions based on anisotropic lossy mapping of space," *Microwave and Guided Wave Letters*, Vol. 5, pp. 90-92, March, 1995.
- [6] Z. S. Sacks, D. M. Kingsland, R. Lee, and J. F. Lee, "A perfectly matched anisotropic absorber for use as an absorbing boundary condition," *IEEE Trans. Antennas Propagat.*, AP-43, pp. 1460-1463, Dec. 1995.
- [7] M. Gribbons, S. K. Lee, and A. C. Cangellaris, "Modification of Berenger's perfectly matched layer for the absorption of electromagnetic waves in layered media," *Proc. of 11th Annual Review of Progress in Applied Computational Electromagnetics*, Vol. 1, pp. 498-503, March, 1995.
- [8] D. Gaitonde and J. Shang, "High-order finite-volume schemes in wave propagation phenomena," 27th AIAA Plasmadynamics and Lasers Conference, New Orleans, June 1996.
- [9] B. Van Leer, "Flux-vector splitting for the Euler Equations." *Lecture Notes in Physics*, No. 170, pp. 507, 1982.
- [10] J. S. Shang and D. Gaitonde, "Characteristic-based, time-dependent Maxwell equations solvers on a general curvilinear frame," *AIAA J.*, vol. 33, pp. 491, 1995.

# DEVELOP AN EXPLOSIVE SIMULATED TESTING APPARATUS FOR IMPACT PHYSICS RESEARCH AT WRIGHT LABORATORY

Junghsen Lieh  
Associate Professor  
Mechanical & Materials Engineering

Wright State University  
3640 Colonel Glenn Highway  
Dayton, Ohio 45435

Final Report for:  
Summer Faculty Research Program  
Wright Laboratory

Sponsored by:  
Air Force Office of Scientific Research  
Bolling Air Force Base, DC

and

Wright Laboratory

September 1997

# DEVELOP AN EXPLOSIVE SIMULATED TESTING APPARATUS FOR IMPACT PHYSICS RESEARCH AT WRIGHT LABORATORY

Junghsen Lieh  
Associate Professor  
Mechanical & Materials Engineering  
Wright State University

## Abstract

The research task is intended to develop a simulated process that may be used to test different materials for resistance to failure from internal explosions. Theoretical derivations and analyses were made of the design of the test device. The equation for the stress intensity of multiple bar impact theory was evolved. The formula for reflective and transmitted stress intensity on varied areas for the impact was also derived. Three scaled down models were used to obtain pressure data in order to analyze the feasibility of the design, which will simulate the characteristics of the larger design. Various tests were conducted at Range A (Building 22B) of Wright Laboratory. An analysis was conducted in order to develop a full-scale model that will be eventually fabricated and tested.

# DEVELOP AN EXPLOSIVE SIMULATED TESTING APPARATUS FOR IMPACT PHYSICS RESEARCH AT WRIGHT LABORATORY

Junghsen Lieh

## Introduction

The use of real explosion processes to test plates of different materials for their resistance to failure is an expensive, time consuming, and hazardous task. The idea to develop a low cost and safe testing procedure to mimic a real explosion has been recommended by Dr. Arnold Mayer of Wright Laboratory. The purpose of this idea is to test plates of different materials for their resistance to failure when subjected to internal explosion. A good example to resist failure is the wing of an airplane to make up the fuel cell. To test the materials, a system is necessary which utilizes a cylindrical pressure tank. The tank will be filled with water, with a plunger in one end, and the test plate mounted on the opposite end. A stress pulse can be created by a projectile pressurized and released through a gun barrel that transmits the impulse to the water by striking the plunger in the cylinder.

As a preliminary step in this continuing project, three scaled-down devices were created to verify the feasibility of the full-scale test machine. The scaled-down devices were simplified, for it is only necessary to attain design parameters, not to test plates. The devices are composed of: 1) One piston and one projectile per test, 2) Three cylinders each with 0.5", 0.75" and 1.0" diameter bore, respectively, and 3) Two pressure transducers. These three cylinders were completely similar with exception of the internal diameter, or bore diameter. Three separate bore dimensions are necessary in order to study the effects of a smaller bullet striking larger plungers. Each cylinder configuration has a piston of the same diameter as its internal bore (i.e., 1/2", 3/4", and 1"). The pressure transducers were mounted in holes at the end and the side of each cylinder. The cylinder, bullets and pistons were all fabricated from carbon steel. The pressure transducers were purchased from Kistler.

A number of tests were conducted in the summer, ranging from low to medium projectile speeds, and from small pistons to large pistons at various helium pressures. Test data were analyzed and used for tuning the next tests. The results from the tests are to be utilized as the design criteria of the full-size impact machine.

## **Methodology**

Figures 1 and 2 illustrate the testing system and the scaled-down cylinders. Each bored cylinder contains two mounting holes for pressure transducers (one on the sidewall and the other at the end), and two water holes on the top. Two types of pressure sensors from Kistler were used, one with a rated pressure of 15,000 psi and the other 70,000 psi. A transducer may require a high-insulation-resistance, a low-noise signal cable, a charge amplifier operating CHARGE mode. The system was connected to a Kontron data acquisition unit. A high-speed CCD camera and a VCR were used to record the impact between the bullet and plunger. Two different mounting schemes were recommended in Kistler's operation manual (see Figure 3). For real explosions where high-speed particles may be created, **Recess Mounting** should be utilized. In the earlier tests, the cylinders were fabricated based on this arrangement. **Flush Mounting** was later recommended due to the fact that there were no particles generated in the water during testing. All three cylinders were later modified based on the Flush Mount requirements (see Figure 4).

The setup procedure for each test includes the following steps:

1. Mount and align the cylinder on the supporting structures,
2. Measure and record the dimension and weight of bullet and plunger,
3. Insert two-third length of plunger into the cylinder,
4. Insert the bullet into the gun barrel until it reaches the front end,
5. Fill the water using the top holes into the cylinder until overflow,
6. Use set screws to cover and seal both water holes,
7. Connect the pressure transducers to the charge amplifier and check the setup,
8. Open the helium valve on the supply line of gun barrel,
9. Setup the high-speed camera on the PLAY mode,
10. Evacuate personnel to control room and close the security door,
11. Set the helium pressure to a desired value,
12. Setup the Kontron parameters: sampling times, channels, lasers, voltage levels, offsets, etc.,
13. Turn the security key, arm the system and shot the gun,
14. Calculate the bullet speed using  $v = \Delta L / \Delta t$ , where  $\Delta L$  is the distance of two lasers, and  $\Delta t$  is the measured time between the lasers,
15. Zoom and examine the time history of each transducer channel and record the pressure data.



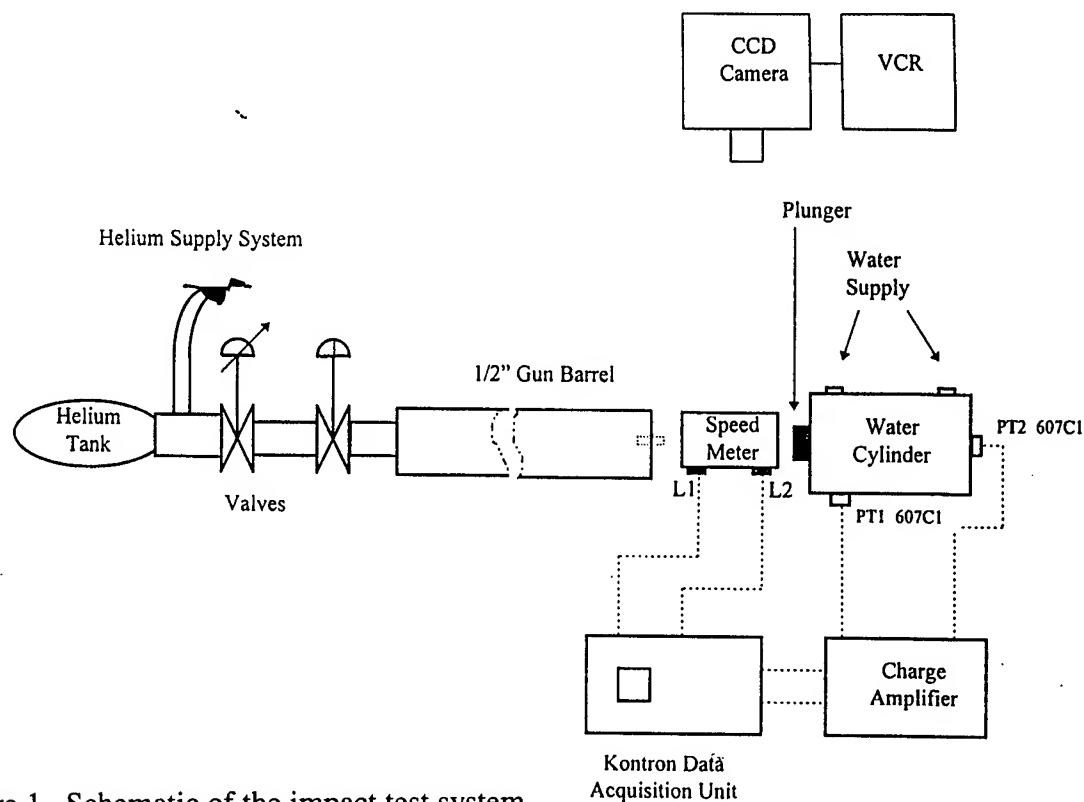


Figure 1. Schematic of the impact test system.

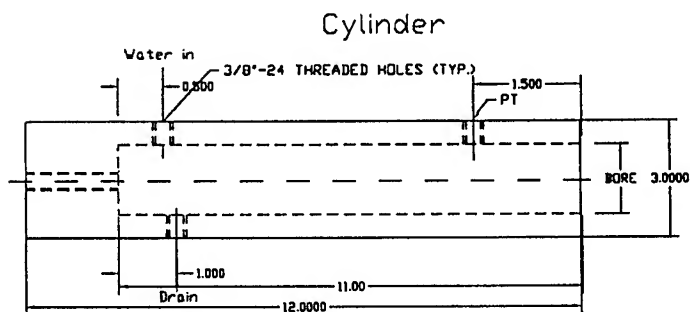


Figure 2. Original design of water cylinders.

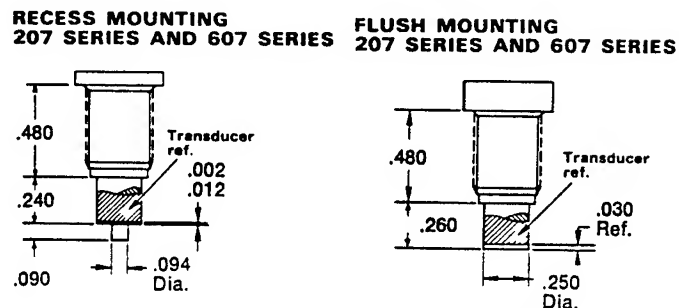


Figure 3. Pressure transducer mountings.

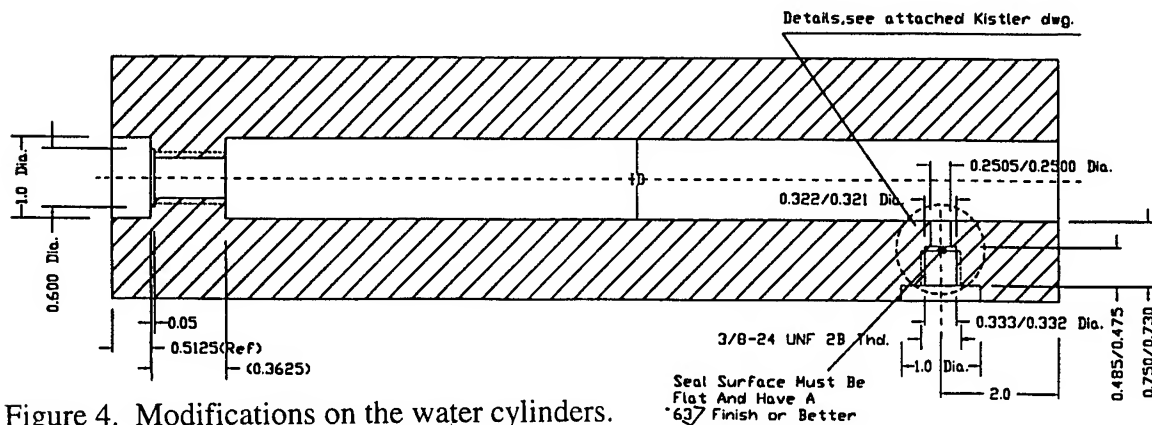


Figure 4. Modifications on the water cylinders.

## Calculation of Cylinder Stresses

Denote the outer and inner radii as  $r_o$  and  $r_i$ , and the internal pressure as  $p_i$ , the radial and tangential stresses may be expressed as follows [1]:

$$\sigma_t = \frac{r_i^2 p_i}{r_o^2 - r_i^2} \left( 1 + \frac{r_o^2}{r^2} \right) \quad (1)$$

$$\sigma_r = \frac{r_i^2 p_i}{r_o^2 - r_i^2} \left( 1 - \frac{r_o^2}{r^2} \right) \quad (2)$$

Since both have maximum values at the inner surface, by substituting  $r = r_i$  yields the maximum radial and tangential stresses as shown in Table 1.

**Table 1. Max. tangential and radial stresses of the scaled-down cylinder models, ( $p_i = 10,000$ psi,  $r_o = 1.5''$ ), material yield strength  $\sigma_y = 32,000$  psi.**

Stresses $r_i$ (Bore)	Tangential Stress (psi), $\sigma_t$	Radial Stress (psi), $\sigma_r$
0.250	10,570	-10,000
0.375	11,333	-10,000
0.500	12,500	-10,000

For a regular carbon steel with  $S_y = 32,000$  psi, the above design is quite safe. For a small outer diameter (say  $d_o = 2.5''$ ), the tangential stress will become 11,330, 13,270, 16,670 psi, respectively, with a safety factor of nearly 2.

## Impact Theory

From the measured explosion data, the water pressure generated in the cylinder should rise up to 10,000 psi within 10  $\mu$ sec and drops to 500 psi within 100  $\mu$ sec. The theory used to obtain the conclusions of this section are an extension of theory derived about elementary one-dimensional elastic stress waves in long uniform bars due to impact [2,3]. The assumptions acquired narrow the scope of analysis to the coaxial collision of four bars of identical cross-sectional area but unequal impedance: an example of energy and momentum transmission. For the report, the initial assumptions were used:

- Identical cross-sectional area but unequal impedance ( $\rho_o c$ )
- Constrained with the condition that  $l_1/c_1 = l_2/c_2 = l_3/c_3 = T$  (where  $l$  = length of a bar, and  $c$  = speed of the longitudinal stress wave in the material)

Figures 5(a) and (b) show the stress and speed situation at time  $t=0$  and  $t=T$ . The compressive force and hence stress at the interface between the first and second bar during the period  $0 < t < T$  is the same in both bars. Denote the initial velocity of bar 1 is  $v_o$ , the following are the stresses at each interval. In period 1,  $0 < t < T$ :

$$\sigma_1 = \rho_1 c_1 (v_o - v_2) \quad (3)$$

$$\sigma_2 = \rho_2 c_2 v_2 \quad (4)$$

where both stresses are assumed to be the same, i.e.,  $\sigma_1 = \sigma_2$ .  $v_2$  is the particle speed in the second bar when supporting the stress  $\sigma_2$ . Hence,

$$v_2 = \frac{\rho_1 c_1}{\rho_1 c_1 + \rho_2 c_2} v_o \quad (5)$$

and

$$\sigma_2 = \sigma_1 = \frac{\rho_1 c_1 \rho_2 c_2}{\rho_1 c_1 + \rho_2 c_2} v_o \quad (6)$$

The head of the stress wave in each of the first and second bars reaches the end of the bar opposite to that at which impact took place, at the same instant and after time  $T$ . In period 2,  $T < t < 2T$ :

(i) The compressive wave in the first bar reflected from its free end after  $t=T$ , as an unloading wave of tension; the first bar is completely stress free at  $t=2T$ . But each particle of the bar will have a speed to the left, see Figure 5(c), of

$$v_2 - (v_o - v_2) = 2v_2 - v_o = (\rho_1 c_1 - \rho_2 c_2) v_o / (\rho_1 c_1 + \rho_2 c_2) \quad (7)$$

(ii) Because the stress at the interface between the second and third bars is the same and if  $v_3$  denotes the particle speed in the third bar when stressed to the level  $\sigma_3$

$$\sigma_2' = \rho_2 c_2 (v_2 - v_3) \quad (8)$$

$$\sigma_3 = \rho_3 c_3 v_3 \quad (9)$$

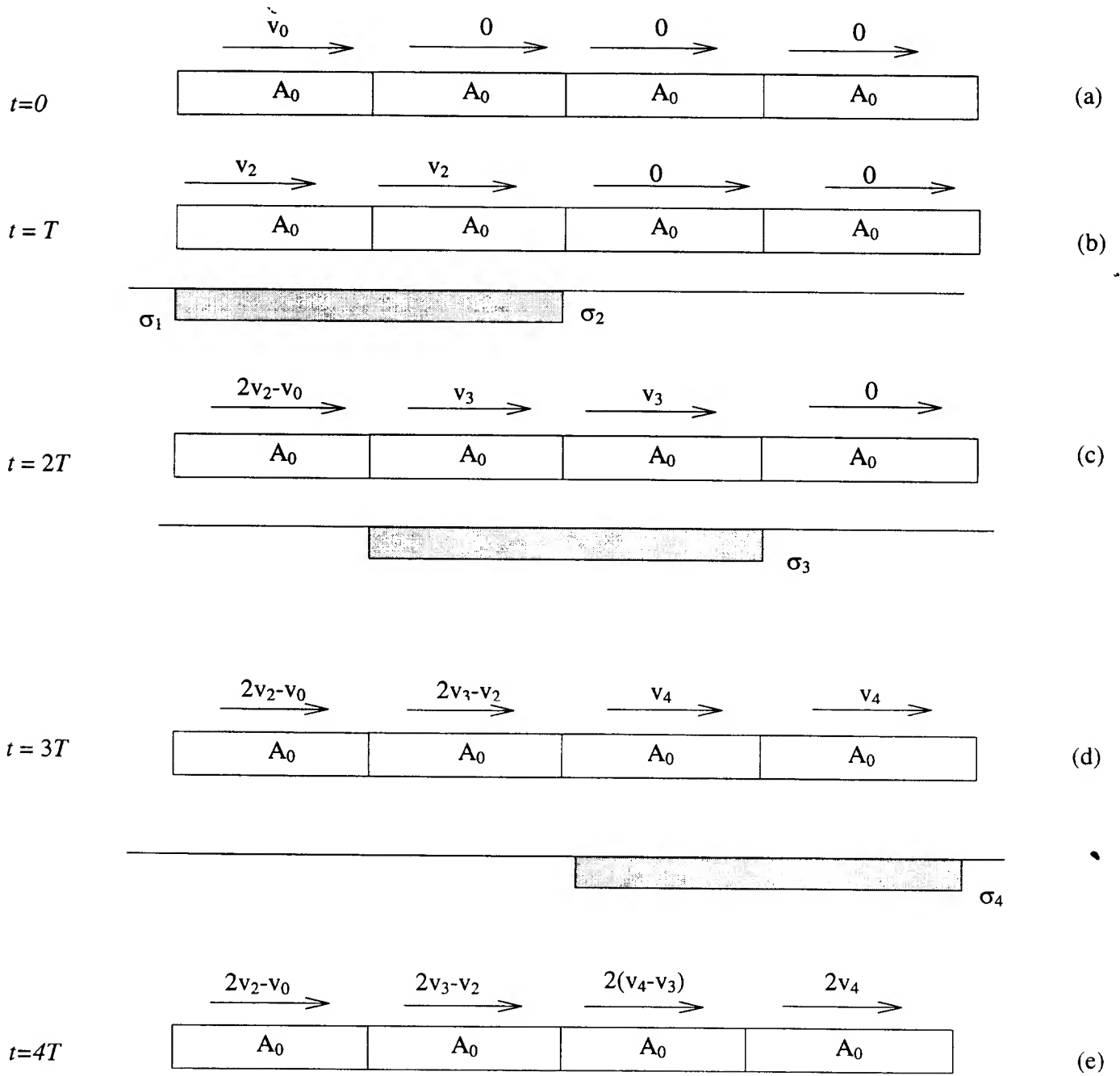


Figure 5. 4-bar impact diagram.

$$\sigma_3 = \sigma_2 + \sigma_2' \quad (10)$$

$$\begin{aligned} v_3 &= \frac{2\rho_2 c_2}{\rho_2 c_2 + \rho_3 c_3} v_2 \\ &= \frac{2\rho_1 c_1 \rho_2 c_2}{(\rho_1 c_1 + \rho_2 c_2)(\rho_2 c_2 + \rho_3 c_3)} v_o \end{aligned} \quad (11)$$

$$\sigma_3 = \frac{2\rho_1 c_1 \rho_2 c_2 \rho_3 c_3}{(\rho_1 c_1 + \rho_2 c_2)(\rho_2 c_2 + \rho_3 c_3)} v_o \quad (12)$$

The above 3-bar theory can be easily extended to obtain 4-bar equations, i.e. for the period  $2T < t < 3T$ , the wave from bar 3 reaches the interface of bars 3 and 4. Bar 4 will get a speed  $v_4$ , and a stress acting on the surface between bars 3 and 4 is

$$\sigma_3' = \rho_3 c_3 (v_3 - v_4) \quad (13)$$

$$\sigma_4 = \rho_4 c_4 v_4 \quad (14)$$

But  $\sigma_4 = \sigma_3 + \sigma_3'$  therefore,

$$v_4 = \frac{2\rho_3 c_3}{\rho_3 c_3 + \rho_4 c_4} v_3 = \frac{4\rho_1 c_1 \rho_2 c_2 \rho_3 c_3}{(\rho_1 c_1 + \rho_2 c_2)(\rho_2 c_2 + \rho_3 c_3)(\rho_3 c_3 + \rho_4 c_4)} v_o \quad (15)$$

$$\sigma_4 = \frac{4\rho_1 c_1 \rho_2 c_2 \rho_3 c_3 \rho_4 c_4}{(\rho_1 c_1 + \rho_2 c_2)(\rho_2 c_2 + \rho_3 c_3)(\rho_3 c_3 + \rho_4 c_4)} v_o \quad (16)$$

### Stress Transmission in Varied Cross Sections

Use an approach concerning longitudinal wave propagation and consider the momentum to acquire a relationship between stress and area (see Figure 6).

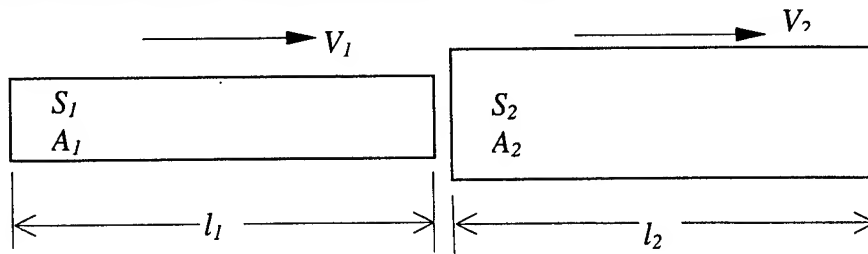


Figure 6. Bar  $S_1$  and  $S_2$  coaxial impact ( $A_1 \neq A_2$ ,  $v_1 > v_2$ ).

Let  $u_0$  be the speed common to both bars after  $S_1$  and  $S_2$  coaxial impact. The force acting on both bars at the common interface is the same. Denote  $\sigma_1$  and  $\sigma_2$  the stresses generated, then

$$A_1 \sigma_1 = A_2 \sigma_2 \quad (17)$$

and

$$A_1 \rho_1 c_1 (v_1 - u_0) = A_2 \rho_2 c_2 (u_0 - v_2) \quad (18)$$

It yields

$$u_0 = \frac{v_2 + \frac{A_1 \rho_1 c_1}{A_2 \rho_2 c_2} v_1}{1 + \frac{A_1 \rho_1 c_1}{A_2 \rho_2 c_2}} \quad (19)$$

It is now straightforward to calculate  $\sigma_1$  and  $\sigma_2$  resulting in

$$\sigma_1 = \frac{\rho_1 c_1 v_1}{1 + \frac{A_1 \rho_1 c_1}{A_2 \rho_2 c_2}} \left[ 1 - \frac{v_2}{v_1} \right] \quad (20)$$

and

$$\sigma_2 = \frac{\rho_2 c_2 v_2}{1 + \frac{A_1 \rho_1 c_1}{A_2 \rho_2 c_2}} \left[ \frac{v_1}{v_2} - 1 \right] \frac{A_1 \rho_1 c_1}{A_2 \rho_2 c_2} \quad (21)$$

Assume  $\rho_1 c_1 = \rho_2 c_2 = \rho c$ , and define the area ratio as  $\mu = A_1/A_2$ , then

$$u_0 = \frac{v_2 + \mu v_1}{1 + \mu} \quad (22)$$

If the starting speed of bar  $S_2$  is zero (i.e.,  $v_2 = 0$ ),

$$u_0 = \frac{\mu}{1 + \mu} v_1 \quad (23)$$

then,

$$\sigma_1 = \rho c v_1 \frac{1}{1 + \mu} \quad (24)$$

$$\sigma_2 = \rho c v_1 \frac{\mu}{1 + \mu} \quad (25)$$

Now consider an incident elastic wave of compressive stress of intensity  $\sigma_1$  moving to the right (See Figure 7), through a stationary bar of material  $S_1$  of cross-sectional area  $A_1$ . The stress is partially transmitted and partially reflected at the surface of discontinuity  $AB$  where the second

bar of material  $S_2$  and cross-sectional area  $A_2$  is perfectly attached to  $S_1$ . Note that if  $A_2$  were zero the wave would be wholly reflected while if  $S_1$  and  $S_2$  were identical the wave would be wholly transmitted. Since  $S_1$  and  $S_2$  are of different areas and materials, then, at  $AB$ , the incident wave must be both reflected and transmitted.

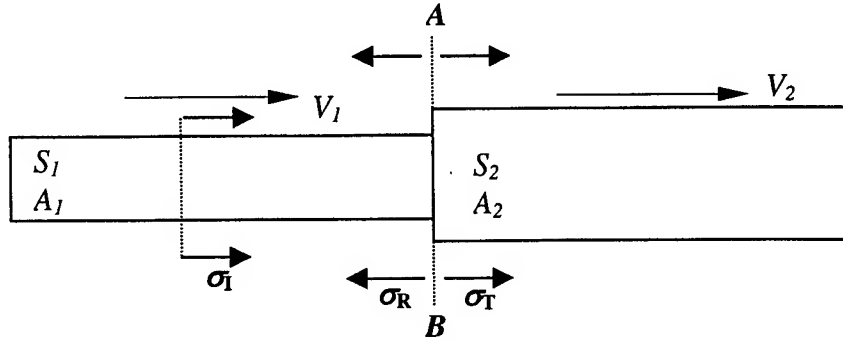


Figure 7. The relationship of  $\sigma_I$ ,  $\sigma_T$ , and  $\sigma_R$  in elastic wave transmission.

The transmitted stress wave intensity through  $S_2$  is defined as  $\sigma_T$ , and that reflected back through  $S_1$  is  $\sigma_R$ . With  $\sigma_0 = \rho_0 c_L v_0$ , it may be found that the conditions to be satisfied at  $AB$  are: (1) The force on plane  $AB$  acting on  $S_1$  and  $S_2$  are at all the time equal; (2) The particle velocity in plane  $AB$ , in the material, for  $S_1$  and  $S_2$  are equal. If both  $\sigma_R$  and  $\sigma_T$  are taken to be compressive then

$$A_1(\sigma_I + \sigma_R) = A_2\sigma_T \quad (26)$$

Noting that  $\sigma_I$  and  $\sigma_R$  are associated with waves traveling in opposite directions, therefore,

$$v_I - v_R = v_T \quad \text{or} \quad \rho_1 c_1 (\sigma_I - \sigma_R) = \rho_2 c_2 \sigma_T \quad (27)$$

in which  $v$  denotes the particle speed and subscripts  $I$ ,  $R$  and  $T$  refer to the incidence, reflection and transmission, respectively. Hence,

$$\sigma_R = \frac{A_2 \rho_2 c_2 - A_1 \rho_1 c_1}{A_2 \rho_2 c_2 + A_1 \rho_1 c_1} \sigma_I \quad (28)$$

$$\sigma_T = \frac{2A_1 \rho_2 c_2}{A_2 \rho_2 c_2 + A_1 \rho_1 c_1} \sigma_I \quad (29)$$

In case same material is used, i.e.,  $\rho_1 = \rho_2$  and  $c_1 = c_2$ , the transmitted and reflective stresses may be simplified as

$$\sigma_R = \frac{1 - \mu}{1 + \mu} \sigma_I = \frac{A_2 - A_1}{A_2 + A_1} \sigma_I \quad (30)$$

$$\sigma_T = \frac{2\mu}{1+\mu} \sigma_I = \frac{2A_1}{A_2 + A_1} \sigma_I \quad (31)$$

## Empirical Data and Calculations

The data collected during testing at Wright-Patterson Range A are listed in full in the Appendix. The comparisons that follow show the relationships necessary to verify the feasibility of the full-scale test device. A tabulation of data acquired to show velocity relationships of the bullets to pressure is shown in the Appendix. These relationships were necessary to determine which pressures were required for the tests.

The data acquired from the tests are compared to theoretical calculations from the theory section in the Table 2 that follow. Figures 8, 9, and 10 show a graphical representation of the data.

**Table 2. Comparison between empirical and theoretical data.**

(a) 0.5" BULLET - 0.5" PISTON,					(b) 0.5" BULLET - 0.75" PISTON,					(c) 0.5" BULLET - 1.0" PISTON				
test date	bullet (ft/s)	measured $\sigma$ (psi)	calculated $\sigma$ (psi)	error (%)	test date	bullet (ft/s)	measured $\sigma$ (psi)	calculated $\sigma$ (psi)	error (%)	test date	bullet (ft/s)	measured $\sigma$ (psi)	calculated $\sigma$ (psi)	error (%)
7/23/97	182	10360	10926	5	7/24/97	182	7600	7285	4	8/21/97	183	18235	5492	232
7/23/97	190	9180	11446	20	7/24/97	191	7680	7666	0	8/21/97	182	6909	5479	26
7/23/97	186	10480	11176	6	8/19/97	183	12960	7325	77	8/21/97	177	0	5324	100
7/24/97	267	18622	16069	16	8/19/97	220	12640	8822	43	8/21/97	188	6644	5654	17
7/24/97	193	13200	11590	14	8/19/97	202	17600	8120	117	8/22/97	190	6112	5724	7
7/24/97	183	9000	10994	18	8/19/97	180	20320	7238	181	8/22/97	170	10365	5118	103
8/20/97	180	13356	10799	24	8/20/97	185	11362	7427	53	8/22/97	171	11693	5137	128
8/20/97	186	16340	11184	46	8/20/97	182	11760	7284	61					
8/20/97	189	14113	11373	24	8/20/97	211	14352	8477	69					
8/20/97	153	9048	9192	2	8/20/97	197	0	7904	100					
8/21/97	168	13330	10116	32										

Although some of the data were erratic due to the defective pressure transducers (15,000psi), it seems that the desired criteria can be reached. More tests will be needed in order to design a full-scaled model.



## CONCLUSIONS AND SUGGESTIONS

A number of tests were conducted, ranging from low to medium high helium pressures, and from small to large plungers. The objective was intended to verify the impact theories, and to use the data as the design criteria for a full-scale cylinder model. Although the data acquired does not completely compare evenly with the theoretical calculations, a trend can be shown that follows the theory. The large discrepancy is partially due to the defective pressure transducers. It is also possible that the calibration and other technical errors within the data acquisition setup could cause this difference. Environmental factors and air in the water along with differences in the consistency of the other materials also add to error. In order to reduce the amount of air in the sensor area it is suggested that the sensor be mounted flush. A mobile support is also recommended, as to allow the placement of the sensors be changed to deal with the problem of air near the sensors. With all problems set aside, the full-scale project should proceed with the calculations provided from the scaling section. It is shown that all criteria are satisfied and the project is feasible. In summary, the following improvements are needed for accurate results:

- (1) All pressure transducers used in the study should be calibrated to avoid uncertainties.
- (2) A low-pass filter should be installed to eliminate unnecessary noise (see Appendix D).
- (3) The Kontron acquisition unit should be calibrated (or upgraded) to prevent potential bias.
- (4) A careful setup procedure is needed to avoid human errors that may induce testing errors. Typical example is the contamination in the transducer body and connectors.
- (5) More tests are needed after the above conditions being corrected. The design of a full-scale model may include the parameters for pressure rise and decay time.

## References

1. Shigley JE and Mischke CR, Mechanical Engineering Design, 5th Edition, McGraw-Hill, New York, 1989.
2. Meyers M, Dynamic Behavior of Materials, John Wiley & Sons, New York, 1994.
3. Johnson W, Impact Strength of Materials, Edward Arnold Ltd., London, 1972.

# VELOCITY VS. STRESS 0.5" BULLET - 0.5" PISTON

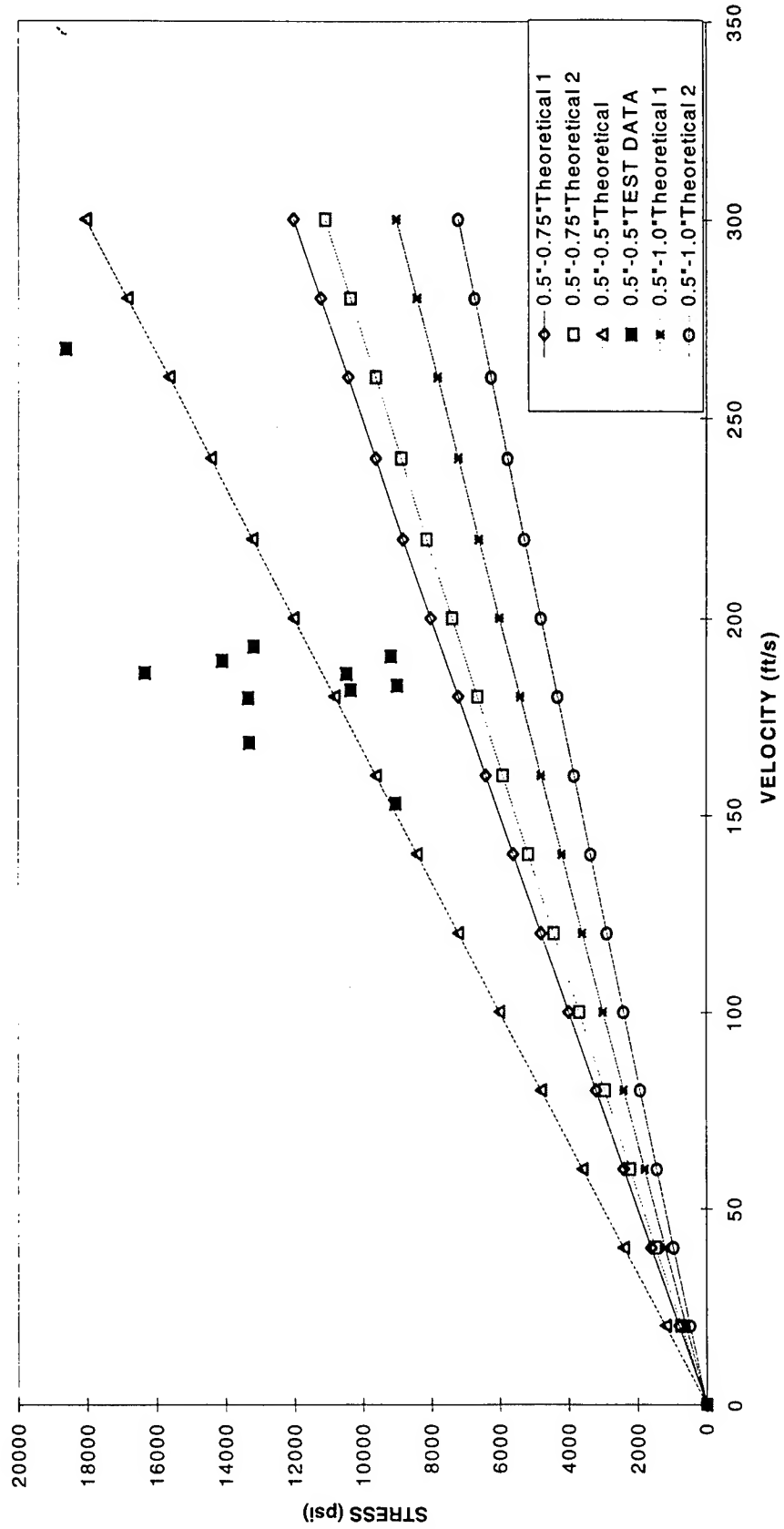


Figure 8. Comparison between empirical and theoretical data for 0.5"-0.5" impact.

# VELOCITY VS. STRESS 0.5" BULLET - 0.75" PISTON

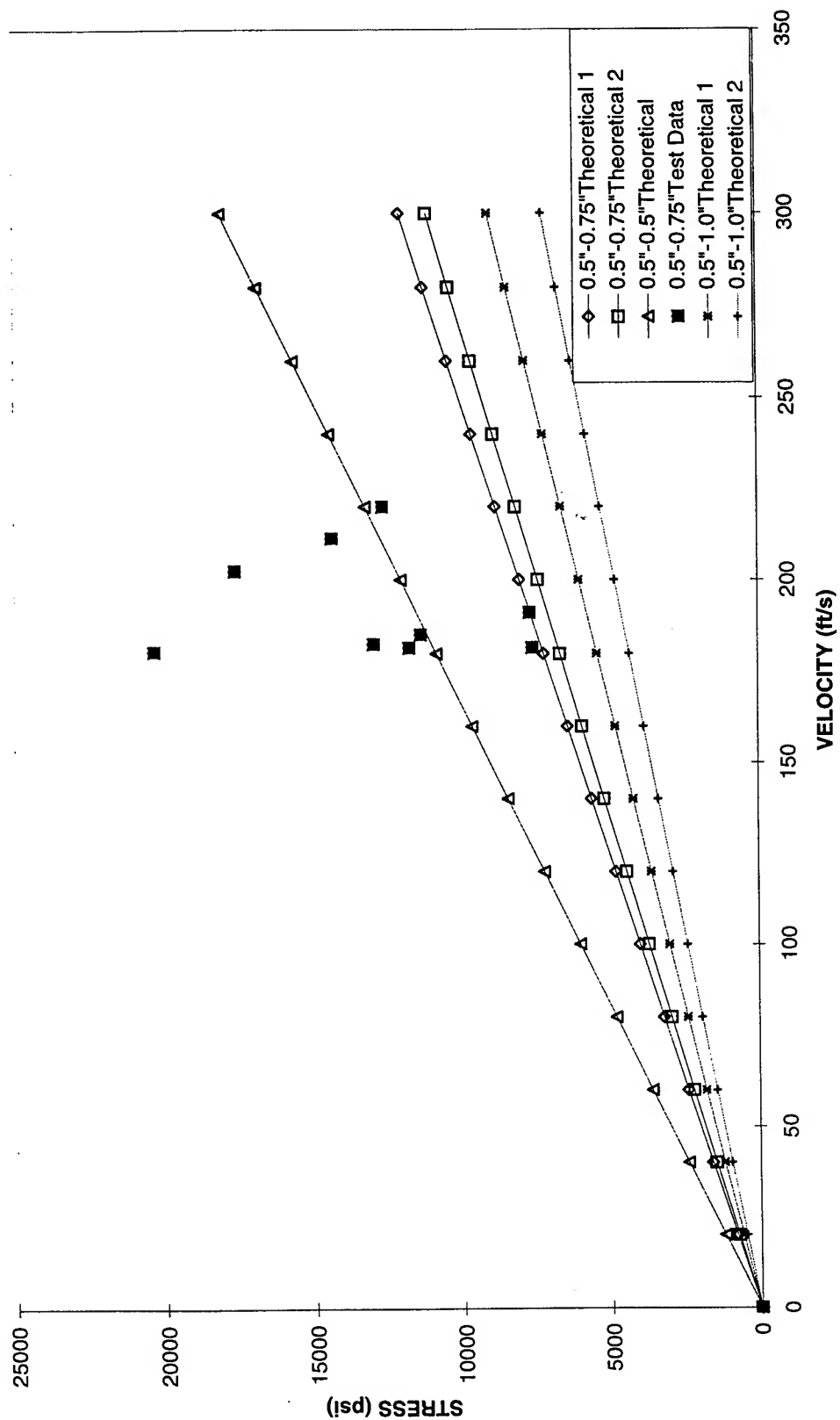


Figure 9. Comparison between empirical and theoretical data for 0.5"-0.75" impact.

# VELOCITY VS. STRESS 0.5" BULLET - 1.0" PISTON

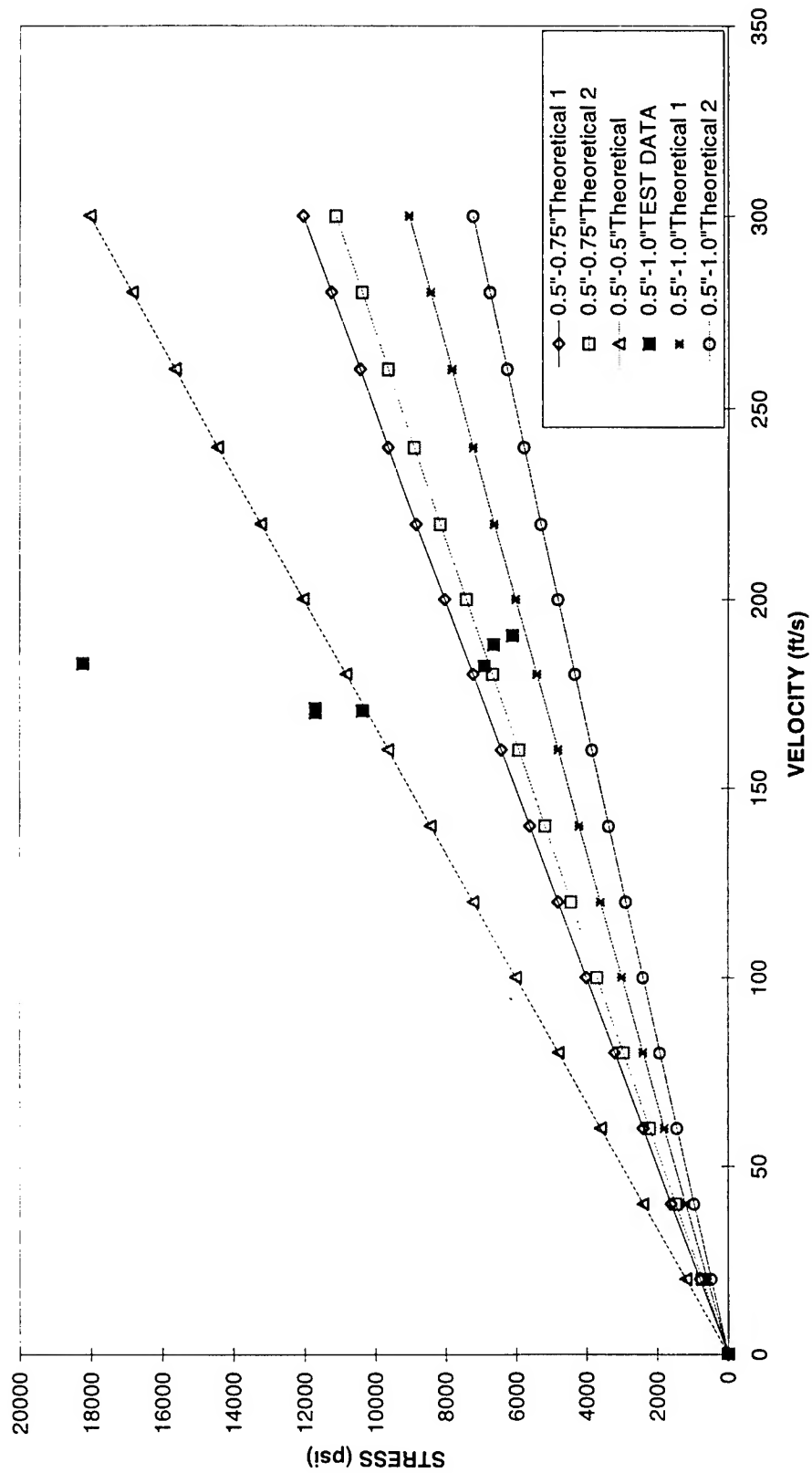


Figure 10. Comparison between empirical and theoretical data for 0.5"-1.0" impact.

# Appendix A: Actual Testing Data

## ACTUAL DATA

test date	test no.	BULLET		PISTON		L (in)	mass (g)	dia.(in)	L (in)	mass (g)	B/P area ratio	pressure	1_2 v(ft/s)	1_2 TIME(ms)	Actual Stress in Water	
		dia.(in)	L (in)	mass (g)	dia.(in)										P.T. 1 (psi)	P.T. 2 (psi)
7/23/97	1	0.5	1.011	25.35	0.5	1	25	1	1	25	1	50.4	181.611	0.001606	10360	
7/23/97	2	0.5	1.015	25.45	0.5	1	25	1	1	25	1	50.2	190.259	0.001533	9180	
7/23/97	3	0.5	1.022	25.65	0.5	1	25	1	1	25	1	50.6	185.775	0.00157	10480	
7/24/97	1	0.5	1.512	38	0.5						1	125.8	267.094	0.001092	18622	
7/24/97	2	0.5	1.015	25.49	0.5						1	50.4	192.646	0.001514	13200	11000
7/24/97	3	0.5	1.02	25.6	0.5						1	50.1	182.749	0.001596	9000	15040
7/24/97	4	0.5	1.05	25.06	0.75	1.501	84.66				2.25	50.4	181.633	0.001606	7600	17741
7/24/97	5	0.5	1	24.84	0.75	1.526	85				2.25	60.2	191.131	0.001526	7680	
8/19/97	1	0.5	0.997	24.84	0.75	1.504	85				2.25	50.2	182.646	0.001597	12960	
8/19/97	2	0.5	0.998	24.99	0.75	1.525	85.13				2.25	70.4	219.96	0.001326	12640	
8/19/97	3	0.5	0.997	24.91	0.75	1.499	84.81				2.25	60.2	202.462	0.001441	17600	
8/19/97	4	0.5	1.005	25.27	0.75	1.506	85.23				2.25	70	180.476	0.001616	20320	
8/20/97	1	0.5	1	24.94	0.75	1.498	84.86				2.25	50.8	185.185	0.001575	11362	
8/20/97	2	0.5	1	24.99	0.75	1.498	84.86				2.25	50.2	181.622	0.001606	11760	
8/20/97	3	0.5	0.998	24.93	0.75	1.498	84.86				2.25	60.2	211.353	0.00138	14352	
8/20/97	4	0.5	0.998	24.94	0.75	1.499	84.85				2.25	60.2	197.072	0.00148		
8/20/97	5	0.5	0.995	24.95	0.5	1.5	37.52				1	50.8	179.5		13356	
8/20/97	6	0.5	1.002	25.09	0.5	1.499	37.54				1	50.2	185.9		16340	
8/20/97	7	0.5	1	25.03	0.5	1.504	37.55				1	50.3	189.038	0.001543	14113	
8/20/97	8	0.5	1.504	37.55	0.5	1.504	37.55				1	50.8	152.785	0.001909	9048	
8/21/97	1	0.5	1	25	0.5	1.5	37.58				1	50	168.146	0.001735	13330	
8/21/97	2	0.5	1	25	1	1.5	150.8				4	50.1	182.577	0.001598	18235	
8/21/97	3	0.5	1	25.02	1	1.504	151				4	50.4	182.15		6909	
8/21/97	4	0.5	1	25.28	1	1.5	150.77				4	50	177			
8/21/97	5	0.5	1	24.97	1	1.5	150.45				4	50.3	187.978	0.001552	6644	
8/22/97	1	0.5	1	25	1	1.5	150.8				4	50.5	190.296	0.001533	6112	
8/22/97	2	0.5	1.496	37.5	1	1.497	150.79				4	60.3	170.153	0.001714	10365	
8/22/97	3	0.5	1.497	37.49	1	1.5	150.17				4	60.3	170.775	0.001708	11693	
8/22/97	4	0.5	1.5	37.5	1	1.5	150.17				4	60.2	169.7		11690	

## Appendix B: Theoretical Data

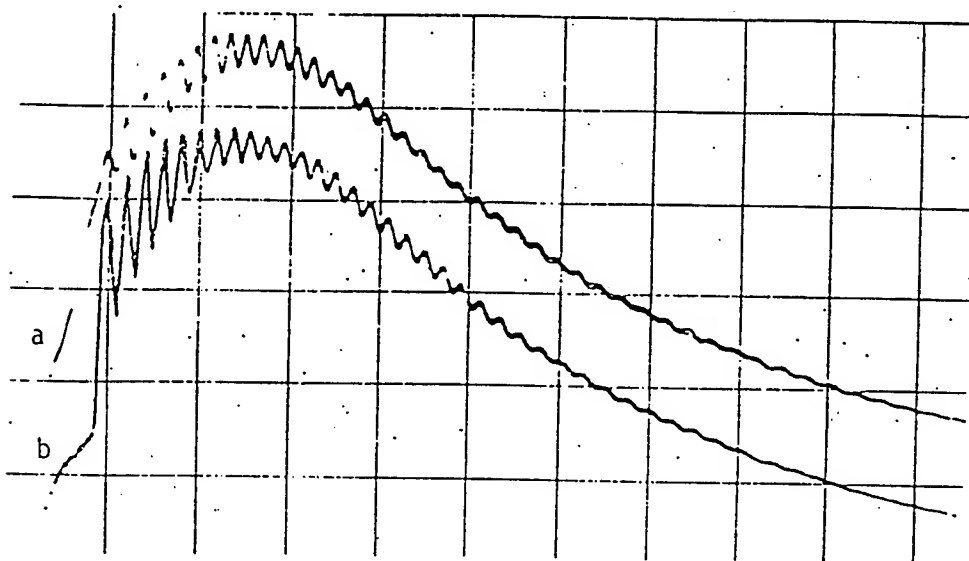
### THEORETICAL DATA

test date	test no.	AREA REL			Stress in wa error (psi) percentage	time for wave to travel		1l of bullet	1l of piston barrel pressure (psi)		A1	A2
		momentum p (g ft/S)	stress in water (psi)	M. Meyers ftn		1l of water	2l of water					
7/23/97	1	4603.829	10925.91892	10925.91892	10925.919	5.1796	0.0001711	0.00034228	4.9852E-06	4.93E-06	51.5	0.19635
7/23/97	2	4842.085	11446.20077	11446.20077	11446.201	19.79872	0.0001711	0.00034228	5.0049E-06	4.93E-06	119.4	0.19635
7/23/97	3	4765.127	11176.44954	11176.44954	11176.45	6.23140238	0.0001711	0.00034228	5.0394E-06	4.93E-06		0.19635
7/24/97	1	10149.57	16068.70493	16068.70493	16068.705	15.88986	0.0001711	0.00034228	7.4556E-06	0		0.19635
7/24/97	2	4910.557	11589.8453	11589.8453	11589.845	13.89281	0.0001711	0.00034228	5.0049E-06	0		0.19635
7/24/97	3	4678.363	10994.37706	10994.37706	10994.377	18.13997	0.0001711	0.00034228	5.0296E-06	0		0.19635
7/24/97	4	4551.729	7284.85315	6724.479831	10927.28	4.326056	0.0001711	0.00034228	5.1775E-06	7.4E-06	45.25	0.19635
7/24/97	5	4747.706	7665.804186	7076.126941	11498.706	0.185184	0.0001711	0.00034228	4.931E-06	7.52E-06		0.19635
8/19/97	1	4536.915	7325.453809	6761.957362	10988.181	76.91737	0.0001711	0.00034228	4.9162E-06	7.42E-06		0.19635
8/19/97	2	5496.795	8822.034078	8143.416072	13233.051	43.27761	0.0001711	0.00034228	4.9211E-06	7.52E-06		0.19635
8/19/97	3	5043.327	8120.239614	7495.605798	12180.359	116.7424	0.0001711	0.00034228	4.9162E-06	7.39E-06		0.19635
8/19/97	4	4560.619	7238.4241	6681.622246	10857.636	180.7241	0.0001711	0.00034228	4.9556E-06	7.43E-06		0.19635
8/20/97	1	4618.519	7427.3125	6855.980769	11140.969	52.97593	0.0001711	0.00034228	4.931E-06	7.39E-06		0.19635
8/20/97	2	4538.732	7284.399519	6724.061095	10926.599	61.4409	0.0001711	0.00034228	4.931E-06	7.39E-06		0.19635
8/20/97	3	5269.022	8476.824049	7824.760661	12715.236	69.30869	0.0001711	0.00034228	4.9211E-06	7.39E-06		0.19635
8/20/97	4	4914.977	7904.065667	7296.060616	11856.099	100	0.0001711	0.00034228	4.9211E-06	7.39E-06		0.19635
8/20/97	5	4478.525	10798.94101	10798.94101	10798.941	23.67879	0.0001711	0.00034228	4.9063E-06	7.4E-06		0.19635
8/20/97	6	4664.231	11183.97289	11183.97289	11183.973	46.10193	0.0001711	0.00034228	4.9408E-06	7.39E-06		0.19635
8/20/97	7	4731.62	11372.75636	11372.75636	11372.756	24.09481	0.0001711	0.00034228	4.931E-06	7.42E-06		0.19635
8/20/97	8	5737.079	9191.736921	9191.736921	9191.7369	1.563762	0.0001711	0.00034228	7.4162E-06	7.42E-06		0.19635
8/21/97	1	4203.659	10115.89172	10115.89172	10115.892	31.77286	0.0001711	0.00034228	4.931E-06	7.4E-06		0.19635
8/21/97	2	4564.424	5492.026849	4393.621479	10984.054	232.0268	0.0001711	0.00034228	4.931E-06	7.4E-06		0.19635
8/21/97	3	4557.393	5479.184136	4383.347309	10958.368	26.09542	0.0001711	0.00034228	4.931E-06	7.42E-06		0.19635
8/21/97	4	4474.56	5324.268966	4259.415173	10648.538	100	0.0001711	0.00034228	4.931E-06	7.4E-06		0.19635
8/21/97	5	4693.811	5654.494	4523.5952	11308.988	17.49946	0.0001711	0.00034228	4.931E-06	7.4E-06		0.19635
8/22/97	1	4757.4	5724.220585	4579.376468	11448.441	6.774362	0.0001711	0.00034228	4.931E-06	7.4E-06		0.19635
8/22/97	2	6380.751	5118.317577	4094.654061	10236.635	102.508	0.0001711	0.00034228	7.3767E-06	7.38E-06		0.19635
8/22/97	3	6402.356	5137.017911	4109.614329	10274.036	127.6223	0.0001711	0.00034228	7.3817E-06	7.4E-06		0.19635
8/22/97	4	6363.75	5104.680472	4083.744377	10209.361	129.0055	0.0001711	0.00034228	7.3964E-06	7.4E-06		0.19635

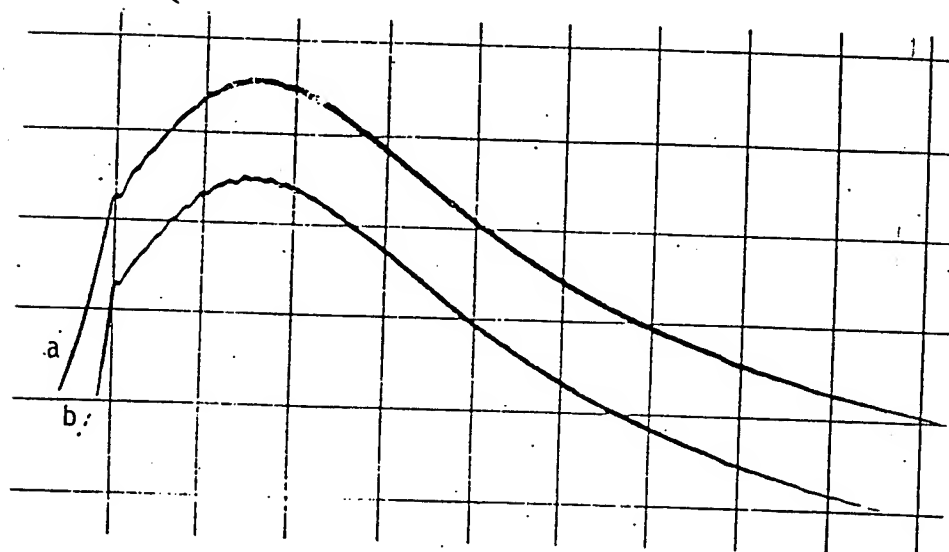
## Appendix C: Material data

material	C (in/s)	$\rho$ (lbm/in <sup>3</sup> )
steel	202800	0.28
water	55510.8	0.0361
aluminum	200400	0.096

**Appendix D. Testing data without and with a low-pass filter.**



Unfiltered Ballistic Pressure-Signal Waveforms.



Filtered Ballistic Pressure-Signal Waveforms

**DISTORTION COMPENSATION AND ELIMINATION  
IN HOLOGRAPHIC RECONSTRUCTION.**

James S. Marsh  
Professor  
Department of Physics

The University of West Florida  
Pensacola, FL 32514

Final Report for:  
Summer Faculty Research Program  
Wright Laboratory  
Eglin AFB

Sponsored by:  
Air Force Office of Scientific Research  
Bolling Air Force Base, DC

and

Wright Laboratory  
Eglin AFB

August, 1997



**DISTORTION COMPENSATION AND ELIMINATION IN  
HOLOGRAPHIC RECONSTRUCTION**

James S. Marsh  
Professor  
Department of Physics  
The University of West Florida

**ABSTRACT.**

I discuss the quantitative location of objects from holographic images when the reconstruction wavelength differs from the recording wavelength. The holographic image equations are interpreted in a way that clarifies the meaning of stereo pairs of holographic images and indicates how back projection methods can be used in holography to locate objects. Alternate methods involving the production of distortion free regions in the holographic image field during reconstruction, the use of self calibrating objects in the object field during recording, and triangulation, can be used to locate objects.

## 1. INTRODUCTION.

The quantitative location of objects from the positions of their holographic images turns out to be unexpectedly complex, unless the holographic reconstruction is made under ideal conditions. By ideal conditions we mean that the reconstruction wavelength is the same as the recording wavelength, and the reconstruction beam is in the same position as the recording beam. In this case the optical position of the image coincides with the position of the object, and aberrations inherent in the process of holographic reconstruction are eliminated.

If circumstances require reconstruction under non-ideal conditions, especially if the reconstruction wavelength must differ from the recording wavelength, relating the optical position of the image to the position of the object in a quantitative way becomes more difficult. In general they do not coincide. For a given object position, the image position depends on the ratio of reconstruction wavelength to recording wavelength, on the position of the reconstruction beam relative to the recording beam, and on the piece of the hologram through which the image is observed.

We refer to the piece of the hologram through which the image is observed as the pupil. The difference in position between the image and the object we call distortion.

The distortions inherent in holographic reconstructions under non-ideal conditions are well described by the holographic image equations, which have been known for thirty years<sup>1-4</sup>. Distortion fields calculated using these equations agree well with what we see when examining, for example, large format (18" diameter) cylindrical holograms recorded at 694 nm and reconstructed at 632 nm. We can distinguish several different phenomena in the distortion fields, such as non-linear distortion, shearing of the image field, magnification, etc. Because of the pupil dependence of the image position, the appearance of the distortion field will depend on the placement of the eye when viewing visually or the camera when recording the holographic image. We need to understand each of these phenomena in a simple physical way if we are to exploit or eliminate them on the optical table or, failing that, compensate for them on the computer.

In a simple object field containing few particles, it is in principal straightforward to optically measure the positions of the

holographic images and then, noting the location of the pupil for each image as well as the location of the reference and reconstruction beam relative to each pupil, to locate the corresponding objects from the image equations. However in a complicated object field containing many particles, such as a debris field, it is impractical to measure the positions of images individually. Rather more wholesale methods such as stereo pairs or back projections analogous to CAT scan methods are required<sup>5-7</sup>. If, for example, you make a stereo pair of photographs of a given image, the two views of the image will be through different pupils of the hologram. The shifting pupils cause the position of the image itself to shift, relative to the hologram. What then does the stereographic location of the image mean, and what is the relationship between this stereographically located image position and the position of the object? In back projection and CAT scan methods, which use bundles of rays from a variety of viewpoints, the questions of interpretation are similar.

In the first part of this paper we will develop a simple physical interpretation of what the holographic image equations are saying. It turns out that determining an object position from the position of its holographic image, under non-ideal conditions, is similar to determining the position of a fish swimming in a bowl by looking at the fish through the sides of the bowl. The fish bowl model gives us a conceptual model of holographic reconstruction that allows discussion, in simple terms, of the issues involved in compensating for the distortions inherent in holographic reconstruction. This picture allows us to see what the stereo pairs or back projections of images mean and shows us how to use them to locate the object positions. It shows us how to interpret holographic interferograms reconstructed at a wavelength different from the recording wavelength. And it shows us how to interpret the additional distortions that arise if the surface of the hologram is deformed at reconstruction.

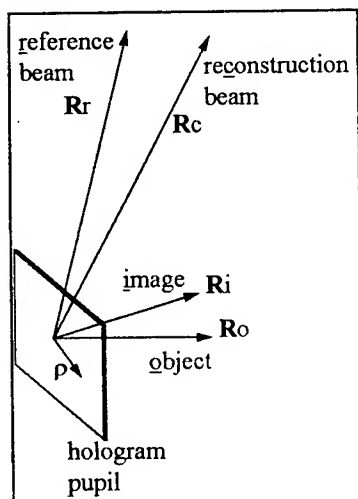
In the second part of the paper we discuss some alternate methods that can be used to eliminate or compensate for distortions. These involve the production of distortion free regions in the holographic image field during reconstruction, the use of self calibrating objects in the object field during recording, and triangulation of image points with fiducial image points.

Our discussion will mostly be framed in terms of cylindrical

holograms, which is the context in which this work was done<sup>11</sup>. However, our conclusions will be applicable to any kind of hologram reconstructed with monochromatic light.

## 2. IMAGE EQUATIONS.

For our application to cylindrical holograms we need to use the non-paraxial image equations as formulated by Champagne in his non-paraxial aberration theory of holograms<sup>8</sup> and refined by Rebordao<sup>9</sup> and Peng and Frankena<sup>10</sup>. This allows the reference and reconstruction beams to be far from the axis of the hologram. The reference beam and reconstruction beam are assumed to be spherical waves emanating from particular points.



Relative to the center of a pupil in the hologram, we let  $\mathbf{R}_r$  be the vector that points to the point of origin of the reference beam,  $\mathbf{R}_c$  points to the origin of the reconstruction beam,  $\mathbf{R}_o$  points to the object, assumed to be a point, and  $\mathbf{R}_i$  points to the corresponding holographic image, as in figure 1. We let  $R_j = |\mathbf{R}_j|$  be the magnitude of  $\mathbf{R}_j$  and  $\mathbf{u}_j = \mathbf{R}_j/R_j$  be the unit vector in the direction of  $\mathbf{R}_j$  for  $j=r, c, o$ , or  $i$ .

Letting  $\mu = \lambda/\lambda_0$ , where  $\lambda_0$  is the recording

**Figure 1.**  $\rho$  points to wavelength and  $\lambda$  is the reconstruction positions in the pupil (cf. appendix). wavelength, the image equations become<sup>8-10</sup>

(c.f. the appendix)

$$\frac{1}{R_i} = \frac{1}{R_c} + \mu \left( \frac{1}{R_o} - \frac{1}{R_r} \right) \quad (1)$$

and

$$\mathbf{u}_i = \mathbf{u}_c + \mu(\mathbf{u}_o - \mathbf{u}_r) \perp \quad (2)$$

The symbol  $\perp$  at the end of equation 2 means that this a relation between the components of the vectors in the plane of the hologram, or perpendicular to the hologram normal. Used to calculate  $\mathbf{u}_i$ , equation 2 gives  $\mathbf{u}_{i\perp}$ , the components of  $\mathbf{u}_i$  in the plane of the hologram, in terms of

$u_{c1}$ ,  $u_{o1}$ , and  $u_{r1}$ . The fact that  $u_i$  is a unit vector determines the component of  $u_i$  normal to the plane of the hologram. Equation 2 is a cleverly disguised form of the diffraction equations.

Rewriting these in a way to emphasize the connection between the object and the corresponding image, we have

$$\frac{1}{R_i} = \frac{\mu}{R_o} + \Delta \quad (1')$$

and

$$u_i = \mu u_o + v|_1 \quad (2')$$

where

$$\Delta = \frac{1}{R_c} - \frac{\mu}{R_r} \quad (3)$$

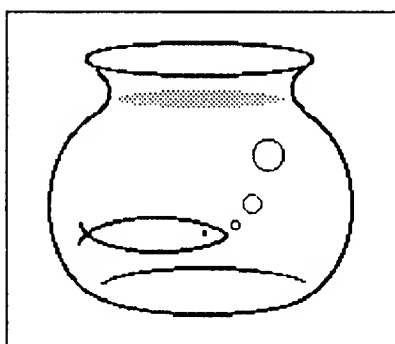
and

$$v = u_c - \mu u_r. \quad (4)$$

### 3. INTERPRETATION.

The interpretation of equation 1' is straightforward and familiar. The pupil acts as a refracting surface separating object space, where the index of refraction is  $\mu$ , from image space which has index equal to one. The relation between the object distance and image distance is given by the thin lens equation 1' with  $\Delta$  playing the role of the optical power of the surface.  $\Delta$  is adjustable by positioning of the reconstruction beam relative to the pupil.

Now we look at equation 2' without the  $v$  term,  $u_i = \mu u_o|_1$ . Given that  $u_i$  is a unit vector, we can write  $|u_{i1}| = \sin\theta_i$ , where  $\theta_i$  is the



angle  $u_i$  makes with respect to the normal to the pupil. Similarly  $|u_{o1}| = \sin\theta_o$ , where  $\theta_o$  is the angle  $u_o$  makes with respect to the pupil normal.  $u_i = \mu u_o|_1$  is Snell's law with the interpretation that the object, in its actual place in the holographic volume, sends out a ray in the direction  $-u_o$  to the pupil. The ray from the object travels in a medium with index of refraction  $\mu$ . On reaching the pupil

the ray refracts at surface of the hologram and emerges into observation space travelling in direction  $-u_1$ . In observation space the index of refraction is equal to one. For this reason we call  $\mu_0$  the refraction term in equation 2'. This is the origin of the fishbowl model.

Finally, we consider the effect of  $v$  in equation 2'. Suppose the object is on the pupil normal, so that  $u_{o1} = 0$ . Then, since  $u_1 = v|_1$ , the ray from the object is still bent at the surface of the hologram, even though there is no refraction at the surface. The ray from the object behaves like an extraordinary ray emerging from a crystalline medium. This behavior makes the image field look sheared, so we call  $v$ , or  $v_1$ , the shearing vector. The shearing vector is adjustable by adjusting the position of the reconstruction beam.

The refraction term in equation 2' is the basis of the fish bowl model of holographic reconstruction. For those portions of the hologram for which the shearing vector has been nullified or may be ignored as a first approximation, the reconstruction occurs as if the object is in its actual position within the holographic volume, but embedded in a medium with index of refraction equal to  $\mu$ . Light rays emanating from the object emerge through the surface of the hologram into air, refracted by the surface of the hologram. The emergent rays are what is observed in the reconstruction, and it is from these that the actual location of the object within the holographic volume is to be determined. To locate the object, the emergent rays must be traced back to the surface of the hologram, the pupils. The bending of the rays by refraction at the surface is taken into account, after which they may be traced back into the holographic volume to locate the object.

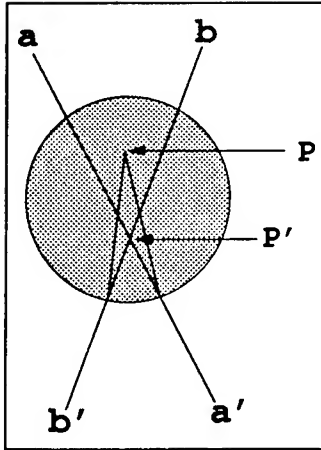


**Figure 2.** A similar construction applies to back projections.

If the effect of the shearing vector is not negligible, the additional bending of the light ray at the surface of the hologram by this term must be included before the ray can be traced back into the holographic volume to locate the object.

This is illustrated in the figure 2. In a cylindrical hologram seen from the top, two views of the image of the same object are seen along the lines  $a'a$  and  $b'b$ . If these were rays from a real object then the intersection of the lines of direction  $a'a$  and  $b'b$  would locate the object at

the point  $P'$ . However, the rays emerging from the hologram moving in the direction of  $a'$  and  $b'$  must have been considered to bent at the surface of the hologram according to equation 2'. So in tracing the rays back into the holographic volume, they intersect at the point  $P$ . This locates the object point.

In tracing these rays, it is necessary to know the position of the reference and reconstruction beams and to locate the pupil for each ray. In the next sections we explore some methods that may be used in which the dependence on some of these parameters is reduced.

#### 4. DISTORTION FREE REGIONS

The image forming equations say that for a particular object as seen through a particular pupil, it is always possible to place the reconstruction beam so that the image point and the object point coincide. That point is called distortion free. Now, since the distortion field varies smoothly, there should be a nearly distortion free region in the hologram enclosing the distortion free point. The shape and extent of the nearly distortion free region will depend on the viewing method, such as the placement of the camera used to record the image field.

In order to produce a distortion free point, equations 1' and 2' are used, under the assumption that  $R=R$ , to produce a position  $R$  for the reconstruction beam. Actually, we may distinguish two distinct forms of distortion which may be manipulated independently of each other.

The difference between  $u_i$  and  $u_o$  we call angular distortion. To nullify angular distortion, set  $u_i = u_o$  in equation 2' and solve for  $u_c$ . This determines the direction of the reconstruction beam from the pupil without determining how far away from the pupil the beam should be. If object positions are to be determined from stereograms of the image field or by back projection methods, it may simplify things if angular distortion only is nullified as much as possible over a region of the hologram, while a different criterion, such as reducing aberrations, is used to determine how far away from the pupil the reconstruction beam should be.

A simple situation is when the object point is on the pupil normal. Then  $u_o|_1 = 0$ , and the condition for nullifying angular distortion at this pupil is to choose  $v_1 = 0$ , i.e. to nullify the shearing vector for this pupil. This leads to the condition  $u_c = \mu u_r|_1$  for this pupil. To the extent that  $v_1 = 0$  for neighboring pupils, angular distortion appears only because of the refraction effect at neighboring pupils.

The difference between  $R_i$  and  $R_o$  we call radial distortion. To nullify radial distortion, set  $R_i = R_o$  in equation 1' and solve for  $R_c$ . This determines the distance of the reconstruction beam from the pupil.

If we refer to distortion free points or regions without qualifications we mean that both angular distortion and radial distortion have been eliminated or reduced at the points in question.

A calculation to test this procedure was performed and the results are shown in the figure 3. The hologram was a 10 inch diameter cylinder. The camera was at infinity below the hologram in the diagram. The recording wavelength was at 694 nm and the reconstruction wavelength was 688 nm. The recording beam was on the axis of the cylinder, 40 inches along the axis from the center of the cylinder. The distortion free point was chosen to be on axis in the middle

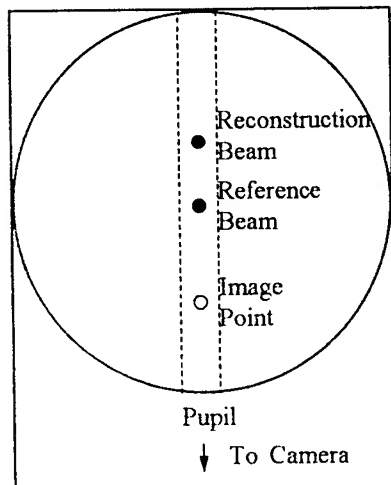


**Figure 3.** The nearly distortion free region is, roughly, the slab between the dotted lines.



of the cylinder viewed from a direction perpendicular to the axis. The reconstruction beam then had to be at 37.37 in. along the axis from the center of the cylinder and 1.83 in. off axis on the opposite side of the axis from the pupil in order to make this point distortion free.

Calculations with the image forming equations showed that the nearly distortion free region (distortion less than 1/40 inch) was a narrow slab in the hologram about an inch thick. The narrowness of the slab was probably due to increasing refraction from the curved surface as we move away from viewing along the diameter of the cylinder. This indicates that for plane holograms it may be possible to produce larger distortion free regions. However, in the cylindrical format and with this optical setup, all portions of the hologram could be sequentially brought into the distortion free region simply by rotating the hologram about its axis.

The advantage of using a distortion free region is that dependence on the pupil is reduced, and objects are where they appear to be. However a problem with distortion free regions is that, in general, placement of the reconstruction beam to achieve the effect is not the same placement that minimizes aberrations.

## **5. SELF CALIBRATING OBJECTS.**

Using the image forming equations to locate objects within the holographic volume requires location of the reference and reconstruction beams to an accuracy consistent with the required accuracy of object location. Though careful external measurements of the reference and reconstruction beam positions at recording and reconstruction times naturally suggest themselves, it would be desirable if the hologram itself could be made to yield information about these positions.

One of the schemes considered to accomplish this was a calibrating object, reintroduction of a real object into the holographic volume at reconstruction in the same location an identical object had when the hologram was made. By comparing the image location with the actual object location, some information about the locations of the reference and reconstruction beams could be obtained. However, re-introducing and registering an object, at reconstruction time, to sufficient accuracy to

its original position at recording time turned out to be impractical. Only developing and reconstructing the hologram *in situ*, in effect without moving the object at all relative to the hologram seems to offer any hope of success.

An alternative is to use a self calibrating object, which is an object such that by measuring the position of its image you can calculate where the object actually was, without using the image forming equations. This makes it unnecessary to know where the reference and reconstruction beams are in order to locate the object. However, once the object is located from the image, information about the location of the reference and reconstruction beams becomes available.

The possibility of a self calibrating object comes from the observation that if two object points are aligned with a particular pupil when the hologram is made, then the images of those points will be aligned with the same pupil at reconstruction, no matter how the reconstruction is performed. This follows from the fact that each pupil records the object field as seen from the perspective of that pupil. This also follows from the image forming equations.

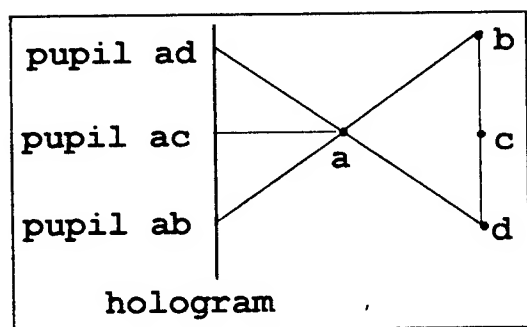


**Figure 4**

Figure 4 shows an example. Working in two dimensions for simplicity, if a triangle with points a,b,c,d is an object, and the images of points a and b line up with the pupil ab in the reconstruction, etc., then from the location of the pupils ab, ac, and ad, you can find the

unique location occupied by the triangle when the hologram was made. In three dimensions, something like a pyramidal object would do the job.

Thus, placing one or more self calibrating objects into the object field at recording time gives a permanent record in the hologram itself that relates the positions of the images of those objects to the original positions of the objects.

## 6. TRIANGULATION

The results of the last two sections may be used in a procedure to locate object points without any precise knowledge of reference and reconstruction beams. Indeed, the reconstruction beam could be placed in such a way as to satisfy some other criterion than minimum distortion, minimum aberration for example.

The idea is to locate at least two object points called fiducial points in the hologram, using points in a distortion free region or points on a self registering object, as in the previous two sections, or

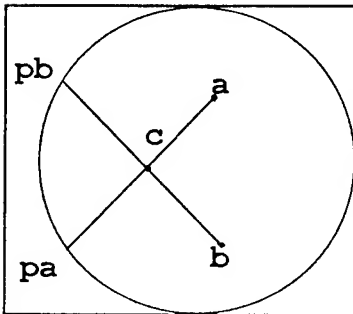


Figure 5.

by straightforward application of the image equations. Two of these fiducial points are represented by a and b in the figure 5.

A third image point c is observed and lined up with the image of point a and with the image of point b. The corresponding pupils through which these alignments are achieved, pa and pb, are noted. Since aligned images correspond to aligned objects, we know that the object point c is aligned with the object point a and the pupil pa, and with the object point b and the pupil pb. Thus the object point c may be located by triangulation.

Proceeding in this way, adding new points to the roster of fiducial points if desirable, we may ultimately locate all the object points in the hologram.

## 7. SUMMARY.

The interpretation of the image forming equations presented here allows discussion of the issues of holographic image formation in a simple qualitative way. In addition to explaining the meaning of stereographic and back projection imaging, it furnishes a framework in terms of which the effects of distortion of the hologram surface at reconstruction time can be seen.

Exploitation of a nearly distortion free region allows reconstructions which do not depend so critically on pupil locations as in the generic case. The use of self calibrating objects and triangulation methods allows reconstructions in which dependence on reference and reconstruction beam locations is eliminated.

## APPENDIX.

The notation in this paper is different from that used in the references, so this is a sketch of the derivation of the image forming equations. In the pupil of the hologram at reconstruction is the wave  $\exp(ikr_c)\exp(ik_0r_o)\exp(-ik_0r_r)$  comprising spherical waves arriving at the pupil from the reconstruction beam, object point, and reference beam.  $k$  is the wave number,  $2\pi/\lambda$ , of the reconstruction wave and  $k_0 = 2\pi/\lambda_0$  is that of the recording wave. These are supposed to be equivalent to a spherical wave  $\exp(ikr_i)$ , emanating from an image point, times an aberration wave,  $\exp(i\Delta\phi)$ . We write  $\mathbf{r}_j = \mathbf{p} - \mathbf{R}_j$ , for  $j=c, o, r$ , or  $i$ .  $\mathbf{R}_j$  points from the center of the pupil to the point source in question and  $\mathbf{p}$  indicates points in the pupil relative to the center of the pupil, as in figure 1. Then the magnitudes

$$r_j = (R_j^2 - 2\mathbf{p} \cdot \mathbf{R}_j + \rho^2)^{1/2} \approx R_j - \mathbf{p} \cdot \mathbf{u}_j + \rho^2/2R_j$$

where the unit vectors  $\mathbf{u}_j = \mathbf{R}_j/R_j$ .

We require that the phase aberration,  $\Delta\phi$ , be constant to second order in  $\rho$ . This means that  $kr_c + k_0r_o - k_0r_r \equiv k(r_c - \mu(r_o - r_r)) = kr_i + \text{const}$  to second order in  $\rho$ . Using the expansion of the  $r_j$  gives, ignoring constant terms,

$$- \mathbf{p} \cdot (\mathbf{u}_c + \mu(\mathbf{u}_o - \mathbf{u}_r)) + \frac{1}{2}\rho^2 \left( \frac{1}{R_c} + \mu \left( \frac{1}{R_o} - \frac{1}{R_r} \right) \right) = - \mathbf{p} \cdot \mathbf{u}_i + \frac{1}{2}\rho^2 \frac{1}{R_i}.$$

Equating the terms in  $\rho^2$  gives equation 1 in the text, while equating the terms in  $\rho$  gives equation 2. The fact that  $\mathbf{p}$  lies in the plane of the pupil explains why equation 2 is a relation between the components,  $\mathbf{u}_{j\perp}$ , of the  $\mathbf{u}_j$  perpendicular to the pupil normal.

## REFERENCES

1. R. W. Meier, "Magnification and third-order aberrations in holography", J. Opt. Soc. Am., **55**, 987-92, (1965)

2. R. J. Collier, C. B. Burkhardt, and L. H. Lin, *Optical Holography*, (Academic Press, New York, 1971)
3. R. R. A. Syms, *Practical Volume Holography*, (Clarendon Press, Oxford, 1990)
4. P. Hariharan, *Optical Holography, 2nd Ed.*, (Cambridge University Press, New York, 1996)
5. Anil K. Jain, *Fundamentals of Digital Image Processing*, Ch. 10, (Prentice Hall, Englewood Cliffs, NJ, 1989) Ch. 10
6. A. C. Kak, "Image Reconstruction from Projections," in M. P. Ekstrom (Ed.). *Digital Image Processing Techniques*, New York: Academic Press, 1984, pp 111-171
7. S. W. Rowland in G. T. Herman (ed.). *Image Reconstruction from Projections. Topics in Applied Physics*, vol. 32. New York: Springer-Verlag, 1979. pp. 9-79
8. E. B. Champagne, "Nonparaxial imaging, magnification and aberration properties in holography", *J. Opt. Soc. Am.* **57**, 51-5 (1967)
9. J. M. Rebordao, "General form for aberration coefficients in holography", *J. Opt. Soc. Am.* **A1**, 788-90 (1984)
10. K-O Peng and H. J. Frankena, "Nonparaxial theory of curved holograms", *Appl. Opt.* **25**, 1319-26 (1986)
11. C. Anderson, J. Gordon, E. Watts, and J. Marsh, "Measurement of behind-armor debris using cylindrical holograms", *Practical Holography IX, SPIE Proceedings*, vol **2406**, 132-146, (1995) and *Opt. Eng.* **36**(1), 40-46 (January 1997)

A MOLECULAR ORBITAL THEORY ANALYSIS OF OLIGOMERS OF 2,2'-BITHIAZOLE AND PARTIALLY  
REDUCED 3,3'-DIMETHYL-2,2'-BITHIAZOLIUM CATIONS

Mark D. McClain  
Assistant Professor of Chemistry  
Department of Science and Mathematics

Cedarville College  
P. O. Box 601  
Cedarville, OH 45314-0601

Final Report for:  
Summer Faculty Research Program  
Wright Laboratory

Sponsored by:  
Air Force Office of Scientific Research  
Bolling Air Force Base, Washington DC

and

Wright Laboratory

September 1997

A MOLECULAR ORBITAL THEORY ANALYSIS OF OLIGOMERS OF 2,2'-BITHIAZOLE AND PARTIALLY  
REDUCED 3,3'-DIMETHYL-2,2'-BITHIAZOLIUM CATIONS

Mark D. McClain  
Assistant Professor of Chemistry  
Department of Science and Mathematics  
Cedarville College

Abstract

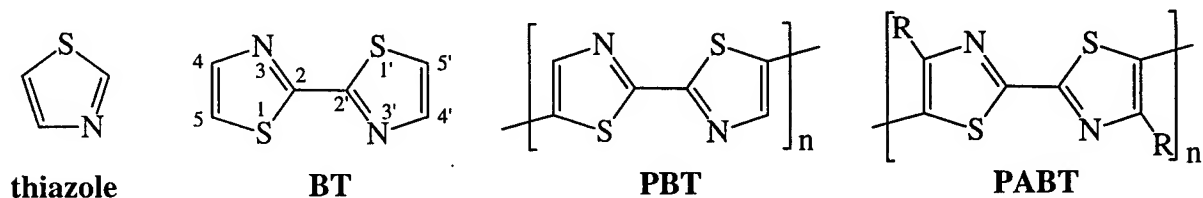
The geometry of model compounds for poly(2,2'-bithiazole) (**PBT**), poly(3,3'-dimethyl-2,2'-bithiazole) (**PMBT**), and reduced **PMBT** were optimized at the AM1 level. Electronic transitions were computed using ZINDO/S. By extrapolation, **PBT** and **PMBT** were predicted to have  $\lambda_{\text{max}}$  values of 702 and 546 nm, respectively. Fully reduced **PMBT** showed no chain length dependence as expected. Significant charge delocalization was observed for some mixed valent oligomers as evidenced by shift of  $\lambda_{\text{max}}$  into the near-IR.

# A MOLECULAR ORBITAL THEORY ANALYSIS OF OLIGOMERS OF 2,2'-BITHIAZOLE AND PARTIALLY REDUCED 3,3'-DIMETHYL-2,2'-BITHIAZOLIUM CATIONS

Mark D. McClain

## INTRODUCTION

Conjugated aromatic and heteroaromatic polymers continue to be studied in the search for low density, environmentally stable, solution processible electrical conductors. Potential uses in aircraft are for anti-static films, EMF shielding, flexible gap sealants, and lightweight wires. While thiazole and derivatives have been known for a hundred years, polymers containing 2,2'-bithiazole (BT) had only been investigated as optical brighteners<sup>1</sup> or high temperature materials<sup>2</sup> until the last several years. Fully aromatic copolymers containing bithiazole have been produced only recently via electrochemical polymerization.<sup>3,4</sup> The solubility of poly(2,2'-bithiazole-5,5'-diyl) (PBT) is poor, as is the case for other unsubstituted polyarylenes such as polythiophene. By alkyl substitution at the 4-position, well defined, thermally stable, soluble homopolymers and copolymers of 4,4'-dialkyl-2,2'-bithiazoles (PABT) were prepared by metal-catalyzed dehalogenative coupling simultaneously in the Curtis<sup>5</sup> and Yamamoto<sup>6</sup> research groups.



As an electronic "blend" of thiophene with pyridine, the thiazole ring displays interesting reactivity. PABTs are found to resist oxidation to form p-doped conductors, but rather to be reduced under mild conditions (-1.93 V vs. Ag/Ag+). N-methylation of PABT lowers the reduction potential by 0.55 V (-1.38 V vs Ag/Ag+).<sup>7</sup> Orange films of N-methylated PABT turn blue-black upon reduction (n-doping) and  $\lambda_{\text{max}}$  shifts into the near IR. Electrical conductivity of the reduced films has been estimated to be ~5 S/cm.

Small molecules can serve an important role as model compounds for understanding polymers. As part of a study of azabiaryl ligands as organic conductors, N-methylation and reduction of BT has already been investigated.<sup>8</sup> BT can



be easily methylated to form the bithiazolium salt **1BTM2** and reduced to the corresponding bithiazolinyldiene, **1BTM** (FIGURE 1). Larger analogs, however, have not been studied.

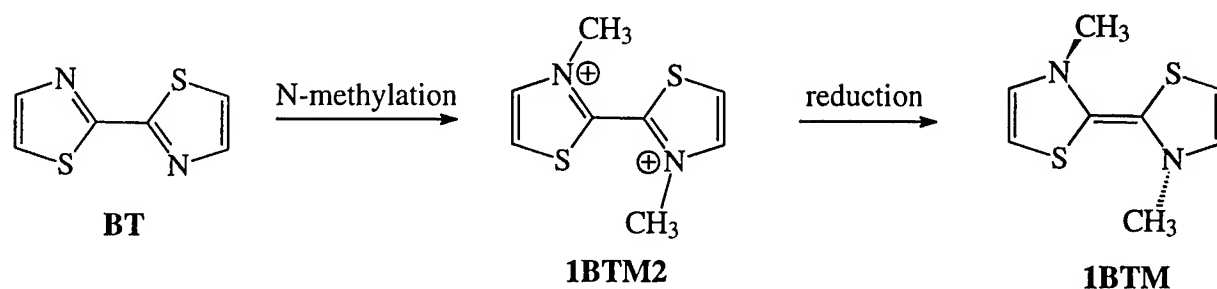
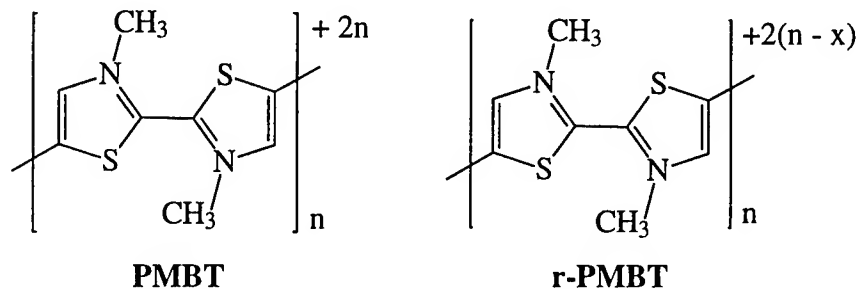


FIGURE 1: N-methylation and reduction of BT.

## PROJECT FOCUS

By using longer bithiazole oligomers ( $n = 1$  to  $7$ ), the electronic effects of conjugation could be studied. As a preliminary step, a computational study of model compounds would help refine synthetic polymer targets. The goal of this research is to calculate the expected UV-visible electronic transitions for geometry optimized model compounds of **PBT**, fully N-methylated **PBT** (**PMBT**), and reduced (partially and fully) N-methylated **PMBT** (**r-PMBT**) where  $x = 1$  to  $n$ . The change in the lowest energy transition within a given series of compounds will be used to determine which polymers should exhibit the lowest band gap.



## METHOD

Molecular coordinate files were generated with HyperChem<sup>TM9</sup>. Geometry optimizations were performed without symmetry constraints on a Silicon Graphics Power x2 workstation using GAMESS<sup>10</sup> set for the restricted closed Hartree-Fock method at the AM1 level. Electronic transitions were predicted using HyperChem<sup>TM</sup> based on a ZINDO/S single point calculation<sup>11</sup> for the optimized geometry using singly excited configuration interaction of the

fifteen highest occupied and fifteen lowest unoccupied molecular orbitals. Transitions with  $\lambda < 150$  nm or oscillator strengths  $< 0.250$  were ignored. A complete listing of calculated total energies and  $\lambda$  values can be found in

**Appendix A.** The model compounds were abbreviated according to the following convention:

**xBT**      x = number of 2,2'-bithiazole units linked at the 5 and 5' positions

**xBTMy**   x = # of 3,3'-dimethyl-2,2'-bithiazolium units linked at the 5 and 5' positions

y = net positive charge on the molecule (omitted for neutral species)

## RESULTS AND DISCUSSION

### xBT series: neutral bithiazole oligomers

Neutral **BT**<sup>12</sup> and alkyl substituted derivatives (R = methyl<sup>13</sup>, *tert*-butyl<sup>14</sup>, and nonyl<sup>14</sup>) are known to prefer the *trans*-planar geometry ( $\Theta = \sim 180^\circ$ ;  $\Theta = \text{S-C-C-S}$  torsion angle) in the solid state. This arrangement maximizes the  $\pi$ -conjugation between the rings and minimizes steric interactions between the sulfur atoms. The optimized geometry for **BT** is in good agreement with the crystallographically determined geometries (TABLE 1). A *cis* geometry ( $|\Theta| < 90^\circ$ ) is so energetically disfavored that one ring turns around to the *trans*-planar conformation during optimization.

Bond	BT	BT	Methyl BT	<i>tert</i> -butyl BT	Nonyl BT
S - C2	1.711	1.722	1.718	1.724	1.720
C2 - N	1.349	1.304	1.332	1.310	1.316
N - C4	1.376	1.377	1.395	1.382	1.378
C4 - C5	1.395	1.337	1.334	1.364	1.363
C5 - S	1.659	1.708	1.744	1.709	1.720
C2 - C2'	1.444	1.449	1.468	1.457	1.446
Ref.	this work	12	13	14	14

TABLE 1: Comparison of calculated and crystallographic bond distances for **BT** and 4,4'-dialkylated **BT**.

The longer members of the **xBT** series are made up of *trans*-planar **BT** units connected with a slight rotation ( $25^\circ$ ) out of planarity between adjacent units, resulting in a helical conformation (FIGURE 2). No crystallographic information for **xBT** ( $x \geq 2$ ) is presently known, however, one measure of the reliability of optimized geometries is the convergence of the difference in the total energy between successive oligomers (TABLE 2).



FIGURE 2: Optimized geometry for **7BT**.

x	Energy (Hartrees)	$\Delta$ Energy (Hartrees)
1	-59.6920575165	
2	-118.3775896478	-58.6855321313
3	-177.0630406381	-58.6854509903
4	-235.7484706528	-58.6854300147
5	-294.4338942798	-58.6854236270
6	-353.1193156081	-58.6854213283
7	-411.8047360015	-58.6854203934
8	-470.4901559652	-58.6854199637

TABLE 2: Convergence of total energy difference for **xBT** series.

The predicted  $\lambda_{\text{max}}$  for **1BT** (362 nm) compares very well with experimental value for 4,4'-dimethyl **BT** (356 nm).<sup>6a</sup>

The high level of planarity for **xBT** results in increasing  $\lambda_{\text{max}}$  with additional bithiazole units (FIGURE 3). This increase in conjugation length can be correlated with molecular length by plotting  $1/\lambda_{\text{max}}$  v.  $1/n$  where  $n$  = number of bithiazole units (FIGURE 4). An estimate for the electronic absorption energy of **PBT** ( $\lambda_{\text{max}}$  = 702 nm) can be extrapolated from the y-intercept (infinite chain length). An experimental study of oligomers of 4,4'-dinonyl-2,2'-bithiazole showed good correlation with a somewhat lower predicted  $\lambda_{\text{max}}$  for the polymer (536 nm).<sup>5a</sup> A well-ordered film, however, was found to have a  $\lambda_{\text{max}}$  of 618 nm.

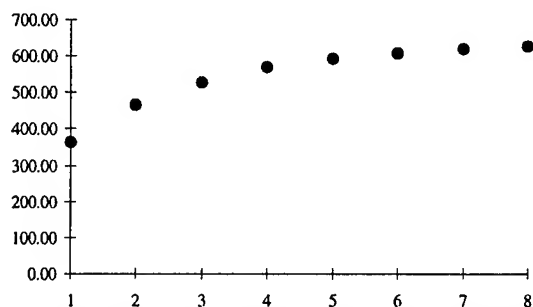


FIGURE 3: Plot of  $\lambda_{\text{max}}$  (nm) vs.  $n$  for **xBT** series.

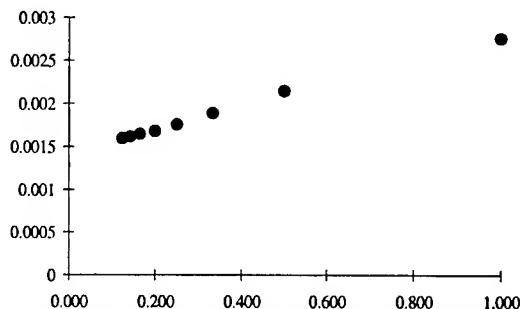


FIGURE 4: Plot of  $1/\lambda_{\text{max}}$  vs.  $1/n$  for **xBT** series.

**xBTM(2x) series: fully charged bithiazolium oligomers**

N-methylation of BT produces 1BTM2 (FIGURE 1), which has an optimized geometry in which the rings twist nearly orthogonal to each other ( $\Theta = 75^\circ$ ). This increases the separation of positive charges to reduce coulombic repulsion. The calculated  $\lambda_{\text{max}}$  (351 nm) shifts to slightly lower energy.

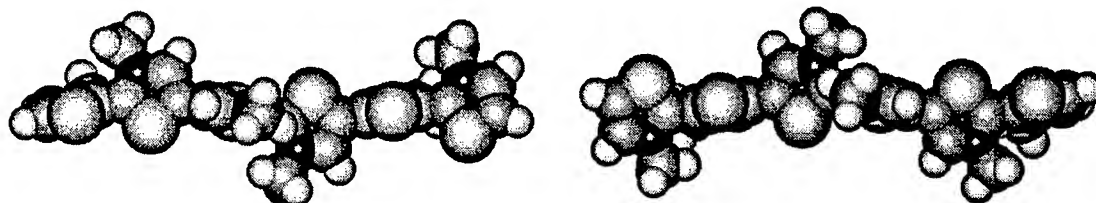


FIGURE 5: Views of 3BTM6.

As additional bithiazolium units are added in this series, an extended kinked chain is produced in which the rings of bithiazolium units are nearly orthogonal to each other ( $\Theta = 75 - 90^\circ$ ) and adjacent units are nearly orthogonal to each other ( $\Theta = 95 - 110^\circ$ ) as well. (FIGURE 5). The calculated  $\lambda_{\text{max}}$  does increase with the number of bithiazolium units, indicating some conjugation along the  $\pi$ -system. The incremental increase per additional bithiazolium unit is smaller, however, than the corresponding member of the **xBT** series. Thus, the predicted  $\lambda_{\text{max}}$  for **PMBT** is only 546 nm by extrapolation (FIGURE 6).

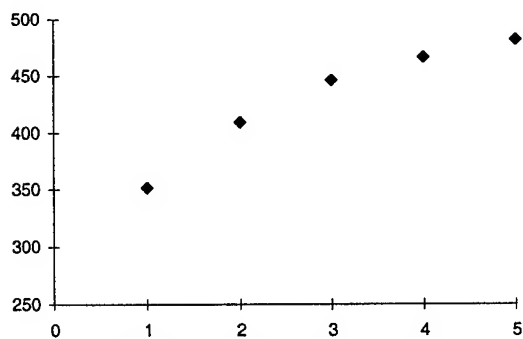


FIGURE 5: Plot of  $\lambda_{\text{max}}$  (nm) vs. n.

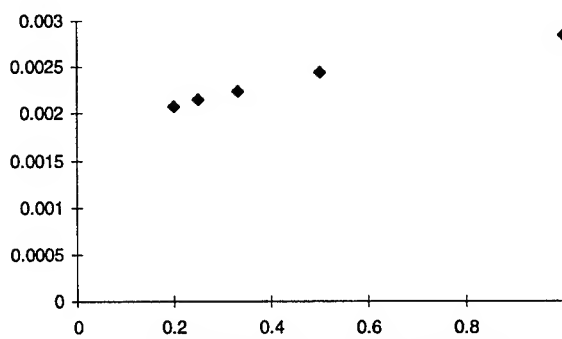


FIGURE 6: Plot of  $1/\lambda_{\text{max}}$  vs.  $1/n$ .

**xBTM series: neutral (fully reduced) bithiazolinylidene series**

Reduction of **1BTM2** by two electrons produces **1BTM** (FIGURE 1). The optimized geometry contains coplanar rings, approximately trigonal pyramidal nitrogens with *trans* methyl groups, and a short inter-ring carbon-carbon bond (1.36 Å vs. 1.45 Å for **1BTM2**). This is consistent with the valence bond description of a bithiazolinylidene. The calculated  $\lambda_{\text{max}}$  (275 nm) is quite a bit lower than for **BT** (362 nm) or **1BTM2** (351 nm) since the double bond is essentially isolated.

The higher members of this series consist of planar bithiazolinylidene units connected to adjacent units with a small S-C-C-S torsion angle ( $\Theta = \sim 40^\circ$ ) (FIGURE 7). The calculated  $\lambda_{\text{max}}$  increases greatly between **1BTM** and **2BTM**, due to conjugation *between* bithiazolinylidene units. No significant increase in  $\lambda_{\text{max}}$  with more bithiazolinylidene units is predicted (FIGURE 8), however, since the  $\text{sp}^3$  nitrogens prevent conjugation.

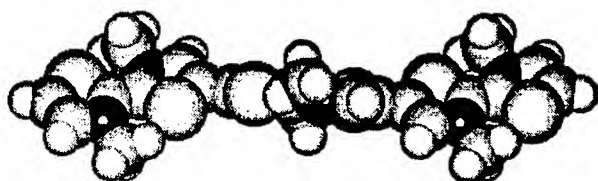


FIGURE 7: Structure of **3BTM**

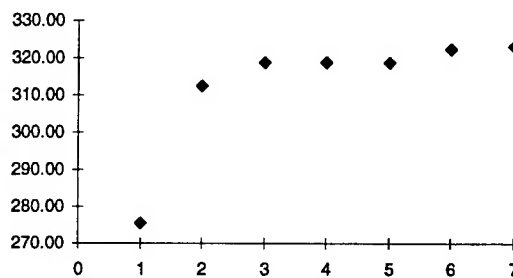


FIGURE 8: Plot of  $\lambda_{\text{max}}$  (nm) vs. n

#### **xBTMy** molecules: partially reduced oligomers

The partially reduced oligomers (and polymers) are expected to be the most interesting by analogy to “doped” or mixed valent states of other polymer systems such as polythiophene. For example, if **2BTM4** (a fully kinked structure) is reduced by two electrons, **2BTM2** is produced. A further two electron reduction would yield **2BTM** (planar bithiazolinylidene units). If the +2 charge on **2BTM2** is localized on one bithiazole unit, an asymmetric molecule would be expected with one bithiazolium unit and one bithiazolinylidene unit. The calculated structure, in fact, has the +2 charge delocalized over all four rings (FIGURE 9). The planar molecule has a *cis* linkage between two identical *trans*-bithiazole units. As expected from the conjugation of  $\pi$ -bonds over four rings, the  $\lambda_{\text{max}}$  for **2BTM2** is predicted to be 831 nm.

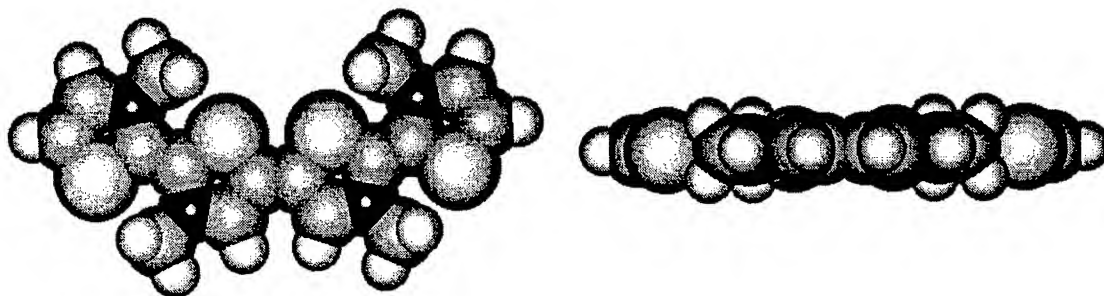


FIGURE 9: Views of planar **2BTM2**.

Some of the longer mixed valent model compounds show similar charge delocalization over several rings. **6BTM2** has the most planarity observed so far in this study (FIGURE 10), having a  $\lambda_{\text{max}}$  of 1680 nm due to charge delocalization over the central eight rings. Several structures were predicted to have relatively little charge delocalization (not more than three or four rings) over the length of the molecule. This inconsistency is under investigation.

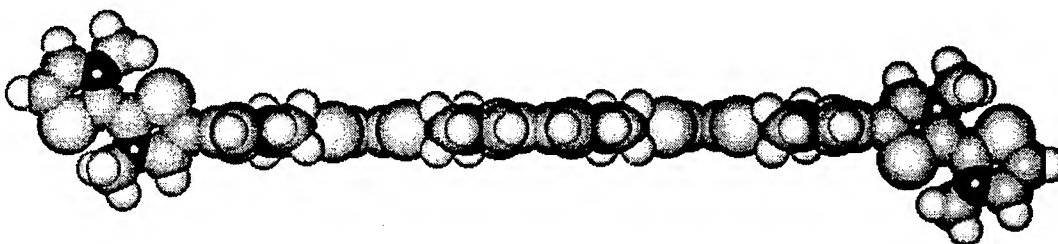


FIGURE 10: View of **6BTM2** showing planarity over most of the molecule.

## CONCLUSIONS

The geometries for several series of polymeric model compounds were optimized and electronic transitions were calculated. The internal consistency of calculations and reasonable agreement of predicted geometries with structural characterization for the model compounds studied confirmed the value of the method.

Significant charge delocalization for several of the mixed-valent compounds was predicted. The extension of the electronic absorption into the near-IR indicated that these materials are promising candidates for low band-gap materials. Further calculations are needed to more fully understand some of the mixed-valent structures, perhaps

involving a higher level of computational theory. Chemical synthesis and structural characterization of some promising molecules under study will be the focus of a Summer Research Extension Proposal.

---

<sup>1</sup> Craven, J. M. US Patent 3330811, 7-11-67.

<sup>2</sup> (a) Longone, D. T.; Un, H. H. *J. Polym. Sci., Part A* **1965**, *3*, 3117-3130. (b) Preston, J.; Black, W. B. *J. Polym. Sci., Part C* **1968**, *23(1)*, 441-448. (c) Bach, H. C. US Patent 3598768, 8-10-71. (d) Sybert, P. D. in *Encyclopedia of Polymer Science and Engineering*, J. I. Kroschwitz, Ed.; Wiley: New York, **1987**, Volume 11, 644-647. (e) Sun, W. L.; Lu, F. C. *Chin. Chem. Lett.* **1996**, *7(4)*, 313-316.

<sup>3</sup> Jenkins, I. H.; Pickup, P. G. *Macromolecules* **1993**, *26*, 4450-4456.

<sup>4</sup> Wolf, M. O.; Wrighton, M. S. *Chem. Mater.* **1994**, *6*, 1526-1533.

<sup>5</sup> (a) Nanos, J. I.; Kampf, J. W.; Curtis, M. D. *Chem. Mater.* **1995**, *7*, 2232-2234. (b) Curtis, M. D.; Nanos, J. I.; McClain, M. D. US Patent 5536808, 10-5-94. (c) Ronda, L. G.; Martin, D. C. *Macromolecules* **1997**, *30*, 1524-1526. (d) Politis, J. K.; Nanos, J.; He, Y.; Kanicki, J.; Curtis, M. D. *Mat. Res. Soc. Symp. Proc.* **1997**, *424*, 495-500.

<sup>6</sup> (a) Yamamoto, T.; Suganuma, H.; Maruyama, T.; Kubota, K. *J. Chem. Soc., Chem. Commun.* **1995**, 1613-14. (b) Yamamoto, T.; Suganuma, H.; Saitoh, Y.; Maruyama, T.; Inoue, T. *Jpn. J. Appl. Phys.* **1996**, *35*, L1142-1144. (c) Yamamoto, T.; Suganuma, H.; Maruyama, T.; Inoue, T.; Muramatsu, Y.; Arai, M.; Komarudin, D.; Ooba, N.; Tomaru, S.; Sasaki, S.; Kubota, K. *Chem. Mater.* **1997**, *9*, 1217-1225. (d) Yamamoto, R.; Marutama, H.; Suganuma, H. Jpn Patent, 09077854, 9-13-95.

<sup>7</sup> Curtis, M. D., unpublished results.

<sup>8</sup> Goulle, V.; Chirayil, S.; Thummel, R. P. *Tetrahedron. Lett.* **1990**, *31(11)*, 1539-1542.

<sup>9</sup> Hypercube, Inc. and Autodesk, Inc., 1993, Release 3 for Windows.

<sup>10</sup> General Atomic and Molecular Electronic Structure System. Schmidt, M. W., Baldrige, K. K., Boatz, J. A., Elbert, S. T., Gordon, M. S., Jensen, J. H., Koseki, S., Matsunaga, N., Nguyen, K. A., Su, S. J., Windus, T. L., Dupuis, M., Montgomery, J. A. *J. Comput. Chem.* **1993**, *14*, 1347-1363.

<sup>11</sup> ZINDO/S is an INDO quantum mechanical method which is parameterized to calculate UV-visible electronic transitions.

<sup>12</sup> Craig, D. C.; Goodwin, H. A.; Onggo, D.; Rae, A. D. *Aust. J. Chem.* **1988**, *41*, 1625-1644.

<sup>13</sup> Bolognesi, A.; Catellani, M.; Destri, S.; Porzio, W. *Acta Cryst.* **1987**, *C43*, 1171-1173.

<sup>14</sup> Curtis, M. D., unpublished results.

# APPENDIX A

## Calculated Total Energies and Electronic Transitions for Optimized Geometries

<i>n</i>	<i>Compound</i>	<i>Total energy (Hartrees)</i>	<i>λ in nm (oscillator strength)</i>
1	BT	-59.6920575165	361.7 (0.646), 189.28 (0.806)
	1BTM2	-71.5168398300	351.43 (0.432), 180.31 (0.368), 178.96 (0.498)
	1BTM	-72.1192940142	275.47 (0.395), 253.32 (0.200), 163.35 (0.332)
2	2BT	-118.3775896478	465.41 (1.533), 196.83 (0.336), 187.00 (0.409), 186.76 (0.339)
	2BTM4	-141.7469924888	409.49 (0.506), 319.07 (0.622), 187.53 (0.366), 179.31 (0.326), 175.31 (0.422), 174.90 (0.332), 174.32 (0.286), 174.05 (0.376)
	2BTM2	-142.6941439483	830.69 (1.605), 169.95 (0.275), 166.73 (0.373), 151.19 (0.359)
	2BTM	-143.2322931356	312.56 (0.782), 268.48 (0.286), 254.58 (0.250)
3	3BT	-177.0630406381	529.62 (2.266), 188.82 (0.496), 185.76 (0.688)
	3BTM6	-211.8326909159	445.71 (0.609), 357.58 (0.367), 327.70 (0.521), 310.16 (0.319), 191.09 (0.256), 178.31 (1.885), 175.27 (1.180), 155.88 (0.346)
	3BTM4	-213.0182531927	838.38 (2.186), 458.93 (0.627), 231.52 (0.329), 207.74 (0.532), 183.84 (0.307), 178.00 (0.215), 171.38 (0.208), 158.58 (0.683)
	3BTM2	-213.8309357881	979.11 (1.101), 475.92 (0.335), 280.07 (0.392)
	3BTM	-214.3453055349	319.02 (1.431), 267.40 (0.312), 153.57 (0.414)
4	4BT	-235.7484706528	570.93 (2.912), 385.88 (0.283)
	4BTM8	-281.8211101766	466.35 (0.687), 357.88 (0.859), 328.44 (0.214), 306.20 (0.618), 197.94 (0.271), 188.87 (0.507), 179.53 (0.601), 179.02 (0.640)
	4BTM6	-283.1854800991	789.93 (2.168), 440.78 (1.161), 233.44 (0.410), 211.95 (0.325), 202.33 (0.456), 183.92 (0.741)
	4BTM4	-284.2299721355	897.37 (2.805), 499.61 (0.414), 284.37 (0.307), 165.65 (0.241), 165.13 (0.245)
	4BTM2	-284.9490453480	1645.55 (2.714), 853.30 (0.576), 419.85 (0.776), 305.85 (0.344), 168.92 (0.330)
	4BTM	-285.4583151157	319.07 (2.078), 253.14 (0.261), 219.45 (0.283)
5	5BT	-294.4338942798	594.55 (3.557), 421.53 (0.358), 238.08 (0.605), 218.05 (0.349)
	5BTM10	-351.7417970274	481.51 (0.420), 473.75 (0.349), 371.93 (0.288), 355.17 (0.429), 342.88 (0.598), 314.40 (0.341), 194.65 (0.256), 194.42 (0.301), 184.52 (0.420), 182.59 (0.628),
	5BTM8	-353.2409887449	906.15 (3.125), 465.40 (0.348), 434.83 (0.256), 308.32 (0.259), 259.34 (0.378), 227.14 (0.525)
	5BTM6	-354.4550762212	1088.67 (3.184), 669.35 (0.340), 479.10, (0.780), 404.90 (0.254), 225.98 (0.676)



	<b>5BTM4</b>	-355.4014547791	837.60 (3.204), 517.91 (0.310), 441.09 (0.332), 293.31 (0.232)
	<b>5BTM2</b>	-356.0668218308	1172.67 (0.701), 839.03 (0.644), 364.32 (0.324), 362.45 (0.278)
	<b>5BTM</b>	-356.5713246144	319.07 (2.562), 258.30 (0.287), 218.82 (0.316)
<b>6</b>	<b>6BT</b>	-353.1193156081	610.02 (4.195), 452.90 (0.427), 238.20 (0.837), 217.81 (0.468)
	<b>6BTM12</b>	-421.6048918743	*
	<b>6BTM10</b>	*	*
	<b>6BTM8</b>	*	*
	<b>6BTM6</b>	-425.6896577497	898.65 (3.717), 729.96 (0.273), 485.03 (0.466), 484.49 (0.480)
	<b>6BTM4</b>	*	*
	<b>6BTM2</b>	-427.1785011423	1679.57 (2.901), 875.63 (0.673), 424.41 (0.642), 311.54 (0.439)
	<b>6BTM</b>	-427.6843339734	322.70 (3.262), 257.41 (0.449), 251.30 (0.278), 219.41 (0.554)
<b>7</b>	<b>7BT</b>	-411.8047360015	620.83 (4.834), 479.36 (0.492), 242.94 (0.442), 236.86 (0.321), 233.98 (0.723), 220.22 (0.312)
	<b>7BTM2</b>	-498.2929668648	*
	<b>7BTM</b>	-498.7973433217	323.51 (3.859), 309.46 (0.267), 264.38 (0.259), 256.73 (0.544), 255.11 (0.264), 250.24 (0.390), 218.63 (0.601)
<b>8</b>	<b>8BT</b>	-470.4901559652	628.48 (5.467), 501.47 (0.560), 240.24 (0.363), 236.74 (0.371), 233.62 (0.660), 231.14 (0.748)

\* indicates incomplete calculation

**SOME OBSERVATIONS ON TARGET RECOGNITION USING HIGH RANGE  
RESOLUTION RADAR**

**William S. McCormick  
Professor  
Department of Electrical Engineering**

**Wright State University  
Colonel Glenn Highway  
Dayton, OH 454535**

**Final Report for:  
Summer Research Program  
Wright Laboratory**

**Sponsored by:  
Air Force Office of Scientific Research  
Bolling Air Force Base, Washington, DC**

**And**

**Wright Laboratory**

**August 1997**

# SOME OBSERVATIONS ON TARGET RECOGNITION USING HIGH RANGE RESOLUTION RADAR

William S. McCormick  
Professor  
Department of Electrical Engineering  
Wright State University

## Abstract

Four topics involving target recognition using high range resolution (HRR) radar are considered. The first topic considers target recognition using the raw radar return (transform of HRR profile) rather than the HRR profile itself; the second topic considers what target recognition potential, if any, resides in the phase component of the HRR profile; the third topic considers the usefulness of a new template feature called the "histogram matrix." The final topic is the application of forward dynamic programming to the multiple aspect angle processing problem. The four investigations provide interesting insights and potentially useful results for the overall recognition problem.

## SOME OBSERVATIONS ON TARGET RECOGNITION USING HIGH RANGE RESOLUTION RADAR

William S. McCormick

### I) Introduction

Accurate target recognition using all-weather radar sensors has been an important USAF priority for a number of years. Of particular interest to the Model Based Vision Laboratory (MBVL) at WPAFB is the use of high range resolution (HRR) radar profiles to correctly identify moving ground targets on a single or multiple look basis. The HRR radar profile provides target recognition capability for short observation times and for moving targets. In contrast, traditional SAR imaging requires long observation times and suffers azimuth resolution degradation in the moving target case. A major shortcoming of HRR processing, however, is its extreme sensitivity to azimuth angle, a direct result of the coherent cancellation/reinforcement of reflections from the target scatterer complex. In operation, the HRR radar system is a stepped frequency radar which transmits  $n$  pulses shifted in frequency by a fixed amount,  $\Delta f$ , to give a large bandwidth,  $n \Delta f$  with corresponding high range resolution. The coherent stored (inphase and quadrature) raw returns can be shown to be the discrete Fourier transform of the scattering complex. Taking the modules of the inverse Fourier transform will then provide the HRR profile for a given azimuth angle.

The HRR target classification techniques usually employed are standard techniques from statistical pattern recognition. For each target type, a template of returns over a correlated increment in azimuth angle is stored in a library of feature vectors varying over 360 degrees of azimuth angle. Upon reception of an unknown target signature, the feature vectors of the template libraries are correlated with the target signature and a class declaration is made based on the highest correlation.

In approaching my rather short eight-week AFOSR summer program, I decided to take a fresh look at the entire problem and try to identify some different approaches. The report is organized as follows: section II reviews some of the MBVL activities in the HRR area and also discusses the data set and simulation software used; section III discusses the processing of the raw radar return directly thereby avoiding the inverse transform operation; section IV considers

the meaning and possible utilization of the HRR phase component as added information in target classification; section V proposes a histogram matrix as a new template feature that offers good separability and reduced azimuth sensitivity as well as providing a natural information theory interpretation that could lead to some useful performance bounds. Section VI presents a dynamic programming algorithm that provides impressive target classification results for multiple, independent aspect angle "looks" without requiring the gaussian data assumption. The report concludes with a listing of topics for further investigation.

## II. Review of MBVL Activities and Discussion of Data Sets and Software Used in Studies

Up to the present, the MBVL has only used the HRR profile for classification, i.e., the modulus of the inverse Fourier Transform of the raw received radar signal. The MBVL group has considered a number of feature vectors including the mean vector per range pixel averaged over angle and the left eigenvector matrix (i.e., range information) of a singular value decomposition (SVD) of the  $(R, \theta)$  matrix. Worrell et al. of VEDA Inc. {2} have used a Hughes Aircraft Adaptive Gaussian classifier to generate discriminate distances where classifier declaration thresholds were set to reject a fixed percentage of in-class signatures. Since this classifier assumes gaussian data for maximum likelihood performance, a power transformation was made on the Rayleigh distributed HRR profile to make it more gaussian. The performance measure for target classification is the confusion matrix which gives estimated probabilities of classification/misclassification for the targets of interest.

The data set used throughout the summer was the synthetic data set called "xpatch" {3} which includes 2 tanks, a school bus, and a fire truck measured at VHF, L, and X band for elevation angles of 10, 25, and 40 degrees respectively. In each target case, the vehicle is represented by a CAD model consisting of triangular patches covering the surface of the vehicle and a simulated rough ground surface in the vicinity of the vehicle.

The specific software program used to generate confusion matrices was a modification of a program developed by A. Shaw and V. Bhatnagar {4} using xpatch data. The confusion matrix is developed in a supervised learning mode where every 20th radar return for each target is stored in a test set and reference templates are generated from the remaining signatures in 2.5 degree increments. The HRR profiles are assumed gaussian and are further assumed to be uncorrelated with a diagonal covariance matrix that is equal over the four target classes. Using standard

Bayesian statistics, the discriminator is a simple correlator or matched filter which correlates each test observation with a stored template {varies with azimuth} and bases the classification on a comparison with a threshold as defined above. Excellent confusion matrices results (diagonal terms  $\geq 0.98$ ) have been obtained using the dominant eigenvector of the left (range) eigenvector matrix of the SVD of the  $(R, \theta)$  template matrix.

### III. The Direct Processing of the Raw Radar Return

Within the MBVL group, there has been some discussion as to the significance of the phase sequence present when the raw radar is inverse Fourier transformed. If target discrimination information is present in the phase sequence, it will be irretrievably lost when the HRR profile or modulus of the inverse transform is formed. While the significance of the phase sequence is specifically considered in the next section, the above consideration raises the possibility of target classification using the raw radar return directly thereby avoiding the usual inverse transform operation. In theory, the raw data should contain at least as much information as the HRR profile since the transform operation is invertible. One obvious concern is the clutter issue since each frequency bin of the raw data will contain a clutter contribution from each pixel of the entire radar footprint in contrast to the HRR profile where the relevant clutter is from the target or near-vicinity of the target only. Another concern is the loss of easily interpretable profile features (eg. a tank gun barrel) which would rule out "classification-by-inspection" and morphological type processing. In response to the first concern, it is emphasized that much of the clutter will be eliminated with MTI processing which can provide signal-to-clutter ratios as high as 28 db. Since target classification must be a real-time process, the processing must be done in a "black box" which does not allow sufficient time to use interpretable features; this constraint alleviates the second concern.

In order to simulate classification with raw data only, the inverse transform was eliminated in the simulation program. Early SVD inspection of the raw data  $[f, \theta]$  template indicated the same dominant eigenvector property observed in the HRR profile. Therefore, initial runs used the dominant eigenvector as the template feature vector. Table 1 ((a) thru (k)) gives the confusion matrices for a variety of parameter settings. Overall, the classification results are disappointing when compared to the HRR profile results. In the angle ranges greater than 180 degrees, classification percentages rarely exceeded 70%. Clearly, a strong

classification force was at work but for some reason, the classification was not as effective as with the HRR profiles. Since the “dominant eigenvector” property varied with azimuth, an attempt was made in entries (e) thru (g) to use additional eigenvectors weighted according to their singular values. No improvement was noted. Attempts to make the data more gaussian were also attempted in entries (h) thru (k) but again with little noticeable improvement.

Some possible explanations for the mediocre performance are listed below:

- (1) A simple programming error may have been made. This is always a problem when modifying a complex program written by someone else.
- (2) Clutter could be a problem since xpatch data does include a “rough” ground surface near the target. It was difficult to find detailed information about this feature of xpatch however.
- (3) Although the HRR profiles are well enough correlated in azimuth (correlation over 2.5 degrees), it does not appear that the raw data is well correlated over 2.5°. Figure 1 illustrates the relative decorrelation of the raw data compared to the HRR profile. The maintenance of sufficient correlation over a 2.5° angular sector is essential for acceptable target recognition. Unless a feature vector or stored template can well represent an angular sector of 2.5°, the entire foundation for the template matching approach is compromised and a mediocre confusion matrix is to be expected. Figure 2 shows the autocorrelation matrices for modulus and phase of the raw data over a 2.5 degree angle. The matrices are, of course, symmetric and the 0 to 60 interval represents the 60 raw xpatch returns over a 2.5 degree azimuth sector. Clearly, both the modulus and phase are not well correlated over 2.5 degrees.

Item 3 above relates to a fundamental concern. One direct way of verifying the necessity of maintaining correlation over the template would be to progressively reduce the template size and observe whether the confusion matrix improves in the raw data case. Time constraints did not permit this test. As an added item, Table 2 presents confusion matrices when only the modulus and phase of the raw data are used as input. The degraded results demonstrate that both modulus and phase are needed in the raw data case, a situation which is not true in the HRR profile domain.

On a totally separate issue, I noticed that the overlays of the unwrapped phase of the raw data over a 2.5 degree template appeared as random fluctuations about a linear characteristic whose slope, from the Fourier transform delay theorem, provides the registration offset. This property could be useful in profile registration.

#### IV. The Meaning and Possible Utilization of the HRR Profile Phase Component

As mentioned in the previous section, the presence of a phase term in the HRR profile is intriguing since it might add further target discrimination information. Initially, the presence of the non-zero phase was surprising since the inverse transform was thought to be the real scattering impulse response. It was speculated that perhaps the full hermetian-symmetric transform ( $F^*(\omega) = F(-\omega)$ ) was not observed in the xpatch data which would account for the non-zero phase. A more appealing interpretation was given by Wehner {1} in his equation (5.4), for the inverse transform,

$$H_I = \frac{1}{n} \sum_{i=0}^{n-1} G_i e^{+j \left[ \frac{2\pi}{n} \right] i} \quad (1)$$

where  $H_I$  is interpreted as the average reflection coefficient over the bandwidth,  $B$ , of the radar

$$\text{or } H_I = \frac{1}{B} \int_B R(p, f) df \quad (2)$$

where  $R(p, f)$  is the complex coefficient at pixel  $p$ .

The average reflection coefficient could then have a non-zero phase value which would be target material specific. Whether the xpatch data set contains this type of information is not known at the present time.

The most direct test of whether the phase contains discrimination information is to simply generate a confusion matrix using the phase as the only data input. The resulting confusion matrix is given in Table 3 which indicates all entries near the value 0.25 which implies that NO target discrimination has occurred. In order to focus the discussion, the overlaid unwrapped phase of the M1 tank is given in Figure 3 for a 60 response template (i.e., 2.5 degrees). Clearly, no correlation in azimuth is evident which, from the previous section, suggests a poor confusion matrix result. In order to reveal a more subtle target discrimination potential, an autoregressive



(AR) model was fit to the M1 tank and School Bus phase sequences using 4<sup>th</sup> and 7<sup>th</sup> order models. The roots of the polynomials were then factored and overlaid. No obvious clustering between the two targets was observed. In another test, separability between phase templates was plotted versus azimuth for all six possible target pairings. The separability measure used was the absolute value of the difference between the phase template matrices of the two targets; Figure 4 gives the separability measure between M1 tank and school bus and also between M1 tank and fire truck over the full 360 degrees. Good separability is apparent but, as mentioned before, good separability does not guarantee good target classification. The relative lack of correlation of the HRR phase as compared to the HRR profile is illustrated in Figures 4 and 5 and could be a significant factor in the poor confusion matrix of Table 3.

The degree of true target separability inherent in the HRR phase sequence has not yet been determined. The “dips” in the separability measure of Figure 4 at angles 90 and 270 degrees indicate that some target sensitivity is present, yet the confusion matrix indicates a nearly non-existent target discrimination ability. In view of equation (2), the xpatch data set may not contain detailed information on the complex reflection coefficient over the radar bandwidth. It would be interesting to look at the target classification capability of the phase sequence using the MSTAR data set.

## V. The Histogram Matrix and Its Possible Users

At the beginning of the summer, an initial attempt was made to develop performance bounds using the concepts and techniques of information theory. An important concept in information theory is the concept of entropy which is a scalar defined in terms of amplitude probability density functions. It was the consideration of entropy that led to the idea of the histogram matrix which is formed by measuring the amplitude histogram over some azimuth interval of all resolution pixels in a number of contiguous range partitions. The original intent was to develop a template with good target separability that was not as sensitive to azimuth as the HRR profile templates. The histogram approach has less inherent angle sensitivity since it essentially makes no attempt to measure structure or coherence but merely monitors the relative frequency of occurrence of amplitudes in a range/azimuth partition. Figures 7 and 8 illustrate the histogram matrix for the M1 tank and school bus over an 8 degree azimuth sector with four contiguous range partitions each containing ten pixels; reasonable separability is observed.

Figures 8 through 11 show the degree of correlation of the histogram matrix within the 8 degree template while Figure 12 shows separability of three targets (fire truck, school bus, and T 72 tank with respect to the M1 tank over 360 degrees of azimuth.

Due to time constraints, no attempt was made to generate a confusion matrix using the histogram matrix as a template. Assuming there is enough azimuth averaging in the radar return (to reduce scintillation) to form a meaningful measured histogram matrix, a number of ways of correlating the two histogram matrices are available. An important potential application for the histogram matrix template is at X-Band where the HRR profile has an azimuth correlation of only 0.1 degree {3} and requires a prohibitively large template library. Another highly speculative application is to apply rate distortion theory to the histogram matrix formulation. The histogram matrix has a natural entropy value, given using the histogram probabilities,  $p_{il}$ ,

$$H = - \sum_{l=1}^{\text{\#ofPartitions}} \sum_{i=1}^{\text{\#ofBins}} p_{il} \log_2 p_{il} \quad (3)$$

while the rate distortion function for a separable markov image is {5}

$$R(D) = \frac{1}{2} \log_2 \left[ \frac{\sigma^2 (1 - P_R^2)(1 - P_\theta^2)}{D} \right] \quad (4)$$

where  $\sigma^2$  is the mean square value of the image,  $P_R$  and  $P_\theta$  are adjacent pixel correlation factors; and  $D$  is the level of distortion. The  $R(D)$  function gives the minimum information rate (bits/rec.) to transmit the scene at a distortion level  $D$  which could possibly be related to target separability. As a final remark on the histogram matrix, it should be stressed that there are a large number of parameters that can be varied in the formation of the matrix. For example, Figures 6 thru 11 use a non-uniform bin size to emphasize low level returns. The number of partitions can also be varied as well as the template width in azimuth.

## VI. The Use of Forward Dynamic Programming in Multiple Aspect Angle Processing {6}

A multistage optimization problem can be decomposed into a sequence of single optimization stages for which the optimization can be carried out sequentially stage by stage. The global solution is then constructed from the solution at each optimization stage. The

mathematical formulation leads to a recurrence relation which can be evaluated sequentially. The main advantages of dynamic programming are: (1) the problem can be solved without knowing the statistical properties of the signal in detail; (2) due to the formulation in terms of optimization of a global criterion, a high degree of stability against local disturbances (i.e., large tracking error) is achieved; (3) the algorithm is guaranteed to converge to the optimal solution, and (4) the algorithm allows a straight forward machine implementation. Dynamic programming can be defined in terms of seeking a minimum penalty through a weighted graph. The fundamental principle of dynamic programming is the principle of optimality which can be stated as follows: "If the optimal path to a terminal node goes through an intermediate node, then the optimal path includes as its initial portion the optimal path to the intermediate node."

In his dissertation, Liddy {7} extended the work of Larsen and Peschon {8} and was the first to apply dynamic programming to the multiple aspect angle target classification problem using the HRR profile. Liddy used a complex extended Kalman filter tracker and an early HRR profile library to classify airborne targets only. While Liddy's treatment was comprehensive, his dissertation did not describe the algorithm's classification performance in detail.

The other major attempt to look at multiple aspect angle processing was the work of Jacobs, O'Sullivan, and Bekker {3} and S. Worrel of VEDA {9} who used the joint or cumulative likelihood ratio to classify ground based targets with HRR profile returns.

In the application of dynamic programming to the present problem, the following terms are defined:

$\theta_k^T$  = True angle track unknown to the user at update  $\underline{k}$ .

$\theta_k^{Tk}$  = Track output at update  $\underline{k}$ .

$\theta_k^{OB}$  = Estimated angle that is used to access templates of each target to compare to measurement.

The steps of the algorithm are as follows:

1. Assume a lattice of nodes where the number of columns equals the number of aspect angle "looks" and the number of nodes in each column represent the possible tracker error (in degrees) both positive and negative.
2. Assume a random sequence of aspect angle looks and also assume a gaussian (innovation sequence) uncorrelated tracker error sequence,  $\Delta \theta_k$ , where  $|\theta_k| \leq 5$  degrees. The  $\theta_k^T$  always forms the center-node line of the lattice; that is, the lattice column nodes are symmetric with respect to the tracker output.
3. From  $\theta_k^{OB} = \theta_k^T + \Delta \theta_k$ , the appropriate template is accessed and compared to the HRR observation determined by  $\theta_k^T$ .
4. Assume the all node metrics in the first column or update equal zero;  $M_o^i = 0$  for all  $i$ . Define a branch metric, referenced to the  $k^{th}$  update or

$$b_k = \alpha (\Delta \theta_k)^2 + \beta \{1 - [\text{correlation of normalized template at } \theta_k^{OB} \text{ with normalized measurement at } \theta_k^T]\} \quad (5)$$

5. Form

$$M_k^i = \underset{all.j}{Min} \{M_{k-1}^j + b_{jk}\} \quad (6)$$

where  $i$  = column node at  $k^{th}$  update and  $j$  = column node at  $(k-1)$  update.

6. Store path pointer at each node  $i$  for  $k^{th}$  update column as the  $j^{th}$  node resulting from the minimization of (6).
7. After the last update, determine the minimum node metric and compare to a threshold  $D$ . If the node metric is below the threshold  $D$ , the target corresponding to that particular lattice array is declared and the optimum path is output from the path pointers.

The above algorithm was programmed ( $\alpha = 1$ ,  $\beta = 5$ ) for the four xpatch targets over an irregular nine aspect angle look sequence; the results are presented in Figures 12 thru 15.

Excellent classification results were obtained! The described configuration has the following advantages:

- (1) By defining the branch metric as in (6) the node metric of the true target never grows with number of updates which simplifies the choice of threshold value,  $D$ .
- (2) An estimate of the true sequence can be used to update the tracker algorithm {7}.
- (3) The unknown target class can easily be identified if none of the known target node metrics fall below  $D$ .

It would be of interest to compare the performance of the dynamic programming algorithm to the joint or cumulative likelihood ratio approach for both synthetic (xpatch) and real MSTAR data. The robustness of the algorithm to large local tracking errors should also be investigated. With the new data sets now available, the value of the dynamic programming track estimate should also be evaluated in a sensor fusion context.

## VII. Conclusions and Topics for Further Investigation

As with most investigations of this type, there were more questions raised than questions answered. In addition to the topics mentioned in the specific sections, there is a more general problem that deserves attention. Based on previous discussions concerning the effects of target separability and template correlation on target classification, there should be an analytical attempt to develop a statistical model that can accurately predict the confusion matrix without requiring simulations. This non data-driven model could then predict performance for different sensor parameters, template types, etc.

0 degrees thru 75 degrees; fftshift; dominant eigenvector

M1 Tank	T 72	Fire Truck	School Bus
9.1011236e-01	6.7415730e-02	0.0000000e+00	2.2471910e-02
5.6179775e-02	8.7640449e-01	2.2471910e-02	4.4943820e-02
0.0000000e+00	3.3707865e-02	9.5505618e-01	1.1235955e-02
3.3707865e-02	5.6179775e-02	4.4943820e-02	8.6516854e-01

(a)

0 degrees thru 125 degrees; fftshift; dominant eigenvector

7.2297297e-01	1.0810811e-01	4.0540541e-02	1.2837838e-01
9.4594595e-02	7.7702703e-01	2.0270270e-02	1.0810811e-01
5.4054054e-02	2.0270270e-02	8.1081081e-01	1.1486486e-01
1.2837838e-01	1.2837838e-01	1.1486486e-01	6.2837838e-01

(b)

0 degrees thru 180 degrees; fftshift; dominant eigenvector

6.9953052e-01	9.3896714e-02	8.4507042e-02	1.2206573e-01
1.1737089e-01	7.3239437e-01	5.6338028e-02	9.3896714e-02
1.0328638e-01	9.3896714e-02	7.2769953e-01	7.5117371e-02
1.3615023e-01	9.3896714e-02	8.9201878e-02	6.8075117e-01

(c)

0 degrees thru 300 degrees; fftshift; dominant eigenvector

6.2146893e-01	9.8870056e-02	9.8870056e-02	1.8079096e-01
1.1016949e-01	6.7231638e-01	9.3220339e-02	1.2429379e-01
1.2146893e-01	9.0395480e-02	7.0621469e-01	8.1920904e-02
1.2994350e-01	1.4689266e-01	7.3446328e-02	6.4971751e-01

(d)

0 degrees thru 125 degrees; no fftshift; weighted eigenvectors

8.3108108e-01	3.3783784e-02	4.7297297e-02	8.7837838e-02
1.8918919e-01	7.3648649e-01	4.7297297e-02	2.7027027e-02
7.4324324e-02	1.3513514e-02	8.2432432e-01	8.7837838e-02
1.2162162e-01	5.4054054e-02	1.0810811e-01	7.1621622e-01

(e)

0 thru 125 degrees; fftshift; composite template generated from 59 [u] eigenvectors weighted and normalized according to their singular values

7.8378378e-01	1.3513514e-02	7.4324324e-02	1.2837838e-01
4.6621622e-01	3.9864865e-01	4.7297297e-02	8.7837838e-02
1.1486486e-01	6.0810811e-02	5.8783784e-01	2.3648649e-01
1.4864865e-01	8.1081081e-02	1.4189189e-01	6.2837838e-01

(f)

0 degrees thru 180 degrees;fftshift; composite template generated from 59 [u] eigenvectors weighted and normalized according to their singular values

6.3849765e-01	5.6338028e-02	1.2206573e-01	1.8309859e-01
3.5680751e-01	4.8826291e-01	7.5117371e-02	7.9812207e-02
1.3615023e-01	1.1267606e-01	5.6338028e-01	1.8779343e-01
2.1126761e-01	7.9812207e-02	1.4553991e-01	5.6338028e-01

(g)

0 degrees thru 125 degrees;fftsht;power transform(=0.4) of real and imaginary parts; dominant eigenvector

4.3918919e-01	2.8378378e-01	1.2837838e-01	1.4864865e-01
1.2162162e-01	5.2702703e-01	1.4864865e-01	2.0270270e-01
1.1486486e-01	1.0810811e-01	4.3243243e-01	3.4459459e-01
1.0135135e-01	1.7567568e-01	3.1081081e-01	4.1216216e-01

(h)

0 degrees thru 125 degrees;fftshift;power transform(exp=0.2) of modulus of raw data;dominant eigenvector

7.2972973e-01	9.4594595e-02	5.4054054e-02	1.2162162e-01
8.7837838e-02	7.5675676e-01	4.7297297e-02	1.0810811e-01
4.7297297e-02	1.3513514e-02	7.8378378e-01	1.5540541e-01
1.4189189e-01	8.7837838e-02	7.4324324e-02	6.9594595e-01

(i)

0 degrees thru 180 degrees;fftshift;power transform(exp=0.2) of modulus of raw data;dominant eigenvector

6.7605634e-01	1.0328638e-01	9.3896714e-02	1.2676056e-01
1.0328638e-01	7.2769953e-01	7.5117371e-02	9.3896714e-02
8.9201878e-02	6.5727700e-02	7.5117371e-01	9.3896714e-02
1.7840376e-01	8.9201878e-02	8.4507042e-02	6.4788732e-01

(j)

0 degrees thru 180 degrees;fftshift;power transform(exp=0.2) on modulus of raw data;3 dominant eigenvectors

7.6525822e-01	4.6948357e-02	8.4507042e-02	1.0328638e-01
2.3004695e-01	6.8075117e-01	4.2253521e-02	4.6948357e-02
9.8591549e-02	2.3474178e-02	7.8873239e-01	8.9201878e-02
1.9718310e-01	8.4507042e-02	9.8591549e-02	6.1971831e-01

(k)

Table 1: Confusion Matrices Run with Raw Data as Input

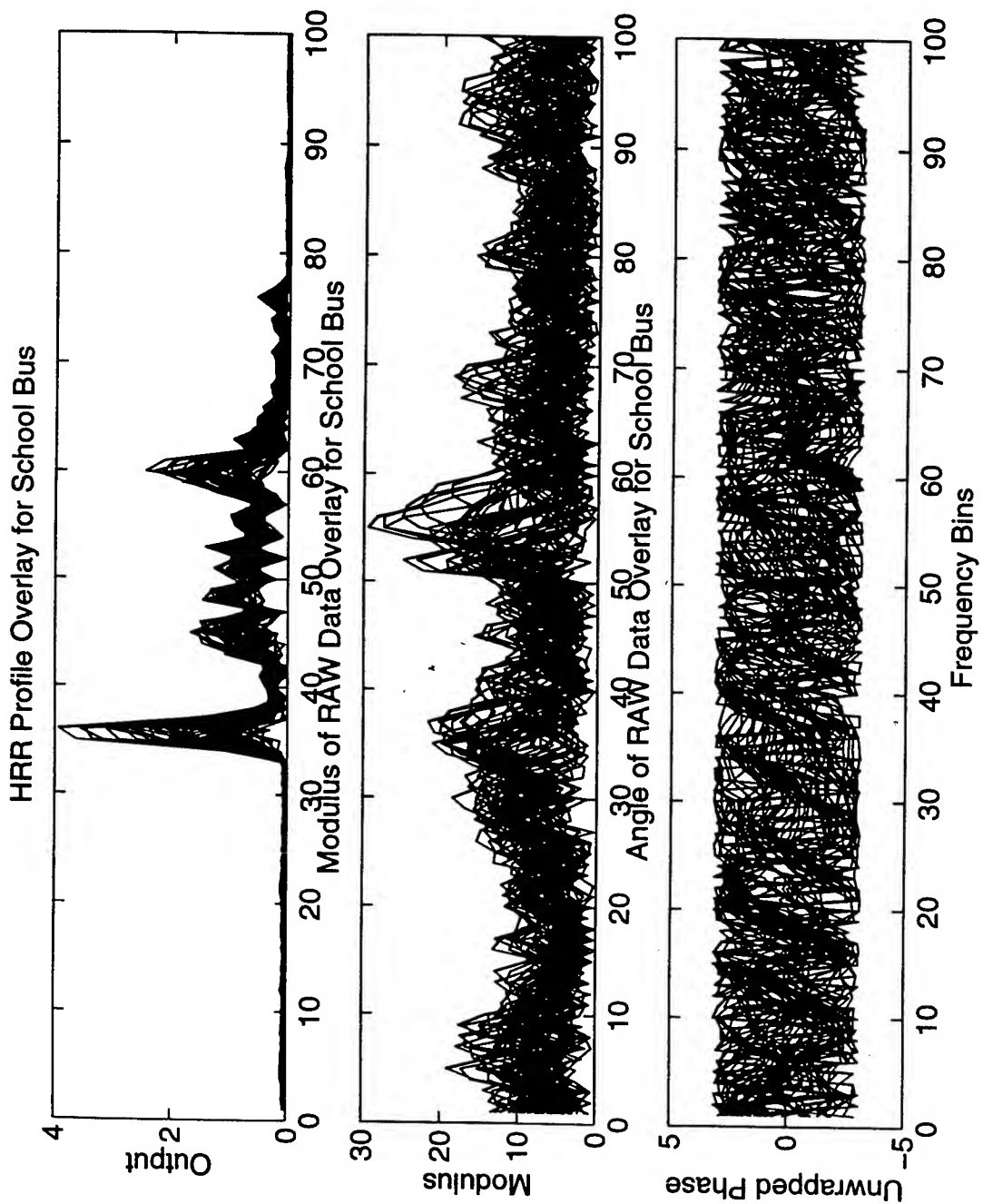
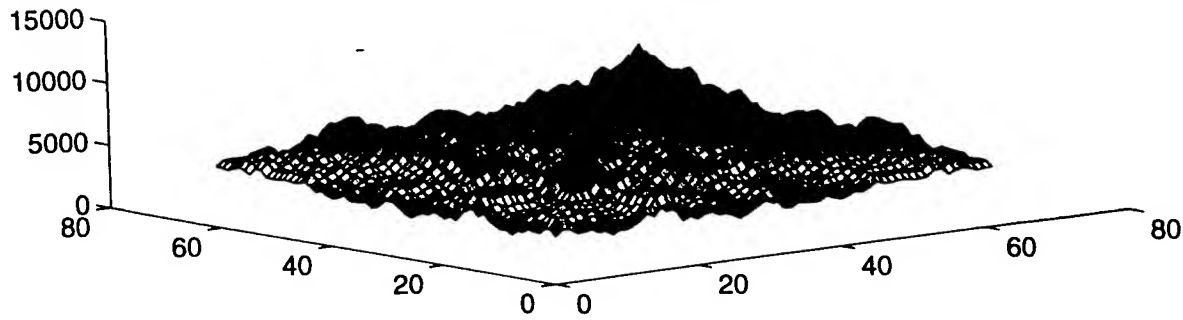


Figure 1: Overlays for the 60 Signatures in a 2.5 Degree Sector



Autocorrelation Matrix of Modulus of RAW for School Bus



Autocorrelation Matrix of Phase of RAW for School Bus

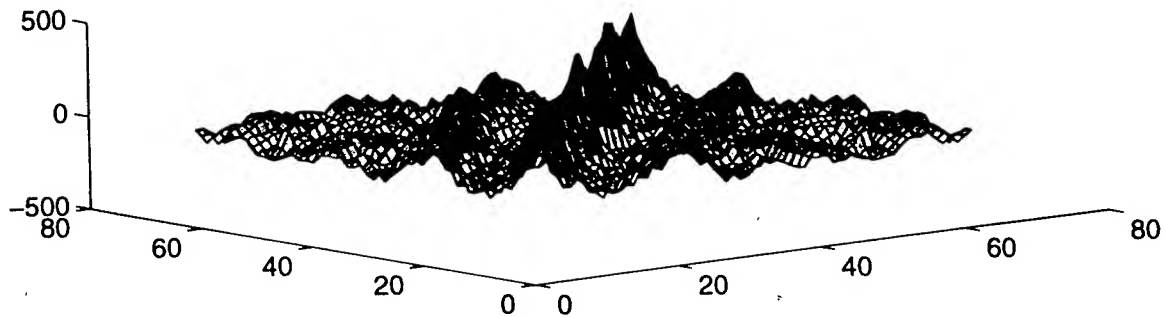


Figure 2: Autocorrelation Matrices for Raw Data

0 degrees thru 180 degrees;no fftshift;abs(raw);dominant  
eigenvector

3.0516432e-01	2.5352113e-01	1.7840376e-01	2.6291080e-01
1.3615023e-01	4.4131455e-01	2.0187793e-01	2.2065728e-01
2.4413146e-01	1.6431925e-01	3.7558685e-01	2.1596244e-01
1.5023474e-01	2.3474178e-01	2.2065728e-01	3.9436620e-01

0 degrees thru 180 degrees;no fftshift;angle(raw);dominant  
eigenvector

4.8356808e-01	1.7370892e-01	1.5962441e-01	1.8309859e-01
2.1596244e-01	5.2112676e-01	9.3896714e-02	1.6901408e-01
1.2676056e-01	1.5023474e-01	5.2112676e-01	2.0187793e-01
1.5023474e-01	1.3615023e-01	1.8779343e-01	5.2582160e-01

Table 2: Confusion Matrices for Abs Only and Phase Only for Raw Data

0 degrees thru 180 degrees; angle of hrr-profile used as  
discriminant; +/-10; dominant eigenvalue

NO TARGET DISCRIMINATION

2.0657277e-01	2.4413146e-01	2.7699531e-01	2.7230047e-01
2.1596244e-01	3.3333333e-01	2.2065728e-01	2.3004695e-01
2.2065728e-01	2.4882629e-01	2.6760563e-01	2.6291080e-01
2.5821596e-01	2.7699531e-01	2.2535211e-01	2.3943662e-01

Table 3: Confusion Matrix with HRR Phase as Input

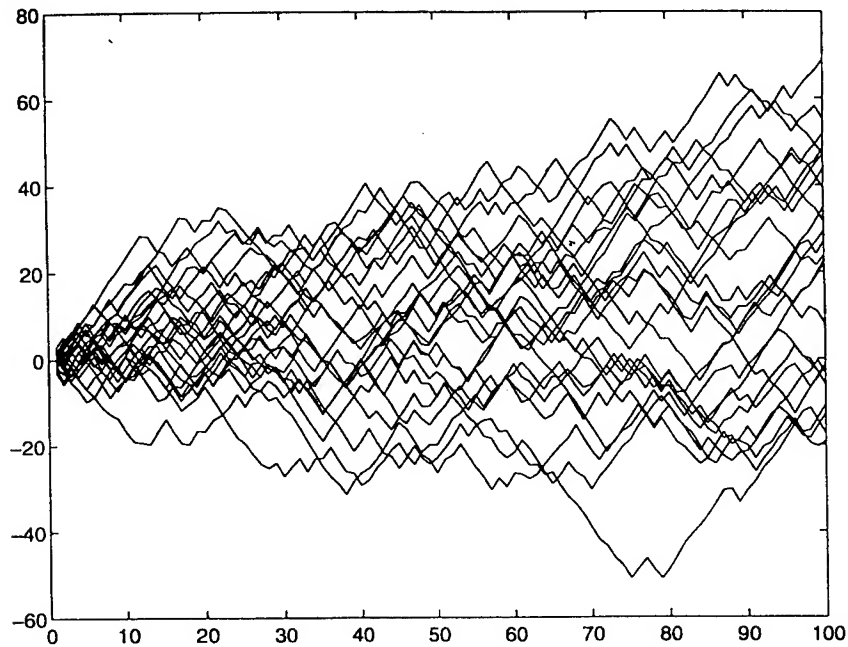


Figure 3: Unwrapped Phase Overlay for M1 Tank Over a 2.5 Degree Template

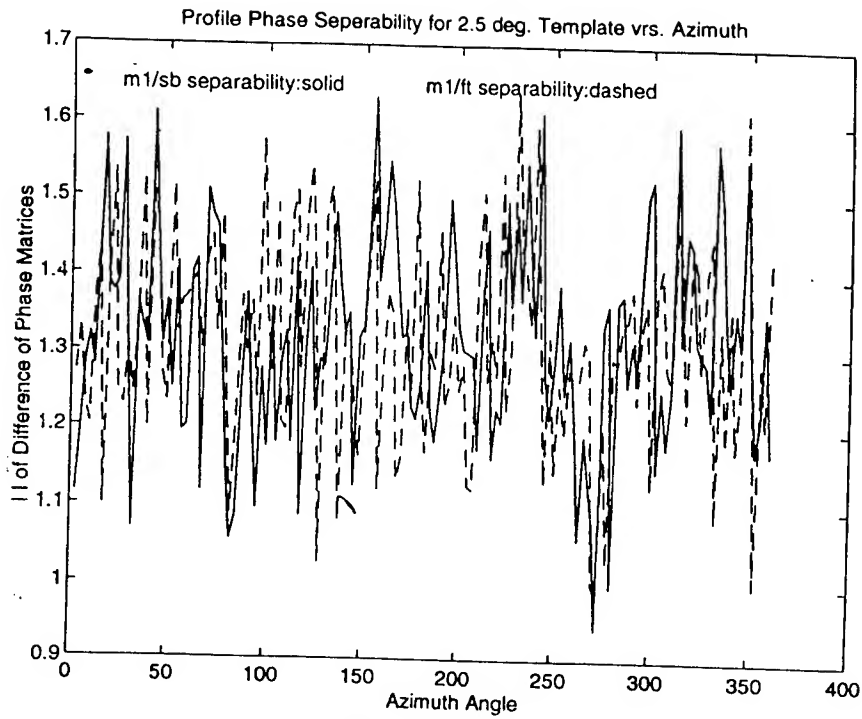


Figure 4: Phase Template Separability

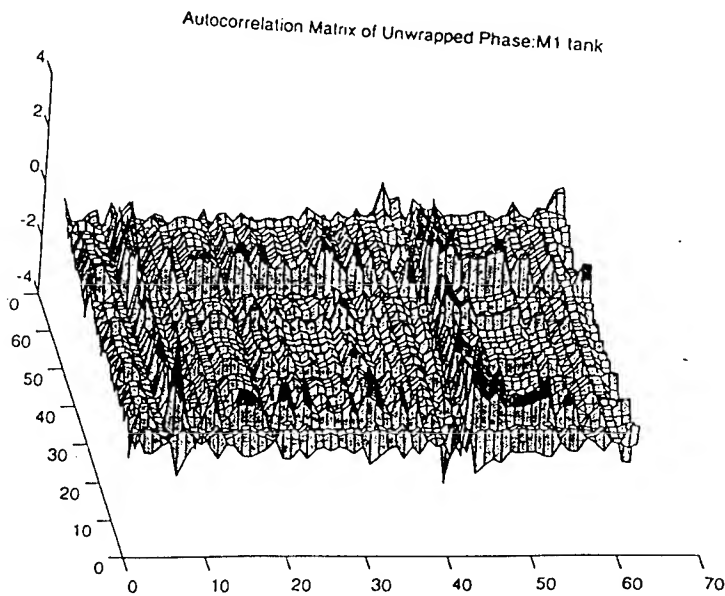


Figure 5: HRR Phase Autocorrelation Azimuth

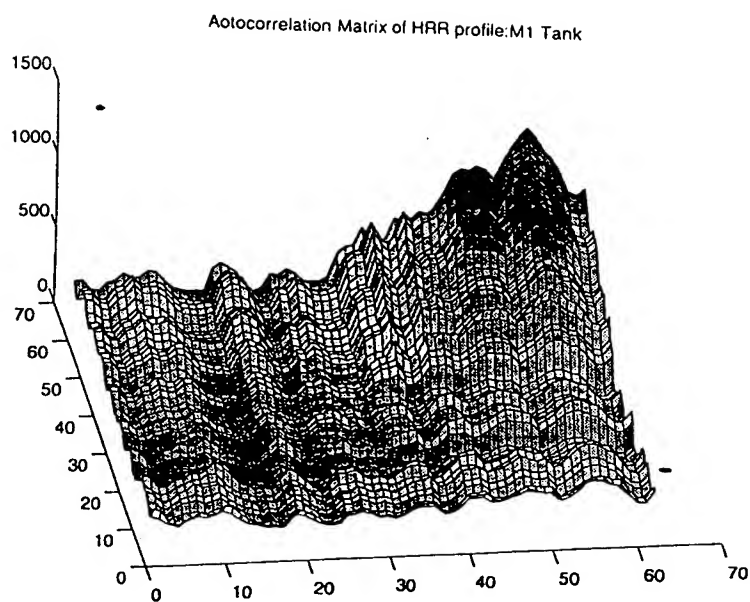


Figure 6: HRR Profile Autocorrelation in Azimuth

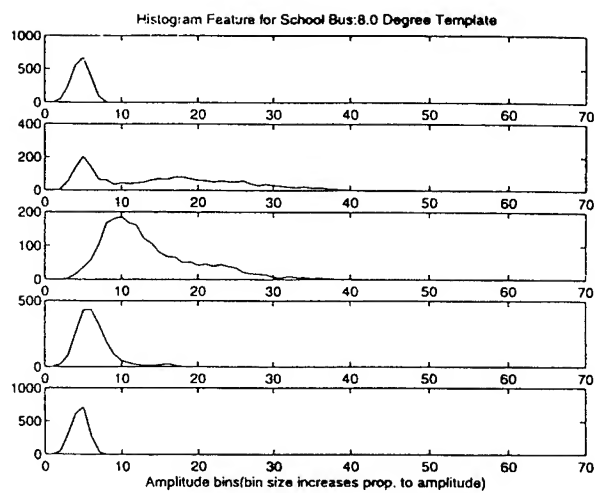


Figure 7

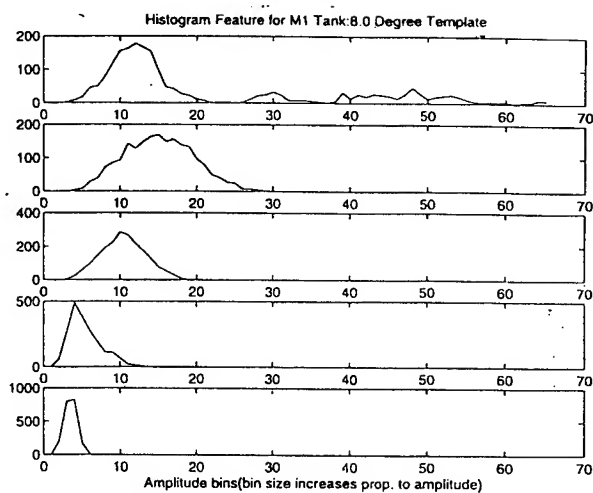


Figure 8

## REFERENCES

1. Wehner, D.R., High Resolution Radar, Norwood, MA, Artech House, 1987, page 164.
2. Worrel, S., "An Air-to-Ground Classification Analysis," Internal VEDA Inc. document, 1996.
3. Jacobs, S.P., O'Sullivan, J.A. and Becker, Z., "Recognition of Ground Targets from High Resolution Radar Range Profiles,"
4. Shaw, A., and Bhatnagar, V., Private Communication 1997.
5. Pratt, W.K., Digital Image Processing, New York, Wiley and Sons, 1978.
6. Nadler, M. and Smith, E.P., Pattern Recognition Engineering, New York, Wiley and Sons Inc., 1993.
7. Liddy, E.W., Application of Sequence Comparison Methods to Multisensor Data Fusion and Target Recognition, Ph.D. Dissertation, Air Force Institute of Technology, 1993.
8. Larson, R.E., and Peschon, J., "A Dynamic Programming Approach to Trajectory Estimation," IEEE Transactions on Automatic Control; July, 1996, pp. 537-540.
9. Worrel, S., VEDA Inc., Private Communication, 1997.